KIT

Karlsruher Institut für Technologie

Search for the production of Dark Matter in hadronic mono-top signatures with the CMS experiment

Zur Erlangung des akademischen Grades eines

DOKTORS DER NATURWISSENSCHAFTEN (Dr. rer. nat.)

von der KIT-Fakultät für Physik des
Karlsruher Instituts für Technologie (KIT)
angenommene

DISSERTATION

von M.Sc. Michael Waßmer

aus Lichtenau

Tag der mündlichen Prüfung: 11.12.2020

| Referent: | Prof. Dr. Ulrich Husemann | Institut für Experimentelle Teilchenphysik |
| Korreferent: | Prof. Dr. Thomas Müller | Institut für Experimentelle Teilchenphysik |

Contents

1 Introduction

High-energy particle physics is currently at a crucial point. On one hand, the underlying theoretical model, called the Standard Model of Particle Physics (SM), keeps being confirmed at unprecedented precision by experiments. On the other hand, several experimental observations show drastic incompatibility with theoretical predictions by the SM, possibly showing signs of new physics. To account for this circumstance, theoretical particle physics is trying to extend the SM to be able to explain observed deviations while staying compatible with other experimental observations. One experiment testing the predictions of the SM is the Compact Muon Solenoid (CMS) experiment at the European Organization for Nuclear Research (CERN) in Geneva, Switzerland. There, collisions of protons at unprecedented energies, provided by the Large Hadron Collider (LHC), are analyzed to learn about nature at the smallest scales currently accessible.

One of the aforementioned deficiencies of the SM is the lack of one ore more Dark Matter (DM) candidates. These particles are motivated by astrophysical and cosmological observations. Observations of galaxy rotations show a much higher rotation speed than theoretical calculations predict based on the amount of visible matter in the galaxies. This observation, among multiple others, led to the hypothesis of Dark Matter, an additional type of matter resulting in additional gravitational pull to keep the observed galaxies stable. Since no additional matter could be observed by experiments, this type of matter does not directly interact with electromagnetic radiation, therefore motivating the term Dark Matter.

The existence of Dark Matter can also be concluded from cosmological observations regarding the formation of structures in the universe. Without the additional gravitational force exhibited by Dark Matter, large scale structures like galaxy clusters and superclusters should have formed at a much later time than observations show. The cosmological influence of Dark Matter on the universe as a whole is observed in the cosmic microwave background (CMB). From temperature fluctuations within this radiation field, the contribution of Dark Matter to the total energy density of the universe can be measured, amounting to around 25%. The amount of visible matter only contributes around 5% to the total energy density. The remaining 70% are due to Dark Energy, an unknown form of energy responsible for the accelerated expansion of the universe.

In order to understand the nature of Dark Matter which, as just explained, constitutes a large amount of the energy content of the universe, large efforts on the experimental and theoretical side of particle physics are made. Three methods are used to search for Dark Matter.

The first method is called direct detection. It relies on the fact that our planet is moving through an accumulation of Dark Matter within our galaxy, called a Dark Matter halo. These experiments search for interactions of atomic nuclei in a target material with Dark Matter particles of the halo. These experiments are situated in underground laboratories to shield them from large backgrounds due to cosmic radiation.

Indirect detection, which is the second method, searches for secondary particles being produced in interactions of Dark Matter particles in the universe. The indirect detection experiments then try to observe the secondary particles created by these interactions. Usually, these searches are performed by telescope or satellite experiments.

The last method is called detection by production. If the mass of the Dark Matter particles is low enough, they might be produced in the collisions created by particle accelerators like the LHC. The accelerator and the detectors analyzing the collisions offer a laboratory environment to search for the production of Dark Matter.

This thesis makes use of the third method. It presents a search for new physics in hadronic mono-top signatures at the CMS experiment. This search is looking for proton-proton collisions in which a single top quark is observed after the collision accompanied by large missing transverse energy. Missing transverse energy emerges if one or more particles escape the detector without being detected. Since Dark Matter at most interacts very weakly, it is expected that these particles escape the detector without leaving a signature to detect, therefore causing missing transverse energy. The top quark is the heaviest fundamental particle in the SM. Due to its short lifetime, it is not affected by hadronization. The top quark decays almost exclusively to a bottom quark and a W boson. The decay of the W boson, either in the hadronic or leptonic decay channel, then determines the overall final-state signature. In the hadronic channel, the final-state signature consists of several quarks, which hadronize and are detected as jets. Large jet radii and jet substructure algorithms are used to reconstruct and tag the top quark in the hadronic decay channel. In the leptonic channel, an additional charged lepton in association with its corresponding neutrino is expected. A kinematic observable, called the transverse mass, can be used to distinguish between SM contributions and possible signal contributions. The analysis presented in this thesis is focused on the hadronic decay channel of the involved top quark. In the SM, mono-top signatures cannot be produced by leading-order processes. In the extension of the SM which is studied in this thesis, the mono-top signature is produced by a flavor-changing neutral current involving a hypothetical spin 1 neutral boson implemented in a simplified model. This model is also called non-resonant mono-top model. If an observation is made, the cross section of the process and the mass ranges of the involved particles are determined. Otherwise, exclusion limits on the non-resonant mono-top model parameters are set.

This thesis is structured as follows. First, general foundations necessary for this analysis are introduced. This includes foundations of particle physics, the experimental environment, and necessary basics of statistical data analysis. The next chapter is an introduction to the concept of Dark Matter describing a set of Dark Matter candidates, theoretical approaches towards Dark Matter, and the different methods to search for Dark Matter, especially the collider approach. Next, basic foundations needed specifically for the hadronic mono-top analysis described in this thesis are introduced. Then, the search for Dark Matter in hadronic mono-top signatures performed within the scope of this thesis is explained in detail and the results are presented. Finally, a conclusion is drawn and an outlook with possible improvements for the analysis is given.

2 General foundations

In this chapter, basic foundations of theoretical particle physics as well as the experimental environment are briefly introduced.

2.1 Theoretical foundations of particle physics

In the following, a short overview of the Standard Model of Particle Physics (SM) is given, followed by basics of collider physics. Afterwards, event generation and simulation are introduced. Finally, a short summary of physics going beyond the Standard Model is given.

2.1.1 The Standard Model of Particle Physics

The Standard Model of Particle Physics (SM) is the current theoretical description of all known elementary particles and their interactions except for gravity. The mathematical description is based on relativistic quantum field theory (QFT), which connects classical field theory, special relativity, and quantum mechanics. The objects of interest are consequently called quantum fields. For every known elementary particle, there exists a corresponding quantum field. The particles correspond to excitations of the field. Interactions are also described by quantum fields whose corresponding particles are called mediators of the respective interaction. The physics of the quantum fields is usually described within the Lagrangian formalism, which is also adopted in this section. The Lagrangian function $\mathcal{L}$ encodes the physical behavior of the quantum fields and the equations of motion govern the space-time evolution of the fields.

Particle content

The elementary particles contained in the SM are presented in Fig. 2.1. These particles can be divided into fermions (half-integer spin) and bosons (integer spin).

The fermions of the SM can further be split into quarks and leptons, which differ in the interactions they take part in. Quarks interact via the strong and electroweak interactions while the leptons only take part in the electroweak interaction. This is due to the fact that quarks carry an additional quantum number compared to leptons named color charge, which can have three distinct values. Also, there exists an antiparticle for each of the quarks and leptons. Both quarks and leptons can be further divided into different generations. The
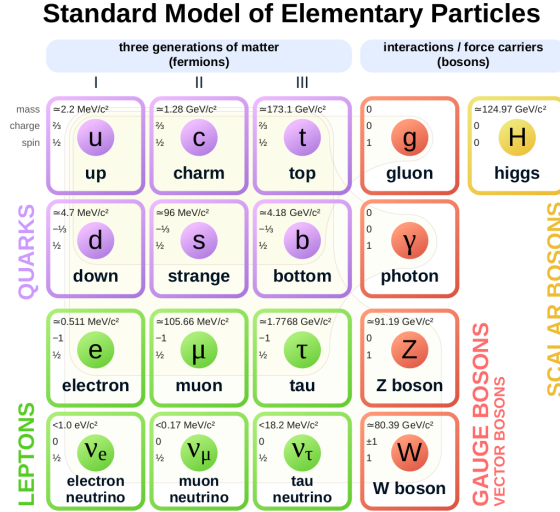
Figure 2.1: Graphical representation of the Standard Model of Particle Physics. Taken from [1].

most striking difference between the generations is given by the masses of the particles in different generations. All other quantum numbers relevant for the interactions are mirrored between the different generations. For more information regarding the properties of quarks and leptons, see the summary tables regarding *Quarks* and *Leptons* in [2].

The bosons in the SM mediate the different interactions. For each interaction, there is at least one mediator serving as a force carrier. Except for the Higgs boson, which takes a special role in the SM, all known force mediators are vector bosons which means that they carry spin 1. The mediators are also called gauge bosons because their introduction renders the SM invariant under specific symmetries, called gauge symmetries, which will be explained in the following subsection. For more information regarding the properties of the SM bosons, see the summary table regarding *Gauge and Higgs bosons* in [2].

Interactions

The interactions in the Standard Model are introduced by requiring invariance of the Lagrangian $\mathcal{L}$ under local transformations. These transformations are then called gauge transformations. To ensure invariance, additional fields, called gauge fields, are introduced, which render the Lagrangian $\mathcal{L}$ invariant by means of their own transformation behavior. In the following, the different interactions of the SM will be briefly introduced.

Strong interaction or Quantum Chromodynamics (QCD)

The following explanations rely on the *Quantum Chromodynamics* review article in [2]. The gauge transformation introduced to obtain the Lagrangian for QCD is an SU(3) transformation in the color space of the quarks. After requiring invariance of the Lagrangian and introducing the gauge fields, which are called gluons and are the mediators of the strong force, the Lagrangian has the following form:

$$\mathcal{L} = \sum_q \bar{\psi}_{q,a}(i\gamma^\mu \partial_\mu \delta_{ab} - g_s \gamma^\mu t^C_{ab} G^C_\mu - m_q \delta_{ab})\psi_{q,b} - \frac{1}{4}F^A_{\mu\nu}F^{A\mu\nu} \tag{2.1}$$

The sum runs over all quark flavors q. The quarks with flavor q, mass m_q, and color a, are represented by the spinor-fields $\psi_{q,a}$ whereas the eight possible gluons are represented by

G_μ^C with $C = 1 .. 8$. The constant g_s is called the strong coupling constant and represents the strength of the strong interaction. The matrices t^C are the generators of the SU(3) group and enable rotations in the color space of the quarks or gluons. The object $F_{\mu\nu}^A$ is called the field strength tensor. The first part of $\mathcal{L}$ contains the kinetic term, the interaction of the quarks with the gluons, and the mass term of the quarks. The second part represents the kinetic term of the gluons and their interactions with one another.

Quantum Chromodynamics has two distinct properties called confinement and asymptotic freedom [3–6]. Confinement describes the fact that the QCD coupling constant becomes large for low energies and large distances. Because of this, quarks and gluons cannot be observed as free particles but only as color-neutral bound states. These states are called hadrons. For more details on the possible hadronic states of quarks, see the *Quark Model* review article in [2]. Asymptotic freedom on the other hand means that the coupling decreases for high energies or short distances and therefore allows for a perturbative description of the process at high energies. Such a process is then often called hard process.

Electroweak interaction

The following explanations rely on the *Electroweak Model and Constraints on New Physics* review article in [2]. The electroweak (EWK) interaction is introduced to the SM with the gauge group SU(2)×U(1) [7–9]. The quarks and leptons are part of left-handed SU(2) doublets.

$$\Psi_i = \begin{pmatrix} \nu_i \\ l_i^- \end{pmatrix}_L \text{ for leptons, } \Psi_i = \begin{pmatrix} u_i \\ d_i' \end{pmatrix}_L \text{ for quarks} \tag{2.2}$$

with $i = 1 .. 3$. Here, $d_i' = \sum_j V_{ij} d_j$ represents a superposition of the mass eigenstates of the down-type quarks d_j. The matrix V is called Cabibbo-Kobayashi-Maskawa (CKM) mixing matrix. The right-handed states $l_{i,R}, u_{i,R}, d_{i,R}$ transform as singlets under the SU(2) transformation. The corresponding gauge fields are the $W^i (i = 1 .. 3)$ fields with the coupling constant g. All of the quarks and leptons transform under the U(1) transformation with the corresponding gauge field B and the coupling constant g'. After including the Higgs mechanism with spontaneous symmetry breaking to account for the fermion masses, the Lagrangian for the fermions takes the following form:

$$\mathcal{L} = \sum_i \bar{\psi}_i \left(i \slashed{\partial} - m_i - \frac{m_i H}{v} \right) \psi_i - \frac{g}{2\sqrt{2}} \sum_i \bar{\Psi}_i \gamma^\mu (1 - \gamma^5)(T^+ W_\mu^+ + T^- W_\mu^-) \Psi_i \tag{2.3}$$

$$- e \sum_i Q_i \bar{\psi}_i \gamma^\mu \psi_i A_\mu - \frac{2}{g \cos\theta_W} \sum_i \bar{\psi}_i \gamma^\mu (g_V^i - g_A^i \gamma^5) \psi_i Z_\mu \tag{2.4}$$

Here, ψ_i are the fermion fields with mass m_i and electric charge Q_i in units of the electron charge e. The operators $T^{+,-}$ are the weak isospin ladder operators and θ_W is called the weak angle or Weinberg angle.

The first term represents the kinetic term and the mass term as well as the coupling of the fermions to the Higgs field H which is proportional to the fermion mass. The generation of the masses of the fermions will be explained in more detail in the next section.

The second part describes the coupling of the charged W$^\pm$ bosons to the fermions. This constitutes the charged current of the weak interaction. The W$^\pm$ bosons are superpositions of the aforementioned W^i fields. The charged current of the weak interaction only couples to left-handed fermions and right-handed antifermions.

The third contribution expresses the coupling between the electrically charged fermions and the photon field A_μ proportional to the electrical charge in units of the coupling constant e.

The coupling constant which determines the strength of this interaction is the magnitude of the electrical charge of the electron. This term describes the electromagnetic interaction.

The last term describes the coupling between the fermions of the SM and the Z boson which is a superposition of the B and W^3 fields. This coupling is flavor diagonal and constitutes the neutral current of the weak interaction.

In this Lagrangian, the mass terms of the weak interaction bosons have been neglected. The mass generation of these bosons and the fermions is explained in the next section on the Higgs mechanism.

Higgs mechanism

This section briefly describes how the masses of the electroweak vector bosons are generated and is based on the *Status of Higgs boson physics* review article in [2]. The basic concept on which the Higgs mechanism relies is called electroweak symmetry breaking [10–12]. First of all, an additional left-handed SU(2) doublet is introduced, consisting of two complex components. Consequently, this doublet has four degrees of freedom.

$$\Phi = \frac{1}{\sqrt{2}} \begin{pmatrix} \sqrt{2}\phi^+ \\ \phi^0 + ia^0 \end{pmatrix} \tag{2.5}$$

This doublet is subject to a scalar potential $V(\Phi)$.

$$V(\Phi) = m^2 \Phi^\dagger \Phi + \lambda (\Phi^\dagger \Phi)^2 \tag{2.6}$$

The Higgs Lagrangian can then be written as

$$\mathcal{L} = (D_\mu \Phi)^\dagger (D^\mu \Phi) - V(\Phi) \tag{2.7}$$

with the covariant derivative $D_\mu = \partial_\mu + ig\sigma^a W_\mu^a / 2 + ig'Y B_\mu / 2$. This form ensures the invariance of $\mathcal{L}$ under the electroweak gauge group, which was introduced in the previous section. The first part of the Lagrangian corresponds to the kinetic term of the Higgs doublet and the interactions with the electroweak fields W and B which were also introduced in the previous section.

If $\lambda < 0$, the second component of the Higgs doublet, which is electrically neutral, has a non-vanishing vacuum expectation value (VEV) v, so the ground state of the Higgs doublet has the following form.

$$\langle \Phi \rangle = \frac{1}{\sqrt{2}} \begin{pmatrix} 0 \\ v \end{pmatrix} \tag{2.8}$$

The neutral CP-even component ϕ^0 can then be expressed as $\phi^0 = H + \langle \phi^0 \rangle = H + v$. Rewriting the Higgs doublet around the ground state, putting it into the Higgs Lagrangian, and using the unitarity gauge, three of the four degrees of freedom in the Higgs doublet are absorbed so that the physical electroweak vector bosons $W^\pm$ and Z obtain masses,

$$m_W^2 = \frac{g^2 v^2}{4} \text{ and } m_Z^2 = \frac{(g'^2 + g^2)v^2}{4}. \tag{2.9}$$

The remaining degree of freedom is the scalar CP-even Higgs field H with its corresponding particle, the Higgs boson.

The masses of the fermions are introduced to the SM by adding Yukawa-type interactions coupling the fermion fields to the Higgs doublet in a gauge invariant way. Then, after spontaneous symmetry breaking, the masses are generated and have the form

$$m_f = \frac{y_f v}{\sqrt{2}}, \tag{2.10}$$

with y_f representing the Yukawa coupling constant of fermion f to the Higgs field. The Yukawa couplings are free parameters in the SM and have to be determined by experiment.

2.1.2 Basics of collider physics

Two approaches are followed to collide particles using particle accelerators. One kind of experiment is called fixed-target. This means that particles are accelerated and brought to collision with material at rest. The other approach is the collider approach. There, two beams of moving particles are brought to collision. This approach is followed at the LHC and the most important concepts are introduced in this section.

The most important quantity characterizing a collider besides its center-of-mass energy is called the luminosity L or its instantaneous luminosity dL/dt. These quantities characterize how many interactions or events N_X of a given process X are expected to occur within a time interval Δt.

$$N_X = \sigma_X \cdot L = \sigma_X \cdot \int_t^{t+\Delta t} \frac{dL}{dt'} dt' \tag{2.11}$$

Here, σ_X is called the cross section of process X. The (instantaneous) luminosity depends on the technical parameters of the collider, e.g. the frequency with which particles are collided or how many particles are on average collided at the same time. It can be interpreted as a measure of the amount of delivered data. The instantaneous luminosity can be interpreted as a flux of possible interactions delivered by the collider and the cross section σ_X as the area crossing the flux leading to an interaction X. The cross section σ_X depends on the physics processes involved in the interaction. For more detailed information regarding accelerator physics, see the review article *Accelerator Physics of Colliders* in [2].

The following is based on [13, 14] which are brief introductions to the subject of collider physics. To calculate cross sections at hadron colliders, it has to be taken into account that hadrons are not elementary particles but composite states of elementary quarks and gluons. This poses a challenge since the QCD interactions within the hadrons need to be taken into account together with the interaction of the collision. However, this is a challenge since the QCD processes within the hadrons happen at low energy scales and are therefore not possible to calculate in perturbation theory because of the large value of the strong coupling constant.

The aforementioned problem can be solved by using a property called factorization. This property allows to factorize the low energy QCD interactions within the hadrons and the high-energy interaction of the partons during the collision. The cross section for a process $\mathrm{pp} \to X$, therefore, can be written as

$$\sigma_{\mathrm{pp}\to X} = \sum_{1,2} \int dx_1 \mathrm{PDF}_{1,\mathrm{p}}(x_1, \mu_F^2) \int dx_2 \mathrm{PDF}_{2,\mathrm{p}}(x_2, \mu_F^2) \hat{\sigma}_{1,2\to X}(x_1 p_1, x_2 p_2, \mu_F^2, \mu_R^2). \tag{2.12}$$

Here, p refers to a proton and X to the final state. The proton momenta are described by p_1 and p_2. The colliding partons have momentum $x_1 p_1$ and $x_2 p_2$. Therefore, x_1 and x_2 describe their momentum fractions within the protons. The quantities PDF are called parton distribution functions and describe the probabilities to find specific partons with momentum fraction x within a proton. Consequently, $\mathrm{PDF}_{1,p}(x_1, \mu_F^2)$ is the probability to find parton 1 with momentum fraction x_1 in proton 1 and analogously $\mathrm{PDF}_{2,p}(x_2, \mu_F^2)$ for parton 2 in proton 2. They depend on a scale μ_F^2 which is called the factorization scale. The non-perturbative structure of the proton is absorbed into the PDFs, which have not yet been calculated from first principles but have to be measured. Finally, to obtain the cross section, it has to be integrated over all $x_{1/2}$ and summed over all partons that allow for the production of the final state X.

The partonic cross section $\hat{\sigma}$ of the high-energy interaction of the partons can be calculated using Fermi's golden rule and perturbation theory. It depends on the momenta of the

partons, the factorization scale μ_F^2, an additional renormalization scale μ_R^2, and of course on the hard partonic process itself. For much more details regarding this topic, see e.g. [15].

2.1.3 Collider kinematics

There are several useful quantities applied in the field of collider physics which are briefly introduced here based on [13]. A general purpose detector like CMS, as is explained in section 2.2.2, is built around the nominal interaction point of the colliding protons in a cylindrical fashion. Therefore, a cylindrical coordinate system is used as is shown in Fig. 2.2. At a hadron collider like the LHC, due to the partonic nature of protons, the momentum of the center-of-mass system along the beam axis in the laboratory frame is not known. This means that momentum balance in the z-direction cannot be used in a straightforward way. Moreover, the momenta measured along the z-axis do not resemble the momenta in the center-of-mass frame along the z-axis. To gain information about the partonic collision, variables that are invariant against the boost in z-direction are desirable. One of these variables is the momentum perpendicular to the beam axis, also called the transverse momentum p_T with

$$p_\mathrm{T} = |\vec{p}_\mathrm{T}| \text{ and } \vec{p}_\mathrm{T} = (p_x, p_y) \,. \tag{2.13}$$

Here, p_x and p_y are the momentum components along the x-axis and the y-axis, respectively. Another variable which is consequently invariant against boosts along the z-axis is the azimuthal angle ϕ with

$$\phi = \tan^{-1}\left(\frac{p_x}{p_y}\right) \,. \tag{2.14}$$

In addition, another quantity called the rapidity y is defined by

$$y = \frac{1}{2}\ln\left(\frac{E + p_z}{E - p_z}\right) \,, \tag{2.15}$$

with E being the energy of the particle and p_z being the momentum along the z-axis. The difference between two rapidities y_1 and y_2 is also invariant against a boost along the z-direction. With the two quantities just introduced, it is possible to define an angular distance that is also independent of the boost along the z-axis. This quantity is

$$\Delta R = \sqrt{(\Delta\phi)^2 + (\Delta y)^2} \,. \tag{2.16}$$

Here, $\Delta\phi = \phi_1 - \phi_2$ is the difference in azimuthal angle and $\Delta y = y_1 - y_2$ is the difference in rapidity between the two particles. Furthermore, for massless particles, the rapidity has a relation to the polar angle θ of the particle which is generalized for all particles using the pseudorapidity

$$\eta = \ln\cot\frac{\theta}{2} \,. \tag{2.17}$$

The pseudorapidity is then commonly used instead of the rapidity in the equation for ΔR, which then reads

$$\Delta R = \sqrt{(\Delta\phi)^2 + (\Delta\eta)^2} \,, \tag{2.18}$$
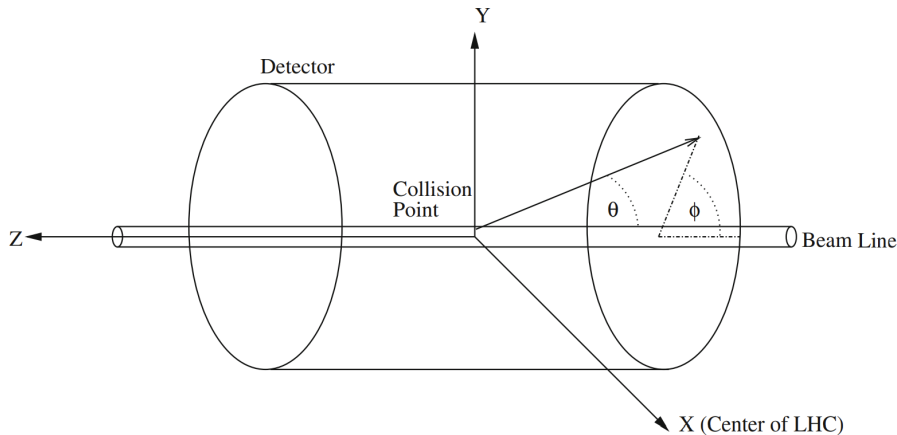
and is used throughout this thesis.

Figure 2.2: Coordinate system used for the CMS experiment. Taken from [16].

2.1.4 Event generation and simulation

In order to compare theoretical predictions and experimental observations, collaborations like the CMS collaboration rely heavily on event simulations. These event simulations establish a connection between the underlying physics of the hard interaction and the observations in the detector by means of Monte Carlo event simulations. A brief overview on Monte Carlo event generation and simulation is given in this section based on the *Monte Carlo Event Generators* review article in [2] and [17], which offer much more detail on this topic.

The generation of an event is split into several stages. This can be done due to the factorization of the different involved energy scales as previously explained. This method has the advantage that different aspects of the simulation can be approached separately. The first stage is the simulation of the hard interaction process involving the partons. The event simulation revolves around the hard process to be studied. Otherwise, an enormous number of events would need to be generated to obtain enough of the desired event type. Furthermore, parton distribution functions are incorporated to account for the structure of the proton. The next stage is called the parton shower. This algorithm handles the radiation of additional partons during the evolution of the partons which are going in and out of the hard interaction process. The next step is the simulation of the hadronization of colored partons into hadrons. Other steps are the simulation of additional partonic interactions besides the hard process, called the underlying event, as well as the decay of heavy resonances. In the following, these steps are explained in some more detail.

Hard process

In order to calculate the cross section for a hard interaction process at a hadron collider like the LHC, the factorization approach already explained in section 2.1.2 is used. This implies that the cross section can be factorized into a convolution of the parton distribution functions and the partonic cross section, see equation 2.12. The partonic cross section depends on the matrix element of the process in question as well as on the final-state phase space integral for the desired final state. The matrix element is calculated at fixed-order perturbation theory. This is done using for example Feynman diagrams. The final-state phase space depends on the momenta of the outgoing states and directly incorporates energy-momentum conservation. The phase space integration is, due to its often high dimensionality, performed with Monte Carlo integration techniques which allow for efficient numerical integration even at high dimensionality. Also, these integration techniques

introduce the possibility of generating events by sampling from the involved probability density functions. As of this time, leading-order matrix elements are fully automated within software tools as for example MADGRAPH5 [18, 19] whereas a large number of processes are also available with automated next-to-leading-order accuracy.

Parton shower

Parton showers are algorithms that connect the physics of high energy scales, as in the hard interaction process, with the physics at low energy scales, the hadronization of partons into hadrons. Partons incoming and outgoing of the hard interaction, analogously to electromagnetic bremsstrahlung, radiate gluons. However, gluons also carry color charge. This implies that the gluons are also able to radiate gluons. This results in a shower of additional partons being created due to QCD radiation. The evolution of this shower is modeled by a stepwise parton splitting criterion until the scale of the hard process has evolved to a scale where non-perturbative QCD effects play a major role. The parton shower is based on the probability to not produce any QCD splitting that is resolvable. This probability is also called the Sudakov form factor. From this, the probability for the first splitting can be calculated. The same procedure can then be applied to the new final state that has an additional radiated parton and to create another possible splitting and so on. This stochastic process can directly be implemented with Monte Carlo techniques. Therefore, with parton showers, the transition from inclusive cross sections to exclusive final states, and therefore final-state events as needed for an event simulation, can be performed.

Hadronization

Since quarks and gluons are confined due to QCD interactions, these particles cannot exist as free particles. Instead, they are only found within hadrons. The transition from partons to hadrons is called hadronization. This process happens at an energy scale at which the strong coupling constant does not allow a perturbative description anymore at approximately $1\,\mathrm{GeV}$. Therefore, these effects have to be modeled. There are two important models used in many applications, the string model [20] and the cluster model [21]. The following short explanations are based on [22]. The string model relies on the observation that the potential energy between color-connected quarks with a distance r grows linearly with r, starting from approximately the proton radius. If enough potential energy is stored, a new color-neutral pair of quarks can be created from the vacuum in a stochastic manner. The cluster model is based on a property observed in parton showers. Well before entering the regime of non-perturbative effects, the partons tend to build clusters in phase space which are neutral in color charge. The hadrons are then created from these clusters.

Underlying event

The underlying event describes the evolution of the additional partons within the colliding protons besides the hard interaction. Since the partons in the hard interaction are removed from the original protons, the state of the former proton is not color-neutral anymore. Therefore, these partons hadronize or interact with one another leading to additional hadronic activity in the event. The description of the underlying event is performed with the concept of multiple parton-parton interactions within one collision. If these additional interactions are at an energy scale that is high enough, perturbative QCD is used. For processes at soft scales where this is not possible, phenomenological models need to be incorporated.

Decay of heavy resonances

During hadronization, also unstable hadrons are created which have a lifetime that is relevant for detection purposes. Therefore, these decays have to be simulated within the event simulation. For this purpose, several multiplets of mesons and baryons are included in the simulation. The decays are often performed using matrix elements exploiting conservation laws but also using knowledge from experimental data.

2.1.5 Beyond the Standard Model Physics

Although the SM is a very successful theory predicting many observations with unprecedented precision, several observations have been made over the last decades that indicate that the SM cannot describe all physical phenomena correctly. A few examples are given in the following based on [2, 23, 24]. In this section, a short overview about the motivations and theoretical approaches for physics beyond the SM (BSM) is given.

It was observed that neutrinos show a phenomenon called neutrino oscillations [25, 26]. This means that the flavor of the neutrinos change while they propagate. This can only be explained by the fact that neutrinos have non-vanishing mass. When a flavor eigenstate is created in an interaction, this flavor eigenstate is a superposition of several different mass eigenstates. During the propagation, the different mass eigenstates travel with a different velocity therefore leading to relative phase differences depending on the distance traveled and the different masses of the mass eigenstates. This leads to the observation that, at a detector, the neutrinos are detected as different flavor eigenstates with distinct probabilities. In the SM, the neutrinos do not have a mass term therefore making this an observation that cannot be explained by the SM. For more details on neutrino oscillations, see e.g. [27] or the *Neutrino Masses, Mixing, and Oscillations* review article in [2].

Astrophysical and cosmological observations indicate that there is an additional form of matter that interacts at most very weakly with SM particles. This new form of matter has to be electrically neutral, colorless, and of non-baryonic nature. This type of matter is also called Dark Matter. This Dark Matter (DM) can indirectly be observed for example by studying galaxy rotation curves, structure formation in the universe, the cosmic microwave background radiation, or gravitational lensing. A more detailed introduction to DM is given in chapter 3. Furthermore, an additional form of energy called Dark Energy is inferred from e.g. observing the redshift of distant supernovae [28–30]. From these observations, it is concluded that the universe is expanding in an accelerated way. The acceleration of the universe is attributed to Dark Energy acting as the cosmological constant in Einstein's equations of general relativity. More details on Dark Matter and Dark Energy can be found in e.g. the review articles *Dark Matter* and *Dark Energy* in [2].

Another observation that indicates the existence of BSM physics is that the universe consists mainly of matter instead of antimatter. Three criteria have been established as necessary for such an asymmetry. These criteria are known as the Sakharov criteria [31]. First, baryon number violation has to occur. Second, electric charge conjugation as well as the combined conjugation of electric charge and parity needs to be violated. Finally, the last requirement is deviation from thermal equilibrium. However, the SM does not allow for such a large observed discrepancy between the matter and antimatter abundance, because the magnitude of the mechanisms for this asymmetry in the SM is too small. More information on the asymmetry between matter and antimatter can be found e.g. in the review article *Big-Bang Cosmology* in [2].

There are also problems from a theoretical perspective, e.g. the hierarchy problem, see [32] for a pedagogical introduction. This problem refers to the fact that in the SM, the mass of

the Higgs boson is modified by quantum corrections mainly due to virtual top quarks and W bosons. These corrections have a larger magnitude than the observed mass of the Higgs boson. Therefore, to obtain the observed mass of the Higgs boson, the mass parameter of the Higgs boson in the SM needs to be tuned to counter the major part of these quantum corrections. This fine-tuning is not explained by the SM and is often called unnatural by theoretical particle physics.

Finally, gravity cannot be added to the SM in a straightforward fashion and reproduce the observations.

2.2 Experimental environment

In this section, the Large Hadron Collider (LHC) and the Compact Muon Solenoid (CMS) detector are introduced. The LHC is a particle accelerator providing several experiments with high-energy proton or ion beams, which are used to produce particle collisions. The CMS detector is a particle detector which records the outcome of these collisions. The data this thesis is based on was produced by the LHC and recorded by the CMS detector.

2.2.1 The Large Hadron Collider

The LHC is a synchrotron used to accelerate protons as well as heavy ions and bring them to collision. It is situated at CERN near Geneva, Switzerland. The LHC is the last stage of the CERN accelerator complex and accelerates protons to a final center-of-mass energy of up to 14 TeV. In this section, the CERN accelerator complex and the most important parts of the LHC are briefly introduced based on the introduction in [33]. More in-depth details can be found in [33–36]. A graphical overview of all accelerators and related experiments at CERN is given in Fig. 2.3.

The acceleration chain is starting with the creation of protons by removing electrons from hydrogen atoms in a strong electric field. Afterwards, the first linear accelerator brings the protons to an energy of 50 MeV. The next step is the first circular accelerator called Booster, resulting in an energy of 1.4 GeV. During this first synchrotron acceleration step, the beam is split into separated packets of protons called bunches. Subsequently, the protons in the bunches are accelerated by the Proton Synchrotron and the Super Proton Synchrotron reaching energies of 25 GeV and 450 GeV, respectively. Finally, the protons are injected into the LHC to accelerate them to their final collision energy of currently 13 TeV.

The LHC is an approximately circular particle-particle collider; the colliding particles are of the same type and therefore carry same electric charge. This leads to the necessity of two separate rings with separate vacua and opposite magnetic fields to obtain beams in opposite directions. The particles which are mainly used in the LHC are protons. The decision for a particle-particle collider was made to allow for high beam intensities.

To accelerate the protons in the LHC, radio-frequency cavities operating at 400 MHz are used. Electromagnetic waves in these cavities accelerate the protons and replenish kinetic energy lost due to synchrotron radiation.

In order to keep the protons on the designed orbit within the vacuum pipes, superconducting electromagnets are used to deflect and focus the beams. The magnets are cooled using superfluid liquid helium at a temperature of around 2 K. The dipole magnets, which keep the beam on an approximately circular orbit, operate at around 8 T. Quadrupole magnets and even higher-order multipole fields are used to focus and stabilize the beams.

After reaching their final energy, bunches of protons are brought to collision at the experimental sites with a frequency of around 40 MHz. The experiments then study the outcome of the collisions with specialized detectors.
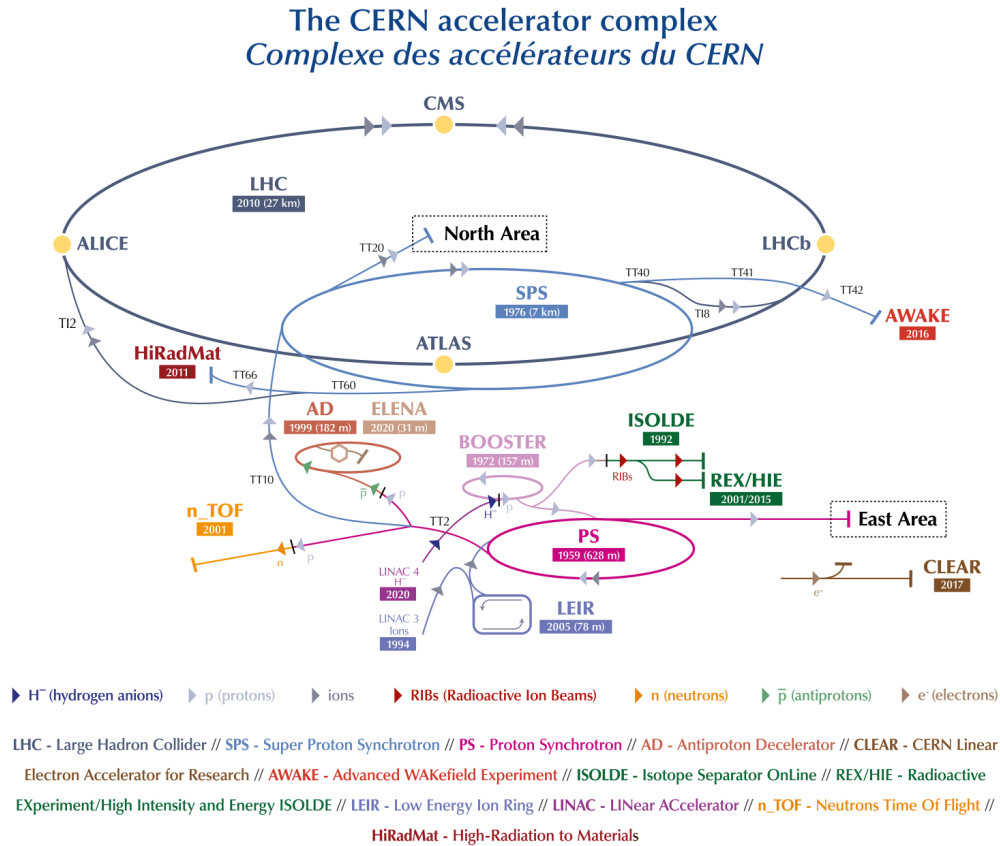
Figure 2.3: Graphical overview of the CERN accelerator complex. Taken from [37].

2.2.2 The CMS detector

The CMS detector is a multi-purpose particle detector operated by the CMS collaboration. The CMS experiment is one of the four largest experiments at CERN. The CMS collaboration studies the physics of the SM as well as possible BSM physics. The data analyzed in this thesis was recorded by the CMS detector in the years 2016 to 2018. In Fig. 2.4, an overview of the CMS detector is shown. The CMS detector consists of several subdetectors each serving a special purpose. The subdetectors are arranged in an onion-like structure around the main interaction point. In this introduction, only the most important subdectectors will be briefly explained based on [38] which also offers much more detailed descriptions.

Tracking detectors

Closest to the interaction point are the silicon tracking detectors. These detectors are used to infer the trajectories of charged particles from which primary interaction vertices as well as secondary vertices from particle decays are reconstructed. In conjunction with the 3.8 T magnetic field created by the superconducting solenoid, the momentum of charged particles as well as the sign of their charge can be extracted by measuring the curvature and direction of the trajectories of the charged particles in the magnetic field. The sensors of the silicon tracking detectors work on the basis of diodes in reverse bias voltage direction. Charged particles passing through the depletion zone create free charge carriers which lead to a current due to the applied voltage. This current can be detected by electronics. More details regarding silicon sensors can be found in e.g. [40].
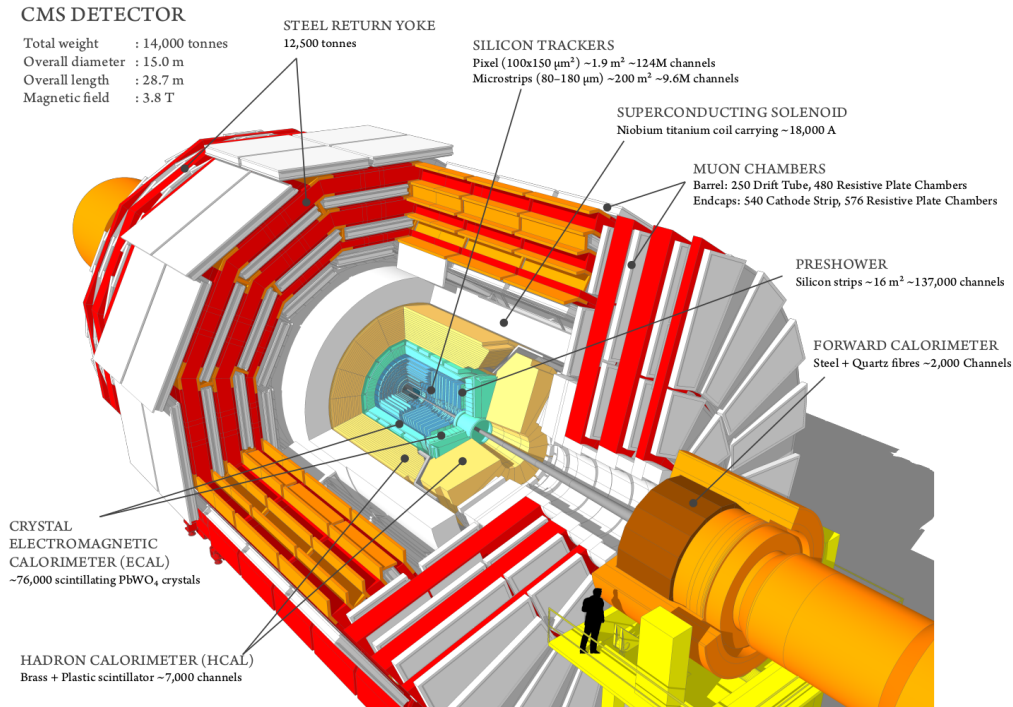
Figure 2.4: Graphical overview of the CMS detector. Taken from [39].

The tracking detectors are split further into pixel and strip detectors. Both are arranged in several cylindrical (barrel region) and disk-like (endcap region) layers around the main interaction point. The pixel detectors are closest to the interaction point and provide high-granularity with 2D position measurements. Outside of the pixel detector region, the silicon microstrip detectors are located. Their granularity is lower and they provide 1D position measurements. However, several layers are using stereo modules able to perform 2D position measurements as well. Both the pixel and strip detectors have to withstand high amounts of radiation due to their proximity to the main interaction point and the large particle flux. A more detailed description of the tracking system and the current pixel detector is given in [41, 42] and [43], respectively. A performance overview can be found in [44].

Calorimeters

The energies of particles are measured using the electromagnetic (ECAL) and hadron (HCAL) calorimeters. The first one is used to measure the energy of mainly electrons, positrons, photons, and to a smaller extent charged hadrons. The latter one is used to measure the energy of particles interacting mainly with the nuclei within a material.

The principle of the ECAL relies on the interaction of charged particles and photons in material. The main mechanisms are ionisation, bremsstrahlung, and the creation of electron-positron pairs. When an energetic charged particle or photon enters a material, the two latter effects lead to the formation of an electromagnetic shower of electrons, positrons, and photons traversing the material. By measuring how much energy these secondary particles lose in the material, it is possible to infer the initial energy of the primary particle. The CMS ECAL is made of $PbWO_4$. Due to its high density, this material induces large energy loss and it also serves as a detector of the energy lost by the secondary particles due to its scintillating properties. The secondary particles ionize the atoms in the material which in turn emit light. This light is detected and the amount of light is proportional to

the energy of the primary particle. For a lot more technical details regarding the ECAL, see [45, 46], which are however quite outdated. For a more recent but shorter overview including performance reviews, see e.g. [47, 48].

The HCAL works in a comparable way to the ECAL. The differences are that the absorber material and the detection material are not the same. Instead, alternating layers of brass absorber material and plastic scintillator material is used. Since hadrons interact less by electromagnetic processes but instead with nuclei, brass as a very dense material is used. Comparable to the electromagnetic shower in the ECAL, a hadronic shower emerges in the HCAL when an energetic hadron enters the absorber material. Due to the detection layers, the amount of energy loss within the scintillating material can be measured during the evolution of the shower to infer the energy of the primary hadron. Many more technical details can be found in [49] or for shorter and more recent overviews including performance studies in [50–52].

Muon chambers

Outside of the solenoid are the muon chambers and the steel return yoke in alternating order. The steel return yoke guides the magnetic field outside of the solenoid and acts as an additional absorber for particles which managed to penetrate the calorimeters. Only a very small fraction of particles other than muons should be able to traverse the calorimeters without being stopped. Since muons however interact only very weakly in material, they are the only type of visible particle which are expected to occur outside of the calorimeters. Therefore, the muon chambers are placed at the outermost of the CMS detector. There, they can be reliably used to identify muons. Though using different techniques, namely gas detectors like drift tubes, resistive plate chambers, and cathode strip chambers, they are used analogously to the silicon trackers to measure the positions of the muons in several layers to be able to reconstruct their trajectories. More detailed information are to be found in [53]. A shorter overview and information about the performance of the muon system can be found in [54].

2.2.3 Triggering and event reconstruction

In this section, it is described how interesting proton-proton collisions are distinguished from less interesting ones using the CMS trigger system and how a global description of a collision event is created using the particle-flow (PF) algorithm.

Trigger system

The LHC has a bunch crossing frequency of 40 MHz resulting in proton-proton collisions every 25 ns. Since saving each event to disk, is at this point in time, technically impossible, the CMS experiment uses a trigger system to decide if an event needs to be saved for further analysis because it probably contains interesting physics or not. This section is based on [55]. The CMS trigger system is separated into two levels.

The first level is called L1 trigger. This stage is comprised of custom electronics to reconstruct signatures compatible with electrons, photons, muons, τ leptons, jets, or missing transverse momentum. To achieve this task, the L1 trigger uses information from the calorimeters and the muon system to reconstruct candidates for the aforementioned objects. Afterwards, a collection of several selection algorithms, called a trigger menu, is run using the object candidates. If the event fulfills the criteria of one of the selection algorithms, it is accepted. This decision has to be performed by the L1 trigger within 4 µs of a collision. If the event is accepted, a signal is sent to the detector subsystems and their information is read out by the data acquisition system and forwarded to the next

trigger level called the high-level trigger (HLT). The total output rate of the L1 trigger is set around 100 kHz, which is the upper limit given by the readout electronics. The total output rate also includes events accepted for calibration and monitoring purposes. For more detailed information, see the technical design report in [56, 57].

The HLT is the second stage of the triggering process. This stage uses more detailed information and is able to use the information from the complete event. The HLT system is a software trigger running on a computing farm with several thousands of CPU cores. The HLT algorithms also reconstruct physics objects like electrons, muons, τ leptons, photons, and jets; however using information from the complete detector, see section 2.2.3 on the particle-flow algorithm for some more details. The HLT uses HLT paths. These are a defined set of operations which need to be performed. At the end of the steps, a selection decision is made whether to keep the event or not. The HLT paths use the same reconstruction algorithms which are used during offline reprocessing of the events. After an event is accepted, it is first stored on disk locally and afterwards sent to the CMS Tier-0 computing center, where it is reprocessed offline and stored permanently. Furthermore, depending on the HLT decisions, the events are grouped in a non-exclusive way into HLT streams, e.g. physics streams or calibration and monitoring streams. The total output rate of the HLT is around 1 kHz and is limited by the amount of data to store and process. More information on the HLT can also be found in [56, 57].

Particle-flow algorithm

The particle-flow (PF) algorithm is used to optimally combine information from all subdetectors for identification and reconstruction of physics objects which are used in the HLT and offline event reconstruction. In this process, the PF algorithm utilizes the different strengths of the different subdetectors in reconstructing and measuring different particles. It allows to create a complete description of the event by reconstructing all final-state particles coming out of a collision. This section is based on [58] which contains much more detail than what is given in this introduction.

Muons

Muon tracks are reconstructed by using hits from several layers of the tracker and muon system. The PF algorithm uses three types of muon tracks called standalone, global, and tracker muons. They differ in the requirements which are set on the track reconstruction. For standalone muons, only hits in the muon system are used to reconstruct the tracks. Global muons are reconstructed by matching a standalone muon track with a track reconstructed from the silicon tracker. If these tracks are compatible, a new track is reconstructed from the hits associated to the two initial tracks. A tracker muon is reconstructed from a track in the inner tracker which was matched to at least one muon track segment after extrapolating the inner track to the muon system. Afterwards, several selection criteria are applied to the tracks to decide whether the muon tracks are identified as PF muons or not thereby considering the different possible origins of muons e.g. isolated muons from the hard process or non-isolated muons from hadron decays in jets. After reconstructing and identifying the PF muons, the hits in the muon system and the tracker used for this process are removed from further consideration by the PF algorithm.

Electrons

An electron is expected to leave hits in the tracker as well as a measurable electromagnetic shower in the ECAL. Therefore, the PF algorithm uses information from the tracker and the ECAL during electron reconstruction. It uses ECAL-based and tracker-based seeds to

be able to deal with isolated and non-isolated electrons. The ECAL-based approach starts from ECAL clusters and tries to extrapolate back to the expected hits in the inner tracker. To account for the expected radiation of the electron during the passage through the tracker layers, ECAL clusters in an (η, ϕ) window are grouped together into superclusters to account for the radiated energy. For electrons which occur in jets, this procedure does not work well because of the overlap with other charged particles which also lead to ECAL clusters incorrectly associated to the supercluster or because of the additional hits in the inner tracker which prevent an unambiguous matching. The tracker-based seeding starts from hits in the inner tracker and uses an iterative tracking algorithm to build electron seeds. This also allows to recover the electrons missed by the ECAL-based approach. Both approaches are then used as starting points to create the final electron collections. Additional selection and identification criteria as well as corrections are applied depending on whether the electron candidate was seeded by the ECAL-based or tracker-based approach.

Photons

For the reconstruction of isolated photons, ECAL superclusters are used. In addition, these superclusters are required to not be linked to a track to distinguish them from electrons. Furthermore, conversions of photons into pairs of an electron and positron are identified and considered during the reconstruction of the kinematic properties of the photons. Finally, reconstructed photon candidates are required to be isolated from other tracks and the properties of the associated ECAL and HCAL energy distributions need to be in agreement with an electromagnetic shower originating from a photon.

Hadrons

Charged hadrons are identified by the combination of tracks and calorimeter clusters. The relativistic momentum is reconstructed by exploiting the measured momentum of the corresponding track and the energy within the calorimeter clusters. This combination of tracker and HCAL information improves the energy resolution of the hadron energy measurement. Neutral hadrons are reconstructed from HCAL clusters which are not linked to a track if the clusters are within the tracker acceptance. If the clusters are outside of the tracker acceptance, a distinction between charged and neutral hadrons is no longer straightforward. Therefore, ECAL and HCAL clusters that are linked and are outside of the tracker acceptance are treated in the same way.

2.3 Statistical data analysis

In this section, the fundamental principles and terms needed for the statistical data analysis within this thesis are briefly described. First, the distinction between frequentist and Bayesian statistics, followed by the concept of probability density functions and histograms are introduced. Then, the likelihood and the maximum likelihood method for parameter estimation are described. Furthermore, the basics of hypothesis testing are explained. Finally, the method to extract information from data combining the maximum likelihood approach and hypothesis testing is introduced. This section is based on [59, 60] and the *Statistics* review article in [2].

2.3.1 Frequentist and Bayesian approach

There are two viewpoints which are commonly used in statistics, the frequentist approach and the Bayesian approach. In frequentist statistics, probability is defined by counting the outcome of repeated experiments. In this framework, probabilities are only assigned to an

ensemble of outcomes under some hypothesis and not to a specific hypothesis or unknown parameters themselves. In frequentist statistics, the probability of an experiment to have an outcome X is obtained by repeating the experiment a large number of times and then calculating the probability P_X for outcome X as

$$P_X = \frac{\text{number of outcomes X}}{\text{number of experiments}}. \tag{2.19}$$

In Bayesian statistics, probability is extended to single outcomes and also to hypotheses and unknown parameters. Therefore, the term degree of belief is commonly used in Bayesian statistics.

Also commonly used in the field of probability is Bayes' theorem.

$$P(Y|X) = \frac{P(X|Y)P(Y)}{P(X)} \tag{2.20}$$

In this equation, $P(Y|X)$ represents the conditional probability that an outcome Y is found given an outcome X and vice versa for $P(X|Y)$. In addition, $P(X)$ and $P(Y)$ are called priors and represent the general probabilities for the outcome X and Y. Again, in Bayesian statistics, X and Y can also be hypotheses or parameters allowing to update the prior degree of belief for a hypothesis or a parameter after performing an experiment.

2.3.2 Probability density function and histograms

The concept of probability density functions emerges if the concept of probability is extended from random discrete items to random continuous variables. Instead of giving the probability P_x to find an item x from a set, the probability density function states the probability $P(x)$ to find the continuous variable x in the range $[x, x + dx]$. Because of the axioms of probability, this also implies

$$\int_x P(x)dx = 1. \tag{2.21}$$

To measure the probability density function of a random variable x in the range $[A, B]$, the measurements of the variable x can be summarized within a histogram. The range $[A, B]$ is divided in N subranges $[a_i, b_i)$ adjacent to one another, so $b_i = a_{i+1}$ with $i = 1, 2, ..., N$. The subrange $[a_i, b_i)$ is also called bin i. Each bin is assigned a number called the bin content n_i. Consequently, for each measurement of the variable x, it is determined in which bin range or bin the variable x is located. The respective bin content n_i is then increased by one. With the concept of histograms, an approximation for the probability density function of the variable x can be obtained from several measurements of the variable. By decreasing the ranges of the bins and therefore increasing the number of bins, the approximation can be improved. However, when increasing the number of bins, more measurements are needed. By performing the limit $N \to \infty$ and having an infinite number of measurements, the histogram or approximation transforms to the real probability density function $P(x)$.

2.3.3 Likelihood and parameter estimation

The likelihood is the probability for an outcome X of an experiment given a hypothesis H and is written as $L(X) = P(X|H)$. If the hypothesis depends on parameters that are not known, it is referred to as a composite hypothesis. Otherwise, it is called a simple hypothesis. In case of a composite hypothesis, the hypothesis is a function of unknown parameters θ, $H = H(\theta)$, the likelihood is also called likelihood function. Using Bayes theorem,

$$P(H|X) = \frac{P(X|H)\pi(H)}{\int P(X|H')\pi(H')dH'} \tag{2.22}$$

is obtained. Here, $P(H|X)$ is called the posterior probability for the hypothesis H given the experimental outcome X. The quantity $\pi(H)$ is the prior probability for hypothesis H. It has to be noted that the likelihood $P(X|H)$ is a function of H but not a probability density function for H. On the contrary, the posterior $P(H|X)$ is a probability density function for H in context of Bayesian statistics.

The likelihood function can be used to perform an estimation of unknown parameters θ in the frequentist approach of statistics. The motivation behind this approach is to choose the parameters to maximize the likelihood for the given experimental outcome X. Therefore,

$$\frac{\partial L}{\partial \theta} = 0 \text{ or } \frac{\partial \ln L}{\partial \theta} = 0 \tag{2.23}$$

for all parameters θ. Both versions are equivalent, however the one using the logarithm often has advantages for calculations. The parameters $\hat{\theta}$ for which this condition is fulfilled are called maximum likelihood estimators for θ. The maximum likelihood estimators are guaranteed to be unbiased and efficient for large samples. Also, in the case of large samples, they follow a Gaussian distribution under most conditions and the multidimensional surface

$$\ln L(\theta) = \ln L_{\text{Max}} - \frac{s^2}{2} \tag{2.24}$$

can be used to obtain approximate confidence intervals for the parameters corresponding to s standard deviations of the standard normal distribution.

2.3.4 Hypothesis testing and significance tests

Hypothesis testing is used to statistically validate if a hypothesis H_0 is to be preferred over an alternative hypothesis H_1 or vice versa. In the frequentist approach, the basis of hypothesis testing is the probability for the outcome X to be within a certain region W of all possible outcomes. If the region is chosen so that this probability is smaller than a specific value α, the value α is called the significance level of the test. Furthermore, if the actual outcome X of the experiment is found in the aforementioned region W, the hypothesis is rejected. Two important quantities regarding hypothesis tests are the type-1 and type-2 error of the test. The type-1 error is the probability of rejecting the hypothesis H_0 although it is the correct hypothesis. This probability is α. The type-2 error, often called β, is the probability of not rejecting the H_0 hypothesis although the alternative hypothesis H_1 is true. Furthermore, the quantity $1 - \beta$ is the probability of rejecting the hypothesis H_0 if H_1 is true and is often called the power of the test.

In most cases, a scalar quantity called a test statistic $t(X)$ is used for constructing the hypothesis test instead of the outcome X itself because this quantity can be constructed to enhance the power of the test, e.g. with multivariate methods. Furthermore, for a given test statistic and a specific value of α, the test has the maximum power if the ratio of the likelihoods

$$\frac{L(t(X)|H_1)}{L(t(X)|H_0)} \tag{2.25}$$

is used according to the Neyman-Pearson lemma [61].

If the agreement of only one hypothesis H_0 is to be investigated with respect to the outcome X, a significance test or goodness-of-fit test can be used. This test relies on the definition of a test statistic that reflects the agreement of the outcome X with the hypothesis H_0. Then, the p-value is defined which represents the probability to find an outcome X_{obs} or the corresponding test statistic value $t(X_{\text{obs}})$ that has the same or worse compatibility with the hypothesis H_0.

$$p = \int_{t_{\text{obs}}}^{\infty} f(t|H_0)dt \tag{2.26}$$

Here, $f(t|H_0)$ is the probability density function of the test statistic under the hypothesis H_0.

2.3.5 Statistical procedure to extract results

In this section, the statistical procedure used in this thesis in order to extract information from data about possible mono-top signals is explained in more detail. The aim is to evaluate if the observed number of events is compatible with the hypothesis of the SM of Particle Physics or if a possible mono-top signal contribution is found in data. If this is not the case, upper limits are set on the parameters of the mono-top models to exclude the parameter space that is not compatible with the observed data. The probability density functions for the two hypotheses are determined by means of Monte Carlo event simulation. Systematic uncertainties are represented by nuisance parameters that change the probability density functions of the the two hypotheses depending on the source of the systematic uncertainty at hand. In addition, the distributions are used in a binned format.

The method relies on the likelihood

$$L(\text{data}|\mu, \theta) = P(\text{data}|\mu \cdot s(\theta) + b(\theta))p(\tilde{\theta}|\theta). \tag{2.27}$$

This is the likelihood for the observed data under the hypothesis that the expected data is given by the SM background $b(\theta)$ in addition with a signal contribution $s(\theta)$ scaled by the parameter μ, called the signal strength modifier. This form allows to describe the background-only hypothesis and the signal-plus-background hypothesis by just changing the parameter μ. As was already explained, the expected contributions depend on systematic uncertainties described by the nuisance parameters θ. The nuisance parameters are unknown and treated as random variables in the context of Bayesian statistics. Nevertheless, there are auxiliary measurements which obtain knowledge or constraints on these parameters. These constraints can be included in the likelihood with $p(\tilde{\theta}|\theta)$ which represents the probability to obtain the measured nuisance parameters $\tilde{\theta}$ in auxiliary measurements given the values θ.

As was already explained, the analysis works with binned data, therefore

$$P(\text{data}|\mu \cdot s(\theta) + b(\theta)) = \prod_i \frac{(\mu \cdot s_i + b_i)^{n_i}}{n_i!} \exp(-\mu \cdot s_i - b_i). \tag{2.28}$$

This expression represents the probability of observing n_i events in bin i with the number of expected events being $\mu \cdot s_i + b_i$ combined over all bins i. This relies on the fact that the statistical fluctuations in bin i are assumed to be distributed with a Poisson distribution around the expected value.

In the next step, a likelihood ratio is constructed to optimize the power of the hypothesis test. The test statistic is

$$\tilde{q}_\mu = -2 \ln \frac{L(\text{data}|\mu, \hat{\hat{\theta}}_\mu)}{L(\text{data}|\hat{\mu}, \hat{\theta})}, \text{ with } 0 \leq \hat{\mu} \leq \mu. \tag{2.29}$$

This expression is also called the profile likelihood ratio. The only parameter that can be freely chosen in this expression is μ. The parameters $\hat{\mu}$ and $\hat{\theta}$ are the values of the parameters μ and θ that maximize the likelihood, so $L(\text{data}|\hat{\mu}, \hat{\theta})$ is the global maximum of the likelihood with respect to the observed data. The parameters $\hat{\hat{\theta}}_\mu$ are the values of the parameters θ that maximize the likelihood with respect to a chosen value of μ, so $L(\text{data}|\mu, \hat{\hat{\theta}}_\mu)$ is the conditional likelihood with respect to the observed data and the chosen value of μ.

Next, p-values are defined for the background-only hypothesis and the $\mu \cdot$signal+background hypothesis.

$$p_\mu = P(\tilde{q}_\mu \geq \tilde{q}_\mu^{\text{obs}} | \mu \cdot \text{signal} + \text{background}) = \int_{\tilde{q}_\mu^{\text{obs}}}^\infty f(\tilde{q}_\mu | \mu, \hat{\theta}_\mu^{\text{obs}}) d\tilde{q}_\mu \qquad (2.30)$$

This expression is the probability to obtain values of the test statistic that agree equally or worse with the $\mu \cdot \text{signal} + \text{background}$ hypothesis than the value obtained from observation. Then, the probability to obtain values of the test statistic that agree equally or worse with the background-only hypothesis is defined as

$$1 - p_b = P(\tilde{q}_\mu \geq \tilde{q}_\mu^{\text{obs}} | \text{background-only}) = \int_{\tilde{q}_\mu^{\text{obs}}}^\infty f(\tilde{q}_\mu | 0, \hat{\theta}_0^{\text{obs}}) d\tilde{q}_\mu \,. \qquad (2.31)$$

The probability distributions $f(\tilde{q}_\mu | 0, \hat{\theta}_0^{\text{obs}})$ and $f(\tilde{q}_\mu | \mu, \hat{\theta}_\mu^{\text{obs}})$ are determined by creating several sets of pseudo-data under the background-only hypothesis and the $\mu \cdot \text{signal} + \text{background}$ hypothesis, respectively. One instance of such a set of pseudo-data is called a toy. The toys for a specific hypothesis are obtained by sampling from the posterior probability distribution of the test statistic given the hypothesis at hand considering all systematic and statistical uncertainties. Finally, the CL_s value [62–65] defined as

$$\text{CL}_s(\mu) = \frac{p_\mu}{1 - p_b} \qquad (2.32)$$

is used to reject the signal-plus-background hypothesis for $\mu = 1$ and $\text{CL}_s \leq \alpha$ with a $(1 - \alpha) \cdot 100\%$ CL_s confidence level. An upper $(1 - \alpha) \cdot 100\%$ confidence level limit $\mu_{\text{UL}}^{(1-\alpha) \cdot 100\% \text{ CL}}$ is obtained by varying μ upwards until $\text{CL}_s(\mu) = 1 - \alpha$. These limits are called observed limits since the real observation is used to calculate them.

It is also possible to calculate expected limits. These limits are a measure of how sensitive the analysis or hypothesis test is towards a possible signal contribution under the assumption that the background processes behave the same in real data as in the expectation. To calculate these limits, again pseudo-data is generated according to the background-only hypothesis a large number of times. For each toy, the upper 95% confidence-level limit is calculated by replacing the observed values in the above equations by the ones obtained from the toy. After performing this calculation for many toys, a distribution of upper limits is obtained. From this distribution, the median is used as the expected 95% CL_s median upper limit. Uncertainties on this expected limit are stated as e.g. the 16% and 84% quantiles corresponding to the $\pm 1\sigma$ band or the 2.5% and 97.5% quantiles corresponding to the $\pm 2\sigma$ band of the distribution of the upper limits.

Generating toy datasets is very demanding from a perspective of computer calculations. To circumvent this challenge, asymptotic formulae are used [59] which describe the distributions of the test statistic for large datasets in an analytic form. These analytical forms are then used to calculate the upper limits with significantly less computing effort compared to the toy generation approach. Because of this, these asymptotic limits are used throughout this thesis.

2.3.6 Systematic uncertainties

Several sources of systematic uncertainties are considered in this thesis. These uncertainties either affect the normalization of processes and/or the shapes of the corresponding probability distributions. As was explained in section 2.3.5, systematic uncertainties are incorporated into the likelihood fit by nuisance parameters propagating the effect on the

expected events. Also, a probability density function for the respective nuisance parameter is included, representing the auxiliary measurement explained in the previous section.

In case of normalization or rate uncertainties, the probability density function assigned to a nuisance parameter θ is given by a Log-normal distribution:

$$\rho(\theta|\tilde{\theta}) = \frac{1}{\sqrt{2\pi}\ln\kappa}\exp\left(-\frac{(\ln(\theta/\tilde{\theta}))^2}{2(\ln\kappa)^2}\right)\frac{1}{\theta} \tag{2.33}$$

The parameter κ describes the width of this distribution and therefore how compatible a varied normalization due to the corresponding systematic uncertainty is with the previous knowledge regarding this uncertainty. This is represented by an increase or decrease of θ compared to the nominal value $\tilde{\theta}$ and the corresponding value of $\rho(\theta|\tilde{\theta})$.

For uncertainties affecting the shape of a distribution, the unit Gaussian distribution is used:

$$\rho(\theta|\tilde{\theta}) = \frac{1}{\sqrt{2\pi}}\exp\left(-\frac{(\theta-\tilde{\theta})^2}{2}\right) \tag{2.34}$$

For each shape uncertainty, two additional histograms/distributions are used corresponding to the one standard deviation up and down variation of the corresponding uncertainty described by the nuisance parameter θ. In addition, an interpolation procedure is performed to obtain interpolated histograms for values of $\theta \neq 0$ and $\theta \neq \pm 1$. In the range $|\theta| < 1$, the bin contents of the templates are interpolated with a spline given by

$$\alpha(\theta) = \frac{1}{2}\left((\delta^+ - \delta^-)\theta + \frac{1}{8}(\delta^+ + \delta^-)(3\theta^6 - 10\theta^4 + 15\theta^2)\right) \tag{2.35}$$

with $\delta^+ = f(1) - f(0)$ and $\delta^- = f(-1) - f(0)$. For $|\theta| > 1$, a linear interpolation is used.

3 Introduction to Dark Matter

A brief introduction to the field of Dark Matter is given in this section in the context of experimental particle physics at colliders. First, a short historical review pointing out the motivations for the concept of Dark Matter (DM) is given. Then, several possible particle candidates for DM are introduced. Next, theoretical approaches to incorporate DM into theoretical particle physics are explained. Finally, an overview about searches for DM in context of collider physics is given.

3.1 History and motivation

The history and motivation for the concept of Dark Matter is briefly summarized in this section based on [66, 67].

The existence of invisible astronomical objects was started to be predicted after the publication of Newton's laws in 1687. With these laws, it was possible for the first time to relate the motion of astronomical objects with their gravitational mass. This led to several predictions of Dark Stars, e.g. in 1844 [68], and Dark Planets. Furthermore, Dark Nebulae and Dark Clouds referring to more diffusely distributed masses that cannot be seen directly were studied in the 19th century as well [69, 70]. Both of these hypotheses were attributed to discrepancies between the expected motion of astronomical objects and their observed behavior.

Later, at the beginning of the 20th century, first estimates were done to determine the amount of invisible matter in our galaxy by treating the stars in the galaxy as a gas allowing to obtain a relationship between the size of the galaxy and the velocity dispersion of the stars [71–75]. From these experiments it was concluded that the amount of invisible mass is most likely lower than the amount of luminous mass in our galaxy. These were the first hints for mass not directly visible on a galactic scale.

In the 1930s, the astronomer Fritz Zwicky studied the velocity dispersion of galaxies in the Coma Cluster and used the virial theorem to determine the mass of the Coma Cluster [76, 77]. A much higher velocity dispersion was measured compared to the expected dispersion he calculated by estimating the luminous mass from the number of observed galaxies. This resulted in the conclusion that there had to be much more mass due to invisible matter than due to luminous matter. In the following, gases as the most common explanation were concluded not to be able to accommodate for this discrepancy. Therefore, first signs of missing matter on scales of galaxy clusters were found.
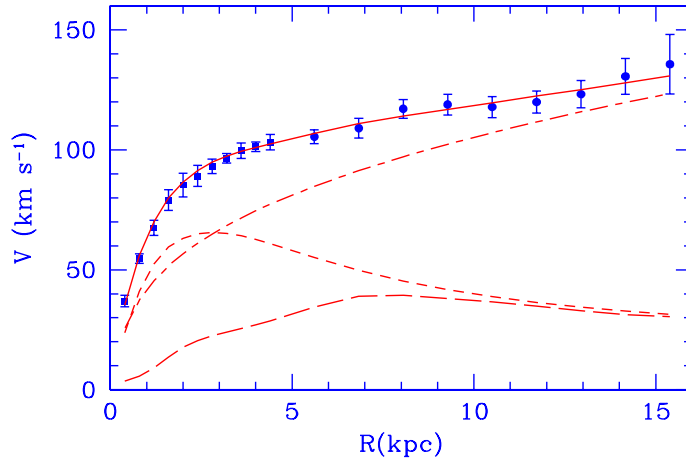
Figure 3.1: Rotation curve of the galaxy M33 showing the rotation velocity of the galaxy as a function of the distance to the center of the galaxy. The blue points with error bars are real measurements. The continuous line is the best-fit model. The model is subdivided into three contributions stemming from the stellar disk (short dashed), the gas contribution (long dashed), and the assumed DM halo (long short dashed). Taken from [86].

The next studies on galactic scales that measured discrepancies between the observed luminous matter and the amount of total matter, inferred from measurements of the dynamics of systems, are rotation curve studies. Rotation curves are created by measuring the rotation speed of galaxies with respect to the distance to the center of the galaxy. From these measurements, the approximate mass distribution of a galaxy can be derived. This was done by several astronomers [78–81]. The results however were not yet conclusive ranging from compatibility with luminous matter measurements to large discrepancies.

In the 1970s, improved measurement methods and experiments [82–85] pioneered by V. Rubin and J. Ford yielded the convincing result that, in order to explain the observed rotation curves, much more mass needs to be present compared to what is actually observed in form of luminous matter. A graphical illustration based on a more modern rotation curve is shown in Fig. 3.1. The rotational velocity v within or close to the center of the galaxy is expected to rise linear with the distance r, $v(r) \propto r$, since the density is assumed to be approximately constant. However, very far from the center of the galaxy, a lot less luminous matter is observed. Therefore, the amount of luminous mass keeping objects on their trajectories is approximately constant. This implies that objects at this distance should behave the same as circular Kepler orbits, $v \propto 1/\sqrt{r}$. As is shown in Fig. 3.1, this is not the case. Instead of becoming slower, the rotation speed reaches a constant level or even increases depending on the rotation curve at hand. This cannot be explained with the amount of observed luminous matter or gas given by the short dashed and long dashed curves in Fig. 3.1. Instead, an additional amount of matter needs to account for the additional gravitational pull necessary to obtain the observed rotation curves. The contribution of this additional type of matter, Dark Matter (DM), is given by the short long dashed curve representing a halo of DM around the galaxy.

Another motivation for DM is gravitational lensing [87]. As the path of light is bent in the presence of heavy objects, large amounts of matter should have a significant influence on gravitational lensing. By analyzing the distortion of gravitationally lensed images, it is possible to derive the amount and the approximate structure of the matter responsible for the lensing effect. This can be seen for example in Fig. 3.2. In this image, it is shown that the largest amount of mass during a galaxy merger is at a different spatial area than
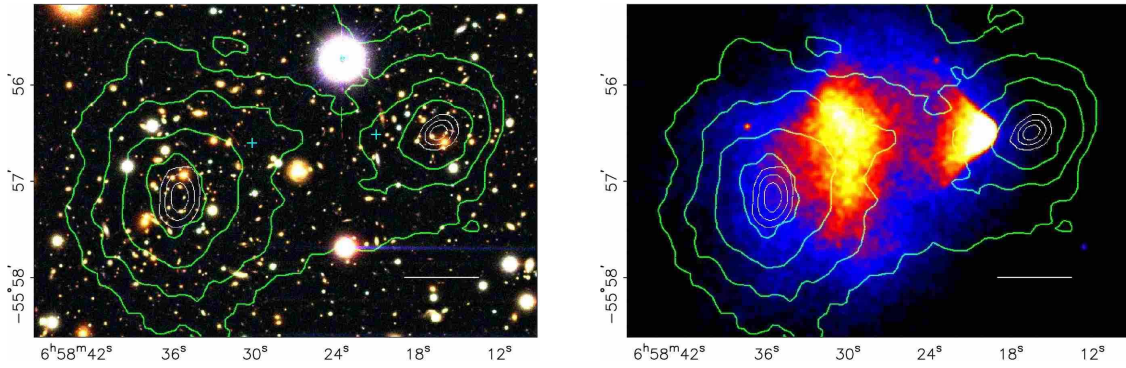
Figure 3.2: Image of the merger of two subclusters within the galaxy cluster 1E0657-558, also called the Bullet cluster. On the left-hand side, the image is shown in visible light with overlaid contours of the mass reconstruction by weak lensing. On the right-hand side, the same image can be seen in X-ray light with the same contours overlaid. Taken from [88].

the largest amount of baryonic matter, which is the X-ray emitting gas. Therefore, the gravitational potential resulting in the weak lensing has to be due to a non-visible amount of mass outside of the visible mass.

On cosmological scales, the cosmic microwave background (CMB) [89] can be used to infer the role of DM during the evolution of the universe. The CMB represents an image of the temperature and density distributions in the universe at the moment it became transparent. These distributions are extremely uniform in all visible directions. Only very small temperature fluctuations of the order of $\mathcal{O}(10^{-5})$ are detected. If the distribution of these temperature fluctuations is studied with respect to their angular distance, a power spectrum can be calculated. This power spectrum is shown in Fig. 3.3. From the first peak of the power spectrum, it is possible to extract the total amount of energy in the universe and whether its geometry is flat or not. From the second and third peak, the ratio of baryonic matter and DM can be inferred. This ratio is found to be such that there must be approximately five to six times more DM than baryonic matter, see e.g. [90].

3.2 Dark Matter candidates

As is shown in the previous section, several observations point to the conclusion that an additional form of matter is likely to exist in the universe, which seems to interact only by gravity. In this section, several particle candidates for Dark Matter are briefly introduced based on [92–94] and the *Dark Matter* review article in [2]. First, general classes of Dark Matter are described, followed by brief explanations of specific candidates.

3.2.1 Dark Matter classes

Hot Dark Matter

The term Hot Dark Matter (HDM) refers to DM candidates with masses up to $\mathcal{O}(1\,\mathrm{eV})$ that are highly relativistic. A candidate belonging to the class of HDM is e.g. the neutrino due to its very low mass. Due to the high velocities of neutrinos, large density fluctuations in the early universe would be required for structure formation to happen. This implies that a top-down formation would occur, meaning that larger objects like galaxy superclusters form before clusters and single galaxies. This results in late formation of galaxies, which is in contradiction to observation. Therefore, HDM as the dominant amount of DM is excluded by cosmology.
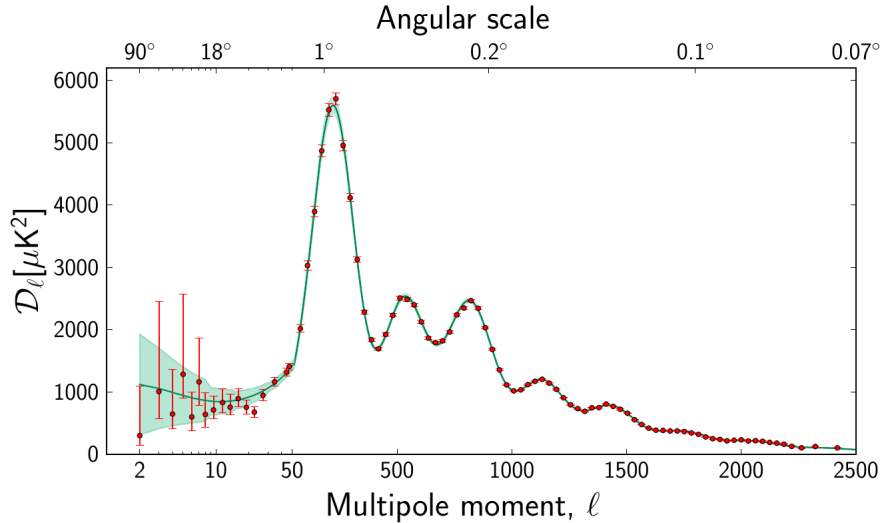
Figure 3.3: The CMB power spectrum is shown. On the lower x-axis, the moment of a multipole expansion is given which relates to the angular distance given on the upper x-axis. The y-axis shows the Fourier coefficient of the multipole expansion, which is a direct measure of the temperature fluctuations on the corresponding angular scale. Taken from [91].

Cold Dark Matter

Dark Matter candidates with non-relativistic velocities are called Cold Dark Matter (CDM). Due to their low velocity, structure formation happens in a bottom-up approach meaning that galaxies form first followed by clusters and superclusters. A candidate for CDM is the Weakly Interacting Massive Particle (WIMP). The concept of CDM is in good agreement with experimental observations except for structures smaller than $\mathcal{O}(1\,\text{Mpc})$, as is explained in the next section regarding WDM.

Warm Dark Matter

Warm Dark Matter (WDM) candidates are at the keV mass scale. Therefore, these particles are neither highly relativistic nor completely in the non-relativistic regime. In the WDM scenario, the large-scale structure formation is comparable to the CDM case in which a bottom-up structure formation takes place. Only at scales smaller than $\mathcal{O}(1\,\text{Mpc})$, the concept of WDM shows a different structure formation addressing for example problems arising with the model of Cold Dark Matter (CDM), see [95, 96]. A candidate for WDM is the sterile neutrino [97].

3.2.2 Dark Matter candidate particles

WIMPs

Weakly Interacting Massive Particles (WIMPs) are a generic class of particles with a mass in the range of $\mathcal{O}(10\,\text{GeV})$ to $\mathcal{O}(1\,\text{TeV})$ and a cross section comparable to SM weak interaction cross sections of $\mathcal{O}(1\,\text{pb})$. These particles are motivated by calculating their current energy density Ω_{DM} in the universe under the assumption that they were in equilibrium with the SM particles in the early universe. Due to the expansion of the universe and the corresponding decrease in temperature, the reactions keeping the thermal equilibrium between the DM particles and the SM particles become slower than the expansion rate of the universe. Therefore, the DM candidates can no longer be kept in thermal equilibrium

with the SM particles and consequently drop out of equilibrium. This is also called freeze-out. An approximation under the assumption that the freeze-out temperature is much lower than the DM mass leads to

$$\Omega_{\mathrm{DM}}h^2 \approx \frac{0.1\,\mathrm{pb}\cdot c}{\langle \sigma_A v \rangle}. \tag{3.1}$$

Here, c is the speed of light, h is the Hubble constant, and $\langle \sigma_A v \rangle$ is the thermal average of the total annihilation cross section σ_A of the two WIMPs into two SM particles times the relative velocity of the two WIMPs v. Using this formula, the currently measured values for the relic density of DM are obtained by $\langle \sigma_A v \rangle$ being in the range of SM weak interaction cross sections. This is called the WIMP miracle. Prominent candidates for WIMPs are for example the lightest supersymmetric particles in supersymmetric extensions of the SM.

Sterile neutrinos

Sterile neutrinos are particles that can be motivated by the observation that at least two of the known neutrinos are massive and that neutrinos have properties desirable for viable DM candidates as for example they only interact by the weak interaction. However, due to their low mass, the SM neutrinos cannot be responsible for the total amount of DM observed in the universe due to bounds of structure formation. By adding a heavier neutrino state with lower interaction strength, these bounds can be circumvented. In its simplest form, the principle of sterile neutrinos relies on adding an additional right-handed neutrino field while keeping the three left-handed lepton doublets of the SM. This means that there is a difference between the number of neutrinos that couple to the W and Z bosons and the number of neutrinos that do not. Furthermore, a mixing between the neutrino flavors that do couple to the W and Z bosons and that do not couple to these bosons has to be introduced, e.g. a Yukawa interaction. Consequently, after transforming to the mass eigenstates, an additional sterile neutrino state appears that has a tiny coupling to the the weak interaction bosons and is a superposition of four massive neutrino states. If the fourth mass eigenstate is significantly heavier than the SM neutrinos, e.g. in the range of keV, this sterile neutrino is a candidate for DM. The mechanism of adding additional non-interacting neutrino fields can be used as well to generate neutrino mass terms which do not exist in the SM in the first place.

Axions and Axion-like particles

Axions are motivated by the strong CP problem [98]. The term

$$\mathcal{L}_\theta = -\theta \frac{\alpha_s}{8\pi} \tilde{G}^a_{\mu\nu} G^a_{\mu\nu} \,, \tag{3.2}$$

which could be added to the QCD Lagrangian without violating any gauge symmetries, is not symmetric under a combined charge and parity conjugation operation. In this term, α_s represents the strong coupling constant, G and $\tilde{G}$ are the QCD field strength tensor and its dual tensor, and θ is a a-priori free parameter. This term leads to an electric dipole moment of the neutron for $\theta \neq 0$. From experimental measurements of the electric dipole moment of the neutron very strong constraints are imposed on this parameter, i.e. $\theta < 10^{-9}$. To ensure that this parameter is in the range imposed by experiment would require significant fine tuning. This is called the strong CP problem. One other possibility is to introduce a new Peccei-Quinn symmetry, which is a global chiral U(1) symmetry that is spontaneously broken. Due to this symmetry, the constant parameter θ is replaced by a dynamical one $\theta(x)$, called the axion field, associated with an additional potential. In the minimum of this potential, θ vanishes and therefore allows for a dynamical explanation for such a small
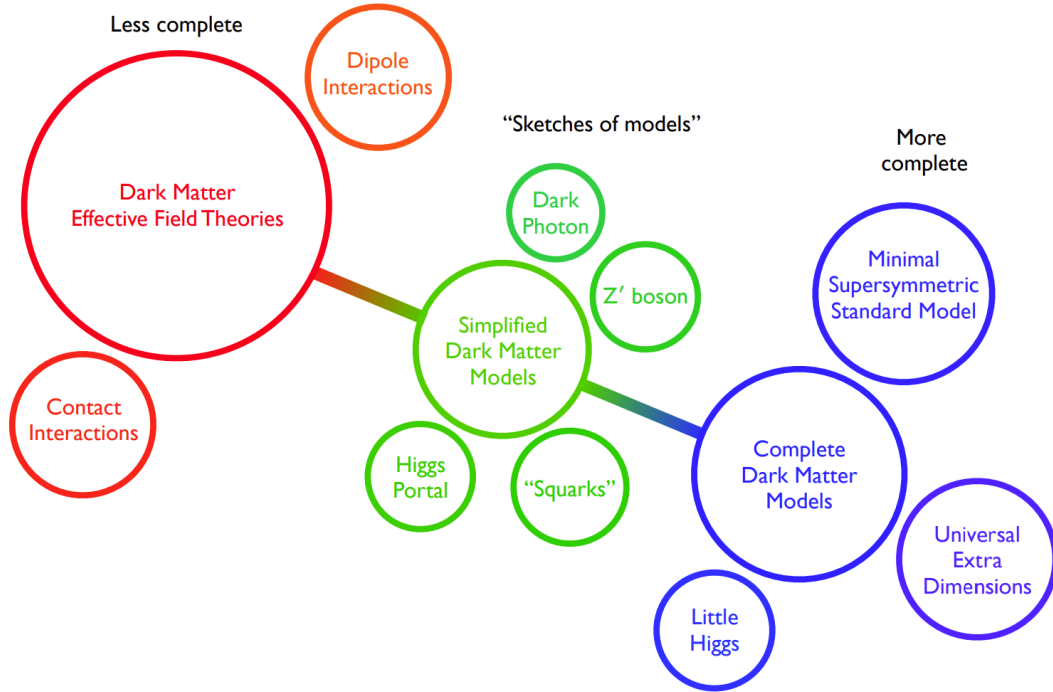
Figure 3.4: Illustration of the different theoretical approaches to include Dark Matter in a model beyond the SM. Taken from [100].

value instead of fine tuning. The mass and coupling of the axion is inversely proportional to the breaking scale of the aforementioned symmetry, which is commonly chosen much higher than the TeV scale. As a result, axions are very light particles in the range of meV to μeV and only couple very weakly. Because of this, they are viable candidates for DM. Because axions are not produced in thermal equilibrium, but by the symmetry breaking, they belong to the CDM class despite their low mass.

Axion-like particles (ALPs) are hypothetical particles which are generated similarly to the Axion but their symmetry breaking scale is chosen even higher than for the original QCD axions. Therefore, their masses and couplings may even be lower than for the original QCD axions.

3.3 Theoretical approaches for Dark Matter searches

Since the SM successfully explains a large number of phenomena, theoretical extensions are designed to contain the SM as a low energy approximation. Three different approaches are commonly used to extend the SM to account for newly observed phenomena while keeping the confirmed predictions of the SM. These approaches are called effective field theories, simplified models, and complete theories. These three approaches are explained in the following in context of Dark Matter searches at colliders based on [99–101]. In Fig. 3.4, a graphical overview of the three approaches is given.

3.3.1 Effective field theories

Using effective field theories is a model-independent method to search for new physics. It is based on the procedure of integrating out physical phenomena that are active at an energy scale M which is much higher than the energy scale E under study. With this approach, interactions connecting the SM particles and the DM can be transformed to

contact interactions which are independent of the exact physics connecting both scales as long as $M \gg E$. If the energy, e.g. at a collider, is high enough that a new mediator might be produced, the effective field theory cannot be used anymore to describe the interaction. The aforementioned contact interactions are described by a set of operators with different mass dimensions which are not renormalizable. These operators are added to the Lagrangian scaled with a power factor of $1/M^n$, with $n \in \mathbb{N}$ and $n = d-4$ depending on the mass dimension d of the operator. One example is the following dimension-six operator, which can describe e.g. the production of a fermionic DM candidate χ and its antiparticle via a scalar interaction starting from a quark q and its antiparticle in the initial state:

$$\frac{1}{M^2} q\overline{q}\chi\overline{\chi} \tag{3.3}$$

In this term, χ and q represent the field operators for the corresponding particles. The kinematic distributions are completely determined by the masses and the types of the involved particles, e.g. Dirac/Majorana fermions, scalar particles, or vector particles, as well as the Lorentz structure of the operator. This implies that the overall production rate is the only free parameter which can be obtained or at least be constrained by measurements. With the effective field theory approach, it is also possible to compare results of collider searches with direct detection experiments in a straightforward manner. A significant advantage of effective field theories is that the only new free parameters which are added to the model are the power factors in front of the operators.

3.3.2 Simplified models

A step further into specifying more details on the physics beyond the SM are simplified models. In simplified models, at least one mediator and a stable DM particle are specified and added to the model. The most important interactions between the SM and the DM particles are then not described by contact interactions but by the resolved mediator. This allows to accurately describe the kinematics of DM production at the LHC by s-channel and t-channel exchanges of the mediator. The necessary operators should fulfill renormalizability as well as respect the symmetries of the SM. This approach is better suited if it cannot be excluded that the energy transfer in the collisions is negligible with respect to the energy scale of the new interactions. However, if the mediator is much heavier than the energy scale of the collisions, the effective field theory is recovered by the simplified model. One disadvantage of simplified models is that more free parameters have to be added to the model, e.g. the masses of the new mediator and the DM candidate as well as the coupling strengths of the new mediator to the SM and the DM particles.

3.3.3 Complete models

The final possibility is to specify a complete model or theory beyond the SM that includes the SM as a low-energy approximation and can be evolved to either arbitrarily high energies or at least energies higher than the current model. A lot more new parameters and particles are added in these types of models. While simplified models cover a specific choice of models and final states, more complex final states and correlations between observables can only be described correctly by complete models. Moreover, from complete models it is possible to obtain motivated parameter ranges for simplified models. Furthermore, complete models are also designed to solve underlying theoretical problems like the already mentioned hierarchy problem as well as other deficiencies at the same time. Examples of such models are Supersymmetry [102], Universal Extra Dimensions [103], or Little Higgs theories [104]. However, the inclusion of a lot more parameters to the theory increases the difficulty to extract reliable information on these parameters from data.
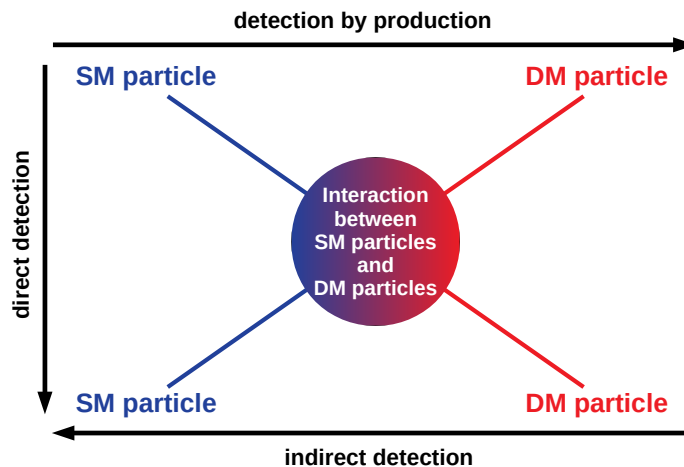
Figure 3.5: Illustration of the basic process between SM particles and DM particles which motivates the different search methods for DM.

3.4 Dark Matter search methods

The experimental searches for DM can be split into three types of searches. These three search methods are called direct detection, indirect detection, and collider-based detection. The methods differ by the initial and final state particles involved in the interaction between SM particles and hypothetical DM particles. A graphical illustration of the basic process, on which the three search methods are based on, is given in Fig. 3.5. In this section, the direct and indirect detection strategies are explained briefly based on [105, 106]. Direct and indirect detection methods provide complementary results to collider-based searches, i.e. they cover different model parameter ranges as well as they would establish a link between a possible collider signal and the hypothesized DM in our universe. The collider-based detection is described in more detail in section 3.5.

Direct detection

Direct detection experiments search for scattering processes between SM particles and DM particles. These experiments rely on the assumption that the earth is moving through a DM halo within our galaxy. Therefore, direct detection experiments use a target material in which DM particles are supposed to scatter on atomic nuclei. Since DM is assumed to be electrically neutral, the electrons of atoms are not assumed to be viable scattering partners. The experiments then try to detect these scattering processes by detecting the effects of the nuclear recoil within the material. The experiments make use of several signal channels, e.g. heat/phonon signals, ionization, or scintillation. The combination of several signal channels can be used to suppress backgrounds. Since the signal is expected to be very small, background processes leading to fake signals need to be suppressed as much as possible. A large background source for these experiments is cosmic radiation. For shielding from this background source, these experiments are situated in underground laboratories. A possible signal in direct detection experiments is expected to be modulated over the time-span of a year due to the relative motion of the earth and the sun, which either increases or decreases the velocities of the incoming DM particles, see the left-hand side of Fig. 3.6. This property can also be used to distinguish between possible signal contributions and background sources that do not show an annular modulation. Among
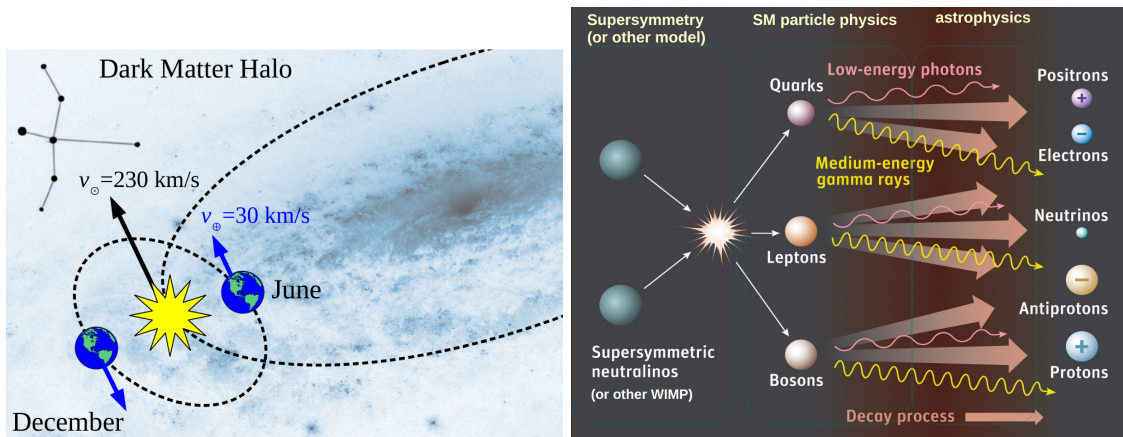
Figure 3.6: Left-hand side: Illustration of the reason behind the expected annular modulation of a possible DM signal in direct detection experiments. Taken from [105]. Right-hand side: Illustration of the production of SM particles via the annihilation of two DM candidate particles. Taken from [107].

others, experiments searching for DM with the direct detection strategy are CRESST I/II, EDELWEISS, (Super)CDMS, XENON 10/100/1T, LUX, PandaX, and the currently planned DARWIN experiment.

Indirect detection

Indirect detection experiments search for SM particles originating from the annihilation, decay, or both, of DM particles in regions of high DM density in the universe. These SM particles, for example, are photons, electrons and positrons, neutrinos, or protons and antiprotons. On the right-hand side of Fig. 3.6, a non-exhaustive illustration of the production of SM particles due to DM annihilation is shown. Depending on the mechanism of the production of the SM particles, either additional continuous contributions to the observed spectral flux of these particles are expected or distinct spectral lines. Experiments, either ground-based or satellite-based telescopes, are therefore searching for possible signals by studying gamma-rays (Fermi LAT, H.E.S.S., MAGIC, ...), cosmic radiation (PAMELA, AMS-02, Fermi LAT, ...), and neutrinos (IceCube, ANTARES, ...).

3.5 Dark Matter searches at colliders

A brief overview on searches for DM at colliders is given in this section. As was already introduced, see section 3.1, cosmological and astrophysical observations motivate the existence of DM. If an interaction between the SM and the DM particles exists, all conservation laws are fulfilled, and the center-of-mass energy of the LHC is high enough, a production of DM particles at the LHC might be possible. Therefore, the CMS collaboration as well as other collaborations search for signs of DM production in their recorded data. The search for DM at colliders follows a general strategy based on the nature of DM. Due to its at most very weak interaction, a direct interaction of the DM particles with the detector is not expected. Because of this, a specific direct signal in the detector is not expected either. However, an indirect signal is expected due to momentum conservation. In the initial state, the interacting partons at the LHC can be assumed to have vanishing transverse momentum compared to the momentum along the beam axis. Consequently, after the hard interaction, the final state still has vanishing transverse momentum due to momentum conservation. If DM particles are produced during the collision, these particles escape the detector without any corresponding interaction or measurement. This implies
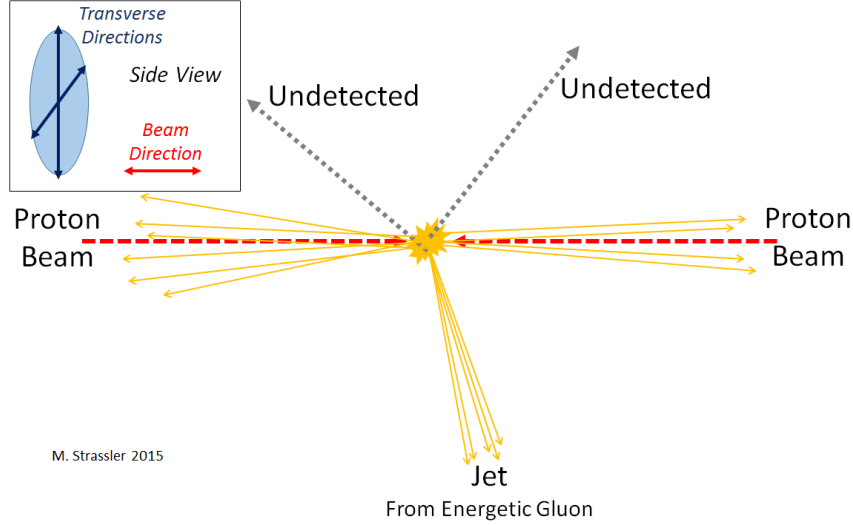
Figure 3.7: Illustration of a mono-jet event in which two DM candidates are recoiling against a jet after the hard collison. Experimentally, such an event would be reconstructed only having an energetic jet without a visible recoil partner since the DM particles escape the detector without interacting. Taken from [108].

that the sum of all transverse momenta of all reconstructed particles is not vanishing because the DM particles are not reconstructed. This signature is called missing transverse momentum or missing transverse energy. It is calculated as

$$\vec{\not{E}}_{\mathrm{T}} = - \sum_{i=\text{reconstructed particles}} \vec{p}_{\mathrm{T},i} \,. \tag{3.4}$$

Most searches for DM at colliders rely on the measurement of a significant amount of $\not{E}_{\mathrm{T}} = |\vec{\not{E}}_{\mathrm{T}}|$, which is the absolute magnitude of the missing transverse momentum, to define their target phase space. However, a large amount of $\not{E}_{\mathrm{T}}$ also implies the existence of one or more other particles that recoil against the missing transverse momentum. Depending on the model at hand, several SM particles, e.g. charged leptons or quarks, are possible candidates to be produced in association with large $\not{E}_{\mathrm{T}}$. The signatures of these particles can then be exploited to identify and to trigger on interesting events. These events and their corresponding searches are often called MET+X or mono-X events and searches. An illustration of such an event is shown in Fig. 3.7.

3.6 Mono-X searches at CMS

Several searches are performed at the CMS collaboration to search for DM in mono-X phase spaces. A short non-exhaustive overview is provided in this section.

3.6.1 Mono-Jet

In the mono-jet search, the production of DM is searched for using events with large missing transverse momentum as well as a jet with a high transverse momentum [109]. Among other models, the analysis uses a simplified model approach in which an additional scalar or vector mediator is added to the SM. Furthermore, this mediator decays exclusively into two Dirac fermion DM candidates. Example Feynman diagrams are given in Fig. 3.8. Important for this analysis is the modeling of the missing transverse momentum in a phase space without any well reconstructed leptons and photons. Moreover, a precise modeling of the main background processes involving the production of a single vector boson in association
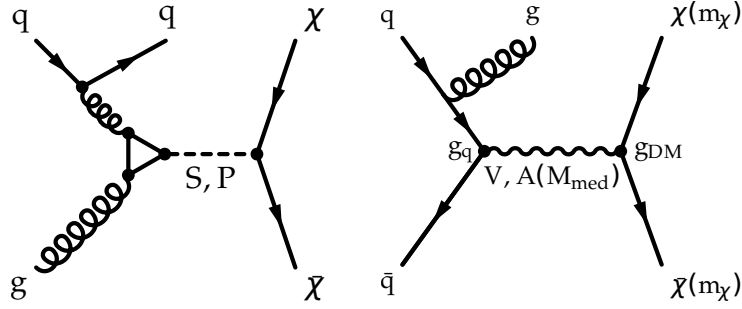
Figure 3.8: Example Feynman diagrams for the production of two DM candidates χ in association with a jet in a simplified model approach initiated by quarks q or gluons g. On the left-hand side, a scalar S or pseudoscalar P mediator is assumed. On the right-hand side, a vector V or axial-vector A mediator is exchanged. The coupling of the quarks and the DM candidates to the mediator is given by g_q and g_{DM}, respectively. Taken from [101]. The masses of the DM candidate and the mediator are represented by m_χ and M_{med}, respectively.

with jets is vital for this analysis. This analysis searches for additional contributions in the tail of the missing transverse momentum distribution in a phase space with a high-p_T jet and no prompt leptons or photons. Background processes are estimated with the help of data using several control regions enriched in events with leptons and photons also in association with high-p_T jets. Finally, exclusion limits are set e.g. on the masses of the mediators and the DM candidate masses, see Fig. 3.9 for a subset of these results. In the vector mediator case, mediator masses up to 1.80 TeV as well as DM masses up to 700 GeV can be excluded for the chosen coupling scenario. For the pseudoscalar mediator scenario, mediator masses up to approximately 400 GeV and DM masses up to 150 GeV are excluded. It has to be noted that these exclusion limits are only valid for the specific choice of couplings used in the simplified model at hand. For the coupling of the mediator to quarks and to the DM candidates $g_q = 0.25$ and $g_{DM} = 1$ was chosen, respectively.

3.6.2 Mono-Z

The search for production of DM in association with a Z boson decaying into charged leptons is called mono-Z search [110]. The signature exploited for this analysis is the reconstruction of two well-identified oppositely charged leptons in association with high $\not{E}_T$. Also in this search, a simplified model approach is used. Either a spin-1 mediator or a spin-0 mediator is added with a subsequent decay into two Dirac fermion DM candidates. In Fig. 3.10 example Feynman diagrams are given. The lepton pair is additionally required to be compatible with originating from a Z boson by a requirement on its invariant mass. Furthermore, angular variables between the leptons, jets, and the missing transverse momentum are exploited to enhance the sensitivity of the analysis. The main backgrounds are the production of two Z bosons, a W boson and a Z boson, and Drell-Yan production of two charged leptons. To estimate these contributions, constraints from additional control regions in data are used. In Fig. 3.11, a subset of preliminary results obtained by this analysis are presented. In the axial-vector coupling scenario, mediator masses up to 900 GeV and DM candidate masses up to 250 GeV are excluded. In the scalar coupling case with an assumed DM candidate mass of 1 GeV, the analysis starts to become sensitive in the range of low mediator masses. Comparable to the mono-jet analysis, the obtained exclusion limits depend on the couplings chosen for the used simplified model. Also in this analysis, the coupling of the mediator to quarks and to the DM candidates was chosen to be $g_q = 0.25$ and $g_\chi = 1$, respectively.
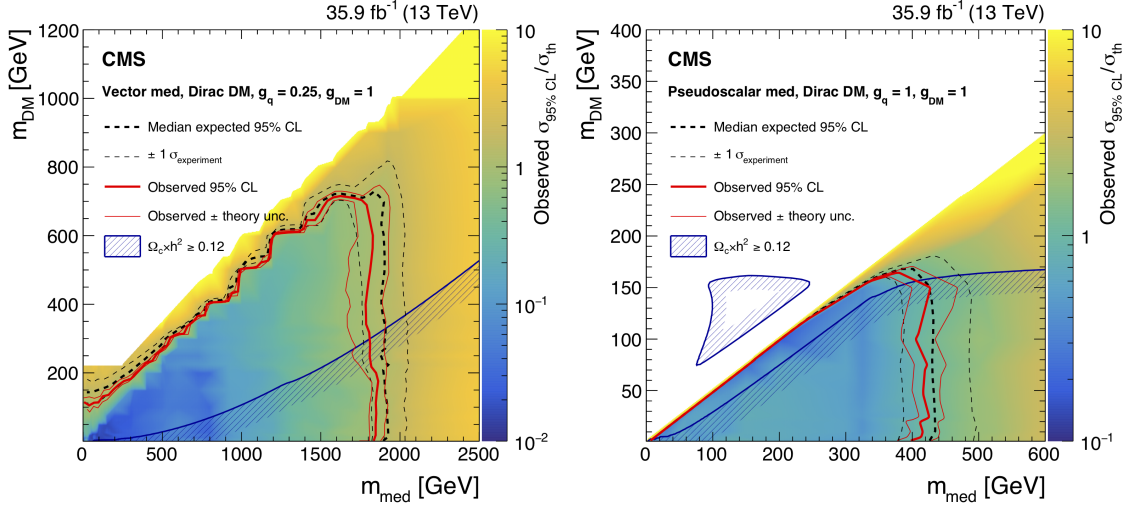
Figure 3.9: Upper exclusion limits on the DM production cross section via simplified models given in the plane of the mediator mass and the DM candidate mass which were obtained by the CMS mono-jet analysis [109]. On the left-hand side, the vector mediator model is shown. On the right-hand side, the model with a pseudoscalar mediator is shown. The coupling of the quarks and the DM candidates to the mediator is given by $g_q = 0.25$ and $g_{DM} = 1$, respectively. The area confined by the blue line and marked by blue shading represents the parameter space of the simplified model which is already excluded by relic abundance measurements. The parameter ranges that lie within the area confined by the red curve are excluded by the mono-jet analysis. Taken from [109].
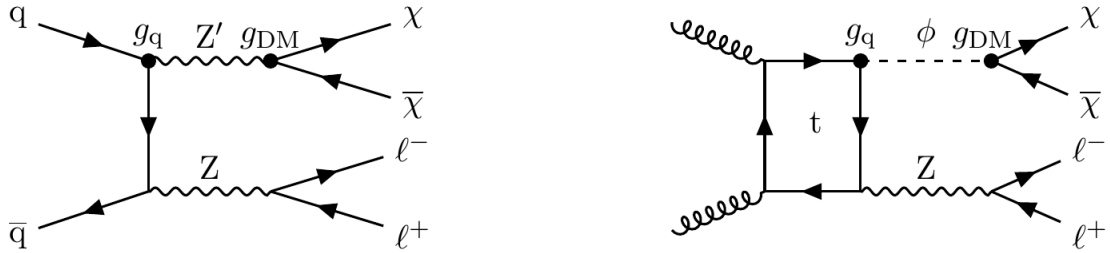

Figure 3.10: Example Feynman diagrams for the production of two DM candidates χ in association with a Z boson decaying into two charged leptons l in a simplified model approach. On the left-hand side, a spin-1 mediator Z' is exchanged. On the right-hand side, a spin-0 mediator ϕ is assumed. The coupling of the quarks and the DM candidates to the mediator is given by g_q and g_{DM}, respectively. Taken from [110].
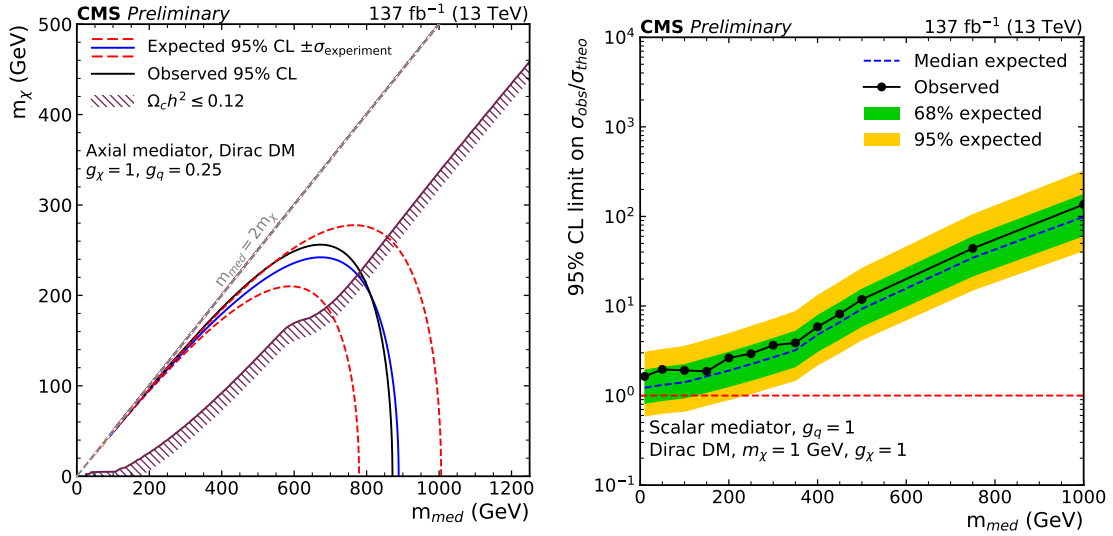
Figure 3.11: Upper exclusion limits on the DM production cross section via simplified models obtained by the mono-Z analysis [111]. On the left-hand side, exclusion limits in the plane of the mediator mass and the DM candidate mass for an axial-vector mediator model are given. The area confined by the purple line and marked by purple shading represents the parameter space of the simplified model which is already excluded by relic abundance measurements. The parameter ranges within the area confined by the black curve are excluded by the mono-Z analysis. On the right-hand side, exclusion limits on the scalar mediator model are given as a function of the mediator mass for a fixed DM candidate mass of $1\,\mathrm{GeV}$. Mediator masses for which the upper limit is below one are excluded. The coupling of the quarks and the DM candidates to the mediator is given by $g_q = 0.25$ and $g_\chi = 1$, respectively. Taken from [111].
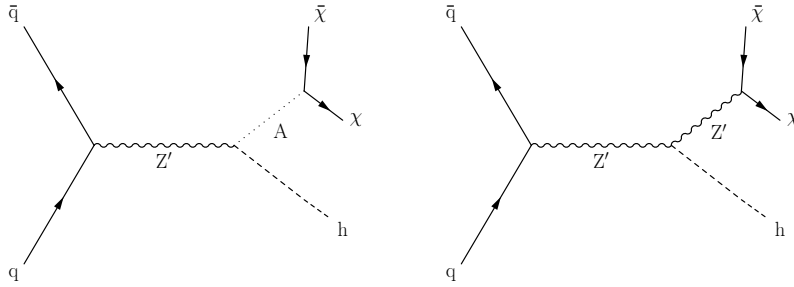
Figure 3.12: Example Feynman diagrams for the production of two DM candidates χ in association with a SM Higgs boson h. On the left-hand side, a mono-Higgs signature is created by a Z'-2HDM model involving a pseudoscalar Higgs boson A and on the right-hand side by a baryonic Z' model. Taken from [112].

3.6.3 Mono-Higgs

The mono-Higgs analysis [112] is searching for SM Higgs bosons in association with large missing transverse momentum due to the associated production of two DM candidates. In order to obtain this final state, two simplified models are investigated. The first model is a type-II Higgs doublet model (2HDM) with an additional spin-1 boson, called Z', and its corresponding $U(1)_{Z'}$ symmetry group [113]. This boson couples to the pseudoscalar Higgs boson A of the 2HDM. In addition, the pseudoscalar Higgs boson couples to the DM particles. The second model introduces a new baryon number $U(1)$ symmetry, also with its corresponding spin-1 boson Z', which is spontaneously broken by an additional baryonic Higgs boson [114]. This baryonic Higgs boson mixes with the SM Higgs boson and therefore allows for a coupling of the Z' to the SM Higgs boson. Furthermore, the baryonic Z' couples to the DM candidates. Example Feynman diagrams for these two models are presented in Fig. 3.12.

For the statistical analysis, several analyses are combined, each targeting a different decay channel of the SM Higgs boson, specifically bb [115, 116], $\gamma\gamma$ [117], $\tau\tau$ [117], WW [112], and ZZ [112]. In the decay channel to bottom-like quarks, large radius jets are used to reconstruct the Higgs boson decay and depending on the model either the recoil or the transverse mass of the Z' boson are used as final discriminants. In the diphoton decay channel, the invariant mass of the two photons is exploited to search for additional contributions to the invariant mass distribution of the photon pair. The analysis including two tau leptons extracts information about a possible signal in the distribution of the transverse mass of the reconstructed Higgs boson. The decay channel of the Higgs boson into two W bosons is analyzed by requiring one electron-like and one muon-like lepton and using a multivariate classifier. The analysis targeted at the decay of the Higgs boson into two Z bosons exploits the final state with four charged leptons and the missing transverse momentum distribution.

After combining the different analyses, for a benchmark point of the Z'-2HDM model, Z' masses in the range of approximately 500 GeV up to 3200 GeV and masses of the pseudoscalar Higgs boson in the range of 300 GeV up to 800 GeV, see the left-hand side of Fig. 3.13, are excluded. On the right-hand side of Fig. 3.13, it is shown that in the baryonic Z' model for the given coupling values, Z' masses up to 1500 GeV and DM candidate masses up to 420 GeV are excluded. Also for these searches, the exclusion limits are only valid for the chosen coupling scenario, see Fig. 3.13.
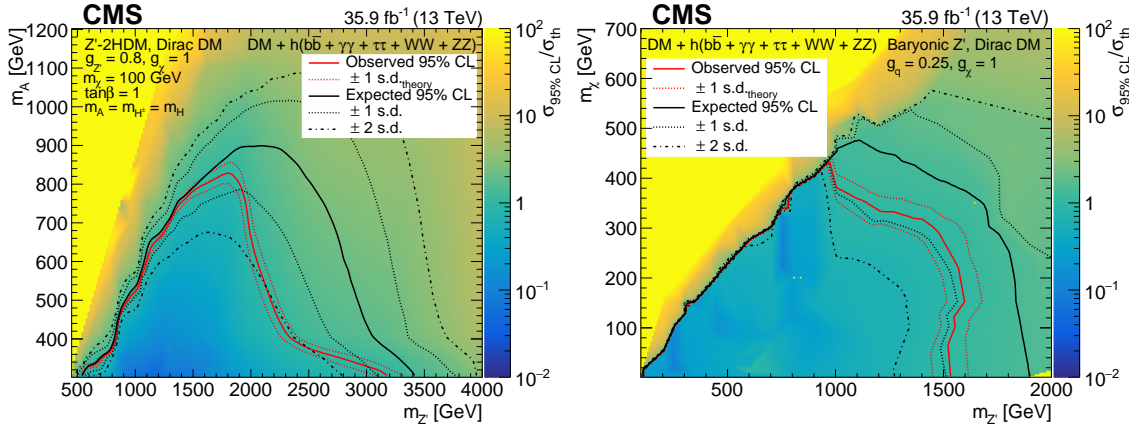
Figure 3.13: Upper exclusion limits on the DM production cross section via simplified models obtained by the mono-Higgs analysis [112]. On the left-hand side, exclusion limits are shown in the plane of the Z' mass and the pseudoscalar Higgs boson A in the Z'-2HDM model for a specific benchmark point. The coupling of the quarks to the Z' boson and the coupling of the DM candidates to the pseudoscalar Higgs boson A are given by $g_{Z'} = 0.8$ and $g_\chi = 1$, respectively. On the right-hand side, exclusion limits are given in the plane of the Z' mass and the DM candidate mass for the baryonic Z' model. The coupling constant of the quarks and the DM candidates to the Z' boson is given by $g_q = 0.25$ and $g_\chi = 1$, respectively. The parameter ranges within the area confined by the red solid curves are excluded. Taken from [112].

3.6.4 Mono-Photon

Another search studying possible new physics is the mono-photon search [118]. Similar to the mono-jet and the mono-Z analyses, a simplified model is used among other models. The simplified model contains a hypothetical spin-1 mediator, which either couples in a vector or axial-vector coupling scenario to the quarks of the SM and to Dirac fermion DM candidates. A mono-photon signature is obtained if one of the quarks in the initial state radiates a photon, see Fig. 3.14. The analysis is therefore searching for events with a high-p_T photon in association with large missing transverse momentum. Comparable to the mono-jet and the mono-Z analyses, this search uses several control regions to constrain major backgrounds with the help of recorded data. These major backgrounds are the production of a Z boson in association with a photon with the Z boson decaying into two neutrinos. Another important background is the production of a W boson decaying into a charged lepton and a neutrino either in association with a photon or not. In the first case, the lepton is out of acceptance or not identified. In the second case, the lepton is misidentified as a photon. Several quality criteria on ECAL-related quantities of the photon candidates are applied to reject incorrectly identified photons from electrons or from ECAL activity due to charged hadrons. In Fig. 3.15 results for the two simplified models are shown. Both models use $g_q = 0.25$ and $g_{DM} = 1$ as coupling constants to SM quarks and to the DM candidates, respectively. In the vector coupling scenario, mediator masses up to approximately 1 TeV and DM candidates masses up to 350 GeV are excluded by this analysis. In case of an axial-vector coupling, mediator masses up to approximately 1 TeV and DM candidates masses up to 250 GeV are excluded.
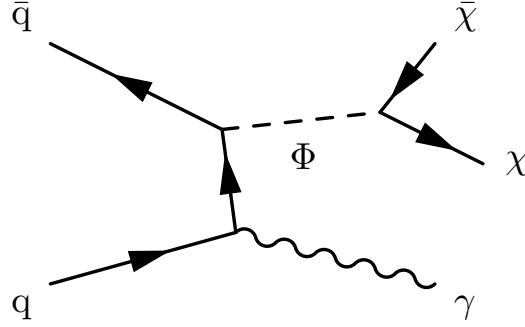
Figure 3.14: Example Feynman diagram for the production of two DM candidates χ in association with a photon γ initiated by a quark q and its antiquark. Taken from [118].
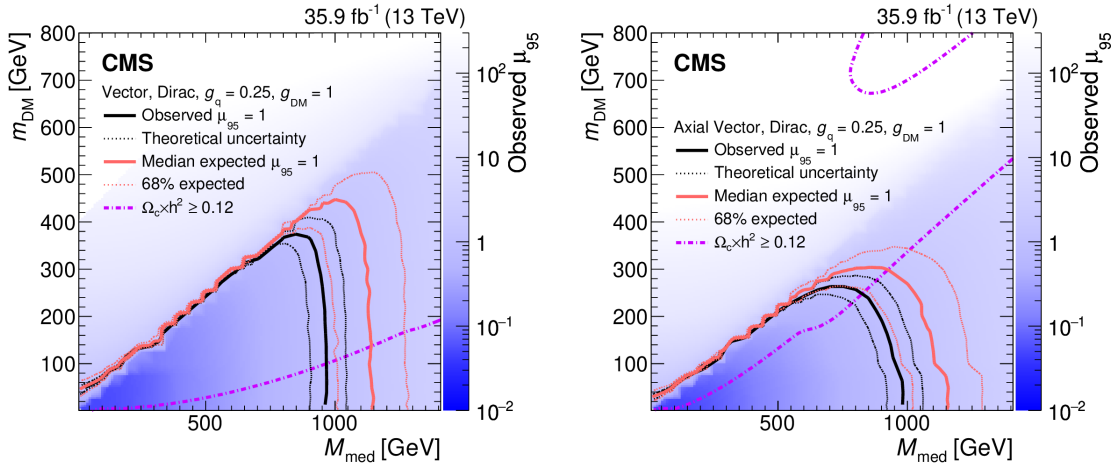

Figure 3.15: Upper exclusion limits on the DM production cross section via two simplified DM models obtained by the mono-photon analysis [118]. On the left-hand and the right-hand side, the vector and axial-vector coupling scenario is shown, respectively. The coupling of the quarks and the DM candidates to the mediator is given by $g_q = 0.25$ and $g_{DM} = 1$, respectively. The area confined by the purple line represents the parameter space of the simplified model which is already excluded by relic abundance measurements. The parameter ranges within the area confined by the black solid curves are excluded. Taken from [118].

3.6.5 Mono-Top

For the mono-top analysis, events with a large missing transverse momentum in association with a top quark are searched for in order to study possible new physics and DM production in association of the heaviest fundamenal fermion currently known. To account for the two different decay channels of the top quark, two separate analyses were performed to search for mono-top signatures in the hadronic decay channel [119] and in the leptonic decay channel [120]. Both analyses employ simplified models containing a Dirac fermion DM candidate and one of two hypothetical mediators allowing interactions between SM particles and DM candidates. Two example Feynman diagrams for these models are given in Fig. 3.16. The first simplified model, called the non-resonant model, allows for the production of a single top quark in association with two DM candidates χ by a flavor-changing neutral interaction mediated by the vector boson V. In the second model, called resonant model, an invisible fermion χ and a top quark are produced by a baryon-number-violating interaction by the scalar ϕ. These models are explained in more detail in section 4.2.

In the hadronic analysis, events with a large missing transverse momentum and a large radius jet are enriched. This is done to cluster the decay products of the hadronic top quark, which are expected to be collimated due to the top quark recoiling against a heavy state, within one jet. In order to distinguish large radius jets originating from top quarks from jets initiated by generic QCD radiation, jet substructure variables are used. Then, a boosted decision tree is trained based on these substructure variables to discriminate between QCD-initiated jets and jets originating from the hadronic decay of a top quark. Furthermore, several control regions are designed to be able to constrain the major backgrounds using recorded data. This is done using a variable called the hadronic recoil. The hadronic recoil approximates the distribution of the missing transverse momentum in the control regions under exclusion of prompt leptons and photons. How this is done is explained later in this thesis. The major backgrounds are the production of single Z and W bosons in association with additional jets as well as the production of top-quark-antiquark pairs. Finally, exclusion limits are set on the masses of the mediators and the DM candidates using e.g. the non-resonant model under the assumption of a vectorial coupling to quarks $g_q = 0.25$ and to the DM candidates $g_\chi = 1$, see Fig. 3.17.

The leptonic analysis searches for events containing an energetic muon in association with large missing transverse momentum and a jet identified as originating from a bottom quark. In order to discriminate between SM events producing this signature, i.e. W boson production, a kinematic variable called the transverse mass is used. This variable allows to separate a state with a charged lepton in association with $\vec{E}_T$ originating from a W boson and the same state originating from a W boson in association with invisible states. The two most important backgrounds are W boson production in association with additional jets and the production of top-quark-antiquark pairs. The signal region and control regions to constrain the most important backgrounds are therefore constructed using the number of jets identified as originating from a bottom-like quark. A major challenge of this analysis is the modeling of the transverse mass above the W boson mass of approximately 80 GeV. In this range SM backgrounds are heavily suppressed and significant mismodeling could be incorrectly interpreted as possible signal contributions if not accounted for by uncertainties. Also the leptonic analysis derived exclusion ranges on e.g. the mass of the scalar mediator in the resonant model, see the right-hand side of Fig. 3.17, under the assumption that the mass of the invisible fermion is 10 GeV and for two chosen coupling values.
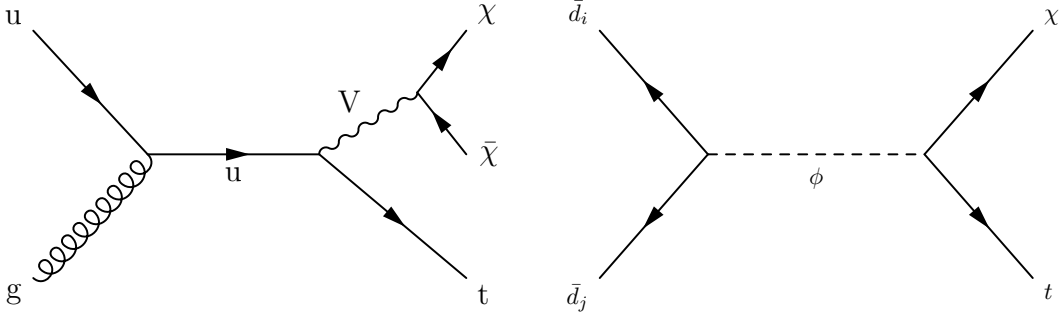
Figure 3.16: Example Feynman diagrams for the production of DM with two simplified models. On the left-hand side, DM is produced by a flavor-changing neutral current (non-resonant model) and on the right-hand side by a baryon-number-violating interaction (resonant model). Taken from [119].
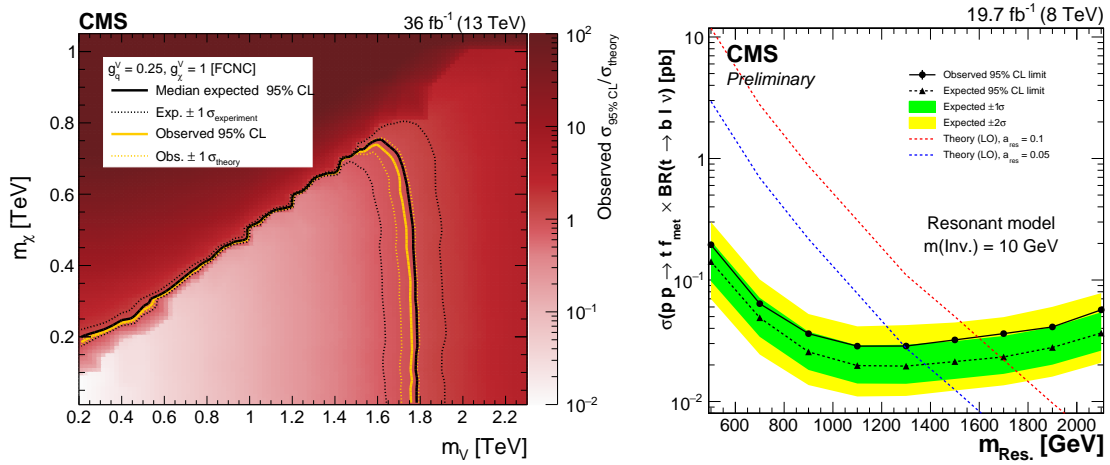

Figure 3.17: Left-hand side: Upper exclusion limits on the DM production cross section via a simplified DM model in the plane of the mass of the mediator V and the mass of the DM candidate χ obtained by the hadronic mono-top analysis [119]. The coupling of the quarks and the DM candidates to the mediator, which is assumed to be only vectorial, is given by $g_q = 0.25$ and $g_{DM} = 1$, respectively. The area confined by the yellow-orange line represents the parameter space of the simplified model which is excluded by the hadronic mono-top analysis. Taken from [119]. Right-hand side: Upper exclusion limits on the DM production cross section via the resonant model as a function of the mass of the scalar mediator derived by the leptonic mono-top analysis [120]. The mass ranges for which the red curve or the blue curve is above the solid black curve are excluded, depending on the chosen coupling value, $a_{res} = 0.1$ or $a_{res} = 0.05$.

4 Foundations of the mono-top analysis

In this chapter, foundations needed for the mono-top analysis are introduced. First, a short overview about top quark physics is given. Then, an introduction to the mono-top model is presented. Finally, the basics of boosted event topologies and jet substructure are described.

4.1 Top quark physics

This brief introduction regarding the properties of the top quark, which are relevant for this thesis, is based on the *Top Quark* review article in [2]. The top quark is the heaviest fundamental fermion currently known. Its mass is approximately $173\,\text{GeV}$ and its absolute charge is $2/3\,\text{e}$ with e representing the absolute electric charge of the electron. Due to its high mass and $|V_{tb}| \gg |V_{td}||V_{ts}|$, with V being the CKM matrix [121, 122], the top quark has a very short lifetime of around $0.5 \times 10^{-24}\,\text{s}$ and decays almost exclusively into an on-shell W boson and a bottom quark. Due to its lifetime being shorter than the mean QCD hadronization timescale of $\Lambda_{\text{QCD}}^{-1} \approx 10^{-23}\,\text{s}$, the top quark decays before hadronizing [123]. Therefore, the signature of a top quark in a detector is given by its decay products. Since the W boson is an unstable elementary particle as well, the final-state signature of a top quark is given by a bottom quark and the decay products of a W boson. A W boson decays into a quark and an antiquark with different flavor (hadronic decay channel) or to a charged lepton and a neutrino (leptonic decay channel) with the following branching ratios (see the *Gauge and Higgs bosons* summary table in [2]):

$$W^{\pm} \rightarrow q\overline{q}' \quad (67.41\%)$$
$$W^{+} \rightarrow l^{+}\nu_l \quad (10.86\%)$$
$$W^{-} \rightarrow l^{-}\overline{\nu}_l \quad (10.86\%)$$

These branching fractions consequently determine the leptonic and hadronic decay probabilities of the top quark. This implies that in approximately two thirds of all cases, the top quark effectively decays into three quarks, which hadronize and result in jets. One of the jets originates from a bottom quark. In approximately one third of the cases, the top quark decays into a lepton and a neutrino as well as a jet originating from a bottom quark. The decay into a τ lepton and the corresponding neutrino can also result in additional hadronic activity since the τ lepton has a hadronic decay channel as well.
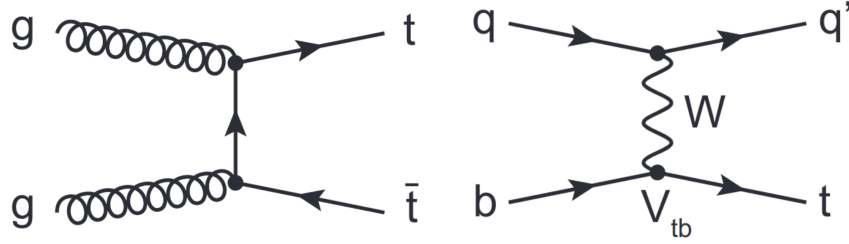
41

Figure 4.1: Left-hand side: One of the leading-order Feynman diagrams for top-quark-antiquark-pair production via the strong force. Right-hand side: Leading-order Feynman diagram for the production of a single top quark in the t-channel production mode via the weak interaction. Taken from [124].

At hadron colliders, top quarks can be produced by the strong interaction as top-quark-antiquark pairs or as single top quarks via the weak interaction considering only SM physics, see Fig. 4.1 for two example Feynman diagrams. In the next section, an extension of the SM is introduced that is able to explain the production of a single top quark, though in association with missing transverse energy due to two DM particles. For more details regarding top quark physics, see e.g. [124, 125].

4.2 The mono-top model

In this section, the mono-top model is introduced based on [126–128]. The term mono-top refers to a final state consisting of a top quark or top antiquark and missing transverse energy due to one or more invisible particles. In the SM, such a process can only occur via higher-order effects in perturbation theory and is therefore strongly suppressed, see the left-hand side of Fig. 4.2. There, a loop consisting of a W boson and two strange quarks allows for the production of a Z boson and a top quark in the final state. This process is therefore loop-suppressed and additionally suppressed by the Glashow–Iliopoulos–Maiani (GIM) mechanism [129]. If the Z boson decays into two neutrinos, a mono-top signature is found. To allow the production of such a mono-top signature at tree level, the SM Lagrangian is extended using a simplified model based on two interactions, baryon-number-violating processes or flavor-changing neutral interactions. The model including baryon-number-violating processes is also called resonant mono-top model since the new hypothesized mediator can be produced in the s-channel. The flavor-changing neutral interaction model is consequently called non-resonant mono-top model. In this thesis, the focus lies on the non-resonant model. The flavor-changing neutral interaction model is explained in more detail in the following.

In this model, an additional neutral bosonic particle, with spin 0 (S) or spin 1 (V), is added, which induces a flavor-changing neutral interaction between two up-type quarks from different generations. The Lagrangian for this model is

$$\mathcal{L} = \mathcal{L}_{\text{kin}}(\text{V}, \text{S}) + \underbrace{\text{S}\bar{u}\left(a^0 + b^0\gamma_5\right)u}_{\text{(pseudo-)scalar interaction}} + \underbrace{\text{V}_\mu\bar{u}\left(a^1\gamma^\mu + b^1\gamma^\mu\gamma_5\right)u}_{\text{(axial-)vector interaction}} + \text{h.c.} \qquad (4.1)$$

with $\mathcal{L}_{\text{kin}}$ containing the kinetic, mass, and gauge interaction terms of the newly introduced fields. Here, u represents the up-type quarks (u, c, t) with the color indices implied and $a^{0/1}, b^{0/1}$ are called flavor-matrices parameterizing the interaction strength of the different up-type quarks with the bosonic final states S or V_μ. The diagonal and non-diagonal elements of the flavor-matrices represent the interaction strengths between up-type quarks of the same and different flavor, respectively.
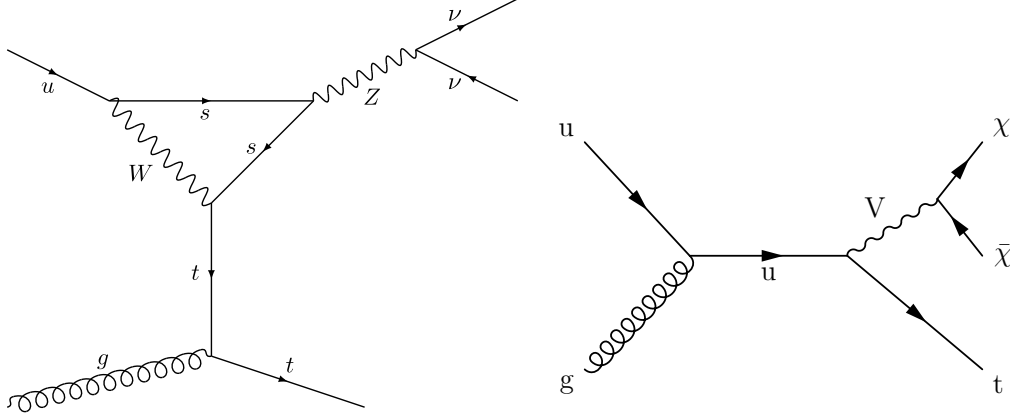
Figure 4.2: Left-hand side: Example Feynman diagram for the production of a mono-top signature in the SM. Right-hand side: Leading-order Feynman diagram for the production of mono-top signatures in a simplified DM model. A flavor-changing neutral interaction is mediated by the hypothetical vector boson V which decays into two DM candidates χ. Right-hand side figure taken from [119].

To retain gauge invariance under SM gauge transformations, couplings to left-handed down-type quarks are required in the Lagrangian as well. These couplings lead to mono-bottom final states. However, since this thesis concentrates on mono-top signatures, these couplings are omitted by setting the couplings to left-handed down-type quarks to zero. This is already done in equation 4.1. Furthermore, the models are chosen such that the flavor-changing neutral current only relates the up-type quarks of the first and third generation of quarks. This implies that only $a_{13}^{0/1}, a_{31}^{0/1} \neq 0$ and $b_{13}^{0/1}, b_{31}^{0/1} \neq 0$ whereas all other couplings are set to zero. This is motivated by the fact that these production modes are favored by parton density functions at the LHC.

The bosonic final states can be long-lived or decay invisibly to result in a final state consisting of significant missing transverse energy. The models studied in this thesis belong to the latter class in which the bosonic state decays into two invisible DM candidates χ with a dominant branching fraction. More details on the decay of the bosonic mediator are given below.

Depending on the top quark decay, the expected experimental final states then are

$$\mathrm{p\,p} \to \mathrm{t} + \vec{\not{E}}_\mathrm{T} \to \mathrm{bq\bar{q}'} + \vec{\not{E}}_\mathrm{T} \ \text{(hadronic mono-top)}\,,$$

$$\mathrm{p\,p} \to \mathrm{t} + \vec{\not{E}}_\mathrm{T} \to \mathrm{bl} + \vec{\not{E}}_\mathrm{T} \ \text{(leptonic mono-top)}\,,$$

with the neutrino from the leptonic channel being absorbed into $\vec{\not{E}}_\mathrm{T}$. In the following, the specifics of a vector and a scalar mediator are explained in more detail.

4.2.1 Vector mediator V

In the simplest case of an electroweak singlet vector mediator, which is the focus of this thesis, the corresponding decay term for the Lagrangian is

$$\mathcal{L}_{\mathrm{V}\to\chi\bar{\chi}} = \mathrm{V}_\mu \bar{\chi} \gamma^\mu \left(g_{\chi V} + g_{\chi A} \gamma_5 \right) \chi \tag{4.2}$$

for a Dirac DM candidate χ which is assumed to be a singlet under all SM gauge interactions. Here, $g_{\chi V}$ and $g_{\chi A}$ represent the coupling strength of the vector and axial-vector coupling of the mediator to the DM candidates. A kinetic term and a mass term for the DM
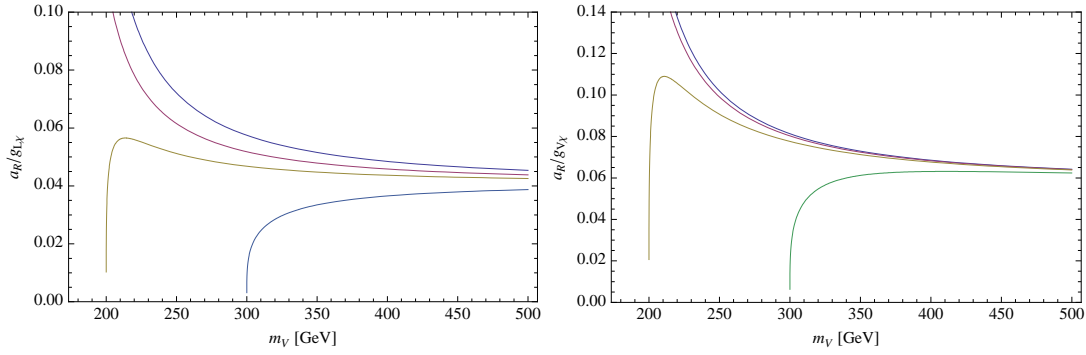
Figure 4.3: The necessary maximum coupling strength a of the mediator to quarks relative to the coupling strength to the DM candidates g_{L_χ} or g_{V_χ} depending on the mass of the vector mediator m_V resulting in a $V \to \chi\bar{\chi}$ branching fraction of 99% is shown. On the left-hand figure, a chiral coupling scenario ($g_{R_\chi} = 0$ or $g_{L_\chi} = 0$) is assumed whereas on the right-hand figure, a vector coupling scenario ($g_{L_\chi} = g_{R_\chi} = g_{V_\chi}$) is used. The four graphs correspond to four scenarios of DM masses m_χ. The values of the masses m_χ are 5, 75, 100 and 150 GeV corresponding to the colors dark blue, red, yellow and light blue. Taken from [128].

candidate combined in $\mathcal{L}_{\text{kin}}(\chi)$ is included as well. A leading-order Feynman diagram for the production of mono-top signatures is given on the right-hand side of Fig. 4.2.

Since the couplings to left-handed down-type quarks have been omitted, the mediator can only decay into two DM candidates or in reverse direction of the production process meaning $V \to t\bar{u}$ or $V \to \bar{t}u$. Depending on the mass hierarchy of the mediator and the top quark, different decays are predominant. Two scenarios can be distinguished. First, the mediator has more mass than the top quark ($m_V > m_t$), or second, the mediator is lighter than the top quark ($m_V < m_t$). The two cases will be explained in more detail in the following.

$m_V > m_t$:

The mediator can decay into a top quark and a light-flavor quark. Because of this, the mediator cannot be long-lived. This means that a missing transverse energy signature can only be obtained if the mediator decays invisibly into two DM candidates with a large branching fraction. For the invisible decay to be dominant under the assumption that none of the two decay modes is heavily suppressed by the kinematic phase space, the coupling strength to the quarks needs to be significantly lower than the coupling to the DM candidates.

This can be observed in Fig. 4.3 for two different coupling scenarios, a chiral coupling scenario and a vector coupling scenario. A chiral coupling implies that the left-handed and right-handed chiralities are not treated on equal footing by the interaction at hand. An example of a chiral interaction is the weak interaction of the SM, which only couples to left-handed fermions and right-handed antifermions. An interaction which couples with the same magnitude to left-handed and right-handed chiralities, often called a vector coupling scenario, is e.g. QCD. The curves corresponding to DM masses of 100 and 150 GeV show a large drop of the maximum coupling strength to quarks at 200 and 300 GeV. This happens because the phase space of the on-shell mediator to decay into two DM candidates becomes smaller the closer the mediator mass is to $2 \times m_V$. Therefore, the kinematic phase space

suppression of the DM decay channel has to be compensated by decreasing the coupling to the quarks in order to retain a predominant invisible branching ratio. Furthermore, the curves corresponding to m_χ of 5 and 75 GeV show a large increase of the maximum allowed coupling to quarks for lower masses of the mediator. This can be explained with the decrease of the allowed kinematic phase space for the decay channel into a top quark and a light quark. Since this channel then becomes suppressed by kinematics, the maximum coupling is allowed to increase. In addition, all four curves behave comparably for large mass values of the mediator. This is because the masses of the top quark and the DM candidates become less important for very high values of the mediator mass. This means that the impact of the decay kinematics decreases and only the relative coupling strength is relevant for the branching fraction. The differences between the two coupling scenarios only show a small impact on the shape and behavior of the curves. The vector scenario however shows higher values of the maximum allowed coupling to quarks compared to the chiral coupling scenario.

The measured DM relic abundance can be used to derive constraints on the allowed couplings to quarks and the DM candidates. Assuming that χ is stable and V is the only portal between the SM and the DM candidates, the only important process for the relic abundance is

$$\chi\bar{\chi} \to V \to t\bar{u}/\bar{t}u.$$

The rate for this process directly depends on the product of the coupling to quarks and the coupling to the DM candidates. Therefore, the measured relic abundance can be used to extract constraints on the product of these couplings. If this product becomes smaller, the annihilation rate decreases as well. The DM abundance consequently increases. This implies that with the currently measured abundance, it is possible to calculate a lower bound on the coupling product resulting in an abundance equal or smaller than the measured one. To do this, the relation

$$\Omega_{\text{DM}}h^2 \approx \frac{1.04 \cdot 10^9}{M_{\text{Pl}}} \frac{x_F}{\sqrt{g*}} \frac{1}{\langle \sigma v \rangle} \tag{4.3}$$

between the DM relic abundance Ω_{DM} and the mean annihilation cross section $\langle \sigma v \rangle$ can be used. Here, M_{Pl} refers to the Planck mass, $x_F = m_\chi/T_F$ to the ratio of the DM candidate mass and the freeze-out temperature $T_F \approx 25$ GeV of the DM candidates, and $g* = 92$ to the number of degrees of freedom at freeze-out. For more details, see [130].

The left-hand graph of Fig. 4.4 shows an example of coupling constraints derived from the DM relic abundance for a vectorial coupling model. In this example, the lowest considered DM mass is half of the top quark mass to kinematically allow the annihilation process shown above. Furthermore, $m_V \geq 2 \times m_\chi$ is required for a possible invisible decay channel. Towards the red line, with $2 \times m_\chi = m_V$, the lower bound on the coupling product needs to decrease since the annihiliation cross section increases close to the resonance. If the mass of the DM candidate m_χ becomes close to half of the top quark mass, the annihilation cross section decreases since the kinematic phase space for this process becomes smaller. This results in a higher relic abundance and therefore the lower bound on the coupling needs to increase to obtain the currently measured abundance or a smaller one to not be in conflict with observation.

It is also possible to combine the lower bounds derived of the relic abundance ($a \times g \geq Y$) with the upper bounds derived to ensure a large invisible branching fraction of the mediator ($a/g \leq X$), with X, Y being arbitrary bounds, to obtain a lower bound on the coupling of the mediator to the DM candidate. This is done on the right-hand side of Fig. 4.4. The
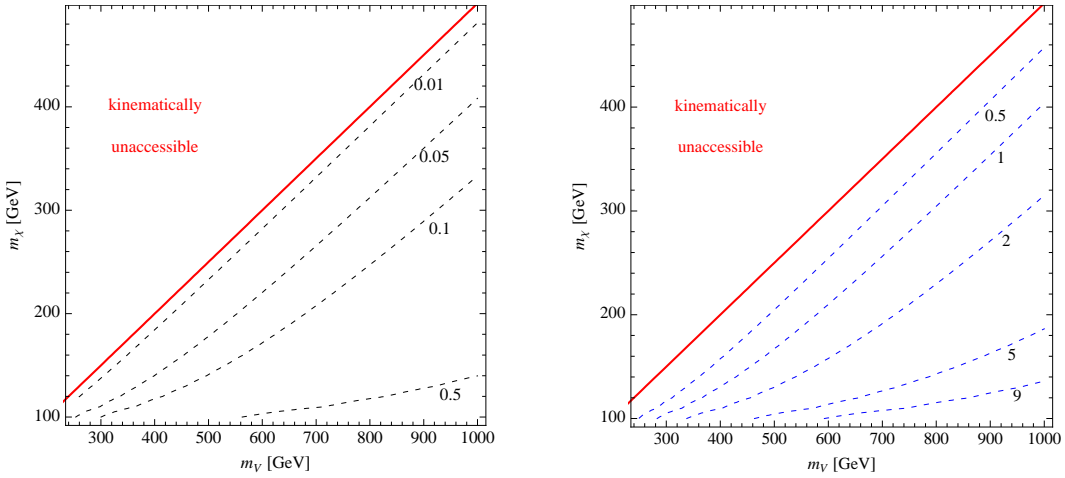
Figure 4.4: On the left-hand side, lower bounds on the product $a \times g_{V_\chi}$, derived from the measured DM relic abundance, are shown for a vector model ($g_{L_\chi} = g_{R_\chi} = g_{V_\chi}$) dependent on the mass of the DM candidate and the mediator mass. On the right-hand side, lower bounds on g_{V_χ} are shown after the DM relic abundance constraints are combined with the requirement of an invisible 99% branching fraction of the mediator ($V \to \chi\bar{\chi}$). Taken from [128].

lower bound on the coupling to the DM candidate increases for decreasing values of the DM mass.

Finally, constraints on the coupling to quarks can also be derived using mono-top collider searches in combination with DM relic abundance constraints. The collider searches commonly assume an invisible branching fraction of 100%. This has to be accounted for if general constraints on the quark couplings are derived from these searches. Due to the assumed 100% invisible branching fraction, the bound of a collider search (CS) $a^2 \leq a_{\mathrm{CS}}^2$ needs to be reinterpreted as

$$a^2 \times \frac{\Gamma_{\chi\chi}}{\Gamma_{\chi\chi} + \Gamma_{\mathrm{tu}}} \leq a_{\mathrm{CS}}^2 \tag{4.4}$$

to account for a non-vanishing $V \to tu$ branching fraction using the partial widths of V decaying into two DM candidates $\Gamma_{\chi\chi}$ and V decaying into a top quark and a light quark Γ_{tu}. Then, to incorporate the relic abundance bound involving the product of a and g, it is necessary to factor out of the partial widths $\Gamma_{\chi\chi}$ and Γ_{tu} the coupling g of V to χ and the coupling a of V to quarks. This yields

$$a^2 \times \frac{g^2 \Gamma'_{\chi\chi}}{g^2 \Gamma'_{\chi\chi} + a^2 \Gamma'_{\mathrm{tu}}} \leq a_{\mathrm{CS}}^2 \,. \tag{4.5}$$

Here, the coupling constant independent partial widths into DM candidates and quarks are represented by $\Gamma'_{\chi\chi}$ and Γ'_{tu}. Finally, by defining $k = a \times g$ as the product of the two different couplings, it is possible to include this product into the expression above. By doing this, the relic abundance bounds on this product can be directly included in the reinterpretation. This results in

$$a^2 \times \frac{(k^2/a^2)\Gamma'_{\chi\chi}}{(k^2/a^2)\Gamma'_{\chi\chi} + a^2 \Gamma'_{\mathrm{tu}}} \leq a_{\mathrm{CS}}^2 \tag{4.6}$$

under the assumption that χ is the only DM particle and makes up all of the DM relic abundance. Again, the lower bound on the coupling product from the DM relic abundance measurements mentioned above is represented by $k = a \times g \geq Y$. This relation can then be used to reinterpret limits obtained from a collider search under the requirement of the correct DM relic abundance.

$\mathbf{m_V} < \mathbf{m_t}$:

The mediator can only decay to quarks via a virtual top quark $V \rightarrow u\bar{b}W^-/\bar{u}bW^+$ due to energy-momentum conservation. If the mass of the mediator is smaller than the W boson mass, then the W boson is virtual as well. These states are called multibody final states and are suppressed by the virtuality of the involved top quark and/or W boson. Furthermore, loop-induced decays of the mediator become important in this regime. A decay into a dijet signature becomes possible through a W boson triangle loop into two down-type quarks. Without adding a decay into two invisible DM candidates, this scenario is a possibility for the mediator to be long-lived due to the strong suppression of all decay modes. However, the studies in [128] show that the lifetime is not long enough with a reasonable choice of parameters to obtain events with missing transverse energy due to a long-lived mediator.

Moreover, in the $m_V < m_t$ scenario the top quark can decay on tree-level via $t \rightarrow Vu$. A possible new decay channel of the top quark could be studied by measurements of the top quark width or by the analysis of top-quark-antiquark pair events. More information regarding the long-lived approach or the new possible decay channel of the top quark can be found in [128].

For a mono-top signal to be possible, a decay of the mediator into two DM candidates has to be added, leading to constraints from the DM relic abundance. Since the top quark is heavier than the mediator, the annihilation process $\chi\bar{\chi} \rightarrow V \rightarrow t\bar{u}$ is not possible. As was already explained, this means that only loop-suppressed or kinematically suppressed processes can contribute to the annihilation, leading to a rather small annihilation rate. This would consequently result in an overabundance of DM. Therefore, the mass regime $m_V < m_t$ is excluded by the observed dark matter density in the universe.

4.2.2 Scalar mediator

The scalar case is more complicated because it directly couples left-handed and right-handed quarks. Therefore, the scalar field cannot be an electroweak singlet but has to be a doublet consisting of a neutral and a charged component. Also, the DM candidate cannot be a singlet anymore but has to be a doublet again resulting in a charged and neutral component. Due to these complications, the scalar mediator model is not considered further in this thesis. For more details on this model, see [128] and the references therein.

4.3 Boosted objects and jet substructure

In this section, a short overview regarding boosted objects and the inner structure of jets is given based on [131–133]. First, the basics of jets are briefly introduced. Then, the specifics of jets in events with large transverse momentum transfer are explained. Finally, basics of the substructure of these jets are described.

4.3.1 Jet physics

As was described in section 2.1.1, quarks and gluons cannot exist as free particles due to the confinement property of QCD. If one of these elementary particles is created in the final state of a particle collision, quark-antiquark pairs from the vacuum are created around the original particle direction until a color-neutral final state is achieved. The final state after hadronization therefore consists of a collimated spray of particles around the direction of the original parton. To be able to combine theoretical calculations, which are performed using the partons of a collision, with experimental measurements, which can only measure the effects of physical particles in the detector, it is necessary to define a set of objects that can be used by experimental measurements as well as theoretical calculations. These objects are called jets and provide a correspondence between experiment and theory. Jets are defined by a clustering and combination procedure, which can be performed with experimental objects like calorimeter towers or particle-flow objects as well as with theoretical objects like partons.

A desirable property of a jet algorithm is infrared-safety and collinear-safety. This implies that the jets obtained with the algorithm do not change due to very low energy radiation or collinear QCD splitting. From a theoretical point of view, these features are helpful for perturbative calculations and from an experimental point of view, they provide a jet definition robust against noise and limited detector granularity.

The currently available jet algorithms can be classified into two types, cone algorithms and sequential recombination algorithms. Cone algorithms work by clustering all objects within a cone of fixed size. After the clustering, the four-momenta of all particles in the cone are summed to obtain the final jet. In contrast to that, sequential recombination algorithms cluster and recombine the objects one after another in a specific sequence depending on a distance measure until a stopping criterion is reached.

The jet algorithm used most commonly for analyses within the CMS experiment is called the anti-k_{T} (AK) algorithm [134]. This algorithm belongs to the sequential recombination class and relies on the following distance measure between two objects (d_{ij}) and on a reference measure for the stopping criterion ($d_{i,B}$).

$$d_{ij}(p_i, p_j) = \min(p_{\mathrm{T},i}^{2k}, p_{\mathrm{T},j}^{2k})\frac{\Delta R^2}{R^2} \text{ and } d_{i,B} = p_{\mathrm{T},i}^{2k} \tag{4.7}$$

with $\Delta R^2 = (\Delta\phi)^2 + (\Delta y)^2$ the squared distance between object i and j in the plane of the azimuthal angle ϕ and the rapidity y as well as $k = -1$ for the AK algorithm. The free parameter R is called the jet radius and is an approximate measure of the size of the jet in the aforementioned plane. The parameter k basically determines in what order the recombination is performed. As soon as $d_{i,B}$ is smaller than all other distances d_{ij}, object i will no longer be combined with other objects and is considered a final jet. For $k = 1$, the algorithm starts by clustering soft and collinear particles and is then known as the k_{T}-clustering algorithm [135]. In the case $k = 0$, the algorithm is called Cambridge-Aachen algorithm [136] and only uses the angular distance. Finally, the AK algorithm starts by clustering high-p_{T} objects first and fulfills the infrared-safety as well as the collinear-safety requirement. In addition, the shapes of the AK clustered jets are almost conical, providing, together with the jet radius, an intuitive idea of an AK jet. Most analyses within the CMS collaboration use AK jets with a jet radius of 0.4 (AK 4). However, in this thesis also very large jets with a radius of 1.5 are extensively used to cluster the decay products of a hadronic top quark decay into one jet. This jet is then studied using jet substructure techniques as well as machine learning methods to identify it as originating from a top quark. This is explained in more detail in the following sections.
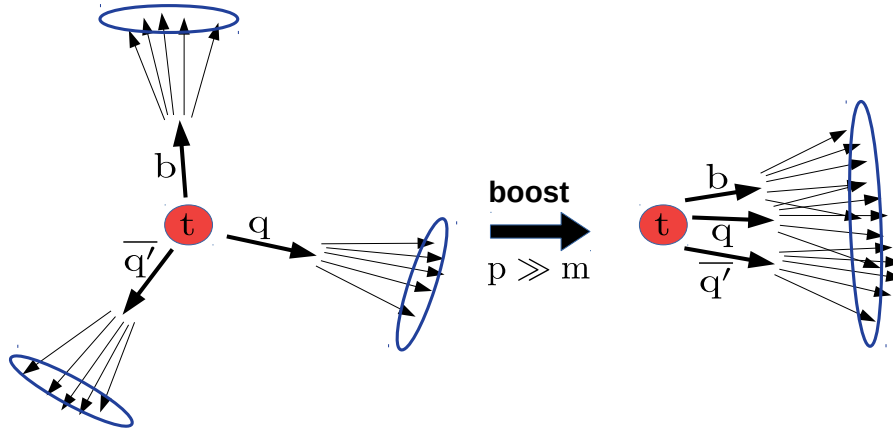
Figure 4.5: Graphical illustration of the hadronic top quark decay. On the left-hand side, the top quark decays in its rest frame. On the right-hand side, the top quark is heavily boosted leading to a collimation of its decay products. The blue circles are an illustration of possible jets clustered with a small jet radius on the left-hand side and a larger jet radius on the right-hand side.

Finally, the jets used in an experimental environment also have to be calibrated. This is required to account for detector effects as well as the underlying event and pileup. This is done by using the balance of a jet with a reference object which is measured very well, e.g. a Z boson reconstructed from two charged leptons.

4.3.2 Boosted objects

The term boosted object refers to a particle with a high momentum compared to its rest mass ($p \gg m$) in the laboratory frame. This implies that the decay products of a boosted object are collimated due to the Lorentz boost of the particle. This behavior is illustratively depicted in Fig. 4.5 in case of a hadronic top quark decay. For a two body decay, the approximate relation

$$\Delta R \approx \frac{2m}{p_{\mathrm{T}}} \tag{4.8}$$

holds with m being the mass of the original particle and p_{T} being its transverse momentum. If the particle is not boosted, the decay products do not overlap and the resulting sprays of hadrons are clustered into separate small radius jets, e.g. AK jets with a radius of 0.4. From these jets, the parent particle can be approximately reconstructed and identified using e.g. b-tagging requirements as well as mass constraints. This cannot be done in the boosted regime because the resulting jets strongly overlap. A possible solution to this problem is to increase the jet radius to cluster all decay products of the parent decay into a larger fat jet. Typical radii for these fat jets range from 0.8 for e.g. W bosons to 1.5 for e.g. top quarks. Using fat jets, however, also has disadvantages. Due to their larger radius, by construction, more contamination from the underlying event and pileup is clustered into the jets. Therefore, these effects are mitigated using pileup reduction techniques, e.g. CHS [137] or PUPPI [138]. The fat jets can be studied in a more detailed manner using jet substructure to identify whether the fat jet is a QCD jet, i.e. originated from a light quark or gluon, or if it is the result of the decay of a heavy resonance like the W/Z/Higgs boson or of the top quark decay. Furthermore, jet substructure techniques can help in removing soft contributions from pileup and the underlying event. Jet substructure is explained more thoroughly in the next section.

4.3.3 Jet substructure

Jet substructure deals with the inner structure of fat jets and how this structure can be used to distinguish different origins of jets, e.g. to discriminate between jets initiated by light quarks or gluons as well as to distinguish fat jets originating from the decay of a heavy resonance. These jet substructure algorithms exploit one or more of three properties that can be studied looking at the structure of fat jets. These are prongs, radiation patterns, and the contamination by soft and wide-angle radiation.

Prongs

Prongs refer to the number of hard cores inside a fat jet. If a heavy resonance decays, the momentum fraction distribution of the daughters is approximately flat leading in most cases to the same number of hard cores inside a fat jet as the number of decay products of the parent object. In contrast to this, quarks or gluons mostly radiate soft partons resulting in only one hard core. The algorithms searching for the number of prongs inside a jet are called prong finders.

Radiation patterns

The color structure of a color-charged state determines the radiation of soft gluons. For a color-neutral state decaying to two quarks, less soft gluon radiation occurs than in gluon-initiated or quark-initiated jets. This is exploited by jet shape variables like angularities [139], N-subjettiness [140, 141], and energy-correlation functions [142].

Soft contamination

As was already explained earlier, the jet area of fat jets is much larger and therefore the contamination due to pileup and the underlying event is larger. Algorithms designed to remove these contributions are called groomers. These algorithms remove soft radiation and wide-angle radiation from the fat jets since these forms of radiation are most probable to originate from pileup or the underlying event. Since soft radiation is removed by grooming, these algorithms help to improve the jet mass resolution, which is heavily affected by soft radiation. Because of this, the groomed jet mass is a better estimator of the mass of the original parton than the ungroomed jet mass. This can be exploited to distinguish QCD jets, which have a groomed jet mass closer to zero, from heavy-resonance-initiated fat jets, which have a groomed jet mass closer to the mass of the resonance.

Groomers and prong finders are related because both algorithms have the aim of working out the partonic structure of the fat jet. Common algorithms are the Mass-drop tagger [143, 144], SoftDrop [145, 146], Filtering [143], Trimming [147], and Pruning [148].

In the following, the grooming algorithm employed in this thesis, called the SoftDrop algorithm, is explained in more detail.

4.3.4 The SoftDrop algorithm

For the SoftDrop (SD) algorithm to work, the constituents of the jet at hand are reclustered using the Cambridge-Aachen algorithm. Then, the clustering sequence is reversed starting from the final Cambridge-Aachen jet. The idea behind this algorithm is to remove soft and wide-angle radiation during the declustering process. Therefore, the combination step of combining object i and j is studied using

$$\frac{\min\left(p_{\mathrm{T},i}, p_{\mathrm{T},j}\right)}{p_{\mathrm{T},i} + p_{\mathrm{T},j}} > z_{\mathrm{cut}}\left(\frac{\Delta R_{ij}}{R}\right)^{\beta} . \tag{4.9}$$

This relation is designed to compare the p_T of the softer object with the p_T of the combined object. If the two objects are significantly far apart compared to the jet radius (wide angle), the softer object is required to have a significant transverse momentum fraction of the combined object not to be recognized as a soft and wide-angle radiation. The parameter β controls how aggressive the algorithms works. For $\beta = 0$ the angular distance is not considered at all and only the momenta are important. For larger positive β values, the z_cut value is more and more suppressed with the angular distance ratio. On the contrary, for larger negative values of β, the algorithm becomes more aggressive and the z_cut is enhanced by the angular distance ratio. If the condition is not fulfilled, the softer of the two objects is rejected and the algorithm continues with the harder one. In case that the condition is fulfilled, the two objects are kept as the result of the algorithm. These objects are then referred to as SD subjets.

As is explained later in this thesis, the SD algorithm is applied to the AK15 jets used in this thesis to get a better estimator of their jet mass. Then, a cut is applied to this SD jet mass around the mass of the top quark to enrich fat jets originating from a top quark and suppress fat jets originating from generic QCD radiation.

4.3.5 Top-tagging and DeepAK15

The term top-tagging refers to a procedure that aims to discriminate fat jets originating from top quarks against fat jets originating from generic QCD radiation. Classical approaches use the methods introduced previously in this chapter, e.g. the number of prongs, the radiation patterns, or grooming. In order to enrich fat jets originating from top quarks, possible criteria could be:

- The jet shape is more compatible with three hard cores than two or one hard core. This can be done using for example ratios of the N-subjettiness variables.

- After removing soft radiation with e.g. the SD algorithm, the jet mass is required to be in a window around the top quark mass.

- One of the subjets obtained after running the SD algorithm has to be compatible with originating from a bottom quark. This requirement can be checked by running a b-tagging algorithm on the subjets.

Another approach to perform top-tagging, which has gained increasing popularity over the last years, is to apply methods from the field of machine learning for this task. In the CMS collaboration, a rather new algorithm to perform tagging of boosted fat jets, called DeepAK, has been developed [149–151]. This tagger is used in this thesis and is explained briefly in the following.

The DeepAK tagger is a deep neural network (DNN) designed to classify the origin of boosted jets. It distinguishes boosted jets originating from several heavy resonances, e.g. the top quark and the W/Z/H boson, and boosted jets originating from QCD radiation. In order to achieve this task, it is designed as a multi-class DNN with outputs corresponding to the different resonances or QCD radiation. The information used by this DNN are the properties of the PF candidates and of the reconstructed secondary vertices contained within the cone of the jets. The PF candidates contain kinematic information and additional information, e.g. the weights of the PUPPI [138] algorithm. In addition, properties of tracks associated to the charged candidates are exploited. Regarding the secondary vertices, kinematics and quality criteria are provided to the DNN. The general idea is that the PF candidates provide information about the substructure of the jet to the DNN, whereas the secondary vertices give information about the flavor structure.
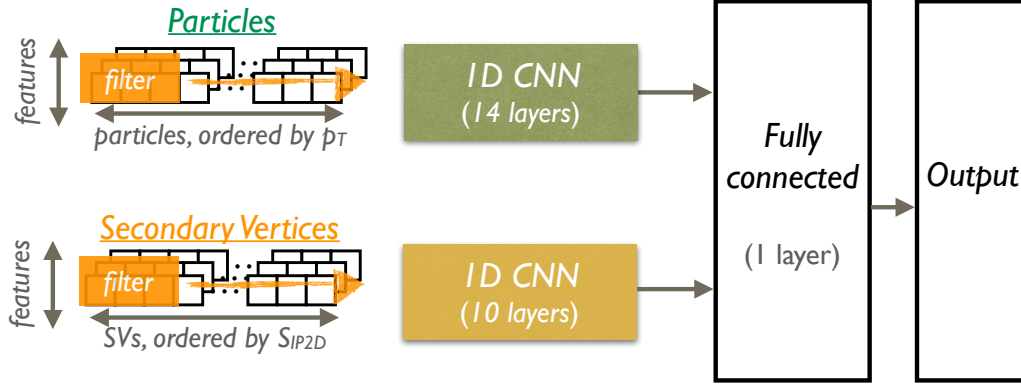
Figure 4.6: Graphical illustration of the architecture of the DeepAK tagger taken from [150].

The structure of the DNN is based on two convolutional neural networks (CNN) which outputs are combined by a fully-connected neural network. The two CNNs are designed to find effective features of the particles/vertices by doing a convolution over several particles/vertices and their properties. A graphical representation of the architecture is given in Fig. 4.6. The output consists of five categories (W, Z, H, Top, QCD) which are further divided according to the flavor of the decay products. For this thesis, only the Top and QCD categories are relevant. The Top (T) category is divided into the subclasses Tbcq, Tbqq, Tbc, and Tbq. The QCD category is subdivided into QCDbb, QCDcc, QCDb, QCDc, and QCDothers. These classes are defined using generator-level information and are used as training labels for the training of the network. For a fat jet to get a specific training label, the following generator particles are required to be found within a ΔR radius of 1.5 around the fat jet.

Top: Exactly one b quark originating from a top quark decay

> bcq: Exactly one c quark and exactly one light-flavor quark both originating from a W boson decay
>
> bqq: Exactly two light-flavor quarks both originating from a W boson decay
>
> bc: Exactly one c quark originating from a W boson decay and no other quark from a W boson decay.
>
> bq: Exactly one light-flavor quark originating from a W boson decay and no other quark from a W boson decay.

QCD: At least one gluon or one quark however not from the decay of a W/Z/H boson or top quark

> bb: Exactly two b quarks and no c quark
>
> bc: Exactly one b quark and exactly one c quark
>
> b: Exactly one b quark and no c quark
>
> c: Exactly one c quark and no b quark
>
> others: None of the above

For each subclass in each category, the DeepAK tagger provides a output number between 0 and 1 which can be interpreted as an probability. Higher values correspond to higher
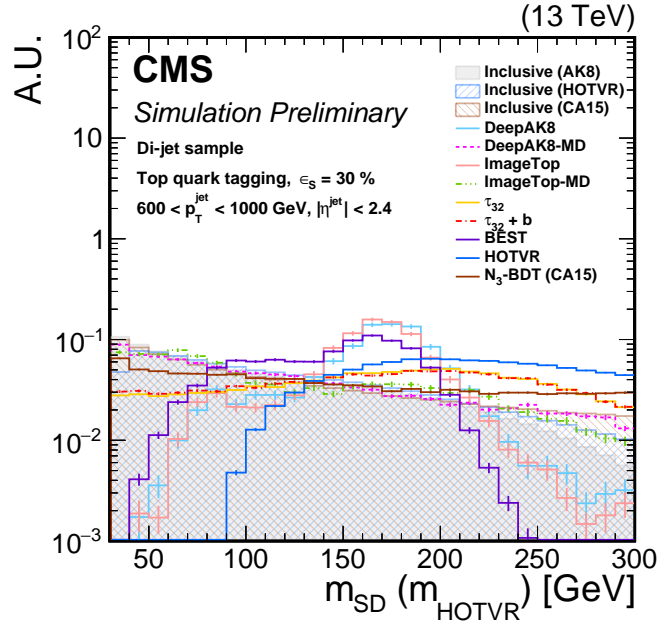
Figure 4.7: Distribution of the SD mass of several kinds of boosted jets after applying top-tagging with different tagging algorithms at a working point of 30% signal efficiency [150].

probabilities for the jet to belong to the predicted class. From these output classes, new taggers can be created or aggregated. In this thesis, a tagger composed of several Top subclasses and QCD subclasses is used to discriminate boosted jets originating from top quarks from QCD jets. This composite tagger has the form of a likelihood ratio and can be calculated for the respective jet as

$$D_{\text{TvsQCD}} = \frac{P(\text{Tbqq}) + P(\text{Tbcq})}{\left(\sum_{i=\text{QCD subclasses}} P(i)\right) + P(\text{Tbqq}) + P(\text{Tbcq})} \ . \tag{4.10}$$

This tagger compares the probabilities for the jet to originate from the two most important Top classes with the sum of the former probability and the probability to belong to one of the QCD classes.

One challenge involving a jet tagger learning a large number of features is the fact that some of these features are highly correlated with the jet mass. This results in the challenge that the distribution of the jet mass of events selected with such a tagger is significantly sculpted. This can be seen e.g. in Fig. 4.7 for a sample of QCD di-jet events. Several of the taggers, among them the DeepAK tagger, show that the distribution of the SD mass is significantly changed compared to the inclusive distributions. To address this behavior, a mass-decorrelated version of the DeepAK tagger is available. This version is trained such that it does not learn features which are highly correlated to the jet mass. This training procedure is called adversarial training [152]. The general principle of this method is to add an additional neural network called adversary that tries to predict the variable that the original classifier is not supposed to be correlated with. Then, a joint loss function containing the loss function of the original network and an additional loss function serving as a penalty term for the degree of correlation with this variable is introduced. This joint loss function is then minimized to simultaneously optimize the classification performance of the original network and to reduce the correlation with the desired variable, in this case the jet mass. A graphical illustration of this method is given in Fig. 4.8. As is presented
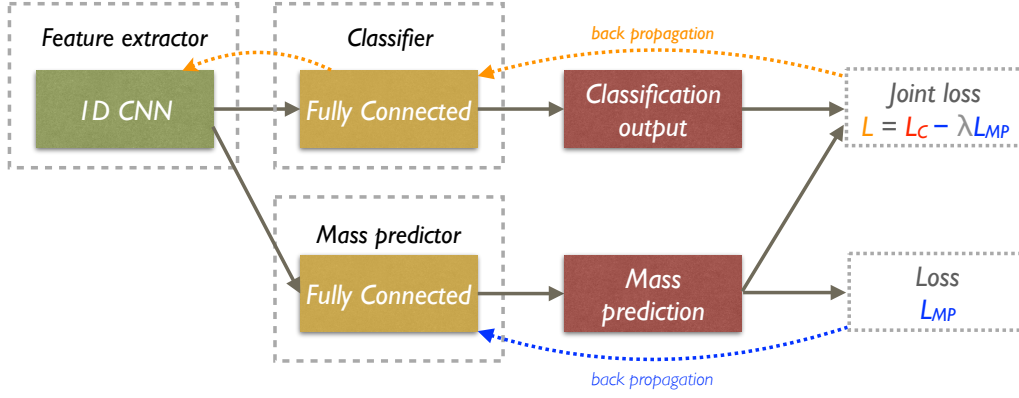
Figure 4.8: Graphical representation of the adversarial training used to decorrelate the
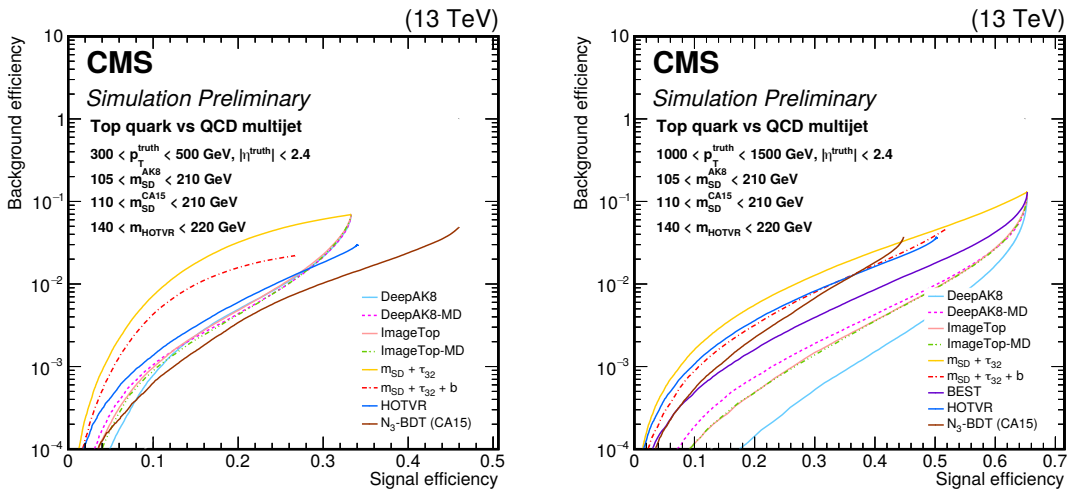DeepAK tagger from the jet mass [150].

Figure 4.9: Background efficiency over signal efficiency for two different regimes of the p_T
of the top quark evaluated for several top-tagging techniques [150].

in Fig. 4.7, the mass-decorrelated (MD) version significantly reduces the aforementioned
sculpting of the jet mass distribution. However, a loss of performance is expected after
adversarial training.

The performance of the DeepAK tagger on simulated events is shown in Fig. 4.9 compared to
other tagging techniques used in the CMS collaboration. Even after mass decorrelation, the
DeepAK algorithm has a significantly improved performance compared to the traditional
techniques of using cuts on the N-subjettiness ratio and the SD mass as well as using
b-tagging information from the subjets.

As was shown in this section, the DeepAK tagger offers significantly higher performance
than traditional techniques for top-tagging. Therefore, this tagger is used in this thesis.
However, the original version of this tagger, which is developed for AK jets with a radius
parameter of $R = 0.8$, is exchanged with a recent version developed for AK jets with
$R = 1.5$, which are used in thesis. The inputs to the tagger and its architecture for $R = 1.5$
AK jets are exactly the same as for the $R = 0.8$ version. In the following of this thesis, the
tagger is referred to as DeepAK15.

4.3.6 B-tagging and DeepJet

Although the tagging of jets originating from a bottom quark is not necessarily related to boosted event topologies, the technique used for this purpose in this thesis is explained in this section because it shares a lot of similarities to the top-tagging with the DeepAK15 algorithm.

The tagging of bottom jets relies on the comparably long lifetime of hadrons consisting of bottom quarks. This long lifetime is due to the suppressed CKM elements V_{ub} and V_{cb} which govern the decay of the bottom quark since the decay into a top quark is not possible because of the higher mass of the top quark. These CKM elements are on the off-diagonal of the CKM matrix and are significantly smaller than the V_{tb} element. Also, due to the high energy of LHC collisions, the resulting particles have a very large Lorentz boost. This results in a time dilation effect which increases the time of flight of these particles before decaying even more. Because of the aforementioned effects, hadrons containing a bottom quark are able to travel a much larger distance before decaying than other hadrons. This can be exploited by reconstructing the decay vertices of these more long-lived hadrons from the reconstructed tracks of their decay products. These secondary vertices and tracks, which do not originate from primary interaction vertices, and are found within a jet, can be used to gain information about the origin of the jet. More information regarding the tagging of heavy-flavor jets can be found e.g. in [153].

Comparable to the DeepAK15 algorithm, the DeepJet tagger [151, 154] is using a multivariate approach in shape of a complex neural network. A schematic of the neural network is given in Fig. 4.10. Inputs to the DeepJet neural network are several charged and neutral PF candidates with their respective properties which are used as input features for the network. Furthermore, a collection of secondary vertices and their properties are also given as input arguments. The neutral and charged PF candidates as well as the secondary vertices are processed separately by several convolutional layers making use of a varying number of 1×1 convolutions. In the next step, the outputs of these convolutional neural networks are passed to three separate long short-term memories (LSTM). The LSTM is a special implementation of a recurrent neural network (RNN). These networks are sensitive to the order of the inputs. Parallel to the processing of the PF candidates and the secondary vertices, several high-level jet variables are also used as input to the tagger. The outputs of the three RNN stages are combined with the global variables in a multi-layer dense network after the global variables were processed by one dense layer beforehand.

The DeepJet tagger has six output nodes which can be interpreted as measures of how certain the algorithm is that the jet at hand belongs to one of the six classes. The six classes are b, bb, lepb, c, l, and g and are designed to be sensitive to jets matched to the following generator particles.

   b: Exactly one B hadron decaying hadronically

 bb: At least two B hadrons

lepb: Exactly one B hadron decaying leptonically

   c: At least one C hadron and no B hadron

   l: None of the above with the hardest matched parton being a light-flavor quark (u, d, s)

   g: None of the above with the hardest matched parton being a gluon

For the decision whether a jet is identified as originating from a bottom quark, the sum of three output nodes is used as recommended by the CMS Collaboration [155–157].

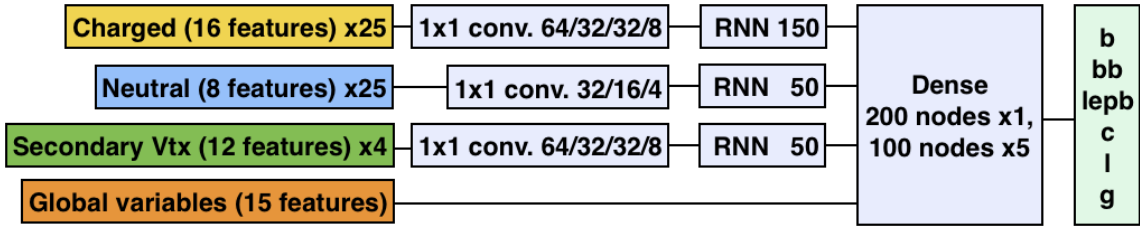$$\text{DeepJet b discrminant} = P(\text{b}) + P(\text{bb}) + P(\text{lepb}) \tag{4.11}$$

Figure 4.10: Schematic of the DeepJet tagger [154].

Here, $P(\mathrm{b})$, $P(\mathrm{bb})$, and $P(\mathrm{lepb})$ are the output values of the DeepJet tagger for the corresponding output nodes.

5 Mono-top analysis

The search for hadronic mono-top signatures is explained in detail in this chapter. First, the analysis strategy is motivated and explained. Next, generator studies are presented to validate the analysis strategy. Following the generator studies, the Monte Carlo simulation samples used to model the background and signal processes are introduced followed by the data recorded by the CMS detector. Consequently, corrections applied to the Monte Carlo simulation, necessary to obtain a satisfying agreement with recorded data, are explained. Special focus is put to corrections for events containing a single electroweak vector boson (Z, W, γ) in association with jets (V + jets). Next, the definitions of the physics objects used in this analysis are given. After the object definitions, the event selection implementing the analysis strategy is introduced. Afterwards, the statistical model used to extract information about the signal process from the recorded data is explained in detail. In the final section of this chapter, the results of this analysis are given and interpreted.

5.1 Analysis strategy

The analysis strategy to search for hadronic mono-top signatures is motivated and described in this section. As was explained in section 4.2, the final-state signature expected from mono-top events consists of missing transverse momentum and the signatures of the top quark decay, which can either happen leptonically or hadronically. The focus of this analysis lies on the hadronic decay channel of the top quark. The analysis strategy relies on the expectation that, for the mono-top models studied in this thesis, a large missing transverse momentum is expected due to the assumed high mass of the new hypothetical mediator, against which the top quark is recoiling, and its subsequent decay into two invisible DM candidates. In this section, the focus is put on the motivation for the analysis strategy. Specific selection requirements used to follow the analysis strategy are given later in the section on event selections.

The presence of large missing transverse momentum in conjunction with the hadronic decay of the top quark is the targeted signature. As was already explained in section 4.3, the decay products of highly boosted objects become collimated. This can be used to cluster the collimated products of the hadronization of the quarks of the hadronic top quark decay within a large radius jet. As was already mentioned, AK jets with a radius parameter of $R = 1.5$ are used for this purpose. Therefore, the expected basic event signature to search for these events is the existence of large missing transverse momentum back-to-back with
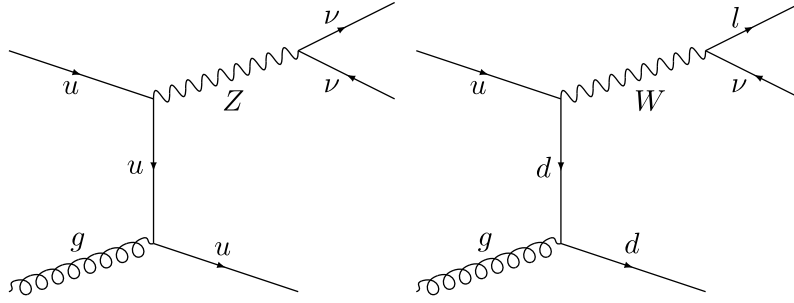
Figure 5.1: Left-hand side: Leading-order Feynman diagram for the production of a Z boson decaying into two neutrinos in association with additional jets. Right-hand side: Leading-order Feynman diagram for the production of a W boson decaying into a charged lepton and a neutrino in association with additional jets.

an AK15 jet, corresponding to the signature of the hadronic top quark decay, without any additional prompt leptons or photons present in the event. However, there are several SM processes with the same kinematic signature. These processes are briefly explained in the following.

The production of a Z boson subsequently decaying into two neutrinos which recoils against quarks or gluons from additional QCD radiation can produce $\vec{\not{E}}_T$ and an AK15 jet with large momentum. On the left-hand side of Fig. 5.1, a leading-order Feynman diagram of this process is given. Although the production of Z bosons with a large transverse momentum becomes highly suppressed, the total production cross section of several hundred pb (see Tab. 5.1) is much higher than the expected total cross section of the mono-top models (see Tab. 5.3) considered in this thesis. Moreover, this process is irreducible without any top/b-tagging techniques because the final-state signature is exactly the same as the mono-top signature from a detector perspective. Furthermore, there is no straightforward orthogonal control region in data that could be used to constrain this background. Therefore, this process is one of the most important background processes and has to be estimated with high precision.

Furthermore, the production of a W boson decaying into a charged lepton and a neutrino in association with additional jets can result in the aforementioned signature as well if the charged lepton, in case of electrons or muons, is not reconstructed, misidentified, or out of detector acceptance. A leading-order Feynman diagram corresponding to this process is shown on the right-hand side of Fig. 5.1. In case the charged lepton is a τ lepton decaying hadronically, this signature is also possible. In addition, the production of a W boson has a large cross section of a few thousand pb, although being heavily suppressed for high transverse momentum of the W boson (see Tab. 5.1), which results in a significant contribution to the targeted phase space despite the reconstruction inefficiency and the misidentification rate of leptons in the CMS detector being low.

In addition, the production of top-quark-antiquark pairs ($t\bar{t}$) is an important background as well. An example Feynman diagram for the production of a top-quark-antiquark pair is given on the left-hand side of Fig. 4.1. The total cross section of approximately $832\,\mathrm{pb}$ (see Tab. 5.1) is much higher than the cross section of any of the mono-top models considered. This background becomes very important as soon as top-tagging techniques are applied since the other background processes then become significantly reduced rendering production of top-quark-antiquark pairs a comparable background. However, only the semileptonic decay channel has a significant contribution to the targeted phase space. If one of the top quarks decays hadronically, resulting in a high-p_T AK15 jet, and the other top quark decays leptonically, while the charged lepton is again not detected or a hadronically

decaying τ lepton, the same signature is measured. The fully-hadronic decay channel of the top-quark-antiquark pair does not generate a significant amount of $\vec{\slashed{E}}_{\mathrm{T}}$ whereas the contribution of dileptonic $t\bar{t}$ events is suppressed because of the low probability that none of the two leptons is detected.

As was just explained, several SM backgrounds can result in the same detector signature as the mono-top process and in addition have much larger cross sections than the mono-top process even in the phase space of large missing transverse momentum and high-p_{T} jets. Consequently, in order to become sensitive to possible signals, it is essential to optimize the phase space of the search in a way to improve the relative contribution of the signal and the background towards the signal. Furthermore, it is necessary to estimate the background contributions with high precision to be able to distinguish a possible signal contribution from fluctuations of the background prediction within its uncertainties.

For further enhancement of signal relative to the background processes, top-tagging techniques are exploited. First, the mass of the AK15 jet after running the SD algorithm, see section 4.3.4, is used. As was described, jets originating from QCD activity have, on average, lower masses whereas jets originating from the top quark decay products center around the mass of the top quark. Therefore, a window around the mass of the top quark is used to reduce the contribution of the production of single electroweak vector bosons in association with jets (V + jets) and QCD multijet processes since the AK15 jets in these processes originate from QCD activity. Next, the DeepAK15 algorithm, see section 4.3.5, is employed to discriminate AK15 jets originating from top quarks against AK15 jets originating from generic QCD activity by making use of complementary information from the PF candidates and the reconstructed secondary vertices. This multivariate tagger helps to significantly reduce the amount of V + jets and QCD multijet contributions in the signal region as well. Both of these methods, however, do not significantly suppress backgrounds like the production of top-quark-antiquark pairs or the production of single top quarks. Therefore, after applying these selections, also $t\bar{t}$ events have a large contribution in the signal region despite the cross section of $t\bar{t}$ production being significantly smaller than for the V + jets processes.

Although the amount of SM background contributions to the signal region is now reduced by several orders of magnitude, the final result depends on how precise and reliable the prediction for the remaining SM background processes in this phase space is. In order to achieve a reliable high precision prediction, the results are based on two procedures. First, the Monte Carlo predictions used for the very important V + jets process are corrected to the latest theoretical calculations, see section 5.5.1. Second, a statistical model is employed that relates the contributions of the most important background processes in the signal region to similar processes in control regions of this analysis and thereby determines their contributions by exploiting information from recorded data. This twofold approach allows to combine the latest theoretical calculations with information from recorded data resulting in a precise and reliable background prediction in the signal region. The basis for this approach is explained in the following.

The analysis and the statistical model rely on a variable called the hadronic recoil $\vec{U}_{\mathrm{T}}$. This variable is closely related to the missing transverse momentum $\vec{\slashed{E}}_{\mathrm{T}}$ and is defined as

$$\vec{U}_{\mathrm{T}} = \vec{\slashed{E}}_{\mathrm{T}} + \sum_{i=\mathrm{e},\mu,\gamma} \vec{p}_i \;, \tag{5.1}$$

with the sum running only over prompt electrons, muons, and photons. The magnitude of $\vec{U}_{\mathrm{T}}$ is labeled as U_{T}. This variable can be motivated by trying to determine the distribution of the missing transverse momentum of Z + jets with $\mathrm{Z} \to \nu\bar{\nu}$ in the signal region where

no prompt leptons or photons are expected. In these events, missing transverse energy is basically the transverse momentum of the Z boson. Since there is no appropriate high-purity control region in data to enrich Z + jets events with $Z \to \nu\bar{\nu}$ which is also orthogonal to the signal region of this analysis, an alternative is to use Z + jets events with $Z \to l\bar{l}$ and $l = e, \mu$ while accounting for the different branching fractions of the Z boson as well as lepton reconstruction, identification, and trigger efficiencies. Such events can be enriched in data with high purity because of the clear signature of the Z boson mass peak which can be reconstructed from the charged leptons. In order to calculate the transverse momentum of the Z boson in Z + jets events with $Z \to l\bar{l}$ in a way comparable to how the transverse momentum of the Z boson is calculated for Z + jets events with $Z \to \nu\bar{\nu}$, which is done by calculating the missing transverse momentum, the hadronic recoil needs to be calculated. By calculating the hadronic recoil, as the name suggests, an approximate measure of the transverse momentum of all hadronic activity is obtained. In Z + jets events with $Z \to \nu\bar{\nu}$, the hadronic recoil is the missing transverse momentum and therefore an approximation of the transverse momentum of the Z boson. In Z + jets events with $Z \to l\bar{l}$, the hadronic recoil is a measure of the recoil of all hadronic activity against the Z boson and is therefore also an approximation of the transverse momentum of the Z boson. The same thought process can be applied to W + jets with $W \to l\nu$ and $\gamma +$ jets events to obtain the transverse momentum of the W boson and the photon whether the charged lepton and photon are reconstructed or not. For these processes, straightforward control regions can be constructed in data from which the transverse momentum of the bosons can be extracted by calculating the hadronic recoil. As these examples show, the hadronic recoil in events with prompt charged leptons or photons is the analogue to the missing transverse momentum in events in which these prompt leptons or photons are not detected or reconstructed.

By exploiting the hadronic recoil, a control region can be constructed for every important process in order to obtain a proxy of the distribution of the missing transverse momentum of this process in the signal region by means of determining the distribution of the hadronic recoil of this process in the control region. Then, by also considering experimental effects like reconstruction, identification, and trigger efficiencies as well as theoretical branching fractions, e.g. for $Z \to l\bar{l}$ and $Z \to \nu\bar{\nu}$, the aforementioned proxy can be converted to a real estimation of a process in the signal region by its corresponding process in the control region. Instead of doing this by hand for every relevant process, this approach is directly implemented into the statistical model of this analysis. This is done in the statistical model by directly connecting the different processes in the different regions by numbers called transfer factors. These transfer factors encode how the contributions of different processes in different analysis regions relate to one another. They encode the effects of the different phase spaces as well as experimental effects like reconstruction, identification, and trigger efficiencies. Furthermore, systematic uncertainties are implemented into the transfer factors as well. More details on these transfer factors and how exactly they are calculated and applied are given in section 5.8 on the statistical model of the analysis.

Using the signal region and the control regions connected by transfer factors, a flexible statistical model is built that extracts a possible signal contribution from the hadronic recoil distribution in the signal region while simultaneously estimating the major backgrounds from data in the control regions.

5.2 Generator studies

In this section, the main features of the mono-top model are studied from the point-of-view of an experimental particle physicist. The expectations used to develop the analysis strategy, which is explained in the previous section, are checked for their validity on

generator level. Therefore, several MC simulation samples implementing a concrete choice for the non-resonant mono-top model, see section 4.2, are studied in the context of their signature and properties at a collider like the LHC. This means that the process

$$pp \to tV \to t\chi\overline{\chi} \qquad (5.2)$$

is studied using the matrix element generator MADGRAPH5_AMC@NLO [18, 19]. The different models differ by the assumed mass of the mediator and the assumed mass of the DM candidates and are intended as representative examples covering a large part of the experimentally accessible phase space in order to design the analysis as general as possible. The exact choice of couplings of the vector mediator V to the SM quarks and the DM candidates is given in section 5.3. The studies are focused first on general kinematic features of the mono-top model. Then, the hadronic top quark decay is studied with respect to the clustering of the decay products.

5.2.1 General properties

Three different hierarchies regarding the relation between the mediator mass M_V and the DM mass M_χ are studied. The first scenario is the case in which the mediator is lighter than two times the DM candidate mass. This means that the mediator is only produced as a virtual state. This heavily suppresses the cross section for such models as can be seen in Tab. 5.3. The second mass hierarchy is defined by the mass of the mediator being two times the mass of the DM candidates. Therefore, the on-shell decay into the two DM candidates is possible and in the rest frame of the mediator, the two DM candidates are created at rest. In the third case, the mass of the mediator is larger than two times the DM candidate mass. This implies that the on-shell decay is possible as well and in the rest frame of the mediator, the two DM candidates have a non-vanishing momentum.

For the low mass range, simulation samples implementing a mono-top model with a mediator mass of 200 GeV and DM masses of 50 GeV, 100 GeV, and 150 GeV are used. In the intermediate mass range, samples containing mediators with a mass of 1000 GeV and DM masses of 150 GeV, 500 GeV, and 1000 GeV are studied. In order to study the mono-top model in the high mass range, a mediator mass of 2500 GeV and DM masses of 750 GeV, 1250 GeV, and 2000 GeV are used.

The distribution of the transverse momentum of the mediator V is shown in Fig. 5.2. The general shape of the distributions is quite similar in all regions. The distribution rises sharply for low transverse momenta of the mediator, then reaches a maximum between approximately 100 GeV and 200 GeV, and consequently falls off with increasing mediator p_T. As expected, for configurations with a lower mediator mass, the distributions fall off more quickly than for configurations with higher mediator masses. Consequently, these configurations have a larger relative contribution in the lower p_T range. For the same mediator masses, the distributions involving higher DM masses have, as expected, larger contributions in the high-p_T range. This effect is strongest for the off-shell configurations. The on-shell configurations for the same mediator masses have comparable distributions. The maximum transverse momenta reached by the mediators in the configurations used in this thesis are in the approximate range from 1.5 TeV to 2 TeV.

Next, the distributions of the transverse momenta of the individual DM candidates are studied in more detail. The corresponding distributions are given in Fig. 5.3. The three mass hierarchy regions each show different behavior. For the $M_V < 2 \cdot M_\chi$ region, the distributions are more stretched out over the p_T range and reach higher values of transverse momentum. This is due to the higher masses of the DM candidates that directly relate to higher p_T. In the $M_V = 2 \cdot M_\chi$ region, the peak of the distributions tends towards lower
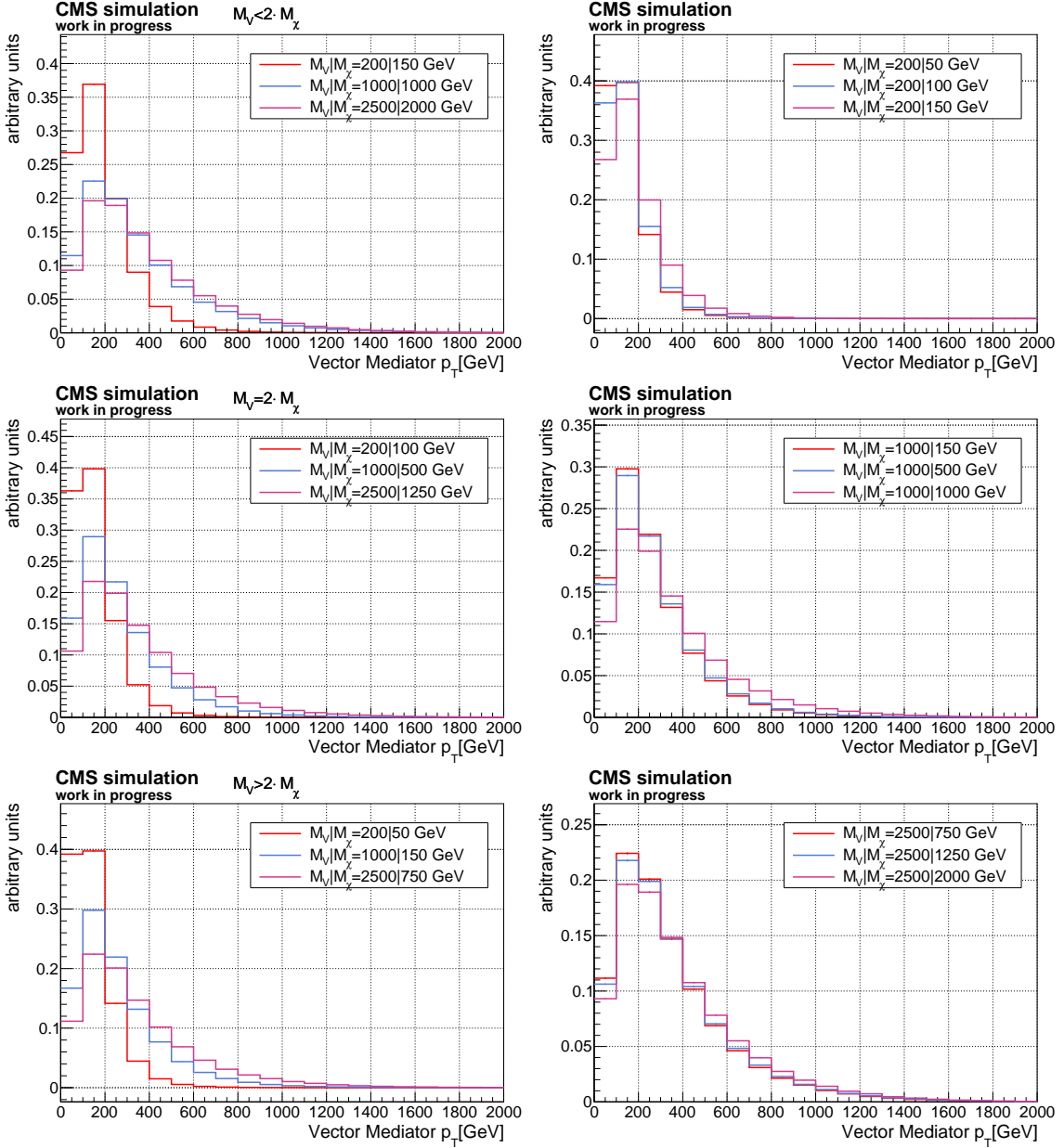
Figure 5.2: Distribution of the transverse momentum of the mediator V in mono-top models with different mediator and DM candidate (χ) masses, M_V and M_χ, respectively. In the left-hand column, the distributions are split according to the mass hierarchy of the mediator and the DM candidates. In the upper left-hand panel, the mediator mass is lower than two times the mass of the DM candidate. In the center left-hand panel, the mediator mass is two times the DM candidate mass. In the bottom left-hand panel, the mediator is heavier than two times the DM candidate mass. In the right-hand column, the distributions are split according to the mediator mass. All distributions are normalized to a yield of one event.

values and the decrease of the distributions after the peak is the steepest compared to the other two mass hierarchies. In this region, the energy contained in the mass of the mediator is completely turned into the energy needed for the mass of the two DM candidates. Therefore, the transverse momentum of the DM candidates is only driven by the boost of the mediator. Finally, in the $M_V > 2 \cdot M_\chi$ region, the samples with high mediator masses show an increase of the distribution over a larger range compared to the other two mass regions and peak positions at higher mediator p_T. This can be explained by the fact that the total energy contained in the mass of the mediator is not completely needed to create the two DM candidates. The energy that is left is turned into kinetic energy for the two DM candidates increasing their transverse momenta. The DM candidates of the mono-top models studied in this thesis reach transverse momenta of up to approximately 2 TeV.

In addition, the transverse momentum of the top quark is studied in Fig. 5.4. The expectation for this distribution, considering the final state of the mono-top signature, is that the top quark recoils against the mediator and therefore should be approximately similar to the distributions of the mediator p_T. The distributions show that this is mostly the case. However, due to the next-to-leading-order (NLO) QCD simulation and the involved parton shower, differences between the distributions can arise. Therefore, the p_T of the top quark and the mediator do not have to be exactly the same.

As a conclusion, the transverse momenta of the mediators in the mono-top models considered for this thesis are in the range of several hundred GeV even for the samples with the lowest mediator masses of 200 GeV and even much higher for models with larger masses involved. As was shown, the same holds for the transverse momenta of the top quarks. This validates the choice to aim at events with high missing transverse momentum and high-p_T top quarks. As the distributions in Fig. 5.2 and Fig. 5.4 show, at least a dominant part of the signal distribution is contained in the range of transverse momenta larger than 200 GeV. Although a significant part of the phase space is also in the low p_T range for the low mass samples, this region is not suitable for a search because SM background processes have an overwhelming contribution there. The final lower threshold applied to the missing transverse momentum and hadronic recoil is, as will be explained later, also driven by trigger efficiency requirements. Furthermore, at a top quark p_T threshold of approximately 200 GeV to 250 GeV, the decay products of the hadronic decay of the top quark start to be within a cone of radius 1.5 as is shown in the next section. This approximate range therefore is also motivated by the requirement to be able to cluster the decay products of the hadronic top quark decay within one AK15 jet.
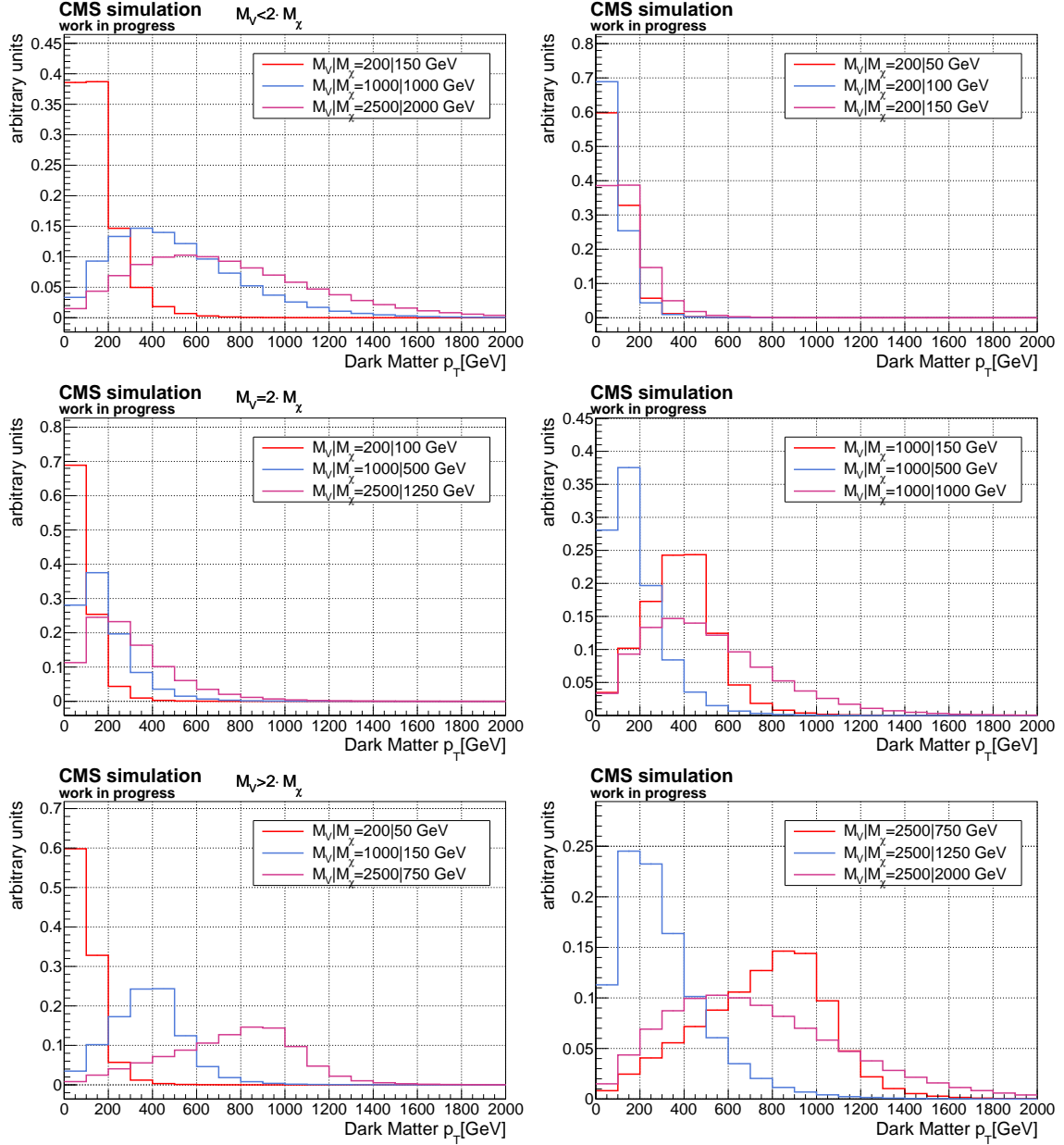
Figure 5.3: Distribution of the transverse momentum of the DM candidates in mono-top models with different mediator (V) and DM candidate (χ) masses, M_V and $M_χ$, respectively. In the left-hand column, the distributions are split according to the mass hierarchy of the mediator and the DM candidates. In the upper left-hand panel, the mediator mass is lower than two times the mass of the DM candidate. In the center left-hand panel, the mediator mass is two times the DM candidate mass. In the bottom left-hand panel, the mediator is heavier than two times the DM candidate mass. In the right-hand column, the distributions are split according to the mediator mass. All distributions are normalized to a yield of one event.
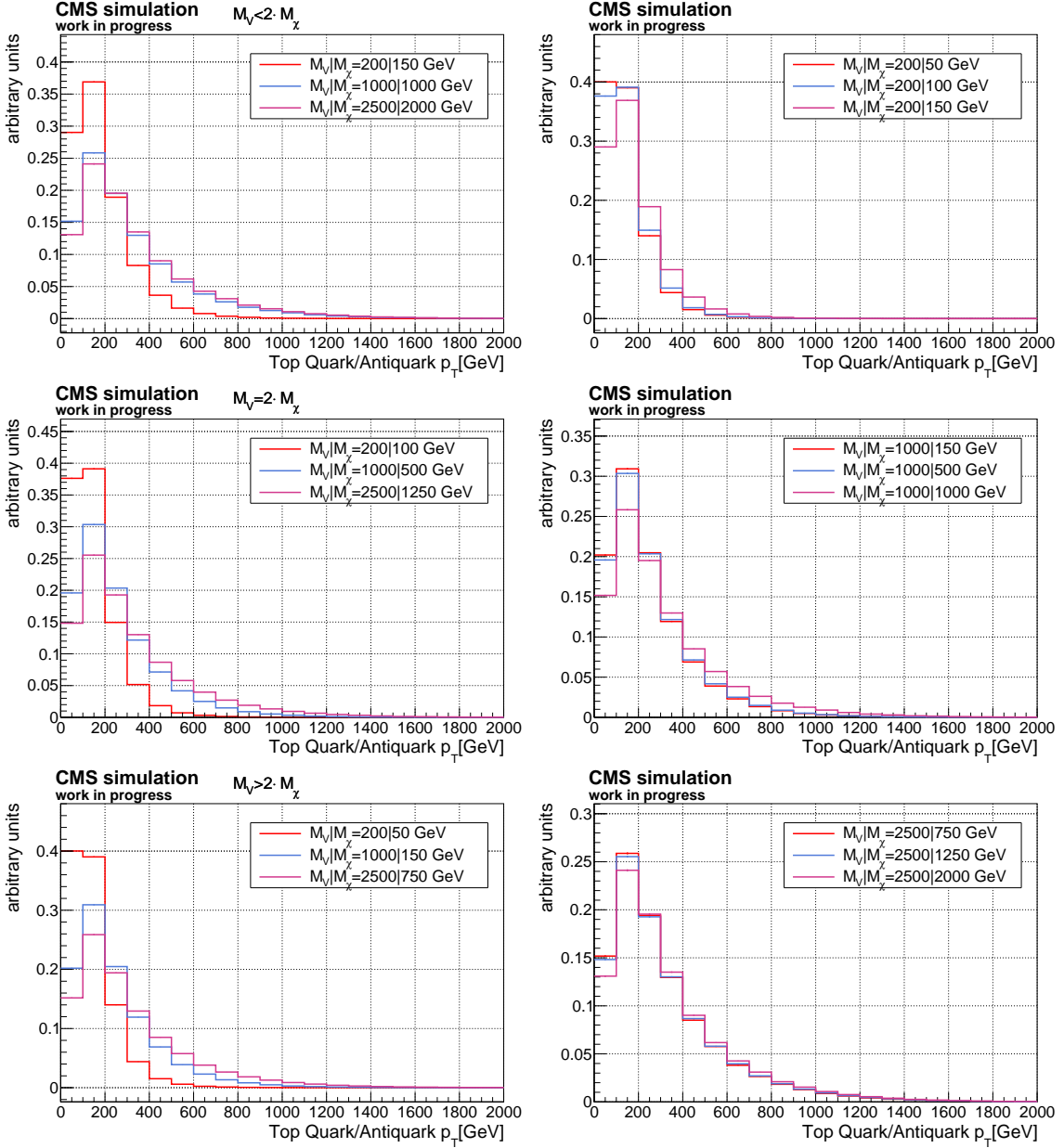
Figure 5.4: Distribution of the transverse momentum of the top (anti-)quark in mono-top models with different mediator (V) and DM candidate (χ) masses, M_V and M_χ, respectively. In the left-hand column, the distributions are split according to the mass hierarchy of the mediator and the DM candidates. In the upper left-hand panel, the mediator mass is lower than two times the mass of the DM candidate. In the center left-hand panel, the mediator mass is two times the DM candidate mass. In the bottom left-hand panel, the mediator is heavier than two times the DM candidate mass. In the right-hand column, the distributions are split according to the mediator mass. All distributions are normalized to a yield of one event.
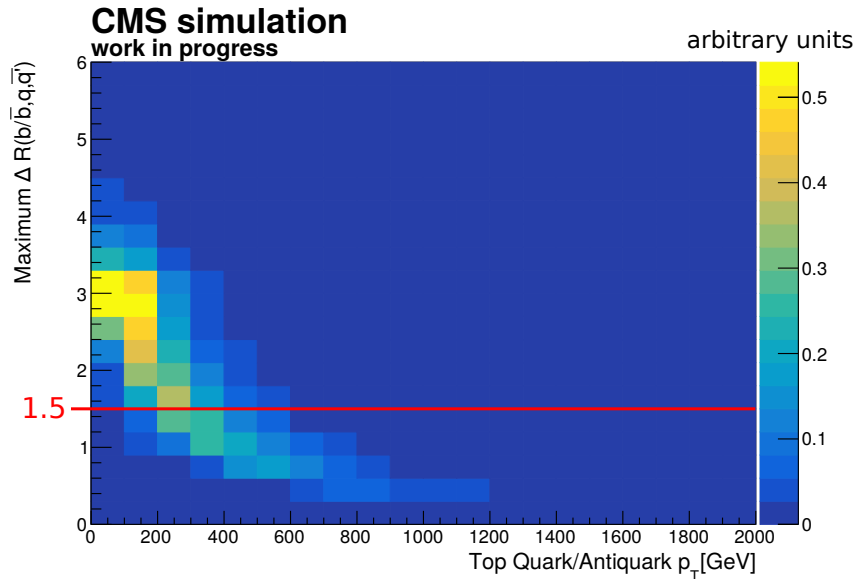
Figure 5.5: Two-dimensional distribution of the transverse momentum of the top quark and the maximum ΔR distance between any two of the three decay products of the top quark.

5.2.2 Hadronic top quark decay

As already mentioned several times, the plan for this analysis is to cluster the particles resulting from the hadronic top quark decay into one large jet with a radius parameter of 1.5. Therefore, the relation between the p_T of the top quark and the ΔR distance between the top quark decay products is studied. In Fig. 5.5, this relation is presented as a two-dimensional distribution. It is clearly observed that for increasing transverse momentum of the top quark, the maximum ΔR between all pairs of the three top quark decay products is decreasing. Moreover, it can be noted that starting from 200 GeV to 250 GeV transverse momentum of the top quark, the decay products start to lie within a ΔR distance of 1.5 allowing to cluster the major part of the resulting spray of particles in a jet with radius parameter of 1.5. Since the hadronic recoil in hadronic mono-top events is mainly driven by the top quark, this confirms the aforementioned range of 200 GeV to 250 GeV as a lower threshold for the hadronic recoil.

More studies regarding the reconstruction of hadronically decaying top quarks with AK jets using jet radius of 1.5 can be found in [158]. This bachelor thesis was advised within the scope of the analysis described in this thesis. In this bachelor thesis, studies were performed evaluating the benefit of using AK jets with jet radius 1.5 compared to a jet radius of 0.8, which is the standard jet radius for fat jets within the CMS collaboration. As a conclusion of this work, it was found that significantly more top quarks can be reconstructed using jets with radius parameter 1.5 instead of 0.8.

5.3 Simulation samples

In the following, information about the simulation of the relevant background processes as well as the simulated signal processes is provided.

Production of a single electroweak vector boson in association with jets

One of the most important backgrounds is the production of a single electroweak vector boson (W, Z, γ) in association with additional jets (V + jets) as was already explained in

section 5.1. The hard process of these simulated V+jets events is generated at leading-order QCD with the ME generator MADGRAPH5 [18, 19] with up to four additional partons in the final state of the matrix element. Furthermore, the events are generated split into bins of the scalar sum of the transverse momenta of all the jets on parton level (H_T). This ensures a sufficiently large number of events in the range of high transverse momenta of the vector boson.

For Z + jets production, the decays $Z \rightarrow \nu\overline{\nu}$ and $Z \rightarrow l\overline{l}$ are considered with ν representing all known neutrino flavors and $l = e, \mu, \tau$ representing all charged lepton flavors. The process $Z \rightarrow \nu\overline{\nu}$ is a major background in the signal region of this analysis and $Z \rightarrow l\overline{l}$ is a major process in one of the control regions. The decay of Z bosons into quarks is negligible in all regions of this analysis since no significant missing transverse momentum or hadronic recoil is present in such events. The simulated Z + jets events which decay into charged leptons originate from simulations of the Drell-Yan process. Therefore, these events have a lower threshold on the invariant mass of the two charged leptons of 50 GeV to enrich the production of Z bosons over the production of two leptons via virtual photons.

For W + jets production, only the decay $W \rightarrow l\overline{\nu}$ is considered because the contributions of the hadronic W boson decay in the signal and control regions of this analysis are negligible since neither leptons are found nor significant missing transverse momentum.

The γ + jets process is required to have an on-shell prompt final-state photon and is a major process in the photon control region of this analysis. For the final results of this analysis, samples at next-to-leading-order QCD perturbation theory are used in the 2017 and 2018 data eras. The samples are split by the transverse momentum of the generated photon $p_{T,\gamma}$ and reach a better agreement with data in the γ + jets control regions compared to the γ + jets samples split by H_T, which were described above. This was found in the studies described in section 5.5.1. In the 2016 data era, the aforementioned γ + jets samples at higher-order perturbation theory are not available. Therefore, in this data era the leading-order γ + jets samples split by H_T are used.

Top-quark-antiquark pair ($t\overline{t}$) and single top-quark production

The production of $t\overline{t}$ as well as of single top quarks (except for s-channel production) is performed at NLO QCD accuracy with the ME generator POWHEG [159–161] with up to two additional jets. The $t\overline{t}$ events [162, 163] are generated separately for the three different decay modes of the $t\overline{t}$ system. The single top quark events are generated according to the three different production channels (s-channel, t-channel [164], tW-channel [165]). The s-channel production of single top quark events is simulated with MADGRAPH5_AMC@NLO. In the simulation of single top quark events, the top quark can either decay in the hadronic channel or the leptonic channel.

QCD multijet production

QCD multijet production is simulated by MADGRAPH5 [18, 19] at leading-order QCD with up to four partons in the final state.

Diboson production

The production of two weak interaction bosons WW, WZ, ZZ is simulated with PYTHIA 8.2 [166–168]. The weak interaction bosons can either decay in the leptonic or hadronic channels.

Non-resonant vector mono-top production

The non-resonant mono-top production via a vector mediator V, see section 4.2, is simulated by MADGRAPH5_AMC@NLO [18, 19] at next-to-leading-order QCD using the DMsimp model [169, 170] of the FeynRules package [171]. Different samples with different mediator and DM masses are generated, see Tab. 5.3. The coupling of the hypothetical mediator V is chosen to be purely vectorial to the DM candidates as well as to the SM quarks. The magnitude of the coupling constant to the quarks and the DM candidates is chosen to be $g_{V,q} = 0.25$ and $g_{V,\chi} = 1.0$, respectively. All couplings involving flavor-diagonal interactions as well as second generation quarks are set to zero. The specific choice for these coupling values follows the recommendations of the LHC Dark Matter Working Group [172].

For all simulation samples explained above, the fragmentation and hadronization is performed with PYTHIA 8.2 [166–168]. The simulation of the CMS detector is performed with the software package GEANT4 [173–175].

In Tab. 5.1 and 5.2, all background samples which were processed for this thesis are listed together with the number of simulated events. In addition, cross sections are provided for the different processes. If there is no additional reference given for a cross section, it is the value predicted by the simulation sample. Otherwise, a theoretical cross section with better accuracy is available, used, and cited in the table. The complete grid of signal samples with different mediator and DM candidate masses is given in Tab. 5.3. The cross sections of the signal samples are taken as calculated by the MC simulation.

For the V+jets samples, the cross sections given by the generator are used at first. However, since the corresponding processes are among the most important backgrounds for this analysis and they are generated at leading-order accuracy, a dedicated correction is derived and applied, which significantly improves their modeling. This will be explained in section 5.5. The cross sections for the production of $t\bar{t}$ and single top quarks are theoretical cross sections at NNLO QCD accuracy. The cross sections regarding the diboson processes are theoretical cross sections at NNLO QCD accuracy as well. The cross sections for the QCD multijet process is taken from the generator.

Simulation samples are produced within the CMS collaboration in campaigns. These campaigns define the settings and conditions used for the production of simulation samples. In this thesis, simulation samples generated in three different campaigns are used. For each year of data taking, there is a dedicated simulation campaign to be able to compare data recorded in the respective year with MC simulation. In Tab. 5.4, the three campaigns are given. As already mentioned, for all simulation samples in this thesis, fragmentation and hadronization is performed by PYTHIA 8.2. However, for the 2016 MC era, the parton shower tune is different than for 2017/2018 except for the $t\bar{t}$ and single top simulation samples which are also available in the 2016 campaign with the same tune as for the 2017/2018 campaigns. The two parton shower tunes are also given in Tab. 5.4. In addition, several data tiers are available. A data tier defines how much information is contained in the samples. For this thesis, the data tier called MINIAOD [184] is used. This format only contains compressed high-level objects like leptons, photons, jets, and $\vec{\not{E}}_T$ for direct use within an analysis. Furthermore, particle-flow candidates are saved in a reduced format and trigger information is contained as well. Finally, a reduced set of generated particles is included.

Finally, a global tag is used to describe the conditions and calibrations of the CMS detector in simulation. If calibrations or conditions change, a new global tag is created and can be applied to the analysis to incorporate these changes. For the results of this thesis, the global tags used during the processing of the simulation samples are given in Tab. 5.5. The software release used to process the simulation samples is `CMSSW_10_2_18` [185].

Table 5.1: Vector boson plus additional jets simulation samples used in this thesis split according to the physical process. The first column describes the phase space of the sample in more detail. The second column shows the cross section predicted by the MC sample split according to the MC era. In the third column, the number of events contained in the MC sample is given split according to the MC era.

| Phase space | Process | | | | | |
| | Cross section [pb] | | | Number of events | | |
	2018	2017	2016	2018	2017	2016
Z + jets with $Z \to \nu\bar{\nu}$						
$100 \leq H_{\mathrm{T}}\,[\mathrm{GeV}] < 200$	3.03×10^2	3.05×10^2	9.36×10^1	23,702,894	22,737,266	24,272,858
$200 \leq H_{\mathrm{T}}\,[\mathrm{GeV}] < 400$	9.17×10^1	9.19×10^1	2.59×10^1	23,276,346	21,675,916	24,761,211
$400 \leq H_{\mathrm{T}}\,[\mathrm{GeV}] < 600$	1.31×10^1	1.31×10^1	3.59	9,511,100	9,542,035	9,862,869
$600 \leq H_{\mathrm{T}}\,[\mathrm{GeV}] < 800$	3.25	3.26	8.57×10^{-1}	5,748,975	5,649,241	5,766,322
$800 \leq H_{\mathrm{T}}\,[\mathrm{GeV}] < 1200$	1.50	1.50	3.93×10^{-1}	2,066,798	2,058,077	2,170,137
$1200 \leq H_{\mathrm{T}}\,[\mathrm{GeV}] < 2500$	3.43×10^{-1}	3.43×10^{-1}	9.55×10^{-2}	343,198	340,873	513,471
$2500 \leq H_{\mathrm{T}}\,[\mathrm{GeV}] < \infty$	5.27×10^{-3}	5.15×10^{-3}	2.30×10^{-3}	359,639	6,734	405,030
Z + jets with $Z \to l\bar{l}$						
$70 \leq H_{\mathrm{T}}\,[\mathrm{GeV}] < 100$	1.47×10^2	1.47×10^2	1.70×10^2	10,019,684	9,344,037	9,691,660
$100 \leq H_{\mathrm{T}}\,[\mathrm{GeV}] < 200$	1.61×10^2	1.61×10^2	1.49×10^2	11,530,510	11,197,488	11,017,086
$200 \leq H_{\mathrm{T}}\,[\mathrm{GeV}] < 400$	4.86×10^1	4.86×10^1	4.09×10^1	11,225,887	10,728,447	9,609,137
$400 \leq H_{\mathrm{T}}\,[\mathrm{GeV}] < 600$	6.98	6.99	5.68	9,697,098	10,219,524	9,725,661
$600 \leq H_{\mathrm{T}}\,[\mathrm{GeV}] < 800$	1.76	1.74	1.36	8,862,104	8,743,640	8,292,957
$800 \leq H_{\mathrm{T}}\,[\mathrm{GeV}] < 1200$	8.09×10^{-1}	8.04×10^{-1}	6.24×10^{-1}	3,138,129	3,114,980	2,673,066
$1200 \leq H_{\mathrm{T}}\,[\mathrm{GeV}] < 2500$	1.93×10^{-1}	1.93×10^{-1}	1.51×10^{-1}	536,416	625,517	596,079
$2500 \leq H_{\mathrm{T}}\,[\mathrm{GeV}] < \infty$	3.51×10^{-3}	3.48×10^{-3}	3.66×10^{-3}	427,051	419,308	399,492
W + jets with $W \to l\bar{\nu}$						
$70 \leq H_{\mathrm{T}}\,[\mathrm{GeV}] < 100$	1.29×10^3	1.29×10^3	1.35×10^3	28,084,244	22,255,124	10,020,533
$100 \leq H_{\mathrm{T}}\,[\mathrm{GeV}] < 200$	1.39×10^3	1.40×10^3	1.35×10^3	29,521,158	35,862,893	78,043,017
$200 \leq H_{\mathrm{T}}\,[\mathrm{GeV}] < 400$	4.10×10^2	4.09×10^2	3.59×10^2	25,468,933	21,250,517	38,984,322
$400 \leq H_{\mathrm{T}}\,[\mathrm{GeV}] < 600$	5.79×10^1	5.79×10^1	4.90×10^1	5,932,701	14,313,274	7,759,701
$600 \leq H_{\mathrm{T}}\,[\mathrm{GeV}] < 800$	1.30×10^1	1.29×10^1	1.21×10^1	19,771,294	21,709,087	18,687,480
$800 \leq H_{\mathrm{T}}\,[\mathrm{GeV}] < 1200$	5.45	5.40	5.49	8,402,687	20,432,728	7,830,536
$1200 \leq H_{\mathrm{T}}\,[\mathrm{GeV}] < 2500$	1.08	1.08	1.33	7,633,949	20,258,624	6,872,441
$2500 \leq H_{\mathrm{T}}\,[\mathrm{GeV}] < \infty$	8.06×10^{-3}	8.05×10^{-3}	3.22×10^{-2}	3,273,980	21,495,421	2,637,821
γ + jets (H_{T})						
$40 \leq H_{\mathrm{T}}\,[\mathrm{GeV}] < 100$	1.86×10^4	1.86×10^4	2.08×10^4	9,371,355	4,754,796	9,326,139
$100 \leq H_{\mathrm{T}}\,[\mathrm{GeV}] < 200$	8.60×10^3	8.63×10^3	9.24×10^3	9,798,176	9,912,980	10,104,155
$200 \leq H_{\mathrm{T}}\,[\mathrm{GeV}] < 400$	2.19×10^3	2.20×10^3	2.30×10^3	19,062,809	10,231,017	20,527,506
$400 \leq H_{\mathrm{T}}\,[\mathrm{GeV}] < 600$	2.58×10^2	2.59×10^2	2.75×10^2	4,655,985	4,646,958	5,060,070
$600 \leq H_{\mathrm{T}}\,[\mathrm{GeV}] < \infty$	8.49×10^1	8.52×10^1	9.35×10^1	4,981,121	3,289,629	5,080,857
γ + jets $(p_{\mathrm{T},\gamma})$						
$100 \leq p_{\mathrm{T},\gamma}\,[\mathrm{GeV}] < 250$	1.18×10^3	1.18×10^3	-	13,598,404	16,221,540	-
$250 \leq p_{\mathrm{T},\gamma}\,[\mathrm{GeV}] < 400$	2.58×10^1	2.58×10^1	-	8,226,000	7,535,790	-
$400 \leq p_{\mathrm{T},\gamma}\,[\mathrm{GeV}] < 650$	3.15	3.15	-	17,171,322	9,469,410	-
$650 \leq p_{\mathrm{T},\gamma}\,[\mathrm{GeV}] < \infty$	2.89×10^{-1}	2.89×10^{-1}	-	1,150,600	4,051,500	-

Table 5.2: MC simulation samples used in this thesis split according to the physical process. The first column describes the phase space of the sample in more detail. The second column shows the cross section. In the third column, the number of events contained in the MC sample is given.

Phase space	Process Cross section [pb]	Number of events 2018	2017	2016
$t\bar{t}$ [176, 177]				
hadronic	3.78×10^2	133,808,000	130,262,440	68,518,800
semileptonic	3.65×10^2	101,550,000	110,085,096	107,604,800
dileptonic	8.83×10^1	64,310,000	69,155,808	67,860,400
Single top [178–180]				
s-channel hadronic	6.96	9,706,000	9,652,000	4,876,400
s-channel leptonic	3.36	19,952,000	9,914,948	9,842,599
t-channel top	1.36×10^2	154,307,600	122,688,200	31,848,000
t-channel antitop	8.10×10^1	79,090,800	64,818,800	17,780,700
tW-channel top	3.59×10^1	9,598,000	7,945,242	4,983,500
tW-channel antitop	3.59×10^1	7,623,000	7,745,276	4,980,600
Diboson [181–183]				
WW	1.19×10^2	7,958,000	7,765,828	7,982,180
WZ	4.67×10^1	3,893,000	3,928,630	3,997,571
ZZ	1.69×10^1	1,979,000	1,925,931	1,988,098
QCD				
$50 \leq H_{\mathrm{T}}\,[\mathrm{GeV}] < 100$	1.85×10^8	38,754,230	40,456,172	4,180,469
$100 \leq H_{\mathrm{T}}\,[\mathrm{GeV}] < 200$	2.80×10^7	93,972,378	93,231,801	82,293,477
$200 \leq H_{\mathrm{T}}\,[\mathrm{GeV}] < 300$	1.71×10^6	54,289,442	59,427,619	38,857,977
$300 \leq H_{\mathrm{T}}\,[\mathrm{GeV}] < 500$	3.48×10^5	54,661,579	59,569,132	54,552,852
$500 \leq H_{\mathrm{T}}\,[\mathrm{GeV}] < 700$	3.21×10^4	55,152,960	56,207,744	62,622,029
$700 \leq H_{\mathrm{T}}\,[\mathrm{GeV}] < 1000$	6.83×10^3	48,158,738	46,840,955	37,233,786
$1000 \leq H_{\mathrm{T}}\,[\mathrm{GeV}] < 1500$	1.21×10^3	15,466,225	16,882,838	15,210,939
$1500 \leq H_{\mathrm{T}}\,[\mathrm{GeV}] < 2000$	1.20×10^2	10,955,087	11,634,434	11,839,357
$2000 \leq H_{\mathrm{T}}\,[\mathrm{GeV}] < \infty$	2.52×10^1	5,475,677	5,941,306	6,019,541

Table 5.3: Non-resonant mono-top signal samples split according to the mass of the mediator M_V and the mass of the DM candidates M_χ. The cross section as well as the number of generated events are provided. A purely vectorial coupling of V to the DM candidates as well as to the SM quarks is assumed. The magnitude of the coupling constant to the quarks and the DM candidates is chosen to be $g_{V,q} = 0.25$ and $g_{V,\chi} = 1.0$, respectively. All couplings involving flavor-diagonal interactions as well as second generation quarks are set to zero.

M_V [GeV]	M_χ [GeV]	Cross section [pb]	Number of events		
			2018	2017	2016
200	50	5.82×10^1	2,937,000	2,789,000	2,963,200
195	100	4.96	2,900,000	2,976,000	2,967,200
200	150	2.49×10^{-1}	2,993,000	2,935,000	2,996,400
300	100	1.89×10^1	2,936,000	2,868,000	2,857,599
295	150	2.35	2,888,000	2,979,000	3,000,000
300	300	1.79×10^{-2}	2,898,000	2,600,000	2,995,000
500	150	4.20	2,952,000	2,988,000	2,991,700
495	250	6.81×10^{-1}	2,952,000	3,000,000	3,000,000
500	500	2.07×10^{-3}	2,529,000	2,735,000	2,998,300
1000	150	3.48×10^{-1}	2,973,000	2,901,999	2,929,200
995	500	6.61×10^{-2}	3,000,000	2,778,000	2,895,500
1000	1000	4.65×10^{-5}	2,941,998	2,955,000	3,000,000
2000	500	1.15×10^{-2}	3,000,000	2,996,000	2,998,900
1995	1000	2.34×10^{-3}	2,880,000	2,606,000	2,999,000
2000	1500	3.58×10^{-6}	2,960,000	2,999,999	3,000,000
2500	750	2.81×10^{-3}	2,970,000	2,999,997	2,988,000
2495	1250	5.84×10^{-4}	2,940,000	2,904,000	3,000,000
2500	2000	2.09×10^{-7}	2,939,998	2,956,996	2,998,399
3000	1000	7.58×10^{-4}	2,878,000	2,992,000	2,998,900
2995	1500	1.60×10^{-4}	2,968,000	2,907,000	2,964,600
3000	2000	3.38×10^{-7}	2,984,000	3,000,000	2,993,100

Table 5.4: Simulation campaigns, data tiers, and parton shower tunes split according to the data era.

year	simulation campaign	data tier	parton shower tune
2018	RunIIAutumn18	MiniAOD	CP5
2017	RunIIFall17	MiniAODv2	CP5
2016	RunIISummer16	MiniAODv3	CUETP8M1 (CP5 for $t\bar{t}$ and single top)

Table 5.5: Global tags used for the simulation samples split according to the data era.

year	simulation campaign	global tag
2018	RunIIAutumn18	`102X_upgrade2018_realistic_v21`
2017	RunIIFall17	`102X_mc2017_realistic_v8`
2016	RunIISummer16	`102X_mcRun2_asymptotic_v8`

Table 5.6: Datasets of recorded data split according to the triggered HLT path and the data era.

HLT Path	Number of events		
	2018	2017	2016
Single Electron	-	479,291,000	962,168,100
Single Photon	-	116,681,806	215,141,438
Single Electron or Single Photon	1,384,292,955	-	-
Missing transverse momentum	275,968,905	436,531,938	176,078,993

5.4 Recorded data

The data recorded by the CMS detector which is used for this thesis is given in the same dataformat (MINIAOD) as the simulation samples. The data is split according to the year it was recorded in. This thesis is based on data recorded in the years 2016, 2017, and 2018. The data relevant for this analysis is chosen according to trigger decisions. The CMS collaboration provides the data split into different datasets according to the logical OR of several HLT trigger paths based on specific signatures of particles in the detectors. The datasets used for this thesis are given in Tab. 5.6. As was already explained, the dominant signature of the hadronic mono-top process is given by missing transverse momentum and the signatures of the hadronic top quark decay, i.e. jets. The missing transverse momentum dataset consists of all events which triggered at least one trigger path searching for missing transverse momentum on trigger level. Events from this dataset are enriched in the signal region, the single muon control region, and the double muon control region of this analysis. The events from the single electron dataset mainly contribute to the single and double electron control regions. Finally, the events originating from the single photon dataset are enriched in the photon control region of the analysis. In the 2018 era, the single electron and the single photon datasets are combined into one dataset.

Similar to simulation, changing calibrations and conditions of the detector are propagated to the already recorded data by using global tags. For recorded data, a combined global tag is used for the years 2016, 2017, and 2018. The identifier for this global tag is `102X_dataRun2_v13`. Also for recorded data, the used software release is `CMSSW_10_2_18`.

5.5 Corrections for simulated events

In this section, several corrections applied to simulated events are motivated and explained. These corrections improve the agreement between data and simulation significantly and are needed to obtain an acceptable level of agreement.

5.5.1 Higher-order corrections for single vector boson events

One of the main backgrounds in many searches looking for large missing transverse momentum in association with a SM particle is the production of an electroweak vector boson with additional jets (V + jets) due to possible invisible decay products of the vector bosons creating a $\vec{E}_\mathrm{T}$ signature in the detector. Especially important is the modeling of the transverse momentum of the vector boson since it dominantly determines the modeling of the missing transverse momentum or hadronic recoil in such events from a theoretical perspective. Consequently, a correct modeling of the transverse momentum of the vector boson in V + jets processes is vital to these searches.
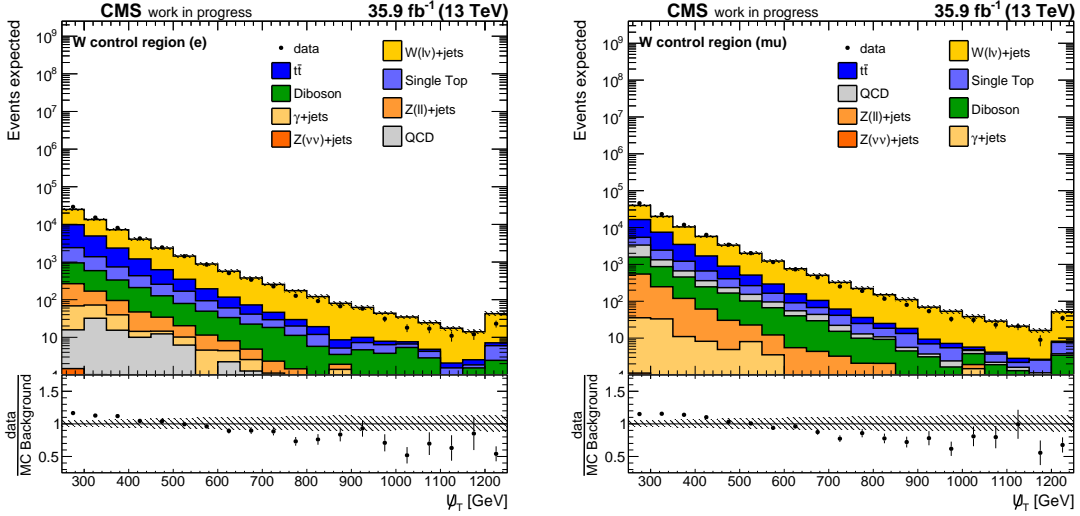
Figure 5.6: Hadronic recoil distributions in the W + jets control region in the 2016 data era based on the predictions of the leading-order W + jets MC simulation. The uncertainty band corresponds to the square root of the quadratic sum of indepedent variations of the matrix element renormalization scale and factorization scale by a factor of 2 and 1/2.

The simulations for events containing an electroweak vector boson and additional jets used in this thesis are, as already explained, based on the matrix element generator MadGraph [18, 19] at leading-order in QCD perturbation theory with up to four additional partons in the final state. These events are then processed further by Pythia 8 [166–168] for fragmentation and hadronization. In phase space regions in which such events are enriched and the largest contribution, the signal and control regions of this analysis, the predictions of such a simulation is not accurate enough to describe the data to a satisfying extent due to missing higher-order QCD effects as well as missing electroweak (EWK) corrections. The effect of the missing higher-order corrections can for example be observed in Fig. 5.6 showing the agreement between data and simulation in the W + jets control region in the 2016 data era for the distribution of the hadronic recoil. A clear mismodeling is observed in the ratio of data and simulation showing a severe underestimation and overestimation by the MC sample predictions for low and high hadronic recoil, respectively, or equivalently low and high transverse momentum of the vector boson.

In Appendix A.1 in Fig. A.1, Fig. A.2, and Fig. A.3, the agreement of data and MC prediction is also shown for the other control regions and MC production eras based on the vector boson plus jets samples used in this thesis. The hadronic recoil is shown in these control regions because it is a direct proxy for the transverse momentum of the vector bosons and it is also the final discriminant used in this analysis as explained in section 5.1. Furthermore, the total yields are shown in the signal regions without applying any top-tagging. Only studying the total yield without any top-tagging techniques applied ensures that no unblinding happens in any signal-sensitive region while still being able to check the modeling to a reduced extent. The uncertainty band in these plots consists of independent variations of the renormalization and factorization scales of the matrix element by a factor of 2 and 1/2 in order to have an estimation of the size of missing higher-order QCD effects. The variations due to these uncertainties are added in quadrature and then the square root of the sum is used as the total uncertainty. The mismodeling is especially pronounced in the 2017 and 2018 data era. In the 2016 data era, at low hadronic
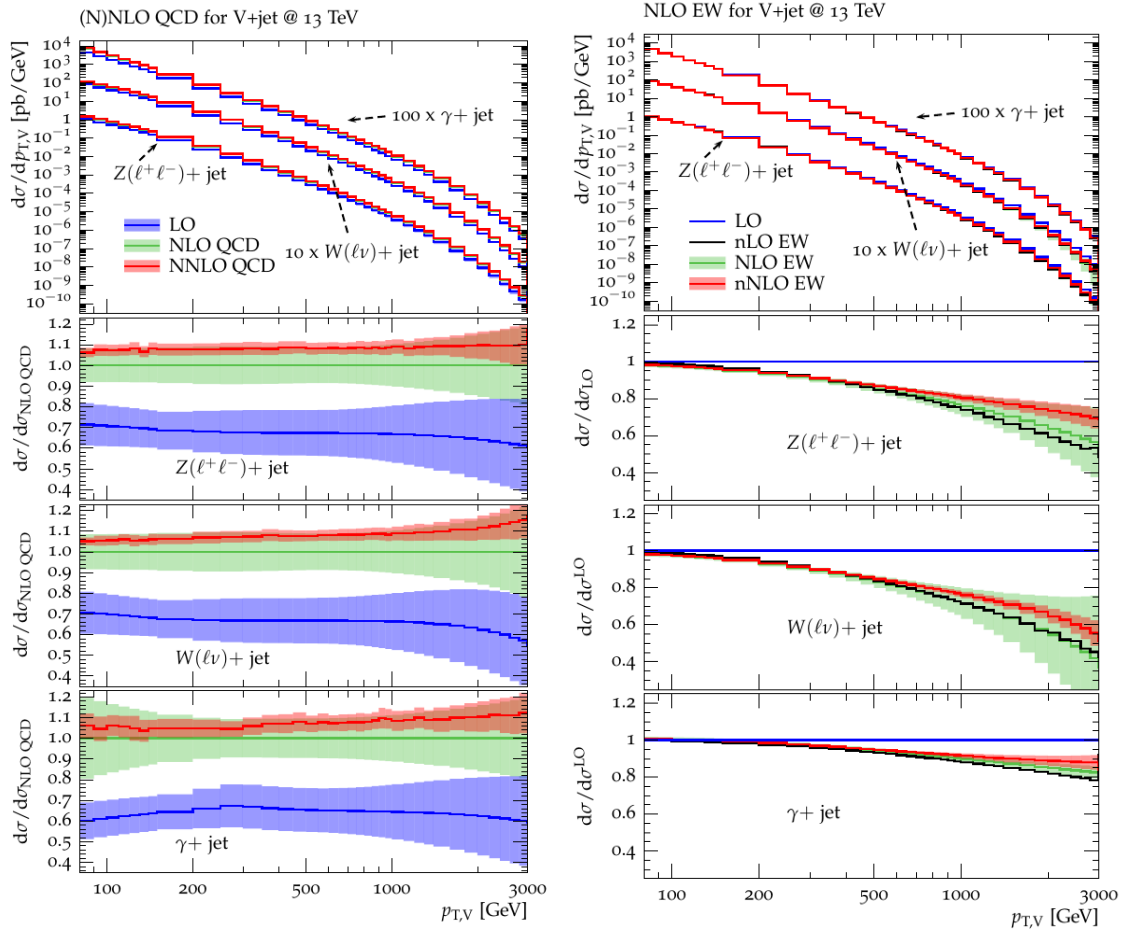
Figure 5.7: Fixed-order differential cross sections as a function of the transverse momentum of the vector boson for different V + jets processes at different QCD and EWK correction orders on the left-hand and right-hand side, respectively. Figures taken from [189].

recoil, the data is underestimated by the MC prediction with an overestimation starting at higher hadronic recoil compared to the 2017 and 2018 data era. The significantly different behavior of the 2016 MC prediction compared to the 2017 and 2018 prediction is due to a MadGraph5 setting affecting emission vertices which was incorrectly activated in the 2017 and 2018 MC production, severely changing the behavior of the transverse momentum of the vector boson. Not only was this setting activated mistakenly but studies within the CMS collaboration showed that this setting was probably also not working correctly [186–188]. In addition, the total yields in the signal region without top-tagging techniques applied are not predicted correctly. This mismodeling cannot be accounted for by the renormalization and factorization scale uncertainties of the matrix element. As a conclusion, it has to be noted that the leading-order V + jets samples do not describe the data to a an acceptable extent. In order to change this situation, corrections need to be applied which improve the prediction of the total yield of the V + jets processes as well as the shape of the distribution of the transverse momentum of the vector bosons.

Most important for predicting the correct rate of the V+jets processes are higher-order QCD corrections as can be observed on the left-hand side of Fig. 5.7. The NLO QCD corrections increase the cross section by approximately 30% to 40% depending on the V + jets process and the transverse momentum of the vector boson. The NNLO QCD corrections increase the cross section as well, by approximately 5% to 10%, also depending on the process and

the transverse momentum of the vector boson. Moreover, the theoretical uncertainties, as expected, decrease significantly comparing LO, NLO, and NNLO predictions.

The dominant reason for the overestimation with increasing hadronic recoil is the influence of missing electroweak corrections as is shown on the right-hand side of Fig. 5.7. With increasing transverse momentum of the vector boson, the NLO electroweak corrections become more important and decrease the differential cross section significantly. At 100 GeV transverse momentum of the vector boson, the corrections are approximately equal to one therefore resulting in no correction. However, for increasing transverse momentum, the corrections range between 10% and 30% in the range of 200 GeV to 1 TeV.

One possible solution to obtain improved predictions is to use simulations which are able to calculate the predictions at a higher order in perturbation theory. However, these samples are often hard to generate with high statistics and available NLO QCD samples created with MadGraph5_aMC@NLO suffer from negative event weights after merging with a parton shower. Therefore, the statistical power of these samples after generating the same number of events is significantly worse than the statistical power of leading-order samples. This is especially severe in the suppressed phase space regions of large transverse momentum of the vector boson. This phase space, however, is especially important for an analysis searching for high missing transverse momentum or hadronic recoil.

In order to retain larger statistics and also to improve the modeling of the LO simulation, a reweighting procedure is tested following [189]. This reweighting procedure aims to enhance the modeling of MC simulation samples by assigning each V + jets event a weight depending on the value of a specific variable which will be explained in more detail in the following based on [189]. Such a reweighting is, however, only an approximate approach. Nevertheless, it can directly be used with existing V + jets MC simulation samples therefore making it an attractive option for experimental analyses.

Reweighting procedure

The reweighting method is based on next-to-next-to-leading-order (NNLO) QCD and next-to-leading-order (NLO) electroweak (EWK) corrections and uncertainties. The simulated events are assigned a weight according to the reweighting formula

$$\frac{d}{dx}\frac{d}{d\mathbf{y}}\sigma^{(\mathrm{V})}(\epsilon_{\mathrm{MC}}, \epsilon_{\mathrm{TH}}) = \frac{d}{dx}\frac{d}{d\mathbf{y}}\sigma_{\mathrm{MC}}^{(\mathrm{V})}(\epsilon_{\mathrm{MC}}) \times \frac{\frac{d}{dx}\sigma_{\mathrm{TH}}^{(\mathrm{V})}(\epsilon_{\mathrm{TH}})}{\frac{d}{dx}\sigma_{\mathrm{MC}}^{(\mathrm{V})}(\epsilon_{\mathrm{MC}})} \,. \tag{5.3}$$

Here, σ represents the cross section, x is a generic reweighting variable, $\mathbf{y}$ is a vector of all possible other variables, MC refers to Monte Carlo sample prediction, and TH refers to a higher-order theoretical prediction. Furthermore, ϵ_{MC} and ϵ_{TH} are nuisance parameters modeling systematic uncertainties regarding the Monte Carlo sample prediction and the higher-order theoretical prediction, respectively. The left-hand side of the equation is the reweighted Monte Carlo prediction which is obtained by multiplying the unreweighted simulation with a reweighting factor

$$R_{\mathrm{TH/MC}}(x) = \frac{\frac{d}{dx}\sigma_{\mathrm{TH}}^{(\mathrm{V})}}{\frac{d}{dx}\sigma_{\mathrm{MC}}^{(\mathrm{V})}} \tag{5.4}$$

that can be obtained from calculating the ratio of the theoretical cross section prediction in a variable x and the MC simulation prediction in the same variable. For eq. 5.3 to hold, the variable x and the binning of its distribution needs to be consistent for all three terms while the selection requirements on all remaining variables only have to be identical in $R_{\mathrm{TH/MC}}$. This means that the prediction of the simulation sample has to be derived

inclusively in **y**. Also, the samples should not have any selection requirements applied that are not present in the theoretical calculation. Theoretical parameters like the QCD and EWK input parameters, the involved scales, and the PDFs need to match in

$$R_{\text{MC}} = \frac{\frac{d}{dx}\frac{d}{d\mathbf{y}}\sigma_{\text{MC}}^{(\text{V})}}{\frac{d}{dx}\sigma_{\text{MC}}^{(\text{V})}} \, , \tag{5.5}$$

which is naturally the case when using the same Monte Carlo sample for deriving and applying the reweighting factors. The phase space in which the reweighting factors are applied does not have to be similar to the phase space in which the correction factors are derived.

In order to benefit in the best possible way of higher-order calculations and available MC simulation samples, the distribution of the reweighting variable x should be modeled with the same or better precision by the fixed-order theoretical predictions. The variable x should therefore be chosen in a way to have reduced sensitivity to effects that are modeled better by MC simulation. However, correlations between the reweighting variable x and other variables **y** should be modeled more precisely by the MC simulation.

A natural candidate for the reweighting variable x is the transverse momentum of the vector boson since it directly relates to the measured missing transverse momentum or hadronic recoil. In addition, this variable has theoretical advantages as for example a reduced sensitivity to multiple jet emissions which is one of several aspects modeled more accurately in MC samples. The region in which the transverse momentum of the vector boson is much smaller than its mass, however, has to be excluded. This is due to the fact that for this region the theoretical calculations would need to have resummation of QCD Sudakov logarithms to all orders. The threshold for this range is chosen to be $30\,\text{GeV}$ in [189].

In order to derive and later apply this reweighting procedure, the $V + \text{jets}$ processes need to be handled as $\text{pp} \rightarrow \text{ll}/\text{l}\nu/\nu\nu/\gamma$ with particle-level objects that have a strong correspondence to theoretical fixed-order calculations. This implies that, from a MC simulation perspective, the objects considered (l, ν, γ) have to fulfill several criteria and need to be reconstructed in a specific way to reduce differences to the corresponding theoretical objects. This will be explained in more detail for the massive vector bosons first and afterwards for photons, which have to be handled in a more specific way.

W and Z boson in association with jets:

As was already explained, the W and Z bosons have to be reconstructed from particle-level leptons. The criteria for these particle-level leptons are given in the following.

- The leptons have to be in the final-state generator status except for τ leptons. This implies that the lepton is in the last state of the event generator before entering the detector simulation. Since the τ lepton is highly unstable, it is not considered as a final-state object by MC event generators. Therefore, τ leptons are allowed to have a different generator status which refers to a decayed particle.

- The leptons need to be prompt. This requirement serves to make sure that the leptons do not originate from a τ lepton decay, a muon decay, or a hadron decay which is a possibility in MC simulation events.

- Charged leptons have to be reconstructed as dressed leptons. Therefore, all collinear ($\Delta R < 0.1$ between lepton and photon) prompt final-state photons are added back to the lepton to obtain a dressed lepton. This is done to minimize biases in the

reweighting due to differences in the handling of photon radiation between theory and simulation. In addition, this procedure minimizes differences between electrons and muons.

After obtaining the correct leptons, the massive vector boson is reconstructed from these leptons by adding their momentum Lorentz vectors.

$$p_{\mathrm{W}}^{\mu} = p_{\mathrm{l}}^{\mu} + p_{\nu}^{\mu}$$
$$p_{\mathrm{Z}}^{\mu} = p_{\mathrm{l}}^{\mu} + p_{\mathrm{l}}^{\mu}$$
$$p_{\mathrm{Z}}^{\mu} = p_{\nu}^{\mu} + p_{\nu}^{\mu}$$

Photon in association with jets:

In case of the $\gamma +$ jets events, only events containing photons which fulfill a specific photon isolation requirement are considered for reweighting. This is due to the fact that perturbative $\gamma +$ jets predictions suffer from collinear singularities involving QCD radiation and $q \to q\gamma$ splittings at higher orders in QCD leading to non-finite results. To obtain finite results, isolation requirements rejecting $q \to q\gamma$ splittings and keeping QCD infrared singularity cancellation have to be used. This is done with an adapted Frixione isolation [190] method. The isolation requirement is fulfilled if

$$\sum_{i=\mathrm{partons/hadrons}} p_{\mathrm{T},i}\Theta(R - \Delta R_{i\gamma}) \leq \epsilon_0 p_{\mathrm{T},\gamma} \left(\frac{1 - \cos R}{1 - \cos R_0} \right)^n \forall R \leq R_0 \tag{5.6}$$

with $p_{\mathrm{T},\gamma}$ representing the transverse momentum of the photon and Θ representing the Heaviside function. In this formula, ϵ_0, R_0 and n refer to parameters that can be chosen freely and which regulate how much QCD radiation is allowed close to the photon. The parameter ϵ_0 can be interpreted as a momentum fraction, R_0 as a cone size, and n as a parameter to tighten or loosen the isolation criterion. This isolation is further adapted such that the behavior of QCD corrections at large transverse momentum of the vector bosons is comparable between $\gamma +$ jets and $\mathrm{V} +$ jets production with massive vector bosons. This is achieved by using a cone radius which is a function of the transverse momentum of the photon.

$$R_{\mathrm{dyn}} = \frac{M_{\mathrm{Z}}}{p_{\mathrm{T},\gamma}\sqrt{\epsilon_0}} \tag{5.7}$$

Here, M_{Z} is the mass of the Z boson. However, the maximum allowed cone radius is chosen to be 1.0. This is done to limit the collinear QCD radiation veto around the photon. The values of the parameters are chosen to be $\epsilon_0 = 0.1$ and $n_{\mathrm{dyn}} = 1$ as recommended in [189]. To derive and apply the reweighting factors, only events containing at least one isolated photon are considered. If there is more than one isolated photon, the hardest photon is chosen.

Finally, a cut on the transverse momentum of the vector bosons of $p_{\mathrm{T,V}} > 30\,\mathrm{GeV}$ is applied for theoretical reasons explained above.

Higher-order corrections and uncertainties

The theoretical prediction for the differential cross section as a function of the reweighting variable x consists of several parts, pure QCD corrections up to NNLO, pure electroweak corrections up to NLO, and approximate mixed QCD and EWK corrections.

$$\frac{d}{dx}\sigma_{\mathrm{TH}}^{(\mathrm{V})} = \frac{d}{dx}\sigma_{\mathrm{QCD}}^{(\mathrm{V})} + \frac{d}{dx}\Delta\sigma_{\mathrm{EW}}^{(\mathrm{V})} + \frac{d}{dx}\Delta\sigma_{\mathrm{mix}}^{(\mathrm{V})} \tag{5.8}$$

The QCD predictions and uncertainties at a given order are parameterized in terms of leading-order cross sections combined with correction factors $K_{\text{QCD}}^{(V)}$ and $\delta K_{\text{QCD}}^{(V)}$ at this order of perturbation theory.

$$\frac{d}{dx}\sigma_{\text{QCD}}^{(V)} = \left(K_{\text{QCD}}^{(V)}(x) + \sum_{i=1}^{3} \epsilon_{\text{QCD},i}\delta^{(i)}K_{\text{QCD}}^{(V)}(x) \right) \times \frac{d}{dx}\sigma_{\text{LO QCD}}^{(V)} \tag{5.9}$$

The nuisance parameters ϵ_{QCD} describe uncertainties related to variations of the renormalization and factorization scales which are performed to estimate the uncertainty of the theoretical prediction due to missing higher-order contributions. This uncertainty is split into three parts, a normalization uncertainty $\epsilon_{\text{QCD},1}$, a shape uncertainty $\epsilon_{\text{QCD},2}$, and an additional uncertainty estimating unknown correlations between the QCD uncertainties of the different vector boson plus jets processes $\epsilon_{\text{QCD},3}$. All three nuisance parameters need to be treated as uncorrelated, however each parameter is correlated for all V + jets processes and all bins of x, i.e. the transverse momentum of the vector boson.

Similar to the QCD predictions, the EWK corrected predictions are modeled in terms of the leading-order QCD prediction with correction factors $\kappa_{\text{EW}}^{(V)}$ and $\delta\kappa_{\text{EW}}^{(V)}$.

$$\frac{d}{dx}\sigma_{\text{EW}}^{(V)} = \left(\kappa_{\text{EW}}^{(V)}(x) + \sum_{i=1}^{3} \epsilon_{\text{EW},i}\delta^{(i)}\kappa_{\text{EW}}^{(V)}(x) \right) \times \frac{d}{dx}\sigma_{\text{LO QCD}}^{(V)} \tag{5.10}$$

The nuisance parameters ϵ_{EW} describe uncertainties related to missing even higher-order (NNLO) EWK contributions. The first parameter $\epsilon_{\text{EW},1}$ describes a universal effect of the missing higher-order corrections and can therefore be used correlated across all V + jets processes. The two other uncertainties parameterized by $\epsilon_{\text{EW},2}$ and $\epsilon_{\text{EW},3}$ describe subleading higher-order effects with unknown process correlation. Therefore, these parameters are considered to be uncorrelated for the different V + jets processes.

The combination of QCD and EWK corretions is performed in a multiplicative fashion instead of an additive approach because this contains at least to some extent mixed QCD and EWK contributions. The full mixed QCD and EWK corrections are not known at this point in time. As a final result, this yields the full correction formula

$$\begin{aligned}
K_{\text{TH}}^{(V)}(x, \epsilon_{\text{QCD}}, \epsilon_{\text{EW}}, \epsilon_{\text{mix}}) = & \left(K_{\text{QCD}}^{(V)}(x) + \sum_{i=1}^{3} \epsilon_{\text{QCD},i}\delta^{(i)}K_{\text{QCD}}^{(V)}(x) \right) \\
& \times \left(1 + \kappa_{\text{EW}}^{(V)}(x) + \sum_{i=1}^{3} \epsilon_{\text{EW},i}\delta^{(i)}\kappa_{\text{EW}}^{(V)}(x) \right) \\
& + \epsilon_{\text{mix}}\delta K_{\text{mix}}^{(V)}(x)
\end{aligned}$$

with an additional uncertainty described by ϵ_{mix} regarding mixed QCD and EWK contributions that cannot be described with the multiplicative/factorized approach. This nuisance parameter is considered to be completely uncorrelated between the different V + jets processes. The final higher-order prediction is then given by

$$\frac{d}{dx}\sigma_{\text{TH}}^{(V)} = K_{\text{TH}}^{(V)}(x, \epsilon_{\text{QCD}}, \epsilon_{\text{EW}}, \epsilon_{\text{mix}}) \times \frac{d}{dx}\sigma_{\text{LO QCD}}^{(V)}. \tag{5.11}$$

Scale factor calculation

For the calculation of the reweighting factors, the prediction given by the MC samples has to be obtained. This is done by iterating over the complete samples without any
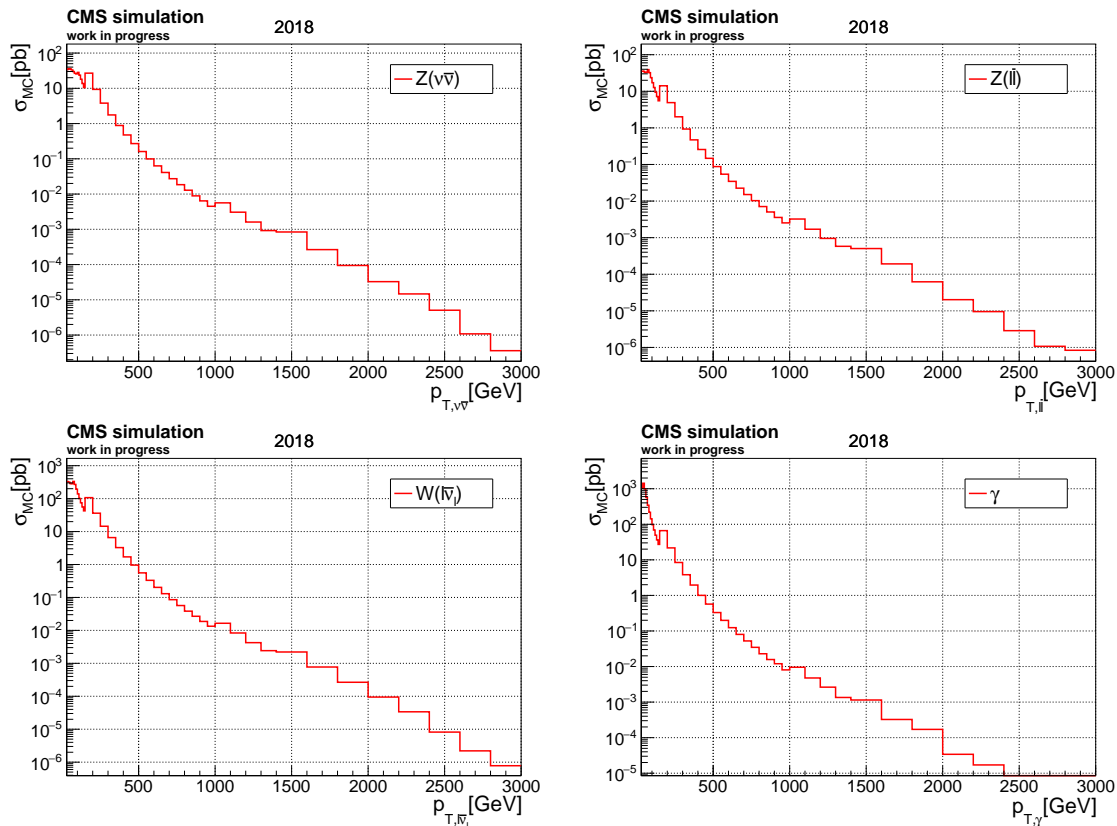
Figure 5.8: Differential cross sections from MC simulation as a function of the transverse momentum of the vector boson for the 2018 MC production era.

selection, reconstructing the respective vector boson according to the prescriptions given in the previous section, and finally filling the transverse momentum of the vector boson into a histogram while considering the correct normalization of the cross section and the weights given by the generator. In Fig. 5.8, the nominal cross sections obtained for the different vector boson processes in association with additional jets are given for the 2018 MC production era. The corresponding cross sections for the 2017 and 2016 MC production eras are given in Fig. A.4 and Fig. A.5 in Appendix A.1.

The differential cross sections obtained from the MC samples behave as expected. The production of a photon in association with possible jets or of a leptonically decaying W boson in association with possible jets have the highest overall cross sections, followed by the production of a Z boson decaying into two neutrinos in association with possible jets. The smallest cross section is given by the production of a Z boson decaying into two charged leptons in association with possible additional jets due to the smaller branching fraction of the Z boson into charged leptons. As was already stated earlier, the cross section strongly decreases with increasing p_T of the vector boson. The cross sections range from $\mathcal{O}(10\,\mathrm{pb}$ - $100\,\mathrm{pb})$ for low transverse momenta of the vector boson in the range of $100\,\mathrm{GeV}$ to $\mathcal{O}(10^{-6}\,\mathrm{pb})$ for very high momenta in the range of around $3\,\mathrm{TeV}$. A notable feature of these distributions can be observed for very low transverse momentum of the vector boson. There, all samples except for γ + jets seem to reach a plateau where the cross section does not increase anymore. This is due to the fact that the available MC samples were not generated completely inclusively but have a lower threshold on the scalar sum of all final-state partons H_T of $70\,\mathrm{GeV}$ for $W \to l\overline{\nu}$ and $Z \to l\overline{l}$, $100\,\mathrm{GeV}$ for $Z \to \nu\overline{\nu}$, and $40\,\mathrm{GeV}$ for γ + jets. Since H_T is highly correlated with the transverse momentum of the vector
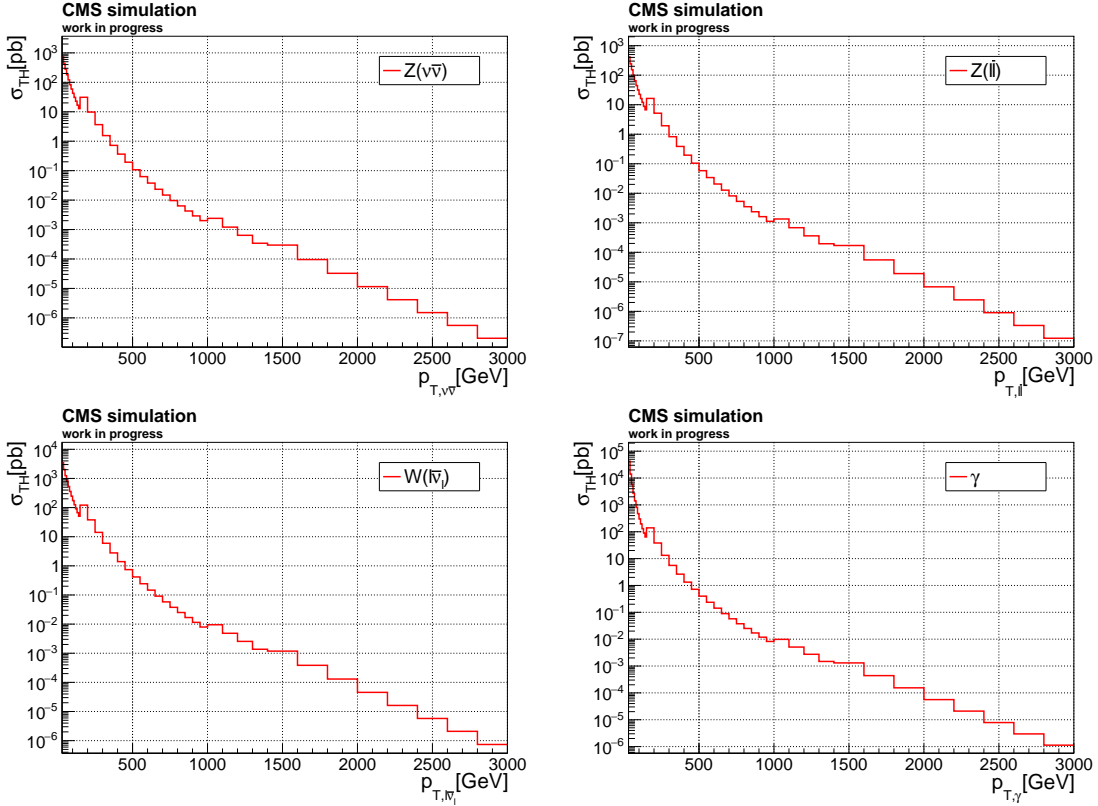
Figure 5.9: Fixed-order NNLO QCD and NLO EWK differential cross sections as a function of the transverse momentum of the vector boson for different V + jets processes.

boson in these events ($p_{\mathrm{T,V}} \leq H_{\mathrm{T}}$), these thresholds are also visible in the distribution of the p_{T} of the vector bosons.

Following this, the final theoretical prediction has to be calculated using equation 5.11. This can be done using the leading-order cross sections and the correction factors for the higher-order predictions explained in the previous section which can be found in [191]. After combining the leading-order cross sections together with the higher-order QCD and EWK corrections, the final NNLO QCD and NLO EWK prediction is presented in Fig. 5.9. The theoretical predictions show the same expected behavior as the predictions obtained from the MC simulation regarding the cross section hierarchy of the different V + jets processes. However, since these fixed-order predictions do not have a threshold on H_{T} comparable to the MC predictions, the distributions do not show the same plateau effect as the MC samples at low transverse momentum of the vector boson. Consequently, this effect will be visible in the reweighting factors.

Finally, to obtain the reweighting factors, the theoretical differential cross sections in Fig. 5.9 have to be divided by the differential cross sections predicted by MC simulation in Fig. 5.8. This yields the reweighting factors shown in Fig. 5.10. The reweighting factors for the other MC production eras are given in Fig. A.6 and Fig. A.7 in Appendix A.1.

Although the reweighting factors show that the theoretical predictions and the MC predictions are of the same order of magnitude over a large range of the vector boson p_{T}, the reweighting factors show very high deviations regarding the different predictions especially for very low vector boson p_{T}. This is the range in which the aforementioned plateau effect is visible in the MC predictions. Therefore, the reweighting factors show a large peak to very high factors to compensate the missing cross section due to the applied lower H_{T}
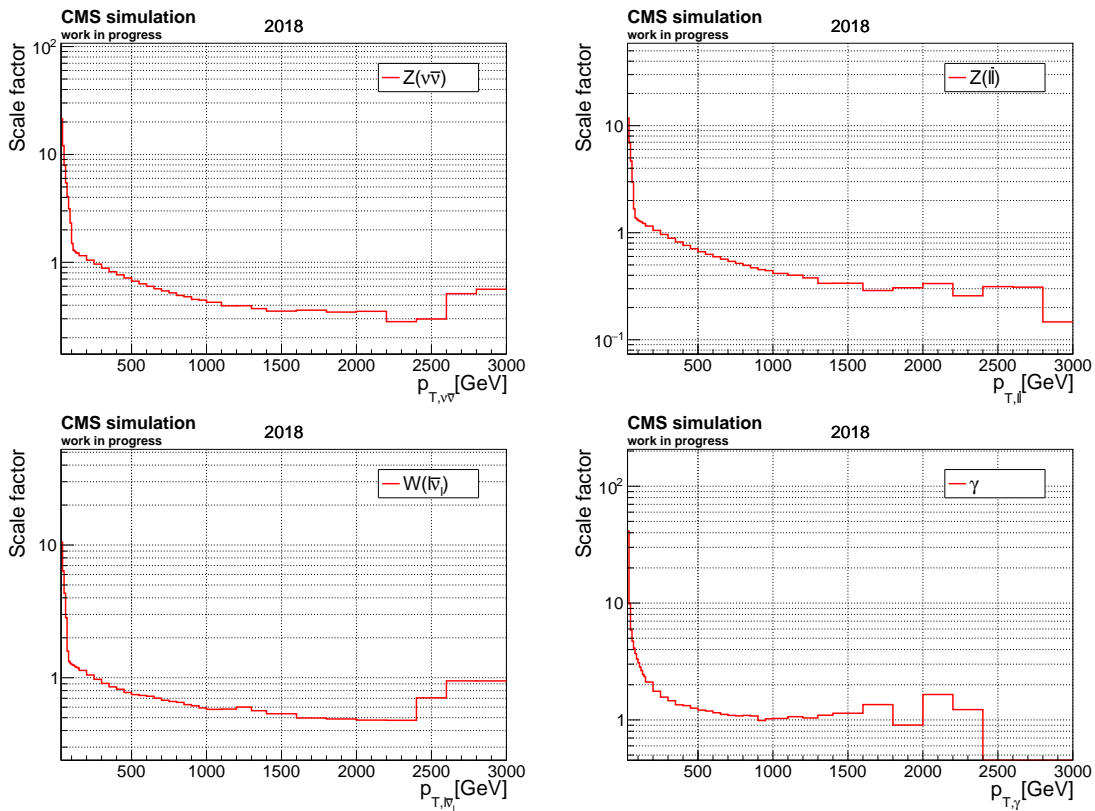
Figure 5.10: Differential reweighting factors as a function the transverse momentum of the vector boson in the 2018 MC production era.

threshold. However, since in [189] it is recommended to use the theoretical predictions only for transverse momenta of the vector boson larger than $100\,\text{GeV}$ and also the final event selection only leaves a negligible number of events in the very low vector boson p_T range, these large reweighting factors are not a problem.

For the massive vector bosons, at low values in the range of approximately $100\,\text{GeV}$ to $250\,\text{GeV}$ of the vector boson p_T, the scale factors are greater than one in the range of 1.0 to 1.3, therefore lifting the MC prediction up if applied. These are the higher-order QCD corrections outweighing the EWK corrections, which are close to zero in this range, see Fig. 5.7. For transverse momenta starting from around $250\,\text{GeV}$, the scale factors fall below one and further decrease down to the range of 0.3 to 0.5 depending on the V + jets process. These are the higher-order electroweak corrections outweighing the higher-order QCD corrections in this phase space of larger vector boson p_T. These reweighting factors are therefore in good agreement with what would be expected for the corrections from a theoretical perspective in Fig. 5.7 and from the observed agreement of data and simulation in Fig. A.1 and Fig. A.2 in Appendix A.1. However, it should be stressed here again that no recorded data is used to derive these correction factors.

Regarding the γ + jets process, the reweighting factors behave differently at first sight. For very high transverse momentum of the photon of approximately $750\,\text{GeV}$, the reweighting factors show a rather stable behavior and are close to unity. For transverse momenta below $750\,\text{GeV}$, the correction factors are greater than unity increasing with decreasing transverse momentum. However, as can be observed in Fig. 5.7, the QCD corrections are larger and the EWK corrections are smaller for the γ + jets process compared to the V + jets processes with a massive vector boson. Due to these differences in the higher-order corrections, the reweighting factors for the γ + jets process behave somewhat differently

than the reweighting factors for the other V + jets processes. Nevertheless, also the γ + jets reweighting factors match the expectation regarding the agreement between data and simulation in Fig. A.3 in Appendix A.1.

Differences between MC production eras

In most cases, MC predictions from different MC production eras differ because of different settings used for the production, e.g. a different underlying PDF set or a different value of the strong coupling constant α_s. Here, these differences are investigated with respect to the reweighting procedure explained in the previous section. The aforementioned differences will be either removed or at least reduced because of the reweighting to a fixed-order calculation. In Fig. 5.11, the ratios of the MC predictions of different eras are shown compared to the 2018 MC production era as a reference. One immediately visible feature can be observed in the Z + jets distribution with $Z \to \nu\bar{\nu}$ in 2016 compared to the same distribution in the 2017 and 2018 MC production era in the upper-left pad of Fig. 5.11. The cross sections from MC simulation are significantly lower and consequently the reweighting factors are significantly higher for the 2016 MC era compared to 2017 and 2018, see the upper-left pad in Fig. A.6 in Appendix A.1 and the two pads right below. The reason for this is that the 2016 sample was generated only for one flavor of neutrinos whereas for 2017 and 2018 it was generated for three neutrino flavors. This explains the approximate factor of three between the reweighting factors.

The reason why this factor is not exactly three is the aforementioned different generator setting regarding emission vertices that was mistakenly enabled for the 2017 and 2018 official production of Z + jets and W + jets. This setting strongly influences the distribution of the vector boson p_T as can also be observed in the upper-right and bottom-left pads of Fig. 5.11. If this setting is enabled, the differential cross sections, relative to the ones without this setting, increase continuously with increasing vector boson p_T until an approximate plateau is reached. However, since the reweighting factors are derived separately for each MC era and for each process, the reweighting renders the inclusive vector boson p_T behavior of the different sample eras comparable by reweighting them to the theoretical distributions. This is one additional advantage of such a reweighting procedure. However, effects related to this incorrect setting during production which are not directly correlated with the transverse momentum of the vector boson cannot be corrected for by the reweighting. Since the 2017 and 2018 MC samples were generated with the same settings, the cross sections from MC simulation show a ratio of around unity over most of the range of the vector boson p_T. For the γ + jets process, there is also a visible difference in the low p_T range between the 2018 and 2016 MC sample era although the aforementioned incorrect production setting was not activated for γ + jets in any MC production era. This difference could be due to the different settings of the parton shower in 2016 therefore changing the hadronic activity near the photon. This would consequently influence the isolation requirement, which depends on this hadronic activity, and the predicted cross section for the production of isolated photons in association with jets.

In the tail of the ratio graphs, starting at around $1\,\mathrm{TeV}$ vector boson p_T, all graphs in Fig. 5.11 show increasing statistical fluctuations because the MC samples only contain a very limited number of events in such a high-p_T range.

Theoretical systematic uncertainties of the reweighting factors

As was already explained previously, the theoretical predictions are affected by systematic uncertainties regarding the QCD and EWK corrections as well as an uncertainty on the combination procedure of both corrections. In this section, the impact of these uncertainties
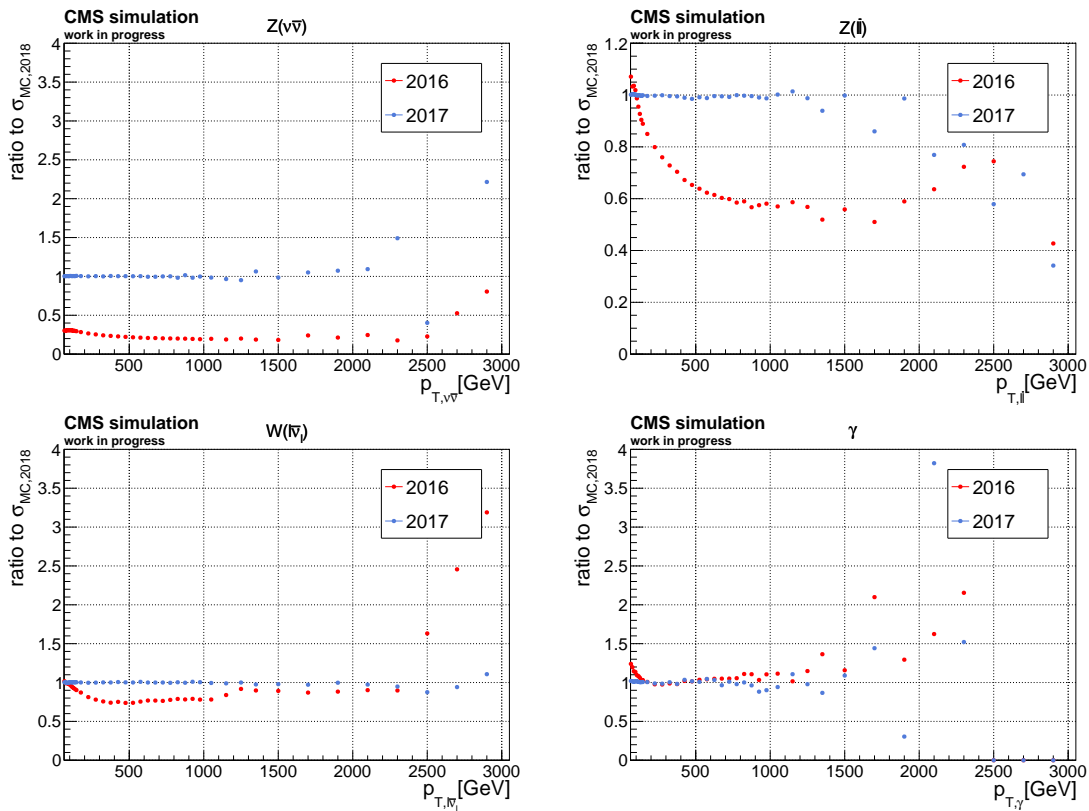
Figure 5.11: Ratios comparing the differential cross sections from MC simulation between different MC production eras for the different V + jets processes as a function of the transverse momentum of the vector boson.

on the reweighting factors is studied. In Fig. 5.12, the ratios of the theoretical predictions varied by a systematic uncertainty to the nominal prediction are shown for the Z + jets process with $Z \to \nu\bar{\nu}$. The corresponding ratios for the other V + jets processes are given in Fig. A.8 and Fig. A.9 in Appendix A.1.

The QCD uncertainties show a very comparable behavior between all processes. This can intuitively be understood since the QCD interactions should not be affected in a significant way by the type of the EWK vector boson involved in the process. The different parts of the QCD uncertainties behave as expected. As already described, the parameter $\epsilon_{QCD,1}$ acts mainly as a normalization uncertainty, however the uncertainty becomes larger with increasing p_T of the vector boson. The parameter $\epsilon_{QCD,2}$ is able to introduce a shape shift or slope. The rate change of $\epsilon_{QCD,1}$ starts from around $\pm 5\%$ to $\pm 10\%$ and increases with the vector boson p_T to almost $\pm 15\%$ depending on the V + jets process. The shape of the vector boson p_T distribution changes due to $\epsilon_{QCD,2}$ around an ankle point of around 700 GeV and the size of the uncertainty ranges from between $\pm 5\%$ and $\pm 10\%$ to around $\mp 10\%$. The parameter $\epsilon_{QCD,3}$ has a very small impact on the Z+jets processes. For W+jets its impact is larger but still significantly smaller than the two other ϵ_{QCD} parameters. Only for γ + jets, the parameter $\epsilon_{QCD,3}$ seems to have a significantly larger impact on the predictions, especially for the very low photon momentum range.

The EWK uncertainties are significantly smaller than the QCD uncertainties especially for low transverse momenta of the vector bosons. This is compatible with the fact that in this range also the EWK corrections are quite small. For increasing values of the transverse momentum, their impact increases as well up to around $\pm 5\%$ to $\pm 10\%$ depending on the process. For the parameters $\epsilon_{EW,1}$ and $\epsilon_{EW,2}$, the uncertainties show a rising trend over
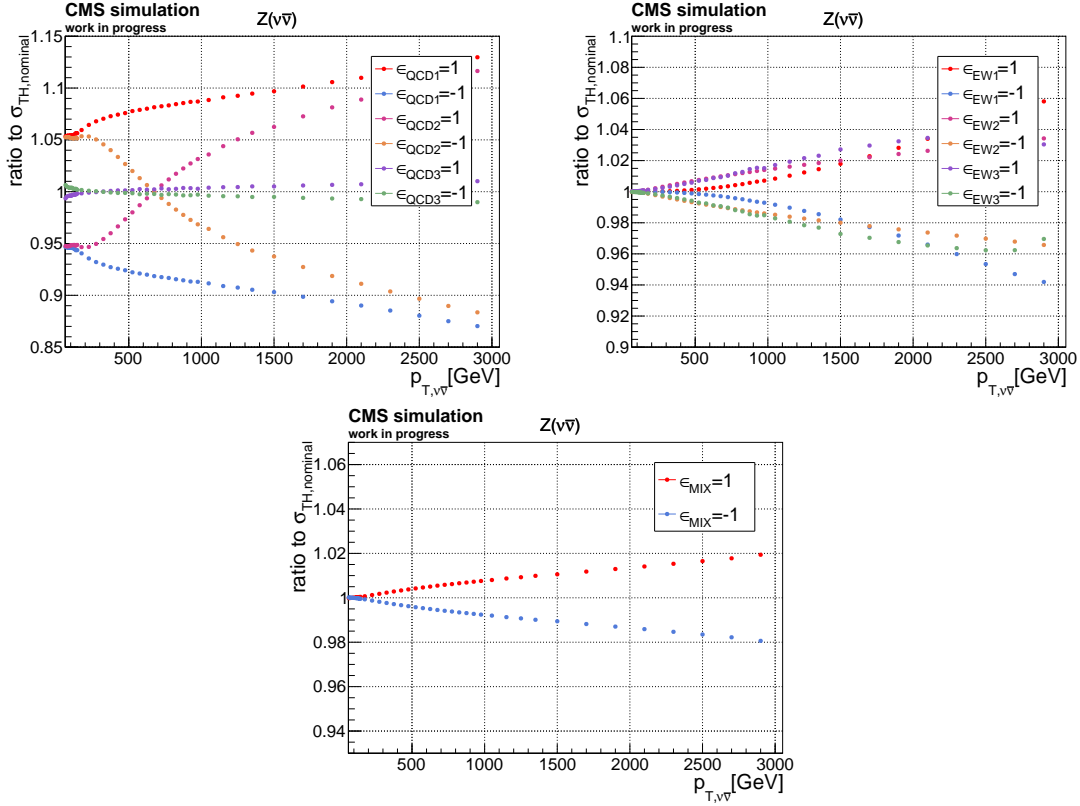
Figure 5.12: Ratios comparing systematically varied fixed-order differential cross sections with the nominal fixed-order differential cross sections for Z+jets with $Z \to \nu\bar{\nu}$ as a function of the transverse momentum of the Z boson. The parameters ϵ are the nuisance parameters described in section 5.5.1. Those parameters ϵ which are not explicitly stated in a specific legend entry are set equal to zero. The top-left pad shows the impact of QCD uncertainties, the top-right pad shows EWK uncertainties, and the bottom pad shows the uncertainty on the combination procedure of QCD and EWK corrections.

the complete p_T range. The corresponding uncertainties are again larger for W + jets than for Z + jets. The uncertainty corresponding to $\epsilon_{EW,3}$ shows a different behavior. This is especially well visible for W + jets for which the corresponding uncertainty switches sign after reaching a maximum or minimum. The Z + jets processes are starting to show this turn-around behavior as well but at much higher p_T of approximately 2.5 TeV.

The uncertainty on the combination of QCD and EWK corrections parameterized by ϵ_{MIX} shows a rising trend for increasing vector boson p_T for all processes. The uncertainty has a quite small impact for Z + jets and γ + jets below 2% over the complete vector boson p_T range. Only for W + jets, the impact increases to around 5% well beyond 2 TeV.

All of the aforementioned theoretical uncertainties are considered in this analysis corresponding to $\pm 1\sigma$ variations of the respective nuisance parameters ϵ which are incorporated into the statistical model of this analysis.

MC simulation systematic uncertainties of the reweighting factors

Also the MC simulation predictions are prone to systematic uncertainties. These uncertainties also have to be considered as shown in the equations in section 5.5.1. The reweighting factors are rederived for all the systematic uncertainties regarding the particle-level MC predictions. The main systematic uncertainties regarding the MC samples are
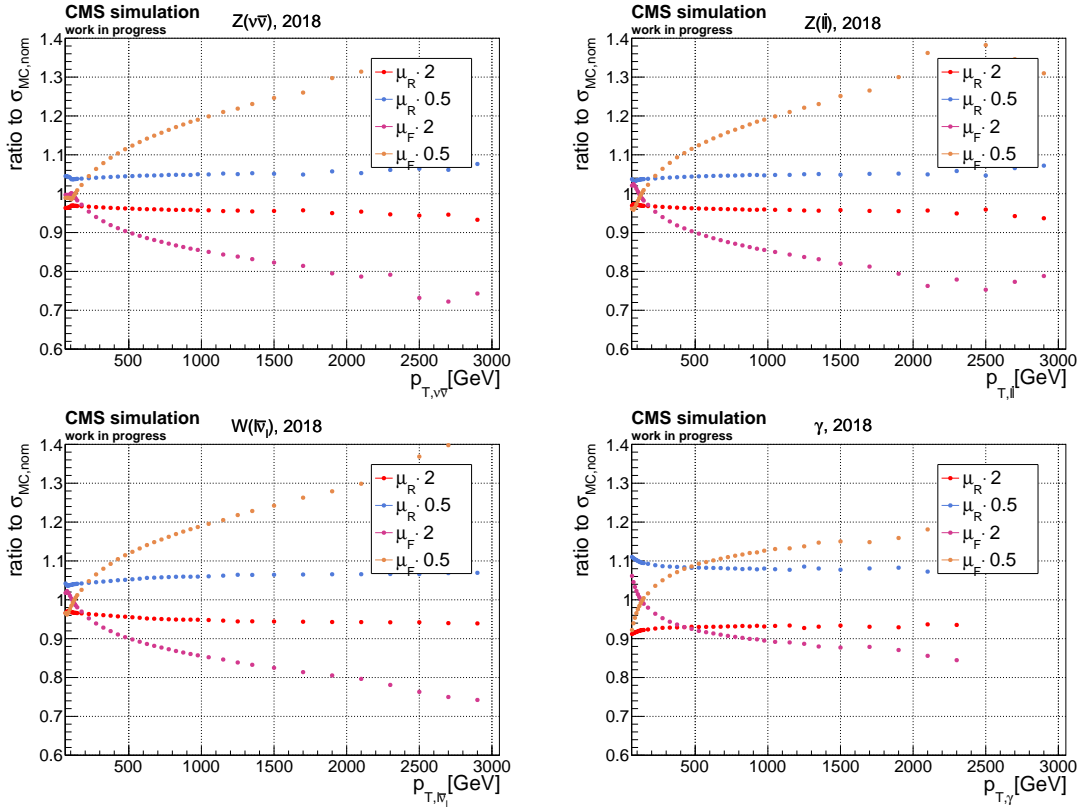
Figure 5.13: Ratios comparing systematically varied differential cross sections from MC simulation with the nominal differential cross sections from MC simulation for the V + jets processes as a function of the transverse momentum of the vector boson in the 2018 MC production era. The renormalization scale μ_R and the factorization scale μ_F are varied with a factor of 2 or $1/2$ in an uncorrelated fashion. The scale which is not explicitly given in a specific legend entry is always set to its nominal value.

the renormalization and factorization scale uncertainties of the matrix element generator. In Fig. 5.13 the effect of these uncertainties on the MC prediction is shown compared to the nominal simulation predictions for the V + jets processes in the 2018 MC production era. In Fig. A.10 and Fig. A.11 in Appendix A.1, the effect of these uncertainties is also shown for the 2016 and 2017 MC production eras.

The general shapes of the ratios look very comparable between all processes and MC eras. The variation of the renormalization scale results in an uncertainty of around 4% to 5% for very low values of the transverse momentum of the massive vector bosons. For increasing values of the massive vector boson p_{T}, the uncertainty increases as well up to approximately 6% to 8% depending on the V + jets process. The increase of the cross section over the vector boson p_{T} range is hence not very large resulting mostly in a rate impact. On the contrary, the γ + jets MC samples have an uncertainty due to the variation of the renormalization scale of approximately 10% for very low photon transverse momenta which decreases slowly with increasing photon p_{T}.

The factorization scale uncertainties are smaller than the renormalization scale uncertainties for low transverse momenta of the vector boson but increase quickly with increasing vector boson p_{T}. At approximately 200 GeV to 300 GeV vector boson p_{T}, the factorization scale uncertainty becomes larger than the uncertainty due to renormalization scale variation for the V + jets processes with massive vector bosons. For the γ + jets process, this happens
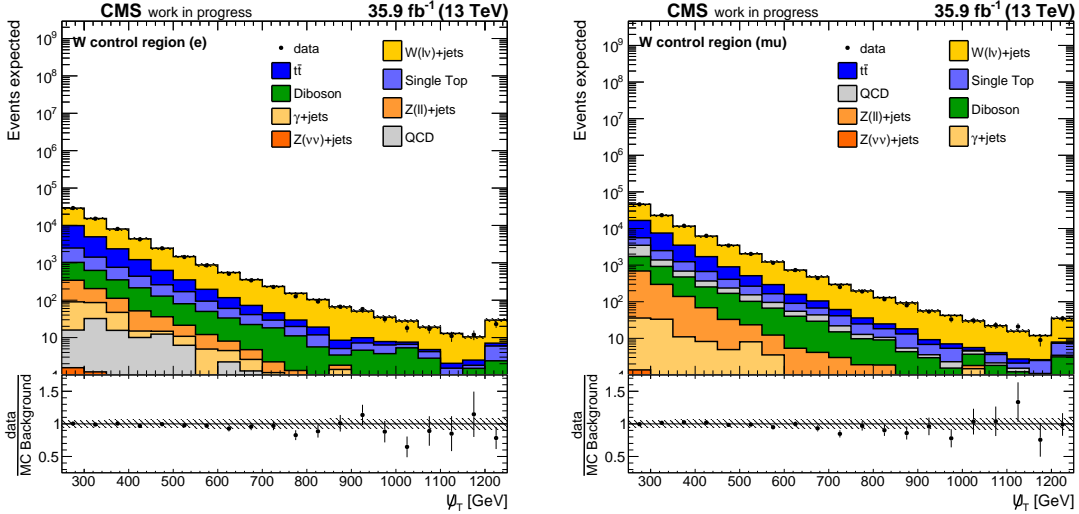
Figure 5.14: Hadronic recoil distributions in the W + jets control region in the 2016 data era after applying the theory-based V+jets reweighting procedure. The uncertainty band corresponds to the square root of the quadratic sum of indepedent variations of the matrix element renormalization scale and factorization scale by a factor of 2 and 1/2 and the theoretical V + jets uncertainties described in section 5.5.1.

later at around $500\,\text{GeV}$ photon momentum. For high vector boson p_T starting from around $500\,\text{GeV}$, the factorization scale uncertainty is approximately twice as large as the renormalization scale uncertainty becoming the dominant uncertainty for the high-p_T range of $Z + \text{jets}$ and $W + \text{jets}$. Again, for $\gamma + \text{jets}$, this happens later at around $1.5\,\text{TeV}$.

The renormalization and factorization scale uncertainties of the matrix element generator are included into the statistical model of this analysis.

Scale factor application and impact

In this section, the reweighting factors derived for the $V + \text{jets}$ processes are applied to the MC simulation and their impact regarding the agreement between data and simulation is studied. The scale factors are applied depending on the MC simulation at hand. For each MC production era and for each $V + \text{jets}$ process, the corresponding reweighting factors are applied to the nominal MC simulation prediction. In addition, the varied reweighting factors representing the theoretical and MC simulation uncertainties are used as well from which an approximate error band is constructed.

The predictions given by the reweighted MC simulations compared to the data are shown for example in the $W + \text{jets}$ control region in the 2016 data era in Fig. 5.14. In Fig. A.12, Fig. A.13, and Fig. A.14 in Appendix A.1 the reweighted distributions compared to data are also given for the other $V + \text{jets}$ control regions and data eras. The reweighting procedure improves the agreement between data and MC simulation significantly comparing Fig. 5.14 and Fig. 5.6. This statement holds for all data eras and $V + \text{jets}$ processes, compare Fig. A.1, Fig. A.2, and Fig. A.3 in Appendix A.1 with Fig. A.12, Fig. A.13, and Fig. A.14 in Appendix A.1. After the reweighting procedure, the distributions are modeled significantly better than without the reweighting. The shape of the hadronic recoil distribution is modeled well for the $Z + \text{jets}$ and $W + \text{jets}$ control regions in all data eras. In the 2016 data era, which shows a good modeling in all control regions, the modeling is in addition significantly better than in the 2017 and 2018 data era in which a mismodeling of the normalization is still present.

Only in the $\gamma + $ jets control region, a shape mismodeling remains especially in the range of low transverse momentum of the photon. This mismodeling is again worse in the 2017 and 2018 data era compared to the 2016 data era in which the data is mostly described within the uncertainties. The total yield in the signal regions without top-tagging applied also shows a different behavior between the data eras. In the 2016 era, the reweighting procedure significantly improves the description of the total yield although a smaller normalization offset still remains. In contrast to this, the yield is described worse in the 2017 and 2018 era after the reweighting procedure. In these data eras, the normalization offset becomes larger. The aforementioned observations point towards the possibility that the incorrect setting during the MC production of the 2017 and 2018 MC samples has a significant interplay with the reweighting procedure. Due to the reweighting procedure working significantly better in the 2016 data era, in which no incorrect production setting was activated, the reweighting procedure might not be able to account for all of the effects induced by the incorrect production setting. Furthermore, effects that are not directly related to the transverse momentum of the vector boson cannot be accounted for by the reweighting procedure since it is performed inclusively in all other variables. If these effects have a significant impact on the analysis phase space, it seems possible that the performance of the reweighting procedure deteriorates.

In summary, the reweighting procedure for the V + jets processes to implement higher-order corrections and uncertainties is a necessity to obtain improved agreement between data and MC prediction. Furthermore, it enables the usage of well-motivated state-of-the-art uncertainties with a well-defined correlation scheme. However, since a residual mismodeling, especially in the normalization of the Z + jets and W + jets control regions, is still present after applying the theory-based reweighting procedure, another approach to incorporate higher-order corrections is tested and shown in the next section.

Higher-order corrections from MC simulation

As is explained above, the shape of the hadronic recoil is mostly described well after the theory-based reweighting procedure. The total normalizations, however, still show some residual mismodeling, expecially in the 2017 and 2018 eras. The total rate of the processes is dominated by the events at low transverse momentum of the vector boson and in this range, the higher-order QCD corrections are the largest corrections. Therefore, another possibility to incorporate next-to-leading-order QCD corrections into the LO MC simulation is checked. This approach is also based on reweighting the events according to the transverse momentum of the vector boson at hand. However, in contrast to the method explained above, the differential cross section as a function of the transverse momentum of the vector boson of the V + jets process at hand is not reweighted to match a fixed-order theoretical prediction but a higher-order MC simulation prediction. For this purpose, NLO QCD V + jets MC samples generated with MadGraph5_aMC@NLO are used. Comparable to the theory-based reweighting approach, the reweighted prediction is given by

$$\frac{d}{dx}\frac{d}{d\mathbf{y}}\sigma^{(\mathrm{V})} = \frac{d}{dx}\frac{d}{d\mathbf{y}}\sigma^{(\mathrm{V})}_{\mathrm{MC,LO}} \times \frac{\frac{d}{dx}\sigma^{(\mathrm{V})}_{\mathrm{MC,NLO}}}{\frac{d}{dx}\sigma^{(\mathrm{V})}_{\mathrm{MC,LO}}} \tag{5.12}$$

with x representing the transverse momentum of the vector boson in the corresponding V + jets process. The reweighting factors are consequently derived by calculating the ratio of the differential cross sections as a function of the transverse momentum of the vector boson of the LO MC simulation and the NLO MC simulation.

$$R_{\mathrm{MC,NLO/MC,LO}}(x) = \frac{\frac{d}{dx}\sigma^{(\mathrm{V})}_{\mathrm{MC,NLO}}}{\frac{d}{dx}\sigma^{(\mathrm{V})}_{\mathrm{MC,LO}}} \; . \tag{5.13}$$
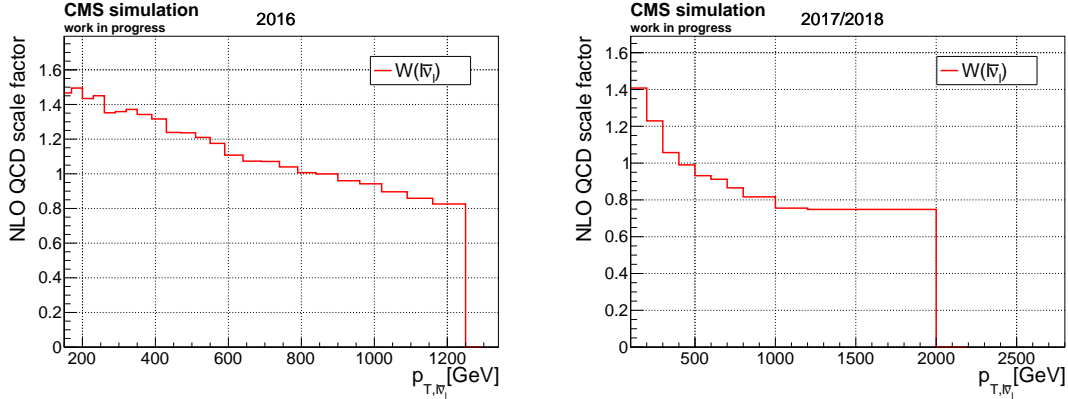
Figure 5.15: Simulation-based differential NLO QCD reweighting factors for the $W + \text{jets}$ process as a function of the transverse momentum of the W boson in the 2016 MC production era and the 2017/2018 production era on the left-hand side and right-hand side, respectively.

Due to the aforementioned incorrect setting in the 2017 and 2018 MC production, separate reweighting factors have to be derived for these eras compared to the 2016 era in which this incorrect setting was not used. Since besides the detector simulation, the 2017 and 2018 simulations are similar, one set of reweighting factors can be derived for the two MC production eras. The NLO QCD reweighting factors have been derived by the CMS mono-jet analysis [192] and are presented for the $W + \text{jets}$ process in Fig. 5.15 comparing the NLO QCD scale factors derived for the 2016 MC production era with scale factors derived for the 2017 and 2018 production eras. In Fig. A.15 and Fig. A.16 in Appendix A.1, the simulation-based NLO QCD reweighting factors are also given for the other $V + \text{jets}$ processes in the different MC production eras. For the 2016 era, only one set of NLO QCD reweighting factors was derived for the $Z + \text{jets}$ process, not distinguishing between $Z \to \nu\bar{\nu}$ and $Z \to l\bar{l}$. The simulation-based NLO QCD reweighting factors show significant differences between the MC production eras similar to the theory-based reweighting factors described above. Especially for high transverse momenta of the massive vector bosons, the reweighting factors for the 2017 and 2018 data eras are significantly lower than the ones for the 2016 data era. This shows again the influence of the aforementioned incorrect MC production setting. Only for the $\gamma + \text{jets}$ process, the reweighting factors behave comparably between the years. This is again expected since the $\gamma + \text{jets}$ samples were not affected by the incorrect MC production setting in the 2017 and 2018 data eras.

The simulation-based NLO QCD reweighting factors are used in conjunction with the NLO EWK corrections from the previous section because no $V + \text{jets}$ MC simulation samples including NLO EWK corrections are available within the CMS collaboration at the time this thesis is written. The agreement between data and simulation after using NLO QCD reweighting factors based on NLO QCD MC simulation together with theory-based NLO EWK corrections are given for example in the $W + \text{jets}$ control region in the 2016 data era in Fig. 5.16. In Fig. A.17, Fig. A.18, and Fig. A.19 in Appendix A.1 the agreement between data and simulation for the other $V + \text{jets}$ control regions in the other data eras is presented. The modeling in the $W + \text{jets}$ control region is improved in all data eras, especially considering the normalization. The total yield in the signal region without applying top-tagging is significantly improved as well comparing to the distributions obtained by using the theory-based NLO QCD reweighting factors. This is especially significant in the 2017 and 2018 data eras although there is a small improvement in the 2016 data era as well. The modeling in the $Z + \text{jets}$ control regions with $Z \to l\bar{l}$ is improved
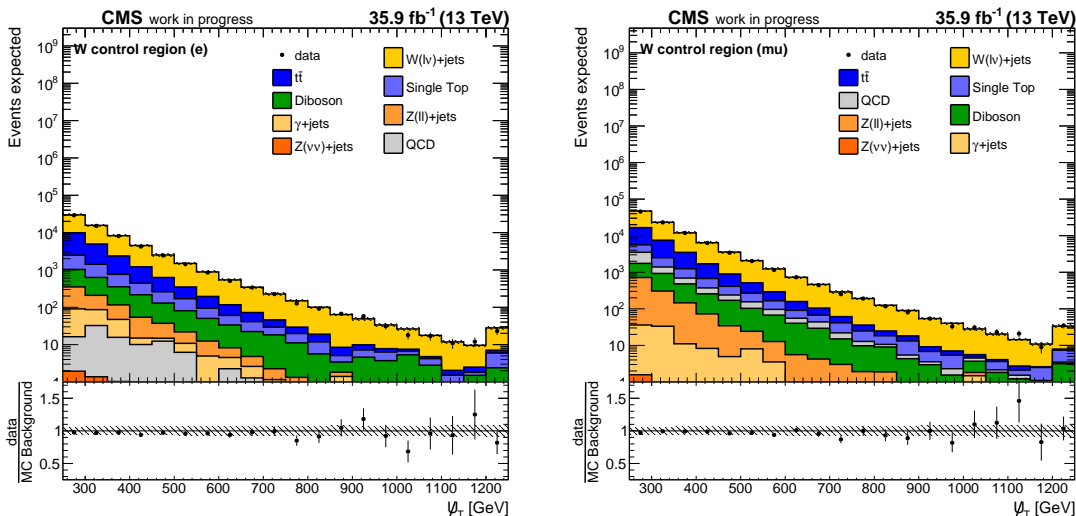
Figure 5.16: Hadronic recoil distributions in the W+jets control region in the 2016 data era after applying the V+jets reweighting procedure based on MC simulation NLO QCD corrections and theory-based NLO EWK corrections. The uncertainty band corresponds to the square root of the quadratic sum of indepedent variations of the matrix element renormalization scale and factorization scale by a factor of 2 and 1/2 and the theoretical V + jets uncertainties described in section 5.5.1.

as well especially in the 2017 data era whereas in the 2018 data era the prediction is too high in the range of lower hadronic recoil. In the γ+jets control region, the modeling is not improved comparing the simulation-based reweighting and the theory-based reweighting. In the 2017 and 2018 eras, the modeling in the γ + jets control region is suboptimal with both approaches. Because of this, large NLO QCD γ + jets MC simulation samples were generated by the CMS mono-jet group [192] in order to obtain an improved modeling also in these control regions. The impact of these samples is shown in the next section.

As a conclusion, the simulation-based NLO QCD correction factors improve the agreement with data compared to the theory-based reweighting factors in most of the phase space regions considered in this analysis. This is especially important for the normalization of the signal region without top-tagging techniques applied in which the theory-based reweighting predictions are significantly worse than the predictions by the simulation-based reweighting procedure. Therefore, these reweighting factors are used in combination with the theory-based NLO EWK corrections for the remainder of this thesis. However, to still be able to use state-of-the-art theoretical uncertainties, the uncertainties based on the theoretical predictions of [189], which are explained in section 5.5.1, are still used although the nominal predictions are derived by the simulation-based reweighting.

The reason why the simulation-based reweighting approach works better is not completely understood at this point in time. One possible reason could be that the aforementioned incorrect MC production setting has a different impact in the signal region of this analysis compared to the control regions. This could be the case if this setting e.g. has a large influence on the transverse momenta of the jets. If this would be the case, a different impact is expected in the signal region because the phase space of this region mainly consists of missing transverse momentum and jets. In the control regions, the reconstructed leptons and photons have a large impact on the hadronic recoil, which could weaken such an effect. Nevertheless, it would not be clear why the simulation-based reweighting can account for

this effect in a better way. Another reason could be that the theory-based reweighting is designed to be applied inclusively regarding the missing transverse momentum. If additional criteria are applied to the analysis phase space, e.g. kinematic requirements on the jets, problems can arise due to missing QCD and EWK corrections for events containing a vector boson in association with 2 jets in MC simulation, see [189]. Then, however, a similar impact would be expected in the control regions. Finally, another reason could be that events with a large number of jet emissions can be more accurately described by MC simulations than by fixed-order calculations [189]. Since especially the signal region is a completely hadronic region, such an effect might have a larger influence there than in the control regions in which well reconstructed leptons and photons are required.

Next-to-leading-order $\gamma + $ jets MC simulation

In order to improve the modeling in the $\gamma + $ jets control region in the 2017 and 2018 data eras, large NLO QCD $\gamma + $ jets samples were generated by the CMS mono-jet group [192] using MADGRAPH5_AMC@NLO. These samples are also processed for this thesis to evaluate their impact on the modeling in the $\gamma + $ jets control region of this analysis. The NLO EWK corrections are used from the theoretical predictions. The distribution of the hadronic recoil in the $\gamma + $ jets control region in the 2017 data era comparing the predictions based on the theoretical reweighting with the NLO QCD $\gamma + $ jets simulation combined with NLO EWK corrections from theory are given in Fig. 5.17. In Fig. A.20 in Appendix A.1 the resulting distributions of the hadronic recoil in the $\gamma + $ jets control region are also shown for the 2018 data era. As can be observed, the modeling is improved with respect to the modeling obtained by the simulation-based reweighting procedure or the theory-based reweighting procedure shown previously. Over most of the range of the hadronic recoil, the agreement between data and simulation is found to be within approximately 5% of unity and the modeling shape is quite flat. Only for low hadronic recoil the discrepancies become slightly larger up to approximately 10%.

Since the agreement between data and simulation is significantly improved in the 2017 and 2018 data eras by using the NLO QCD $\gamma + $ jets MC simulation samples, these samples are used for the $\gamma + $ jets predictions in the 2017 and 2018 data eras. As already stated, NLO EWK corrections are used from theory. For the 2016 data era, the corresponding samples have unfortunately not been generated. Therefore, the $\gamma + $ jets predictions obtained by using the theory-based reweighting approach in combination with LO MC simulation samples are used in the 2016 data era since a good agreement between data and simulation is found, which in addition is comparable to the agreement found in the 2017 and 2018 era with the NLO QCD $\gamma + $ jets MC simulation.

5.5.2 Pileup reweighting

MC simulation events are reweighted to reproduce the distribution of the average number of proton-proton interactions in one luminosity section that is found in data. This can only be done after the data was recorded. Therefore, the distribution of the average number of interactions in one luminosity section in a specific data era is divided by the same distribution in the MC simulation. Then, depending on the average number of interactions used for the simulated event, the value in the corresponding bin is taken as the reweighting factor for this simulated event. The distribution in data can be obtained by using the luminosity profile as well as the total inelastic proton-proton cross section of 69.2 mb. This distribution is provided by the CMS Luminosity POG. As a systematic uncertainty, the minimum bias cross section is varied by $\pm 4.6\%$ and varied weights are derived. The varied pileup weights are used to derive alternate templates and this uncertainty is considered as a nuisance parameter in the statistical model of this analysis.
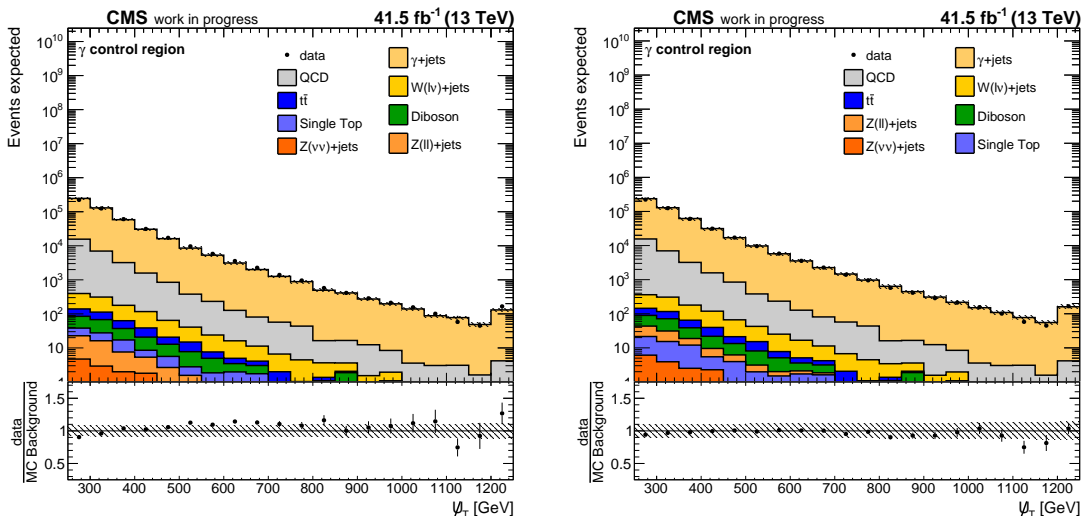
Figure 5.17: Hadronic recoil distributions in the $\gamma + \text{jets}$ control region in the 2017 data era based on the theory-based reweighting approach and the NLO QCD $\gamma + \text{jets}$ simulation on the left-hand and right-hand side, respectively. The uncertainty band corresponds to the square root of the quadratic sum of indepedent variations of the matrix element renormalization scale and factorization scale by a factor of 2 and 1/2 and the theoretical $V + \text{jets}$ uncertainties described in section 5.5.1.

5.5.3 Prefire reweighting

In the 2016 and 2017 data eras, trigger primitives of the L1 trigger located in the endcap of the ECAL were not associated to the correct bunch crossing. A shift in the timing of the ECAL was incorrectly propagated to the L1 trigger causing the aforementioned incorrect assignment. This problem is called the L1 prefire issue [193]. Two consequences arise from this issue. First, the trigger primitives are not found in the correct bunch crossing. Second, due to the rule which prevents the L1 trigger to trigger on two consecutive bunch crossings, an event which would have been accepted by the L1 trigger can be discarded if the prefire issue triggered on the previous bunch crossing. This issue needs to be mitigated because it is not modeled in simulated events.

The prefire issue is mitigated by assigning a weight to each object that can cause the prefire issue, photons and jets. This weight represents the probability for the respective object to cause the prefiring. The total weight which is assigned to the event to mitigate the prefire issue is then the probability that none of the objects causes the prefire issue.

The probabilities of jets and photons to cause a prefiring as a function of the transverse momentum and the pseudorapidity as well as a tool to compute the total prefire weight are provided by the CMS collaboration [193]. Furthermore, a systematic uncertainty for the prefire weights is introduced representing the statistical uncertainties of the derivation of the prefire probabilities of the different objects. The mitigation of the L1 prefire issue and the corresponding systematic uncertainty is propagated to the final result of this analysis.

5.6 Object definitions

After the event reconstruction performed by the PF algorithm, see section 2.2.3, several collections of different PF candidates are used, i.e. electrons, photons, muons, charged

hadrons, and neutral hadrons. From these object collections, several other physics object collections are created for the offline analysis by requiring additional identification and/or reconstruction criteria. Also, the collection of all trigger decisions from all available HLT trigger paths for the respective event is used. In this section, the different available physics objects as well as additional quality criteria applied to these objects are explained in more detail. Furthermore, corrections and uncertainties regarding specific physics objects are introduced.

5.6.1 Trigger decisions

An event contains a list of all trigger path decisions available for the respective event. The trigger decision is either false, which means that a specific trigger did not fire for the event in question, or the trigger decision is true, which means that a specific trigger did fire for the event in question. To be able to compare simulation and data, only events in which a trigger was activated can be used. Depending on the final state of the analysis, different triggers sensitive to different signatures are employed to obtain a sufficient number of events from recorded data. In this thesis, three overall types of triggers are used. These are triggers sensitive to missing transverse momentum or hadronic recoil, electrons, and photons. In Tab. 5.7, the trigger paths used in this thesis are provided dependent on the data era and split according to the event signature the trigger paths are sensitive to.

For this analysis, triggers that are sensitive to missing transverse momentum $\not{E}_T$ or hadronic recoil $\not{U}_T$ are used. These trigger paths remove muons found on trigger level from the $\not{E}_T$ calculation and therefore allow to trigger on $\not{U}_T$ in events with reconstructed muons on trigger level. Therefore, these triggers are employed in the signal region as well as the muon control regions. The threshold for $\not{E}_T$ or $\not{U}_T$ on trigger level is between $90\,\text{GeV}$ and $120\,\text{GeV}$ for these trigger paths, see Tab. 5.7. In addition, in the 2017 and 2018 data era, these trigger paths also apply a threshold on the scalar sum of the transverse momentum of all PF jets (H_T) on trigger level of $60\,\text{GeV}$. One of the paths applies this threshold considering all PF jets and the other only considering jets which fulfill a cut-based discriminator at the tight working point. The tight working point means that jets with a neutral hadron energy fraction larger than 90% are discarded. In the 2016 data era, the threshold on H_T is not applied, however other trigger paths having lower $\not{E}_T$ and $\not{U}_T$ thresholds of 90, 100 and $110\,\text{GeV}$ are used as well.

Next, trigger paths that are sensitive to prompt electrons are employed. These triggers are used in the electron control regions of this analysis. One electron trigger, sensitive to isolated electrons, is used as well as a trigger path that is sensitive to high-p_T electrons, which do not need to fulfill an isolation requirement. The isolation is a measure of additional activity by other PF candidates in the vicinity of the electron at hand. The isolation can be used to distinguish prompt electrons from electrons originating from decays of hadrons or from jets incorrectly reconstructed as electrons. At high transverse momentum of the electrons, the isolated electron trigger path loses efficiency. This loss of efficiency can be at least partly mitigated by using the additional high-p_T trigger path without an isolation requirement. Both trigger paths have a lower threshold on the p_T of the electron on trigger level, see Tab. 5.7, of $35\,\text{GeV}$, $32\,\text{GeV}$, or $27\,\text{GeV}$ for the isolated electron trigger and $115\,\text{GeV}$ or $105\,\text{GeV}$ for the high-p_T electron trigger without an isolation requirement.

Finally, photon triggers are employed which are sensitive to either high-energy photons or electrons. These triggers have thresholds on the transverse momentum of the photons or electrons as well, see Tab. 5.7. In the 2017 and 2018 data era, this threshold is $200\,\text{GeV}$ and in the 2016 data era, it is $175\,\text{GeV}$ or $165\,\text{GeV}$. The trigger path using a threshold of $165\,\text{GeV}$ on the transverse momentum in the 2016 data era also uses a upper threshold on the ratio of the associated energy deposited in the HCAL and the ECAL of 10%.

Table 5.7: HLT trigger paths used in this thesis. The trigger paths are split according to the data era and according to the event signature they are sensitive to.

Signature	HLT path
	2018
$\not{E}_\mathrm{T}$ or $\not{\Psi}_\mathrm{T}$	`HLT_PFMETNoMu120_PFMHTNoMu120_IDTight_PFHT60_vX`
	`HLT_PFMETNoMu120_PFMHTNoMu120_PFHT60_vX`
isolated electron	`HLT_Ele32_WPTight_Gsf_vX`
high-p_T electron	`HLT_Ele115_CaloIdVT_GsfTrkIdT_vX`
high-p_T photon/electron	`HLT_Photon200_vX`
	2017
$\not{E}_\mathrm{T}$ or $\not{\Psi}_\mathrm{T}$	`HLT_PFMETNoMu120_PFMHTNoMu120_IDTight_PFHT60_vX`
	`HLT_PFMETNoMu120_PFMHTNoMu120_PFHT60_vX`
isolated electron	`HLT_Ele35_WPTight_Gsf_vX`
high-p_T electron	`HLT_Ele115_CaloIdVT_GsfTrkIdT_vX`
high-p_T photon/electron	`HLT_Photon200_vX`
	2016
$\not{E}_\mathrm{T}$ or $\not{\Psi}_\mathrm{T}$	`HLT_PFMETNoMu120_PFMHTNoMu120_IDTight_vX`
	`HLT_PFMETNoMu110_PFMHTNoMu110_IDTight_vX`
	`HLT_PFMETNoMu100_PFMHTNoMu100_IDTight_vX`
	`HLT_PFMETNoMu90_PFMHTNoMu90_IDTight_vX`
isolated electron	`HLT_Ele27_WPTight_Gsf_vX`
high-p_T electron	`HLT_Ele105_CaloIdVT_GsfTrkIdT_vX`
high-p_T photon	`HLT_Photon175_vX`
	`HLT_Photon165_HE10_vX`

A defining quantity with respect to triggers is the trigger efficiency. The trigger efficiency describes how many events fulfilling a specific offline selection activate the trigger path in question with respect to all events fulfilling the offline selection. This quantity therefore provides a measure of how many events of the desired offline selection would be triggered on and therefore would also be expected to be found in data. However, trigger efficiencies are found to be different in recorded data and simulation. Therefore, trigger efficiency scale factors are applied to simulated events to obtain the same trigger efficiencies in simulation as in recorded data. These scale factors are derived by measuring the trigger efficiency for a specific trigger path in an independent data sample (ϵ_Data) as well as in simulation (ϵ_MC) dependent on one or more variables relevant for the trigger path in question. The scale factor is then obtained by calculating the ratio of these efficiencies $\epsilon_\mathrm{Data}/\epsilon_\mathrm{MC}$. Therefore, the trigger efficiency scale factors are dependent on the aforementioned variables as well.

The trigger efficiency corrections for the electron, $\vec{\not{E}}_\mathrm{T}$ or $\vec{\not{\Psi}}_\mathrm{T}$, and photon triggers employed in this thesis are derived by the CMS mono-jet analysis [192]. The electron trigger scale factors depend on the transverse momentum of the electrons and the pseudorapidity of the associated ECAL supercluster. The scale factors for the $\not{E}_\mathrm{T}/\not{\Psi}_\mathrm{T}$ triggers are provided as a function of the hadronic recoil. The photon trigger scale factors depend on the transverse momentum of the photon. The trigger efficiency corrections are also affected by uncertainties, e.g. statistical uncertainties relevant for the calculation of the scale factors. The trigger efficiency corrections and their systematic uncertainties are propagated to the final result of this analysis.

Table 5.8: Selection criteria for the two electron collections used in this thesis.

collection	$p_\mathrm{T}[\mathrm{GeV}] \geq$	$|\eta| \leq$	electron ID	$\mathrm{IP}_{xy}[\mathrm{cm}] \leq$	$\mathrm{IP}_z[\mathrm{cm}] \leq$
loose	10	2.5	veto	0.05(EB), 0.1(EC)	0.1(EB), 0.2(EC)
tight	40	2.5	tight	0.05(EB), 0.1(EC)	0.1(EB), 0.2(EC)

5.6.2 Electrons

Two collections of electrons are used in this thesis. Detailed lists of selection criteria for the two collections are given in Tab. 5.8. The first collection is referred to as loose electrons. The criteria for this selection allow for a high efficiency in finding electrons with a moderate misidentification rate. The tight electron collection is designed to contain only high-quality electrons with a very low misidentifaction rate but a lower efficiency than the loose collection to enrich prompt electrons. The electron ID in Tab. 5.8 is a cut-based discriminator of several quantities related to electron reconstruction and identification. The veto electron ID has an average efficiency of around 95% whereas the efficiency of the tight electron ID is around 70% [194]. For more information regarding electron reconstruction and identification, see [195]. The lower threshold of 40 GeV for the tight electron collection is chosen to be in the plateau of the trigger efficiency as determined by the latest CMS mono-jet analysis [192]. On top of the aforementioned selections, the electrons in both collections need to fulfill an upper threshold on the impact parameter in the transverse (IP_{xy}) and longitudinal direction (IP_z) of the detector with respect to the leading primary vertex in the event. This threshold depends on whether the electron is reconstructed within the ECAL barrel (EB) or the ECAL endcap (EC), see Tab. 5.8. Furthermore, all electron candidates within the crack between the ECAL barrel and endcap ($1.4442 < |\eta| < 1.5660$) are removed. As will be explained in the section on event selection, the loose electron collection is mainly used to veto events containing prompt electrons in the signal region, the muon regions, as well as the photon control regions whereas prompt electron events are enriched in the electron control regions using the tight electron collection.

For simulated events, the electrons of the two collections are assigned identification and reconstruction scale factors depending on the p_T of the electron and the pseudorapidity of the corresponding ECAL supercluster. These scale factors are designed to yield similar identification and reconstruction efficiencies in data (ϵ_Data) and MC simulation (ϵ_MC) after applying them. For each electron used within the event selection, the corresponding identification and reconstruction scale factor ($\epsilon_\mathrm{Data}/\epsilon_\mathrm{MC}$) is multiplied to the total event weight. Both of these scale factors are subject to uncertainties arising during their derivation, which are propagated to the final result of this analysis as nuisance parameters. The scale factors and their uncertainties are provided by the CMS collaboration [196] for the 2016 data era and by the latest CMS mono-jet analysis [192] for the 2017 and 2018 data era.

5.6.3 Photons

Similar to electrons, two collections of photons, loose photons and tight photons, are employed. The detailed selection requirements are given in Tab. 5.9. In 2016, the threshold of the single photon trigger is different than in 2017 and 2018, see Tab. 5.7, therefore motivating a different threshold on the transverse momentum of the offline photon. The upper threshold on the pseudorapidity of the tight photons is chosen to be at the end of the ECAL barrel. This region is a fiducial region for the reconstruction and identification of photons. Also in case of the photons, a cut-based discriminant, called photon ID,

Table 5.9: Selection criteria for the two photon collections used in this thesis.

collection	$p_{\mathrm{T}}[\mathrm{GeV}] \geq$			$|\eta| \leq$	photon ID
	2018	2017	2016		
loose		15		2.5	loose
tight	230	230	200	1.479	medium

is used for identifying prompt photons. The medium ID has an average efficiency of around 80% whereas the loose ID reaches approximately 90% efficiency [197]. For more information regarding photon reconstruction and identification, see [198]. If a loose or tight photon is found within $\Delta R < 0.4$ of a loose electron or muon, the photon is discarded. Furthermore, all photon candidates within the crack between the ECAL barrel and endcap ($1.4442 < |\eta| < 1.5660$) are removed. The loose collection is used to veto events with prompt photons in the signal regions as well as in the electron and muon regions of the analysis. The tight collection is used to select a sufficient number of events with medium-quality photons for the photon control region of this analysis.

Similar to the electrons, the photons are assigned efficiency scale factors in simulated events to render the efficiency of the photon ID comparable between data (ϵ_{Data}) and simulation (ϵ_{MC}). The photon identification scale factors ($\epsilon_{\mathrm{Data}}/\epsilon_{\mathrm{MC}}$) depend on the p_{T} of the photon and the pseudorapidity of the corresponding ECAL supercluster for the 2016 data era and are provided by the CMS collaboration [199]. For the 2017 and 2018 data era, the identification scale factors only depend on the pseudorapidity of the associated supercluster and were measured explicitly for high-p_{T} photons by the CMS mono-jet analysis [192, 200]. For each photon used during the event selection, the corresponding identification scale factor is multiplied to the total event weight. In addition, uncertainties on the identification scale factors are considered and propagated to the final result of this thesis. For the 2016 data era, one uncertainty is available for the scale factors derived by the CMS collaboration. For the scale factors derived by the CMS mono-jet analysis [192], two uncertainties are considered. First, a base uncertainty that includes statistical uncertainties as well as uncertainties regarding the fit used to derive the scale factors. Second, an uncertainty to estimate the change of the scale factors with increasing transverse momentum of the photon.

5.6.4 Muons

Analogous to the electrons, there are two collections of muons referred to as loose muons and tight muons corresponding to the working points of the employed identification discriminants. The loose muon ID has a high efficiency of $> 99\%$ for real muons with a small fraction of $< 0.5\%$ of misidentified muons whereas the tight ID has a lower misidentification rate of $< 0.3\%$ with a lower efficiency of $> 96\%$, see [54]. Furthermore, another quantity called muon isolation is used. This isolation is a measure of electromagnetic and hadronic activity within a cone around the muon. It can therefore be used to suppress muons from hadron decays in a jet [54]. The offline cuts on the loose muon collections are chosen to be in the range in which identification and isolation scale factors are available, see Tab. 5.10.

For the muons, efficiency scale factors for the identification discriminant and the muon isolation dependent on the transverse momentum and the pseudorapidity of the muon are used. Comparable to electrons, these scale factors render the identification and isolation efficiencies the same between simulation (ϵ_{MC}) and data (ϵ_{Data}). Also, uncertainties on these scale factors are propagated to the final result of this analysis. The scale factors and their uncertainties are provided by the CMS collaboration [201–203].

Table 5.10: Selection criteria for the two muon collections used in this thesis.

collection	p_{T}[GeV] $\geq$			$\|\eta\| \leq$	muon ID	muon isolation
	2018	2017	2016			
loose	15	20	20	2.4	loose	loose
tight		30		2.4	tight	tight

5.6.5 Tau leptons

Since there is no dedicated control region enriched in tau leptons in this analysis, only one collection is used to reject events with hadronically decaying tau leptons with a high efficiency. Therefore, an algorithm called the hadron-plus-strips algorithm [204] is used to identify jets that are compatible to the signature of a hadronically decaying tau lepton and simultaneously distinguish these candidates from quark or gluon induced jets. Furthermore, the tau candidates need to fulfill an isolation requirement considering charged PF candidates and PF photon candidates in a cone around the tau candidate. An isolation discriminant based on a boosted decision tree is used for this purpose [204] at the very loose working point. The lower p_{T} cut on these tau candidates is 18 GeV and they have to fulfill $\|\eta\| \leq 2.3$.

Isolation efficiency corrections $\epsilon_{\mathrm{Data}}/\epsilon_{\mathrm{MC}}$ for simulation are employed to obtain a comparable behavior of the isolation discriminant comparing data and simulation. Since the tau candidates are only used to veto events, the effect of the efficiency corrections is propagated to the tau veto. This is done by not rejecting the events with at least one hadronically decaying tau lepton, but each reconstructed tau lepton is assigned a veto weight as $1 - \epsilon_{\mathrm{Data}}/\epsilon_{\mathrm{MC}}$. The tau veto event weight is then the product of all veto weights assigned to each reconstructed tau lepton. Also uncertainties on these corrections are propagated to the final result of this analysis.

5.6.6 Jets

Two types of jet collections are used. As was explained previously, boosted top quarks are expected for a large phase space of the hadronic mono-top signal. Therefore, fat jets are used to cluster the decay products of the hadronic top quark decay. Jets with a smaller jet radius are used for further requirements on the number of b-tagged jets present in an event.

AK15 Particle-flow Puppi jets

The AK15 PF PUPPI jet collection is used to cluster the decay products of hadronically decaying top quarks within one jet. The jets are clustered starting from PF candidates with the AK algorithm, see section 4.3.1, using $R = 1.5$ as the jet radius. Also, the PUPPI algorithm [138] is used to mitigate pileup effects. Only jets with a minimum p_{T} of 150 GeV and $\|\eta\| \leq 2.4$ are kept in the first selection step because the DeepAK15 tagger was trained on jets fulfilling these requirements.

After the jets are clustered, additional information is added. The SoftDrop (SD) algorithm is applied to the jets and the resulting subjets are kept as daughters of the original jets. Next, the DeepAK15 algorithm, see section 4.3.5, is applied and the resulting tagger outputs are appended to the original jet as well. Furthermore, the DeepJet algorithm [151, 154] is applied on the SD subjets.

In addition, jet energy corrections, see section 5.6.8 consisting of jet energy scale corrections and jet energy resolution corrections are applied to the AK15 jets. However, since dedicated corrections are not provided by the CMS collaboration for AK15 jets, the jet energy

Table 5.11: Working points of the DeepJet algorithm [155–157]. The mistagging probability is the probability that the DeepJet algorithm tags a jet as originating from a bottom quark although it originated from a light-flavor quark or gluon.

working point	discriminant value $\geq$			mistagging probability
	2016	2017	2018	
loose	0.0614	0.0521	0.0494	10%
medium	0.3093	0.3033	0.2770	1%
tight	0.7221	0.7489	0.7264	0.1%

corrections derived for AK8 PF PUPPI jets are applied to the AK15 jets used in this thesis. Nevertheless, as is shown later, the modeling of the jets with these corrections is satisfactory.

To obtain the final collection used during event selection, only jets are kept that fulfill the tight jet ID criteria provided by the CMS collaboration [205–207] to suppress jets originating from detector noise or which have a poor reconstruction quality. Because there are no dedicated jet IDs for AK15 PF PUPPI jets, the recommended ones for AK4 PF PUPPI jets are used. In addition, a procedure called jet cleaning is performed. This procedure removes jets if a loose electron, loose muon, or loose photon is found within a cone with a specific radius around the jet. Commonly, the cone radius is chosen to be the jet radius of the corresponding jet collection. Therefore, the cleaning radius is chosen to be 1.5.

AK4 Particle-flow CHS jets

The jets in this collection are also clustered with the AK algorithm from PF candidates but with the more common jet radius of $R = 0.4$. For pileup reduction, the Charged Hadron Substraction (CHS) algorithm [137] is used. In a preselection step, all jets with a p_T lower than $20\,\mathrm{GeV}$ or $|\eta| > 2.4$ are removed.

In the next step, the DeepJet algorithm [151, 154] is applied and the jet energy corrections, see section 5.6.8, for AK4 PF CHS jets are applied.

The final collection is created by requiring the jets to have a minimum p_T of $30\,\mathrm{GeV}$, to fulfill the tight jet ID criteria for AK4 PF CHS jets [205–207], and not to be removed by a jet cleaning procedure with a radius of 0.4.

Heavy-flavor tagged AK4 jets

The AK4 jets are evaluated with the DeepJet algorithm to decide whether they originate from the hadronization of a bottom quark or not (b-tagging). For more details on the DeepJet algorithm, see section 4.3.6. The discriminant value to decide whether a jet is identified as originating from a bottom quark depends on the working point at which the tagger is operated at. For the DeepJet algorithm, there are three working points which are shown in Tab. 5.11 [155–157]. These working points differ by the misidentification rate to b-tag a jet originating from a light-flavor quark or gluon. In this thesis, collections containing jets that are b-tagged at the loose working point are used. These collections are created from the AK4 PF CHS jets described above.

The b-tagging efficiencies are found to be different in simulation and data. Therefore, corrections are needed to predict the correct rates using simulated events in conjunction with b-tagging. These corrections rely on the b-tagging efficiencies found in simulation and

on scale factors derived by the CMS collaboration [155–157, 208]. The scale factors per jet depend on the transverse momentum and the pseudorapidity of the jet. Furthermore, there is also a dependence on the hadron flavor of the jet at generator level. There are three flavors that are considered for the b-tagging scale factors and efficiencies, light-flavor, c-flavor, and b-flavor jets. The b-flavor and c-flavor jets are determined by a generator-level B or C hadron being part of the jet at hand. If this is not the case, the jet belongs to the light-flavor class. The b-tagging efficiencies in simulation are defined as

$$\epsilon_{\mathrm{MC}} = \frac{\#\mathrm{jets}(p_{\mathrm{T}}, \eta, \mathrm{f}, \text{b-tagged at working point WP})}{\#\mathrm{jets}(p_{\mathrm{T}}, \eta, \mathrm{f})} \, . \tag{5.14}$$

In this equation, the numerator refers to the number of jets which are b-tagged using the working point WP and have transverse momentum p_{T}, pseudorapidity η, and generator-level hadron flavor f. The denominator is the number of all jets with the same properties but not having to be b-tagged at working point WP.

The b-tagging efficiencies need to be calculated for the specific kinematic phase space the analysis is covering because the efficiencies depend on event kinematics. Furthermore, only the jets of which the b-tagging information is used need to be considered for the efficiency calculation. The b-tagging information is only used for the AK4 jets which, by a $\Delta R > 1.5$ criterion, lie outside of the leading AK15 jet in the event. Furthermore, the loose working point is used. Because of this, the b-tagging efficiencies at the loose working point are calculated specifically for the aforementioned AK4 jets which are outside of the leading AK15 jet in the event. These efficiencies are shown in Fig. 5.18 split according to the data era.

The efficiencies show that the DeepJet algorithm performs in a comparable way in all data eras with a slightly better performance in the 2017 and 2018 data era. This is could be due to the pixel detector upgrade which was performed after the 2016 data era and improves the tracking performance of the CMS detector, therefore having a direct influence on b-tagging performance.

The scale factors which are derived by the CMS collaboration are defined as

$$\mathrm{SF}(p_{\mathrm{T}}, \eta, \mathrm{f}, \text{working point WP}) = \frac{\epsilon_{\mathrm{Data}}}{\epsilon_{\mathrm{MC}}} \, . \tag{5.15}$$

Therefore, the scale factors also depend on the transverse momentum, pseudorapidity, and generator flavor of the jets as well as the working point at which the tagger is operated at.

The final event weight which is applied to simulated events to correct the b-tagging efficiencies can then be calculated depending on the number of b-tagged jets which is required in the final event selection of an analysis category. In the following, only the weights necessary for this analysis are given.

For events required to have exactly zero b-tagged jets, the following event weight needs to be used.

$$w(0 \text{ b-tags}) = \left(\prod_i (1 - P_{\mathrm{Data},i}) \right) \bigg/ \left(\prod_i (1 - P_{\mathrm{MC},i}) \right) \tag{5.16}$$

Here, the products run over all jets considered in conjunction with b-tagging information and $P_{\mathrm{Data},i}$ represents the scale factor corrected probability to b-tag this jet $P_{\mathrm{Data},i} = \mathrm{SF}_i \times \epsilon_{\mathrm{MC},i}$ and $P_{\mathrm{MC},i} = \epsilon_{\mathrm{MC},i}$ represents the nominal probability to b-tag this jet in simulation. Therefore, the expression above is just the ratio of the probability to not find any b-tagged jet in data and in simulation.
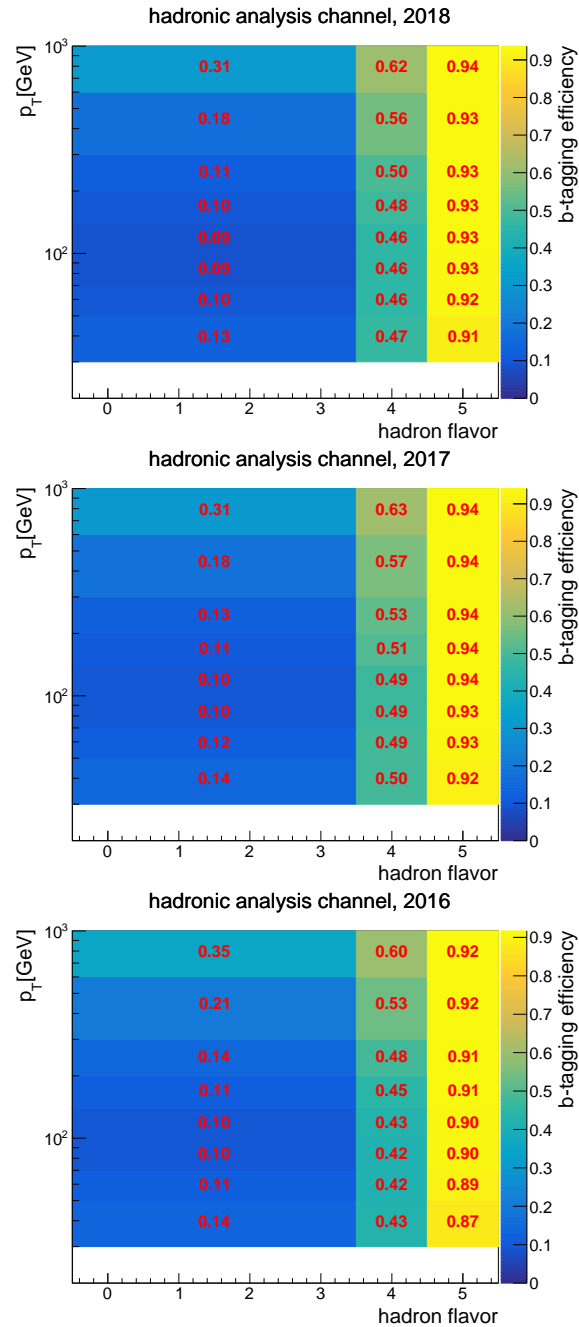
Figure 5.18: Binned b-tagging efficiencies derived for this analysis. The x-axis represents the hadron flavor of the jet at generator level and the y-axis the transverse momentum of the jet. The hadron flavor range from -0.5 to 3.5 represents the light-flavor jets, the range from 3.5 to 4.5 the c-flavor jets and the range from 4.5 to 5.5 the b-flavor jets. The color palette represents the b-tagging efficiency with the red numbers showing the exact number in the used bins.

Consequently, the event weight for simulated events with exactly one required b-tagged jet can be calculated as

$$w(1 \text{ b-tag}) = \left(\sum_i \left(P_{\text{Data},i} \prod_j (1 - P_{\text{Data},j}) \right) \right) \Bigg/ \left(\sum_i \left(P_{\text{MC},i} \prod_j (1 - P_{\text{MC},j}) \right) \right) \quad (5.17)$$

with $i \neq j$. This expression represents the probability to find exactly one b-tagged jet in data divided by the probability to find exactly one b-tagged jet in simulation.

Finally, simulated events with exactly two required b-tagged jets are analogously assigned the weight

$$w(2 \text{ b-tags}) = \left(\sum_i \sum_j \left(P_{\text{Data},i} P_{\text{Data},j} \prod_k (1 - P_{\text{Data},k}) \right) \right) \Bigg/ \left(\sum_i \sum_j \left(P_{\text{MC},i} P_{\text{MC},j} \prod_k (1 - P_{\text{MC},k}) \right) \right)$$
$$(5.18)$$

with $j > i$ and $k \neq i, j$.

Inclusive requirements on the number of b-tagged jets in an analysis category can be incorporated as well. For events fulfilling the selection of at least one b-tagged jet, the corresponding event weight is calculated as

$$w(\geq 1 \text{ b-tag}) = 1 - w(0 \text{ b-tags}). \quad (5.19)$$

Accordingly, for categories requiring at least two b-tagged jets, the weight

$$w(\geq 2 \text{ b-tags}) = 1 - w(0 \text{ b-tags}) - w(1 \text{ b-tag}) \quad (5.20)$$

has to be used.

The weights introduced here are used in this analysis to correct the b-tagging efficiencies in simulation and therefore predict the correct rate in analysis categories using the associated requirements on the number of b-tagged jets. The b-tagging scale factors are also subject to uncertainties, split according to heavy-flavor (b-jet or c-jet) jets and light flavor (no b-jet and no c-jet) jets. These uncertainties are provided by the CMS collaboration [155–157, 208] and are propagated to the final result of this analysis.

For more information about the calibration of the b-tagging discriminant, see [153, 208].

5.6.7 Missing transverse momentum and hadronic recoil

The missing transverse momentum that is used in this thesis is calculated from the PF candidates by using

$$\vec{\not{E}}_{\text{T}} = - \sum_{i=\text{PF candidates}} \vec{p}_{\text{T},i} . \quad (5.21)$$

In addition, the jet energy corrections, see section 5.6.8, in case of the jet energy scale corrections and the jet energy resolution corrections are propagated to $\vec{\not{E}}_{\text{T}}$. This is done by replacing all the PF candidates in the sum that are clustered in a jet by the corresponding jet. Then, the jet energy corrections are applied to these jets. Furthermore, the total uncertainty on the jet energy scale and resolution are propagated to $\vec{\not{E}}_{\text{T}}$. Another uncertainty which is considered for the missing transverse momentum is the unclustered energy uncertainty. For this uncertainty, all PF candidates that are not clustered into jets are varied within their energy resolution and the effect is propagated to the missing transverse momentum. For more information regarding the reconstruction of missing transverse momentum with the CMS detector, see e.g. [209, 210].

The hadronic recoil is calculated from the aforementioned missing transverse momentum by adding the transverse momentum vectors of loose electrons, loose muons, and loose photons:

$$\vec{\mathcal{U}}_T = \vec{\mathcal{E}}_T + \sum_{i=\text{loose electrons/muons/photons}} \vec{p}_{T,i} \tag{5.22}$$

Since the total jet energy scale, total jet energy resolution, and unclustered energy contributions are propagated to the missing transverse momentum, these corrections and their uncertainties are also propagated to the hadronic recoil.

5.6.8 Jet energy corrections

The jet energy corrections are explained briefly based on [211]. A lot more details on these corrections, their derivation, as well as their performance can be found in [212–214].

Jet energy scale corrections

The jet energy scale corrections aim to improve the approximation of the parton kinematics by the measured jet kinematics. Within the CMS collaboration, this is done with a factorized approach meaning that different effects are corrected for with different correction steps. Each step scales the four momentum of a jet depending on its properties, e.g. its transverse momentum and pseudorapidity. The steps are briefly summarized in the following.

1. Due to pileup collisions, energy contributions not originating from the hard process are clustered into the jet. The aim of this step is to remove these contributions from the jet. This is done using a QCD dijet simulation sample with and without pileup effects considered. After this correction, residual differences between data and detector simulation are corrected for.

2. The next step is to correct for the detector response. Again, a QCD dijet sample is used to determine the relation between the energy of a jet on particle-level and on detector-level. These differences are corrected for depending on the transverse momentum and pseudorapidity of the jet.

3. After the aforementioned corrections, only small differences in the response to jets in transverse momentum and pseudorapidity are found comparing data and simulation. This last step corrects for the different response in pseudorapidity using corrections from dijet events whereas Z+jets events and γ+jets events are used for the corrections as a function of the transverse momentum.

The jet energy scale corrections are provided by the CMS collaboration [215] and their total uncertainty is propagated to the final result of this analysis.

Jet energy resolution corrections

The jet energy resolution corrections aim to adapt the resolution in simulation to better describe the resolution in data. If a particle-level jet is found that matches a reconstructed jet with $\Delta R \leq R/2$, with R being the cone radius of the jet at hand, then the four-momentum of the reconstructed jet is scaled according to

$$c_{\text{JER}} = 1 + (s_{\text{JER}} - 1)\frac{p_T - p_T^{\text{particle}}}{p_T} \tag{5.23}$$

with c_{JER} being truncated at zero. Here, p_T is the transverse momentum of the reconstructed jet and p_T^{particle} is the transverse momentum of the matched particle-level jet. If a matching

particle-level jet cannot be found, a stochastic smearing procedure is applied and the four-momentum is scaled according to

$$c_{\text{JER}} = 1 + \mathcal{N}(0, \sigma_{\text{JER}}) \sqrt{\max(s_{\text{JER}}^2 - 1, 0)} \tag{5.24}$$

with σ_{JER} being the relative p_{T} resolution in simulation. The quantity s_{JER} is the resolution scale factor. The symbol $\mathcal{N}(0, \sigma_{\text{JER}})$ represents a randomly sampled number from the Gaussian distribution with mean zero and standard deviation σ_{JER}. Both the resolution in simulation as well as the resolution scale factor are a function of the transverse momentum and the pseudorapidity of the jet at hand and are provided by the CMS collaboration [216]. In this thesis, the total uncertainty on the jet energy resolution is propagated to the final result of this analysis.

5.7 Event selection

As was explained in section 5.1 regarding the analysis strategy, selection requirements are applied to define regions of phase space in which possible signal contributions are enhanced as well as phase space regions in which specific background events are enriched. In this section, the event selections to define these regions of phase space are described in detail.

As was already motivated, the variable used to search for hadronic mono-top signatures is the hadronic recoil $\vec{\slashed{U}}_{\text{T}}$ which allows to use a comparable quantity across phase space regions with and without prompt leptons and photons. Because of this, a basic event selection motivated by the expected event signature is applied in every analysis region used in this analysis. Then, by requiring different multiplicities of charged leptons and photons on top of the basic event selection, the signal and control regions are defined.

5.7.1 Basic event selection

In the signal region, a significant amount of missing transverse energy is expected due to the heavy invisible DM candidates. In addition, the top quark approximately recoils against the DM candidates before decaying hadronically. To reconstruct the top quark, AK15 PF jets are used, see section 5.6.6. From the mono-top signature, at least one AK15 jet with high transverse momentum is expected. To identify the AK15 jet as originating from a top quark decay, the SoftDrop (SD) mass and the DeepAK15 tagger, see section 4.3, are exploited. These top-tagging techniques are applied at a later stage to be able to compare the modeling of the simulation with data before applying the final top-tagging methods. No sensitivity towards mono-top signatures is expected without any top-tagging techniques. Therefore, recorded data can be studied without unblinding the analysis if only signal-depleted phase spaces and/or signal-insensitive variables are studied. This is done to check the simulation in phase spaces in which the modeling is expected to not be optimal and to motivate requirements used to improve this modeling. Distributions which are shown to motivate a selection requirement are only shown for the 2018 data era since no differences for these arguments are expected for the 2017 or 2016 data eras. Furthermore, for all shown distributions, the best description of the $V + \text{jets}$ processes is used as found in the studies of section 5.5.1. The general preselection applied in all regions before using top-tagging techniques is given in the following.

1. The magnitude of the hadronic recoil $\slashed{U}_{\text{T}}$ is at least $250\,\text{GeV}$. This lower threshold is chosen to be approximately in the plateau of the trigger efficiency of the missing transverse momentum or hadronic recoil triggers as determined by the latest CMS mono-jet analysis [192]. In addition, at $250\,\text{GeV}$ transverse momentum, the top quark decay products which recoil against the hadronic recoil start to be clustered within a jet with a radius parameter of 1.5, see Fig. 5.5 in section 5.2.
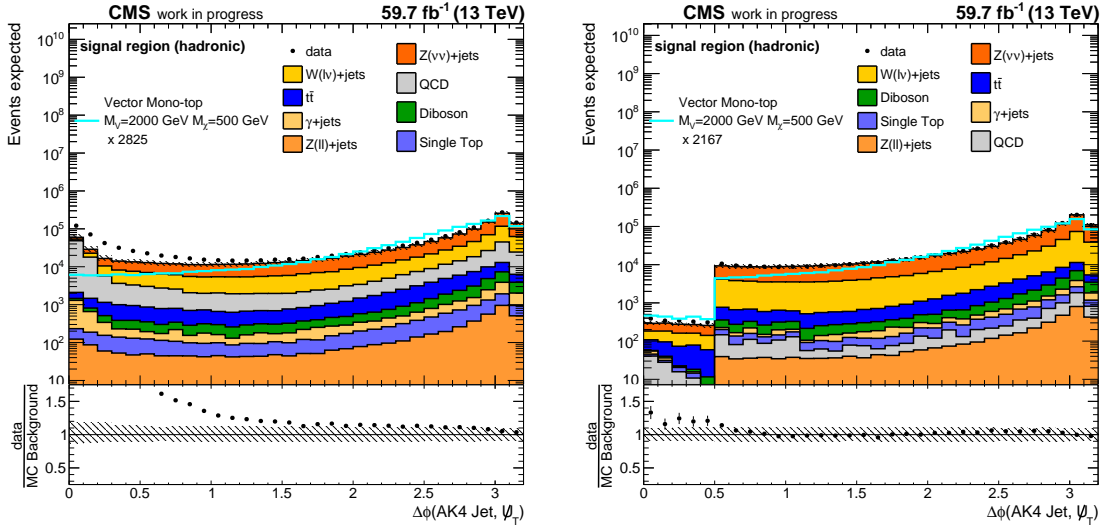
Figure 5.19: Left-hand side: Distribution of the angle in the transverse detector plane between all selected AK4 jets and the hadronic recoil without any requirement on this angle. Right-hand side: Distribution of the angle in the transverse detector plane between all selected AK4 jets and the hadronic recoil after requiring this angle to be larger than 0.5 radians for the four leading AK4 jets. The distribution of one mono-top simulation sample is overlaid as the cyan curve. The rate of the signal distribution is scaled to the total background yield with the scale factor given in the legend.

2. At least one AK15 jet with a p_T of at least $160\,\mathrm{GeV}$ needs to be present in the event. The threshold on p_T is chosen at $160\,\mathrm{GeV}$ to also select events in which the hadronic recoil is not completely driven by the leading AK15 jet. Possibly problematic QCD contributions at lower transverse momentum of the leading AK15 jet are heavily suppressed as soon as top-tagging techniques are applied. Therefore, the cut is chosen at this rather low value for the preselection requirements.

3. The angle between the hadronic recoil and the four leading AK4 jets in the transverse detector plane has to be larger than 0.5 radians. This cut is performed to veto QCD multijet events and events in which the missing transverse momentum is measured incorrectly along the AK4 jet momentum. These events are not modeled well in simulation, which is shown on the left-hand side of Fig. 5.19. There, the angle between an AK4 jet and the hadronic recoil in the transverse detector plane is shown for all selected AK4 jets, see section 5.6.6, without any requirement on this angle. As can be observed, the QCD multijet contribution becomes significantly enhanced for small angles between the AK4 jets and the hadronic recoil. Starting from approximately 0.5 radians, the QCD multijet contribution becomes one of the most important processes. In this range, the simulation does not model the data well. After applying the requirement on the angle between the hadronic recoil and the AK4 jets, the modeling is significantly improved, see the right-hand side of Fig. 5.19. A residual mismodeling in the aforementioned range remains for events with more than four jets, however, this phase space is negligible compared to the total number of events. In addition, the overlaid signal distribution shows that no significant amount of signal is removed by this requirement.

4. The angle in the transverse detector plane between the leading AK15 jet and the hadronic recoil is required to be larger than 1.5 radians. This requirement removes a
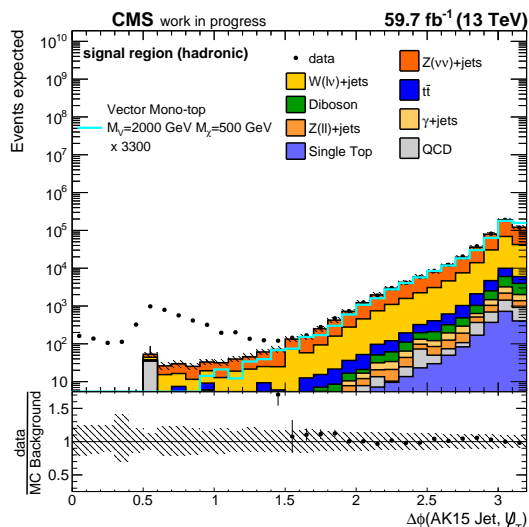
Figure 5.20: Angle in the transverse detector plane between the leading AK15 jet and the hadronic recoil in the signal region without applying any top-tagging techniques. The distribution of one mono-top simulation sample is overlaid as the cyan curve. The rate of the signal distribution is scaled to the total background yield with the scale factor given in the legend.

residual mismodeling observed in the signal region without top-tagging techniques applied as can be observed in Fig. 5.20. This mismodeling is probably due to QCD multijet events in which the missing transverse momentum is measured incorrectly along the direction of the leading AK15 jet. This requirement is also compatible with the assumption that the leading AK15 jet represents the top quark which should recoil against the missing transverse momentum. In the control regions of the analysis, this requirement has a negligible effect. Furthermore, the overlaid signal distribution shows that no significant amount of signal is removed by this requirement.

5. The charged hadron energy fraction of the leading AK15 jet has to be larger than 10% and the neutral hadron energy fraction of the leading AK15 jet is required to be smaller than 80%. These requirements remove anomalous sources or large missing transverse momentum in the signal region. In the control regions, these requirements have a negligible effect.

6. Veto any event that contains at least one reconstructed hadronically decaying τ lepton. This is done because none of the desired event signatures contains hadronically decaying τ leptons.

7. In the 2018 data era, any event that contains an AK4 jet with $p_T > 30$ GeV in the region $-3.2 \leq \eta \leq -1.3$ and $-1.57 \leq \phi \leq -0.87$ is vetoed, with η representing the pseudorapidity of the AK4 jet and ϕ the azimuthal angle in the transverse detector plane. This selection is performed due to a problem called the HEM issue [217, 218]. Due to a broken HCAL submodule, a region of the detector ($-3.2 \leq \eta \leq -1.3$ and $-1.57 \leq \phi \leq -0.87$) was completely depleted of HCAL energy deposits. This leads to a significantly increased number of reconstructed isolated electrons because HCAL information is used to distinguish between real isolated electrons leaving energy deposits in the ECAL and jets that would also leave deposits in the HCAL. Because of these fake isolated electrons, these events are triggered on. Furthermore, the jet energy reconstruction relies heavily on information from the HCAL. Therefore, the
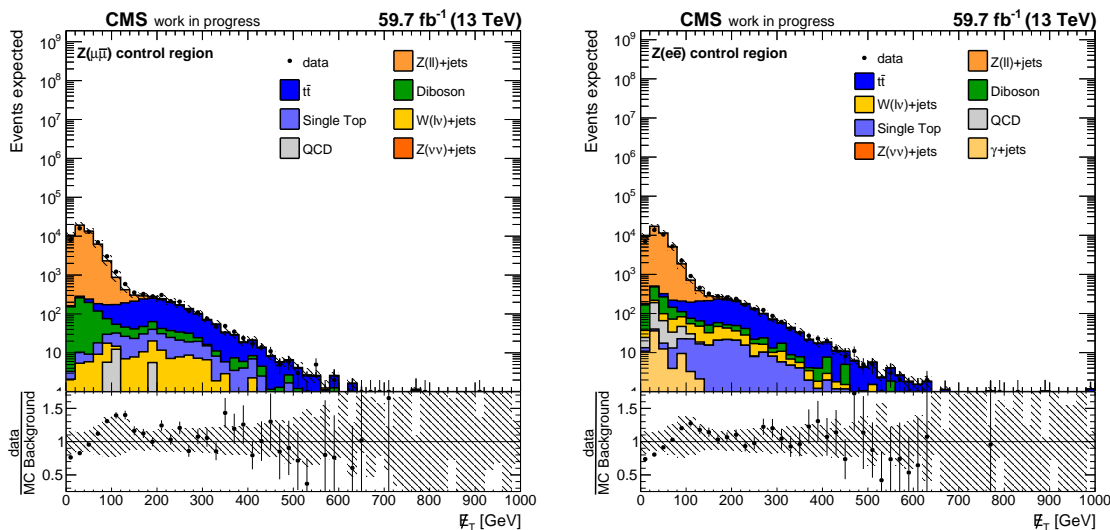
Figure 5.21: Distributions of the missing transverse momentum in the two Z boson control regions split according to the flavor of the two leptons. On the left-hand side, two muons are required. On the right-hand side, two electrons are required.

energy of jets in this region is not calibrated correctly. These effects are not modeled in simulation and therefore these events are removed.

5.7.2 Z boson control regions

In the Z boson control regions, events with $Z \to l\bar{l}$ whereas $l = e, \mu$ are enriched. These events are a direct proxy for events with $Z \to \nu\bar{\nu}$ in the signal region. In addition, this phase space is split between electrons and muons. Therefore, the selections are the following.

1. Exactly two loose electrons and no loose muon or exactly two loose muons and no loose electron are required. Due to the small branching fraction of the Z boson into charged leptons, this region has significantly smaller statistics than the other analysis regions. The issue of limited statistics is even increased after the top-tagging techniques are applied. To retain as much statistics as possible, only loose leptons are required.

2. The invariant mass of the two electron/muon system $m_{ee/\mu\mu}$ has to fulfill the requirement $60\,\text{GeV} \leq m_{ee/\mu\mu} \leq 120\,\text{GeV}$. This requirement is applied to enrich events in which the two lepton system has an invariant mass which is compatible with the Z boson mass. In addition, this requirement suppresses background events with two leptons that do not originate from a Z boson decay, e.g. $t\bar{t}$ production.

3. The missing transverse momentum has to be smaller than $120\,\text{GeV}$. This requirement suppresses $Z + \text{jets}$ events with $Z \to l\bar{l}$ in which the incorrect measurement of the missing transverse momentum is severe. Also, $t\bar{t}$ events with two leptonic W boson decays are suppressed. The aforementioned effects are shown in Fig. 5.21 in which the distributions of the missing transverse momentum are shown without any requirement on the missing transverse momentum for the 2018 data era. Starting from approximately $120\,\text{GeV}$, the production of top-quark-antiquark pairs is the most important background in this region. Since these regions are designed to enrich Z boson events with $Z \to l\bar{l}$, this phase space is removed.

4. No loose photon is found in the event. Since the targeted events of this control region are $Z + \text{jets}$ events with $Z \to l\bar{l}$, no prompt photons are expected.
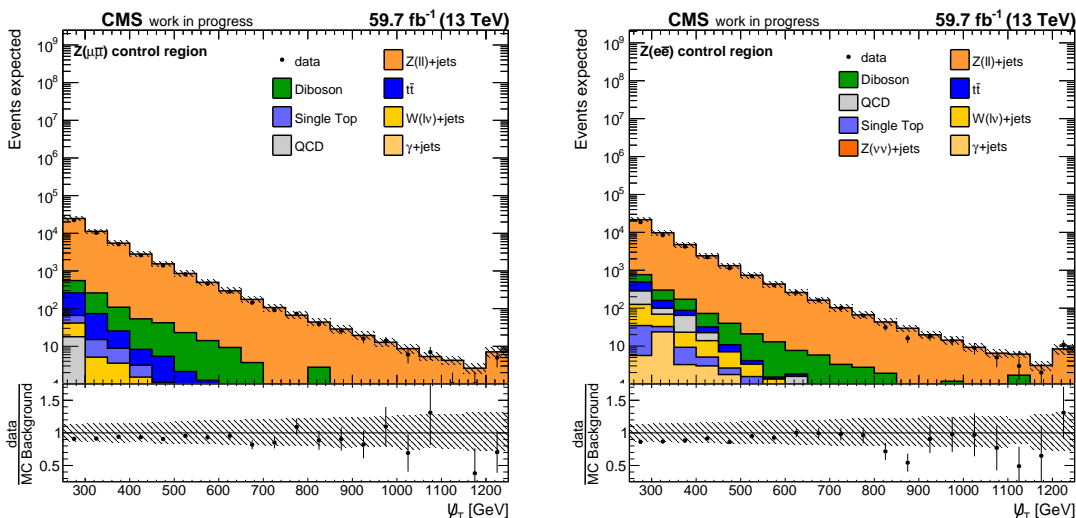
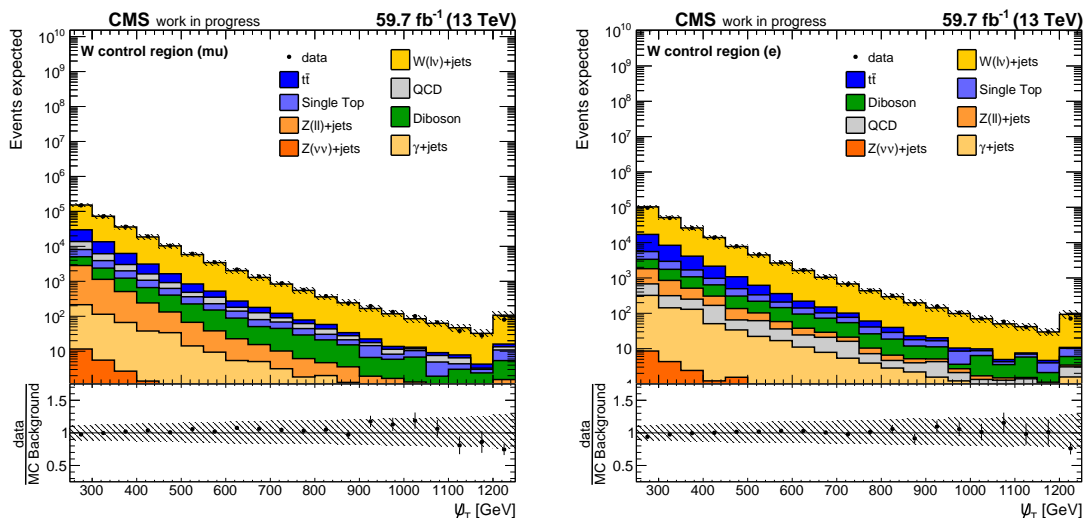Figure 5.22: Distribution of the hadronic recoil in the $Z \to l\bar{l}$ control regions in the 2018 data era with preselection requirements applied. The upper pad shows the absolute prediction of the different processes stacked on top of each other and the observation from data. The lower pad shows the ratio of the observation and the prediction. The uncertainty band corresponds to the square root of the quadratic sum of all uncertainties, see section 5.8.1.

5. At least one of the hadronic recoil triggers has to trigger on the events with muons, see Tab. 5.7.

6. At least one of the electron triggers has to trigger on the events with electrons, see Tab. 5.7.

In Fig. 5.22 the distribution of the hadronic recoil is shown in the 2018 data era as a representative example for this control region. The shown uncertainty band corresponds to the square root of the quadratic sum of all uncertainties considered in this analysis, see section 5.8.1. The distributions show that this region is very pure with only a very small contribution of diboson and $t\bar{t}$ production. As expected, the hadronic recoil distribution as a proxy for the Z boson p_T decreases rapidly with increasing hadronic recoil.

In Appendix B.1, a larger set of kinematic distributions is given and their agreement with data is shown for all data eras. In the 2018 data era, the prediction at low hadronic recoil is too high compared to data both for the electron and muon regions. This effect is, however, found to be larger for the electron region. The overprediction becomes smaller for increasing hadronic recoil. In the 2017 data era, see Fig. B.21, the overprediction compared to data is smaller than in the 2018 data era. The modeling in the 2016 data era is found not to show a significant overprediction by the simulation. All distributions, however, show that the data is modeled mostly within the total uncertainty of the prediction.

The distribution of the transverse momentum of the leading AK15 jet in Fig. B.22 is observed to not be modeled in an optimal way. The agreement between data and simulation in all three data eras shows a slope resulting in an overprediction by the simulation for larger values of the transverse momentum of the AK15 jet. However, the agreement between data and simulation for the distribution of the transverse momentum of the leading AK15 jet after applying the SD algorithm is observed to be better, see Fig. B.23.

In Fig. B.24 the distributions of the transverse momentum of the loose electrons and muons are shown. Besides the general overprediction by simulation in the 2018 and 2017 data era,

which was already mentioned, the modeling is observed to be good. No major slope in the ratio of data to simulation is observed.

The distribution of the jet mass of the AK15 jet after applying the SD algorithm is shown in Fig. B.25. As expected, the distribution is steeply falling at low masses due to the fact that the AK15 jets in this control region almost completely originate from generic QCD activity. The agreement between data and simulation is observed to be acceptable and mostly within the total uncertainty of the prediction.

In Fig. B.26 the distributions of the DeepAK15 discriminant used for top-tagging are given. The distributions show that the $Z + \text{jets}$ events with $Z \to \text{l}\bar{\text{l}}$ are mostly accumulated at low values of the discriminant as expected since the AK15 jets originate from generic QCD activity. In addition, the comparison of data and MC prediction shows a rising trend that becomes more flat to the end of the distribution. Since this discriminant is not calibrated to data, the modeling is not found to be optimal. However, a simplified calibration approach is performed in order to mitigate this mismodeling during the likelihood fit at the end of this analysis.

5.7.3 W boson control regions

Analogously to the Z boson control regions, W boson control regions with $W \to \text{l}\bar{\nu}$, where $\text{l} = \text{e}, \mu$, are defined. These events are a direct proxy for $W + \text{jets}$ events with $W \to \text{l}\bar{\nu}$ in the signal region in which the lepton is not reconstructed or identified. Again, the region is split into two regions depending on the flavor of the charged lepton, electron or muon.

1. Exactly one tight electron, no additional loose electron, and no loose muon is required to enrich events with one prompt electron. In contrast to this, exactly one tight muon, no additional loose muon and no loose electron is required to enrich events with one prompt muon. The leptons need to fulfill the tight identification criteria to retain a high purity for prompt leptons. No additional loose leptons are required to suppress processes with two prompt leptons, e.g. $Z + \text{jets}$ production with $Z \to \text{l}\bar{\text{l}}$.

2. No AK4 jet identified as originating from a bottom quark, using the DeepJet algorithm at the loose working point, outside ($\Delta R > 1.5$) of the leading AK15 jet is found. This requirement suppresses semileptonic $t\bar{t}$ events without setting any requirement on the leading AK15 jet.

3. No loose photon is found in the event. Similar to the Z boson control regions, no photons are expected in the event signature targeted by this control region.

4. The missing transverse momentum needs to be higher than $100\,\text{GeV}$. This lower threshold suppresses QCD multijet events, $\gamma + \text{jets}$ events as well as $Z + \text{jets}$ events with $Z \to \text{l}\bar{\text{l}}$ as is shown in Fig. 5.23 for the 2018 data era. In the electron region (right-hand side), the aforementioned processes have a significant contribution below $100\,\text{GeV}$, which vanishes almost completely after applying this requirement. In order to select the same phase space also for events with reconstructed muons (left-hand side), this requirement is also applied in the region with a tight muon. Furthermore, in both regions the simulation shows a more stable modeling with respect to the data starting from approximately $100\,\text{GeV}$ missing transverse momentum.

5. An upper threshold on the transverse mass of the lepton and missing transverse momentum system of $100\,\text{GeV}$ is applied. This threshold suppresses any leptonic mono-top signal contamination which would be expected in the range of high transverse masses, see section E.1 in Appendix E.
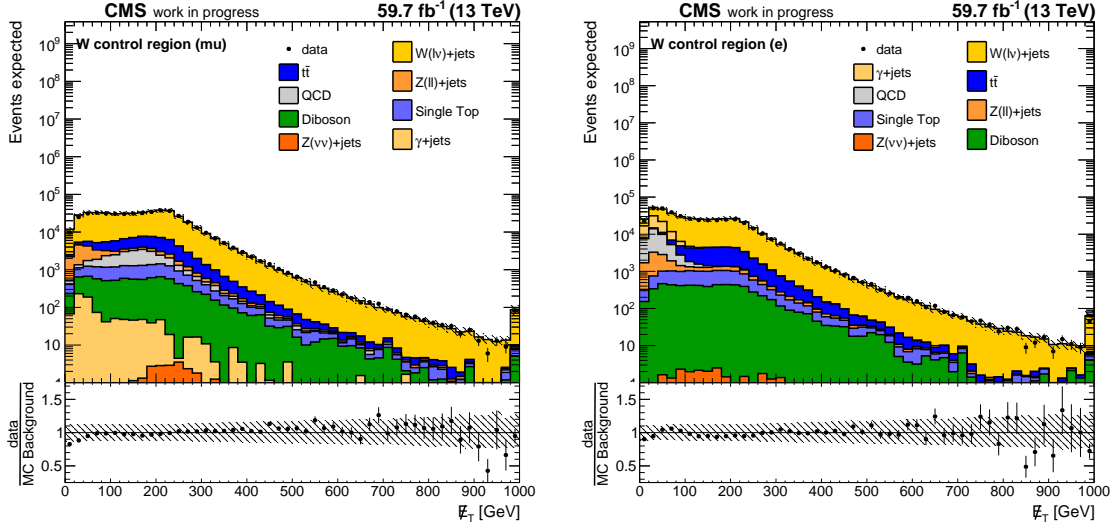
Figure 5.23: Distributions of the missing transverse momentum in the two W boson control regions split according to the flavor of the leptons. On the left-hand side, one muon is required. On the right-hand side, one electron is required.

6. At least one of the hadronic recoil triggers has to trigger on the events with muons, see Tab. 5.7.

7. At least one of the electron triggers has to trigger on the events with electrons, see Tab. 5.7.

The distribution of the hadronic recoil in the 2018 data era is given as a representative example for this control region in Fig. 5.24. The uncertainty band corresponds to the square root of the quadratic sum of all considered uncertainties in this analysis, see section 5.8.1. Both distributions show that the major process in these regions, as desired, is the $W +$ jets process with $W \rightarrow l\overline{\nu}$. A significant contribution of $t\overline{t}$ production is found as well. Comparable to the Z boson control regions, the distributions are falling steeply towards higher recoil values.

In Appendix B.2, distributions of a larger set of variables are given in order to check the modeling in this control region. The distributions of the hadronic recoil, see Fig. B.27, show mostly good agreement of simulation and recorded data. Only in the muon region of the 2017 data era, the discrepancy between data and simulation increases for increasing hadronic recoil. However, this effect is still within the total uncertainty of the prediction.

The distributions of the leading AK15 jet p_T, see Fig. B.28, are modeled in a comparable way to the Z boson control regions. However, the overprediction of the simulation with increasing AK15 jet p_T is not as severe as in the Z boson control regions. Furthermore, at low values of the hadronic recoil in the range between $150\,\mathrm{GeV}$ and $250\,\mathrm{GeV}$, the simulation does not predict enough events. In addition, the transverse momentum of the leading AK15 jet after applying the SD algorithm , see Fig. B.29, is modeled in a significantly improved manner compared to the momentum before applying the SD algorithm. The trend observed for the latter is heavily reduced and a good modeling within the uncertainties is found.

The distributions in Fig. B.30, showing the transverse momentum of the electron and muon, show a good modeling within the uncertainties in all data eras.

In Fig. B.31 and Fig. B.32 the distributions of the AK15 jet mass after applying the SD algorithm as well as the distributions of the DeepAK15 top-tagging discriminant are given,

Figure 5.24: Distributions of the hadronic recoil in the $W \to l\bar{\nu}$ control regions in the 2018 data era with preselection requirements applied. The upper pad shows the absolute prediction of the different processes stacked on top of each other and the observation from data. The lower pad shows the ratio of the observation and the prediction. The uncertainty band corresponds to the square root of the quadratic sum of all uncertainties, see section 5.8.1.

respectively. The distributions of the AK15 jet SD mass, as expected, shows an accumulation of events mostly at lower values for the W+jets events with only suppressed contributions at higher values. The DeepAK15 top-tagging discriminant behaves comparably in the W boson control region and in the Z boson control region. For large values of the discriminant, the $W + \text{jets}$ events are significantly suppressed and the small $t\bar{t}$ contribution in this region is enriched. The agreement between recorded data and simulation is comparable between the Z boson and W boson control regions except for high values of the discriminant. This is due to the $t\bar{t}$ contribution showing a different response to the top-tagging discriminant. As already stated, the top-tagging discriminant is not calibrated to data at this stage, therefore explaining the discrepancies observed in the modeling.

5.7.4 Top-Quark-Antiquark-Pair control regions

The $t\bar{t}$ analysis regions are very similar to the W boson control regions, however, $t\bar{t}$ events are enriched. This region is split depending on the flavor of the charged lepton as well.

1. All selections which are required in the W boson control regions, see above, need to be fulfilled except for the requirement on the number of AK4 jets identified as originating from a bottom quark outside of the leading AK15 jet.

2. At least one AK4 jet identified as originating from a bottom quark, using the DeepJet algorithm at the loose working point, outside ($\Delta R > 1.5$) of the leading AK15 jet is found. This selection ensures that this region is enriched with $t\bar{t}$ events and that $W + \text{jets}$ events with $W \to l\bar{\nu}$ are suppressed.

3. An upper threshold on the transverse mass of the lepton and missing transverse momentum system of $100 \, \text{GeV}$ is applied. This suppresses any leptonic mono-top signal contamination which would be expected in the range of high transverse masses, see section E.1 in Appendix E.
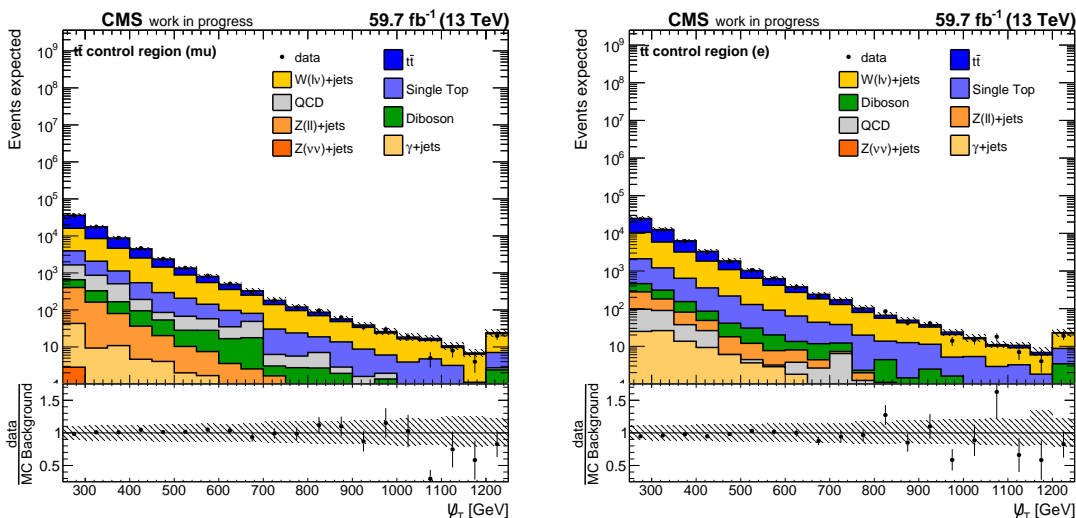
Figure 5.25: Distributions of the hadronic recoil in the $t\bar{t}$ control regions in the 2018 data era with preselection requirements applied. The upper pad shows the absolute prediction of the different processes stacked on top of each other and the observation from data. The lower pad shows the ratio of the observation and the prediction. The uncertainty band corresponds to the square root of the quadratic sum of all uncertainties, see section 5.8.1.

As a representative example for this control region, the distribution of the hadronic recoil in the 2018 data era is shown in Fig. 5.25. The uncertainty band corresponds to the square root of the quadratic sum of all uncertainties considered in this analysis, see section 5.8.1. Both distributions show that the major process in this control region, as desired, is the $t\bar{t}$ process, with some smaller contributions from single top-quark production and W + jets production.

The distributions of several variables in this control region are provided in Appendix B.3. The distributions of the hadronic recoil $\not{p}_{\mathrm{T}}$, see Fig. B.33, again look comparable to the Z boson and W boson control regions. The modeling in this control region is well within the uncertainties in the 2017 and 2018 data eras. Only in the muon region of the 2017 data era, some larger discrepancies are found between 300 GeV and 500 GeV, comparable to the W boson control regions in the 2017 data era. In the 2016 data era, a small overprediction of the simulation, which increases with increasing hadronic recoil, is found.

The modeling of the transverse momentum of the leading AK15 jet is again comparable to the modeling found in the W boson control regions, as can be seen in Fig. B.34. An overprediction by the simulation is observed with increasing transverse momentum of the leading AK15 jet. This effect is more pronounced in the 2016 data era than in the 2017 and 2018 data eras. Again, applying the SD algorithm to the leading AK15 jet improves the modeling of the transverse momentum as is presented in the distributions in Fig. B.35.

The distributions of the transverse momentum of the leptons, given in Fig. B.36, are also modeled well. The aforementioned overprediction by the simulation in the 2016 data era is also visible in these distributions.

The distributions of the SD mass of the leading AK15 jet are given in Fig. B.37. The shape of the distributions is as expected. Since this region is enriched in semileptonic $t\bar{t}$ events, the SD mass of the AK15 jet is expected to be centered around the top quark mass if the decay products of the hadronic top quark decay are clustered within the AK15 jets.
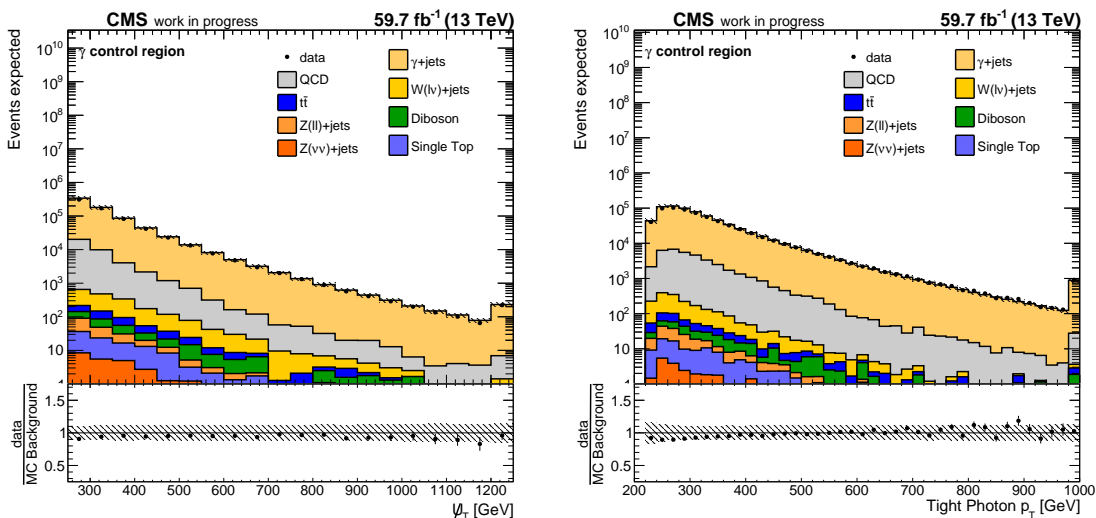
Figure 5.26: Distributions of the hadronic recoil (left-hand side) and the photon p_T (right-hand side) in the γ control region in the 2018 data era with preselection requirements applied. The upper pad shows the absolute prediction of the different processes stacked on top of each other and the observation from data. The lower pad shows the ratio of the observation and the prediction. The uncertainty band corresponds to the square root of the quadratic sum of all uncertainties, see section 5.8.1.

The distributions show a peak close to the mass of the top quark and close to the mass of the W boson. The peak close to the W boson mass is due to events in which only the hadronic decay products of the W boson are clustered within the AK15 jet. The modeling of this variable is mostly within the uncertainties, however, a change of the agreement between data and simulation is observed close to the mass of the top quark. This change in modeling is not observed in the 2016 data era.

The final distribution given in section B.3 is again the top-tagging discriminant, see Fig. B.38. As expected, the backgrounds other than $t\bar{t}$ production, e.g. W + jets production, are mostly enriched for small values of the discriminant whereas $t\bar{t}$ events are enriched towards larger values.

5.7.5 Photon control region

The final control region is used to enrich γ + jets events with a well reconstructed photon as a proxy for γ + jets events in the signal region in which the photon is not reconstructed or identified. The selection requirements on top of the base selections are given in the following.

1. Exactly one tight photon and no additional loose photon has to be found in the event.

2. At least one of the photon triggers has to trigger on the event, see Tab. 5.7.

In Fig. 5.26 the distributions of the hadronic recoil and the transverse momentum of the photon in the 2018 data era are shown as representative examples for this control region. The uncertainty band corresponds to the square root of the quadratic sum of all considered uncertainties in this analysis, see section 5.8.1. The distributions show that, as expected, the largest contribution in this region is given by γ + jets. A smaller contribution is due to QCD multijet events.

Several distributions of variables in the $\gamma + \text{jets}$ control region are given in section B.4. The distributions of the hadronic recoil on the left-hand side of Fig. B.39 show an acceptable modeling within the total uncertainty. All three distributions show a comparable behavior of the agreement between data and simulation regarding the shape. Only in the 2018 data era, the simulation has a slight overprediction compared to the other two data eras. The same observations are made for the distributions of the transverse momentum of the photon, see the right-hand side of Fig. B.39.

In Fig. B.40 the distributions of the transverse momentum of the leading AK15 jet before and after applying the SD algorithm are given on the left-hand side and right-hand side, respectively. The 2017 and 2018 data eras show a comparable behavior of the distributions. In the 2016 data era, the modeling deteriorates for increasing transverse momentum of the AK15 jet. These differences are probably because of the different $\gamma + \text{jets}$ simulations used in the 2016 data era compared to the 2017 and 2018 data eras, see section 5.5.

The final two sets of distributions show again the mass of the AK15 jet after the SD algorithm is applied and the top-tagging discriminant in Fig. B.41. Comparable to the other $V + \text{jets}$ processes in the other control regions, the SD mass distribution for $\gamma + \text{jets}$ is suppressed for large values of the SD mass compared to lower masses. The agreement between data and simulation is found to be different for the different data eras. The top-tagging discriminant also shows the same behavior as in the other $V + \text{jets}$ categories. A large part of the distribution is in the range of low discriminant values since the AK15 jets originate from QCD activity. Also this variable shows a different behavior of the 2016 data era and the 2017 and 2018 data eras. These differences could be again due to the different underlying simulations as well as the different parton shower tunes when comparing the 2016 data era with the 2017 and 2018 data era.

5.7.6 Signal region

By the basic event selections given above, events are selected that have a signature almost compatible with the expectation for hadronic mono-top signatures. The selections given in the following are added on top of these selections to define the signal region, however, still not applying any top-tagging techniques.

1. At least one of the hadronic recoil or missing transverse momentum triggers has to trigger on the event, see Tab. 5.7.

2. Veto any event that contains a loose electron, loose muon, or loose photon. Since in the hadronic mono-top signature no prompt leptons or photons are expected, the loose object collections, which a have a high efficiency for reconstructing and identifying prompt leptons and photons, are used to veto these events.

3. No AK4 jet identified as originating from a bottom quark, using the DeepJet algorithm at the loose working point, outside ($\Delta R > 1.5$) of the leading AK15 jet is found. This requirement is chosen to further suppress background events that are not compatible with the hadronic mono-top signature. Especially $t\bar{t}$ events are enriched after the top-tagging selection. In order to suppress the $t\bar{t}$ background as much as possible, this requirement on the additional expected b-tagged jets outside of the leading AK15 jet can be used.

4. Events which have a missing transverse momentum smaller than $470\,\text{GeV}$ and an azimuthal angle of the missing transverse momentum in the range $-1.62 \leq \phi \leq -0.62$ are vetoed. This requirement is an additional measure to suppress the HEM issue in the signal region and was found by the CMS mono-jet analysis [192].
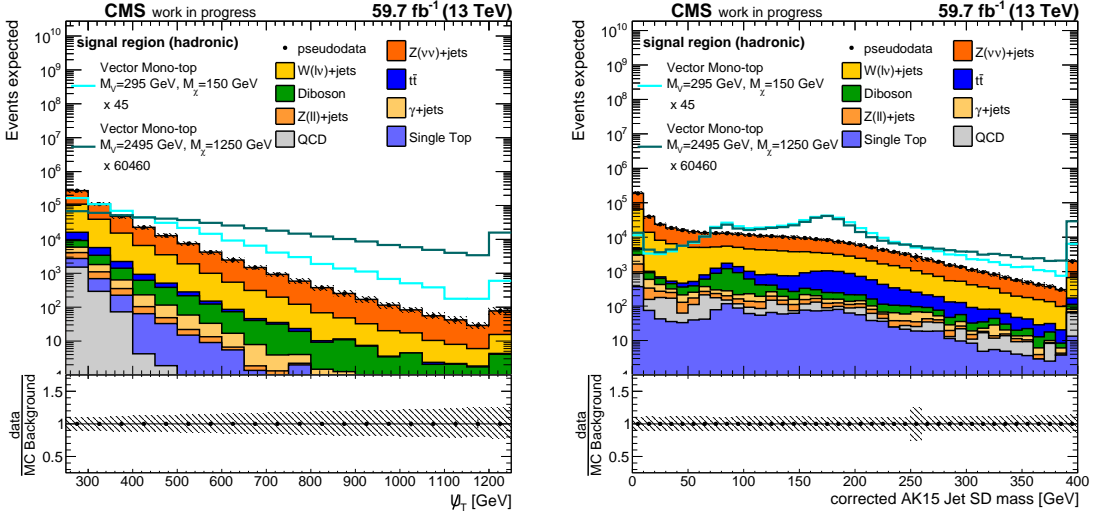
Figure 5.27: Distribution of the hadronic recoil and the mass of the AK15 jet after applying the SD algorithm in the signal region in the 2018 data era with preselection requirements applied. The upper pad shows the absolute prediction of the different processes stacked on top of each other and the observation from background-only pseudodata. The lower pad shows the ratio of the observation and the pseudodata, which is unity by construction. The uncertainty band corresponds to the square root of the quadratic sum of all uncertainties, see section 5.8.1. Two mono-top signal predictions, which are scaled to the total background yield, are overlaid and the corresponding scale factors are given in the legend.

The distribution of the hadronic recoil in the 2018 data era is shown as a representative example in Fig. 5.27. Instead of real data, a set of pseudodata built from all simulated background processes is created and shown. It is observed that the major background processes are $Z + \text{jets}$ with $Z \to \nu\bar{\nu}$ and $W + \text{jets}$ with $W \to l\bar{\nu}$. Furthermore, distributions of two mono-top models in two different mass regimes are overlaid as well.

The most important distributions in the signal region are given in Appendix B.5. The hadronic recoil and the transverse momentum of the AK15 jet are shown in Fig. B.42. As expected, due to the involved high masses of the mediator and the DM candidates, the hadronic recoil and the leading AK15 jet p_T tend towards higher values for the signals compared to the SM background processes. Furthermore, it is observed that, as expected, the relative contributions to regions of high hadronic recoil and AK15 jet p_T become larger with higher masses of the mediator and the DM candidates.

The mass of the leading AK15 jet after applying the SD algorithm and the top-tagging discriminant is presented in Fig. B.43. The SM background processes have a falling distribution of the AK15 SD jet mass with the by far largest contributions at very low masses. This is expected because the jets in these events originate from generic QCD radiation instead of heavy resonances. In contrast, the mono-top signals and the $t\bar{t}$ contributions show a peak at approximately the mass of the W boson and the top quark. The top-tagging discriminant also behaves as expected. Contributions from the $Z + \text{jets}$ and $W + \text{jets}$ processes are accumulated at low values whereas the mono-top signals but also the $t\bar{t}$ contributions are enriched towards larger values. As is explained in the next section, the SD jet mass as well as the top-tagging discriminant are used to further suppress $V + \text{jets}$ background processes for the final event selection.

5.7.7 Top-tagging selection

In order to finally enrich events in which the leading AK15 jet is likely to originate from a hadronically decaying top quark, two additional requirements are applied on top of the selection criteria in the signal region introduced previously. These requirements are also applied in all other regions of the analysis to keep the phase spaces between the signal region and the control regions as similar as possible. This is needed such that the constraints on the different background processes obtained from data in the corresponding control regions are as reliable as possible.

The leading AK15 jet needs to have a SD mass m_{SD} fulfilling $105\,\mathrm{GeV} \leq m_{\mathrm{SD}} \leq 210\,\mathrm{GeV}$. This requirement is motivated by the fact that the SD mass of the AK15 jet should be centered around the top quark mass for AK15 jets originating from a hadronically decaying top quark, see section 4.3.5. The exact values are chosen to be in agreement with the thresholds which were chosen for the DeepAK8 top-tagging scale factors provided by the CMS collaboration [219]. Furthermore, the distributions of the mass of the leading AK15 jet after applying the SD algorithm, see the right-hand side distribution in Fig. 5.27 or the distributions on the left-hand side of Fig. B.43, show that the dominant part of the signal phase space is within this range whereas the dominant part of background phase space is removed by this criterion.

Furthermore, the DeepAK15 top-tagging discriminant value D_{TvsQCD}, see section 4.3.5, has to be greater or equal to 0.3. This lower threshold enriches events with hadronically decaying top quarks by exploiting the multivariate DeepAK15 top-tagging discriminant, see section 4.3.5.

To motivate the exact value that is chosen, the distribution of the discriminant in the signal region is studied in more detail comparing the shape of the distribution for signal events and background events. In this context, signal events do not refer to events originating from the mono-top signal samples but events that fulfill a requirement on the leading AK15 jet. The leading AK15 jet has to be top-matched on generator level. This means that a bottom-type quark originating from the decay of a top quark as well as two quarks originating from the decay of a W boson are matched to the leading AK15 jet using a $\Delta R < 1.5$ criterion. Furthermore, the aforementioned W boson needs to originate from the decay of the aforementioned top quark. The working point of the top-tagger is then defined such that the efficiency to tag these top-matched AK15 jets is 90%. This method of determining the working point has the advantage that it is independent of the process at hand, since the signal definition relies on the property of the AK15 jet instead of being a specific process. On the left-hand side of Fig. 5.28, the distribution of the top-tagging discriminant of the leading AK15 jet is given for the 2018 data era as an example. The corresponding distributions in the 2017 and 2016 data eras are shown on the left-hand side of Fig. B.44 in Appendix B. In these distributions, the mono-top events as well as the $t\bar{t}$ and single top events are chosen to have a top-matched leading AK15 jet. First, it is observed how the top-tagging discriminant separates the contributions from V + jets processes, which by definition cannot have a top-matched leading AK15 jet, and the processes involving the production of top quarks. Furthermore, since the processes involving the production of top quarks ($t\bar{t}$ production, single top quark production, mono-top production) have the additional selection of a top-matched leading AK15 jet, these processes show a similar behavior of the top-tagging discriminant.

The receiver-operator-characteristic shows the relation between signal efficiency and the background rejection given by scanning over possible lower thresholds on the discriminant value. The signal efficiency here is defined as the fraction of events which have a top-matched leading AK15 jet with a top-tagging discriminant value larger than the threshold
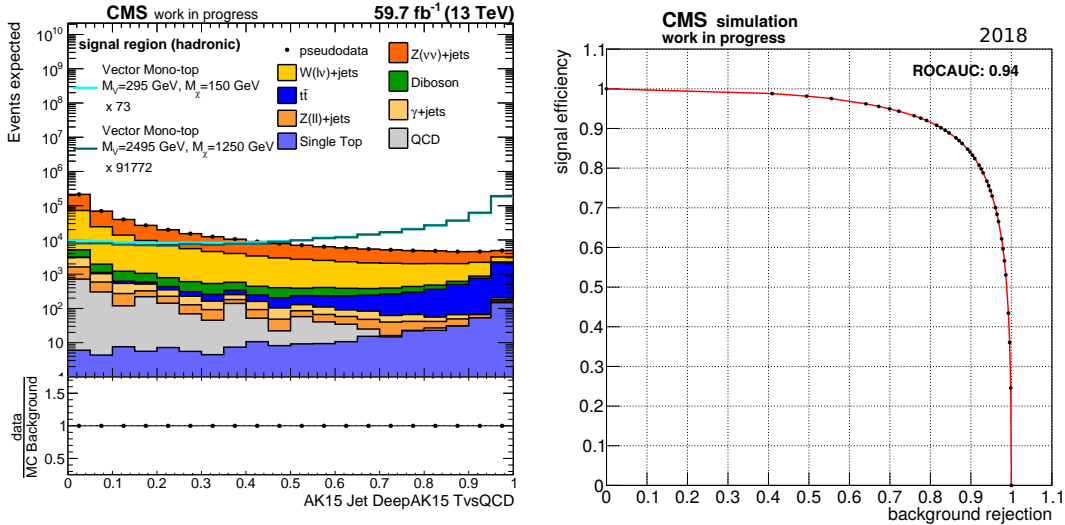
Figure 5.28: Left-hand side: Distribution of the top-tagging discriminant of the leading AK15 jet in the signal region after the preselection is applied in the 2018 data era. The $t\bar{t}$, single top quark, and mono-top events are required to have a top-matched leading AK15 jet, see section 5.7.7. Right-hand side: Receiver-operator-characteristic for the top-tagging discriminant of the leading AK15 jet in the signal region after the preselection. For the definition of signal efficiency and background rejection, see the description in section 5.7.7.

compared to all events which have a top-matched leading AK15 jet. The background rejection is then defined as the fraction of V + jets events which have a leading AK15 jet with a top-tagging discriminant value smaller than the cut value compared to all V + jets events. The relation between the signal efficiency and the background rejection is shown on the right-hand side of Fig. 5.28 for the 2018 data era as an example and in Fig. B.44 on the right-hand side for all data eras. As can be observed, the top-tagging discriminant behaves in a similar way in all data eras. With increasing working point, the background rejection rises significantly whereas the signal efficiency only drops a small amount until a turning point is reached. After the turning point, the signal efficiency starts to drop significantly whereas the background rejection does not increase significantly anymore. The chosen value of 90% signal efficiency is right in front of this turning point at which the top-tagger starts to heavily loose efficiency. Another reason to choose the working point of the top-tagger at a rather low value is that the number of events in the Z boson control regions of the analysis is already limited due to the selection criteria and the small branching fraction of the Z boson into charged leptons. Since the requirement on the SD mass of the leading AK15 jet already removes large amounts of V + jets events, increasing the cut on the top-tagging discriminant even more would render the Z + jets region with Z → l$\bar{\text{l}}$ unusable due to the fact that almost no event would be left. As a conclusion, it is found that the lower threshold on the top-tagging discriminant to obtain the aforementioned 90% efficiency is approximately 0.3 in all eras.

After applying the aforementioned top-tagging selection on top of the event selections explained previously, the final event selection is obtained. In Fig. 5.29 the distributions of the hadronic recoil in a subset of the control regions after applying the final selection criteria are given for the 2018 data era as an example. The remaining distributions of the hadronic recoil in the 2017 and 2016 data eras as well as in all other control regions are given in Appendix C.

It is observed that the agreement between data and simulation is significantly worse after applying the final selection criteria compared to the agreement after the preselection. However, since the top-tagging discriminant is not calibrated to data, this is expected. This can intuitively be understood by examining the distributions of the top-tagging discriminant given in Fig. B.26, Fig. B.32, Fig. B.38, and Fig. B.41 in Appendix B.5. These distributions show that the top-tagging discriminant is not modeled well comparing data and simulation. Therefore, it is expected that the agreement between data and simulation becomes worse as soon as a requirement on the value of the top-tagging discriminant is set. However, it is also observed that the deterioration of the modeling is significantly larger in control regions in which $V + \text{jets}$ processes are the dominant contribution. In the control regions in which processes involving the production of top quarks are the most dominant contribution, the agreement between data and simulation is still significantly better. This points to the possibility that the top-tagging efficiency is more similar in data and simulation than the top-mistagging rate. In order to account for the mismodeling regarding the top-tagging discriminant, scale factors for the top-tagging efficiency and top-mistagging rate are introduced into the statistical model of this analysis as will be explained in section 5.8 on the statistical model.

Furthermore, it is observed in Fig. 5.29 that the Z boson control region with $Z \rightarrow l\bar{l}$ is, as already mentioned, heavily affected by the top-tagging selection criteria regarding the available number of events. In addition, the production of top-quark-antiquark pairs is the dominant background process even in the W boson control regions after applying the top-tagging criteria as is shown in Fig. 5.29.

All parts necessary for the hadronic mono-top analysis are in place after applying the final selection criteria and the statistical model can be built. This is explained in section 5.8.
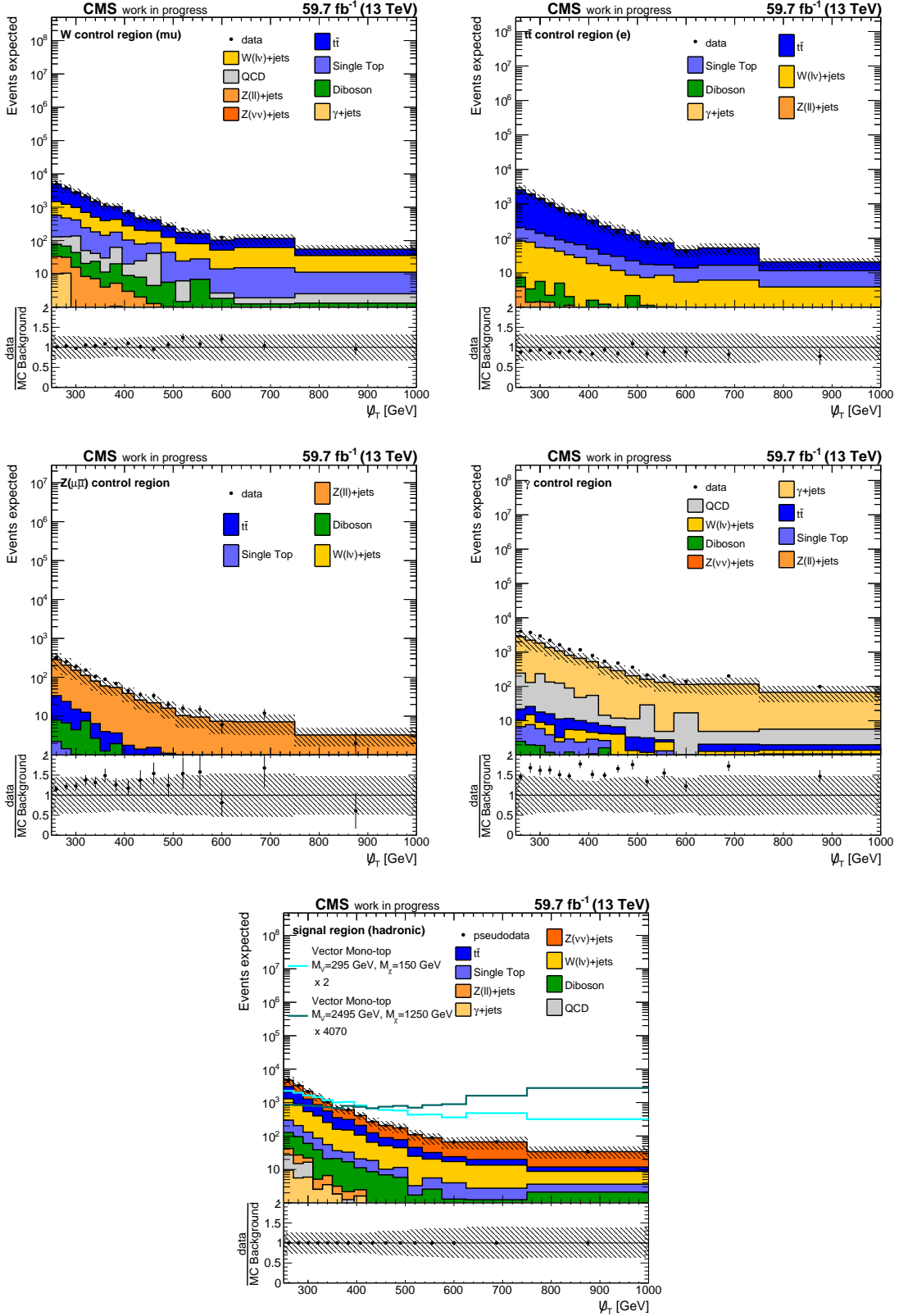
Figure 5.29: Distribution of the hadronic recoil in a subset of control regions of the 2018 data era with the final selection criteria applied. The upper pad shows the absolute prediction of the different processes stacked on top of each other and the observation from data or pseudodata. The lower pad shows the ratio of the observation and the prediction. The uncertainty band corresponds to the square root of the quadratic sum of all considered uncertainties, see section 5.8.1. Two mono-top signal predictions, which are scaled to the total background yield, are overlaid and the corresponding scale factors are given in the legend.

5.8 Statistical model

In this section the statistical model is further explained and validated. This includes the already mentioned transfer factors which connect the predictions of several SM backgrounds in different regions of the analysis. In addition, the different systematic uncertainties considered in this thesis are summarized.

5.8.1 Systematic uncertainties

As was already mentioned in different sections of this thesis, several systematic uncertainties are considered for the final result. These uncertainties can affect the rate and/or the shape of expected distributions of the observables considered, i.e. the distribution of the hadronic recoil. In Tab. 5.12 an overview of the experimental systematic uncertainties considered in this thesis is given. The theoretical systematic uncertainties considered in this thesis are presented in Tab. 5.13 and 5.14. In the following, these uncertainties and the chosen correlation scheme are explained in more detail.

Luminosity

The uncertainties on the measurement of the total integrated luminosity for the different years are rate uncertainties and are provided centrally by the CMS collaboration [220–224]. For each era, the uncertainty consists of uncorrelated and correlated uncertainty sources. The uncorrelated uncertainties are $\pm 2.2\%, \pm 2.0\%, \pm 1.5\%$ for the 2016, 2017, 2018 data era, respectively. One additional uncertainty, on the assumption that the proton bunch densities in x and y direction factorize, is correlated between the three data eras and has an effect of $\pm 0.9\%, \pm 0.8\%, \pm 2.0\%$ for the 2016, 2017, 2018 data era, respectively. Another uncertainty on the length-scale calibration of the beam-beam separation and the calibration of the beam current is correlated only between 2017 and 2018 and has an effect of $\pm 0.4\%$ and $\pm 0.3\%$ for the 2017 and 2018 data era, respectively. The last luminosity uncertainty considered, associated to ghost and satellite fractions as well as the beam-beam deflection, is correlated only between the 2016 and 2017 data eras and results in $\pm 0.8\%$ and $\pm 0.6\%$, respectively. These uncertainties result in overall six nuisance parameters implemented into the statistical model of this analysis.

Jet energy scale and jet energy resolution

The total uncertainty of the jet energy scale and the jet energy resolution corrections, see section 5.6.8, are considered in this analysis. These uncertainties affect the shape and the rate of the distributions of the hadronic recoil due to changing the kinematics of all the jets considered in this analysis. Furthermore, these uncertainties directly affect the measurement of the missing transverse momentum and hence the hadronic recoil. These effects lead to migrations of events into the phase space of the analysis as well as out of the phase space of the analysis. These uncertainties are assumed to be uncorrelated between the three data eras and therefore they are parameterized using six different nuisance parameters (2×3) within the statistical model. Using the total uncertainties of the jet energy scale and the jet energy resolution is a simplified approach which will be replaced by considering all uncertainty sources separately in conjunction with a dedicated nuisance parameter in the future. Nevertheless, effects due to jet energy scale and jet energy resolution are expected to cancel to a significant extent in the transfer factors.

Electron identification and reconstruction

As was explained in section 5.6.2, electron identification and reconstruction scale factors are used as additional weights multiplied to the total event weight of simulated events in this

analysis. These scale factors are subject to uncertainties during their derivation and are provided as two different variations of the scale factors. These uncertainties, which affect the rate and the shape of the distributions, are propagated separately for the identification and reconstruction scale factors to the final result of this analysis. Furthermore, these uncertainties are assumed to be uncorrelated between the three data eras. Because of this, six nuisance parameters (2×3) are used to propagate the effect of electron identification and reconstruction uncertainties to the statistical model of this analysis.

Muon identification and reconstruction

Muon identification and isolation scale factors are used in this analysis to correct the identification and isolation efficiencies found in simulation to match the efficiencies measured in recorded data, see section 5.6.4. These scale factors are subject to uncertainties during their derivation as well comparable to the electron scale factors. The uncertainties are provided as two different sets of varied scale factors. These uncertainties, which affect the rate and the shape of the distributions of the hadronic recoil, are propagated separately for the identification and isolation scale factors to the final result of this analysis. Analogously to the electron scale factors, these uncertainties are assumed to be uncorrelated between the three data eras. Because of this, six nuisance parameters (2×3) are used to propagate the effect of muon identification and isolation uncertainties to the statistical model of this analysis.

Photon identification

As described in section 5.6.3, identification scale factors are used for the photons in simulated events to correct their identification efficiencies such that these efficiencies are comparable to the efficiencies measured in data. In the 2017 and 2018 data era, these scale factors have two different uncertainties associated to them. The first uncertainty is a base uncertainty and the second uncertainty covers the extrapolation of the identification scale factors to high transverse momenta of the photons, see section 5.6.3. The extrapolation uncertainties are only available for the 2017 and 2018 data eras. The uncertainties on the identification scale factors, which affect the rate and the shape of the distributions of the observables, are propagated to the statistical model of this analysis as five different nuisance parameters $(2 \times 3 - 1)$.

Trigger

Scale factors are used in this analysis to render the trigger efficiencies comparable between recorded data and simulation, see section 5.6.1. These scale factors are subject to uncertainties, which are propagated to the final result of this analysis. This is done separately for the combined electron trigger path, photon trigger path, and missing transverse momentum or hadronic recoil trigger path. The uncertainties on the trigger scale factors are provided as two different sets of varied scale factors, affecting the shape and rate of the distributions, and are assumed to be uncorrelated between the three different years. This results in three different nuisance parameters (1×3) for each overall trigger selection and therefore in nine overall nuisance parameters (3×3) considering all three trigger selections used in this thesis.

B-tagging

In section 5.6.6 the usage of b-tagging scale factors was explained. These scale factors are subject to uncertainties which are propagated to the final result of this analysis as separate uncertainties on the scale factors for light-flavor jets and the b-/c-flavor jets, see

section 5.6.6. The b-tagging scale factor uncertainties affect the shape and the rate of the distributions of the hadronic recoil. The uncertainty of the light-flavor jet scale factors is assumed to be uncorrelated to the uncertainty of the b-/c-flavor jet scale factors. However, the uncertainties of the b-/c-flavor scale factors are assumed to be correlated. Furthermore, the b-tagging scale factor uncertainties are assumed to be uncorrelated between the three data eras. This results in six independent nuisance parameters (2×3) included into the statistical model of this analysis.

Pileup

As already explained in section 5.5.2, a reweighting procedure for the simulated events is performed to reproduce the distribution of the average number of proton-proton interactions in one luminosity section that is found in data. As an input to this reweighting procedure, the total inelastic proton-proton cross section of $69.2 \, \mathrm{mb}$ is used. An uncertainty of $\pm 4.6\%$ on this cross section is used to obtain the uncertainty due to pileup as varied reweighting factors. This uncertainty changes the shape and the rate of the distributions of the considered observables. In addition, the pileup uncertainty is assumed to be uncorrelated between all three data eras. Therefore, three independent nuisance parameters are used to propagate this uncertainty to the statistical model of this analysis.

L1 prefire

The systematic uncertainty on the mitigation of the prefire issue of the L1 trigger in the 2016 and 2017 data eras, see section 5.5.3, is also propagated to the final result of this analysis. Since the mitigation of the prefire issue is done using additional event weights, this uncertainty affects the rate and the shape of the distributions of the observables. This uncertainty is assumed to be correlated between the 2016 and 2017 data eras. Therefore, one nuisance parameter representing this systematic uncertainty is introduced into the statistical model.

Top-tagging

In order to identify AK15 jets that are originating from the hadronization of the decay products of a hadronic top quark decay, the DeepAK15 tagger, see section 4.3.5 and section 5.7.7, is used. As was presented in the studies of these sections, the top-tagging discriminant shows a different behavior comparing data and simulation. Then, by applying a lower threshold on the value of the top-tagging discriminant as is done in this analysis, the agreement between data and simulation deteriorates rather significantly.

In order to mitigate this effect, a heavily simplified calibration procedure is performed during the maximum likelihood fit of this analysis since no official scale factors derived by the CMS collaboration are available at this point in time. A full calibration of the top-tagging discriminant is beyond the scope of this thesis. The simplified calibration procedure relies on the same generator information which was used in section 5.7.7 to define the working point of the top-tagging discriminant. This information is whether the AK15 jet at hand is top-matched or not. The AK15 jet is top-matched if a bottom-type quark originating from the decay of a top quark as well as two quarks originating from the decay of a W boson are matched to the AK15 jet using a $\Delta R < 1.5$ criterion. Furthermore, the aforementioned W boson needs to originate from the decay of the aforementioned top quark. In all other cases, the AK15 jet at hand is considered not to be top-matched.

At this stage of the analysis, the leading AK15 jet in every event has a top-tagging discriminant value greater or equal to 0.3, see section 5.7.7, which defines the AK15 jet as top-tagged. An AK15 jet is consequently defined to be correctly top-tagged if it is

also top-matched. If it is not top-matched, it is defined as incorrectly top-tagged or top-mistagged. Then, the top-tagging efficiency is defined as

$$\epsilon_{\text{top-tag}} = \frac{\#\text{AK15 jets top-tagged and top-matched}}{\#\text{AK15 jets top-matched}} . \tag{5.25}$$

In order to equalize the top-tagging efficiencies in data and simulation, a top-tagging efficiency scale factor, analogously to the b-tagging scale factors in section 5.6.6, is introduced for the simultaneously top-matched and top-tagged AK15 jets. These scale factors, comparable to the b-tagging scale factors, are subject to systematic uncertainties. Analogously, the top-mistagging efficiency/rate is defined as

$$\epsilon_{\text{top-mistag}} = \frac{\#\text{AK15 jets top-tagged and not top-matched}}{\#\text{AK15 jets not top-matched}} . \tag{5.26}$$

Similar to the top-tagging efficiency, top-mistagging scale factors are introduced for the leading AK15 jets which are top-tagged but not top-matched. Also the top-mistagging scale factors are subject to systematic uncertainties.

Since the DeepAK15 top-tagging discriminant distinguishes between a large number of different generator-based classes of AK15 jets, see section 4.3.5, a calibration with scale factors would optimally depend on every generator-class of the AK15 jets and the kinematic variables of the AK15 jets. In addition, a calibration would optimally be performed using a large set of independent data in dedicated control regions for the different generator-classes. This is, however, beyond the scope of this thesis. Therefore, a heavily simplified approach is used with the main emphasis on being conservative rather than precise. The top-tagging efficiency scale factors used in this analysis are defined as

$$\text{SF(top-matched, AK15 jet } p_{\text{T}} < 400\,\text{GeV} = 1.0 \pm 0.2$$
$$\text{SF(top-matched, AK15 jet } p_{\text{T}} \geq 400\,\text{GeV} = 1.0 \pm 0.2$$

and the top-mistagging scale factors are

$$\text{SF(not top-matched, AK15 jet } p_{\text{T}} < 400\,\text{GeV} = 1.0 \pm 0.2$$
$$\text{SF(not top-matched, AK15 jet } p_{\text{T}} \geq 400\,\text{GeV} = 1.0 \pm 0.2$$

with ± 0.2 representing the one standard-deviation variation of the associated scale factor and nuisance parameter. The scale factors are implemented as uncertainties affecting the rate and the shape of the hadronic recoil and are determined in-situ during the maximum likelihood fit to data used to extract the results of this analysis. The large 20% uncertainties are chosen to conservatively account for shortcomings of this approach. This method therefore results in twelve (3×4) additional nuisance parameters introduced into the statistical model of this analysis.

Higher-order V + jets reweighting

As was discussed in section 5.5.1, reweighting factors for simulated V + jets events are used to improve the modeling of the simulated V + jets processes. Well-defined theoretical uncertainties as a function of the transverse momentum of the vector bosons and their correlations can be implemented like this into the analysis, see section 5.5.1 and [189]. These uncertainties at NLO in QCD and EWK perturbation theory affect the rate as well as the shape of the distributions of the hadronic recoil. In order to include NLO QCD uncertainties, three nuisance parameters, representing correlated NLO QCD uncertainties between all V + jets processes, are needed. For the NLO EWK uncertainties nine different

nuisance parameters are used. These nuisance parameters represent different uncertainties correlated or uncorrelated between the different V + jets processes, see section 5.5.1. Four nuisance parameters are included to estimate the uncertainties of approximate mixed NLO QCD and EWK corrections which are assumed to be uncorrelated between the V + jets processes. Since all the aforementioned uncertainties are of purely theoretical origin, they are assumed to be correlated between all data eras. This results in overall 16 nuisance parameters added to the statistical model of this analysis.

Matrix element renormalization and factorization scale

A common approach in order to estimate the effects of missing higher-order corrections for a specific process is the variation of the renormalization and factorization scales during the calculation of the corresponding matrix elements. The same approach is followed to estimate this uncertainty for the simulations used in this thesis. A different nuisance parameter is used for the renormalization scale variations and the factorization scale variations. The renormalization and factorization scale is varied by a factor of 2 and $1/2$ corresponding to the $\pm 1\sigma$ variations of the corresponding nuisance parameters. These uncertainties are assumed to be uncorrelated for the following processes V + jets, $t\bar{t}$, single top-quark, and QCD multijet production, however, correlated over all years. Moreover, these uncertainties are further decorrelated between the different V + jets processes. This decorrelation is performed because significant differences in the modeling quality between the different V + jets control regions are observed after the preselection, as was shown in section 5.7.

Using the uncertainties due to the variation of the matrix element renormalization and factorization scales of the simulated V + jets samples in conjunction with the higher-order V + jets uncertainties explained above is a very conservative approach since parts of these uncertainties are then possibly accounted for twice. Nevertheless, this approach is followed here because the uncertainties from the higher-order V + jets reweighting are only formulated in terms of the transverse momentum of the vector boson. Therefore, the effect of these uncertainties on variables that are not completely correlated with the transverse momentum might be underestimated. This is especially severe if the analysis phase space is defined using such variables, e.g. momenta of jets. By using the scale variations obtained from the simulations, which are given as additional event weights calculated during the simulation, the effect of these variations can be propagated to any arbitrary variable in the event. With this approach the effect of missing higher-order QCD effects can at least be estimated also for the other important variables relevant for this analysis, e.g. jet momenta. In addition, since significant modeling differences are observed in the preselection control distributions between the different V + jets control regions, these additional uncertainties allow the statistical model to cover for these differences in a more conservative way. A disadvantage of this approach is, however, that the uncertainties on the final result of this analysis become larger. Nevertheless, for the results of this thesis, the more reliable and conservative approach is preferred over the approach of maximum sensitivity.

Parton distribution functions

In the 2017 and 2018 data eras, the NNPDF3.1 [225] parton distribution function (PDF) set at NNLO in QCD perturbation theory was used as the nominal PDF set during the production of the simulation samples. This set contains 100 PDF variations calculated via the eigenvector or Hessian approach [226, 227]. From this set of 100 Hessian PDF variations, a central 68% confidence interval is calculated around the nominal PDF. The differences of the nominal PDF and the aforementioned envelope are used as an uncertainty. This uncertainty is considered for the $t\bar{t}$ process, the Z + jets process, and W + jets processes since these processes are the dominant background processes in the signal region. In the

2016 data era, the aforementioned PDF set is unfortunately not available for the V + jets processes. Because of this, this uncertainty is currently not considered in the 2016 era. However, at a later stage an uncertainty regarding parton distribution functions needs to be considered in the 2016 era as well.

Diboson normalization

For the production of two massive electroweak vector bosons, WW, ZZ, and WZ, a conservative fully-correlated normalization uncertainty of $\pm 10\%$ is assumed. This uncertainty covers the uncertainties due to variations of the renormalization and factorization scales of the matrix elements as well as the uncertainties due to variations of the underlying PDF set, see [181–183]. A future improvement of this analysis could be to split the diboson processes into its single contributions, however more simulated events would be necessary in order to obtain reliable distributions.

Modeling of top quark p_T

Discrepancies between simulation and measurements of the differential cross section in $t\bar{t}$ events as a function of the transverse momentum of the top quark were found in several analyses, e.g. [228]. The CMS collaboration provides a function to calculate weights in order to reweight the simulated differential cross section obtained by the $t\bar{t}$ simulation samples used in this thesis to the observed differential cross section in data. The scale factor for each top quark in simulated $t\bar{t}$ events as a function of its p_T is calculated via

$$\mathrm{SF}(p_\mathrm{T}) = \exp\left(0.0615 - 0.0005 p_\mathrm{T}[\mathrm{GeV}]\right). \tag{5.27}$$

The final weight to multiply to the total event weight is then calculated as the product of the scale factors calculated for the two top quarks in the event. However, it is not recommended by the CMS collaboration to apply these weights to simulation directly. Instead, the reweighted prediction is used as a systematic uncertainty propagated to the statistical model with one nuisance parameter correlated between all years.

Number of simulated events

Fluctuations caused by the limited number of events simulated for a specific process need to be considered as a systematic uncertainty. This can be done with the Barlow-Beeston method [229, 230]. This uncertainty affects each simulated process, in each analysis region, in each bin of the hadronic recoil separately, therefore introducing a large number of additional nuisance parameters to the statistical model. To limit the number of additional nuisance parameters, a simplified method called the Barlow-Beeston light method is used. With this method, only one additional nuisance parameter is introduced for every bin as far as a minimum number of events is found in this bin. If this is not the case for a specific bin, each process in this bin again is assigned an additional nuisance parameter. The threshold for the minimum number of events in one bin is chosen to be ten in this analysis.

Table 5.12: Experimental systematic uncertainties considered in this thesis. The first column shows the source of the uncertainty. In the second column, a label for the uncertainty is given which is used to identify the corresponding uncertainty in figures. The next three columns indicate in which year the specific uncertainty is considered. The final column indicates whether the uncertainty is taken as correlated between the years it is considered in. The placeholder `YEAR` can represent 2016, 2017, or 2018. More details regarding the uncertainties are given in section 5.8.1.

Source	Label	2016	2017	2018	correlated
Luminosity uncorrelated	`CMS_Lumi_YEAR.`	✓	✓	✓	-
Luminosity correlated 2016, 2017, 2018	`CMS_Lumi_16_17_18`	✓	✓	✓	✓
Luminosity correlated 2017, 2018	`CMS_Lumi_17_18`	-	✓	✓	✓
Luminosity correlated 2016, 2017	`CMS_Lumi_16_17`	✓	✓	-	✓
Jet energy scale	`CMS_JES_YEAR`	✓	✓	✓	-
Jet energy resolution	`CMS_JER_YEAR`	✓	✓	✓	-
Electron identification	`CMS_eff_e_id_YEAR`	✓	✓	✓	-
Electron reconstruction	`CMS_eff_e_reco_YEAR`	✓	✓	✓	-
Muon identification	`CMS_eff_m_id_YEAR`	✓	✓	✓	-
Muon isolation	`CMS_eff_m_iso_YEAR`	✓	✓	✓	-
Photon identification	`CMS_eff_ph_id_YEAR`	✓	✓	✓	-
Photon identification extrapolation	`CMS_eff_ph_id-_extrapol_YEAR`	-	✓	✓	-
Electron trigger	`CMS_Trigger_e_YEAR`	✓	✓	✓	-
$\not{E}_\mathrm{T}/\not{\psi}_\mathrm{T}$ trigger	`CMS_Trigger_met_YEAR`	✓	✓	✓	-
Photon trigger	`CMS_Trigger_g_YEAR`	✓	✓	✓	-
Pileup	`CMS_PU_YEAR`	✓	✓	✓	-
L1 prefire	`CMS_prefire`	✓	✓	-	✓
b-tagging (heavy-flavor)	`CMS_btag_lf_YEAR`	✓	✓	✓	-
b-tagging (light-flavor)	`CMS_btag_hf_YEAR`	✓	✓	✓	-
Top-mistagging rate, AK15 jet $p_\mathrm{T} < 400\,\mathrm{GeV}$	`CMS_DeepAK15_Mistag-_Low_YEAR`	✓	✓	✓	-
Top-mistagging rate, AK15 jet $p_\mathrm{T} \geq 400\,\mathrm{GeV}$	`CMS_DeepAK15_Mistag-_High_YEAR`	✓	✓	✓	-
Top-tagging efficiency, AK15 jet $p_\mathrm{T} < 400\,\mathrm{GeV}$	`CMS_DeepAK15_Eff-_Low_YEAR`	✓	✓	✓	-
Top-tagging efficiency, AK15 jet $p_\mathrm{T} \geq 400\,\mathrm{GeV}$	`CMS_DeepAK15_Eff-_High_YEAR`	✓	✓	✓	-
Top-quark p_T modeling	`CMS_Top_Pt`	✓	✓	✓	✓

Table 5.13: MC generator uncertainties considered in this thesis. The first column shows the source of the uncertainty. In the second column, a label for the uncertainty is given which is used to identify the corresponding uncertainty in figures. The next three columns indicate in which year the specific uncertainty is considered. The final column indicates whether the uncertainty is taken as correlated between the years it is considered in. The symbols μ_R and μ_F represent the renormalization scale and the factorization scale of matrix elements, respectively. More details regarding the uncertainties are given in section 5.8.1.

Source	Label	2016	2017	2018	correlated
μ_R variation for $t\bar{t}$ production	muR_Powheg_tt	✓	✓	✓	✓
μ_F variation for $t\bar{t}$ production	muF_Powheg_tt	✓	✓	✓	✓
μ_R variation for single top-quark production	muR_Powheg_t	✓	✓	✓	✓
μ_F variation for single top-quark production	muF_Powheg_t	✓	✓	✓	✓
μ_R variation for $Z+\text{jets}$ production with $Z \to \nu\bar{\nu}$	muR_madgraph_vvj_norm	✓	✓	✓	see section 5.8.1
μ_F variation for $Z+\text{jets}$ production with $Z \to \nu\bar{\nu}$	muF_madgraph_vvj_norm	✓	✓	✓	see section 5.8.1
μ_R variation for $Z+\text{jets}$ production with $Z \to l\bar{l}$	muR_madgraph_eej_norm	✓	✓	✓	see section 5.8.1
μ_F variation for $Z+\text{jets}$ production with $Z \to l\bar{l}$	muF_madgraph_eej_norm	✓	✓	✓	see section 5.8.1
μ_R variation for $W+\text{jets}$ production with $W \to l\bar{\nu}$	muR_madgraph_evj_norm	✓	✓	✓	see section 5.8.1
μ_F variation for $W+\text{jets}$ production with $W \to l\bar{\nu}$	muF_madgraph_evj_norm	✓	✓	✓	see section 5.8.1
μ_R variation for $\gamma+\text{jets}$ production	muR_madgraph_aj_norm	✓	✓	✓	see section 5.8.1
μ_F variation for $\gamma+\text{jets}$ production	muF_madgraph_aj_norm	✓	✓	✓	see section 5.8.1
μ_R variation for QCD multijet production	muR_madgraph_qcd	✓	✓	✓	✓
μ_F variation for QCD multijet production	muF_madgraph_qcd	✓	✓	✓	✓
Parton distribution functions	PDF	-	✓	✓	✓

Table 5.14: Theoretical systematic uncertainties considered in this thesis. The first column shows the source of the uncertainty. In the second column, a label for the uncertainty is given which is used to identify the corresponding uncertainty in figures. The next three columns indicate in which year the specific uncertainty is considered. The final column indicates whether the uncertainty is taken as correlated between the years it is considered in. More details regarding the uncertainties are given in section 5.8.1. The placeholder `PROCESS` can represent vvj, evj, eej, and aj. These abbreviations represent the following processes in the same order: production of $Z + \text{jets}$ with $Z \to \nu\overline{\nu}$, $W + \text{jets}$ with $W \to l\overline{\nu}$, $Z + \text{jets}$ with $Z \to l\overline{l}$, and $\gamma + \text{jets}$. The index `i` represents the different theoretical $V + \text{jets}$ uncertainties explained in section 5.5.1.

Source	Label	2016	2017	2018	correlated
$V + \text{jets}$ QCD corrections	`TH_vjets_QCDi`	✓	✓	✓	✓
$V + \text{jets}$ EWK corrections	`TH_vjets_EWi_PROCESS`	✓	✓	✓	✓
V+jets mixed QCD-EWK corrections	`TH_vjets_MIX_PROCESS`	✓	✓	✓	✓

5.8.2 Transfer factor model

The statistical procedure to extract information about the mono-top signal is explained in section 2.3.5. This model is used as described, however, changes are made to connect the predictions of SM background processes in the signal region with comparable predictions in the control regions. Therefore, a transfer factor (TF) is defined connecting the prediction $n_{i,Y}^{X}$ of process X in bin i of the hadronic recoil distribution in analysis region Y with the prediction $n_{i,Y'}^{X'}$ of process X' in bin i of the hadronic recoil distribution in analysis region Y'.

$$\mathrm{TF}_{i,Y'/Y}^{X'/X} = \frac{n_{i,Y'}^{X'}}{n_{i,Y}^{X}} \tag{5.28}$$

With this transfer factor, the prediction $n_{i,Y'}^{X'}$ can be expressed as

$$n_{i,Y'}^{X'} = \mathrm{TF}_{i,Y'/Y}^{X'/X} \cdot n_{i,Y}^{X} . \tag{5.29}$$

Since the predictions themselves are subject to systematic uncertainties described by nuisance parameters θ, the transfer factors also depend on systematic uncertainties and their corresponding nuisance parameters θ, $\mathrm{TF} = \mathrm{TF}(\theta)$. This dependence on the nuisance parameters is always implied if not written explicitly.

The relation above allows for the possibility to describe the ratio between the two predictions directly in the statistical model while keeping the overall rate of the two predictions freely-floating. The rate can then be determined from data directly during the maximum likelihood fit. This has the advantage that uncertainties which affect the two predictions in a similar way are reduced or eliminated in the transfer factor and direct information from data is used to determine the appropriate normalization.

The following relations are used to connect the predictions of the Z + jets background with $Z \to \nu\bar{\nu}$ and the $t\bar{t}$ background, both in the signal region (SR), with analogous predictions in control regions (CR) of this analysis.

1. $n_{i,\mathrm{SR}}^{\mathrm{W} \to l\bar{\nu}} = \mathrm{TF}_{i,\mathrm{SR}/\mathrm{SR}}^{\mathrm{W} \to l\bar{\nu}/\mathrm{Z} \to \nu\bar{\nu}} \cdot n_{i,\mathrm{SR}}^{\mathrm{Z} \to \nu\bar{\nu}}$

2. $n_{i,\mathrm{CR(Z)}}^{\mathrm{Z} \to l\bar{l}} = \mathrm{TF}_{i,\mathrm{CR(Z)}/\mathrm{SR}}^{\mathrm{Z} \to l\bar{l}/\mathrm{Z} \to \nu\bar{\nu}} \cdot n_{i,\mathrm{SR}}^{\mathrm{Z} \to \nu\bar{\nu}}$

3. $n_{i,\mathrm{CR(W)}}^{\mathrm{W} \to l\bar{\nu}} = \mathrm{TF}_{i,\mathrm{CR(W)}/\mathrm{SR}}^{\mathrm{W} \to l\bar{\nu}/\mathrm{Z} \to \nu\bar{\nu}} \cdot n_{i,\mathrm{SR}}^{\mathrm{Z} \to \nu\bar{\nu}}$

4. $n_{i,\mathrm{CR(\gamma)}}^{\gamma} = \mathrm{TF}_{i,\mathrm{CR(\gamma)}/\mathrm{SR}}^{\gamma/\mathrm{Z} \to \nu\bar{\nu}} \cdot n_{i,\mathrm{SR}}^{\mathrm{Z} \to \nu\bar{\nu}}$

5. $n_{i,\mathrm{CR(t\bar{t})}}^{t\bar{t}} = \mathrm{TF}_{i,\mathrm{CR(t\bar{t})}/\mathrm{SR}}^{t\bar{t}/t\bar{t}} \cdot n_{i,\mathrm{SR}}^{t\bar{t}}$

6. $n_{i,\mathrm{CR(W)}}^{t\bar{t}} = \mathrm{TF}_{i,\mathrm{CR(W)}/\mathrm{SR}}^{t\bar{t}/t\bar{t}} \cdot n_{i,\mathrm{SR}}^{t\bar{t}}$

In these relations, the subscripts SR, CR(Z), CR(W), CR(γ), and CR($t\bar{t}$) represent the signal region as well as the Z boson, W boson, γ, and $t\bar{t}$ control regions introduced in section 5.7, respectively. The superscripts $Z \to \nu\bar{\nu}$, $Z \to l\bar{l}$, $W \to l\bar{\nu}$, γ, and $t\bar{t}$ symbolize the processes Z + jets with $Z \to \nu\bar{\nu}$ and $Z \to l\bar{l}$, W + jets with $W \to l\bar{\nu}$, γ + jets, and $t\bar{t}$ production. Since the leptonic control regions are generally split into final states with electrons and muons, the transfer factors for the corresponding regions and the above relations exist twice, once for the regions with electrons and once for the regions with muons. As the relations above show, the predictions of four V + jets processes in bin i of the hadronic recoil distribution in seven different analysis regions are connected simultaneously to the number of expected $Z \to \nu\bar{\nu}$ events in bin i of the hadronic recoil distribution in
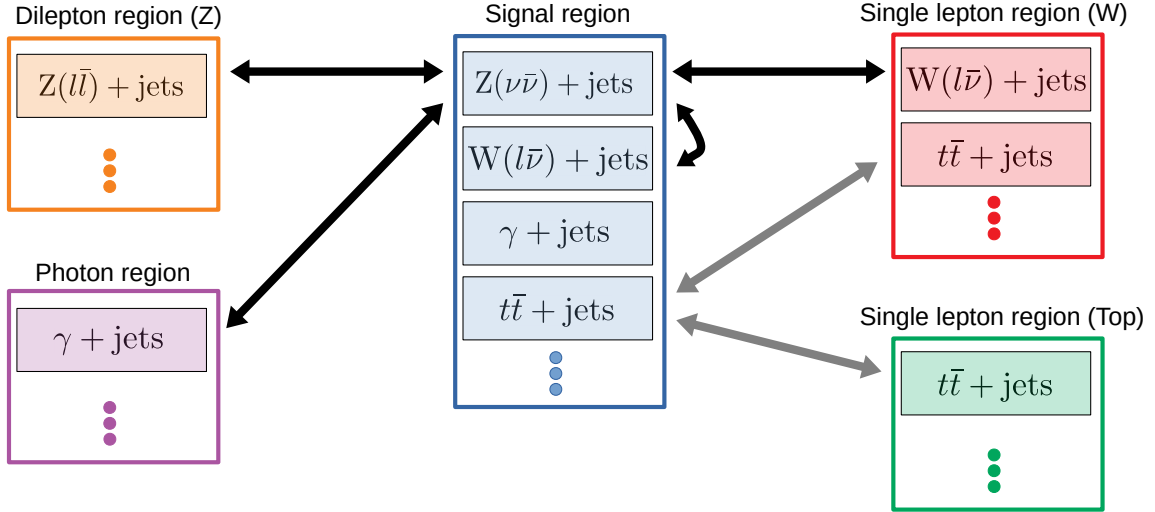
Figure 5.30: Illustration of the statistical model relying on the connection of several background processes among several control regions. The black arrows correspond to transfer factors related to the Z + jets background with $Z \to \nu\bar{\nu}$ and the gray arrows correspond to the transfer factors related to the $t\bar{t}$ background.

the signal region and the corresponding transfer factors. Analogously, the $t\bar{t}$ contribution in bin i of the hadronic recoil distribution in the top control regions and in the W boson control regions is described by the $t\bar{t}$ prediction in bin i of the hadronic recoil in the signal region and the corresponding transfer factors. A graphical illustration of these relations in each bin of the hadronic recoil distribution is given in Fig. 5.30.

The relations above are incorporated into the binned likelihood, see section 2.3.5, for each bin of the hadronic recoil. Furthermore, the predictions $n_{i,\mathrm{SR}}^{Z \to \nu\bar{\nu}}$ and $n_{i,\mathrm{SR}}^{t\bar{t}}$ are promoted to freely-floating parameters of the model which will be determined during the maximum likelihood fit. The result of this procedure is that the complete V + jets and $t\bar{t}$ sector in each bin of the hadronic recoil is predicted simultaneously using data in all regions of the analysis while only relying on Monte Carlo simulation for the ratios of the predictions.

This method, however, relies on the accuracy of the Monte Carlo predictions for the ratios. An acceptable modeling should be given for the V + jets processes since the Monte Carlo predictions are reweighted to NLO QCD and NLO EWK predictions as a function of the p_{T} of the vector bosons. Since the hadronic recoil is the experimental proxy for the vector boson p_{T}, this variable should profit the most from this reweighting and should therefore be modeled reasonably well from a theoretical perspective. The $t\bar{t}$ predictions on which the corresponding $t\bar{t}$ transfer factors rely are based on NLO QCD modeling of $t\bar{t}$ production. Therefore, also for the $t\bar{t}$ process the theoretical predictions should be modeled in an acceptable manner.

As was already stated, the transfer factors also have the advantage that uncertainties having comparable effects on processes in the different regions connected by the transfer factors should cancel at least partially and therefore the final uncertainty gets reduced. One example of this are uncertainties regarding jets. The uncertainties affecting jets in the V + jets processes are expected to have comparable effects on the considered V + jets processes because the only difference in these events are the different electroweak vector bosons either decaying leptonically (Z + jets, W + jets) or not decaying at all (γ + jets).

In addition, incorrect modeling between the predictions and the observations can be accommodated for by the statistical model by adapting the aforementioned freely-floating

parameters $n_{i,\text{SR}}^{Z\to\nu\bar{\nu}}$ and $n_{i,\text{SR}}^{t\bar{t}}$ in order to improve the description as long as the incorrect modeling is comparable in all regions of the analysis. This is especially important regarding the modeling of the top-tagging discriminant described in section 5.7.7. In these studies, a significant mismodeling was observed after applying a lower threshold on the top-tagging discriminant value since the distribution of the top-tagging discriminant is not modeled well due to a lacking calibration. However, the effect of applying a lower threshold on the top-tagging discriminant should be comparable between the different V + jets processes in their corresponding control regions. This is because the jet content in W + jets, Z + jets, and γ + jets events is described in the same manner and the top-tagger should not show large differences regarding these events. The same arguments should hold for $t\bar{t}$ events in the signal region as well as in the $t\bar{t}$ control regions. These events mainly differ by the reconstructed lepton in the events, however the jet content of these events is again similar. This implies that the calibration of the top-tagging discriminant should not play a dominant role for the description of the V + jets processes or the $t\bar{t}$ process, which are the dominant backgrounds of this analysis. Nevertheless, the calibration is very important regarding the mono-top signal processes since large calibration effects will have a dominant effect on the normalization of the signal processes in the statistical model and therefore will have a large effect on the results. This is a disadvantage of the in-situ calibration in conjunction with transfer factors since the statistical model by definition only has limited sensitivity from the control regions towards the calibration scale factors.

The transfer factors for the nominal predictions, implying no variations of nuisance parameters from their central value, are given in Fig. 5.31 for the 2017 data era as an example. Almost all transfer factors show a rising trend towards increasing values of the hadronic recoil except for the transfer factors connecting the Z + jets process ($Z \to \nu\bar{\nu}$) and the W + jets process ($W \to l\bar{\nu}$) both in the signal region. This is probably due to the fact that increasing missing transverse momentum in association with no reconstructed lepton is more likely to be generated by $Z \to \nu\bar{\nu}$ than by $W \to l\bar{\nu}$. In case of the other transfer factors, increasing hadronic recoil or (approximately) increasing transverse momentum of the vector boson probably enhances the selection efficiency of the corresponding processes due to the higher transverse momenta of the involved charged leptons and photons.

Furthermore, it is observed that the transfer factors involving electron and muon control regions behave comparable regarding their shape but always show an offset with higher transfer factors for the control regions involving muons. This is due to the lower transverse momentum thresholds used for the muon collections compared to the electron collections used in this analysis, see section 5.6.2 and section 5.6.4.

The transfer factors connecting the Z + jets process with $Z \to \nu\bar{\nu}$ in the signal region and the Z + jets process with $Z \to l\bar{l}$ in the Z boson control regions can be used as an intuitive sanity-check because the involved processes originate from the same production process with just a different decay of the Z boson. These transfer factors are approximately in the range between 0.1 and 0.2. This is exactly in the range where these transfer factors are expected using the ratio of the branching fractions of the Z boson into neutrinos $\text{BR}(Z \to \nu\bar{\nu}) \approx 20\%$ and into charged leptons $\text{BR}(Z \to l\bar{l}) \approx 3.4\%$. The transfer factors of course also depend on a multitude of detector effects as well as selection, reconstruction, and identification efficiencies resulting in variations and differences from this simple picture. Moreover, the limited statistics in the Z boson control regions after the full event selection is also visible in the transfer factors.

The transfer factors for the other data eras are given in Fig. D.49 and Fig. D.51 in Appendix D.1. The transfer factors in the 2018 data era are found to be mostly comparable to the transfer factors in the 2017 data era. Nevertheless, one significant difference of the

transfer factors is observed between the 2017 and 2018 data eras. All the transfer factors show a dip at approximately 450 GeV to 500 GeV. The reason for this dip is the special HEM veto, see section 5.7.1, applied in the signal region for $\not{E}_T < 470$ GeV in the 2018 data era. As soon as this threshold is exceeded, the special HEM veto in the signal region is not applied anymore resulting in an increase of events in the signal region. This increase of events in the signal region in turn leads to a decrease of the transfer factors. The transfer factors in the 2016 data era are mostly comparable as well, besides the transfer factors for $\gamma + \text{jets}$ in the photon control region. In the 2017 and 2018 data era, these transfer factors show a strong increase with increasing hadronic recoil starting from 250 GeV. In contrast, the aforementioned transfer factors in the 2016 data era show a rather flat behavior before starting to increase at approximately 600 GeV. This difference could be due to the different $\gamma + \text{jets}$ simulations used in the 2016 data era compared to the 2017 and 2018 data eras, see section 5.5.1.

Using the transfer factors, the statistical model of the hadronic mono-top analysis can be built and tested. This is done in the next section.
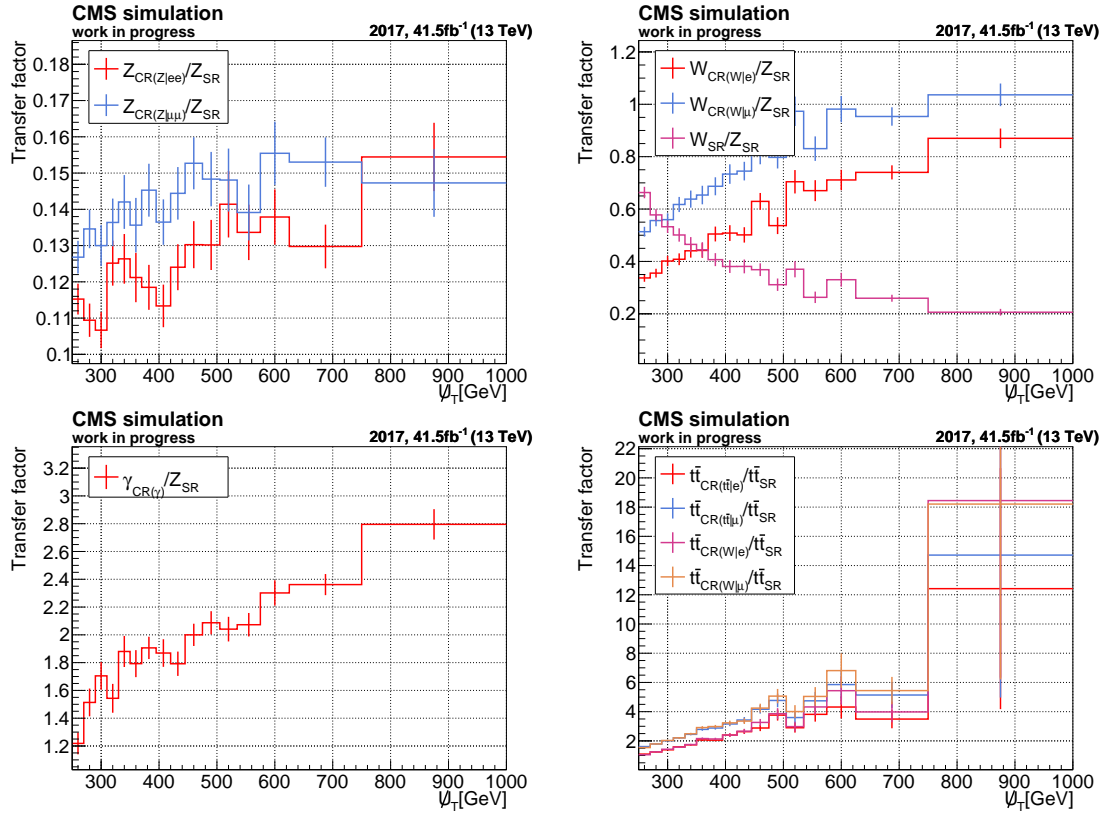
Figure 5.31: Transfer factors used in the 2017 data era as a function of the hadronic recoil. In the upper-left pad, the transfer factors connecting the Z + jets process with Z → $\nu\overline{\nu}$ in the signal region and the Z + jets process with Z → l$\overline{\text{l}}$ in the Z boson control regions are given. The upper-right pad shows the transfer factor connecting the Z + jets process (Z → $\nu\overline{\nu}$) in the signal region and the W + jets process (W → l$\overline{\nu}$) in the signal region as well as the transfer factors connecting the Z + jets process (Z → $\nu\overline{\nu}$) in the signal region and the W + jets process (W → l$\overline{\nu}$) in the W boson control regions. In the lower-left pad, the transfer factors connecting the Z + jets process (Z → $\nu\overline{\nu}$) in the signal region and the γ + jets process in the photon control region are presented. The transfer factors connecting the t$\overline{\text{t}}$ process in the signal region with the t$\overline{\text{t}}$ process in the t$\overline{\text{t}}$ control regions and in the W boson control regions are shown in the lower-right pad. The error bars represent the statistical uncertainties of the transfer factors due to the limited number of simulated events.

5.8.3 Validation of the statistical model

In this section several tests of the statistical model are performed. These tests are done to ensure that the statistical model is self-consistent and that it is able to describe the recorded data to a sufficient extent. In order to perform the aforementioned statistical tests and to extract the results of this analysis, the CMS `combine` tool based on the methods in [59, 60, 229–231] is used.

Maximum likelihood fits to Asimov datasets

The first tests which are performed are used to check whether the maximum likelihood fit which is used to extract the results of this analysis, see section 2.3.5, is able to determine the correct signal strength injected into toy datasets. As was already explained in section 2.3, a toy dataset is an artifically generated dataset sampled from the probability density function of the statistical model itself. For these tests special toy datasets, called Asimov datasets, are used [59]. The Asimov datasets are toy datasets which exactly reproduce the expected observation. This implies that all nuisance parameters representing systematic uncertainties are fixed to their central value and that no sampling of the probability density function is performed. If the statistical model is self-consistent, the Asimov toy dataset should be exactly reproduced by the statistical model when it is fitted to the Asimov toy with the maximum likelihood method.

Two different Asimov datasets are used. The first Asimov toy is the background-only Asimov toy. This means that the signal strength modifier in the statistical model is fixed to zero hence removing any signal contribution. Therefore, the background-only Asimov toy is exactly the expected observation under the assumption that no signal is present. The second Asimov toy is the signal-plus-background Asimov toy. This means that the signal strength modifier in the statistical model is fixed exactly to unity therefore assuming a signal to be present. Because of this, the signal-plus-background Asimov toy is exactly the expected observation under the assumption of the SM background processes and the hypothetical signal. For the statistical model to be considered self-consistent, the maximum likelihood estimator of the signal strength modifier, obtained from the fit to the Asimov toys, has to be exactly zero in case of the background-only Asimov toy and exactly one in case of the signal-plus-background Asimov toy.

In Fig. 5.32 the maximum likelihood estimators of the signal strength modifier after performing the maximum likelihood fit to the background-only Asimov toy as well as the signal-plus-background Asimov toy are shown for the combination of all eras. All mono-top signals are scaled to a cross section of 0.1 pb for this test. This is done in order to account for the largely different cross sections of the different mono-top signals as a function of the mass of the vector mediator and the mass of the DM candidates. Otherwise, mono-top signals in the high mass range are extremely difficult to detect for the fitting procedure since the cross sections are in the range of 10^{-4} pb to 10^{-7} pb, see Tab. 5.3 in section 5.3, resulting in a negligible normalization compared to the SM background. Furthermore, the scaling procedure is beneficial for the minimization during the fit since the range of the signal strength modifier including its uncertainties is comparable for all signals allowing to specify a common range for this parameter for the minimization. It is observed that in case of the background-only Asimov toy, the best-fit signal strength modifier is, as expected, zero for all mono-top signals. In contrast to this, the best-fit signal strength modifier in case of the signal-plus-background Asimov toy is, as expected, one. The shown uncertainty of the maximum likelihood estimator of the signal strength modifier has to be interpreted with care after scaling the cross sections of the mono-top signals. It should not be used to calculate an approximate expected significance for the different mono-top signals. This will
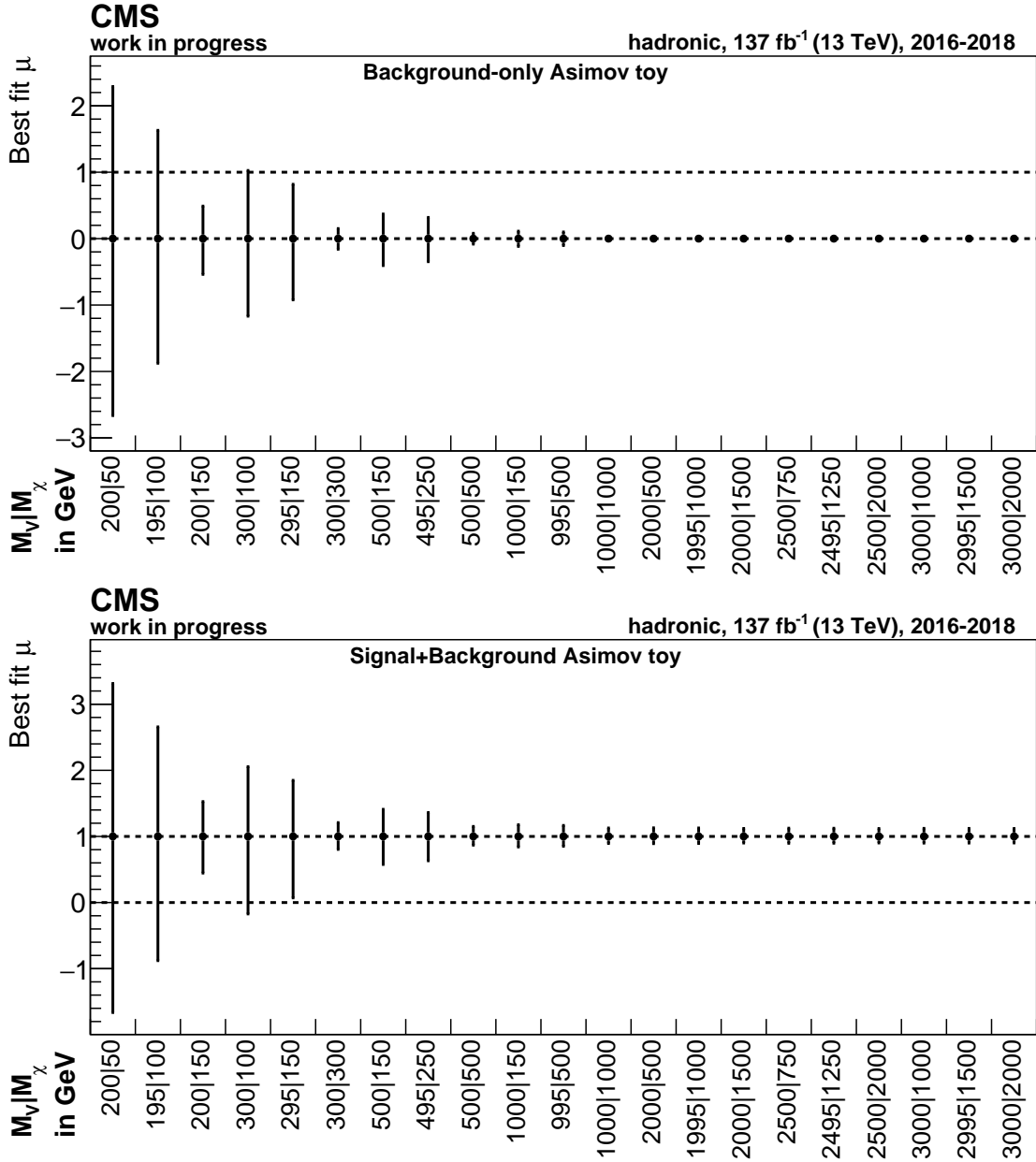
Figure 5.32: Maximum likelihood estimators and their corresponding $\pm 1\sigma$ uncertainty of the signal strength modifier for different mono-top signals after a simultaneous maximum likelihood fit to a background-only Asimov toy (top) and a signal-plus-background Asimov toy (bottom) in all eras. The mono-top signals are scaled to a cross section of $0.1\,\mathrm{pb}$. The mass of the hypothetical vector mediator is represented by $\mathrm{M_V}$ and the mass of the DM candidates by $\mathrm{M_\chi}$.

be done with the correct cross sections in another section. However, a few other conclusions can be drawn. The uncertainties in the upper pad in Fig. 5.32 give an approximate measure of how the sensitivity of the analysis changes depending on the hadronic recoil shape of the mono-top signals since all signals are scaled to the same cross section. As was shown in section 5.2 and section 5.7.6, mono-top signals with larger mediator and DM candidate masses tend towards larger hadronic recoil. Therefore, it is observed that the sensitivity of the analysis increases towards mono-top signals with higher mediator and DM candidate masses or in other words towards increasing hadronic recoil, however, only under the assumption of similar cross sections of the mono-top signals. This is expected since the analysis is designed to search for deviations in the tail of the hadronic recoil. The more signal contribution is found in the high hadronic recoil region, where the SM background is strongly suppressed, the more sensitive the statistical model becomes. For low hadronic recoil or equivalently low mediator and DM candidate masses, the sensitivity becomes worse since more SM background is present in this range. From the perspective of the shape of the signal distributions, the analysis reaches an approximate plateau of sensitivity for the signal points with mediator masses and DM candidate masses of at least 1000 GeV. As soon as not only the shape of the distribution of the hadronic recoil is considered for the mono-top signals but also their correct normalizations corresponding to the respective cross sections, this statement will of course change.

The uncertainties of the maximum likelihood estimators in case of the signal-plus-background Asimov toy show a slightly different behavior for mono-top signals with larger mediator and DM candidate masses. This effect is caused by the scaling of the mono-top cross sections within the signal-plus-background Asimov toy. As soon as a mono-top signal has significant contributions in the high hadronic recoil range, the scaling of the signal cross sections results in the mono-top signal being a dominant contribution in this range in the signal-plus-background Asimov dataset because of the strong suppression of SM backgrounds. Therefore, the uncertainty of the maximum likelihood estimator of the signal strength modifier is changed by the additional statistical uncertainty of the mono-top contribution in the signal-plus-background Asimov toy. This uncertainty is most prominent in range of high hadronic recoil because there the SM contributions are heavily suppressed. This uncertainty is comparable for the different mono-top signals since they are scaled to the same cross section and have comparable shapes of the hadronic recoil distribution.

Similar results for the 2018, 2017, and 2016 eras separately are given in Fig. D.52 and Fig. D.53 in Appendix D.2.

As a conclusion, it is confirmed that the statistical model is able to reproduce the injected signal strength in background-only Asimov datasets as well as in signal-plus-background Asimov datasets.

Behavior of nuisance parameters

The next tests of the statistical model also check the self-consistency of the model, however, with respect to the systematic uncertainties considered. Therefore, the maximum likelihood estimators of the nuisance parameters and their corresponding uncertainties after a maximum likelihood fit (post-fit) are compared to their values before the maximum likelihood fit (pre-fit). Since, as already explained, the Asimov toy datasets are exactly the expected observations under the assumption that all nuisance parameters are at their central values, zero in this analysis, the maximum likelihood fit of the statistical model to the Asimov toys should reproduce these central values as long as the fitted statistical model is the same that was used to generate the Asimov toys. More specifically, this means that the post-fit maximum likelihood estimators of the nuisance parameters should exactly be at the

central values of the pre-fit nuisance parameters. Furthermore, it is checked how the post-fit uncertainties of the nuisance parameters compare to their pre-fit uncertainties. These checks provide information whether the maximum likelihood fit can decrease systematic uncertainties by using information from the observation and how sensitive the fit is to different systematic uncertainties. In addition, these checks also provide a measure of how well the statistical model can describe the recorded data. For these tests, only one mono-top signal with a mediator mass of 995 GeV and a DM candidate mass of 500 GeV is used as a representative example. Comparable to the tests in the previous section, the mono-top signal is scaled to a cross section of 0.1 pb.

The results of the aforementioned tests are shown in Fig. D.54, Fig. D.55, Fig. D.56, and Fig. D.57 in Appendix D.2 for the combination of all eras separately for a maximum likelihood fit to a background-only Asimov dataset and a signal-plus-background Asimov dataset. The maximum likelihood fits reproduce, as expected, the initial central values of the nuisance parameters for both Asimov datasets. The only exception is the fit of the background-only model to the signal-plus-background Asimov dataset. However, this behavior is expected since the background-only model cannot account for the injected signal with the signal itself. Instead, the central values of the nuisance parameters have to be changed to account for the additional signal contributions. Moreover, it is observed that the post-fit uncertainties of several nuisance parameters are reduced with respect to their pre-fit uncertainties. For most of these nuisance parameters, this can, however, be expected as well.

The nuisance parameters representing the jet energy scale and jet energy resolution uncertainties are constrained because these nuisance parameters represent the total uncertainties, which are composed of a multitude of uncertainty sources. Because of this, the corresponding uncertainties are artifically large and are constrained by the maximum likelihood fit. This behavior can be mitigated by using a systematic uncertainty and a corresponding nuisance parameter for each jet energy scale and resolution uncertainty source. This is a planned improvement of this analysis for the near future.

The uncertainty due to unclustered particles during the calculation of the missing transverse momentum is constrained as well. A possible reason for this could be that this uncertainty, similar to the total jet energy scale and resolution uncertainties, consists of several uncertainty sources representing different types of unclustered particles, e.g. electrons, muons, tau leptons, photons, as well as charged and neutral hadrons. This uncertainty needs to be studied further in the future.

Uncertainties regarding the DeepAK15 top-tagging discriminant are constrained as well. This is expected since these uncertainties were chosen conservatively due to missing calibrations. As soon as dedicated calibrations of the top-tagging discriminant are available, or an improved in-situ calibration is implemented, an improvement regarding these uncertainties is expected as well.

Furthermore, the nuisance parameters representing variations of the matrix element renormalization and factorization scales of different processes are constrained. This observation is expected as well since the control regions of this analysis are designed to enrich the corresponding processes allowing the fit to be sensitive to these uncertainties. In addition, as already explained, the uncertainty model of the V + jets processes is chosen very conservatively to account for possible mismodeling of the V + jets processes not accounted for by the purely theoretical uncertainties.

Concluding from the behavior of the nuisance parameters in case of fits to Asimov datasets, the statistical model behaves as expected and seems to work without any major problems.
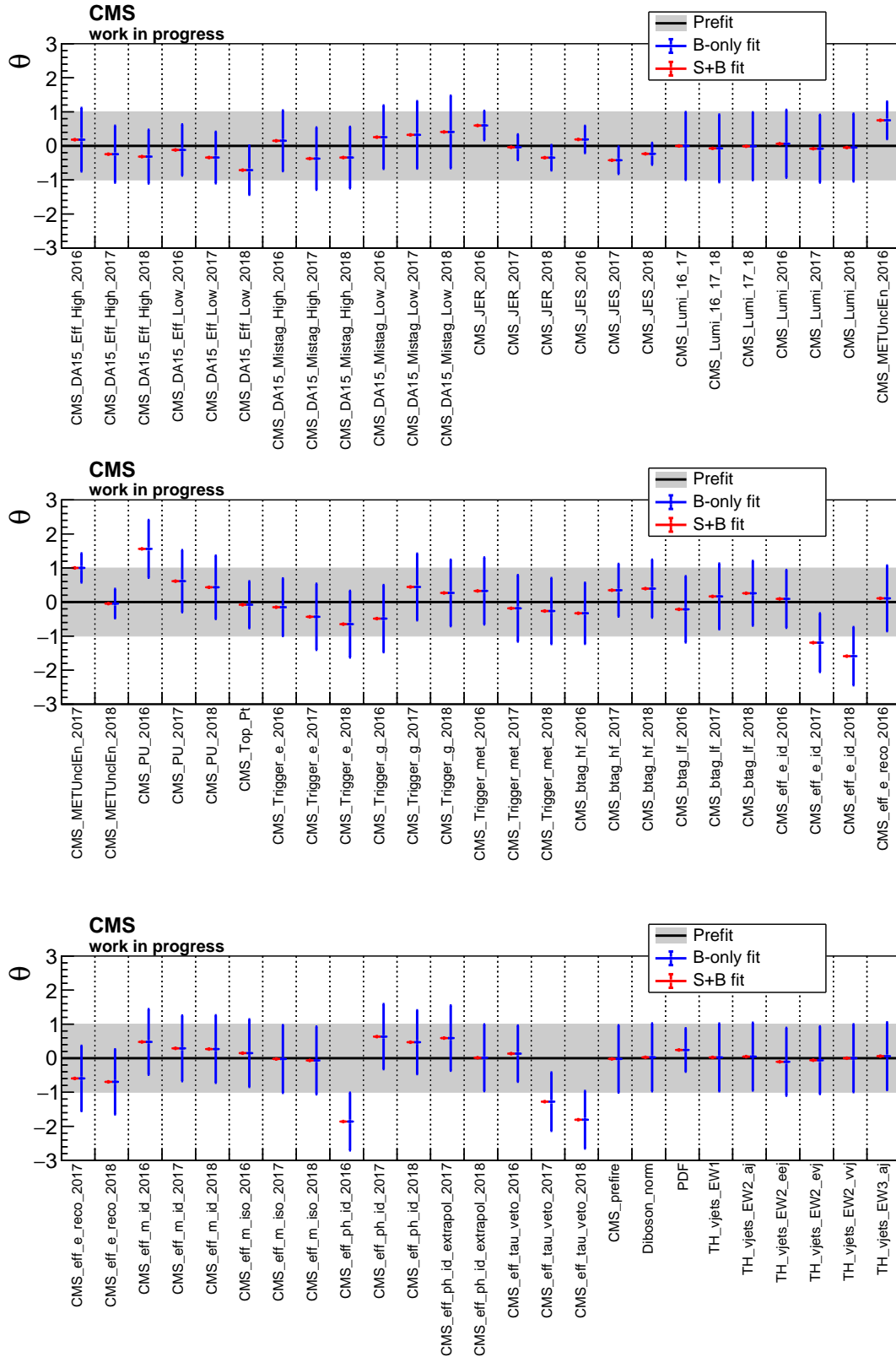
Figure 5.33: Maximum likelihood estimators and their corresponding $\pm 1\sigma$ uncertainty of the nuisance parameters after the maximum likelihood fit of the background-only and signal-plus-background model to the data in the control regions. The points represent the value of the maximum likelihood estimators and the error bars their corresponding $\pm 1\sigma$ uncertainties. The different nuisance parameters can be identified with the corresponding systematic uncertainties by using the labels given in Tab. 5.12, Tab. 5.13, and Tab. 5.14.
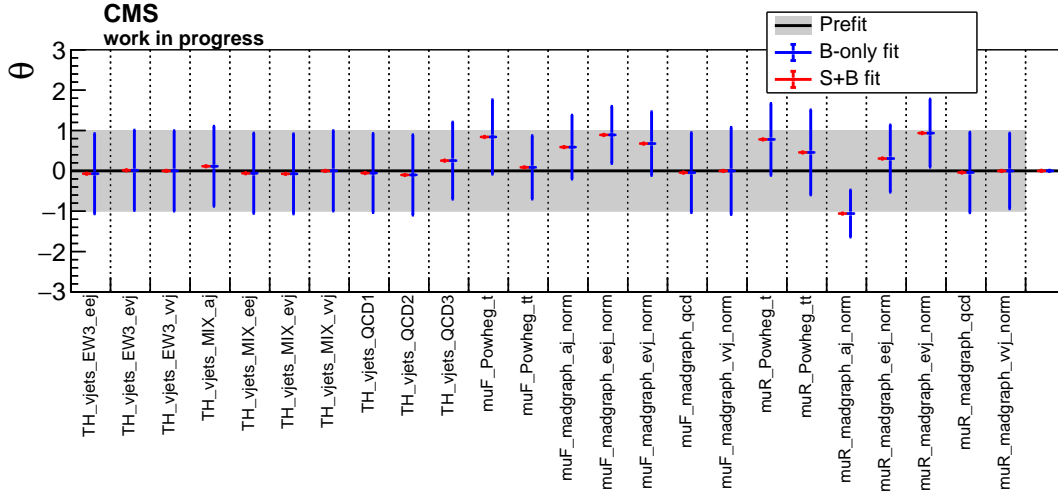
Figure 5.34: Maximum likelihood estimators and their corresponding $\pm 1\sigma$ uncertainty of the nuisance parameters after the maximum likelihood fit of the background-only and signal-plus-background model to the data in the control regions. The points represent the value of the maximum likelihood estimators and the error bars their corresponding $\pm 1\sigma$ uncertainties. The different nuisance parameters can be identified with the corresponding systematic uncertainties by using the labels given in Tab. 5.12, Tab. 5.13, and Tab. 5.14.

Instead of studying the behavior of the nuisance parameters when fitted to Asimov datasets, another possibility is to fit the statistical model only to data in the control regions. With this method, the aforementioned checks can be performed without unblinding the analysis however confronting the statistical model with recorded data. Since the statistical model is based on the aforementioned transfer factors, which are only defined in conjunction with the signal region, the signal region cannot be removed completely from the likelihood. Instead, the signal region is kept in the likelihood, however the contributions of the signal region to the likelihood are masked, i.e. they have no effect on the likelihood function. The results of this test are shown in Fig. 5.33 and Fig. 5.34 for the combination of all data eras.

The results of the maximum likelihood fit of the signal-plus-background model need to be discarded for this test because all the regions in which signal contributions are expected are masked. Because of this, the maximum likelihood fit cannot find a proper minimum with respect to all parameters of the model and the calculation of the a-posteriori uncertainties fails. This is the reason why no error bars are visible for the signal-plus-background fit in Fig. 5.33 and Fig. 5.34.

It is observed that most of the maximum likelihood estimators of the nuisance parameters after the maximum likelihood fit of the background-only model are still compatible to their expected $\pm 1\sigma$ uncertainties. Only a few nuisance parameters show a post-fit value outside of the $\pm 1\sigma$ pre-fit uncertainty and from these nuisance parameters all are compatible again with the $\pm 1\sigma$ pre-fit uncertainty considering the post-fit uncertainties. These parameters are mostly representing uncertainties regarding different physics objects like the electron and photon identification uncertainties or the tau lepton veto uncertainties. The corresponding nuisance parameters are adapted by the fit to mitigate mismodelings observed in the control regions. For example a mismodeling in the control regions with two electrons was observed already before applying the top-tagging selections, see Fig. B.21 in Appendix B.1. This mismodeling was found to be more severe in the 2018 data era than in the 2017

data era and the least severe in the 2016 data era. This observation is reproduced by the corresponding post-fit nuisance parameters showing the largest pull for the 2018 data era, a slightly smaller pull for the 2017 era, and almost no pull in the 2016 era.

The behavior of the post-fit uncertainties of the nuisance parameters is mostly comparable to the Asimov datasets explained above. Similar uncertainties are constrained, e.g. uncertainties regarding the jet energy scale and resolution, the DeepAK15 top-tagging discriminant, the unclustered energy uncertainties as well as the matrix element renormalization and factorization scale uncertainties.

From the results presented in this section, it is concluded that no major problems are observed regarding the statistical model and that the recorded data in the control regions can be described mostly within one standard deviation of the considered uncertainties.

Goodness-of-fit tests

Another method to evaluate whether the statistical model is able to describe the recorded data to a satisfying extent, called a goodness-of-fit test, can be used. This test provides a measure of how well the data is described by a statistical model corresponding to a specific hypothesis without specifying an alternative hypothesis. More precisely, it is a measure of how probable it is to obtain the observed data under the assumption of a specific statistical model, i.e. its probability density function. A goodness-of-fit test is based on a test statistic. This test statistic is evaluated on the observed data. Then, to determine how compatible the data is with the probability density function of the model, the probability density function of the test statistic under assumption of the statistical model needs to be obtained. This can be done with the Monte Carlo method by sampling toy datasets from the probability density function of the statistical model and calculating the test statistic for each toy dataset. After the distribution of the test statistic was determined, a p-value can be calculated using the value of the test statistic obtained for recorded data and the distribution of the test statistic from the toy datasets. This p-value is then again a measure of how compatible the statistical model is with the recorded data. For this analysis, a goodness-of-fit test based on the saturated model method, see [232, 233], is used. Then, as recommended by the CMS statistics committee [234], a-posteriori toy datasets are used in conjunction with the saturated model. This implies that the toys are sampled from the a-posteriori probability density function of the statistical model. This a-posteriori probability density function is obtained by fitting the statistical model to the observed data with a maximum likelihood fit.

The first goodness-of-fit test is performed to test the agreement of the statistical model of the background-only hypothesis with the recorded data only in the control regions of the analysis. This test therefore provides information whether the statistical model is able to describe the data in the control regions reasonably well. Since the statistical model is based on the aforementioned transfer factors, which are only defined in conjunction with the signal region, the signal region cannot just be removed completely from the likelihood, as already explained. Instead, the signal region is kept in the likelihood, however the contributions to the likelihood are masked. The masking of the signal region is done during the fit of the statistical model to data, as explained above, as well as during the calculation of the test statistic. The result of this goodness-of-fit test is shown in Fig. 5.35 for the combination of all eras.

It is observed that the distribution of the test statistic obtained from a-posteriori toy datasets shows a double peak structure with a smaller peak at smaller values of the test statistic and a larger peak at higher test statistic values. In order to understand the origin of this double peak structure, the same goodness-of-fit tests are repeated for the different
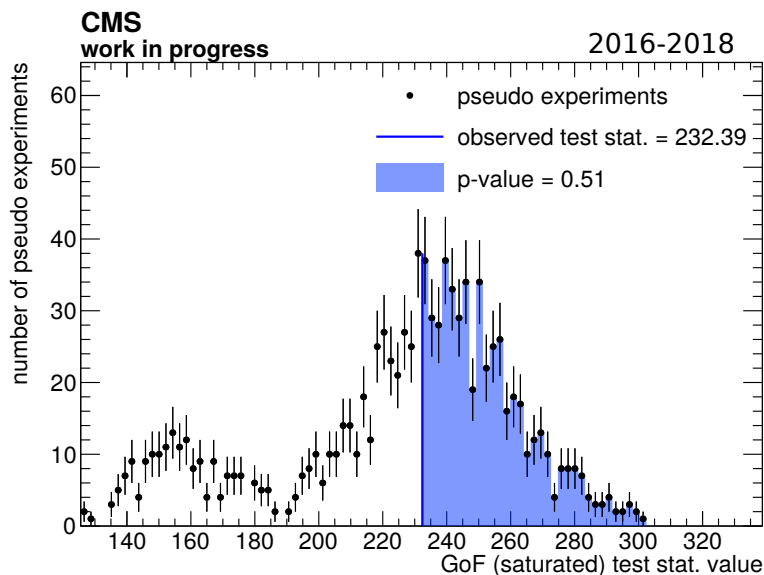
Figure 5.35: Distribution of the test statistic of the saturated goodness-of-fit test for a-posteriori toy datasets sampled from the a-posteriori probability density function of the statistical model after a maximum likelihood fit to all control regions in all data eras.

data eras separately. The result of these goodness-of-fit tests performed separately for each data era are given in Fig. D.58 in Appendix D.2. The distributions generated separately for each data era do not show this double peak structure but show, as expected, a distribution compatible to a χ^2 distribution. The test statistic value obtained from data is always found to be in the bulk of the distribution indicating no problem for the statistical model to describe the data in the control regions. To exclude the possibility that the double peak structure is due to problematic correlations between the different data eras, the same tests were repeated after decorrelating all nuisance parameters between the different data eras. However, the double peak structure was also found for this configuration. One explanation for this double peak structure could be that a large number of uncertainty sources are assumed to be decorrelated between the years. Therefore, if a toy dataset is sampled such that in one year the toy dataset has a configuration with a rather small test statistic value but in the other years is in the bulk of the distributions, such a second smaller peak could emerge. Nevertheless, this double peak structure should be studied more extensively in the future.

The value of the test statistic obtained from data in the control regions is found to be compatible with the distribution of the test statistic obtained from toy datasets in the single data eras but also for the combination of all data eras. Because of this, although the double peak structure should be examined further in the future, it is concluded that the statistical model is able to describe the data in the control regions to a sufficient extent.

Expected significances

In order to obtain a measure of the sensitivity of the analysis for the different mono-top signals, the expected significance is calculated. The significance is determined by calculating the test statistic $\tilde{q}_\mu$ based on the likelihood ratio introduced in section 2.3.5 for a vanishing

signal strength $\mu = 0$.

$$\tilde{q}_0 = -2 \ln \frac{L(\text{data}|0, \hat{\hat{\theta}}_0)}{L(\text{data}|\hat{\mu}, \hat{\theta})} \tag{5.30}$$

Here, data refers to the observation at hand. This can either be the real observation from recorded data, a generated Asimov dataset, or also a toy dataset sampled from the probability distribution of the statistical model. In order to obtain the p-value corresponding to the test statistic evaluated on the aforementioned observation, the distribution of the test statistic needs to be known. This distribution can be calculated with Wilks' theorem. As was already explained, the p-value represents the probability to find a value of the test statistic that is larger than the test statistic evaluated with the observation. This probability, the obtained p-value, is then converted into a Gaussian significance. The Gaussian significance is the number of standard deviations σ for which the corresponding quantile of the standard normal distribution has the same value as the p-value. The significance is a measure to evaluate how compatible the background-only hypothesis is with the a-posteriori signal-plus-background model. If the significance is low, this implies that the data can be well described by the background-only model within the uncertainties. Therefore, no significant deviation of the background-only hypothesis is found. If the significance is high, the background-only hypothesis is unlikely to be able to explain the observation. A high significance consequently implies that the observed deviation from the background-only hypothesis is unlikely due to a fluctuation. A significance larger than 3σ, representing a probability smaller than 0.3% for a fluctuation, is commonly referred to as evidence. A significance larger than 5σ, representing a smaller than $6 \cdot 10^{-5}\%$ probability for a fluctuation, is called a discovery.

The aforementioned expected significance is determined by using a a-posteriori signal-plus-background Asimov dataset as the observation for the calculation of the test statistic value. The expected significance is hence a measure of how well the statistical model is able to detect a signal contribution in the observation under the assumption that the data behaves similar to the Asimov dataset.

The expected significances for a signal-plus-background Asimov dataset are given in Fig. 5.36 for the different mono-top signals after combining all eras. It is observed that the expected significances for mono-top signals involving low masses of the hypothetical mediator and the DM candidates are high and often significantly above the 5σ discovery significance. The main reason for this is the relatively large cross section of the mono-top signals in this mass range of $\mathcal{O}(10\,\text{pb})$ to $\mathcal{O}(0.1\,\text{pb})$. The only low mass signals for which no discovery sensitivity is reached are the ones which involve only off-shell decays of the mediator into the DM candidates. Due to the off-shell decay, the cross section of these signals is heavily suppressed resulting in lower significances. Furthermore, the expected significances decrease with increasing masses of the mediator and the DM candidates. Although, as was shown, the sensitivity of the analysis improves for mono-top signals with increasing masses of the mediator and DM candidates under the assumption of similar cross sections, it is observed here that the decrease of the cross sections significantly outweighs this effect for high masses.

The same significances calculated separately in each data era are given in Fig. D.59 in Appendix D.2. The expected significances calculated separately for each era show a similar behavior to the significances calculated for all eras combined. It is also observed how the additional statistical power due to the combination of the data eras improves the expected significances, e.g. for the mono-top signals with a mediator mass of $995\,\text{GeV}$ and a DM candidate mass of $500\,\text{GeV}$. The expected significances in the single eras do not reach the 5σ discovery threshold for this signal, however the combination approximately does.
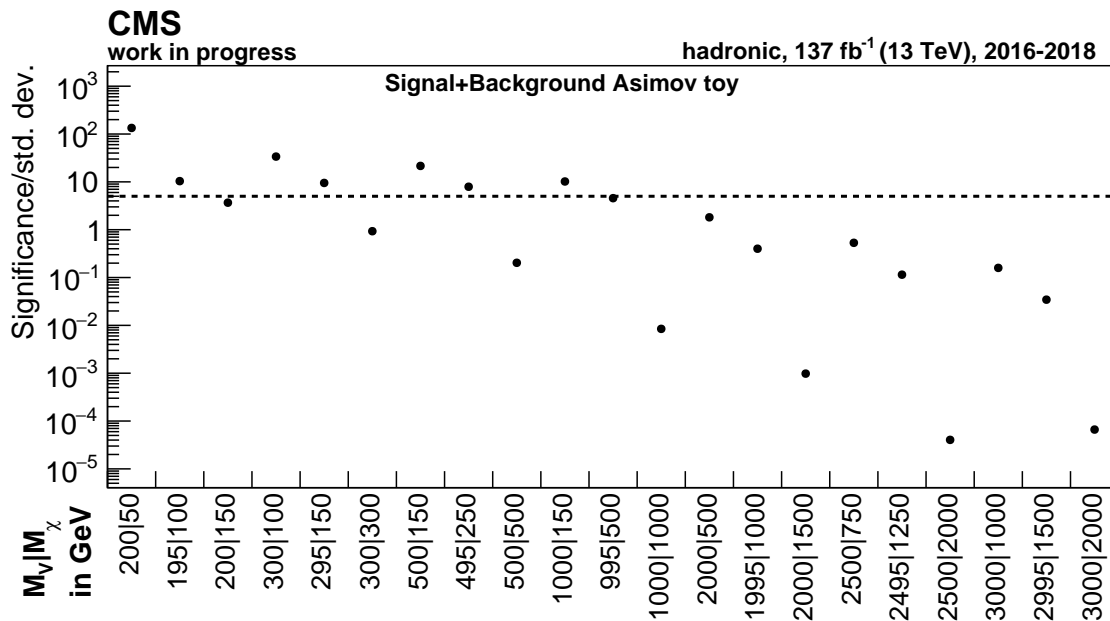
Figure 5.36: Expected significances in units of the standard deviation of the standard normal distribution for different mono-top signals after combining all eras. The mass of the hypothetical vector mediator is represented by M_V and the mass of the DM candidates by M_χ. The 5σ discovery significance is represented by the dashed line.

Expected exclusion limits

If no significant signal contribution is observed, parameter space of the mono-top model can be excluded by calculating upper limits on the observed cross section of the mono-top signals. If the upper limit on the cross section is below the theoretical cross section, the model configuration is excluded at the confidence level the limits are calculated at. In this thesis, upper limits are calculated at 95% confidence level with the asymptotic limit approach and the CL_s construction, see section 2.3 and [59, 62–65].

In order to get a sense of the parameter space which can be excluded by the analysis, expected limits are calculated. Expected limits are calculated using toy datasets. Specifically, the background-only Asimov dataset is used to calculate the expected exclusion limits under the assumption that no signal is present. There are two different possibilities to calculate expected limits.

First, expected limits can be calculated a-priori implying that no information from data is used at all. This also means that the background-only Asimov toy is created from the blind expected distributions. The a-priori expected limits are a good measure to optimize the sensitivity of an analysis without using information from data but only simulation.

However, since the statistical model of this analysis is built to directly use data from control regions in order to constrain the V + jets and the $t\bar{t}$ background in the signal region, a-posteriori expected limits are calculated. For these limits, a maximum likelihood fit of the signal-plus-background model to data is performed to obtain an a-posteriori model describing the data in the best possible way. Then, the background-only Asimov dataset is created from this a-posteriori model. With this method, limits under the best possible description of data given the statistical model are obtained.

In the following, upper limits are always calculated for the signal strength modifier $\mu = \sigma_{\mathrm{obs}}/\sigma_{\mathrm{th}}$ with σ_{obs} representing the observed cross section and σ_{th} representing

the theoretical cross section of a mono-top signal. By calculating upper limits of the signal strength modifier, it is straightforward to determine whether a signal is excluded or not by just comparing the upper limit to unity. However, since effectively an upper limit of the observed signal cross section is calculated, theoretical uncertainties affecting the cross section of the signals are not considered in σ_{obs}. Instead, cross section uncertainties of the signal process are considered in σ_{th}. Varied upper limits are calculated for the variations of the mono-top cross section due to the signal cross section uncertainties. The cross section uncertainty of the mono-top signal process is conservatively taken to be $\pm 10\%$ including effects of missing higher-order matrix elements as well as PDF uncertainties [119].

Since only a specified grid of signal samples is available, see Tab. 5.3 in section 5.3, upper limits can only be calculated for these specific points in the plane of the mediator mass and the DM candidate mass. However, in order to obtain an exclusion area in the aforementioned plane, an interpolation needs to be performed. For this interpolation to work, a sufficient number of dedicated grid points need to be available. Unfortunately, this is not the case in the mediator mass range of 1 TeV to 2 TeV for the available sample grid. Because of this, upper limits are approximated for several points for which no dedicated simulation samples are available.

The aforementioned approximation is done by using the partial decay widths of the hypothetical mediator into DM candidates and quarks obtained from [128]. The partial decay width into quarks is given by $\Gamma_{\mathrm{q}} = \Gamma_d + \Gamma_u$ with Γ_d and Γ_u representing the decay widths into down-type quarks of the first and third generation and up-type quarks of the first and third generation, respectively. As was explained in section 4.2, only couplings mixing first and third generation quarks are considered. The decay width into one down-type quark (antiquark) of the first and one down-type antiquark (quark) of the third generation is given by

$$\Gamma_d = \frac{m_{\mathrm{V}}}{4\pi} g_{\mathrm{V,q}}^2 \, . \tag{5.31}$$

Here, m_{V} represents the mass of the hypothetical vector mediator and $g_{\mathrm{V,q}}$ the coupling constant of the purely vectorial coupling to down-type and up-type quarks. In addition, the decay width into one up-type quark (antiquark) of the first generation and one up-type antiquark (quark) of the third generation is given by

$$\Gamma_u = \frac{m_{\mathrm{V}}}{4\pi} g_{\mathrm{V,q}}^2 \left(1 - \frac{m_{\mathrm{t}}^2}{m_{\mathrm{V}}^2} \right) \left(1 - \frac{m_{\mathrm{t}}^2}{2m_{\mathrm{V}}^2} - \frac{m_{\mathrm{t}}^4}{2m_{\mathrm{V}}^4} \right) \tag{5.32}$$

with m_{t} being the mass of the top quark. As previously explained, the coupling constant to quarks in the mono-top models considered in this analysis is chosen to be $g_{\mathrm{V,q}} = 0.25$.

Analogously, the partial decay width into two DM candidates is given by

$$\Gamma_{\chi} = \frac{m_{\mathrm{V}}}{12\pi} g_{\mathrm{V,\chi}}^2 \sqrt{1 - 4\frac{m_{\chi}^2}{m_{\mathrm{V}}^2}} \left(1 + 2\frac{m_{\chi}^2}{m_{\mathrm{V}}^2} \right) \tag{5.33}$$

assuming a purely vectorial coupling with coupling constant $g_{\mathrm{V,\chi}}$ and a DM candidate mass m_{χ}. The coupling constant to DM candidates is chosen to be $g_{\mathrm{V,\chi}} = 1.0$ for the mono-top models considered in this thesis.

Then, the branching ratio of the mediator into two DM candidates is given by

$$\mathrm{BR}_{\chi} = \frac{\Gamma_{\chi}}{\Gamma_{\chi} + \Gamma_u + \Gamma_d} \, . \tag{5.34}$$

Consequently, in order to approximate the upper limit for a mono-top model with DM candidate mass m_{χ}' and mediator mass m_{V} using the upper limit obtained by a model with
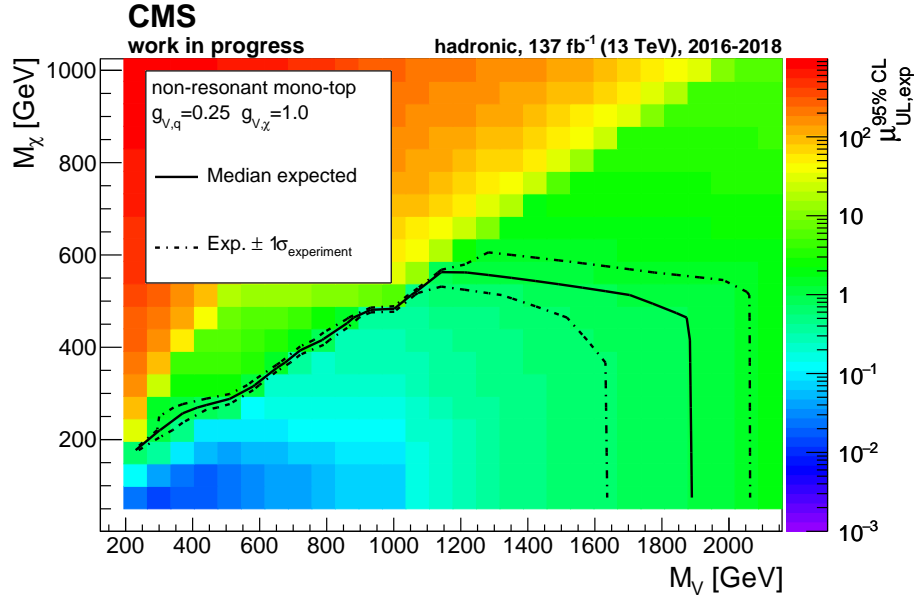
Figure 5.37: Expected upper exclusion limits of the signal strength modifier at 95% confidence-level as a function of the mediator mass M_V and the DM candidate mass M_χ for the combination of all eras. The colored area represents the median expected upper limits. The solid black line represents the contour for which the median expected upper limit is equal to unity. The dashed black lines represent the 68% confidence interval for the expected upper limit to be equal to unity considering all uncertainties relevant for the description of the background processes. The area within the black solid line is the expected exclusion area at 95% confidence-level.

the same mediator mass m_V but different DM candidate mass m_χ, the available upper limit needs to be multiplied by BR_χ/BR'_χ. This approximation only holds if the kinematics of the different signal events are assumed to be comparable. As was presented in Fig. 5.2 in section 5.2 showing some of the performed generator studies, the transverse momentum of the mediator is approximately independent of the mass of the DM candidates for the models with on-shell decays of the mediator. Since the transverse momentum of the mediator is a direct proxy for the missing transverse momentum in hadronic mono-top signatures, the kinematics of these events should be comparable as well. The approximation procedure is only used for mass grid points having on-shell decays of the mediator into the two DM candidates.

In Fig. 5.37 the resulting median expected upper limits of the signal strength modifier at 95% confidence-level are given as a function of the mass of the mediator and the DM candidates for the combination of all data eras. Mediator masses up to approximately 1900 GeV and DM candidate masses up to approximately 500 GeV are excluded by the expected upper limits for the chosen coupling scenario. A dent is observed in the exclusion contour between mediator masses of 1100 GeV and 1900 GeV. The reason for this dent is that no dedicated signal samples are available in this range. Also, the aforementioned approximation procedure to calculate additional limits from existing upper limits cannot be used since this procedure only works for a fixed mediator mass and variable DM candidate masses. An interpolation into x direction, meaning interpolating the upper limits for different mediator masses and fixed DM candidate mass, is not straightforwardly possible from a theoretical perspective and e.g. a spline interpolation would need more points for a reliable interpolation. Therefore, this dent is left as it is for the results of this thesis. In

the future, at least one further signal sample should be generated in the mediator mass range between $1100\,\mathrm{GeV}$ and $1900\,\mathrm{GeV}$.

Mono-top signals in the lower mass regime are expected to be excluded with a high significance. Furthermore, mono-top signals for which the mediator decays off-shell cannot be excluded because of their strongly suppressed cross sections. Expected limits from a previous hadronic mono-top analysis [119] are found to be compatible to the expected limits calculated in this analysis. It is observed that this analysis, although using significantly more data, does not result in significantly improved exclusion limits. The main reasons for this observation are the heavily simplified calibration method for the top-tagging discriminant, the differences of the modeling quality between the different $V + \mathrm{jets}$ control regions, and, resulting from the latter, the overall very conservatively chosen statistical model.

Since the top-tagging calibration is performed in-situ, information from data is used to determine the top-tagging scale factors during the maximum likelihood fit. This information from data could instead be used for additional signal sensitivity if a dedicated calibration would be available. Furthermore, the large uncertainties of the top-tagging scale factors are difficult to reduce during the fit of the statistical model since these uncertainties are strongly decreased for the major background processes due to cancellation effects in the transfer factors. Therefore, the fit only has limited sensitivity towards the top-tagging scale factors.

As stated above, the statistical model of this analysis is chosen to be very conservative regarding the correlations of the included uncertainties in order to account for discrepancies of the simplified top-tagging calibration procedure and for discrepancies observed for the agreement of data and simulation in the $V + \mathrm{jets}$ control regions before applying the top-tagger. One one hand, this ensures that the model is able to describe the data to a satisfying extent despite the aforementioned discrepancies, as was shown in the previous sections, however it also significantly increases the uncertainties and therefore decreases the sensitivity of the analysis. Nevertheless, as already stated before, this approach is preferred in this thesis in order to produce a conservative but reliable result.

Similar exclusion limits calculated for the separate data eras are given in Fig. D.60 and Fig. D.61 in Appendix D.2. The exclusion limits in the separate data eras are found to be compatible with one another within one standard deviation of the considered uncertainties. In addition, the exclusion limits calculated for the 2016 era are found to be slightly better than in the 2017 and 2018 data eras. This is probably due to the significantly different agreement between data and simulation found in the 2016 era compared to the 2017 and 2018 data eras.

5.9 Results

In the previous sections the hadronic mono-top analysis was described in detail and the statistical model used to extract results from data was motivated and validated. In this section the results obtained from recorded data in all analysis regions are presented.

Before extracting the final results, the behavior of the nuisance parameters is studied as well as goodness-of-fit tests are performed analogously to the previous section, however, including data in the signal regions of the analysis.

The behavior of the nuisance parameters is evaluated analogously to the previous section, however, including the recorded data in the signal regions as well. The results are presented in Fig. D.62 and Fig. D.63 in Appendix D.3. Similar behavior is observed as was observed
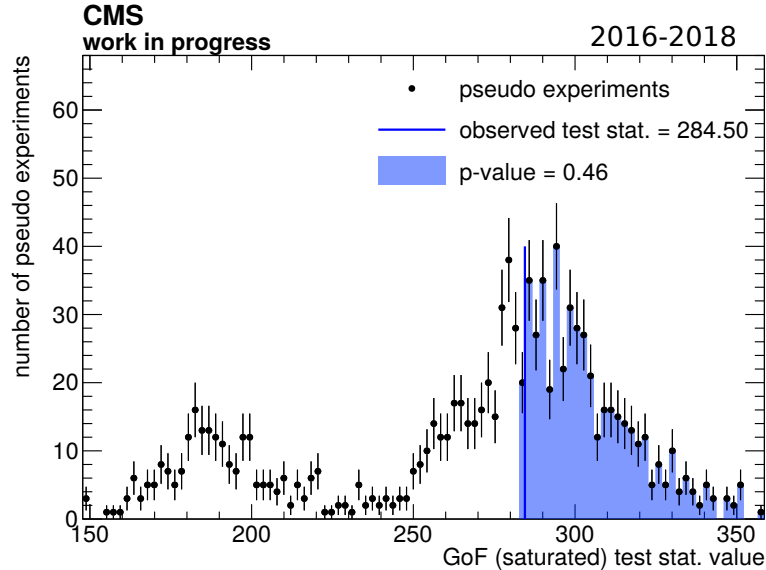
Figure 5.38: Distribution of the test statistic of the saturated goodness-of-fit test for a-posteriori toy datasets sampled from the a-posteriori probability density function of the statistical model after a maximum likelihood fit to all analysis regions in all data eras.

in the studies of the previous section. Most of the nuisance parameters are well within their a-priori uncertainties. Only a small number of nuisance parameters have post-fit values outside of the a-priori uncertainties and from these almost all are compatible with their a-posteriori uncertainties. The only nuisance parameter compatible only at two standard deviations is the nuisance parameter representing the uncertainties of the photon identification efficiencies in the 2016 data era. A reason for this could be the different theoretical modeling of the $\gamma + \mathrm{jets}$ process in the 2016 data era compared to the 2017 and 2018 data eras. In the 2016 data era, the $\gamma + \mathrm{jets}$ process is modeled only at leading-order QCD perturbation theory. In contrast, the $\gamma + \mathrm{jets}$ process is modeled at NLO QCD perturbation theory in the 2017 and 2018 eras. To account for the resulting discrepancies in the photon control regions, the maximum likelihood fit could adapt a nuisance parameter directly related to the $\gamma + \mathrm{jets}$ description in the photon control region of the 2016 data era, which is the aforementioned nuisance parameter. Regarding the nuisance parameters, conclusions similar to those of the previous section are drawn. No major problems with the behavior of the nuisance parameters are observed.

In Fig. 5.38 the result of the goodness-of-fit test using all data eras in all analysis regions is shown for the signal-plus-background model. Similar to what was observed in the previous section, the distribution of the test statistic shows two peaks. The test statistic value observed from data is in the bulk of the distribution of the test statistic which is obtained by sampling a-posteriori toy datasets. This implies that the signal-plus-background model is able to describe the data within its uncertainties. The same conclusions are drawn from the goodness-of-fit tests performed separately in each data era, see Fig. D.64 in Appendix D.3. Also in the separate data eras, no incompatibility between the signal-plus-background model and the data is found. This, however, does not imply the presence of a signal because this goodness-of-fit test does not give any information whether the background-only hypothesis is able to describe the data equally well or not. This latter information is obtained by calculating the observed significances.
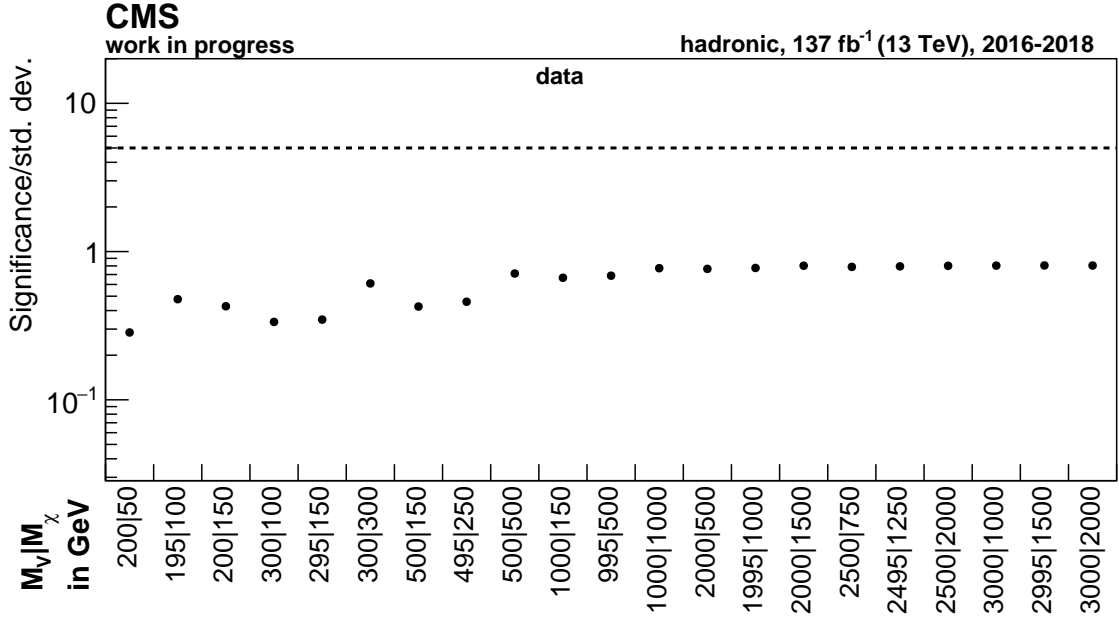
Figure 5.39: Observed significances in units of the standard deviation of the standard normal distribution for different mono-top signals after combining all eras in all analysis regions. The mass of the hypothetical vector mediator is represented by M_V and the mass of the DM candidates by M_χ. The 5σ discovery significance is represented by the dashed line.

Analogously to the previous section, significances are calculated with respect to the background-only hypothesis. Instead of using an a-posteriori signal-plus-background Asimov dataset to calculate the observed value of the test statistic, the recorded data is used to evaluate the observed test statistic. The observed significances are shown in Fig. 5.39. No significant deviations from the background-only hypothesis are found. The observed significances are below one standard deviation for all combinations of DM candidate and mediator masses considered.

This observation can be understood by studying the corresponding maximum likelihood estimators of the signal strength modifiers given in Fig. D.65 in Appendix D.3 for which the cross sections of all mono-top signals were scaled to 0.1 pb. Since the best-fits of the signal strength modifier and their uncertainties both scale with the cross section, the significances do not change due to this scaling. However, after the scaling the best-fit signal strength modifiers are in a more comparable range for all mono-top signals. Nevertheless, it is noted again that the significances are calculated using the respective theoretical cross sections except for the two mono-top models with mediator mass 2500 GeV and 3000 GeV and a DM candidate mass of 2000 GeV. For these two mono-top models, the cross section is scaled up by a factor of ten. This is done because of their extremely low cross section of $\mathcal{O}(10^{-7}\,\text{pb})$. Because of this, the minimization procedure during the maximum likelihood estimation does not find the global minimum but a local minimum resulting in an unexpected drop of the significance. This drop can be recovered by increasing the cross section such that the minimization procedure finds the correct minimum. In order to ensure that the significance does not change by scaling the cross section, the cross sections of other mono-top samples were changed by several orders of magnitude and no change of the reported observed significance was found. The best-fit signal strength modifiers and their uncertainties show that the background-only hypothesis ($\mu = 0$) is always compatible within one standard deviation. Similar observed significances are calculated separately for each data era and are
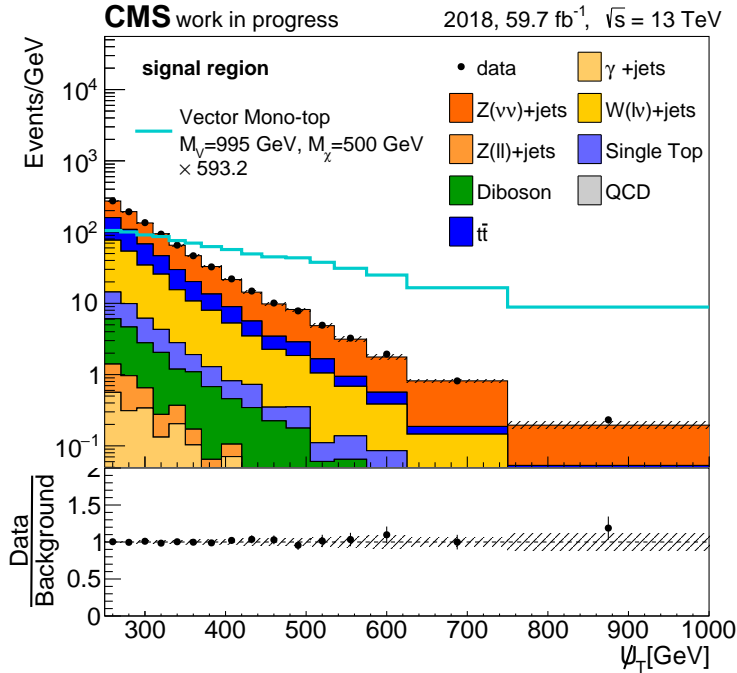
Figure 5.40: A-posteriori distribution of the hadronic recoil in the signal region of the 2018 data era. One mono-top signal sample, scaled to the total yield of all background processes, is overlaid. The corresponding scale factor is given in the legend. The hatched uncertainty band represents the total a-posteriori uncertainty of the background processes. The black error bars represent the inherent statistical uncertainty of the data.

shown in Fig. D.66 in Appendix D.3. The corresponding maximum likelihood estimators of the signal strength modifier are given in Fig. D.67 also in Appendix D.3. In the 2018 data era, the background-only hypothesis is described within slightly larger than one standard deviation of the best-fit signal-plus-background model pointing towards either an upward fluctuation of the data or a residual mismodeling. This is confirmed by the best-fit signal strength modifiers shown in the top of Fig. D.67 in Appendix D.3. In the 2017 data era, the best-fit signal strength modifiers are found to be negative as can be observed in the center of Fig. D.67 in Appendix D.3. This is most likely due to a small downward fluctuation of the data. Nevertheless, the best-fit signal strength modifiers and their uncertainties show that the data is very compatible with the background-only hypothesis also in the 2017 data era which is confirmed by the reported observed significances in the center of Fig. D.66 in Appendix D.3. In the 2016 data era, the observed significances are also found to be below one standard deviation of the best-fit signal-plus-background model. The maximum likelihood estimators of the signal strength modifiers confirm the calculated observed significances in the 2016 data era as is presented in the bottom of Fig. D.67 in Appendix D.3.

Because the maximum likelihood fits have been performed at this stage of the analysis, the a-posteriori distributions of the signal-plus-background model in all years and in all analysis regions can be studied and are given in Fig. D.68, Fig. D.69, Fig. D.70, and Fig. D.71 in Appendix D.3. An exemplary distribution of the hadronic recoil in the signal region of the 2018 data era is given in Fig. 5.40. As the lower pad in Fig. 5.40 shows, the background processes are able to describe the recorded data well within their uncertainties indicating no significant deviation of the SM. The signal regions in the other data eras as well as

the control regions show a good description of the data within the uncertainties of the statistical model as well.
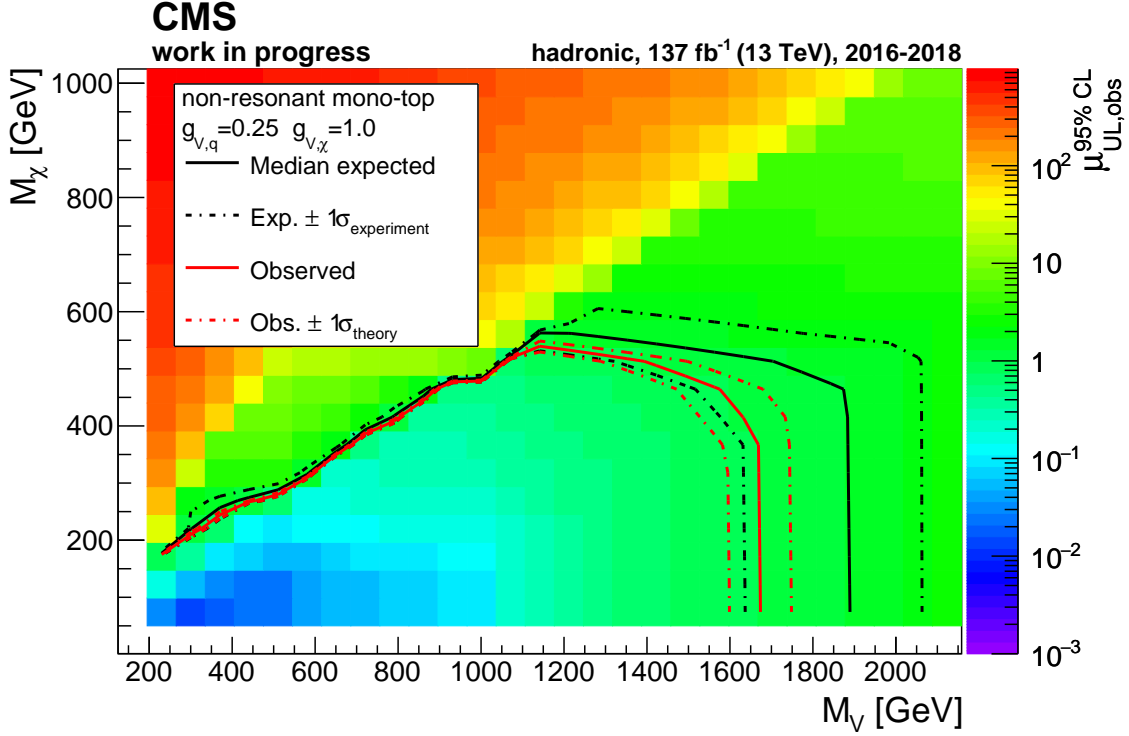
Figure 5.41: Observed upper exclusion limits of the signal strength modifier at 95% confidence-level as a function of the mediator mass M_V and the DM candidate mass M_χ for the combination of all eras. The colored area represents the observed upper limits. The solid black and red line represent the contours for which the median expected upper limit and the observed upper limit is equal to unity, respectively. The dashed black lines represent the 68% confidence interval for the expected upper limit to be equal to unity considering all uncertainties relevant for the description of the background processes. The area within the red solid line is the observed exclusion area at 95% confidence-level. The dashed red lines show the observed exclusion areas assuming a change of the mono-top cross section by $\pm 1\sigma$.

Because no significant deviations from the background-only hypothesis are observed, upper limits of the signal strength modifier are calculated similarly to the previous section but utilizing recorded data in all analysis regions instead of a-posteriori background-only Asimov datasets. The observed exclusion contour of the signal strength modifiers at 95% confidence-level is presented in Fig. 5.41 for the combination of all data eras. Mediator masses of up to approximately 1700 GeV and DM candidate masses of up to approximately 500 GeV are excluded at 95% confidence-level by the recorded data. Furthermore, the observed and the expected exclusion limits are compatible within one standard deviation of the uncertainties. Due to the observed upward fluctuations in the 2016 and 2018 data eras, the observed upper exclusion limits are slightly larger than the expected limits and therefore the observed exclusion area is slightly smaller than the expected exclusion area. The explicit values of the expected and observed upper limits are given in Tab. 5.15. Analogous upper limits and their exclusion contours are given for the separate data eras in Fig. D.72 and Fig. D.73 in Appendix D.3.

The observed exclusion limits are found to be compatible with exclusion limits found in an earlier CMS hadronic mono-top analysis [119] except in the range of mediator masses above 1100 GeV and DM candidate masses above 500 GeV. In this range, the dent already explained in the previous section is observed again. The exclusion contour can be rendered more smooth by producing more MC signal samples in this phase space. This will be done in the near future. No significant improvements of the exclusion limits with respect to the previous analysis are found due to several reasons which offer possibilities for further improvement.

First, the top-tagging discriminant will directly profit from a dedicated calibration which was not available at the time this thesis was written. Because of this, a heavily simplified and conservative in-situ calibration was employed to mitigate the significant deterioration of the modeling quality after using the top-tagging discriminant to define the final phase space of the analysis. Large uncertainties on this calibration were introduced to account for shortcomings of this approach. Another possibility for improvement is to further split all analysis regions into low-purity and high-purity regions according to the top-tagging discriminant. With this approach, the in-situ calibration tested in this thesis could be significantly improved. Not only would this approach introduce additional analysis regions with larger statistics to constrain uncertainties independent of the top-tagging discriminant, but it would also allow the maximum likelihood fit to have a more powerful handle on the top-(mis)tagging efficiencies because events would migrate in and out of the low-purity and high-purity regions therefore also incorporating information from the top-mistagged fat jets.

Moreover, investigating and resolving remaining discrepancies in the modeling of the V+jets control regions before applying top-tagging would be of great benefit for the analysis as well. Because of these discrepancies and the aforementioned missing top-tagging calibration, the statistical model of this analysis was chosen very conservatively giving the model the possibility to account for these effects during the maximum likelihood fit of the statistical model to recorded data. This is done mostly via the matrix element renormalization and factorization scale uncertainties of the different $V + \text{jets}$ processes being the only sizeable uncertainties able to account for differences of the modeling quality in the different $V + \text{jets}$ control regions. Consequently, an improved modeling would allow to choose the statistical model less conservatively and therefore directly decrease the uncertainties of the analysis. Finally, improved simulations of the $V + \text{jets}$ processes including NLO QCD as well as NLO EWK corrections on the level of MC simulation would remove the need of reweighting leading-order simulations to approximate higher-orders, which is a suboptimal solution for analyses not using the inclusve $\vec{\not{E}}_\text{T}$ distribution according to [189].

Further improvement is expected by also considering the leptonic decay channel of the mono-top model. In order to include this channel, an additional analysis category could be added to the analysis based on the transverse mass of the expected charged lepton and missing transverse momentum. A preliminary analysis strategy and corresponding generator studies are presented in Appendix E.

Finally, it has to be noted that the results obtained in this analysis are only valid for the realization of the mono-top model chosen in this thesis. This implies that the exclusion contours in the plane of the mass of the hypothetical mediator and the DM candidates are only valid for a purely vectorial coupling of first and third generation quarks to the hypothetical vector mediator with a coupling constant $g_{\text{V,q}} = 0.25$ as well as a purely vectorial coupling of the DM candidates to the mediator with a coupling constant $g_{\text{V},\chi} = 1.0$. For more general coupling scenarios, dedicated samples would need to be generated or additional weights would need to be provided by the matrix element generator allowing to reweight existing events to different coupling scenarios.

Table 5.15: Median expected upper limits and observed upper limits at 95% confidence-level split according to the mass of the mediator M_V and the mass of the DM candidates M_χ. The subscript and superscript represent the 68% confidence interval around the median expected upper limit considering all uncertainties relevant for the description of the background processes.

M_V [GeV]	M_χ [GeV]	median expected	observed
200	50	$0.010^{+0.004}_{-0.003}$	0.011
195	100	$0.082^{+0.032}_{-0.022}$	0.096
200	150	$0.49^{+0.19}_{-0.13}$	0.58
300	100	$0.013^{+0.005}_{-0.004}$	0.015
295	150	$0.087^{+0.034}_{-0.024}$	0.098
300	300	$2.12^{+0.83}_{-0.60}$	2.63
500	150	$0.022^{+0.009}_{-0.006}$	0.025
495	250	$0.12^{+0.05}_{-0.03}$	0.14
500	500	$9.6^{+3.8}_{-2.6}$	12.5
1000	150	$0.080^{+0.034}_{-0.021}$	0.101
995	500	$0.37^{+0.16}_{-0.10}$	0.48
1000	1000	240^{+100}_{-60}	320
2000	500	$1.1^{+0.4}_{-0.4}$	1.4
1995	1000	$4.8^{+2.3}_{-1.3}$	6.6
2000	1500	2500^{+1000}_{-700}	3400
2500	750	$3.8^{+1.6}_{-1.0}$	4.9
2495	1250	16^{+8}_{-4}	22
2500	2000	43000^{+18000}_{-14000}	56000
3000	1000	13^{+5}_{-4}	17
2995	1500	56^{+27}_{-15}	77
3000	2000	27000^{+9000}_{-9000}	34000

6 Conclusion and outlook

In this thesis, a preliminary search for the production of Dark Matter in hadronic mono-top signatures was presented. This search utilizes data recorded by the CMS detector at 13 TeV center-of-mass energy in the years 2016, 2017, and 2018 corresponding to a total integrated luminosity of $137\,\mathrm{fb}^{-1}$. For this analysis, $\mathcal{O}(10^9)$ simulated events as well as recorded events were analyzed.

The mono-top search presented in this thesis focuses on the non-resonant mono-top model introduced in [126] and is performed in the framework of a simplified model. In this simplified model, a new hypothetical vector mediator as well as a Dirac DM candidate is added to the SM. The new mediator induces a flavor-changing neutral current between up-type quarks of the first and third generation therefore allowing for the production of a single top quark in association with the new mediator. The mediator then decays into two DM candidates generating the mono-top signature.

One of the most important background processes for this search, the production of single electroweak vector bosons (W, Z, γ) in association with jets (V + jets), was studied in context of the modeling of the data in several control regions of this analysis. Only V + jets simulations at leading-order QCD perturbation theory were available with sufficient statistics to perform this search. The modeling of these leading-order samples was found not to be sufficient to describe the recorded data to a satifsying extent. In order to improve this description, a reweighting approach, based on fixed higher-order calculations [189] for the differential cross section of V + jets as a function of the transverse momentum of the vector bosons, was implemented and tested for the simulated V + jets events. Furthermore, dedicated theoretical uncertainties incorporated into this reweighting procedure were studied and compared to uncertainties directly obtained from MC simulation. The reweighting method significantly improved the modeling of the data in the V + jets control regions of this analysis. However, a significant mismodeling was still observed in the normalization of the signal region. This normalization issue was resolved after incorporating a similar reweighting approach, however, based on V + jets MC simulation at NLO QCD perturbation theory instead of fixed-order calculations. The fixed-order calculations were still used to incorporate important NLO electroweak corrections.

The presented search for hadronic mono-top signatures is based on a kinematic variable called the hadronic recoil. Using this quantity, a statistical model was built relating the distributions of the missing transverse momentum of the major background processes in the

signal region with analogous distributions in several control regions. With this approach, the major backgrounds in the signal regions are determined in-situ by using data from the control regions of this analysis.

Furthermore, large radius jets with a jet radius of 1.5 were used to cluster the decay products of a hadronic top quark decay within one jet. A new top-tagging algorithm developed within the CMS collaboration, called DeepAK [149–151], was used to identify the aforementioned jets as originating from the hadronic decay of a top quark.

No significant deviations from the SM expectations were found. Therefore, exclusion limits on the parameter space of the non-resonant mono-top model were set. For a purely vectorial coupling of the quarks and the DM candidates to the hypothetical vector mediator, masses of the mediator up to 1700 GeV and masses of the DM candidates up to 500 GeV can be excluded at 95% confidence-level. The expected exclusions are found to be up to 1900 GeV mediator mass and up to 500 GeV DM candidate mass. The observed and expected exclusion contours are compatible within one standard deviation of the uncertainties affecting the background model. The observed as well as the expected exclusion limits are found to be compatible with corresponding exclusion limits found in an earlier CMS hadronic mono-top analysis [119]. No significant improvements of the exclusion limits with respect to the previous analysis are found due to several reasons which offer possibilities for further improvement, e.g. a dedicated top-tagging calibration, an improved modeling quality in the $V + \text{jets}$ control regions in conjunction with a less conservative statistical model, and more generated non-resonant mono-top signal samples in order to fill currently present gaps in the plane of the mediator mass and the DM candidate mass.

As a conclusion, the analysis presented in this thesis is a first preliminary approach to search for hadronic mono-top signatures with the complete dataset recorded by the CMS detector in the second major run of the LHC. Although not improving the sensitivity compared to a previous analysis, this analysis points towards several challenges which need to be addressed in the near future in order for the official CMS publication to have an improved sensitivity. Some of the aforementioned improvements will be implemented in the near future or their implementation is already in progress. Finally, the analysis will be extended to also be sensitive to the leptonic decay channel of the mono-top model consisting of large missing transverse momentum in association with a charged lepton. This is done by introducing a leptonic analysis channel utilizing the transverse mass of the system of the missing transverse momentum and the charged lepton as a final discriminant. The inclusion of the leptonic analysis channel in conjunction with the improvements explained above should result in a significant enhancement of the sensitivity over previous analyses.

Acronyms

2HDM Two Higgs Doublet Model. 36, 37

AK Anti-k_T algorithm. 48, 49, 54, 57, 66, 96, 97

ALP Axion-like Particle. 28

BSM Beyond the Standard Model. 11, 13

CDM Cold Dark Matter. 26, 28

CERN European Organization for Nuclear Research. 1, 12, 13

CHS Charged Hadron Substraction. 49, 97

CKM Cabibbo-Kobayashi-Maskawa. 5, 41, 55

CMB Cosmic Microwave Background. 1, 25, 26

CMS Compact Muon Solenoid. 1, 2, 8, 9, 12–16, 31, 32, 34, 48, 51, 54, 55, 57, 58, 66, 68, 72, 74, 88–91, 93–98, 100–102, 112, 114, 118, 120, 123, 132, 138, 149, 151, 152

CNN Convolutional Neural Network. 52

DeepAK15 DeepAK boosted jet tagger for anti-k_t jets with jet radius of 1.5. 54, 96

DM Dark Matter. 1, 11, 23–40, 42–47, 57, 61–65, 68, 71, 102, 113, 132–135, 140–143, 146, 148–152, 222, 223, 229–231, 235–237, 242–246

DNN Deep Neural Network. 51, 52

ECAL Electromagnetic Calorimeter. 14–17, 37, 91–95, 104

EWK Electroweak. 5, 73–78, 80–84, 88–90, 121, 122, 128, 149, 179, 180, 187–190

GIM Glashow–Iliopoulos–Maiani. 42

HCAL Hadron Calorimeter. 14, 15, 17, 92, 104

HDM Hot Dark Matter. 25

HLT High-Level Trigger. 16, 72, 92, 93

LHC Large Hadron Collider. 1, 2, 7–9, 12, 15, 29, 31, 43, 55, 61, 68, 152

LO Leading-order. 75, 87, 90

LSTM Long Short-Term Memory. 55

ME Matrix element. 67

NLO Next-to-leading-order. 63, 67, 74, 75, 77, 80, 87–91, 121, 122, 128, 145, 149, 151, 186, 190

NNLO Next-to-next-to-leading-order. 68, 74, 75, 77, 78, 80, 122

PDF Parton Distribution Function. 76, 82, 122, 123, 142

PF Particle-Flow. 15, 16, 51, 55, 59, 91, 92, 96, 97, 100, 102

POG Physics Object Group. 90

PUPPI Pile-up Per Particle Identification. 49, 51, 96, 97

QCD Quantum Chromodynamics. 4, 5, 7, 10, 27, 39, 41, 44, 48–53, 58, 59, 63, 67, 68, 73–78, 80–84, 87–91, 101, 103, 104, 107, 111–113, 121, 122, 128, 145, 149, 151, 179, 180, 186–190, 244

QFT Quantum Field Theory. 3

RNN Recurrent Neutral Network. 55

SD SoftDrop. 50, 51, 53, 54, 59, 96, 102, 106–110, 112–115, 193, 195, 199, 201, 205, 207, 210, 211, 213

SM Standard Model of Particle Physics. 1–6, 11–13, 20, 26–32, 36, 37, 39, 42–45, 58, 59, 61, 63, 68, 71, 72, 113, 118, 127, 132, 134, 147, 151, 152, 244–246

VEV Vacuum Expectation Value. 6

WDM Warm Dark Matter. 26

WIMP Weakly Interacting Massive Particle. 26, 27

Bibliography

[1] Wikimedia Commons. 2019-09-17. URL: https://commons.wikimedia.org/wiki/File:Standard_Model_of_Elementary_Particles.svg (visited on 2019-11-06).

[2] P. Zyla et al. "Review of Particle Physics". In: *PTEP* 2020.8 (2020), p. 083C01. DOI: 10.1093/ptep/ptaa104.

[3] D. J. Gross and F. Wilczek. "Ultraviolet Behavior of Nonabelian Gauge Theories". In: *Phys. Rev. Lett.* 30 (1973), pp. 1343–1346. DOI: 10.1103/PhysRevLett.30.1343.

[4] D. J. Gross and F. Wilczek. "Asymptotically Free Gauge Theories - I". In: *Phys. Rev.* D8 (1973), pp. 3633–3652. DOI: 10.1103/PhysRevD.8.3633.

[5] D. J. Gross and F. Wilczek. "Asymptotically Free Gauge Theories - II". In: *Phys. Rev.* D9 (1974), pp. 980–993. DOI: 10.1103/PhysRevD.9.980.

[6] H. D. Politzer. "Reliable Perturbative Results for Strong Interactions?" In: *Phys. Rev. Lett.* 30 (26 1973-06), pp. 1346–1349. DOI: 10.1103/PhysRevLett.30.1346. URL: https://link.aps.org/doi/10.1103/PhysRevLett.30.1346.

[7] S. L. Glashow. "Partial Symmetries of Weak Interactions". In: *Nucl. Phys.* 22 (1961), pp. 579–588. DOI: 10.1016/0029-5582(61)90469-2.

[8] A. Salam and J. C. Ward. "Electromagnetic and weak interactions". In: *Phys. Lett.* 13 (1964), pp. 168–171. DOI: 10.1016/0031-9163(64)90711-5.

[9] S. Weinberg. "A Model of Leptons". In: *Phys. Rev. Lett.* 19 (1967), pp. 1264–1266. DOI: 10.1103/PhysRevLett.19.1264.

[10] F. Englert and R. Brout. "Broken Symmetry and the Mass of Gauge Vector Mesons". In: *Phys. Rev. Lett.* 13 (1964), pp. 321–323. DOI: 10.1103/PhysRevLett.13.321.

[11] P. W. Higgs. "Broken symmetries, massless particles and gauge fields". In: *Phys. Lett.* 12 (1964), pp. 132–133. DOI: 10.1016/0031-9163(64)91136-9.

[12] P. W. Higgs. "Broken Symmetries and the Masses of Gauge Bosons". In: *Phys. Rev. Lett.* 13 (1964), pp. 508–509. DOI: 10.1103/PhysRevLett.13.508.

[13] M. D. Schwartz. "TASI Lectures on Collider Physics". In: *Proceedings, Theoretical Advanced Study Institute in Elementary Particle Physics : Anticipating the Next Discoveries in Particle Physics (TASI 2016): Boulder, CO, USA, June 6-July 1, 2016.* 2018, pp. 65–100. DOI: 10.1142/9789813233348_0002. arXiv: 1709.04533 [hep-ph].

[14] M. Perelstein. "Introduction to Collider Physics". In: *Physics of the large and the small, TASI 09, proceedings of the Theoretical Advanced Study Institute in Elementary Particle Physics, Boulder, Colorado, USA, 1-26 June 2009.* 2011, pp. 421–486. DOI: 10.1142/9789814327183_0008. arXiv: 1002.0274 [hep-ph].

[15] R. K. Ellis, W. J. Stirling, and B. R. Webber. "QCD and collider physics". In: *Camb. Monogr. Part. Phys. Nucl. Phys. Cosmol.* 8 (1996), pp. 1–435.

[16]   M. Schott and M. Dunford. "Review of single vector boson production in pp collisions at $\sqrt{s} = 7$ TeV". In: *Eur. Phys. J. C* 74 (2014), p. 2916. DOI: 10.1140/epjc/s10052-014-2916-1. arXiv: 1405.1160 [hep-ex].

[17]   A. Buckley et al. "General-purpose event generators for LHC physics". In: *Phys. Rept.* 504 (2011), pp. 145–233. DOI: 10.1016/j.physrep.2011.03.005. arXiv: 1101.2599 [hep-ph].

[18]   J. Alwall et al. "The automated computation of tree-level and next-to-leading order differential cross sections, and their matching to parton shower simulations". In: *JHEP* 07 (2014), p. 079. DOI: 10.1007/JHEP07(2014)079. arXiv: 1405.0301 [hep-ph].

[19]   J. Alwall et al. "MadGraph 5 : Going Beyond". In: *JHEP* 06 (2011), p. 128. DOI: 10.1007/JHEP06(2011)128. arXiv: 1106.0522 [hep-ph].

[20]   B. Andersson et al. "Parton Fragmentation and String Dynamics". In: *Phys. Rept.* 97 (1983), pp. 31–145. DOI: 10.1016/0370-1573(83)90080-7.

[21]   B. Webber. "A QCD Model for Jet Fragmentation Including Soft Gluon Interference". In: *Nucl. Phys. B* 238 (1984), pp. 492–528. DOI: 10.1016/0550-3213(84)90333-X.

[22]   Webber, Bryan. *Parton shower Monte Carlo event generators.* 2011-12-01. URL: http://www.scholarpedia.org/article/Parton_shower_Monte_Carlo_event_generators#Hadronization (visited on 2020-10-20).

[23]   J. Ellis. "Physics Beyond the Standard Model". In: *Nucl. Phys. A* 827 (2009). Ed. by I. Tserruya, A. Gal, and D. Ashery, pp. 187C–198C. DOI: 10.1016/j.nuclphysa.2009.05.034. arXiv: 0902.0357 [hep-ph].

[24]   B. Gripaios. *Lectures on Physics Beyond the Standard Model.* 2015-03. arXiv: 1503.02636 [hep-ph].

[25]   Y. Fukuda et al. "Evidence for oscillation of atmospheric neutrinos". In: *Phys. Rev. Lett.* 81 (1998), pp. 1562–1567. DOI: 10.1103/PhysRevLett.81.1562. arXiv: hep-ex/9807003.

[26]   Q. Ahmad et al. "Direct evidence for neutrino flavor transformation from neutral current interactions in the Sudbury Neutrino Observatory". In: *Phys. Rev. Lett.* 89 (2002), p. 011301. DOI: 10.1103/PhysRevLett.89.011301. arXiv: nucl-ex/0204008.

[27]   G. Fantini et al. "Introduction to the Formalism of Neutrino Oscillations". In: *Adv. Ser. Direct. High Energy Phys.* 28 (2018), pp. 37–119. DOI: 10.1142/9789813226098_0002. arXiv: 1802.05781 [hep-ph].

[28]   A. G. Riess et al. "Observational evidence from supernovae for an accelerating universe and a cosmological constant". In: *Astron. J.* 116 (1998), pp. 1009–1038. DOI: 10.1086/300499. arXiv: astro-ph/9805201.

[29]   S. Perlmutter et al. "Measurements of Ω and Λ from 42 high redshift supernovae". In: *Astrophys. J.* 517 (1999), pp. 565–586. DOI: 10.1086/307221. arXiv: astro-ph/9812133.

[30]   B. P. Schmidt et al. "The High Z supernova search: Measuring cosmic deceleration and global curvature of the universe using type Ia supernovae". In: *Astrophys. J.* 507 (1998), pp. 46–63. DOI: 10.1086/306308. arXiv: astro-ph/9805200.

[31]   A. D. Sakharov. "Violation of CP Invariance, C Asymmetry, and Baryon Asymmetry of the Universe". In: *Soviet Journal of Experimental and Theoretical Physics Letters* 5 (1967), p. 24.

[32] C. Csáki and P. Tanedo. "Beyond the Standard Model". In: *2013 European School of High-Energy Physics*. 2015, pp. 169–268. DOI: 10.5170/CERN-2015-004.169. arXiv: 1602.04228 [hep-ph].

[33] L. R. Evans and P. Bryant. "LHC Machine". In: *JINST* 3 (2008). This report is an abridged version of the LHC Design Report (CERN-2004-003), S08001. 164 p. DOI: 10.1088/1748-0221/3/08/S08001. URL: https://cds.cern.ch/record/1129806.

[34] O. S. Brüning et al. *LHC Design Report*. CERN Yellow Reports: Monographs. Geneva: CERN, 2004. DOI: 10.5170/CERN-2004-003-V-1. URL: https://cds.cern.ch/record/782076.

[35] O. S. Brüning et al. *LHC Design Report*. CERN Yellow Reports: Monographs. Geneva: CERN, 2004. DOI: 10.5170/CERN-2004-003-V-2. URL: https://cds.cern.ch/record/815187.

[36] M. Benedikt et al. *LHC Design Report*. CERN Yellow Reports: Monographs. Geneva: CERN, 2004. DOI: 10.5170/CERN-2004-003-V-3. URL: https://cds.cern.ch/record/823808.

[37] E. Mobs. *The CERN accelerator complex - 2019. Complexe des accélérateurs du CERN - 2019*. General Photo. 2019-07. URL: https://cds.cern.ch/record/2684277.

[38] CMS Collaboration. "The CMS Experiment at the CERN LHC". In: *JINST* 3 (2008), S08004. DOI: 10.1088/1748-0221/3/08/S08004.

[39] T. Sakuma and T. McCauley. "Detector and Event Visualization with SketchUp at the CMS Experiment". In: *J. Phys. Conf. Ser.* 513 (2014). Ed. by D. Groep and D. Bonacorsi, p. 022032. DOI: 10.1088/1742-6596/513/2/022032. arXiv: 1311.4942 [physics.ins-det].

[40] F. Hartmann. "Evolution of Silicon Sensor Technology in Particle Physics". In: *Springer Tracts Mod. Phys.* 275 (2017), pp.1–372. DOI: 10.1007/978-3-319-64436-3.

[41] CMS Collaboration. *The CMS tracker system project: Technical Design Report*. Tech. rep. CERN-LHCC-98-006, CMS-TDR-5. 1997.

[42] CMS Collaboration. *The CMS tracker: addendum to the Technical Design Report*. Tech. rep. CERN-LHCC-2000-016, CMS-TDR-5-add-1. 2000.

[43] CMS Collaboration. *CMS Technical Design Report for the Pixel Detector Upgrade*. Tech. rep. CERN-LHCC-2012-016, CMS-TDR-011. 2012-09.

[44] CMS Collaboration. "Description and performance of track and primary-vertex reconstruction with the CMS tracker". In: *JINST* 9.10 (2014), P10009. DOI: 10.1088/1748-0221/9/10/P10009. arXiv: 1405.6569 [physics.ins-det].

[45] CMS Collaboration. *The CMS electromagnetic calorimeter project: Technical Design Report*. Tech. rep. CERN-LHCC-97-033, CMS-TDR-4. 1997.

[46] CMS Collaboration. *Addendum to the CMS ECAL technical design report: Changes to the CMS ECAL electronics*. Tech. rep. CERN-LHCC-2002-027. 2002-09.

[47] CMS Collaboration. "Energy Calibration and Resolution of the CMS Electromagnetic Calorimeter in pp Collisions at $\sqrt{s} = 7$ TeV". In: *JINST* 8 (2013), P09009. DOI: 10.1088/1748-0221/8/09/P09009. arXiv: 1306.2016 [hep-ex].

[48] CMS Collaboration. "Performance and Operation of the CMS Electromagnetic Calorimeter". In: *JINST* 5 (2010), T03010. DOI: 10.1088/1748-0221/5/03/T03010. arXiv: 0910.3423 [physics.ins-det].

[49] CMS Collaboration. *The CMS hadron calorimeter project: Technical Design Report.* Tech. rep. CERN-LHCC-97-031. Geneva, 1997.

[50] CMS Collaboration. "Performance of the CMS Hadron Calorimeter with Cosmic Ray Muons and LHC Beam Data". In: *JINST* 5 (2010), T03012. DOI: `10.1088/1748-0221/5/03/T03012`. arXiv: `0911.4991` [`physics.ins-det`].

[51] CMS Collaboration. "Performance of CMS Hadron Calorimeter Timing and Synchronization using Test Beam, Cosmic Ray, and LHC Beam Data". In: *JINST* 5 (2010), T03013. DOI: `10.1088/1748-0221/5/03/T03013`. arXiv: `0911.4877` [`physics.ins-det`].

[52] CMS Collaboration. *CMS Technical Design Report for the Phase 1 Upgrade of the Hadron Calorimeter.* Tech. rep. 2012-09. DOI: `10.2172/1151651`.

[53] CMS Collaboration. *The CMS muon project: Technical Design Report.* Tech. rep. CERN-LHCC-97-032, CMS-TDR-3. 1997.

[54] CMS Collaboration. "Performance of the CMS muon detector and muon reconstruction with proton-proton collisions at $\sqrt{s} = 13$ TeV". In: *JINST* 13.06 (2018), P06015. DOI: `10.1088/1748-0221/13/06/P06015`. arXiv: `1804.04528` [`physics.ins-det`].

[55] CMS Collaboration. "The CMS trigger system". In: *JINST* 12.01 (2017), P01020. DOI: `10.1088/1748-0221/12/01/P01020`. arXiv: `1609.02366` [`physics.ins-det`].

[56] CMS Collaboration. *CMS. The TriDAS project. Technical design report, vol. 1: The trigger systems.* Tech. rep. CERN-LHCC-2000-038. 2000-12.

[57] CMS Collaboration. *CMS: The TriDAS project. Technical design report, Vol. 2: Data acquisition and high-level trigger.* Tech. rep. CERN-LHCC-2002-026. 2002-12.

[58] CMS Collaboration. "Particle-flow reconstruction and global event description with the CMS detector". In: *JINST* 12.10 (2017), P10003. DOI: `10.1088/1748-0221/12/10/P10003`. arXiv: `1706.04965` [`physics.ins-det`].

[59] G. Cowan et al. "Asymptotic formulae for likelihood-based tests of new physics". In: *Eur. Phys. J. C* 71 (2011). [Erratum: Eur.Phys.J.C 73, 2501 (2013)], p. 1554. DOI: `10.1140/epjc/s10052-011-1554-0`. arXiv: `1007.1727` [`physics.data-an`].

[60] ATLAS Collaboration and CMS Collaboration. *Procedure for the LHC Higgs boson search combination in Summer 2011.* Tech. rep. CMS-NOTE-2011-005. ATL-PHYS-PUB-2011-11. Geneva: CERN, 2011-08. URL: `https://cds.cern.ch/record/1379837`.

[61] J. Neyman, E. S. Pearson, and K. Pearson. "IX. On the problem of the most efficient tests of statistical hypotheses". In: *Philosophical Transactions of the Royal Society of London. Series A, Containing Papers of a Mathematical or Physical Character* 231.694-706 (1933), pp. 289–337. DOI: `10.1098/rsta.1933.0009`. eprint: `https://royalsocietypublishing.org/doi/pdf/10.1098/rsta.1933.0009`. URL: `https://royalsocietypublishing.org/doi/abs/10.1098/rsta.1933.0009`.

[62] A. L. Read. "Presentation of search results: The CL(s) technique". In: *J. Phys. G* 28 (2002). Ed. by M. Whalley and L. Lyons, pp. 2693–2704. DOI: `10.1088/0954-3899/28/10/313`.

[63] A. L. Read. "Modified frequentist analysis of search results (The CL(s) method)". In: *Workshop on Confidence Limits.* 2000-08, pp. 81–101.

[64] T. Junk. "Confidence level computation for combining searches with small statistics". In: *Nucl. Instrum. Meth. A* 434 (1999), pp. 435–443. DOI: `10.1016/S0168-9002(99)00498-2`. arXiv: `hep-ex/9902006`.

[65] T. Junk. *Sensitivity, Exclusion and Discovery with Small Signals, LargeBackgrounds, and Large Systematic Uncertainties*. 2006-02.

[66] G. Bertone and D. Hooper. "History of dark matter". In: *Rev. Mod. Phys.* 90.4 (2018), p. 045002. DOI: 10.1103/RevModPhys.90.045002. arXiv: 1605.04909 [astro-ph.CO].

[67] G. Bertone, D. Hooper, and J. Silk. "Particle dark matter: Evidence, candidates and constraints". In: *Phys. Rept.* 405 (2005), pp. 279–390. DOI: 10.1016/j.physrep.2004.08.031. arXiv: hep-ph/0404175 [hep-ph].

[68] F. W. Bessel. "On the variations of the proper motions of Procyon and Sirius". In: *Mon. Not. Roy. Astron. Soc.* 6 (1844), pp. 136–141.

[69] A. Secchi. *L'Astronomia in Roma nel pontificato di Pio IX: memoria*. Tipografia della Pace, 1877. URL: https://books.google.de/books?id=01w5PwAACAAJ.

[70] E. E. Barnard and A. C. Ranyard. "Structure of the Milky Way". In: *Knowledge: An Illustrated Magazine of Science* 17 (1894), p. 253.

[71] W. Thomson Baron Kelvin. *Baltimore Lectures on Molecular Dynamics and the Wave Theory of Light*. Cambridge Library Collection - Physical Sciences. Cambridge University Press, 2010. DOI: 10.1017/CBO9780511694523.

[72] H. Poincare. "The Milky Way and the Theory of Gases". In: *Popular Astronomy* 14 (1906), pp. 475–488.

[73] J. H. Oort. *The force exerted by the stellar system in the direction perpendicular to the galactic plane and some related problems*. 1932.

[74] J. H. Jeans. "The Motions of Stars in a Kapteyn-Universe". In: *Monthly Notices of the Royal Astronomical Society* 82.3 (1922-01), pp. 122–132. ISSN: 0035-8711. DOI: 10.1093/mnras/82.3.122. eprint: https://academic.oup.com/mnras/article-pdf/82/3/122/18250702/mnras82-0122.pdf. URL: https://doi.org/10.1093/mnras/82.3.122.

[75] P. O. Lindblad. "Bertil Lindblad's early work: the two-dimensional classification of stellar spectra at low dispersion". In: *Journal of Astronomical History and Heritage* 4.2 (2001), pp. 163–170.

[76] F. Zwicky. "Die Rotverschiebung von extragalaktischen Nebeln". In: *Helvetica Physica Acta* 6 (1933), pp. 110–127.

[77] F. Zwicky. "On the Masses of Nebulae and of Clusters of Nebulae". In: *Astrophysical Journal* 86 (1937), p. 217. DOI: 10.1086/143864.

[78] K. Lundmark. "Über die Bestimmung der Entfernungen, Dimensionen, Massen und Dichtigkeit fur die nächstgelegenen anagalacktischen Sternsysteme." In: *Meddelanden fran Lunds Astronomiska Observatorium Serie I* 125 (1930), pp. 1–13.

[79] H. W. Babcock. "The rotation of the Andromeda Nebula". In: *Lick Observatory Bulletin* 498 (1939), pp. 41–51. DOI: 10.5479/ADS/bib/1939LicOB.19.41B.

[80] M. Schwarzschild. "Mass distribution and mass-luminosity ratio in galaxies". In: *Astronomical Journal* 59 (1954), p. 273. DOI: 10.1086/107013.

[81] H. C. van de Hulst, E. Raimond, and H. van Woerden. "Rotation and density distribution of the Andromeda nebula derived from observations of the 21-cm line". In: *Bulletin of the Astronomical Institutes of the Netherlands* 14 (1957), p. 1.

[82] V. C. Rubin and J. Ford W. Kent. "Rotation of the Andromeda Nebula from a Spectroscopic Survey of Emission Regions". In: *Astrophysical Journal* 159 (1970), p. 379. DOI: 10.1086/150317.

[83] D. H. Rogstad and G. S. Shostak. "Gross Properties of Five Scd Galaxies as Determined from 21-CENTIMETER Observations". In: *Astrophysical Journal* 176 (1972), p. 315. DOI: 10.1086/151636.

[84] M. S. Roberts and A. H. Rots. "Comparison of Rotation Curves of Different Galaxy Types". In: *Astronomy and Astrophysics* 26 (1973), pp. 483–485.

[85] A. Bosma. "The distribution and kinematics of neutral hydrogen in spiral galaxies of various morphological types". PhD thesis. 1978.

[86] E. Corbelli and P. Salucci. "The Extended Rotation Curve and the Dark Matter Halo of M33". In: *Mon. Not. Roy. Astron. Soc.* 311 (2000), pp. 441–447. DOI: 10.1046/j.1365-8711.2000.03075.x. arXiv: astro-ph/9909252 [astro-ph].

[87] R. Massey, T. Kitching, and J. Richard. "The dark matter of gravitational lensing". In: *Rept. Prog. Phys.* 73 (2010), p. 086901. DOI: 10.1088/0034-4885/73/8/086901. arXiv: 1001.1739 [astro-ph.CO].

[88] D. Clowe et al. "A direct empirical proof of the existence of dark matter". In: *Astrophys. J.* 648 (2006), pp. L109–L113. DOI: 10.1086/508162. arXiv: astro-ph/0608407 [astro-ph].

[89] D. Samtleben, S. Staggs, and B. Winstein. "The Cosmic microwave background for pedestrians: A Review for particle and nuclear physicists". In: *Ann. Rev. Nucl. Part. Sci.* 57 (2007), pp. 245–283. DOI: 10.1146/annurev.nucl.54.070103.181232. arXiv: 0803.0834 [astro-ph].

[90] N. Aghanim et al. *Planck 2018 results. VI. Cosmological parameters.* 2018. arXiv: 1807.06209 [astro-ph.CO].

[91] P. A. R. Ade et al. "Planck 2013 results. I. Overview of products and scientific results". In: *Astron. Astrophys.* 571 (2014), A1. DOI: 10.1051/0004-6361/201321529. arXiv: 1303.5062 [astro-ph.CO].

[92] J. R. Primack and M. A. K. Gross. *Hot dark matter in cosmology.* 2000. arXiv: astro-ph/0007165 [astro-ph].

[93] P. Bode, J. P. Ostriker, and N. Turok. "Halo Formation in Warm Dark Matter Models". In: *The Astrophysical Journal* 556.1 (2001-07), pp. 93–107. DOI: 10.1086/321541. URL: https://doi.org/10.1086%2F321541.

[94] D. V. Naumov. "The Sterile Neutrino: A short introduction". In: *EPJ Web Conf.* 207 (2019), p. 04004. DOI: 10.1051/epjconf/201920704004. arXiv: 1901.00151 [hep-ph].

[95] A. A. Klypin et al. "Where are the missing Galactic satellites?" In: *Astrophys. J.* 522 (1999), pp. 82–92. DOI: 10.1086/307643. arXiv: astro-ph/9901240 [astro-ph].

[96] G. Gentile et al. "The Cored distribution of dark matter in spiral galaxies". In: *Mon. Not. Roy. Astron. Soc.* 351 (2004), p. 903. DOI: 10.1111/j.1365-2966.2004.07836.x. arXiv: astro-ph/0403154 [astro-ph].

[97] M. Drewes et al. "A White Paper on keV Sterile Neutrino Dark Matter". In: *JCAP* 1701 (2017), p. 025. DOI: 10.1088/1475-7516/2017/01/025. arXiv: 1602.04816 [hep-ph].

[98] R. Peccei. "The Strong CP problem and axions". In: *Lect. Notes Phys.* 741 (2008), pp. 3–17. DOI: 10.1007/978-3-540-73518-2_1. arXiv: hep-ph/0607268.

[99] A. De Simone and T. Jacques. "Simplified models vs. effective field theory approaches in dark matter searches". In: *Eur. Phys. J. C* 76.7 (2016), p. 367. DOI: 10.1140/epjc/s10052-016-4208-4. arXiv: 1603.08002 [hep-ph].

[100] J. Abdallah et al. "Simplified Models for Dark Matter Searches at the LHC". In: *Phys. Dark Univ.* 9-10 (2015), pp. 8–23. DOI: 10.1016/j.dark.2015.08.001. arXiv: 1506.03116 [hep-ph].

[101] D. Abercrombie et al. "Dark Matter Benchmark Models for Early LHC Run-2 Searches: Report of the ATLAS/CMS Dark Matter Forum". In: *Phys. Dark Univ.* 27 (2020). Ed. by A. Boveia et al., p. 100371. DOI: 10.1016/j.dark.2019.100371. arXiv: 1507.00966 [hep-ex].

[102] M. Drees. "An Introduction to supersymmetry". In: *Inauguration Conference of the Asia Pacific Center for Theoretical Physics (APCTP)*. 1996-11. arXiv: hep-ph/9611409.

[103] D. Hooper and S. Profumo. "Dark Matter and Collider Phenomenology of Universal Extra Dimensions". In: *Phys. Rept.* 453 (2007), pp. 29–115. DOI: 10.1016/j.physrep.2007.09.003. arXiv: hep-ph/0701197.

[104] M. Schmaltz. "Physics beyond the standard model (theory): Introducing the little Higgs". In: *Nucl. Phys. B Proc. Suppl.* 117 (2003). Ed. by S. Bentvelsen et al., pp. 40–49. DOI: 10.1016/S0920-5632(03)01409-9. arXiv: hep-ph/0210415.

[105] M. Schumann. "Direct Detection of WIMP Dark Matter: Concepts and Status". In: *J. Phys. G* 46.10 (2019), p. 103003. DOI: 10.1088/1361-6471/ab2ea5. arXiv: 1903.03026 [astro-ph.CO].

[106] J. M. Gaskins. "A review of indirect searches for particle dark matter". In: *Contemp. Phys.* 57.4 (2016), pp. 496–525. DOI: 10.1080/00107514.2016.1175160. arXiv: 1604.00014 [astro-ph.HE].

[107] C. de los Heros. ISAPP Summer School "The Dark Side of the Universe". 2011. URL: https://www.mpi-hd.mpg.de/lin/events/isapp2011/pages/lectures/de_los_Heros.pdf (visited on 2020-08-30).

[108] M. Strassler. *Searching for Dark Matter at the LHC.* 2015. URL: https://profmattstrassler.com/articles-and-posts/relativity-space-astronomy-and-cosmology/dark-matter/searching-for-dark-matter-at-the-lhc/ (visited on 2020-05-23).

[109] CMS Collaboration. "Search for new physics in final states with an energetic jet or a hadronically decaying W or Z boson and transverse momentum imbalance at $\sqrt{s} = 13$ TeV". In: *Phys. Rev. D* 97.9 (2018), p. 092005. DOI: 10.1103/PhysRevD.97.092005. arXiv: 1712.02345 [hep-ex].

[110] CMS Collaboration. "Search for new physics in events with a leptonically decaying Z boson and a large transverse momentum imbalance in proton–proton collisions at $\sqrt{s} = 13$ TeV". In: *Eur. Phys. J. C* 78.4 (2018), p. 291. DOI: 10.1140/epjc/s10052-018-5740-1. arXiv: 1711.00431 [hep-ex].

[111] CMS Collaboration. *Search for dark matter produced in association with a Z boson in proton-proton collisions at $\sqrt{s} = 13$ TeV.* CMS Physics Analysis Summary CMS-PAS-EXO-19-003. 2020-06.

[112] CMS Collaboration. "Search for dark matter particles produced in association with a Higgs boson in proton-proton collisions at $\sqrt{s} = 13$ TeV". In: *JHEP* 03 (2020), p. 025. DOI: 10.1007/JHEP03(2020)025. arXiv: 1908.01713 [hep-ex].

[113] A. Berlin, T. Lin, and L.-T. Wang. "Mono-Higgs Detection of Dark Matter at the LHC". In: *JHEP* 06 (2014), p. 078. DOI: 10.1007/JHEP06(2014)078. arXiv: 1402.7074 [hep-ph].

[114] L. Carpenter et al. "Mono-Higgs-boson: A new collider probe of dark matter". In: *Phys. Rev. D* 89.7 (2014), p. 075017. DOI: 10.1103/PhysRevD.89.075017. arXiv: 1312.2592 [hep-ph].

[115] CMS Collaboration. "Search for heavy resonances decaying into a vector boson and a Higgs boson in final states with charged leptons, neutrinos and b quarks at $\sqrt{s} = 13$ TeV". In: *JHEP* 11 (2018), p. 172. DOI: 10.1007/JHEP11(2018)172. arXiv: 1807.02826 [hep-ex].

[116] CMS Collaboration. "Search for dark matter produced in association with a Higgs boson decaying to a pair of bottom quarks in proton–proton collisions at $\sqrt{s} = 13$ TeV". In: *Eur. Phys. J. C* 79.3 (2019), p. 280. DOI: 10.1140/epjc/s10052-019-6730-7. arXiv: 1811.06562 [hep-ex].

[117] CMS Collaboration. "Search for dark matter produced in association with a Higgs boson decaying to $\gamma\gamma$ or $\tau^+\tau^-$ at $\sqrt{s} = 13$ TeV". In: *JHEP* 09 (2018), p. 046. DOI: 10.1007/JHEP09(2018)046. arXiv: 1806.04771 [hep-ex].

[118] CMS Collaboration. "Search for new physics in final states with a single photon and missing transverse momentum in proton-proton collisions at $\sqrt{s} = 13$ TeV". In: *JHEP* 02 (2019), p. 074. DOI: 10.1007/JHEP02(2019)074. arXiv: 1810.00196 [hep-ex].

[119] CMS Collaboration. "Search for dark matter in events with energetic, hadronically decaying top quarks and missing transverse momentum at $\sqrt{s} = 13$ TeV". In: *JHEP* 06 (2018), p. 027. DOI: 10.1007/JHEP06(2018)027. arXiv: 1801.08427 [hep-ex].

[120] CMS Collaboration. *Search for monotop in the muon channel in proton-proton collisions at $\sqrt{s} = 8$ TeV*. CMS Physics Analysis Summary CMS-PAS-B2G-15-001. 2016-04.

[121] N. Cabibbo. "Unitary Symmetry and Leptonic Decays". In: *Phys. Rev. Lett.* 10 (1963), pp. 531–533. DOI: 10.1103/PhysRevLett.10.531.

[122] M. Kobayashi and T. Maskawa. "CP Violation in the Renormalizable Theory of Weak Interaction". In: *Prog. Theor. Phys.* 49 (1973), pp. 652–657. DOI: 10.1143/PTP.49.652.

[123] I. I. Y. Bigi et al. "Production and Decay Properties of Ultraheavy Quarks". In: *Phys. Lett.* B181 (1986), pp. 157–163. DOI: 10.1016/0370-2693(86)91275-X.

[124] U. Husemann. "Top-Quark Physics: Status and Prospects". In: *Prog. Part. Nucl. Phys.* 95 (2017), pp. 48–97. DOI: 10.1016/j.ppnp.2017.03.002. arXiv: 1704.01356 [hep-ex].

[125] A. Quadt. "Top quark physics at hadron colliders". In: *Eur. Phys. J. C* 48 (2006), pp. 835–1000. DOI: 10.1140/epjc/s2006-02631-6.

[126] J. Andrea, B. Fuks, and F. Maltoni. "Monotops at the LHC". In: *Phys. Rev.* D84 (2011), p. 074025. DOI: 10.1103/PhysRevD.84.074025. arXiv: 1106.6199 [hep-ph].

[127] J.-L. Agram et al. "Monotop phenomenology at the Large Hadron Collider". In: *Phys. Rev.* D89.1 (2014), p. 014028. DOI: 10.1103/PhysRevD.89.014028. arXiv: 1311.6478 [hep-ph].

[128] I. Boucheneb et al. "Revisiting monotop production at the LHC". In: *JHEP* 01 (2015), p. 017. DOI: 10.1007/JHEP01(2015)017. arXiv: 1407.7529 [hep-ph].

[129] S. L. Glashow, J. Iliopoulos, and L. Maiani. "Weak Interactions with Lepton-Hadron Symmetry". In: *Phys. Rev. D* 2 (7 1970-10), pp. 1285–1292. DOI: 10.1103/PhysRevD.2.1285. URL: https://link.aps.org/doi/10.1103/PhysRevD.2.1285.

[130] E. W. Kolb and M. S. Turner. "The Early Universe". In: *Front. Phys.* 69 (1990), pp. 1–547.

[131] R. Kogler et al. "Jet Substructure at the Large Hadron Collider: Experimental Review". In: *Rev. Mod. Phys.* 91.4 (2019), p. 045003. DOI: 10.1103/RevModPhys.91.045003. arXiv: 1803.06991 [hep-ex].

[132] S. Marzani, G. Soyez, and M. Spannowsky. *Looking inside jets: an introduction to jet substructure and boosted-object phenomenology.* 2019. DOI: 10.1007/978-3-030-15709-8. arXiv: 1901.10342 [hep-ph].

[133] J. Shelton. "Jet Substructure". In: *Proceedings, Theoretical Advanced Study Institute in Elementary Particle Physics: Searching for New Physics at Small and Large Scales (TASI 2012): Boulder, Colorado, June 4-29, 2012.* 2013, pp. 303–340. DOI: 10.1142/9789814525220_0007. arXiv: 1302.0260 [hep-ph].

[134] M. Cacciari, G. P. Salam, and G. Soyez. "The anti-k_t jet clustering algorithm". In: *JHEP* 04 (2008), p. 063. DOI: 10.1088/1126-6708/2008/04/063. arXiv: 0802.1189 [hep-ph].

[135] S. D. Ellis and D. E. Soper. "Successive combination jet algorithm for hadron collisions". In: *Phys. Rev. D* 48 (1993), pp. 3160–3166. DOI: 10.1103/PhysRevD.48.3160. arXiv: hep-ph/9305266.

[136] M. Wobisch and T. Wengler. "Hadronization corrections to jet cross-sections in deep inelastic scattering". In: *Workshop on Monte Carlo Generators for HERA Physics (Plenary Starting Meeting).* 1998-04, pp. 270–279. arXiv: hep-ph/9907280.

[137] CMS Collaboration. *Pileup Removal Algorithms.* CMS Physics Analysis Summary CMS-PAS-JME-14-001. Geneva: CERN, 2014. URL: https://cds.cern.ch/record/1751454.

[138] D. Bertolini et al. "Pileup Per Particle Identification". In: *JHEP* 10 (2014), p. 059. DOI: 10.1007/JHEP10(2014)059. arXiv: 1407.6013 [hep-ph].

[139] A. J. Larkoski, J. Thaler, and W. J. Waalewijn. "Gaining (Mutual) Information about Quark/Gluon Discrimination". In: *JHEP* 11 (2014), p. 129. DOI: 10.1007/JHEP11(2014)129. arXiv: 1408.3122 [hep-ph].

[140] I. W. Stewart, F. J. Tackmann, and W. J. Waalewijn. "N-Jettiness: An Inclusive Event Shape to Veto Jets". In: *Phys. Rev. Lett.* 105 (2010), p. 092002. DOI: 10.1103/PhysRevLett.105.092002. arXiv: 1004.2489 [hep-ph].

[141] J. Thaler and K. Van Tilburg. "Identifying Boosted Objects with N-subjettiness". In: *JHEP* 03 (2011), p. 015. DOI: 10.1007/JHEP03(2011)015. arXiv: 1011.2268 [hep-ph].

[142] A. J. Larkoski, G. P. Salam, and J. Thaler. "Energy Correlation Functions for Jet Substructure". In: *JHEP* 06 (2013), p. 108. DOI: 10.1007/JHEP06(2013)108. arXiv: 1305.0007 [hep-ph].

[143] J. M. Butterworth et al. "Jet substructure as a new Higgs search channel at the LHC". In: *Phys. Rev. Lett.* 100 (2008), p. 242001. DOI: 10.1103/PhysRevLett.100.242001. arXiv: 0802.2470 [hep-ph].

[144] M. Dasgupta et al. "Towards an understanding of jet substructure". In: *JHEP* 09 (2013), p. 029. DOI: 10.1007/JHEP09(2013)029. arXiv: 1307.0007 [hep-ph].

[145] A. J. Larkoski et al. "Soft Drop". In: *JHEP* 05 (2014), p. 146. DOI: 10.1007/JHEP05(2014)146. arXiv: 1402.2657 [hep-ph].

[146] F. A. Dreyer et al. "Recursive Soft Drop". In: *JHEP* 06 (2018), p. 093. DOI: 10.1007/JHEP06(2018)093. arXiv: 1804.03657 [hep-ph].

[147]   D. Krohn, J. Thaler, and L.-T. Wang. "Jet Trimming". In: *JHEP* 02 (2010), p. 084. DOI: 10.1007/JHEP02(2010)084. arXiv: 0912.1342 [hep-ph].

[148]   S. D. Ellis, C. K. Vermilion, and J. R. Walsh. "Techniques for improved heavy particle searches with jet substructure". In: *Phys. Rev.* D80 (2009), p. 051501. DOI: 10.1103/PhysRevD.80.051501. arXiv: 0903.5081 [hep-ph].

[149]   CMS Collaboration. *Boosted jet identification using particle candidates and deep neural networks.* Tech. rep. CMS-DP-2017-049. 2017-11.

[150]   CMS Collaboration. *Machine learning-based identification of highly Lorentz-boosted hadronically decaying particles at the CMS experiment.* CMS Physics Analysis Summary CMS-PAS-JME-18-002. 2019-07.

[151]   M. Stoye et al. *DeepJet : Generic physics object based jet multiclass classification for LHC experiments.* Tech. rep. Workshop on Deep Learning for Physical Sciences, NIPS. 2017.

[152]   G. Louppe, M. Kagan, and K. Cranmer. *Learning to Pivot with Adversarial Networks.* 2016. arXiv: 1611.01046 [stat.ML].

[153]   CMS Collaboration. "Identification of heavy-flavour jets with the CMS detector in pp collisions at 13 TeV". In: *JINST* 13.05 (2018), P05011. DOI: 10.1088/1748-0221/13/05/P05011. arXiv: 1712.07158 [physics.ins-det].

[154]   CMS Collaboration. *Performance of the DeepJet b tagging algorithm using 41.9/fb of data from proton-proton collisions at 13TeV with Phase 1 CMS detector.* Tech. rep. CMS-DP-2018-058. 2018-11.

[155]   CMS collaboration. *Heavy flavour tagging for 13 TeV 2016 Legacy data.* URL: https://twiki.cern.ch/twiki/bin/viewauth/CMS/BtagRecommendation2016Legacy (visited on 2020-04-27).

[156]   CMS collaboration. *Heavy flavour tagging for 13 TeV data in 2017 and 94X MC.* URL: https://twiki.cern.ch/twiki/bin/viewauth/CMS/BtagRecommendation94X (visited on 2020-04-27).

[157]   CMS collaboration. *Heavy flavour tagging for 13 TeV data in 2018 and 102X MC.* URL: https://twiki.cern.ch/twiki/bin/viewauth/CMS/BtagRecommendation102X (visited on 2020-04-27).

[158]   M. Molch. "Untersuchungen zur Effizienz des Einsatzes von AK8- und AK15-Jets bei einer Monotop-Analyse bei CMS". Bachelor's Thesis. Karlsruhe Institute of Technology (KIT), 2020.

[159]   P. Nason. "A New method for combining NLO QCD with shower Monte Carlo algorithms". In: *JHEP* 11 (2004), p. 040. DOI: 10.1088/1126-6708/2004/11/040. arXiv: hep-ph/0409146.

[160]   S. Frixione, P. Nason, and C. Oleari. "Matching NLO QCD computations with Parton Shower simulations: the POWHEG method". In: *JHEP* 11 (2007), p. 070. DOI: 10.1088/1126-6708/2007/11/070. arXiv: 0709.2092 [hep-ph].

[161]   S. Alioli et al. "A general framework for implementing NLO calculations in shower Monte Carlo programs: the POWHEG BOX". In: *JHEP* 06 (2010), p. 043. DOI: 10.1007/JHEP06(2010)043. arXiv: 1002.2581 [hep-ph].

[162]   J. M. Campbell et al. "Top-Pair Production and Decay at NLO Matched with Parton Showers". In: *JHEP* 04 (2015), p. 114. DOI: 10.1007/JHEP04(2015)114. arXiv: 1412.1828 [hep-ph].

[163] S. Alioli, S.-O. Moch, and P. Uwer. "Hadronic top-quark pair-production with one jet and parton showering". In: *JHEP* 01 (2012), p. 137. DOI: 10.1007/JHEP01(2012)137. arXiv: 1110.5251 [hep-ph].

[164] S. Alioli et al. "NLO single-top production matched with shower in POWHEG: s- and t-channel contributions". In: *JHEP* 09 (2009). [Erratum: JHEP 02, 011 (2010)], p. 111. DOI: 10.1088/1126-6708/2009/09/111. arXiv: 0907.4076 [hep-ph].

[165] E. Re. "Single-top Wt-channel production matched with parton showers using the POWHEG method". In: *Eur. Phys. J. C* 71 (2011), p. 1547. DOI: 10.1140/epjc/s10052-011-1547-z. arXiv: 1009.2450 [hep-ph].

[166] T. Sjostrand, S. Mrenna, and P. Z. Skands. "A Brief Introduction to PYTHIA 8.1". In: *Comput. Phys. Commun.* 178 (2008), pp. 852–867. DOI: 10.1016/j.cpc.2008.01.036. arXiv: 0710.3820 [hep-ph].

[167] T. Sjöstrand et al. "An Introduction to PYTHIA 8.2". In: *Comput. Phys. Commun.* 191 (2015), pp. 159–177. DOI: 10.1016/j.cpc.2015.01.024. arXiv: 1410.3012 [hep-ph].

[168] T. Sjostrand. "The Lund Monte Carlo for Jet Fragmentation". In: *Comput. Phys. Commun.* 27 (1982), p. 243. DOI: 10.1016/0010-4655(82)90175-8.

[169] DMsimp - FeynRules. 2020-02-06. URL: http://feynrules.irmp.ucl.ac.be/wiki/DMsimp (visited on 2020-09-21).

[170] M. Backović et al. "Higher-order QCD predictions for dark matter production at the LHC in simplified models with s-channel mediators". In: *Eur. Phys. J. C* 75.10 (2015), p. 482. DOI: 10.1140/epjc/s10052-015-3700-6. arXiv: 1508.05327 [hep-ph].

[171] A. Alloul et al. "FeynRules 2.0 - A complete toolbox for tree-level phenomenology". In: *Comput. Phys. Commun.* 185 (2014), pp. 2250–2300. DOI: 10.1016/j.cpc.2014.04.012. arXiv: 1310.1921 [hep-ph].

[172] G. Busoni et al. "Recommendations on presenting LHC searches for missing transverse energy signals using simplified *s*-channel models of dark matter". In: *Phys. Dark Univ.* 27 (2020). Ed. by A. Boveia et al., p. 100365. DOI: 10.1016/j.dark.2019.100365. arXiv: 1603.04156 [hep-ex].

[173] S. Agostinelli et al. "GEANT4–a simulation toolkit". In: *Nucl. Instrum. Meth. A* 506 (2003), pp. 250–303. DOI: 10.1016/S0168-9002(03)01368-8.

[174] J. Allison et al. "Geant4 developments and applications". In: *IEEE Trans. Nucl. Sci.* 53 (2006), p. 270. DOI: 10.1109/TNS.2006.869826.

[175] J. Allison et al. "Recent developments in Geant4". In: *Nucl. Instrum. Meth. A* 835 (2016), pp. 186–225. DOI: 10.1016/j.nima.2016.06.125.

[176] M. Czakon, P. Fiedler, and A. Mitov. "Total Top-Quark Pair-Production Cross Section at Hadron Colliders Through ". In: *Phys. Rev. Lett.* 110 (2013), p. 252004. DOI: 10.1103/PhysRevLett.110.252004. arXiv: 1303.6254 [hep-ph].

[177] M. Czakon and A. Mitov. "Top++: A Program for the Calculation of the Top-Pair Cross-Section at Hadron Colliders". In: *Comput. Phys. Commun.* 185 (2014), p. 2930. DOI: 10.1016/j.cpc.2014.06.021. arXiv: 1112.5675 [hep-ph].

[178] M. Aliev et al. "HATHOR: HAdronic Top and Heavy quarks crOss section calculatoR". In: *Comput. Phys. Commun.* 182 (2011), pp. 1034–1046. DOI: 10.1016/j.cpc.2010.12.040. arXiv: 1007.1327 [hep-ph].

[179] P. Kant et al. "HatHor for single top-quark production: Updated predictions and uncertainty estimates for single top-quark production in hadronic collisions". In: *Comput. Phys. Commun.* 191 (2015), pp. 74–89. DOI: `10.1016/j.cpc.2015.02.001`. arXiv: `1406.4403 [hep-ph]`.

[180] N. Kidonakis. "Two-loop soft anomalous dimensions for single top quark associated production with a W- or H-". In: *Phys. Rev.* D82 (2010), p. 054018. DOI: `10.1103/PhysRevD.82.054018`. arXiv: `1005.4451 [hep-ph]`.

[181] T. Gehrmann et al. "W^+W^- Production at Hadron Colliders in Next to Next to Leading Order QCD". In: *Phys. Rev. Lett.* 113.21 (2014), p. 212001. DOI: `10.1103/PhysRevLett.113.212001`. arXiv: `1408.5243 [hep-ph]`.

[182] J. M. Campbell, R. K. Ellis, and C. Williams. "Vector boson pair production at the LHC". In: *JHEP* 07 (2011), p. 018. DOI: `10.1007/JHEP07(2011)018`. arXiv: `1105.0020 [hep-ph]`.

[183] F. Cascioli et al. "ZZ production at hadron colliders in NNLO QCD". In: *Phys. Lett.* B735 (2014), pp. 311–313. DOI: `10.1016/j.physletb.2014.06.056`. arXiv: `1405.2219 [hep-ph]`.

[184] G. Petrucciani, A. Rizzi, and C. Vuosalo. "Mini-AOD: A New Analysis Data Format for CMS". In: *J. Phys. Conf. Ser.* 664.7 (2015), p. 7. DOI: `10.1088/1742-6596/664/7/072052`. arXiv: `1702.04685 [physics.ins-det]`.

[185] CMSSW_10_2_18. URL: `https://github.com/cms-sw/cmssw/tree/CMSSW_10_2_18` (visited on 2020-11-06).

[186] CMS Collaboration. *Known issues in centrally produced MC*. 2020-03-30. URL: `https://twiki.cern.ch/twiki/bin/viewauth/CMS/MCKnownIssues#WJetsToLNu_HT_and_DYJets_HT_LO_M` (visited on 2020-10-05).

[187] CMS Collaboration. *PH Generator meeting - Matrix Element and Future Generators - The pdfwgt setting in MG 2.4.2 and its effect on 2017/18 LO V samples*. 2019-09-03. URL: `https://indico.cern.ch/event/841559/#b-345082-matrix-element-and-fu` (visited on 2020-10-05).

[188] CMS Collaboration. *PH Generator meeting - Matrix Element and Future Generators - pdfwgt setting in MG*. 2019-10-22. URL: `https://indico.cern.ch/event/855110/#b-351397-matrix-element-and-fu` (visited on 2020-10-05).

[189] J. M. Lindert et al. "Precise predictions for $V+$ jets dark matter backgrounds". In: *Eur. Phys. J.* C77.12 (2017), p. 829. DOI: `10.1140/epjc/s10052-017-5389-1`. arXiv: `1705.04664 [hep-ph]`.

[190] S. Frixione. "Isolated photons in perturbative QCD". In: *Phys. Lett.* B429 (1998), pp. 369–374. DOI: `10.1016/S0370-2693(98)00454-7`. arXiv: `hep-ph/9801442 [hep-ph]`.

[191] J. M. Lindert et al. *Precise predictions for $V+$ jets dark matter backgrounds*. URL: `https://www.ippp.dur.ac.uk/~jlindert/vjets/` (visited on 2020-11-10).

[192] CMS collaboration. *Run-II monojet / mono-V analysis*. Tech. rep. CMS AN-20-042. 2020.

[193] CMS Collaboration. *Reweighting recipe to emulate Level 1 ECAL prefiring*. 2019-04-08. URL: `https://twiki.cern.ch/twiki/bin/viewauth/CMS/L1ECALPrefiringWeightRecipe` (visited on 2020-10-17).

[194] CMS collaboration. *Electron Cut-based Identification Efficiencies*. URL: `https://twiki.cern.ch/twiki/bin/view/CMS/CutBasedElectronIdentificationRun2#Electron_ID_Working_Points_WP_de` (visited on 2020-04-26).

[195] CMS Collaboration. "Performance of Electron Reconstruction and Selection with the CMS Detector in Proton-Proton Collisions at $\sqrt{s} = 8$ TeV". In: *JINST* 10.06 (2015), P06005. DOI: `10.1088/1748-0221/10/06/P06005`. arXiv: `1502.02701 [physics.ins-det]`.

[196] CMS collaboration. *Electron Cut-based Identification Efficiency Scale Factors.* URL: `https://twiki.cern.ch/twiki/bin/view/CMS/EgammaIDRecipesRun2#Efficiencies_and_scale_factors` (visited on 2020-04-26).

[197] CMS collaboration. *Photon Cut-based Identification Efficiencies.* URL: `https://twiki.cern.ch/twiki/bin/view/CMS/CutBasedPhotonIdentificationRun2#Photon_ID_Working_Points_WP_defi` (visited on 2020-04-26).

[198] CMS Collaboration. *Performance of electron and photon reconstruction in Run 2 with the CMS experiment.* Tech. rep. CMS-DP-2020-037. 2020-07. URL: `https://cds.cern.ch/record/2725004`.

[199] CMS collaboration. *Photon Cut-based Identification Efficiency Scale Factors.* URL: `https://twiki.cern.ch/twiki/bin/view/CMS/EgammaIDRecipesRun2#Photon_efficiencies_and_scale_fa` (visited on 2020-04-26).

[200] S. Yuan. *Measurement of cut-basedID SF medium WP for high pT photons for EXO-20-004.* 2020-05-21. URL: `https://indico.cern.ch/event/879924/contributions/3872624/attachments/2042983/3422039/Photon_ID_EGamma_meeting0521.pdf` (visited on 2020-10-16).

[201] CMS collaboration. *Reference muon id, isolation and trigger efficiencies for 2016 legacy re-reco data.* URL: `https://twiki.cern.ch/twiki/bin/view/CMS/MuonReferenceEffs2016LegacyRereco` (visited on 2020-04-26).

[202] CMS collaboration. *Reference muon id, isolation and trigger efficiencies for 2017 data.* URL: `https://twiki.cern.ch/twiki/bin/view/CMS/MuonReferenceEffs2017` (visited on 2020-04-26).

[203] CMS collaboration. *Reference muon id, isolation and trigger efficiencies for 2018 data.* URL: `https://twiki.cern.ch/twiki/bin/view/CMS/MuonReferenceEffs2018` (visited on 2020-04-26).

[204] CMS Collaboration. "Reconstruction and identification of τ lepton decays to hadrons and ν_τ at CMS". In: *JINST* 11.01 (2016), P01019. DOI: `10.1088/1748-0221/11/01/P01019`. arXiv: `1510.07488 [physics.ins-det]`.

[205] CMS collaboration. *Jet Identification for the 13 TeV data Run2016.* URL: `https://twiki.cern.ch/twiki/bin/view/CMS/JetID13TeVRun2017` (visited on 2020-04-27).

[206] CMS collaboration. *Jet Identification for the 13 TeV data Run2017.* URL: `https://twiki.cern.ch/twiki/bin/view/CMS/JetID13TeVRun2017` (visited on 2020-04-27).

[207] CMS collaboration. *Jet Identification for the 13 TeV data Run2018.* URL: `https://twiki.cern.ch/twiki/bin/view/CMS/JetID13TeVRun2018` (visited on 2020-04-27).

[208] CMS collaboration. *Methods to apply b-tagging efficiency scale factors.* URL: `https://twiki.cern.ch/twiki/bin/view/CMS/BTagSFMethods` (visited on 2020-09-10).

[209] CMS Collaboration. "Performance of missing transverse momentum reconstruction in proton-proton collisions at $\sqrt{s} = 13$ TeV using the CMS detector". In: *JINST* 14.07 (2019), P07004. DOI: `10.1088/1748-0221/14/07/P07004`. arXiv: `1903.06078 [hep-ex]`.

[210] CMS Collaboration. *Mitigation of anomalous missing transverse momentum measurements in data collected by CMS at sqrt(s) = 13 TeV during the LHC Run 2*. Tech. rep. CMS-DP-2020-018. 2020-04. URL: https://cds.cern.ch/record/2714938.

[211] CMS collaboration. *Introduction to Jet Energy Corrections at CMS*. URL: https://twiki.cern.ch/twiki/bin/view/CMS/IntroToJEC (visited on 2020-04-27).

[212] CMS Collaboration. "Determination of jet energy calibration and transverse momentum resolution in CMS". In: *Journal of Instrumentation* 6.11 (2011-11), P11002–P11002. DOI: 10.1088/1748-0221/6/11/p11002. URL: https://doi.org/10.1088%2F1748-0221%2F6%2F11%2Fp11002.

[213] CMS Collaboration. "Jet energy scale and resolution in the CMS experiment in pp collisions at 8 TeV". In: *JINST* 12.02 (2017), P02014. DOI: 10.1088/1748-0221/12/02/P02014. arXiv: 1607.03663 [hep-ex].

[214] CMS Collaboration. *Jet energy scale and resolution performance with 13 TeV data collected by CMS in 2016*. Tech. rep. CMS-DP-2018-028. 2018-06.

[215] CMS collaboration. *Jet energy scale uncertainty sources*. URL: https://twiki.cern.ch/twiki/bin/view/CMS/JECUncertaintySources (visited on 2020-05-09).

[216] CMS Collaboration. *JER Scaling factors and Uncertainty for 13 TeV*. URL: https://twiki.cern.ch/twiki/bin/view/CMS/JetResolution#JER_Scaling_factors_and_Uncertai (visited on 2020-05-09).

[217] CMS Collaboration. *JEC Status Report - HEM issue Studies*. 2019-09-09. URL: https://indico.cern.ch/event/846608/contributions/3556096/attachments/1904250/3144533/JERCMeeting_9_9_2019_V2.pdf (visited on 2020-10-11).

[218] CMS Collaboration. *Treatment of the HEM15/16 region in 2018 data*. 2019-10-18. URL: https://hypernews.cern.ch/HyperNews/CMS/get/JetMET/2000.html (visited on 2020-10-11).

[219] CMS Collaboration. *DeepAK8 (V2) Working Points and Scale Factors for 13 TeV data*. URL: https://twiki.cern.ch/twiki/bin/view/CMS/DeepAK8Tagging2018WPsSFs (visited on 2020-10-01).

[220] CMS Collaboration. *CMS Luminosity Measurements for the 2016 Data Taking Period*. CMS Physics Analysis Summary CMS-PAS-LUM-17-001. 2017. URL: https://cds.cern.ch/record/2257069.

[221] CMS Collaboration. *CMS luminosity measurement for the 2017 data-taking period at $\sqrt{s}$ = 13 TeV*. CMS Physics Analysis Summary CMS-PAS-LUM-17-004. 2018. URL: https://cds.cern.ch/record/2621960.

[222] CMS Collaboration. *CMS luminosity measurement for the 2018 data-taking period at $\sqrt{s}$ = 13 TeV*. CMS Physics Analysis Summary CMS-PAS-LUM-18-002. 2019. URL: https://cds.cern.ch/record/2676164.

[223] CMS Collaboration. *Luminosity Physics Object Group - Year-to-year combinations and correlations*. 2020-09-11. URL: https://twiki.cern.ch/twiki/bin/view/CMS/TWikiLUM#LumiComb (visited on 2020-10-12).

[224] CMS Collaboration. *Luminosity Physics Object Group - Year-to-year combinations and correlations*. 2020-10-07. URL: https://twiki.cern.ch/twiki/bin/view/CMS/TopSystematics#Luminosity (visited on 2020-10-12).

[225] R. D. Ball et al. "Parton distributions from high-precision collider data". In: *Eur. Phys. J. C* 77.10 (2017), p. 663. DOI: 10.1140/epjc/s10052-017-5199-5. arXiv: 1706.00428 [hep-ph].

[226] A. Buckley et al. "LHAPDF6: parton density access in the LHC precision era". In: *Eur. Phys. J. C* 75 (2015), p. 132. DOI: 10.1140/epjc/s10052-015-3318-8. arXiv: 1412.7420 [hep-ph].

[227] J. Butterworth et al. "PDF4LHC recommendations for LHC Run II". In: *J. Phys. G* 43 (2016), p. 023001. DOI: 10.1088/0954-3899/43/2/023001. arXiv: 1510.03865 [hep-ph].

[228] V. Khachatryan et al. "Measurement of the differential cross section for top quark pair production in pp collisions at $\sqrt{s} = 8\,\text{TeV}$". In: *Eur. Phys. J. C* 75.11 (2015), p. 542. DOI: 10.1140/epjc/s10052-015-3709-x. arXiv: 1505.04480 [hep-ex].

[229] R. Barlow and C. Beeston. "Fitting using finite Monte Carlo samples". In: *Computer Physics Communications* 77.2 (1993), pp. 219–228. ISSN: 0010-4655. DOI: https://doi.org/10.1016/0010-4655(93)90005-W. URL: http://www.sciencedirect.com/science/article/pii/001046559390005W.

[230] J. Conway. "Incorporating Nuisance Parameters in Likelihoods for Multisource Spectra". In: *PHYSTAT 2011*. 2011, pp. 115–120. DOI: 10.5170/CERN-2011-006.115. arXiv: 1103.0354 [physics.data-an].

[231] G. Aad et al. "Measurements of the Higgs boson production and decay rates and constraints on its couplings from a combined ATLAS and CMS analysis of the LHC pp collision data at $\sqrt{s} = 7$ and 8 TeV". In: *JHEP* 08 (2016), p. 045. DOI: 10.1007/JHEP08(2016)045. arXiv: 1606.02266 [hep-ex].

[232] Robert D., Cousins. *Generalization of Chisquare Goodness-of-Fit Test for Binned Data Using Saturated Models, with Application to Histograms*. 2013-03-03. URL: http://www.physics.ucla.edu/~cousins/stats/cousins_saturated.pdf (visited on 2020-10-20).

[233] S. Baker and R. D. Cousins. "Clarification of the Use of Chi Square and Likelihood Functions in Fits to Histograms". In: *Nucl. Instrum. Meth.* 221 (1984), pp. 437–442. DOI: 10.1016/0167-5087(84)90016-4.

[234] CMS collaboration. *CMS Statistics Committee*. 2020-10-12. URL: https://twiki.cern.ch/twiki/bin/view/CMS/StatisticsCommittee (visited on 2020-10-20).

Appendix

A Corrections for simulated events

A.1 Higher-order corrections for single vector boson events
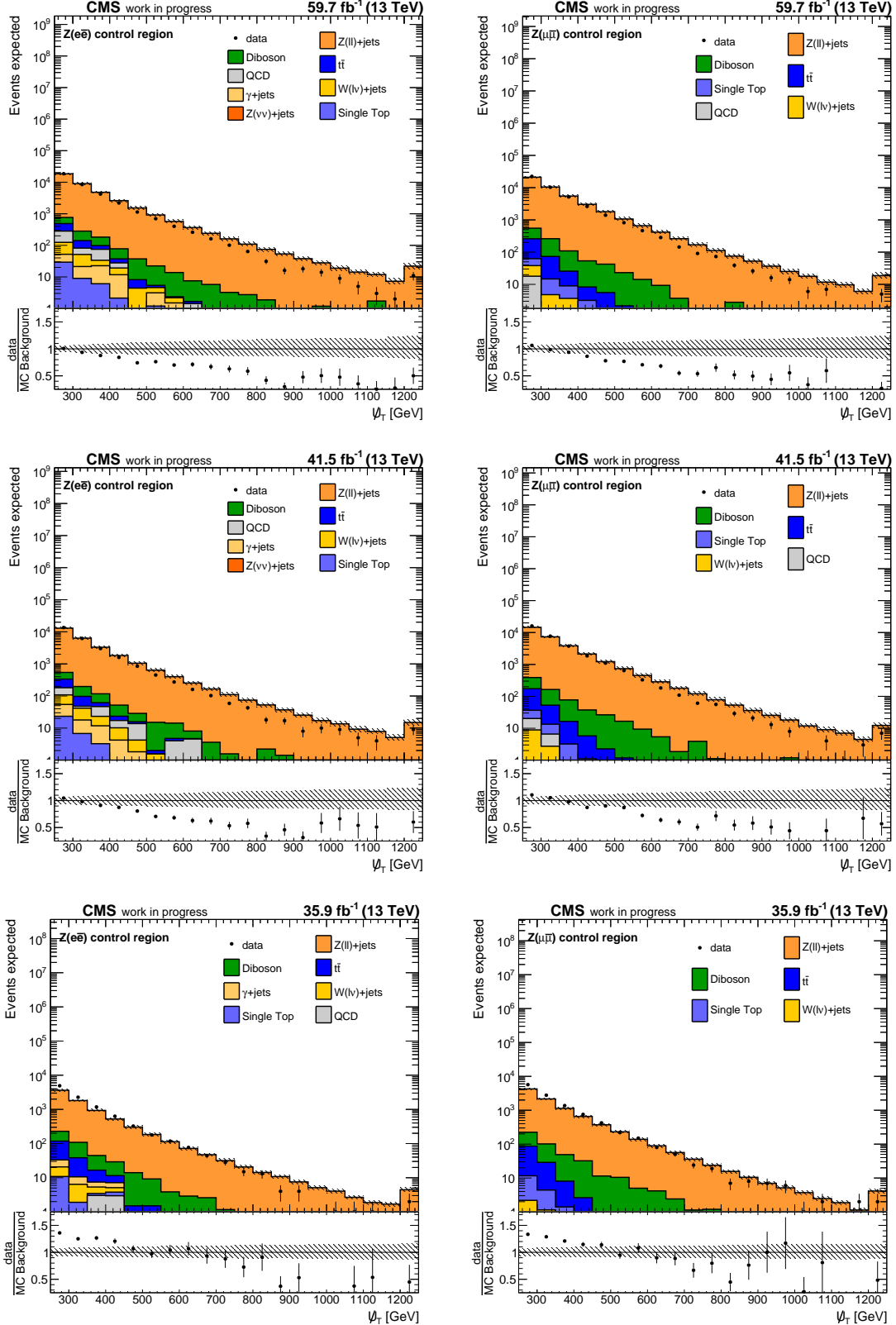
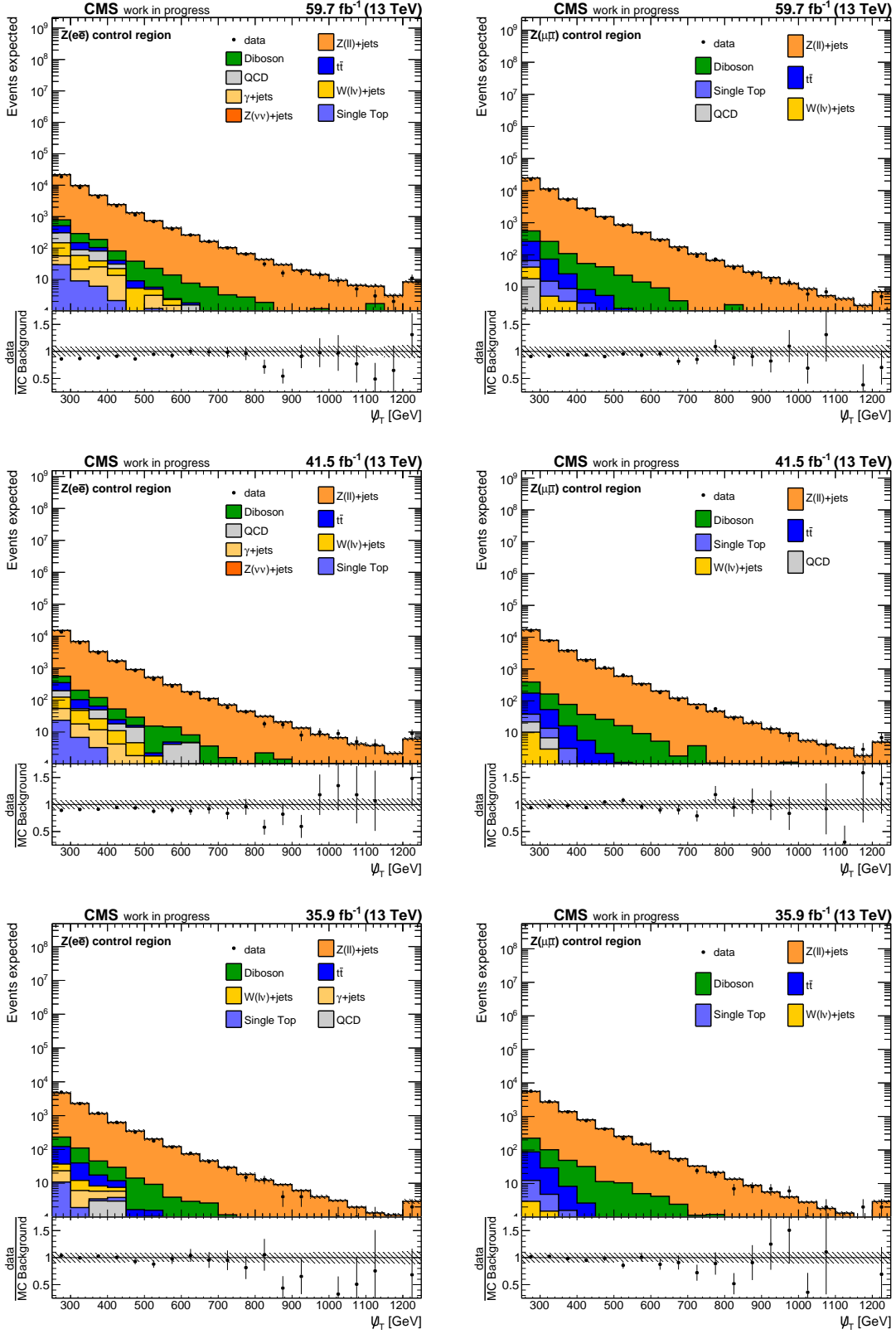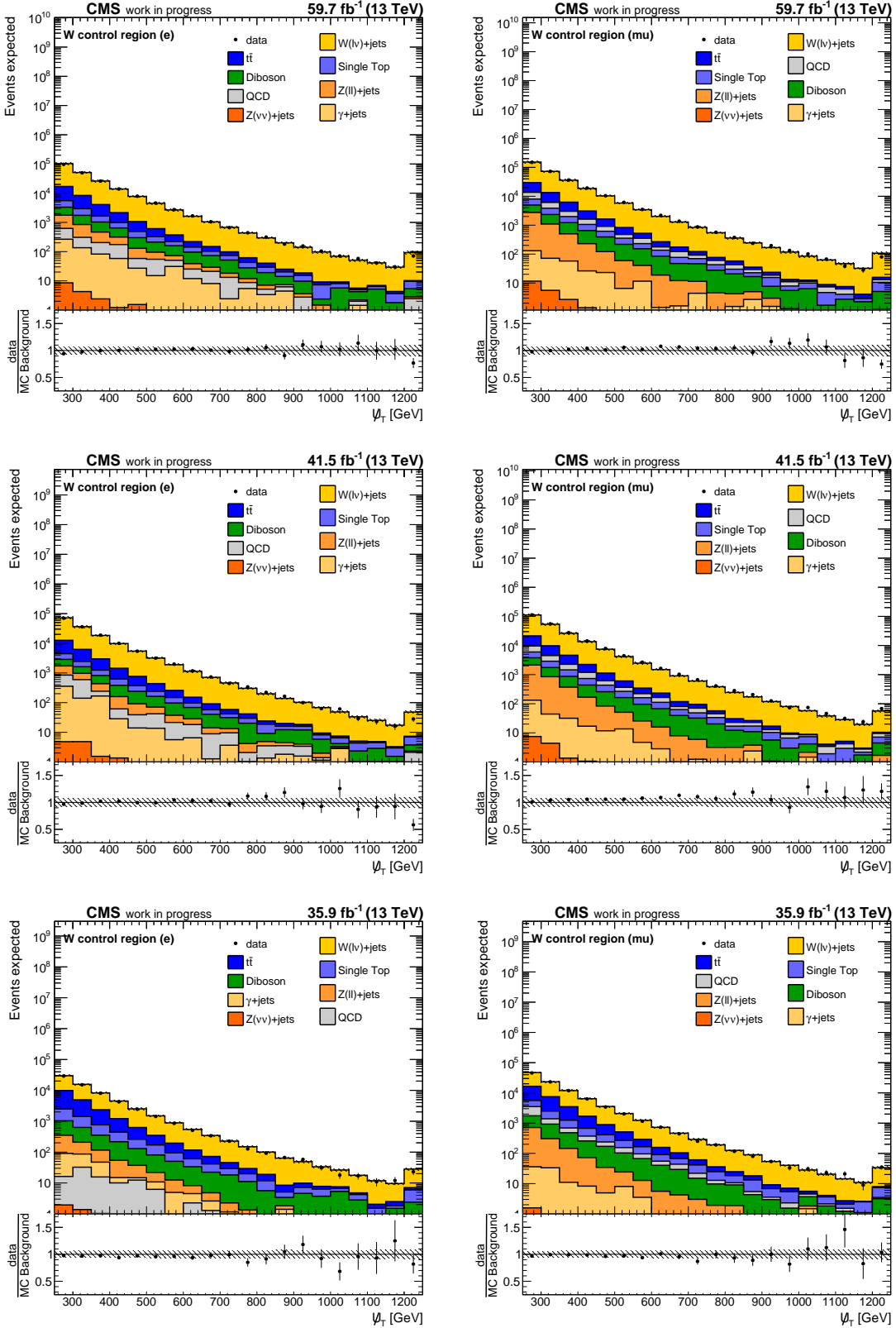
Figure A.1: Hadronic recoil distributions in the Z+jets control region split according to the data era without applying the V+jets reweighting procedure. The uncertainty band corresponds to the square root of the quadratic sum of indepedent variations of the matrix element renormalization scale and factorization scale by a factor of 2 and 1/2.
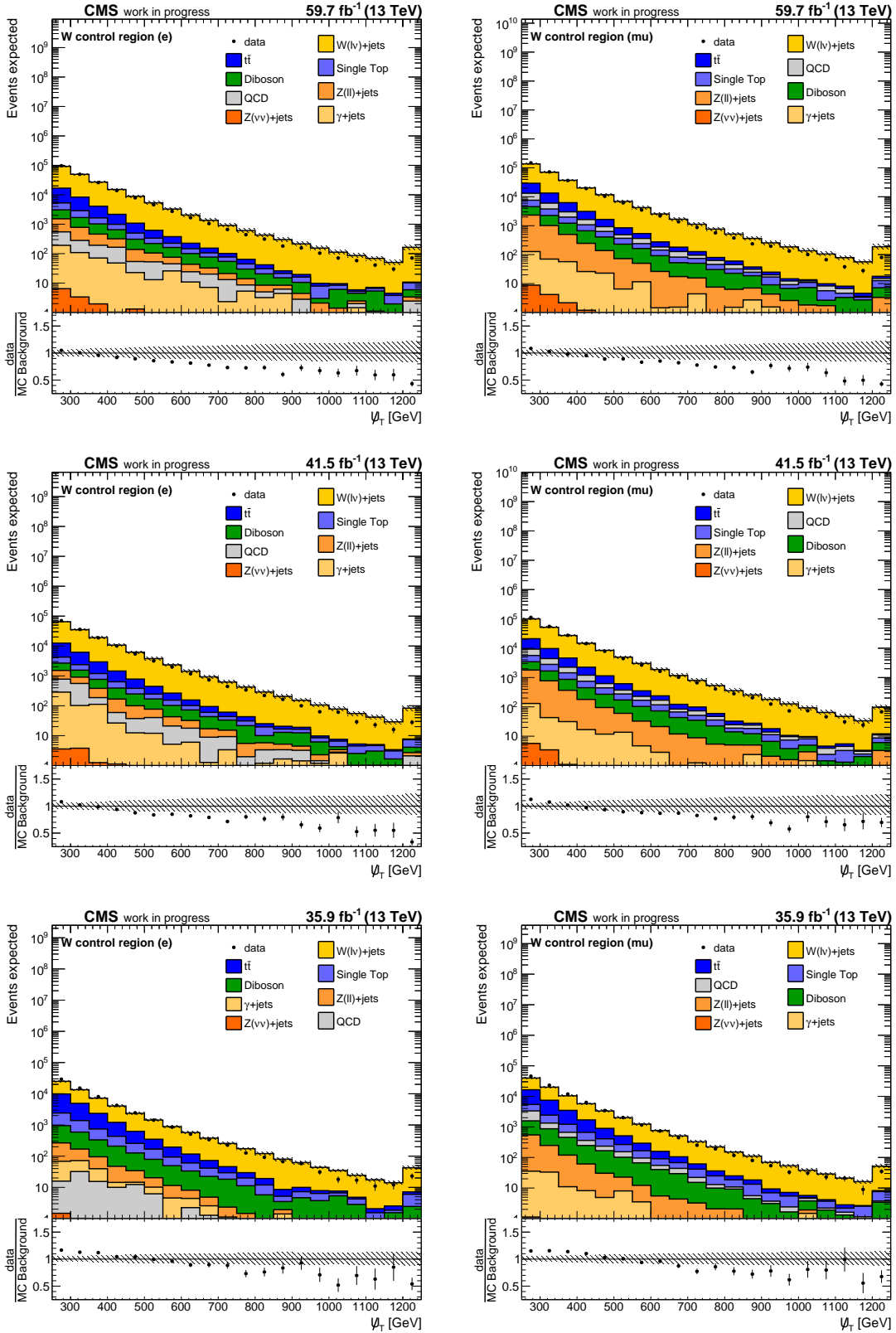
Figure A.2: Hadronic recoil distributions in the W + jets control region split according to the data era without applying the V + jets reweighting procedure. The uncertainty band corresponds to the square root of the quadratic sum of indepedent variations of the matrix element renormalization scale and factorization scale by a factor of 2 and 1/2.
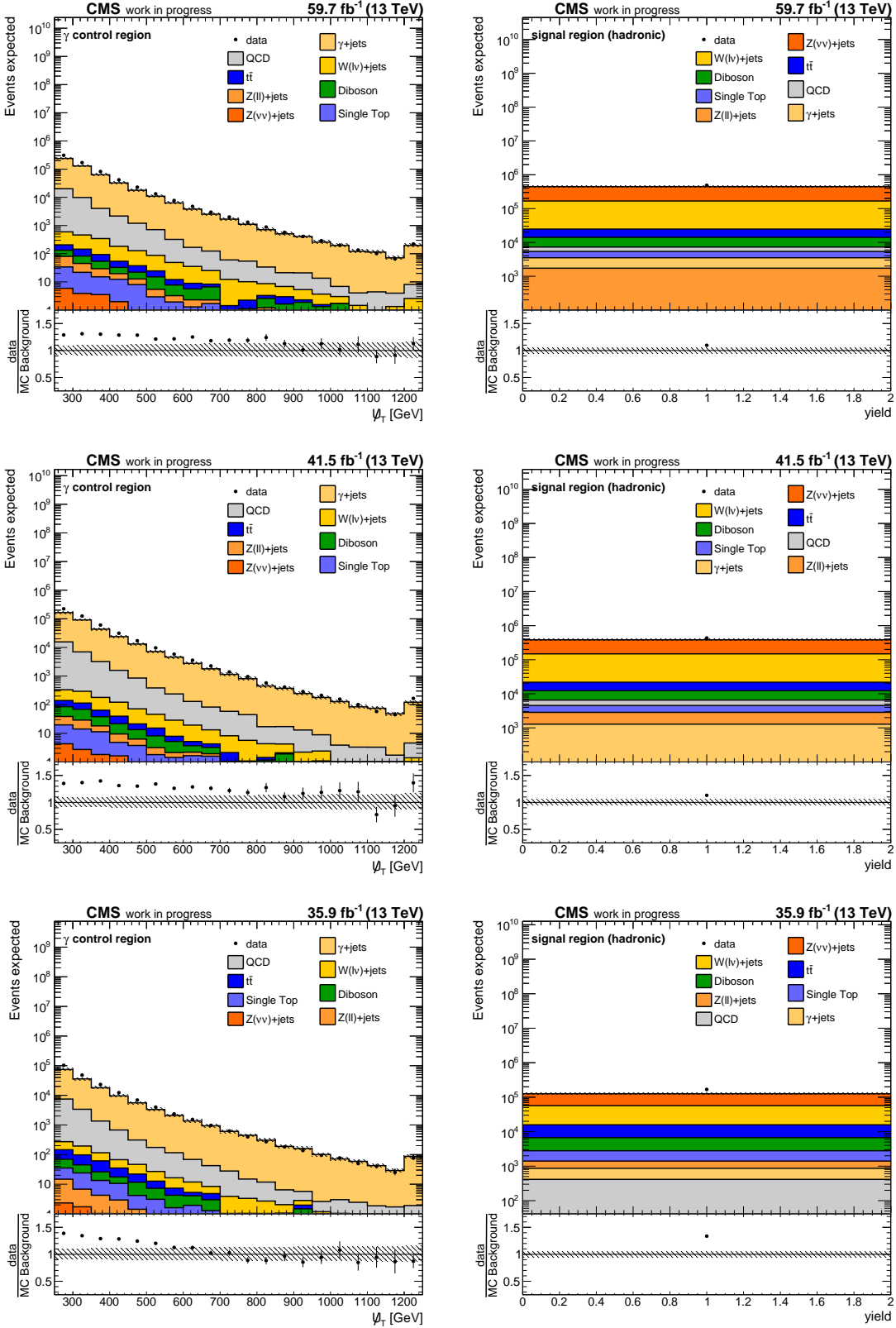
Figure A.3: Hadronic recoil distributions in the $\gamma + \text{jets}$ control region and total yields in the signal region without top-tagging techniques applied split according to the data era without applying the $V + \text{jets}$ reweighting procedure. The uncertainty band corresponds to the square root of the quadratic sum of indepedent variations of the matrix element renormalization scale and factorization scale by a factor of 2 and $1/2$.

Scale factor calculation
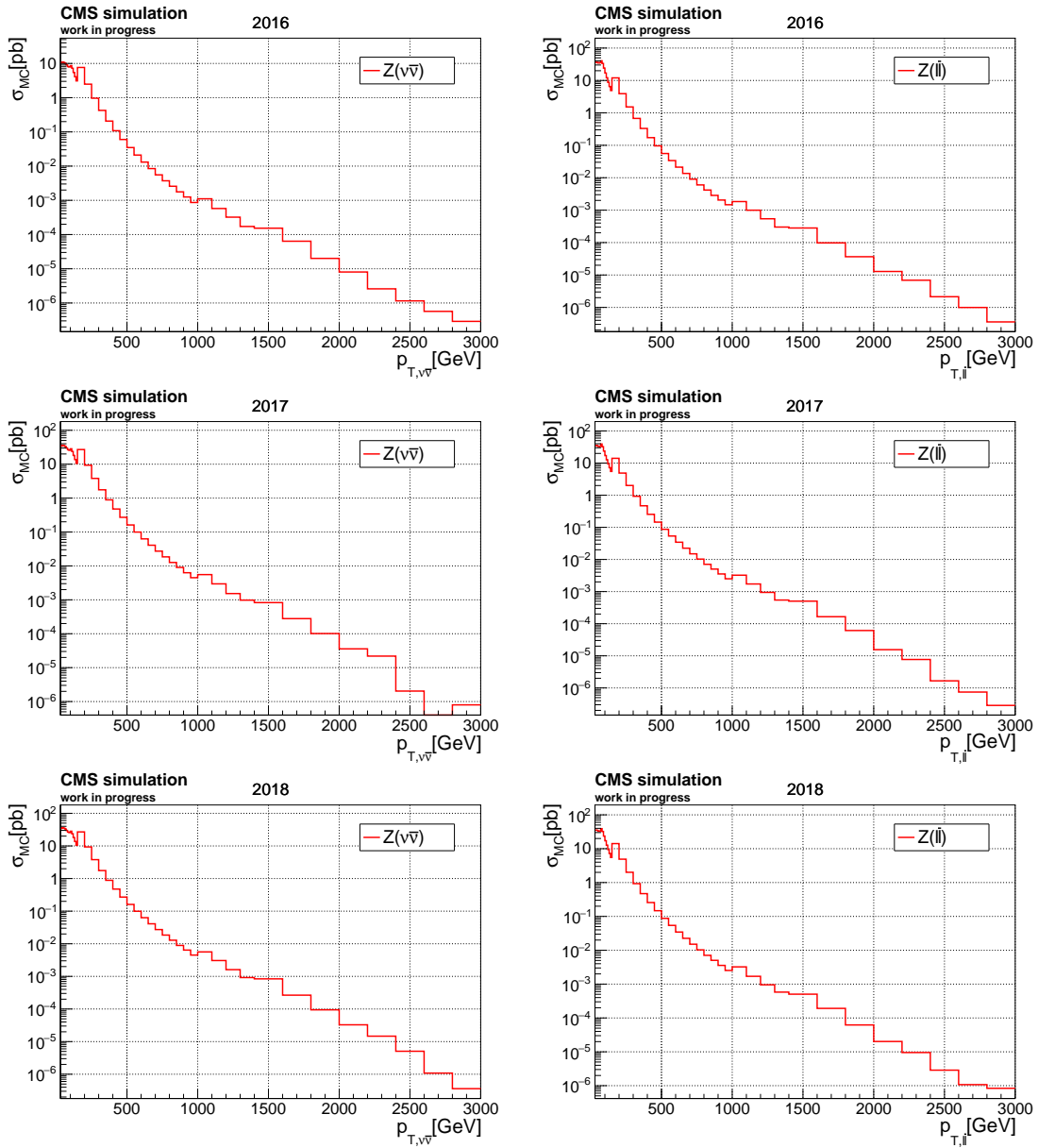
Figure A.4: Differential cross sections from MC simulation as a function of the transverse momentum of the vector boson for $Z \to \nu\bar{\nu}$ and $Z \to l\bar{l}$ as well as for different MC production eras.
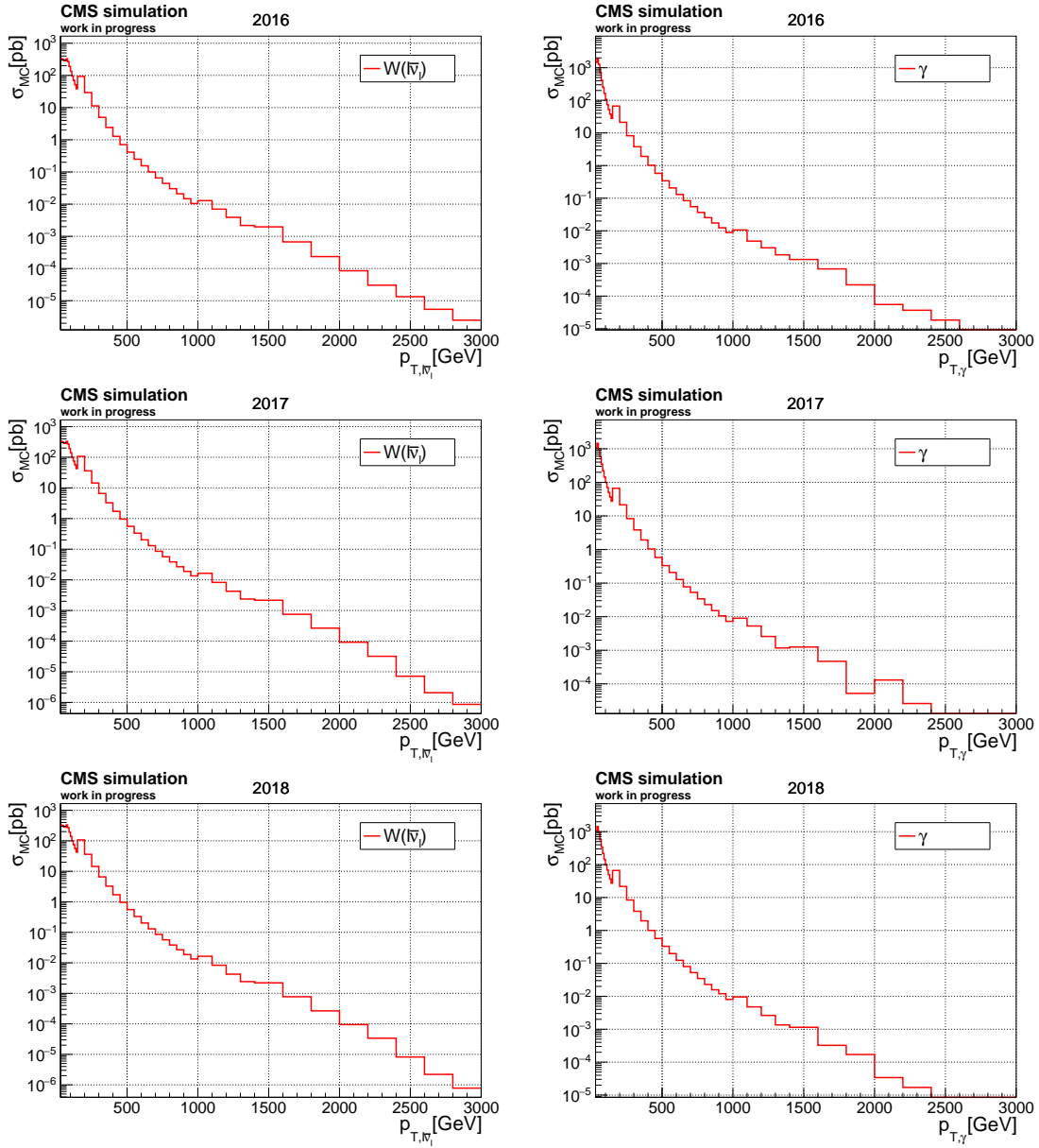
Figure A.5: Differential cross sections from MC simulation as a function of the transverse momentum of the vector boson for $W \to l\bar{\nu}$ and γ as well as for different MC production eras.
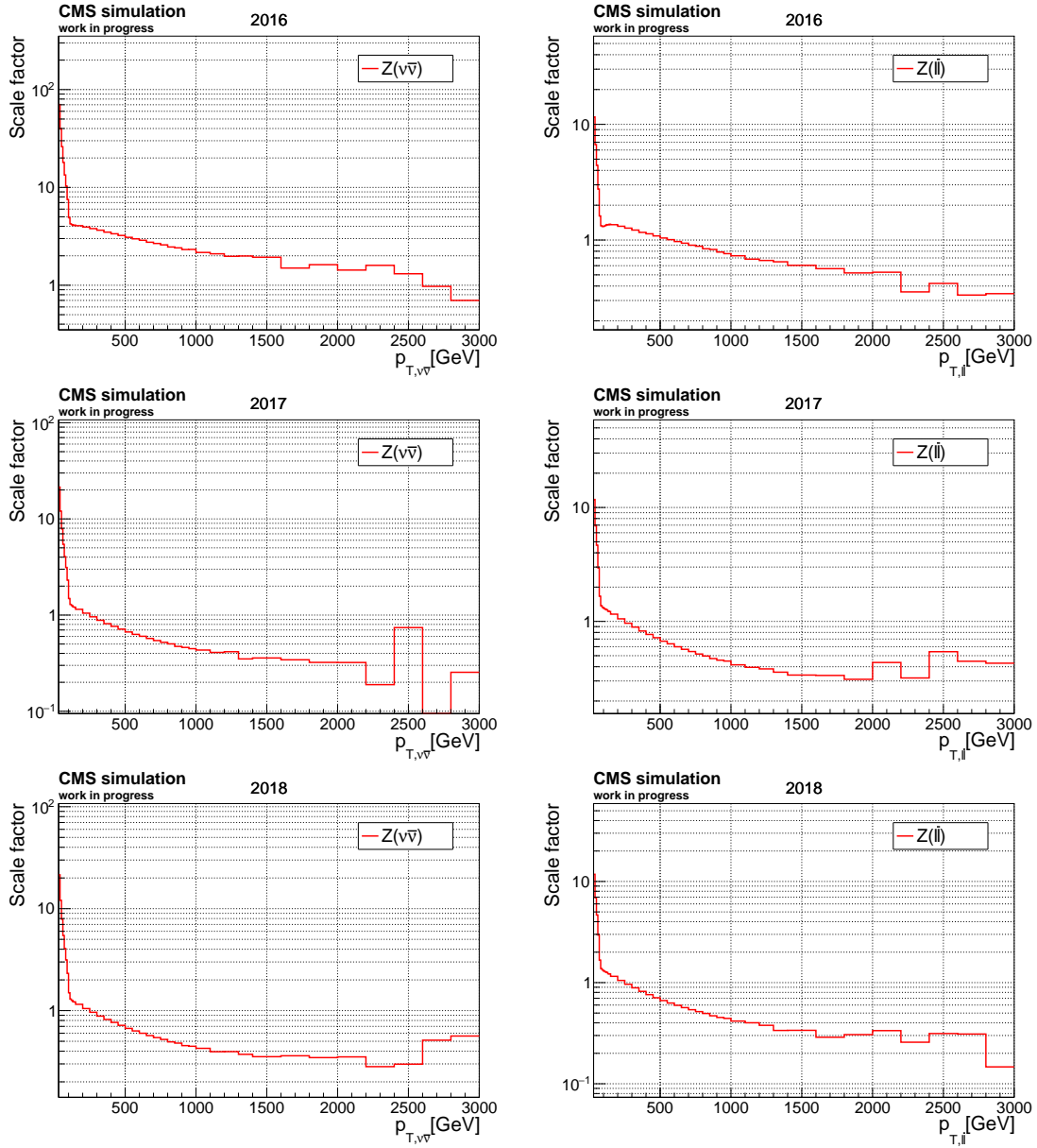
Figure A.6: Differential reweighting factors as a function the transverse momentum of the Z boson for the Z + jets process with Z → $\nu\overline{\nu}$ and Z → l$\overline{\text{l}}$ comparing different MC production eras.
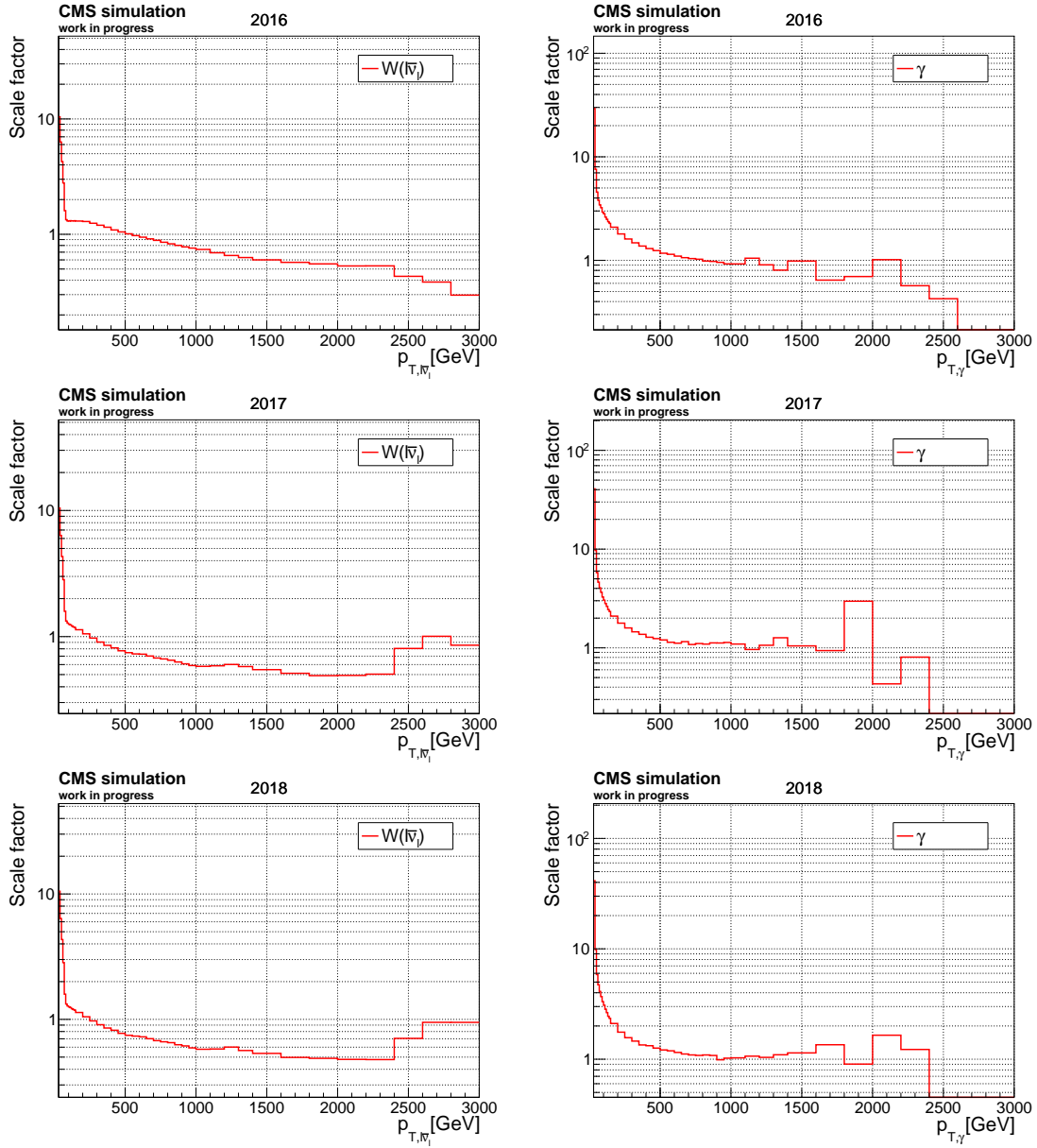
Figure A.7: Differential reweighting factors as a function of the transverse momentum of the vector boson for the W + jets and γ + jets processes comparing different MC production eras.

Theoretical systematic uncertainties of the reweighting factors
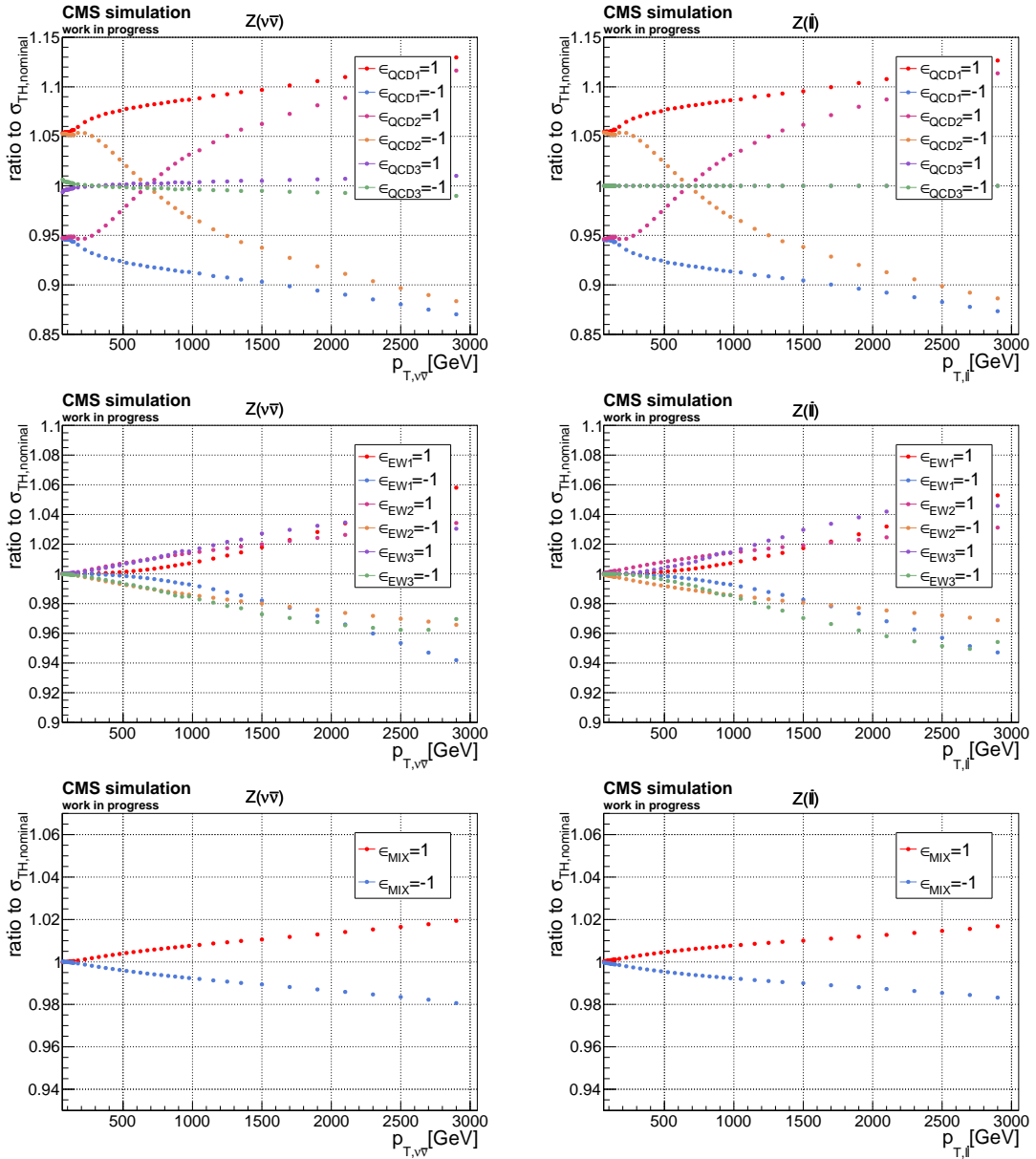
Figure A.8: Ratios comparing systematically varied fixed-order differential cross sections with the nominal fixed-order differential cross sections for Z + jets with $Z \rightarrow \nu\bar{\nu}$ and $Z \rightarrow l\bar{l}$ as a function of the transverse momentum of the Z boson. The parameters ϵ are the nuisance parameters described in section 5.5.1. Those parameters ϵ which are not explicitly stated in a specific legend entry are set equal to zero. The first row shows the impact of QCD uncertainties, the second row shows EWK uncertainties, and the third row shows the uncertainty on the combination procedure of QCD and EWK corrections.
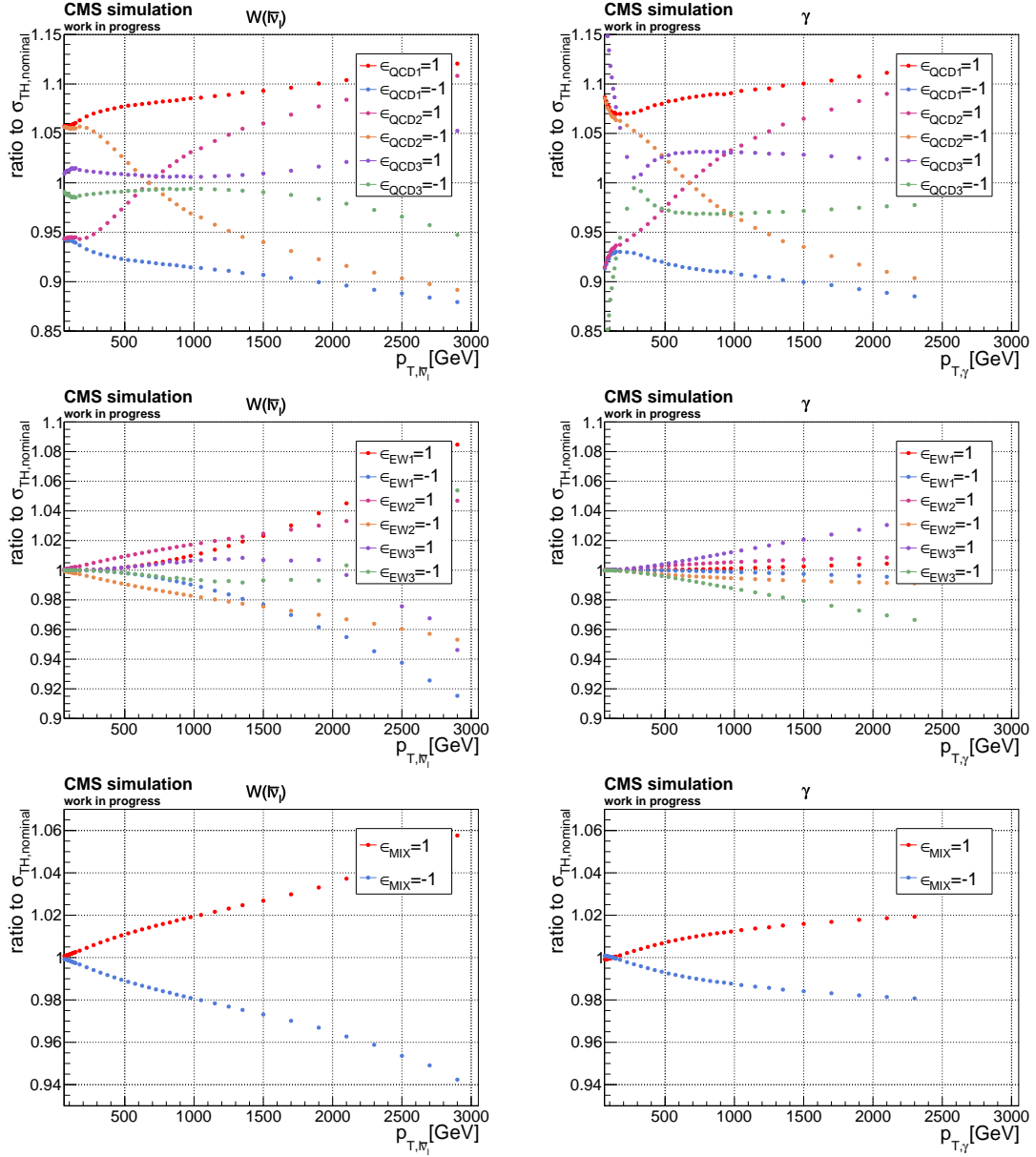
Figure A.9: Ratios comparing systematically varied fixed-order differential cross sections with the nominal fixed-order differential cross sections for W + jets and γ + jets as a function of the transverse momentum of the vector boson. The parameters ϵ are the nuisance parameters described in section 5.5.1. Those parameters ϵ which are not explicitly stated in a specific legend entry are equal to zero. The first row shows the impact of QCD uncertainties, the second row shows EWK uncertainties, and the third row shows the uncertainty on the combination procedure of QCD and EWK corrections.

MC simulation systematic uncertainties of the reweighting factors
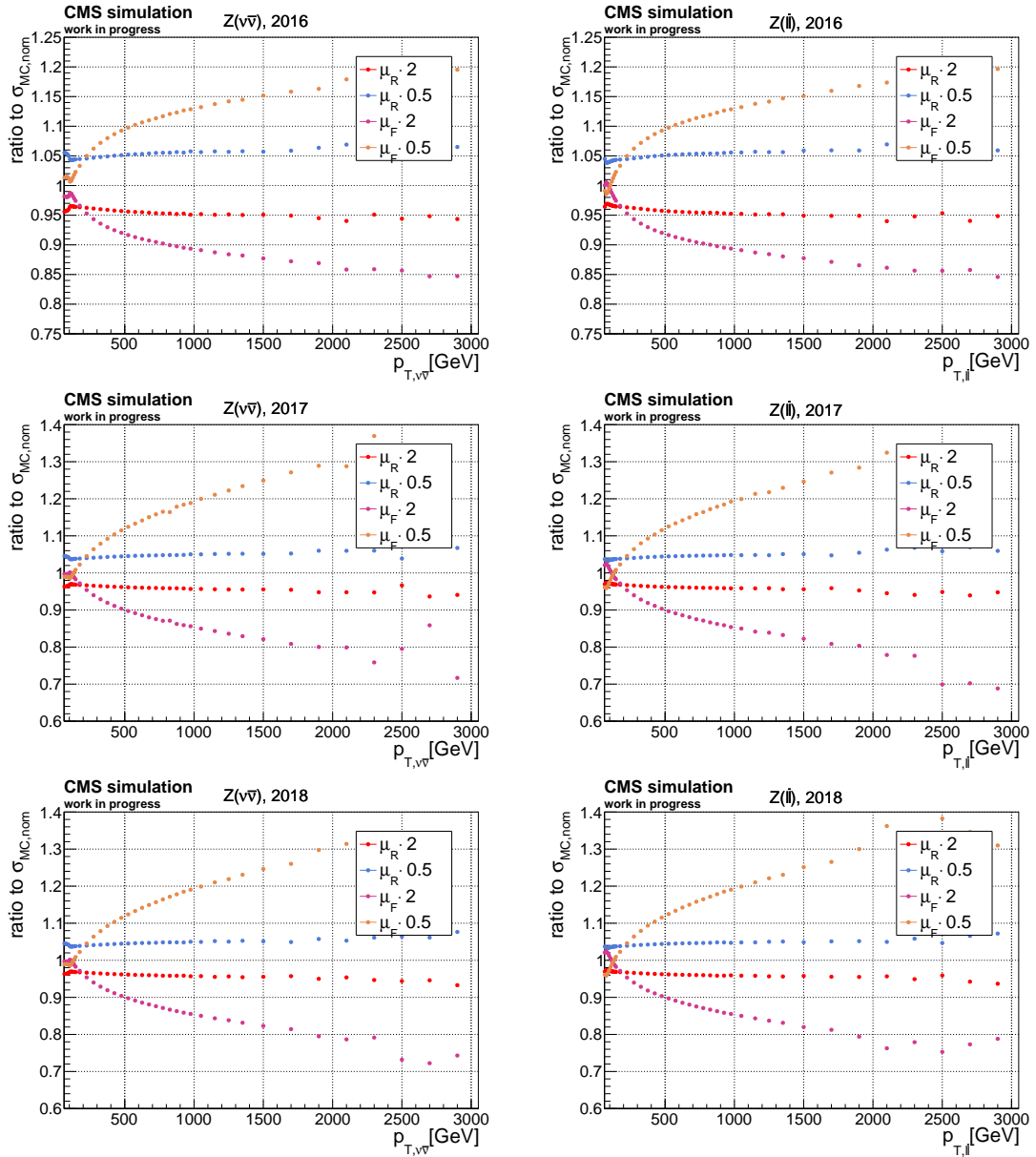
Figure A.10: Ratios comparing systematically varied differential cross sections from MC simulation with the nominal differential cross sections from MC simulation for the Z + jets process as a function of the transverse momentum of the Z boson. The renormalization scale μ_R and the factorization scale μ_F are varied with a factor of 2 or 1/2 in an uncorrelated fashion. The scale which is not explicitly given in a specific legend entry is always set to its nominal value.
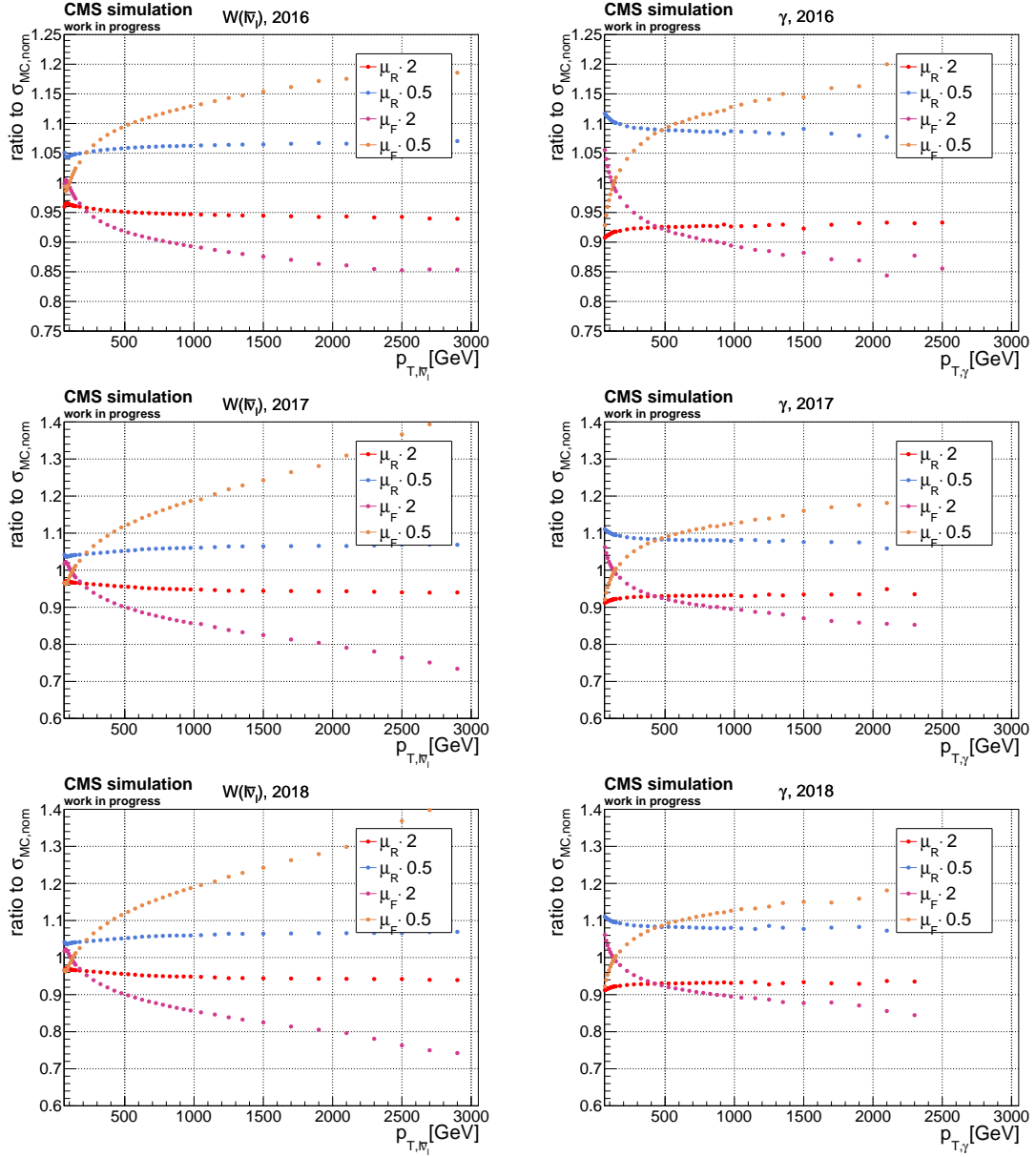
Figure A.11: Ratios comparing systematically varied differential cross sections from MC simulation with the nominal differential cross sections from MC simulation for the W + jets and γ + jets processes as a function of the transverse momentum of the vector boson. The renormalization scale μ_R and the factorization scale μ_F are varied with a factor of 2 or 1/2 in an uncorrelated fashion. The scale which is not explicitly given in a specific legend entry is always set to its nominal value.

Scale factor application and impact
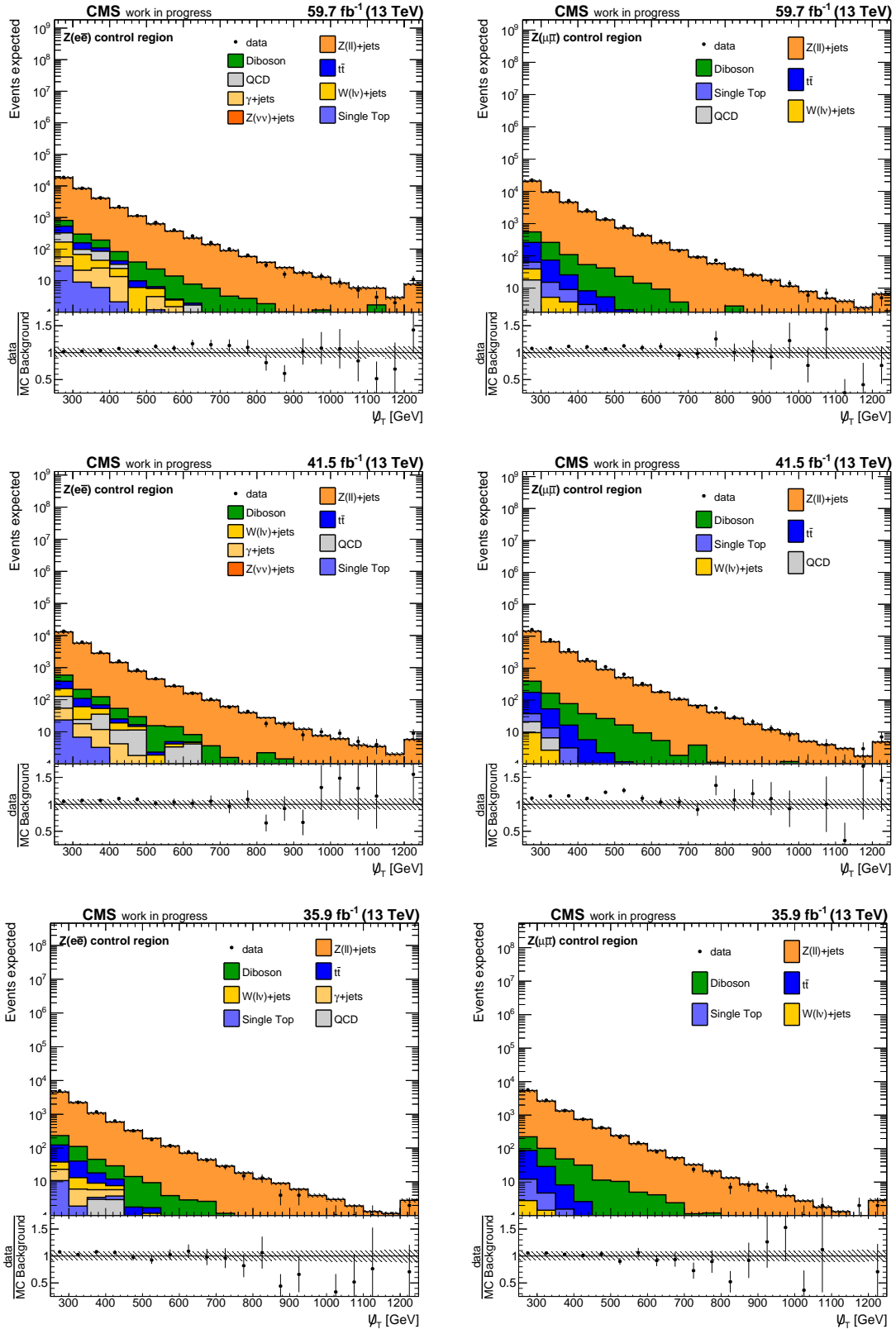
Figure A.12: Hadronic recoil distributions in the Z + jets control region split according to the data era after applying the theory-based V + jets reweighting procedure. The uncertainty band corresponds to the square root of the quadratic sum of indepedent variations of the matrix element renormalization scale and factorization scale by a factor of 2 and 1/2 and the theoretical V + jets uncertainties described in section 5.5.1.
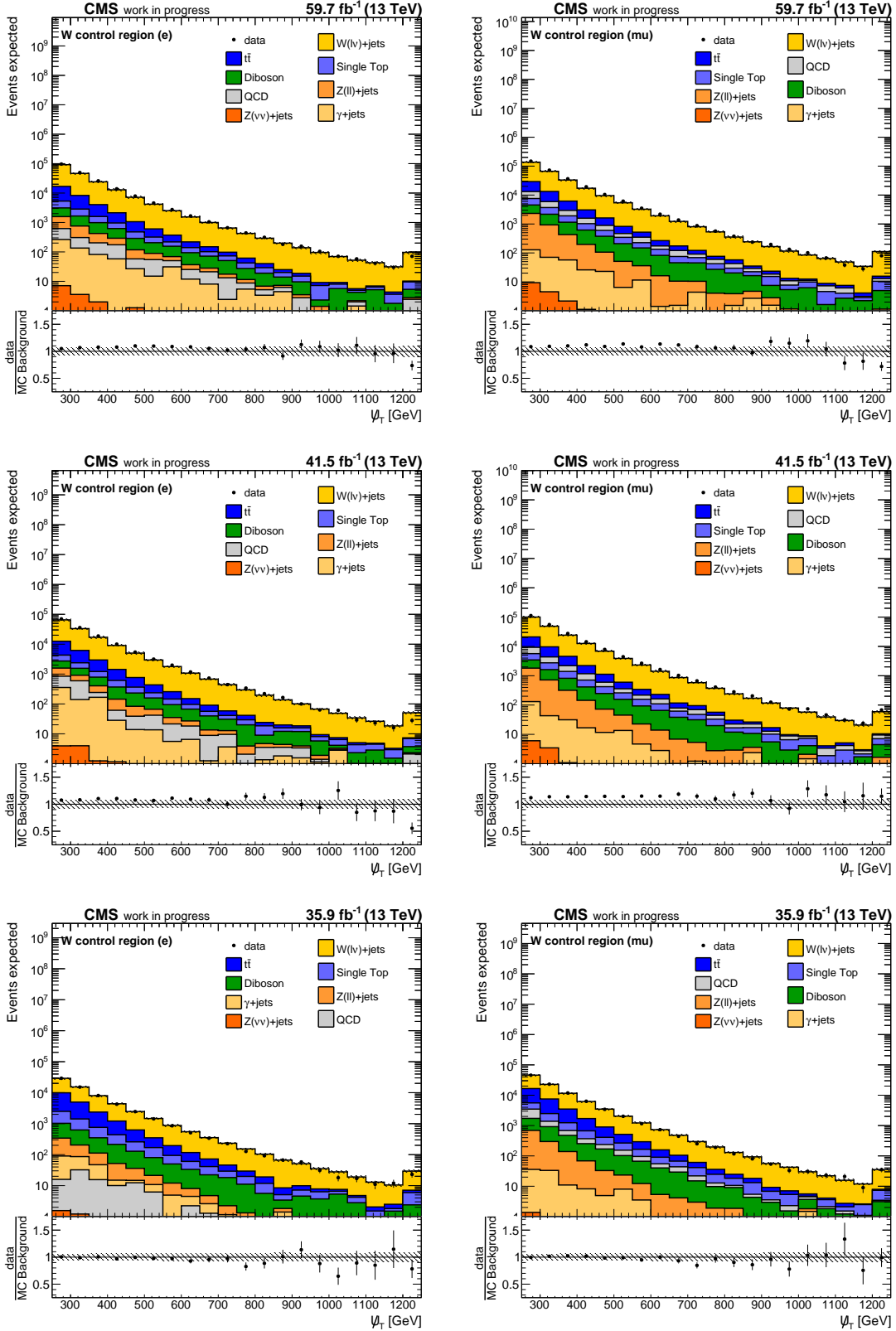
Figure A.13: Hadronic recoil distributions in the W + jets control region split according to the data era after applying the theory-based V + jets reweighting procedure. The uncertainty band corresponds to the square root of the quadratic sum of indepedent variations of the matrix element renormalization scale and factorization scale by a factor of 2 and 1/2 and the theoretical V + jets uncertainties described in section 5.5.1.
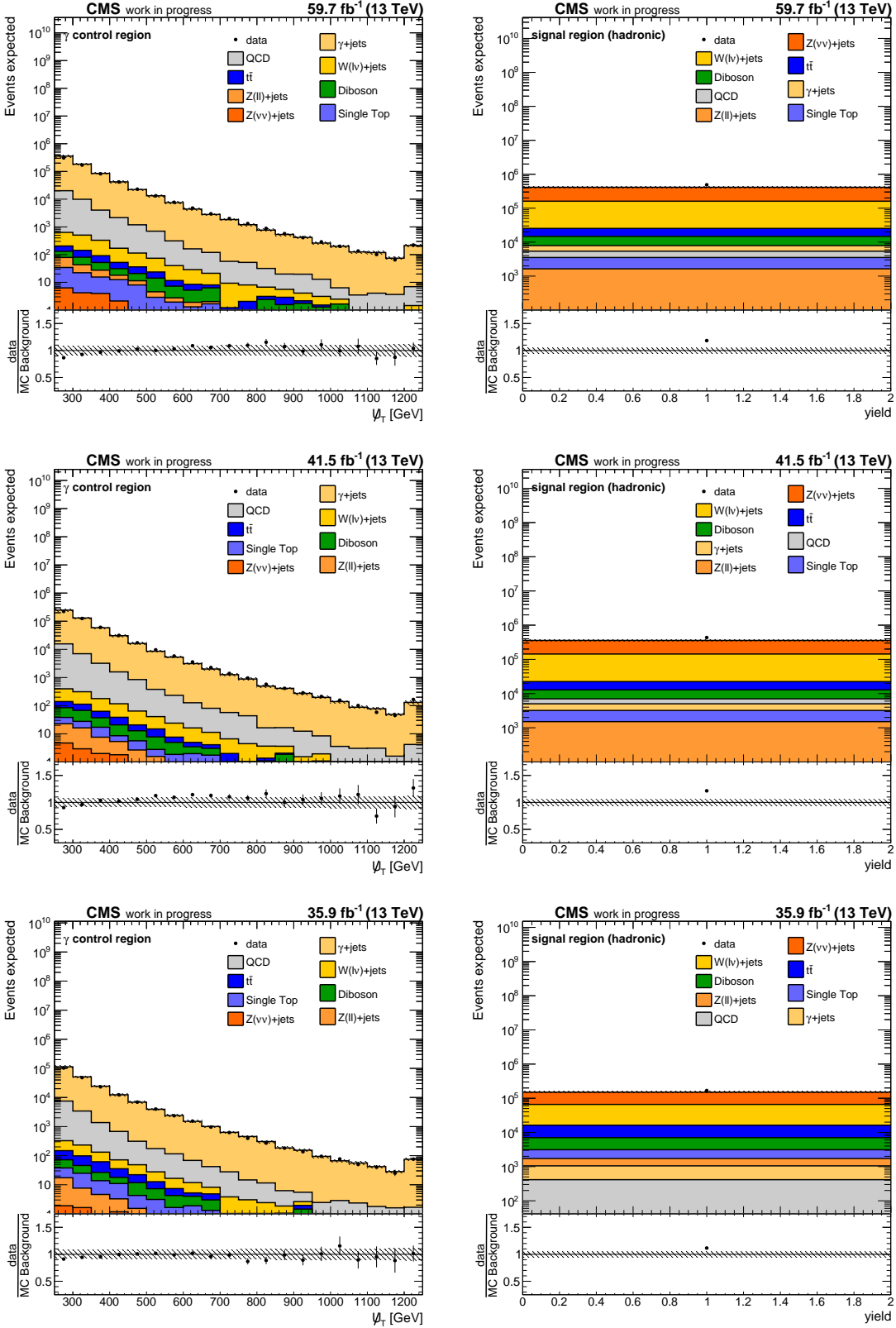
Figure A.14: Hadronic recoil distributions in the $\gamma + $ jets control region and total yields in the signal region without top-tagging techniques applied split according to the data era after applying the theory-based V + jets reweighting procedure. The uncertainty band corresponds to the square root of the quadratic sum of indepedent variations of the matrix element renormalization scale and factorization scale by a factor of 2 and 1/2 and the theoretical V + jets uncertainties described in section 5.5.1.

Higher-order corrections from MC simulation
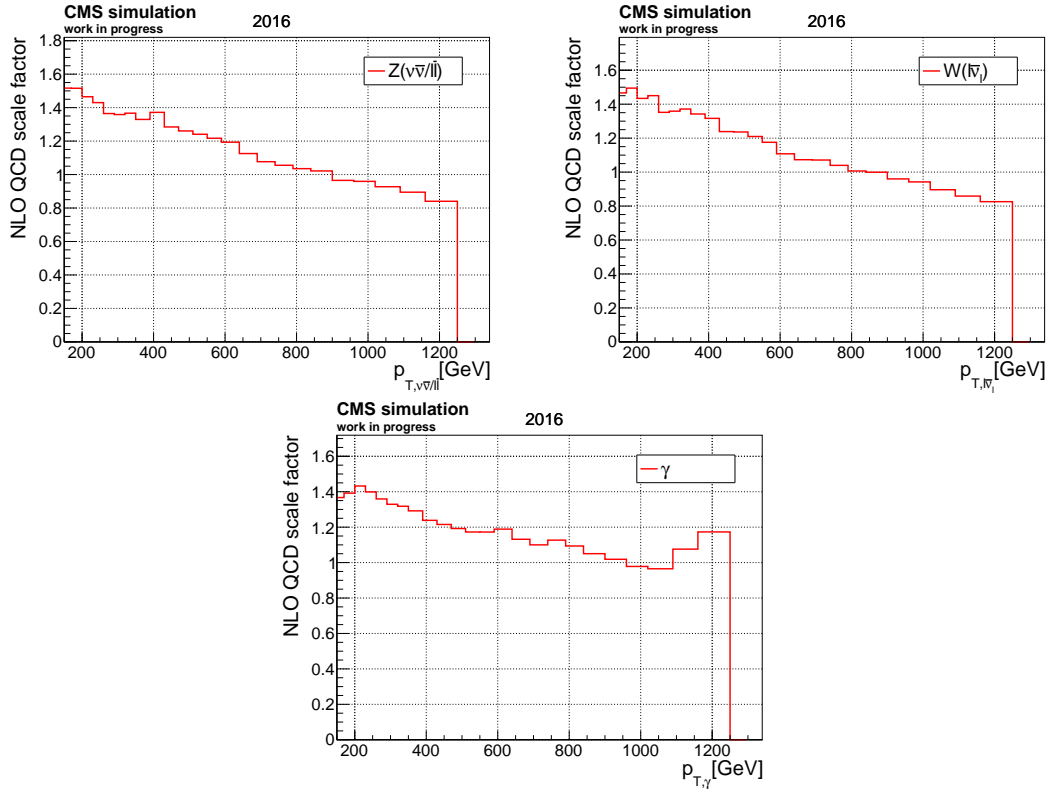
Figure A.15: Simulation-based differential NLO QCD reweighting factors as a function of the transverse momentum of the vector boson for different V + jets processes in the 2016 MC production era.
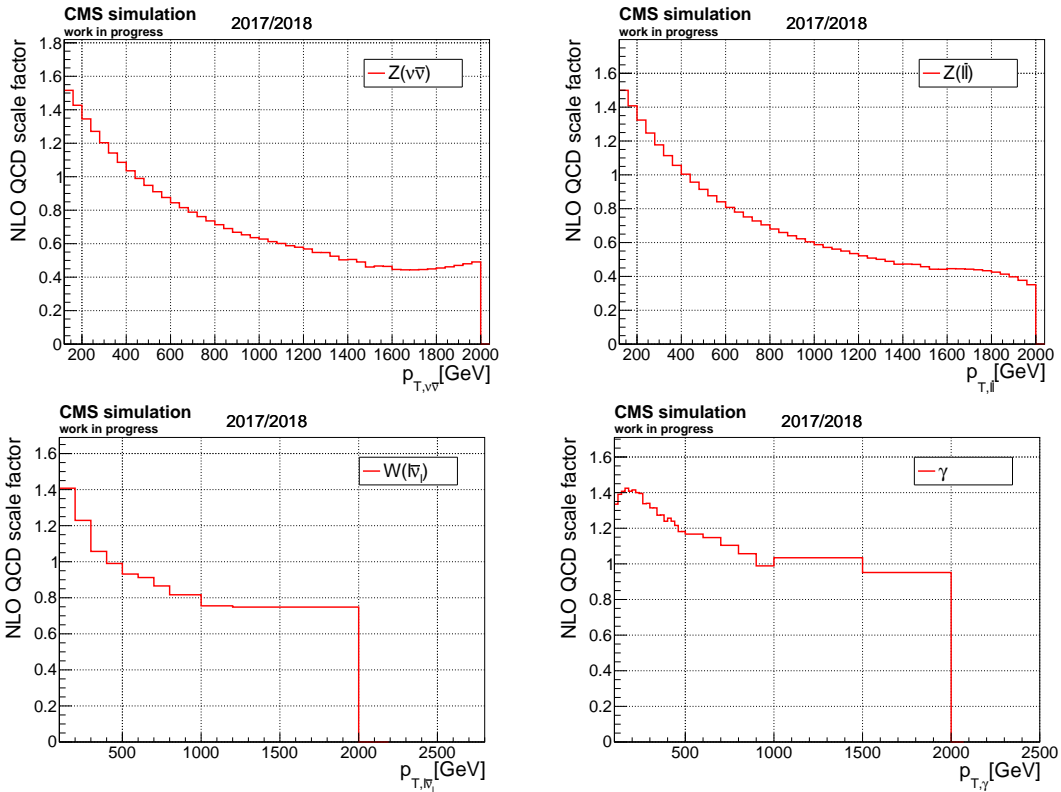
Figure A.16: Simulation-based differential NLO QCD reweighting factors as a function of the transverse momentum of the vector boson for different V + jets in the 2017 and 2018 MC production era.

Figure A.17: Hadronic recoil distributions in the Z + jets control region split according to the data era after applying the V + jets reweighting procedure based on MC simulation NLO QCD corrections and theory-based NLO EWK corrections. The uncertainty band corresponds to the square root of the quadratic sum of indepedent variations of the matrix element renormalization scale and factorization scale by a factor of 2 and 1/2 and the theoretical V + jets uncertainties described in section 5.5.1.

Figure A.18: Hadronic recoil distributions in the W + jets control region split according to the data era after applying the V + jets reweighting procedure based on MC simulation NLO QCD corrections and theory-based NLO EWK corrections. The uncertainty band corresponds to the square root of the quadratic sum of indepedent variations of the matrix element renormalization scale and factorization scale by a factor of 2 and 1/2 and the theoretical V + jets uncertainties described in section 5.5.1.
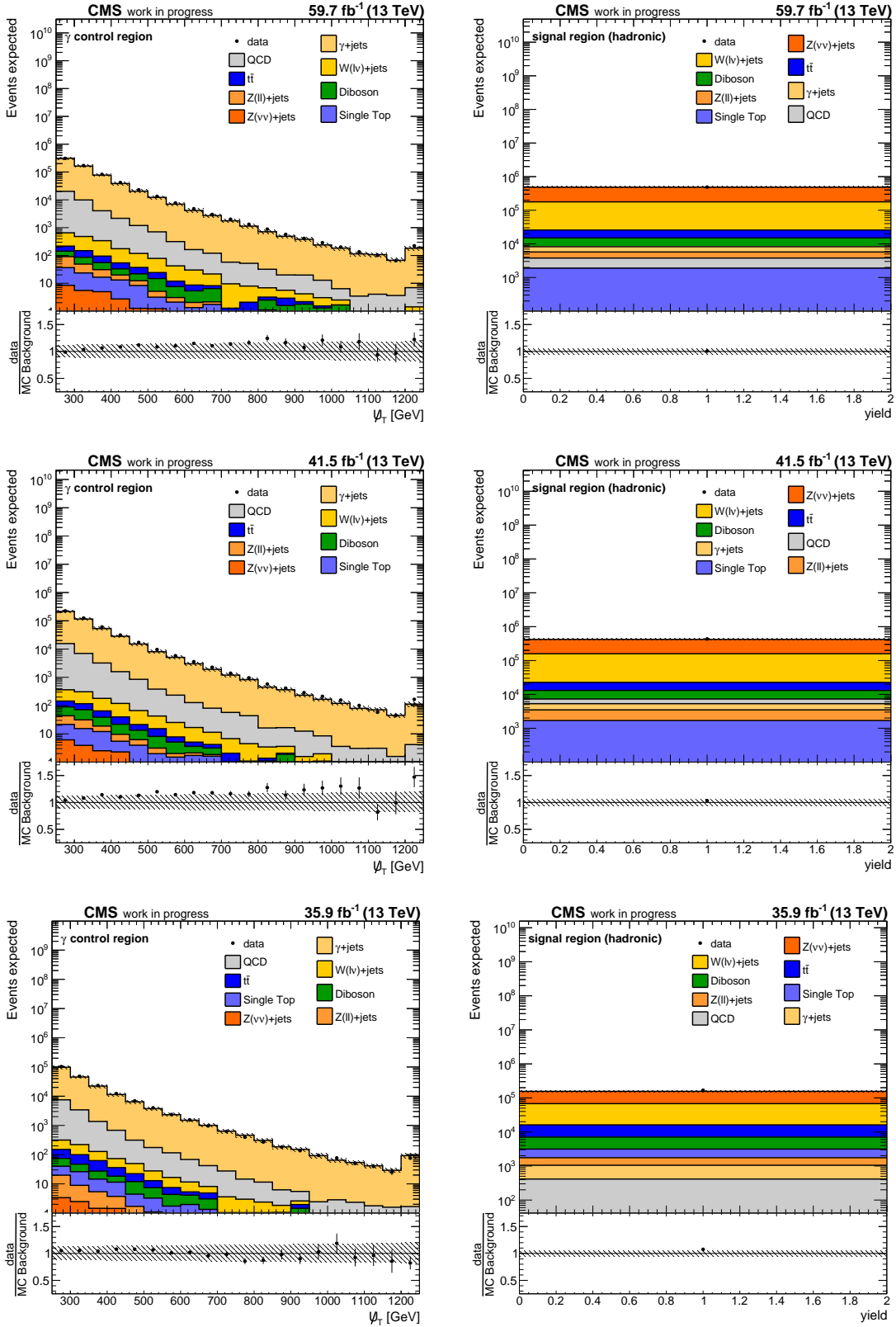
Figure A.19: Hadronic recoil distributions in the γ + jets control region and total yields in the signal region without top-tagging techniques applied split according to the data era after applying the V + jets reweighting procedure based on MC simulation NLO QCD corrections and theory-based NLO EWK corrections. The uncertainty band corresponds to the square root of the quadratic sum of indepedent variations of the matrix element renormalization scale and factorization scale by a factor of 2 and 1/2 and the theoretical V + jets uncertainties described in section 5.5.1.

Next-to-leading-order γ + jets MC simulation
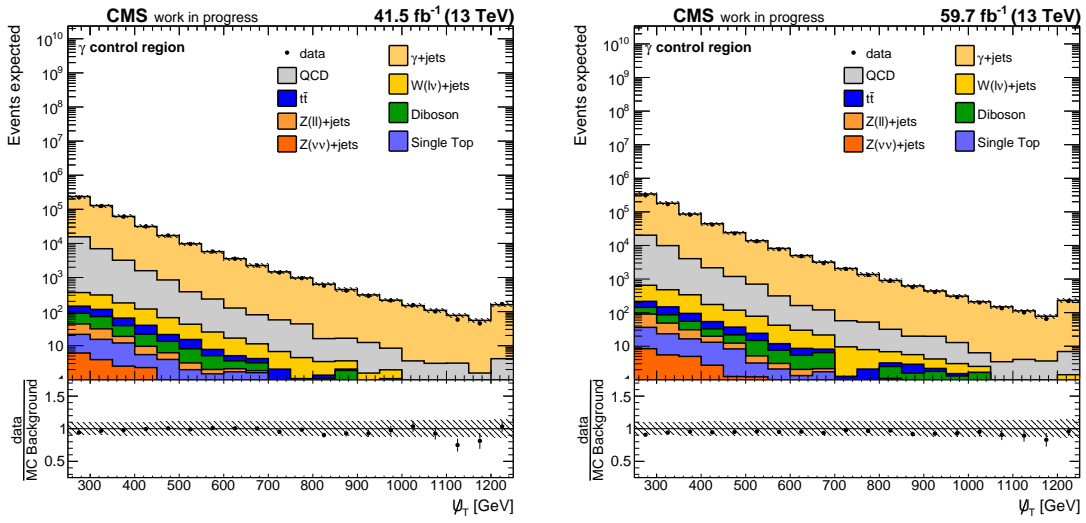
Figure A.20: Hadronic recoil distributions in the γ + jets control region in the 2017 and 2018 data era on the left-hand and right-hand side, respectively. The predictions rely on NLO QCD γ + jets MC simulation combined with NLO EWK corrections from theory. The uncertainty band corresponds to the square root of the quadratic sum of indepedent variations of the matrix element renormalization scale and factorization scale by a factor of 2 and 1/2 and the theoretical V + jets uncertainties described in section 5.5.1.

B Control distributions with preselection requirements
B.1 Z boson control regions
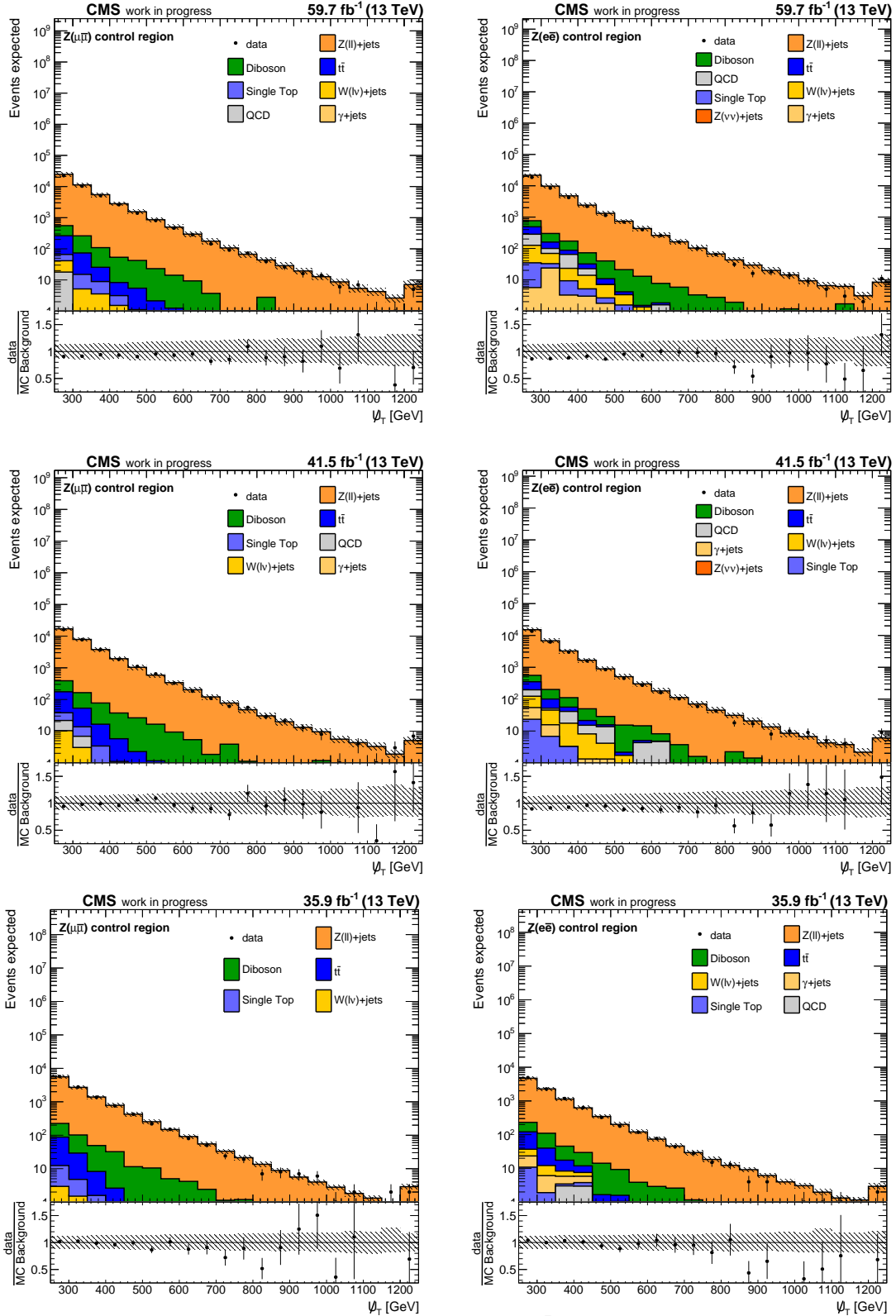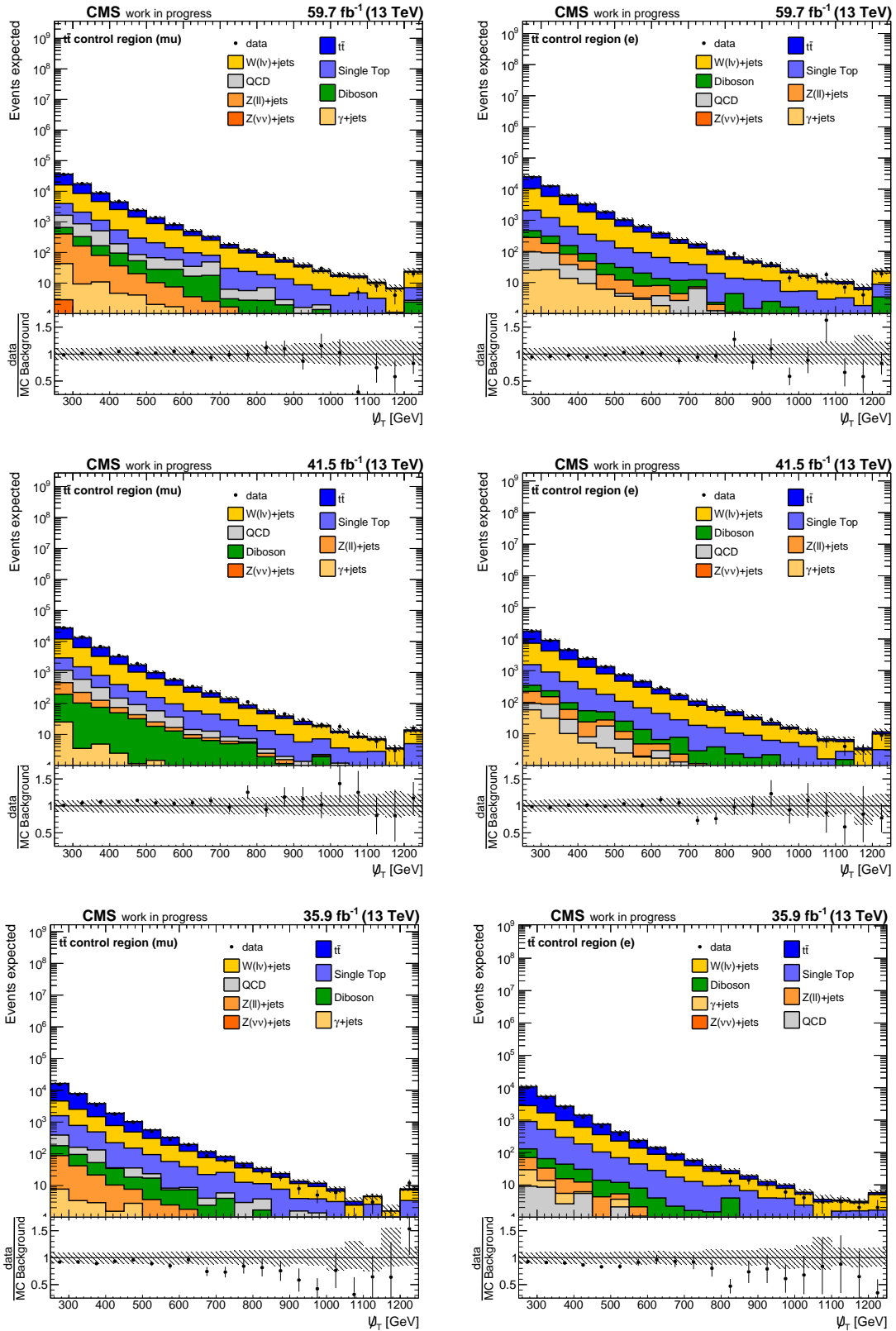

Figure B.21: Distribution of the hadronic recoil in the $Z \to l\bar{l}$ control regions comparing all data eras with preselection requirements applied. The upper pad shows the absolute prediction of the different processes stacked on top of each other and the observation from data. The lower pad shows the ratio of the observation and the prediction. The uncertainty band corresponds to the square root of the quadratic sum of all considered uncertainties, see section 5.8.1.
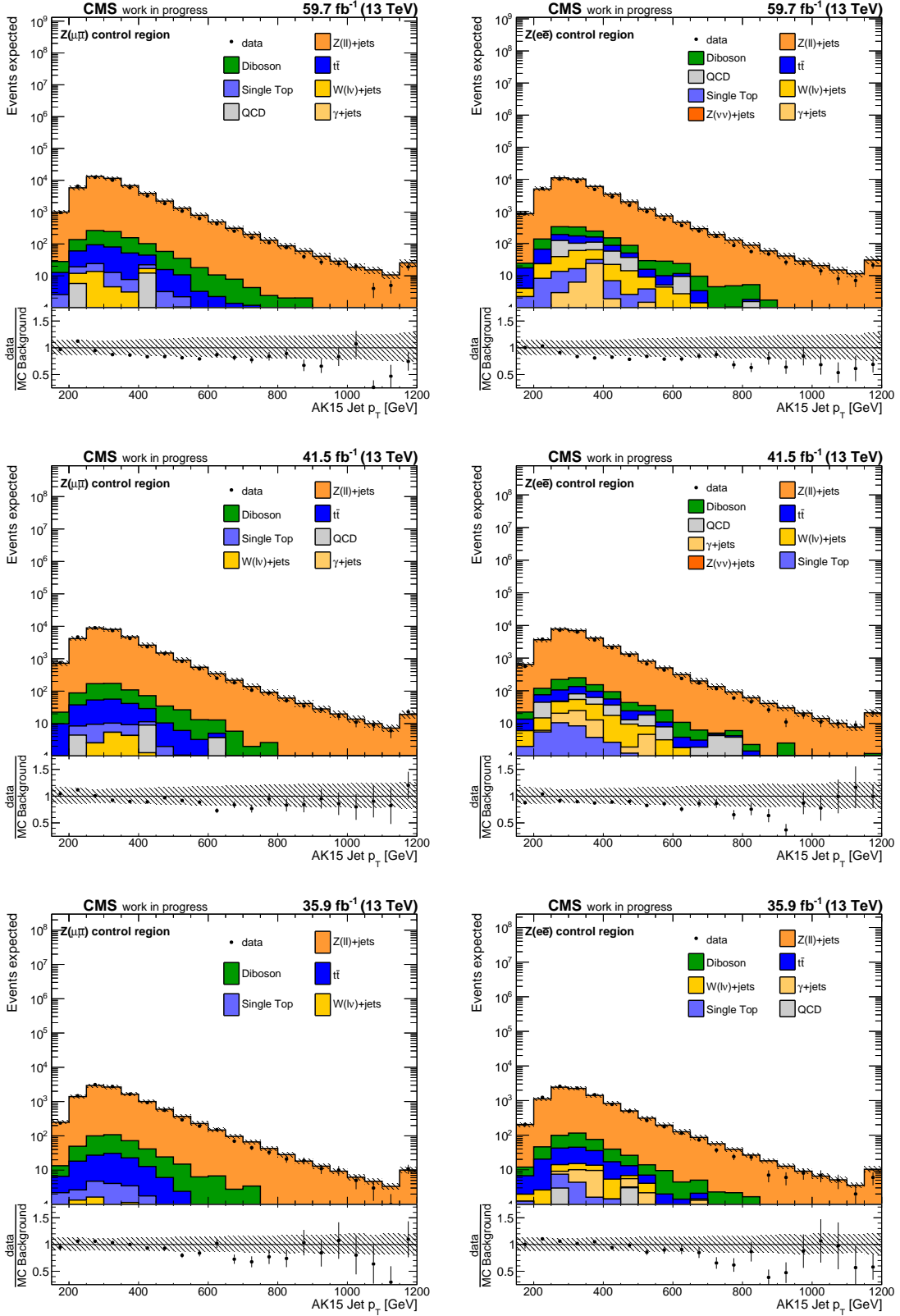
Figure B.22: Distribution of the AK15 jet p_T in the Z → ll̄ control regions comparing all data eras with preselection requirements applied. The upper pad shows the absolute prediction of the different processes stacked on top of each other and the observation from data. The lower pad shows the ratio of the observation and the prediction. The uncertainty band corresponds to the square root of the quadratic sum of all considered uncertainties, see section 5.8.1.
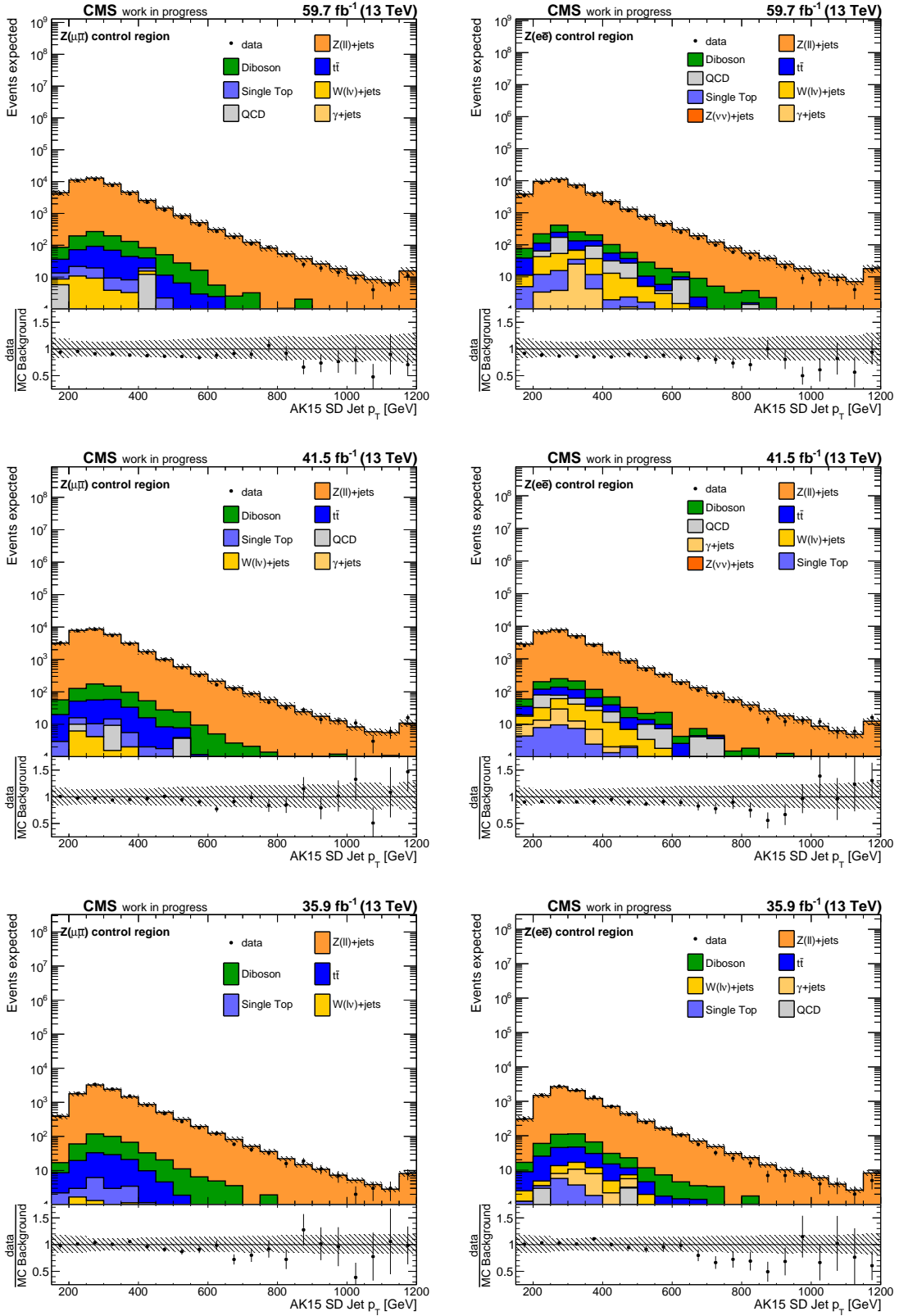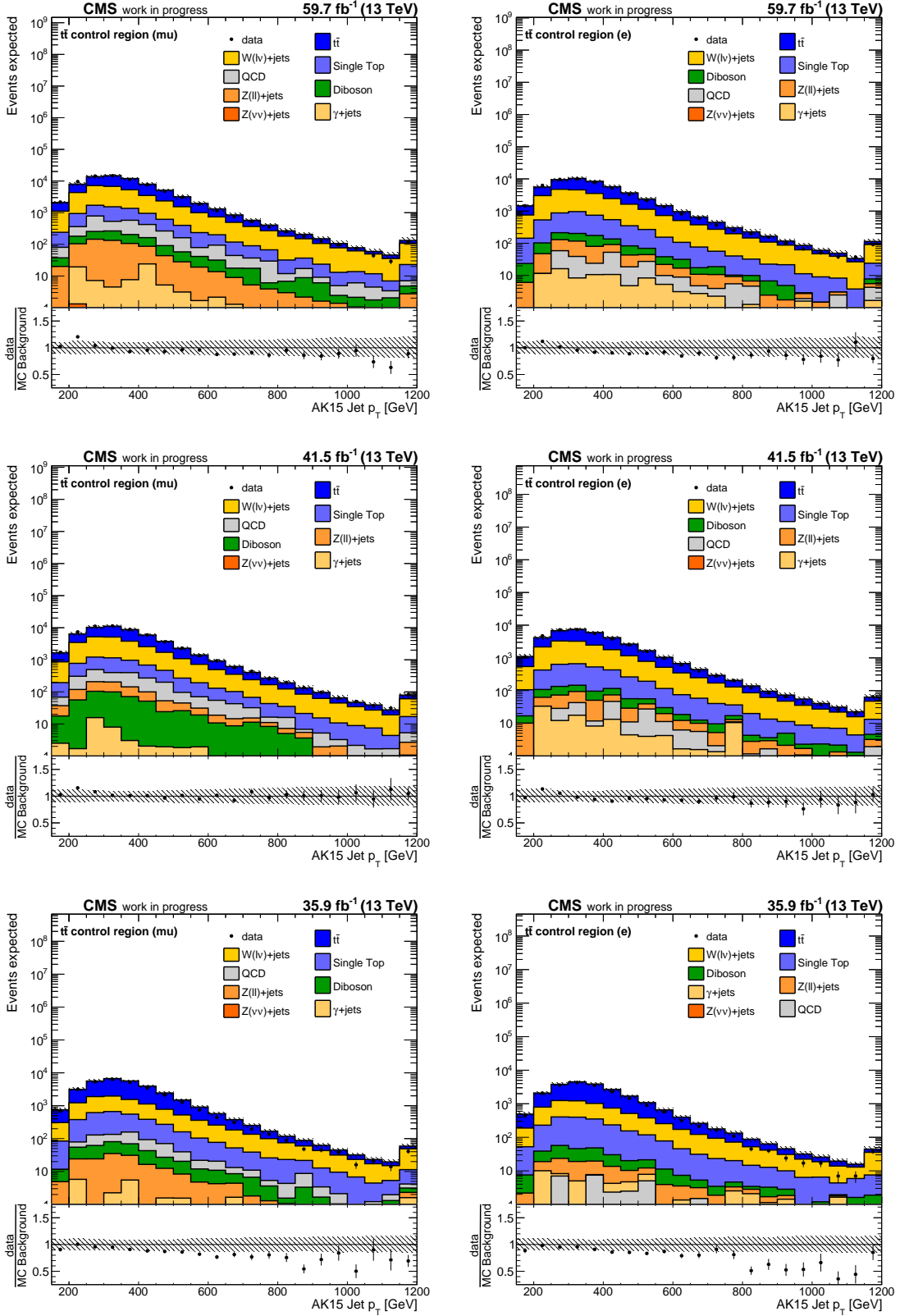
Figure B.23: Distribution of the AK15 jet p_T after applying the SD algorithm in the $Z \rightarrow l\bar{l}$ control regions comparing all data eras with preselection requirements applied. The upper pad shows the absolute prediction of the different processes stacked on top of each other and the observation from data. The lower pad shows the ratio of the observation and the prediction. The uncertainty band corresponds to the square root of the quadratic sum of all considered uncertainties, see section 5.8.1.
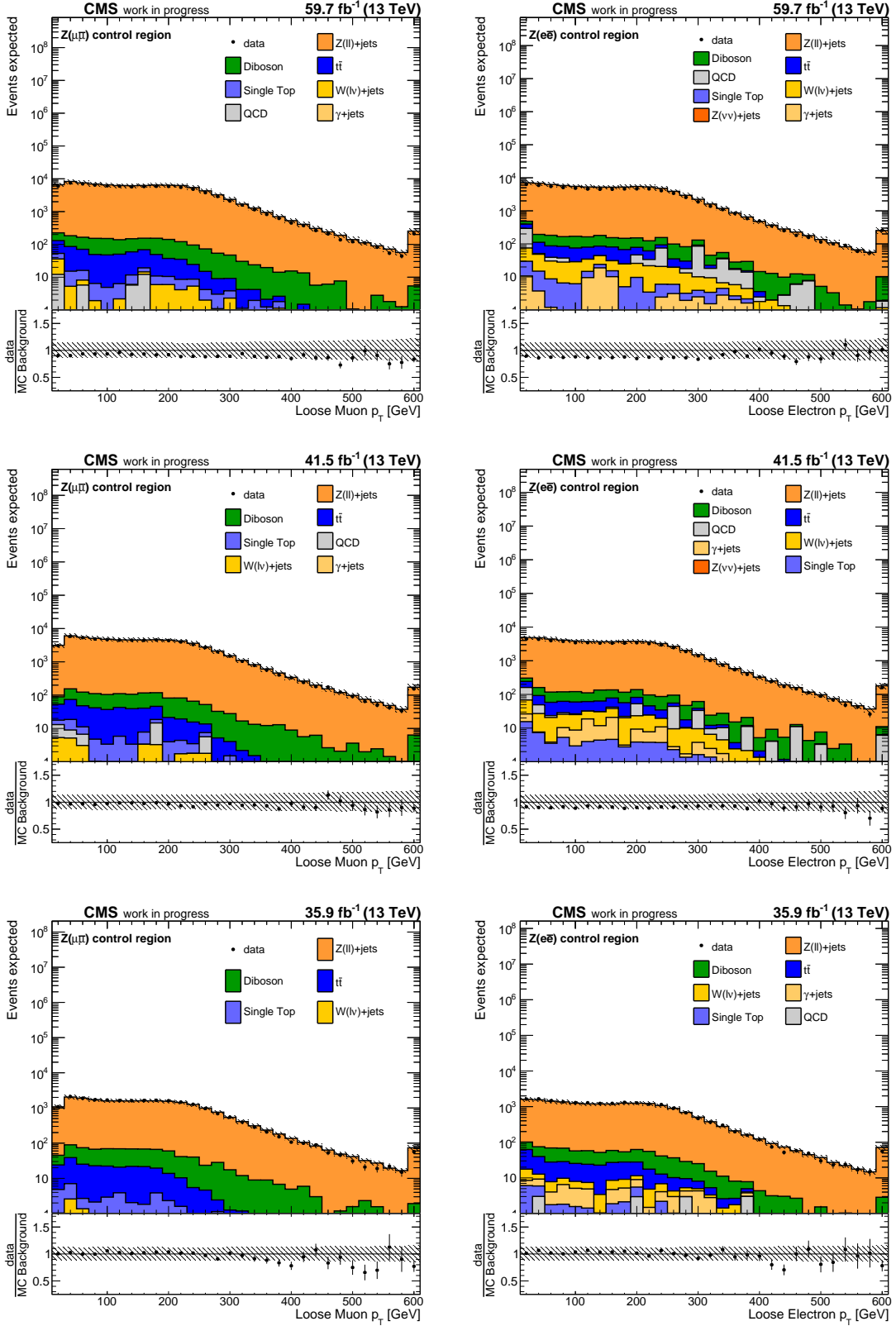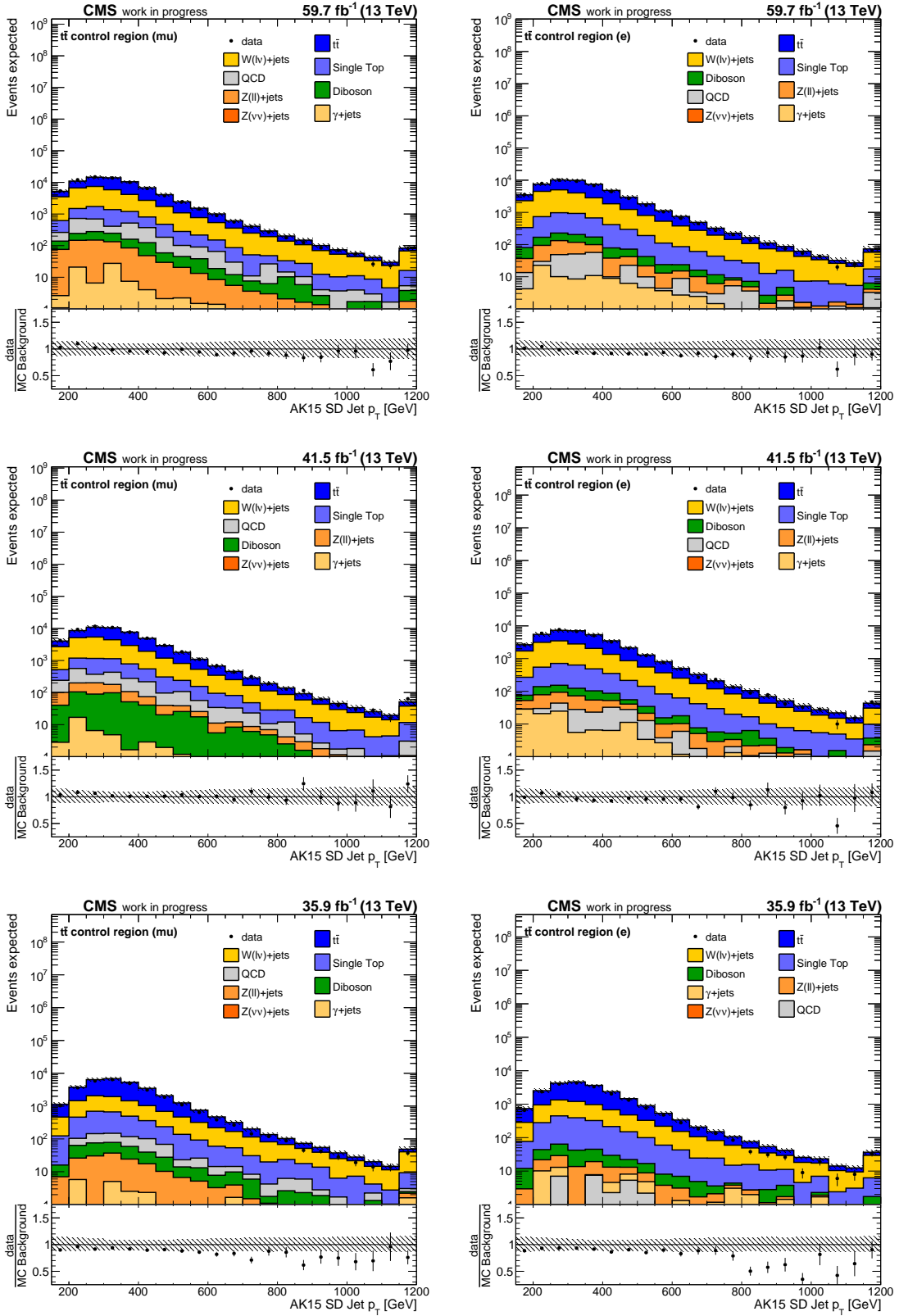
Figure B.24: Distribution of the lepton p_T in the $Z \to l\bar{l}$ control regions comparing all data eras with preselection requirements applied. The upper pad shows the absolute prediction of the different processes stacked on top of each other and the observation from data. The lower pad shows the ratio of the observation and the prediction. The uncertainty band corresponds to the square root of the quadratic sum of all considered uncertainties, see section 5.8.1.
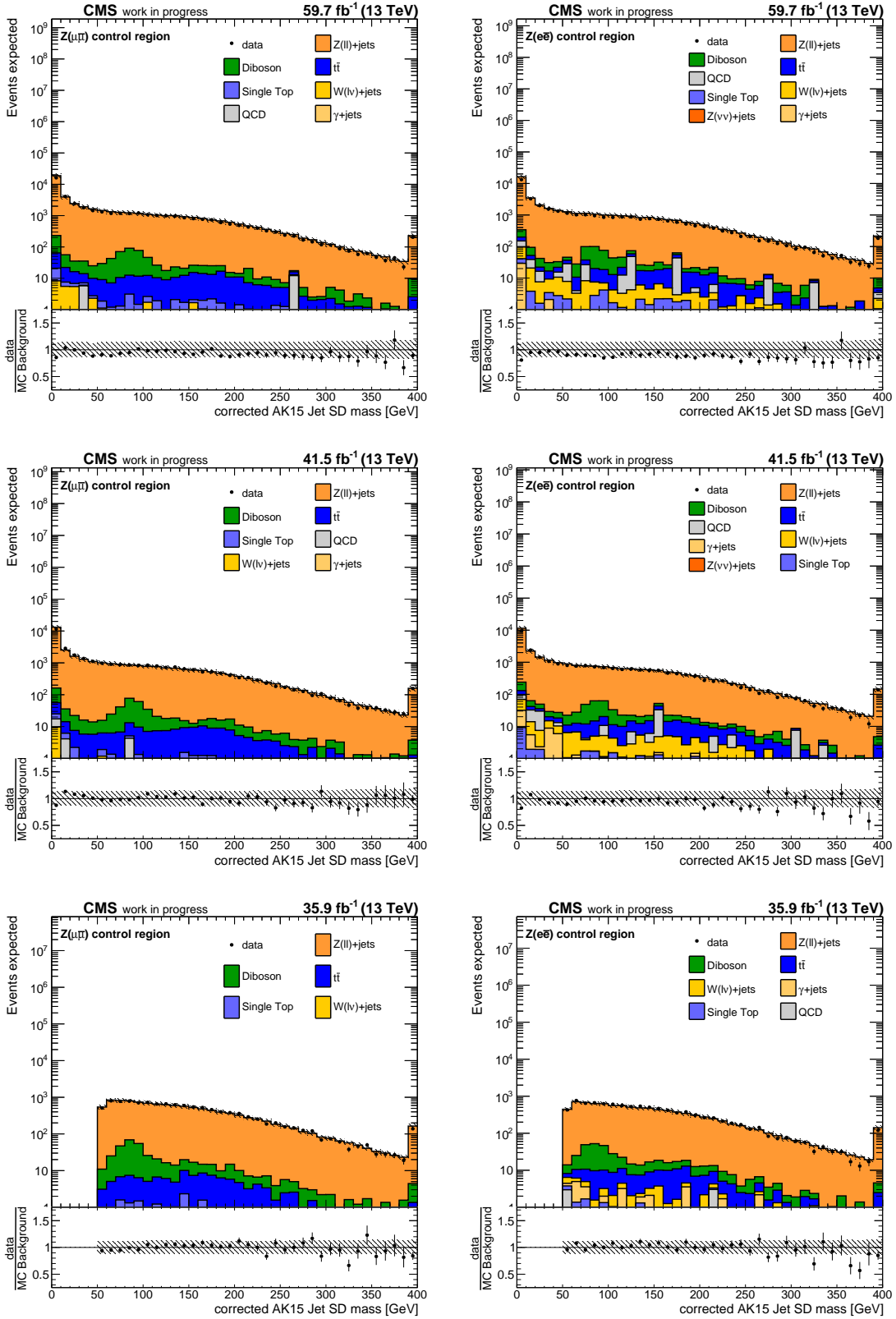
Figure B.25: Distribution of the mass of the AK15 jet after the SD algorithm is applied in the Z → l̄l control regions comparing all data eras with preselection requirements applied. The upper pad shows the absolute prediction of the different processes stacked on top of each other and the observation from data. The lower pad shows the ratio of the observation and the prediction. The uncertainty band corresponds to the square root of the quadratic sum of all considered uncertainties, see section 5.8.1.
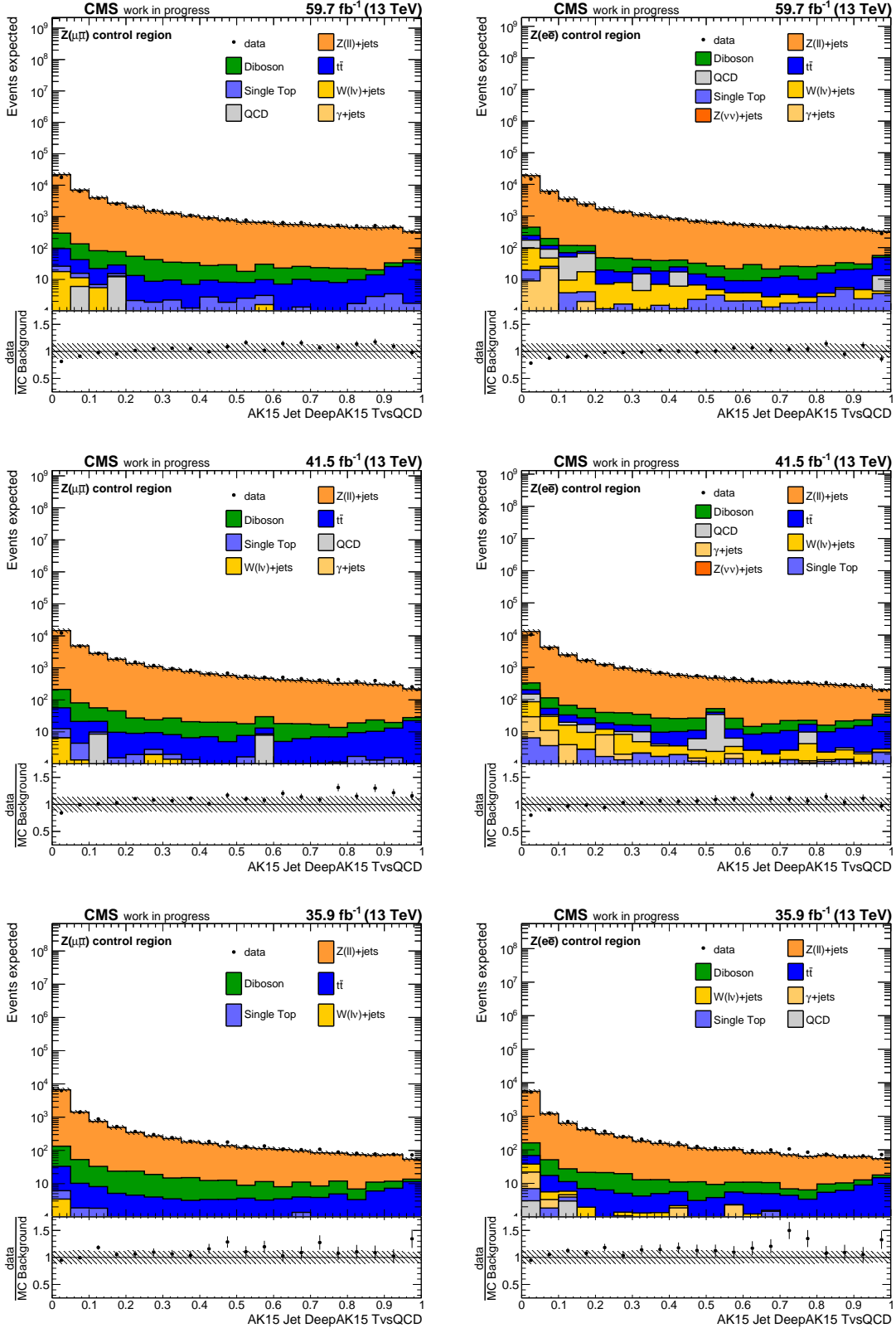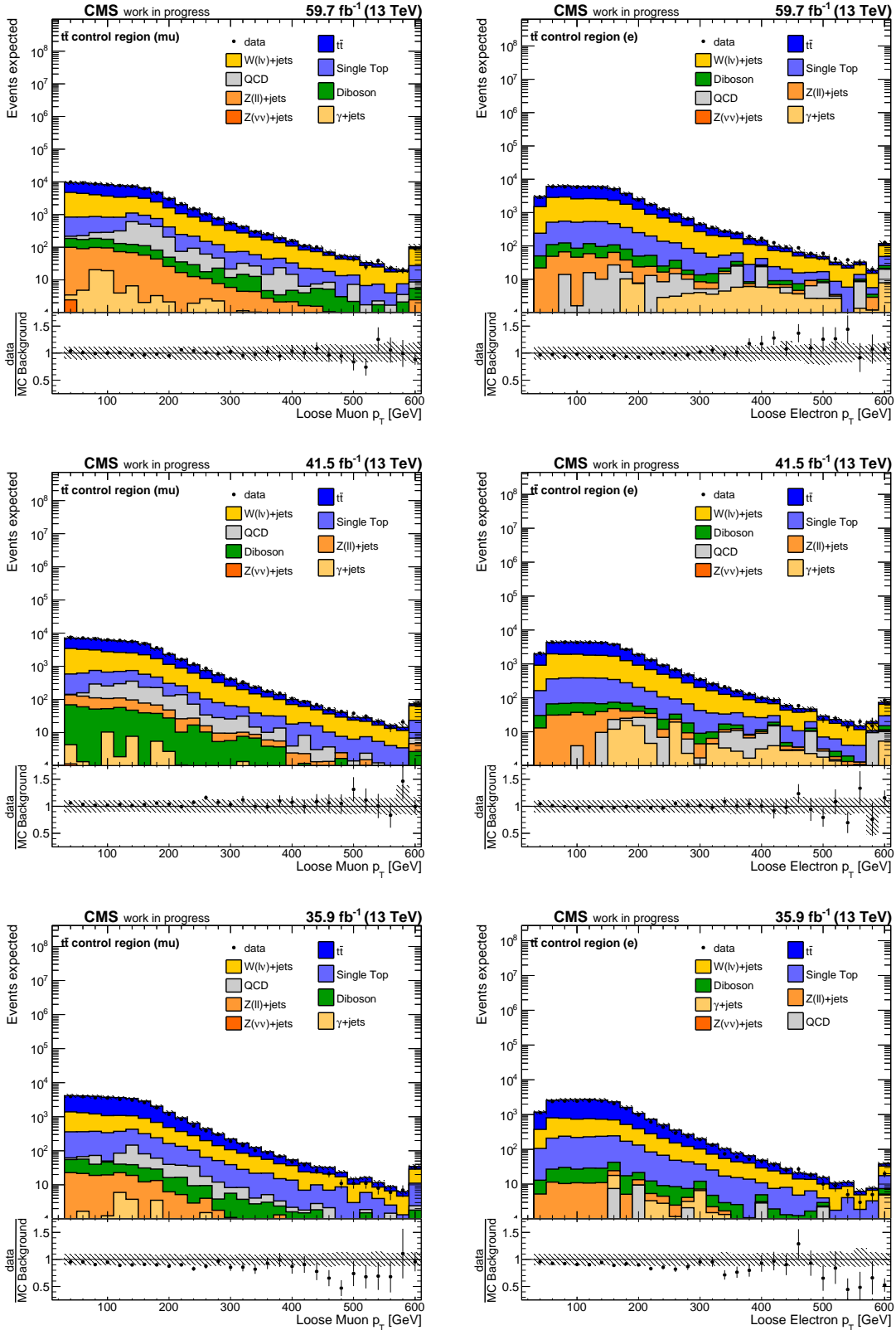
Figure B.26: Distribution of the DeepAK15 top-tagging discriminant in the Z → ll̄ control regions comparing all data eras with preselection requirements applied. The upper pad shows the absolute prediction of the different processes stacked on top of each other and the observation from data. The lower pad shows the ratio of the observation and the prediction. The uncertainty band corresponds to the square root of the quadratic sum of all considered uncertainties, see section 5.8.1.
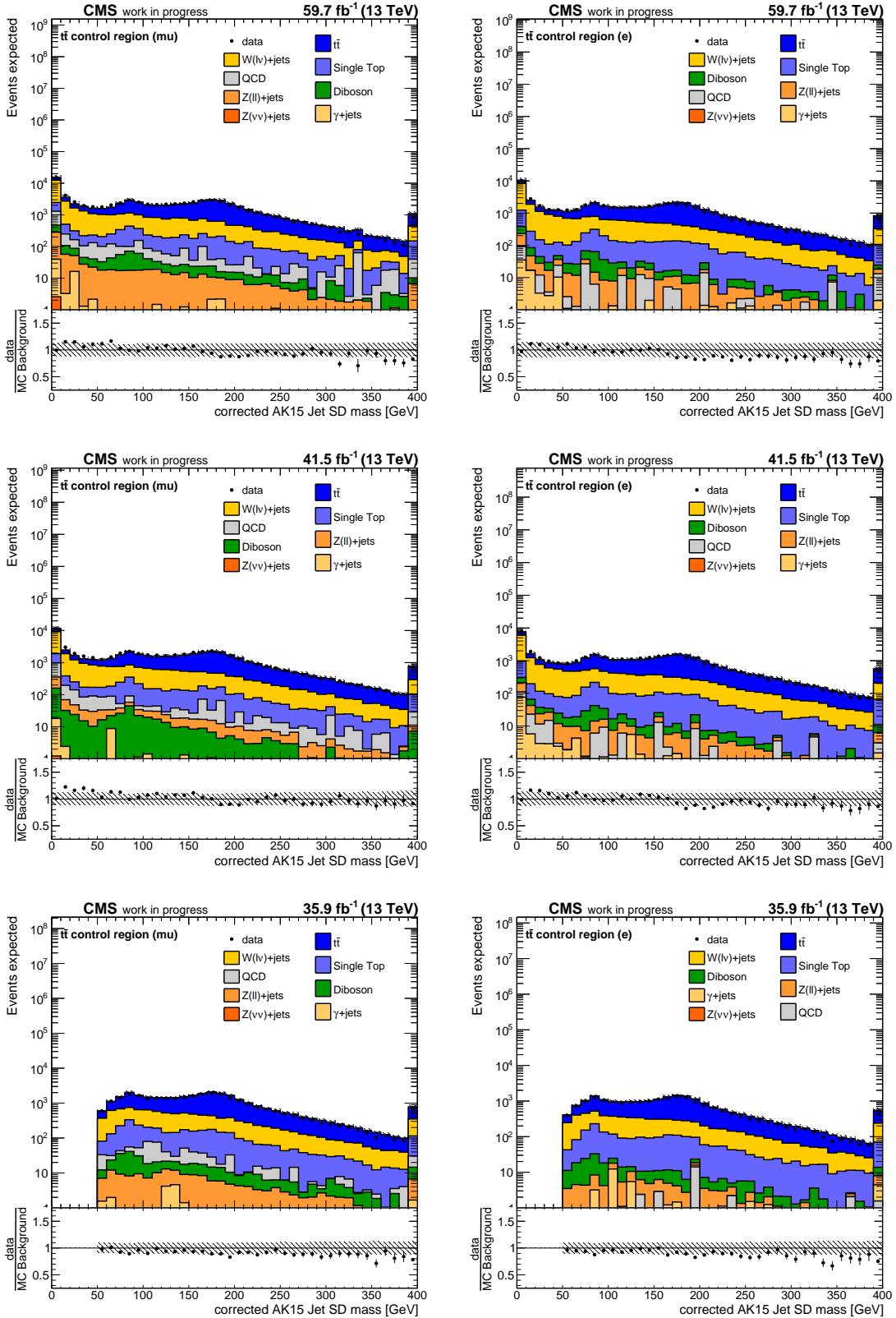
B.2 W boson control regions
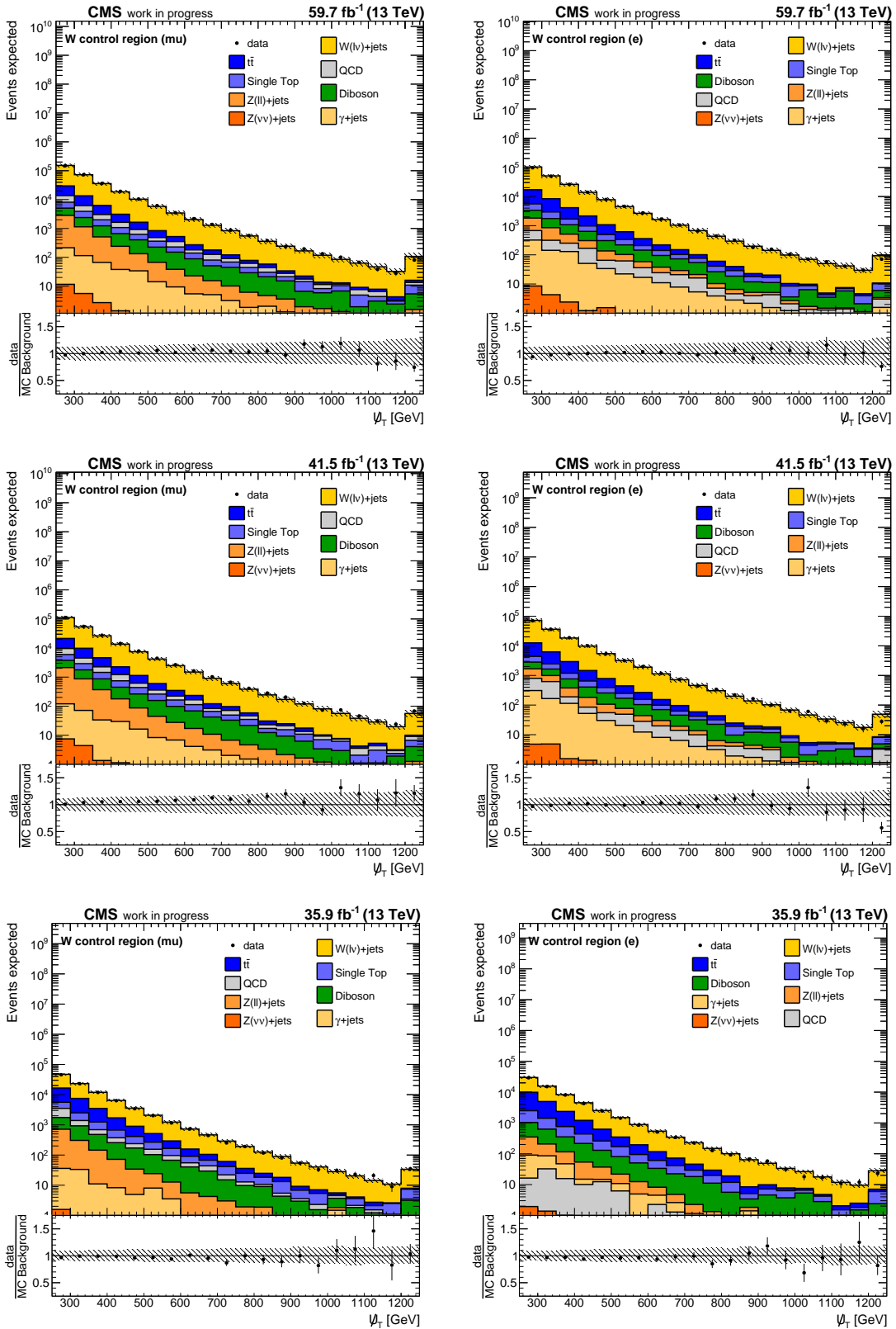
Figure B.27: Distribution of the hadronic recoil in the W → lν̄ control regions comparing all data eras with preselection requirements applied. The upper pad shows the absolute prediction of the different processes stacked on top of each other and the observation from data. The lower pad shows the ratio of the observation and the prediction. The uncertainty band corresponds to the square root of the quadratic sum of all considered uncertainties, see section 5.8.1.
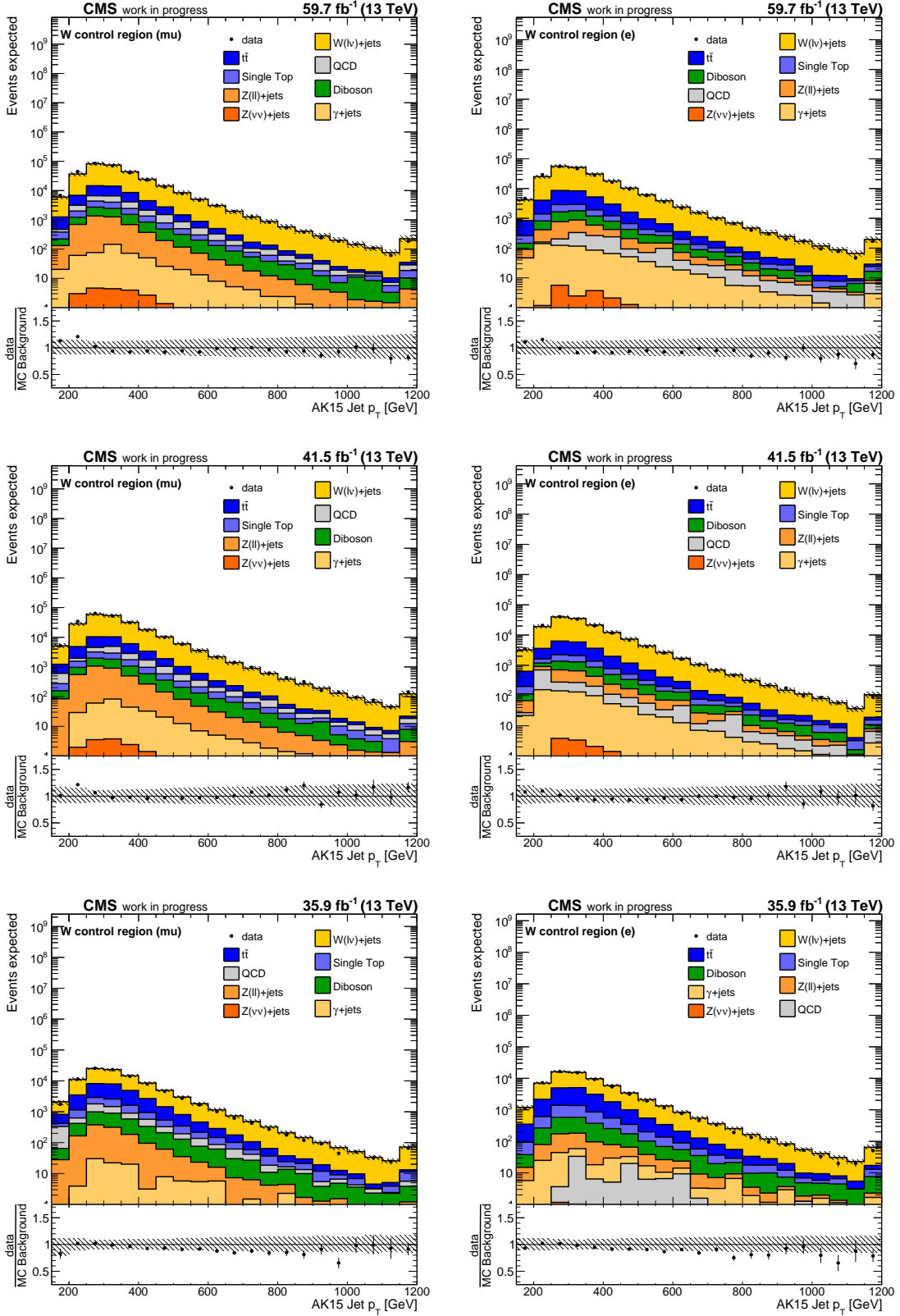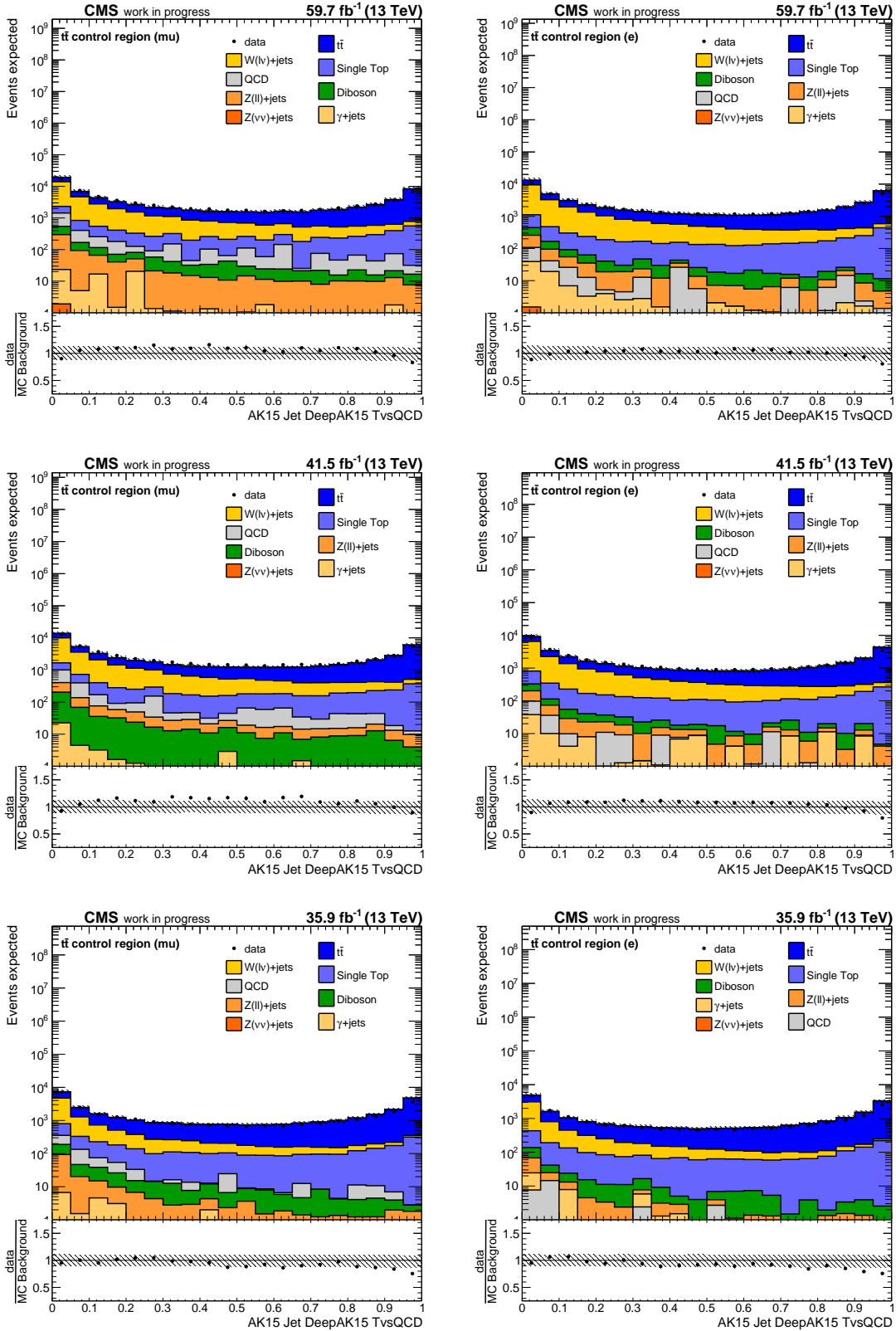
Figure B.28: Distribution of the AK15 jet p_T in the W $\to$ l$\overline{\nu}$ control regions comparing all data eras with preselection requirements applied. The upper pad shows the absolute prediction of the different processes stacked on top of each other and the observation from data. The lower pad shows the ratio of the observation and the prediction. The uncertainty band corresponds to the square root of the quadratic sum of all considered uncertainties, see section 5.8.1.
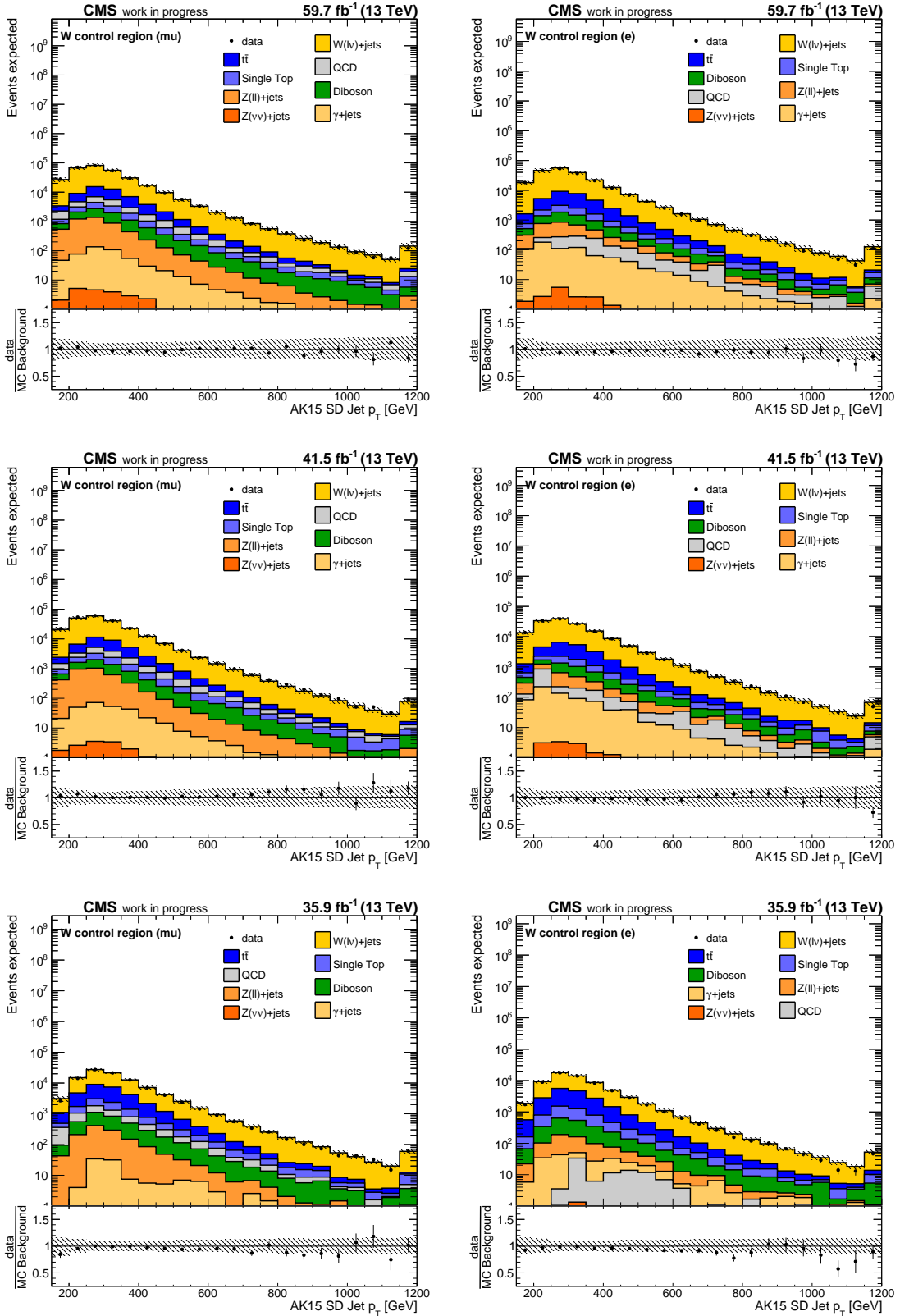
Figure B.29: Distribution of the AK15 jet p_T after applying the SD algorithm in the W $\to$ l$\overline{\nu}$ control regions comparing all data eras with preselection requirements applied. The upper pad shows the absolute prediction of the different processes stacked on top of each other and the observation from data. The lower pad shows the ratio of the observation and the prediction. The uncertainty band corresponds to the square root of the quadratic sum of all considered uncertainties, see section 5.8.1.
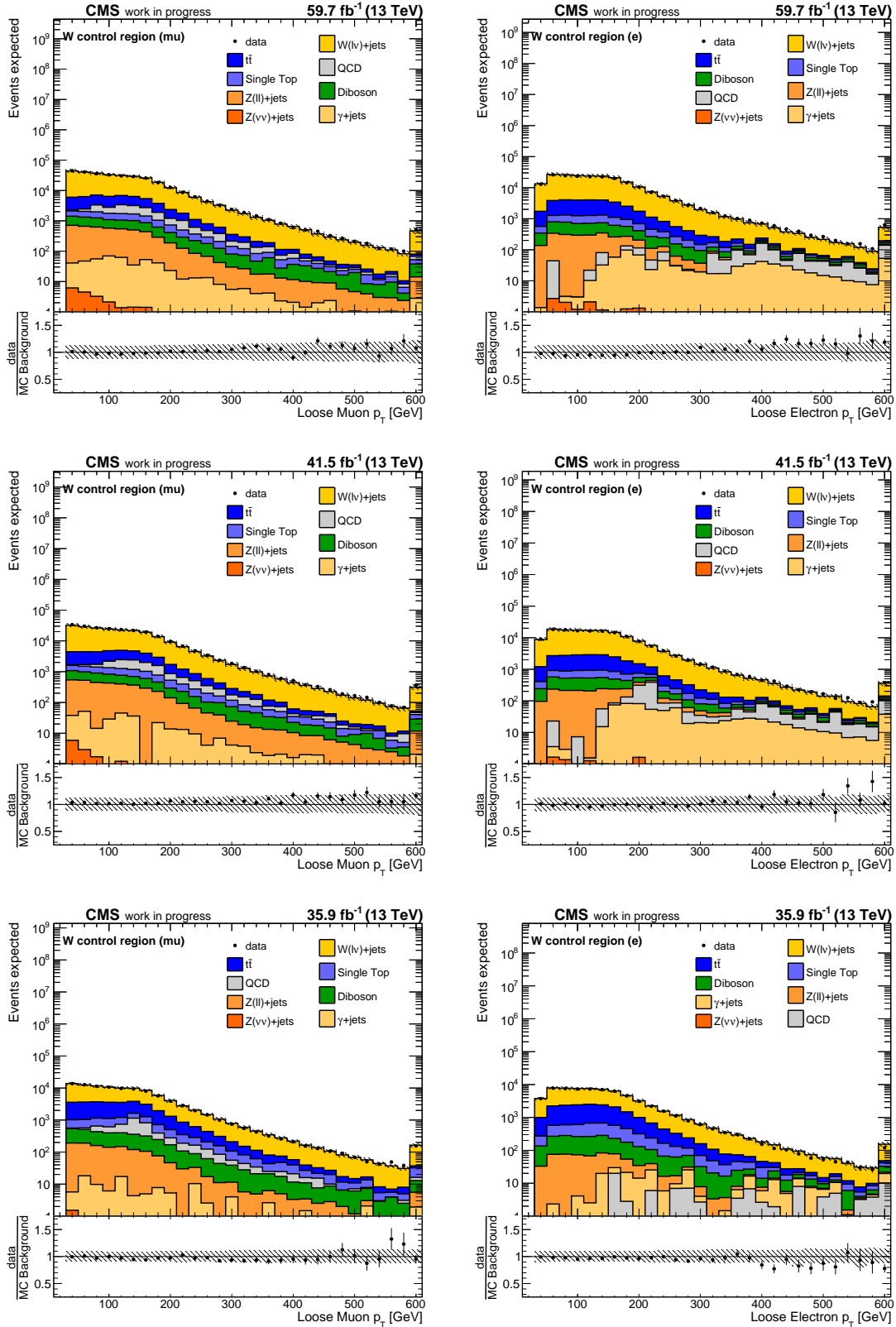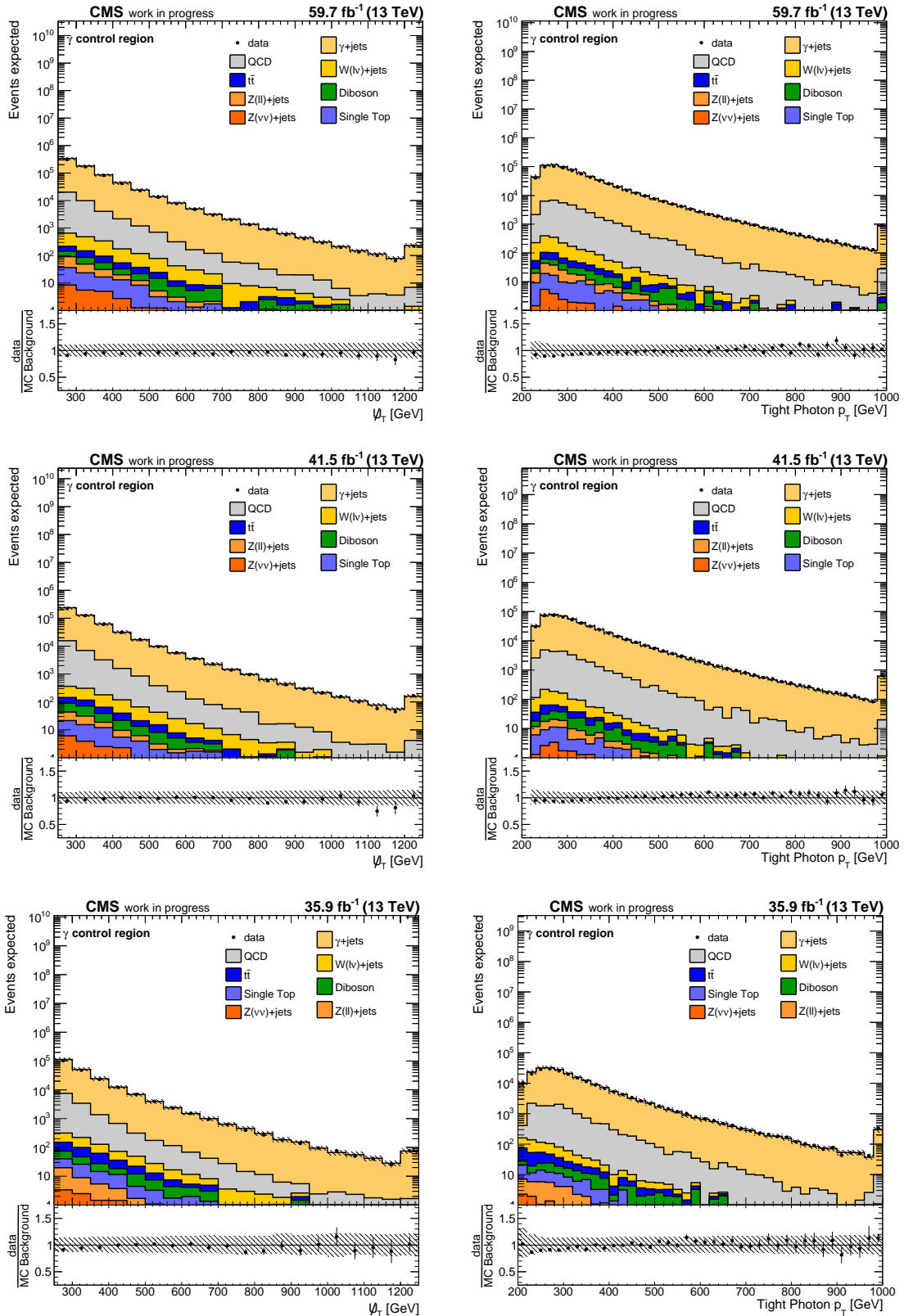
Figure B.30: Distribution of the lepton p_{T} in the $\mathrm{W} \to l\overline{\nu}$ control regions comparing all data eras with preselection requirements applied. The upper pad shows the absolute prediction of the different processes stacked on top of each other and the observation from data. The lower pad shows the ratio of the observation and the prediction. The uncertainty band corresponds to the square root of the quadratic sum of all considered uncertainties, see section 5.8.1.
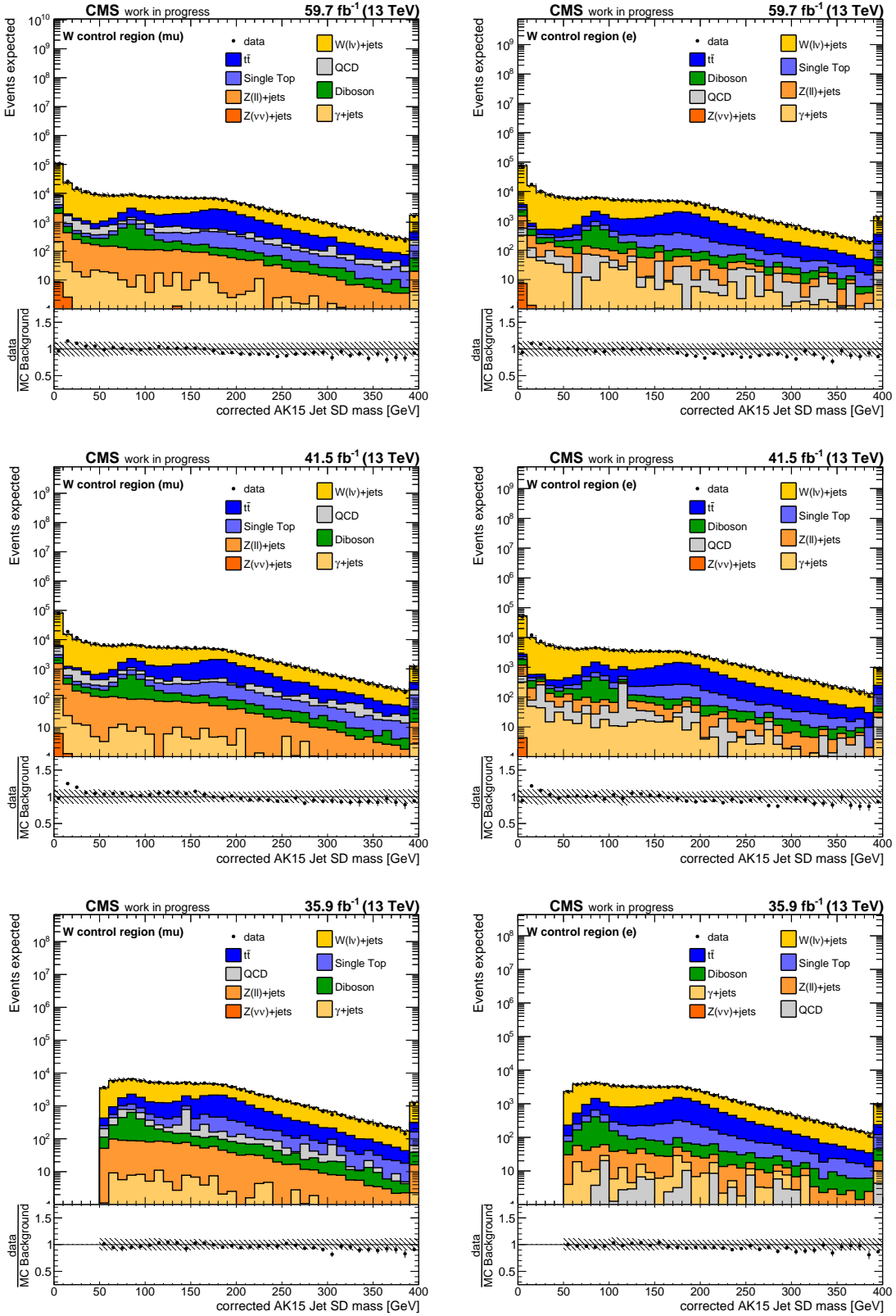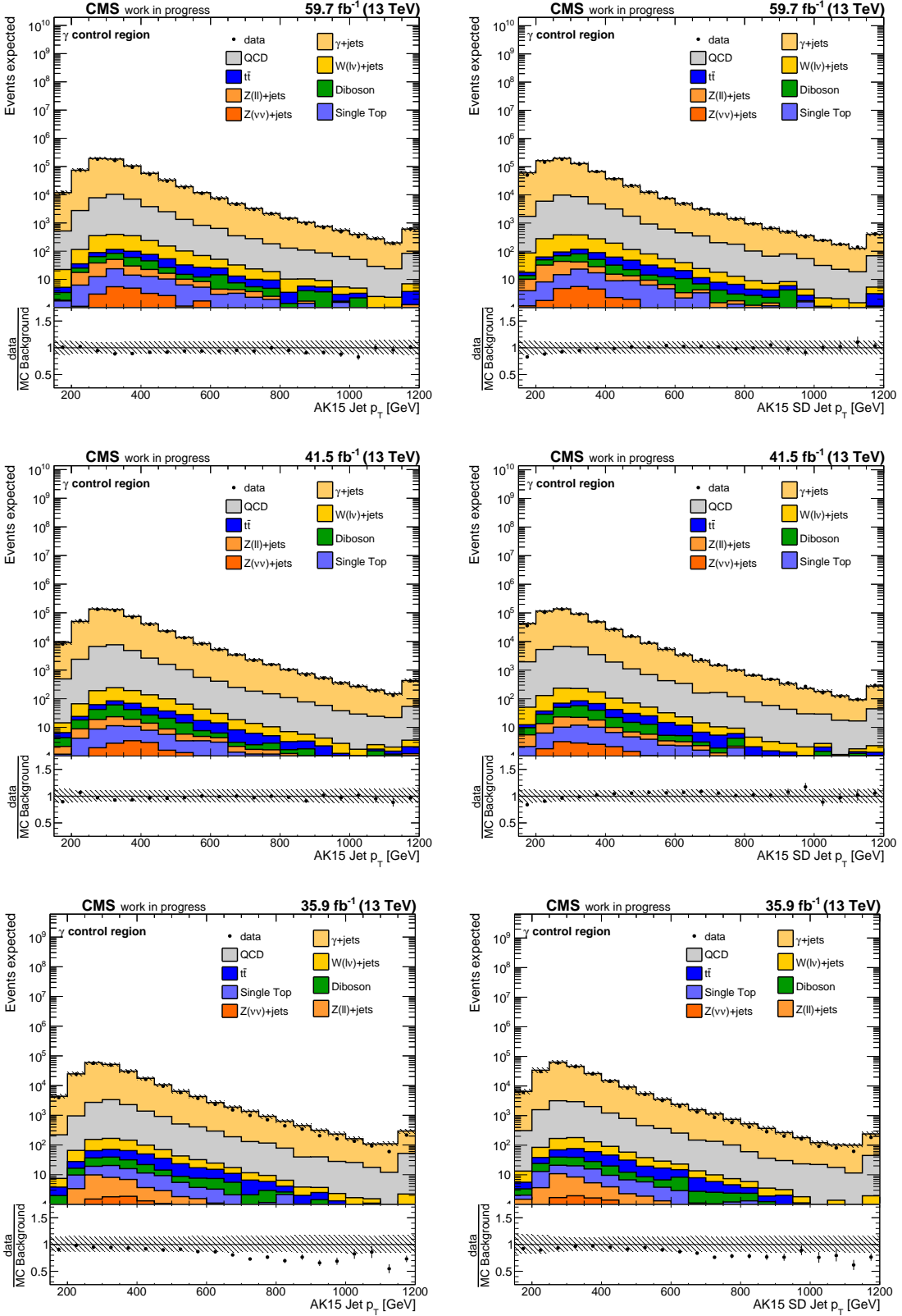
Figure B.31: Distribution of the mass of the AK15 jet after the SD algorithm is applied in the W → lν̄ control regions comparing all data eras with preselection requirements applied. The upper pad shows the absolute prediction of the different processes stacked on top of each other and the observation from data. The lower pad shows the ratio of the observation and the prediction. The uncertainty band corresponds to the square root of the quadratic sum of all considered uncertainties, see section 5.8.1.
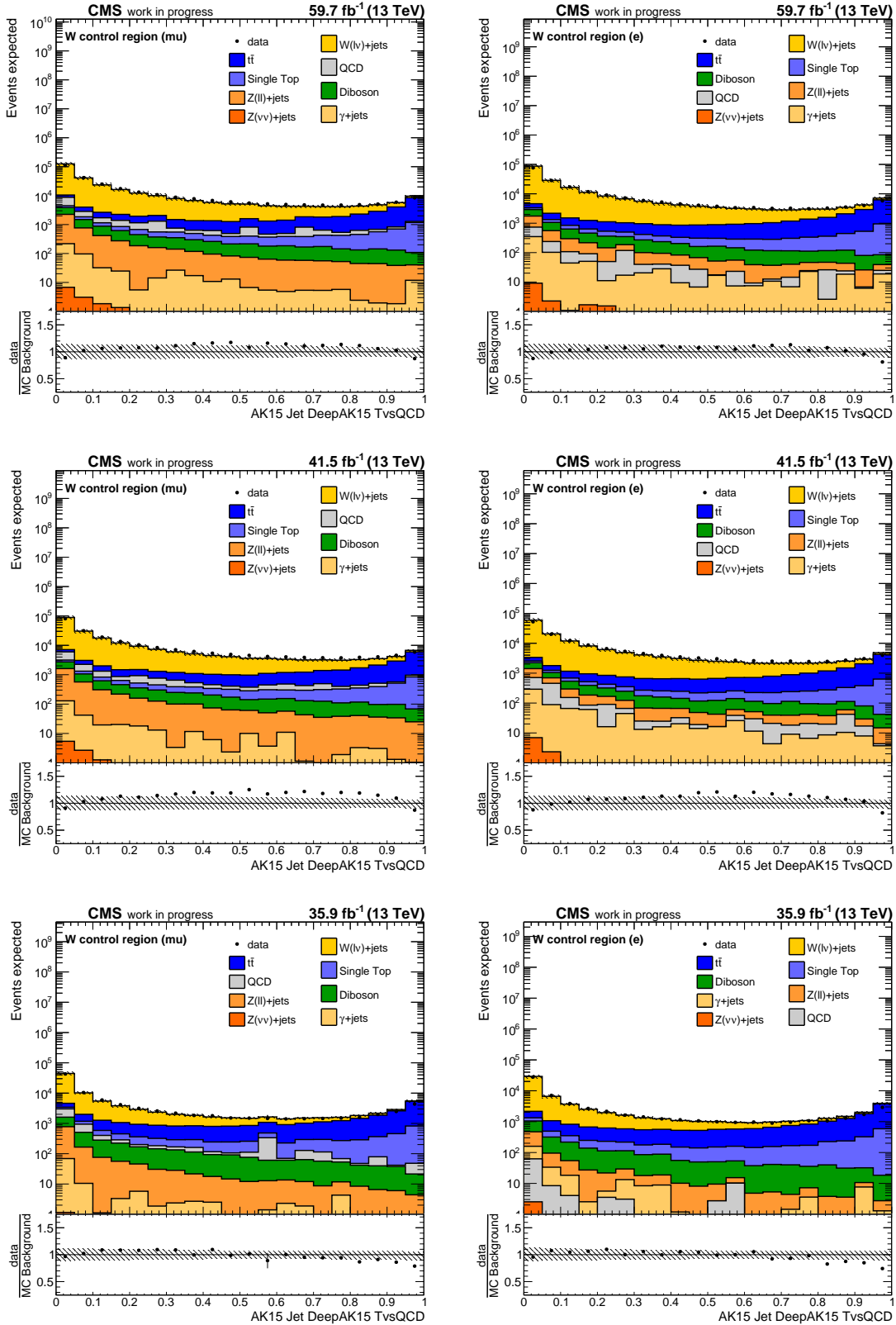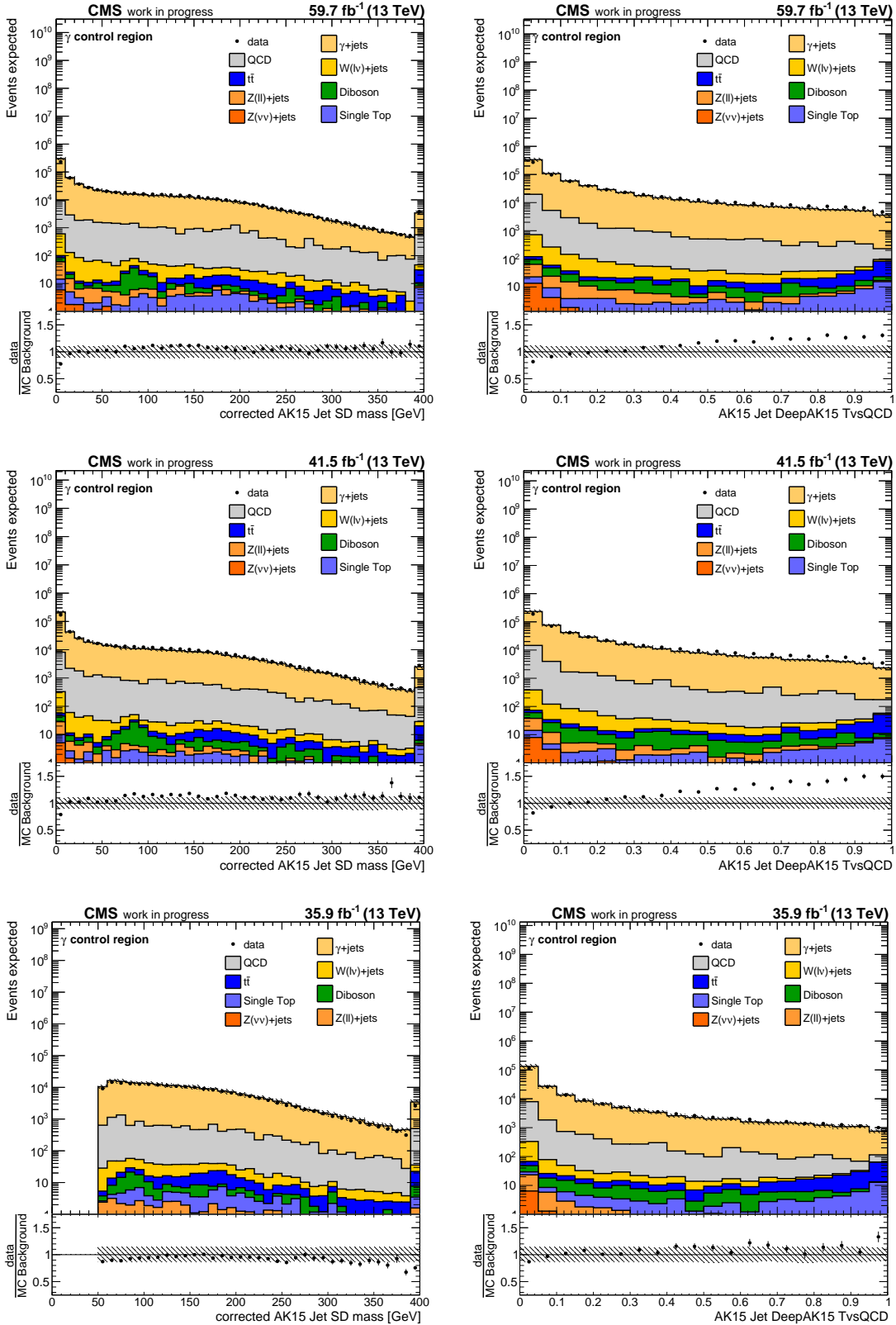
Figure B.32: Distribution of the DeepAK15 top-tagging discriminant in the $W \to l\overline{\nu}$ control regions comparing all data eras with preselection requirements applied. The upper pad shows the absolute prediction of the different processes stacked on top of each other and the observation from data. The lower pad shows the ratio of the observation and the prediction. The uncertainty band corresponds to the square root of the quadratic sum of all considered uncertainties, see section 5.8.1.

B.3 Top-Quark-Antiquark-Pair control regions

Figure B.33: Distribution of the hadronic recoil in the $t\bar{t}$ control regions comparing all data eras with preselection requirements applied. The upper pad shows the absolute prediction of the different processes stacked on top of each other and the observation from data. The lower pad shows the ratio of the observation and the prediction. The uncertainty band corresponds to the square root of the quadratic sum of all considered uncertainties, see section 5.8.1.
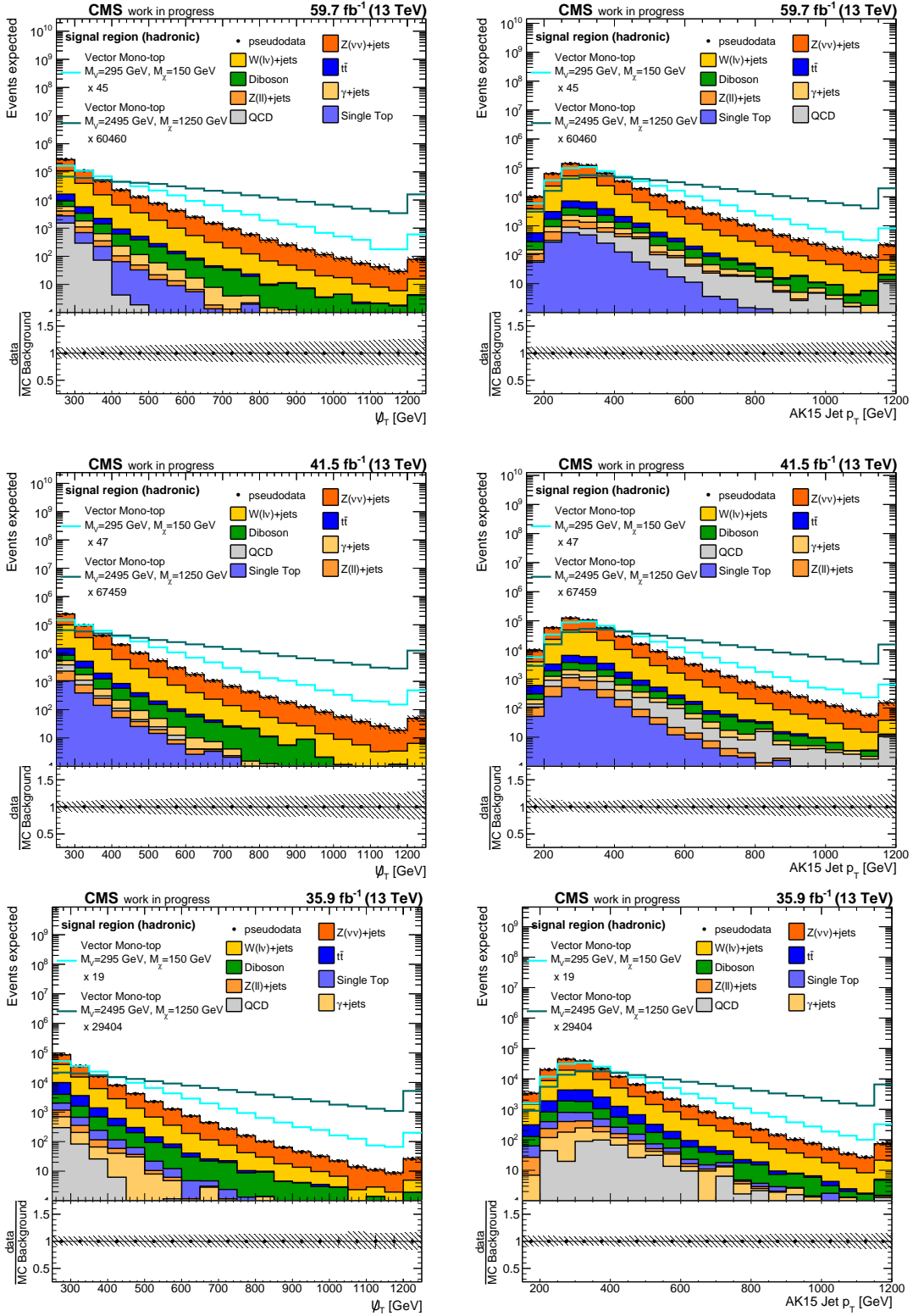
Figure B.34: Distribution of the AK15 jet p_T in the $t\bar{t}$ control regions comparing all data eras with preselection requirements applied. The upper pad shows the absolute prediction of the different processes stacked on top of each other and the observation from data. The lower pad shows the ratio of the observation and the prediction. The uncertainty band corresponds to the square root of the quadratic sum of all considered uncertainties, see section 5.8.1.

Figure B.35: Distribution of the AK15 jet p_{T} after applying the SD algorithm in the $t\bar{t}$ control regions comparing all data eras with preselection requirements applied. The upper pad shows the absolute prediction of the different processes stacked on top of each other and the observation from data. The lower pad shows the ratio of the observation and the prediction. The uncertainty band corresponds to the square root of the quadratic sum of all considered uncertainties, see section 5.8.1.

Figure B.36: Distribution of the lepton p_{T} in the $t\bar{t}$ control regions comparing all data eras with preselection requirements applied. The upper pad shows the absolute prediction of the different processes stacked on top of each other and the observation from data. The lower pad shows the ratio of the observation and the prediction. The uncertainty band corresponds to the square root of the quadratic sum of all considered uncertainties, see section 5.8.1.

Figure B.37: Distribution of the mass of the AK15 jet after the SD algorithm is applied in the $t\bar{t}$ control regions comparing all data eras with preselection requirements applied. The upper pad shows the absolute prediction of the different processes stacked on top of each other and the observation from data. The lower pad shows the ratio of the observation and the prediction. The uncertainty band corresponds to the square root of the quadratic sum of all considered uncertainties, see section 5.8.1.

Figure B.38: Distribution of the DeepAK15 top-tagging discriminant in the t$\bar{t}$ control regions comparing all data eras with preselection requirements applied. The upper pad shows the absolute prediction of the different processes stacked on top of each other and the observation from data. The lower pad shows the ratio of the observation and the prediction. The uncertainty band corresponds to the square root of the quadratic sum of all considered uncertainties, see section 5.8.1.

B.4 Photon control regions

Figure B.39: Distribution of the hadronic recoil (left-hand column) and the photon p_T (right-hand column) in the γ control regions comparing all data eras with preselection requirements applied. The upper pad shows the absolute prediction of the different processes stacked on top of each other and the observation from data. The lower pad shows the ratio of the observation and the prediction. The uncertainty band corresponds to the square root of the quadratic sum of all considered uncertainties, see section 5.8.1.

Figure B.40: Distribution of the AK15 jet p_T before (left-hand side) and after (right-hand side) applying the SD algorithm in the γ control regions comparing all data eras with preselection requirements applied. The upper pad shows the absolute prediction of the different processes stacked on top of each other and the observation from data. The lower pad shows the ratio of the observation and the prediction. The uncertainty band corresponds to the square root of the quadratic sum of all considered uncertainties, see section 5.8.1.

Figure B.41: Distribution of the mass of the AK15 jet after the SD algorithm is applied (left-hand column) and the DeepAK15 top-tagging discriminant (right-hand column) in the γ control regions comparing all data eras with preselection requirements applied. The upper pad shows the absolute prediction of the different processes stacked on top of each other and the observation from data. The lower pad shows the ratio of the observation and the prediction. The uncertainty band corresponds to the square root of the quadratic sum of all considered uncertainties, see section 5.8.1.

B.5 Signal region

Figure B.42: Distribution of the hadronic recoil and the AK15 jet p_T in the signal region comparing all data eras with preselection requirements applied. The upper pad shows the absolute prediction of the different processes stacked on top of each other and the observation from background-only pseudodata. The lower pad shows the ratio of the observation and the prediction. The uncertainty band corresponds to the square root of the quadratic sum of all considered uncertainties, see section 5.8.1. Two mono-top signal predictions, which are scaled to the total background yield, are overlaid and the corresponding scale factors are given in the legend.
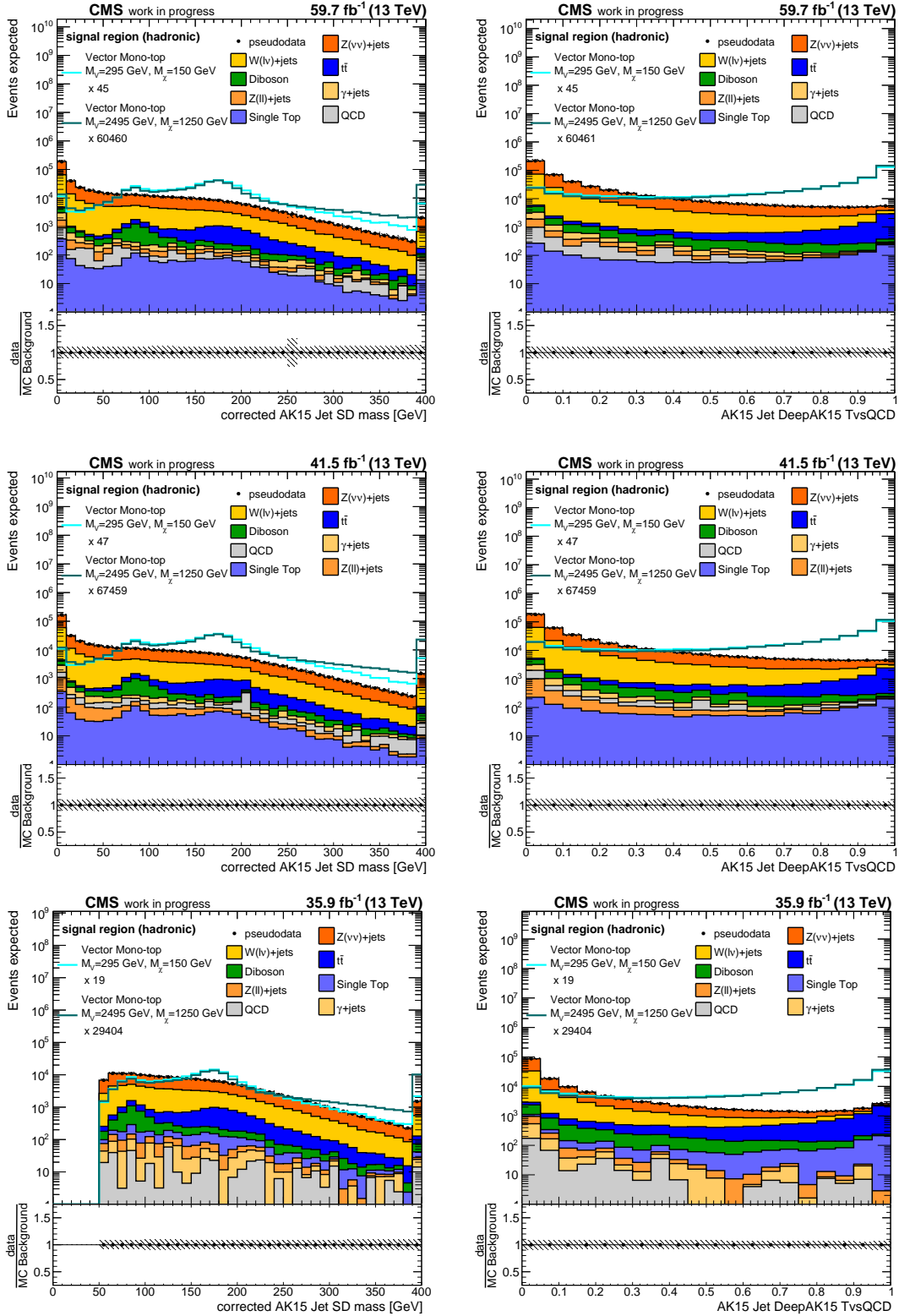
Figure B.43: Distribution of the mass of the AK15 jet after the SD algorithm is applied and the DeepAK15 top-tagging discriminant in the signal region comparing all data eras with preselection requirements applied. The upper pad shows the absolute prediction of the different processes stacked on top of each other and the observation from background-only pseudodata. The lower pad shows the ratio of the observation and the prediction. The uncertainty band corresponds to the square root of the quadratic sum of all considered uncertainties, see section 5.8.1. Two mono-top signal predictions, which are scaled to the total background yield, are overlaid and the corresponding scale factors are given in the legend.
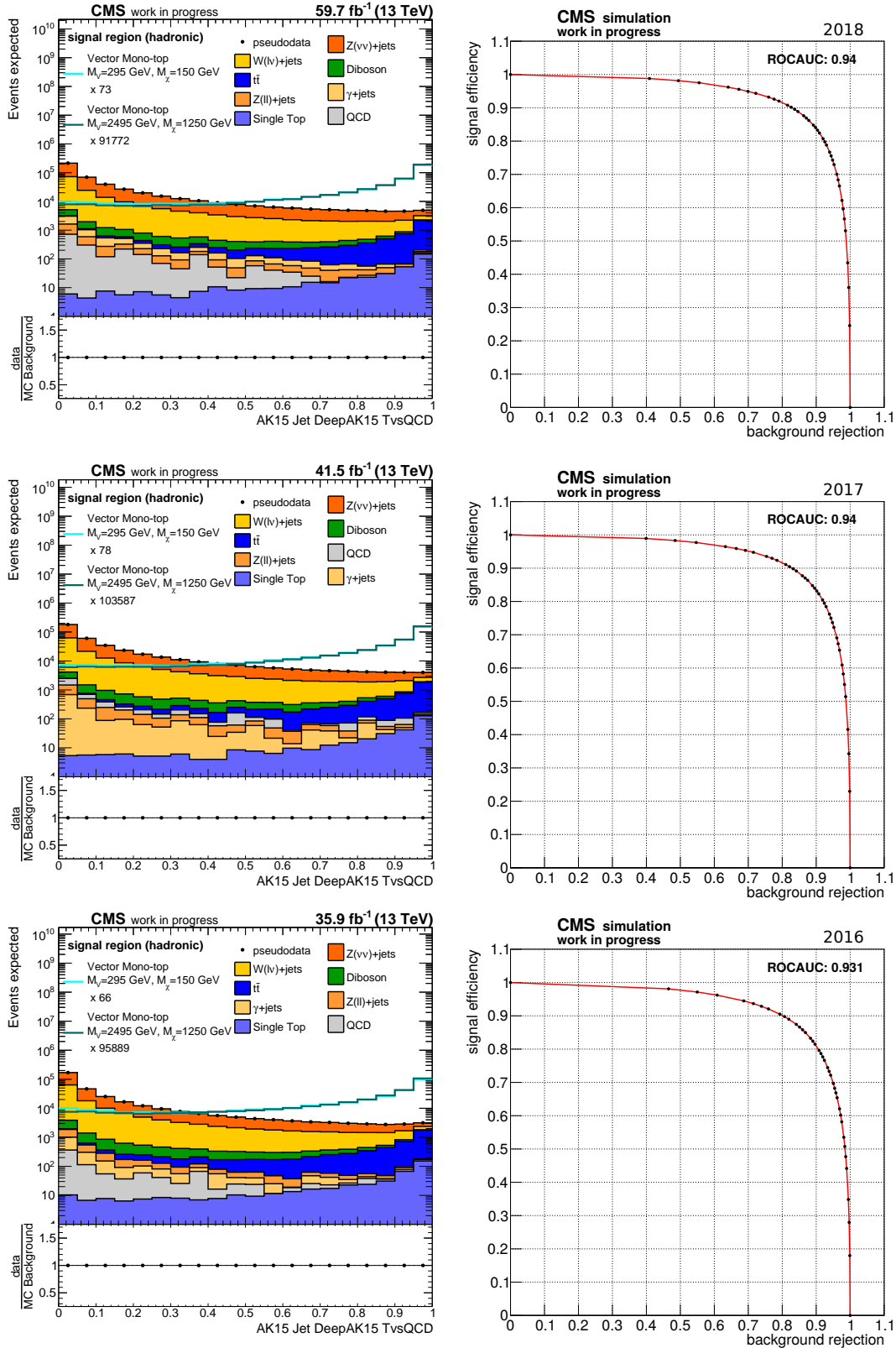
Figure B.44: Left-hand side: Distribution of the top-tagging discriminant of the leading AK15 jet in the signal region after the preselection is applied. The $t\bar{t}$, single top quark, and mono-top events are required to have a top-matched leading AK15 jet, see section 5.7.7. Right-hand side: Receiver-operator-characteristic for the top-tagging discriminant of the leading AK15 jet in the signal region after the preselection. For the definition of signal efficiency and background rejection, see the description in section 5.7.7.

C Control distributions with final selection requirements
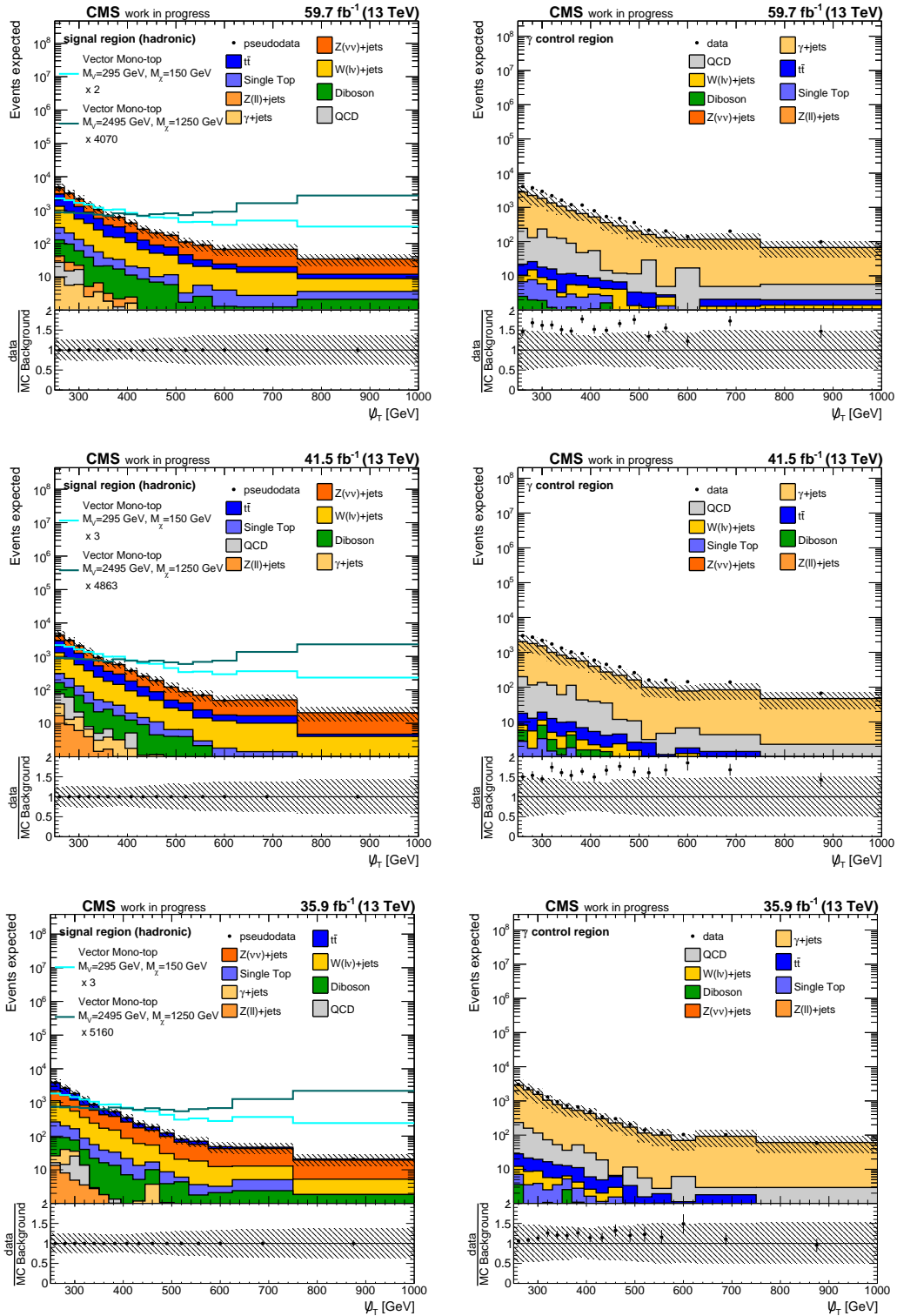
Figure C.45: Distribution of the hadronic recoil in the signal regions (left-hand side) and in the γ+jets control regions (right-hand side) comparing all data eras with the final selection criteria applied. The upper pad shows the absolute prediction of the different processes stacked on top of each other and the observation from data. The lower pad shows the ratio of the observation and the prediction. The uncertainty band corresponds to the square root of the quadratic sum of all considered uncertainties, see section 5.8.1. On the left-hand side, two mono-top signal predictions, which are scaled to the total background yield, are overlaid and the corresponding scale factors are given in the legend.
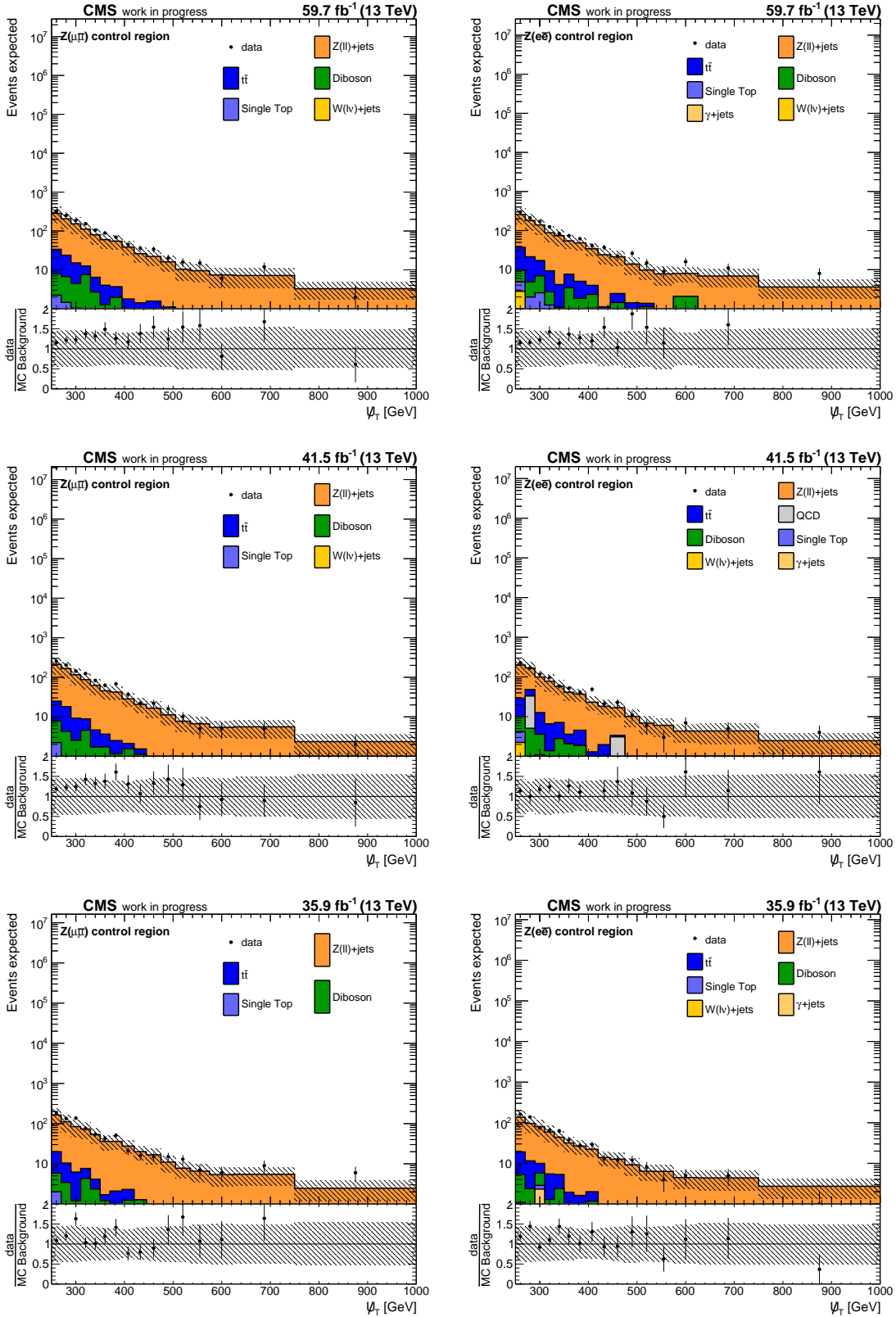
Figure C.46: Distribution of the hadronic recoil in the Z boson control regions comparing all data eras with the final selection criteria applied. The upper pad shows the absolute prediction of the different processes stacked on top of each other and the observation from data. The lower pad shows the ratio of the observation and the prediction. The uncertainty band corresponds to the square root of the quadratic sum of all considered uncertainties, see section 5.8.1.
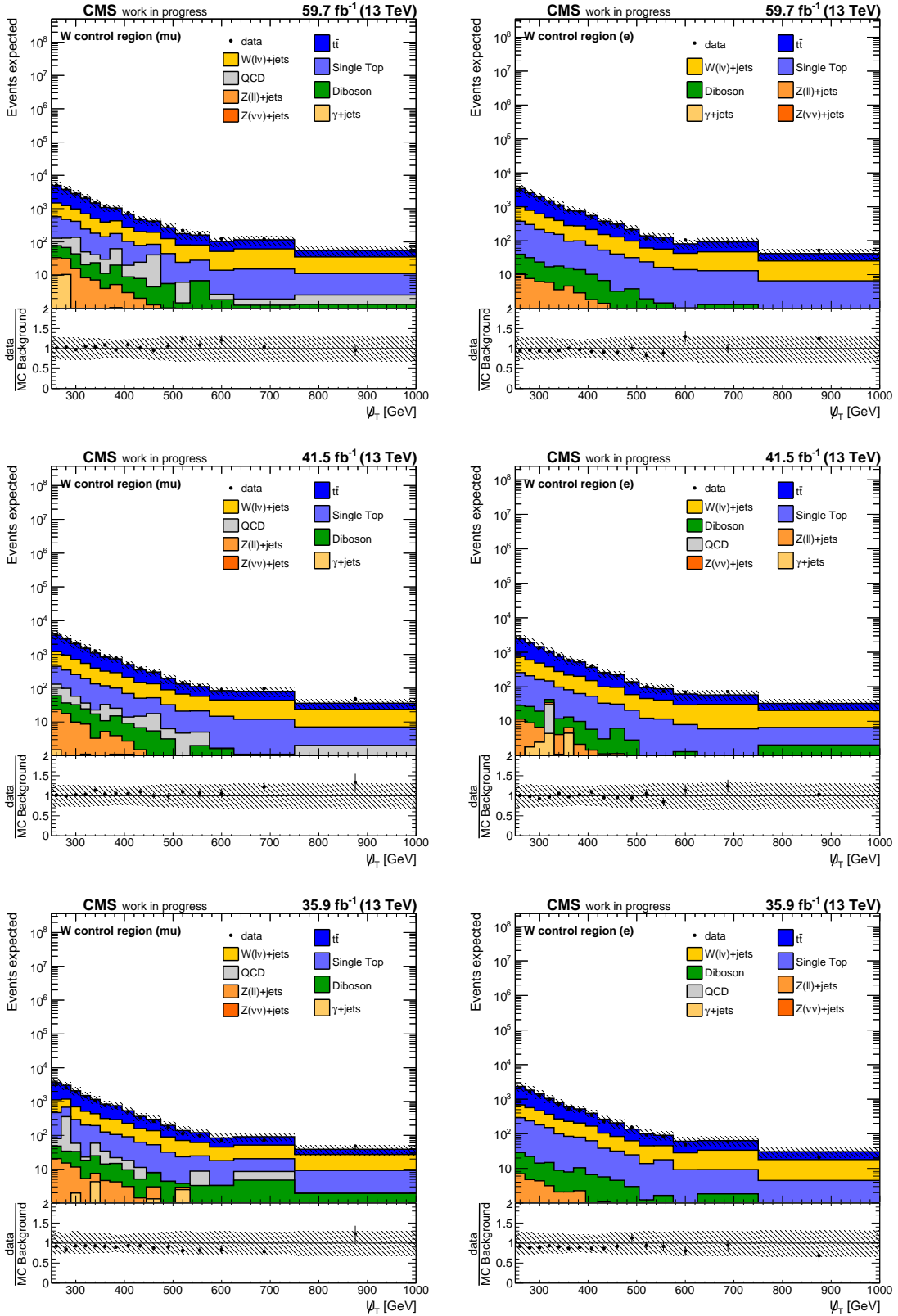
Figure C.47: Distribution of the hadronic recoil in the W boson control regions comparing all data eras with the final selection criteria applied. The upper pad shows the absolute prediction of the different processes stacked on top of each other and the observation from data. The lower pad shows the ratio of the observation and the prediction. The uncertainty band corresponds to the square root of the quadratic sum of all considered uncertainties, see section 5.8.1.
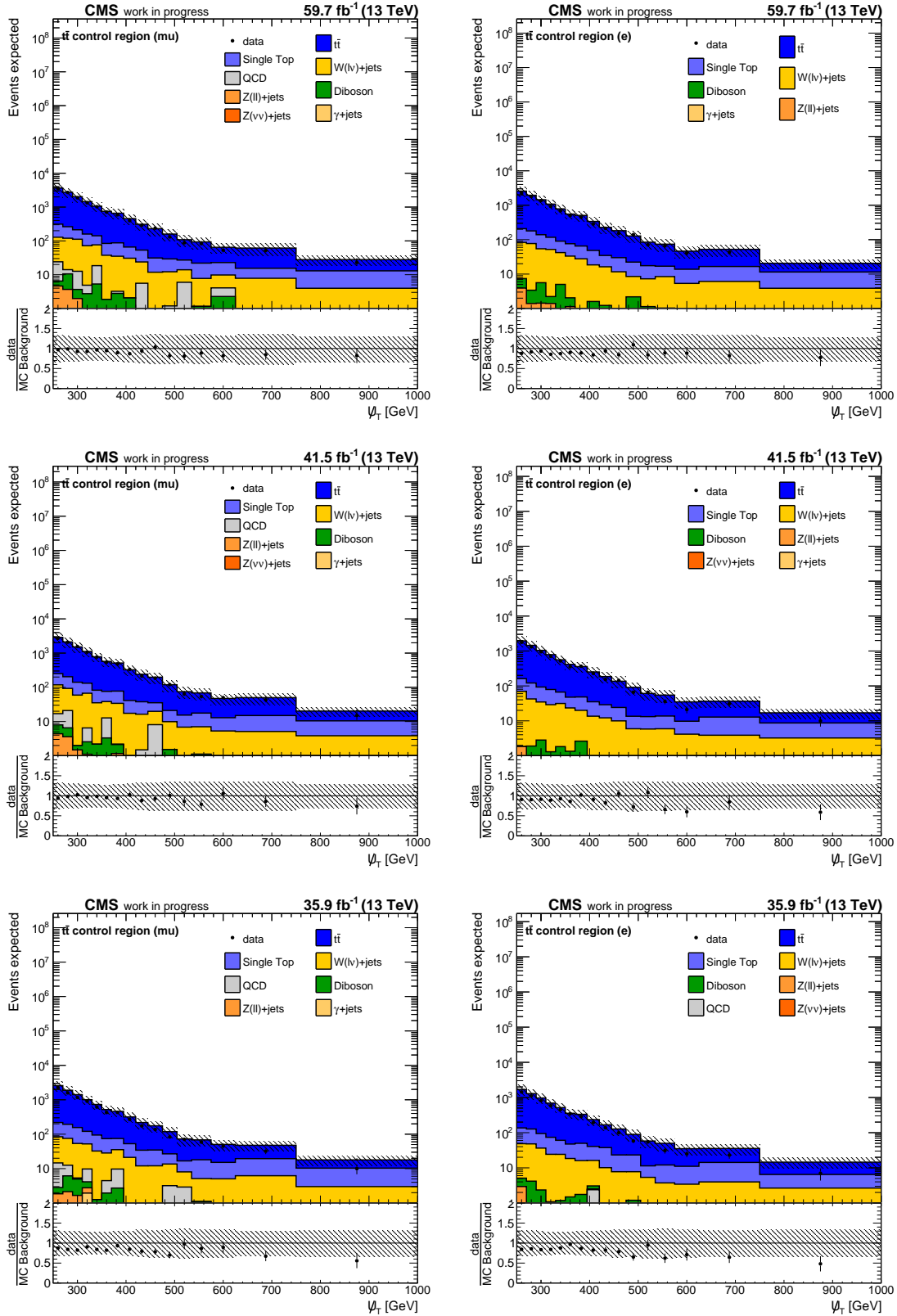
Figure C.48: Distribution of the hadronic recoil in the t$\bar{\text{t}}$ control regions comparing all data eras with the final selection criteria applied. The upper pad shows the absolute prediction of the different processes stacked on top of each other and the observation from data. The lower pad shows the ratio of the observation and the prediction. The uncertainty band corresponds to the square root of the quadratic sum of all considered uncertainties, see section 5.8.1.

D Statistical model

D.1 Transfer factors
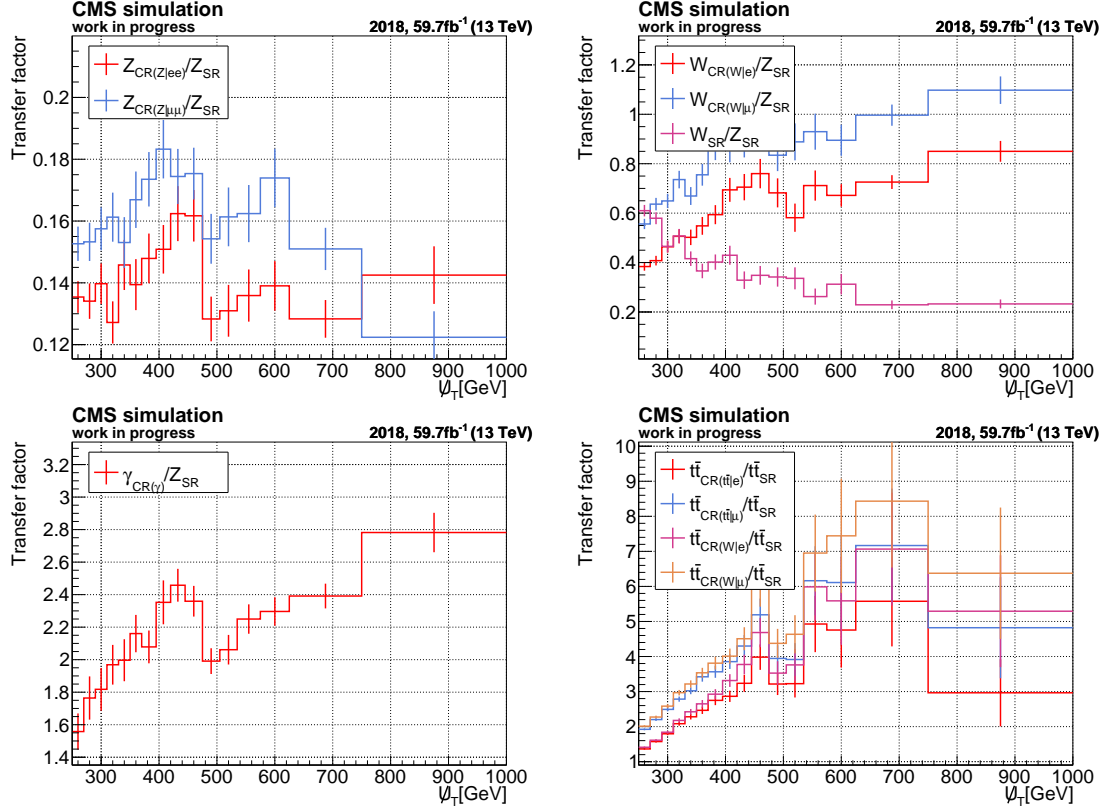
Figure D.49: Transfer factors used in the 2018 data era as a function of the hadronic recoil. In the upper-left pad, the transfer factors connecting the $Z + \text{jets}$ process with $Z \to \nu\bar{\nu}$ in the signal region and the $Z + \text{jets}$ process with $Z \to l\bar{l}$ in the Z boson control regions are given. The upper-right pad shows the transfer factor connecting the $Z + \text{jets}$ process $(Z \to \nu\bar{\nu})$ in the signal region and the $W + \text{jets}$ process $(W \to l\bar{\nu})$ in the signal region as well as the transfer factors connecting the $Z + \text{jets}$ process $(Z \to \nu\bar{\nu})$ in the signal region and the $W + \text{jets}$ process $(W \to l\bar{\nu})$ in the W boson control regions. In the lower-left pad, the transfer factors connecting the $Z + \text{jets}$ process $(Z \to \nu\bar{\nu})$ in the signal region and the $\gamma + \text{jets}$ process in the photon control region are presented. The transfer factors connecting the $t\bar{t}$ process in the signal region with the $t\bar{t}$ process in the $t\bar{t}$ control regions and in the W boson control regions are shown in the lower-right pad. The error bars represent the statistical uncertainties of the transfer factors due to the limited number of simulated events.

Figure D.50: Transfer factors used in the 2017 data era as a function of the hadronic recoil. In the upper-left pad, the transfer factors connecting the $Z + \text{jets}$ process with $Z \to \nu\bar{\nu}$ in the signal region and the $Z + \text{jets}$ process with $Z \to l\bar{l}$ in the Z boson control regions are given. The upper-right pad shows the transfer factor connecting the $Z + \text{jets}$ process $(Z \to \nu\bar{\nu})$ in the signal region and the $W + \text{jets}$ process $(W \to l\bar{\nu})$ in the signal region as well as the transfer factors connecting the $Z + \text{jets}$ process $(Z \to \nu\bar{\nu})$ in the signal region and the $W + \text{jets}$ process $(W \to l\bar{\nu})$ in the W boson control regions. In the lower-left pad, the transfer factors connecting the $Z + \text{jets}$ process $(Z \to \nu\bar{\nu})$ in the signal region and the $\gamma + \text{jets}$ process in the photon control region are presented. The transfer factors connecting the $t\bar{t}$ process in the signal region with the $t\bar{t}$ process in the $t\bar{t}$ control regions and in the W boson control regions are shown in the lower-right pad. The error bars represent the statistical uncertainties of the transfer factors due to the limited number of simulated events.

Figure D.51: Transfer factors used in the 2016 data era as a function of the hadronic recoil. In the upper-left pad, the transfer factors connecting the $Z + \text{jets}$ process with $Z \to \nu\bar{\nu}$ in the signal region and the $Z + \text{jets}$ process with $Z \to l\bar{l}$ in the Z boson control regions are given. The upper-right pad shows the transfer factor connecting the $Z + \text{jets}$ process $(Z \to \nu\bar{\nu})$ in the signal region and the $W + \text{jets}$ process $(W \to l\bar{\nu})$ in the signal region as well as the transfer factors connecting the $Z + \text{jets}$ process $(Z \to \nu\bar{\nu})$ in the signal region and the $W + \text{jets}$ process $(W \to l\bar{\nu})$ in the W boson control regions. In the lower-left pad, the transfer factors connecting the $Z + \text{jets}$ process $(Z \to \nu\bar{\nu})$ in the signal region and the $\gamma + \text{jets}$ process in the photon control region are presented. The transfer factors connecting the $t\bar{t}$ process in the signal region with the $t\bar{t}$ process in the $t\bar{t}$ control regions and in the W boson control regions are shown in the lower-right pad. The error bars represent the statistical uncertainties of the transfer factors due to the limited number of simulated events.

D.2 Validation of the statistical model

Maximum likelihood fits to Asimov datasets
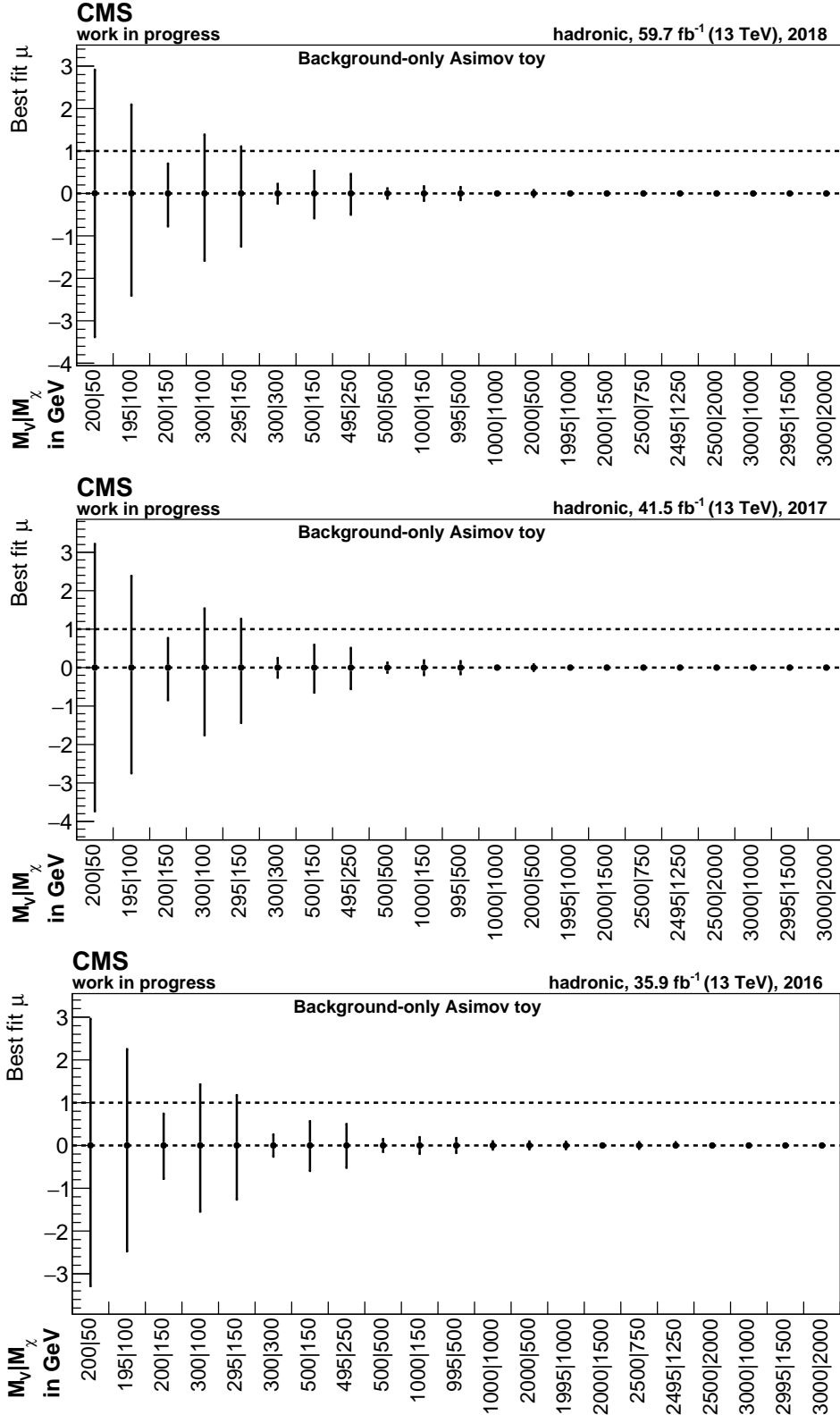
Figure D.52: Maximum likelihood estimators and their corresponding $\pm 1\sigma$ uncertainty of the signal strength modifier for different mono-top signals after a maximum likelihood fit to a background-only Asimov toy in the 2018 (top), 2017 (center), and 2016 (bottom) era. The mono-top signals are scaled to a cross section of 0.1 pb. The mass of the hypothetical vector mediator is represented by M_V and the mass of the DM candidates by M_χ.
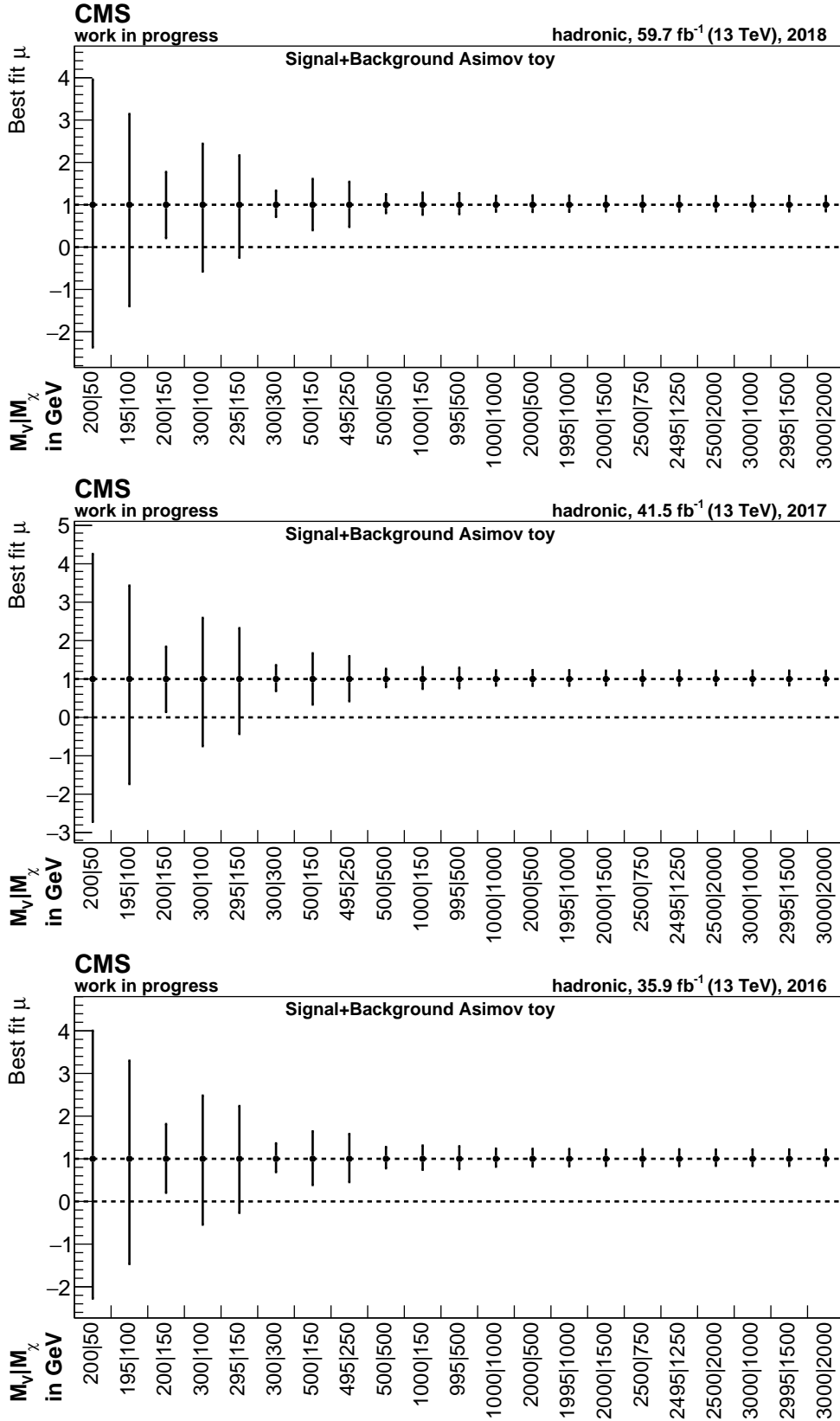
Figure D.53: Maximum likelihood estimators and their corresponding $\pm 1\sigma$ uncertainty of the signal strength modifier for different mono-top signals after a maximum likelihood fit to a signal-plus-background Asimov toy in the 2018 (top), 2017 (center), and 2016 (bottom) era. The mono-top signals are scaled to a cross section of 0.1 pb. The mass of the hypothetical vector mediator is represented by M_V and the mass of the DM candidates by M_χ.

Behavior of nuisance parameters
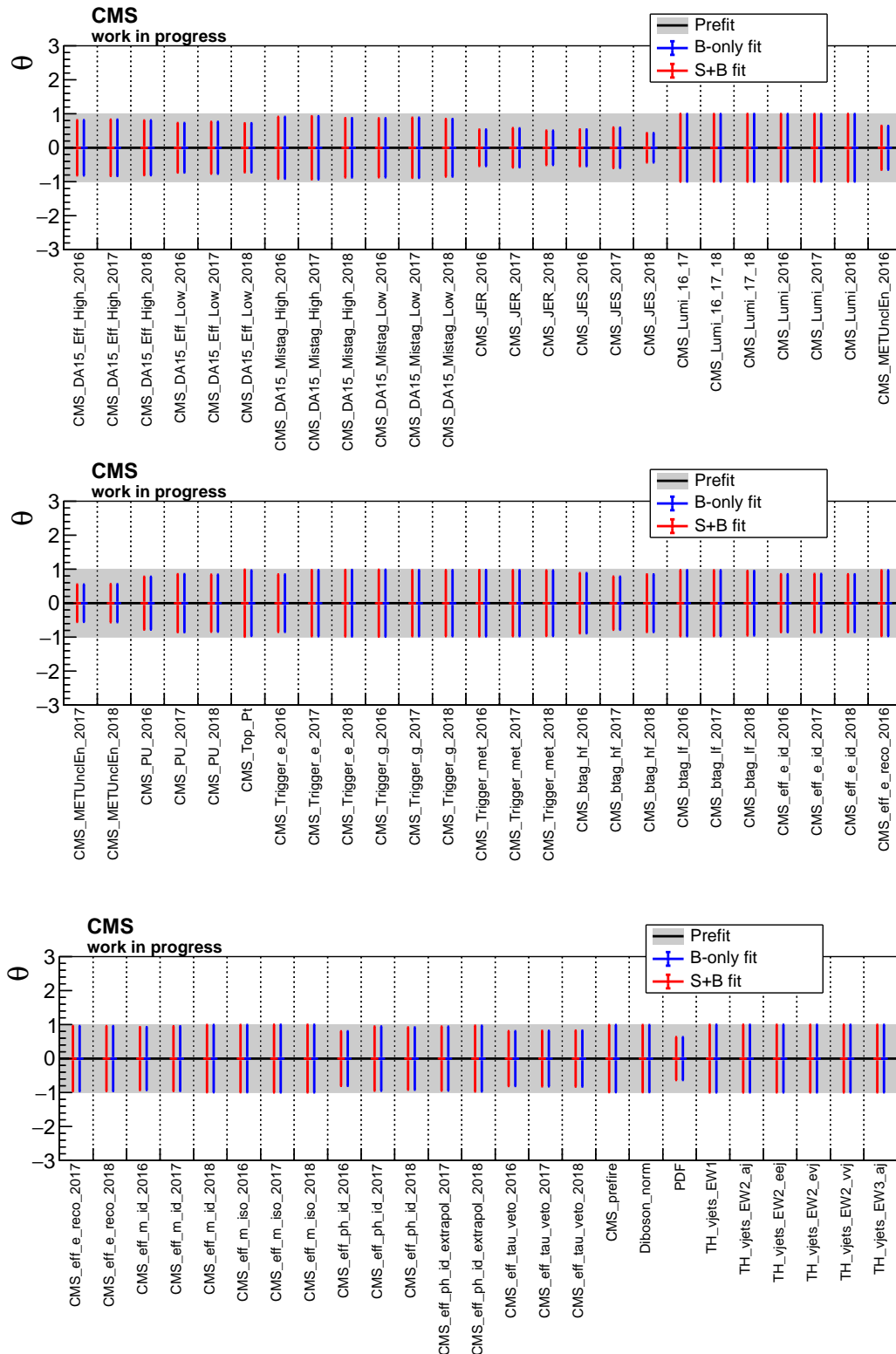
Figure D.54: Maximum likelihood estimators and their corresponding $\pm 1\sigma$ uncertainty of the nuisance parameters after the maximum likelihood fit of the background-only and signal-plus-background model to a background-only Asimov dataset. The points represent the value of the maximum likelihood estimators and the error bars their corresponding $\pm 1\sigma$ uncertainties. The different nuisance parameters can be identified with the corresponding systematic uncertainties by using the labels given in Tab. 5.12, Tab. 5.13, and Tab. 5.14.
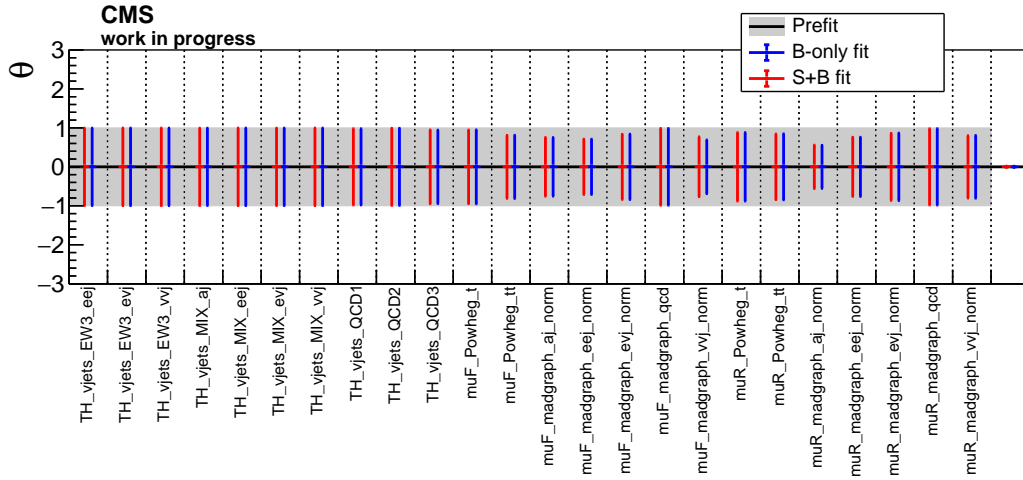
Figure D.55: Maximum likelihood estimators and their corresponding $\pm 1\sigma$ uncertainty of the nuisance parameters after the maximum likelihood fit of the background-only and signal-plus-background model to a background-only Asimov dataset. The points represent the value of the maximum likelihood estimators and the error bars their corresponding $\pm 1\sigma$ uncertainties. The different nuisance parameters can be identified with the corresponding systematic uncertainties by using the labels given in Tab. 5.12, Tab. 5.13, and Tab. 5.14.
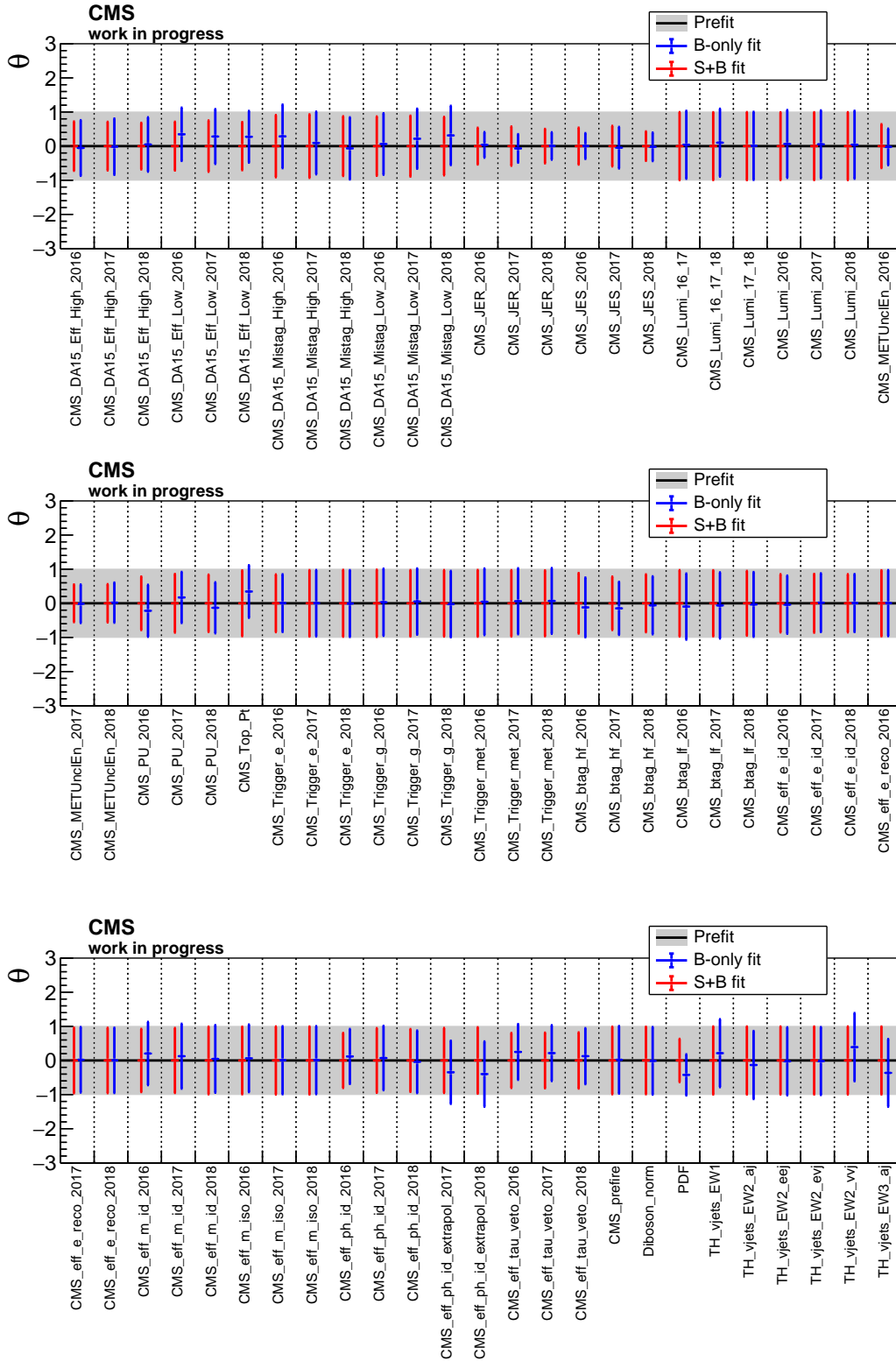
Figure D.56: Maximum likelihood estimators and their corresponding $\pm 1\sigma$ uncertainty of the nuisance parameters after the maximum likelihood fit of the background-only and signal-plus-background model to a signal-plus-background Asimov dataset. The points represent the value of the maximum likelihood estimators and the error bars their corresponding $\pm 1\sigma$ uncertainties. The different nuisance parameters can be identified with the corresponding systematic uncertainties by using the labels given in Tab. 5.12, Tab. 5.13, and Tab. 5.14.
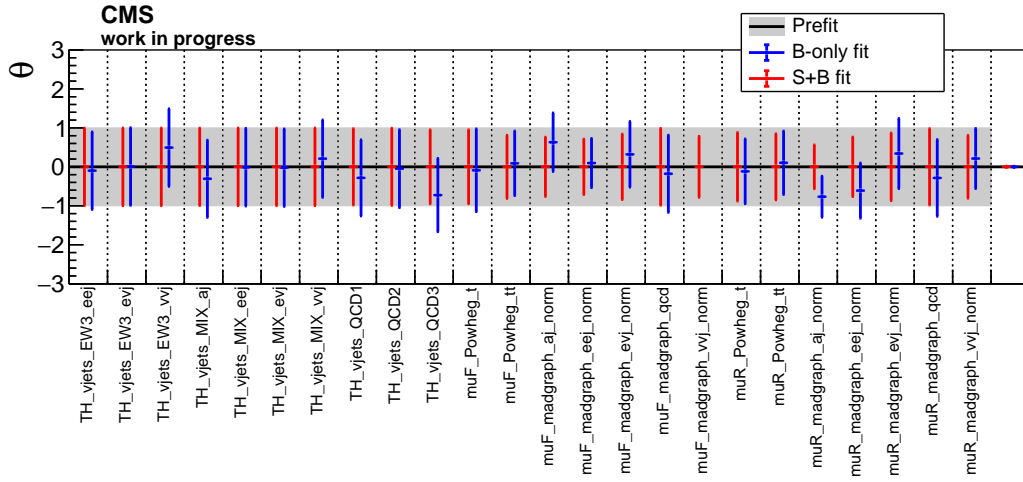
Figure D.57: Maximum likelihood estimators and their corresponding $\pm 1\sigma$ uncertainty of the nuisance parameters after the maximum likelihood fit of the background-only and signal-plus-background model to a signal-plus-background Asimov dataset. The points represent the value of the maximum likelihood estimators and the error bars their corresponding $\pm 1\sigma$ uncertainties. The different nuisance parameters can be identified with the corresponding systematic uncertainties by using the labels given in Tab. 5.12, Tab. 5.13, and Tab. 5.14.

Goodness-of-fit tests
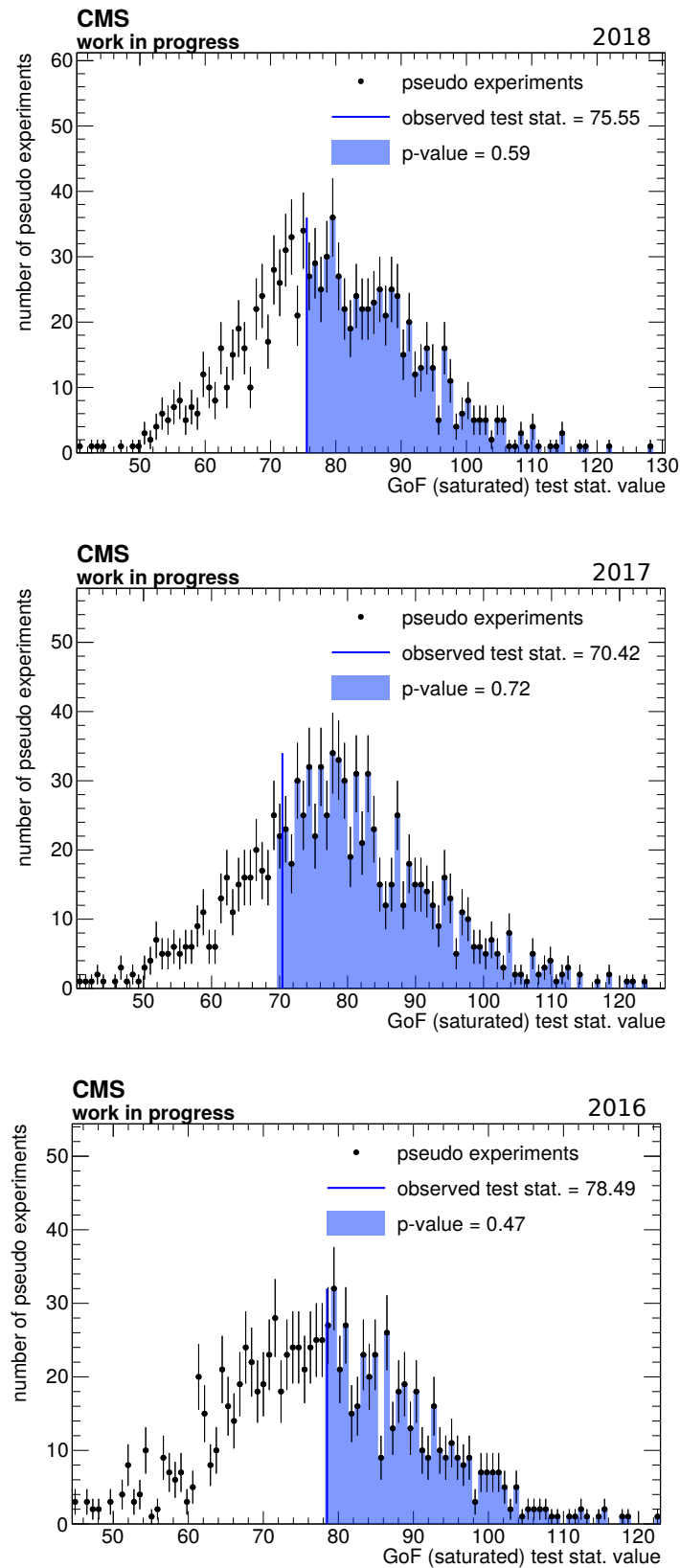
Figure D.58: Distributions of the test statistic of the saturated goodness-of-fit test for a-posteriori toy datasets sampled from the a-posteriori probability density function of the statistical model after a maximum likelihood fit to all control regions in the 2018 (top), 2017 (center), and 2016 (bottom) data era separately.

Expected significances
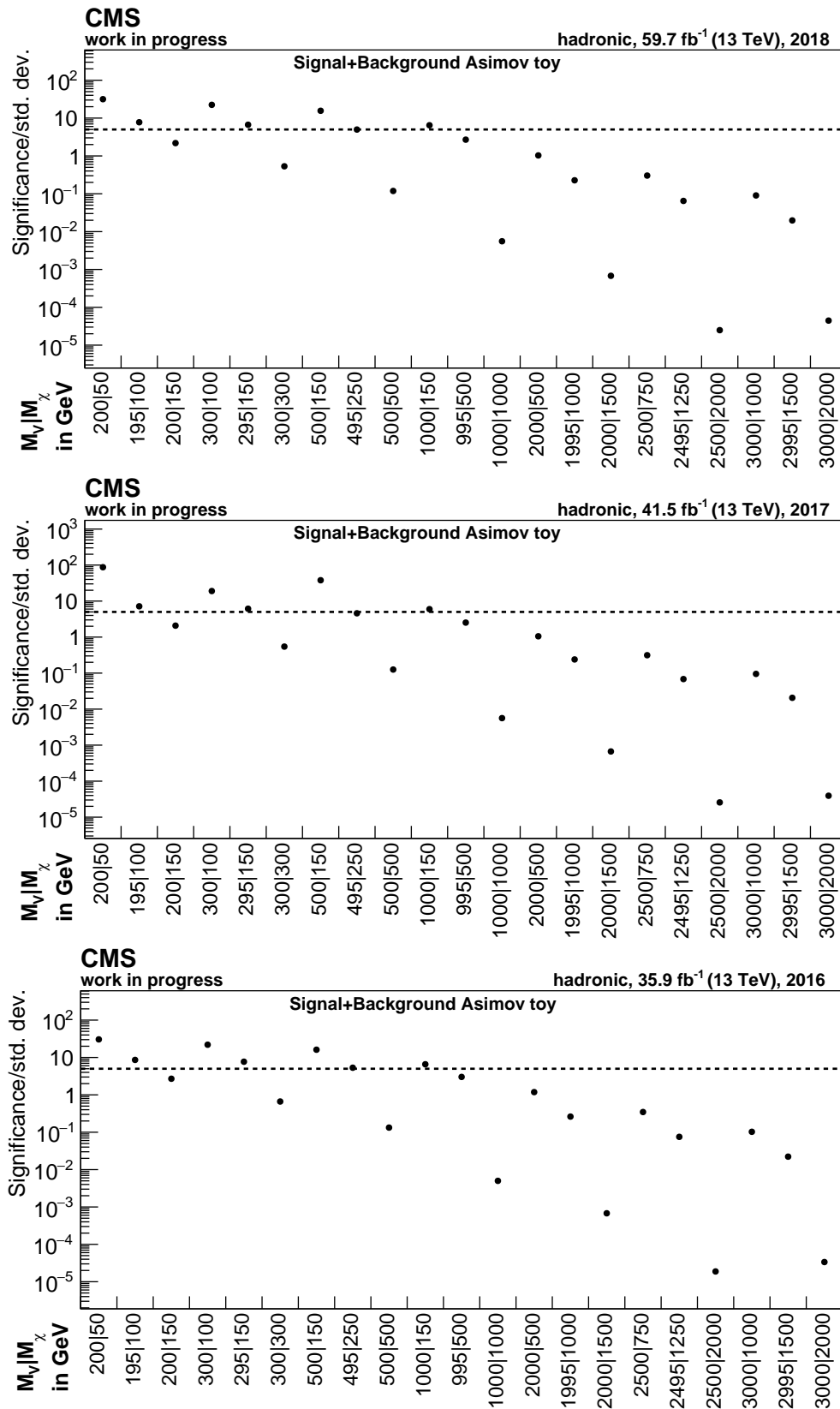
Figure D.59: Expected significances in units of the standard deviation of the standard normal distribution for different mono-top signals in the 2018 (top), 2017 (center), and 2016 (bottom) data era. The mass of the hypothetical vector mediator is represented by M_V and the mass of the DM candidates by M_χ. The 5σ discovery significance is represented by the dashed line.

Expected exclusion limits
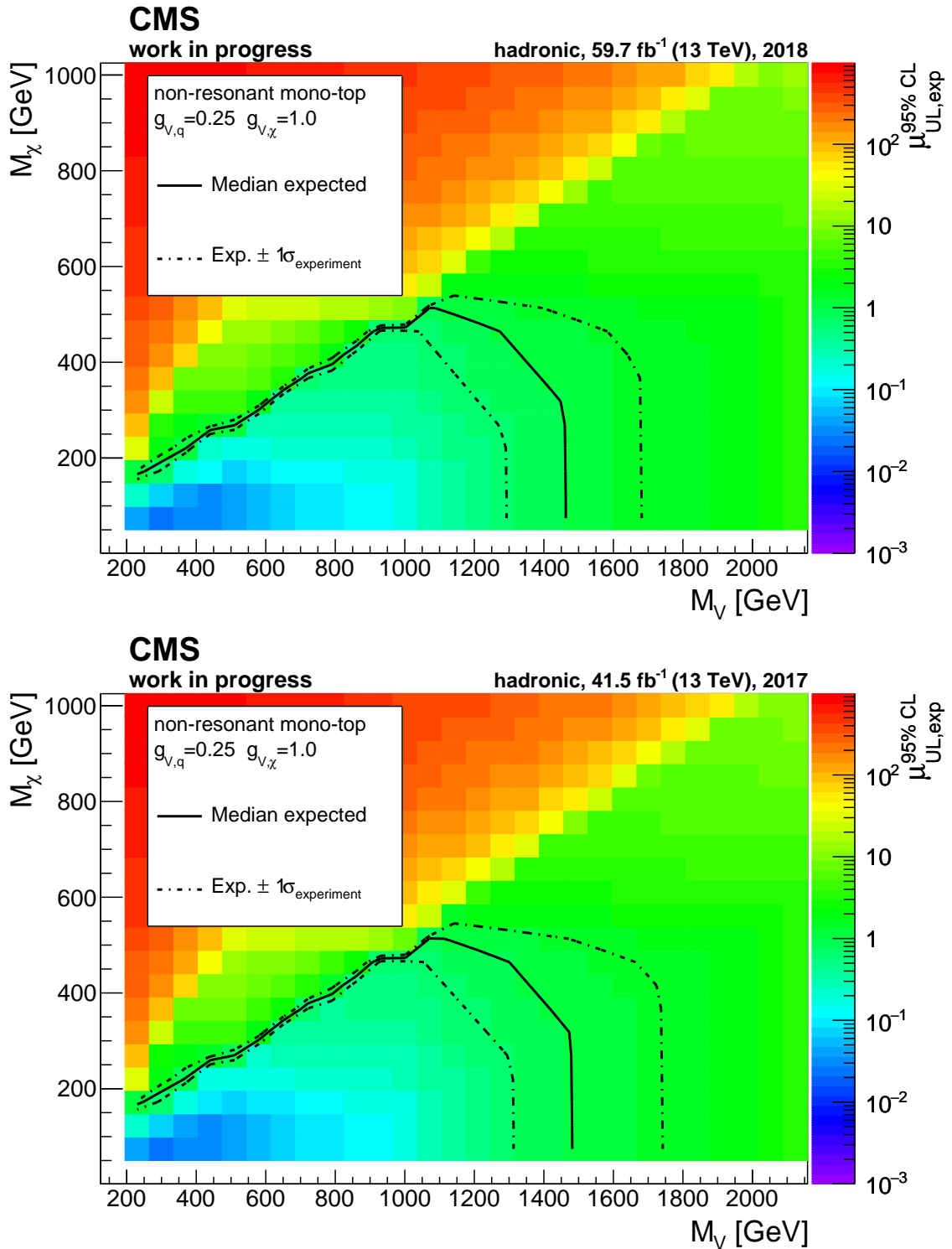
Figure D.60: Expected upper exclusion limits of the signal strength modifier at 95% confidence-level as a function of the mediator mass M_V and the DM candidate mass M_χ for the 2018 (top) and 2017 (bottom) data era. The colored area represents the median expected upper limits. The solid black line represents the contour for which the median expected upper limit is equal to unity. The dashed black lines represent the 68% confidence interval for the expected upper limit to be equal to unity considering all uncertainties relevant for the description of the background processes. The area within the black solid line is the expected exclusion area at 95% confidence-level.
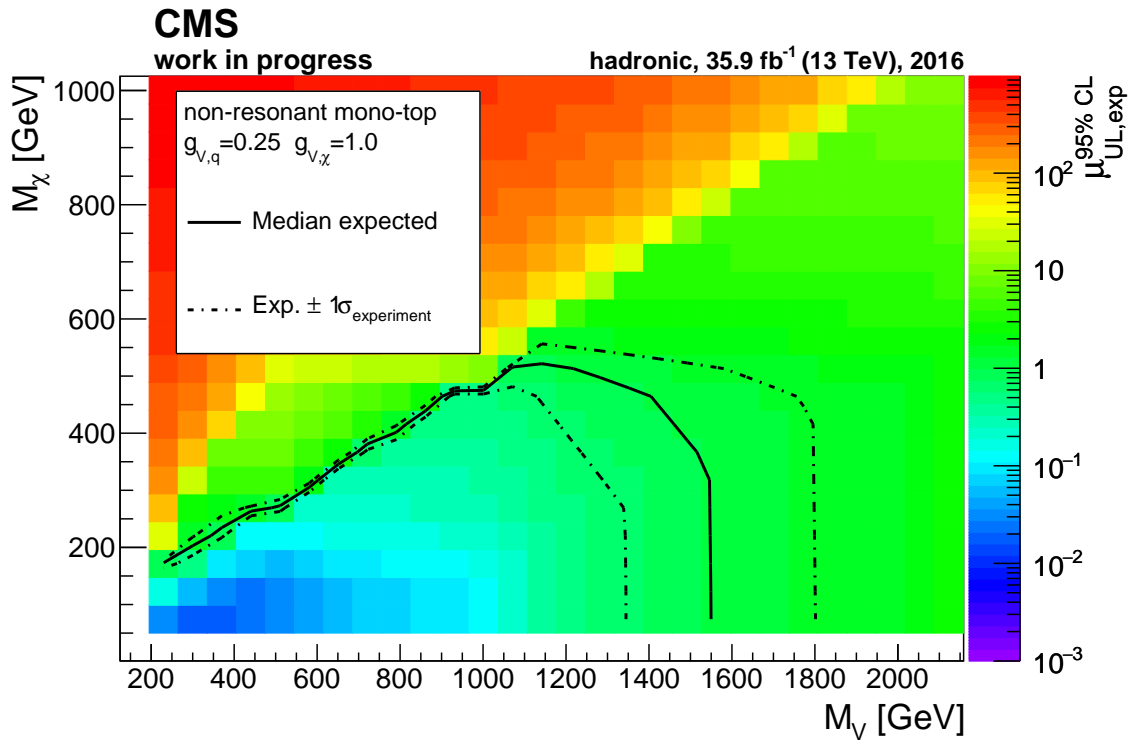
Figure D.61: Expected upper exclusion limits of the signal strength modifier at 95% confidence-level as a function of the mediator mass M_V and the DM candidate mass M_χ for the 2016 data era. The colored area represents the median expected upper limits. The solid black line represents the contour for which the median expected upper limit is equal to unity. The dashed black lines represent the 68% confidence interval for the expected upper limit to be equal to unity considering all uncertainties relevant for the description of the background processes. The area within the black solid line is the expected exclusion area at 95% confidence-level.

D.3 Results
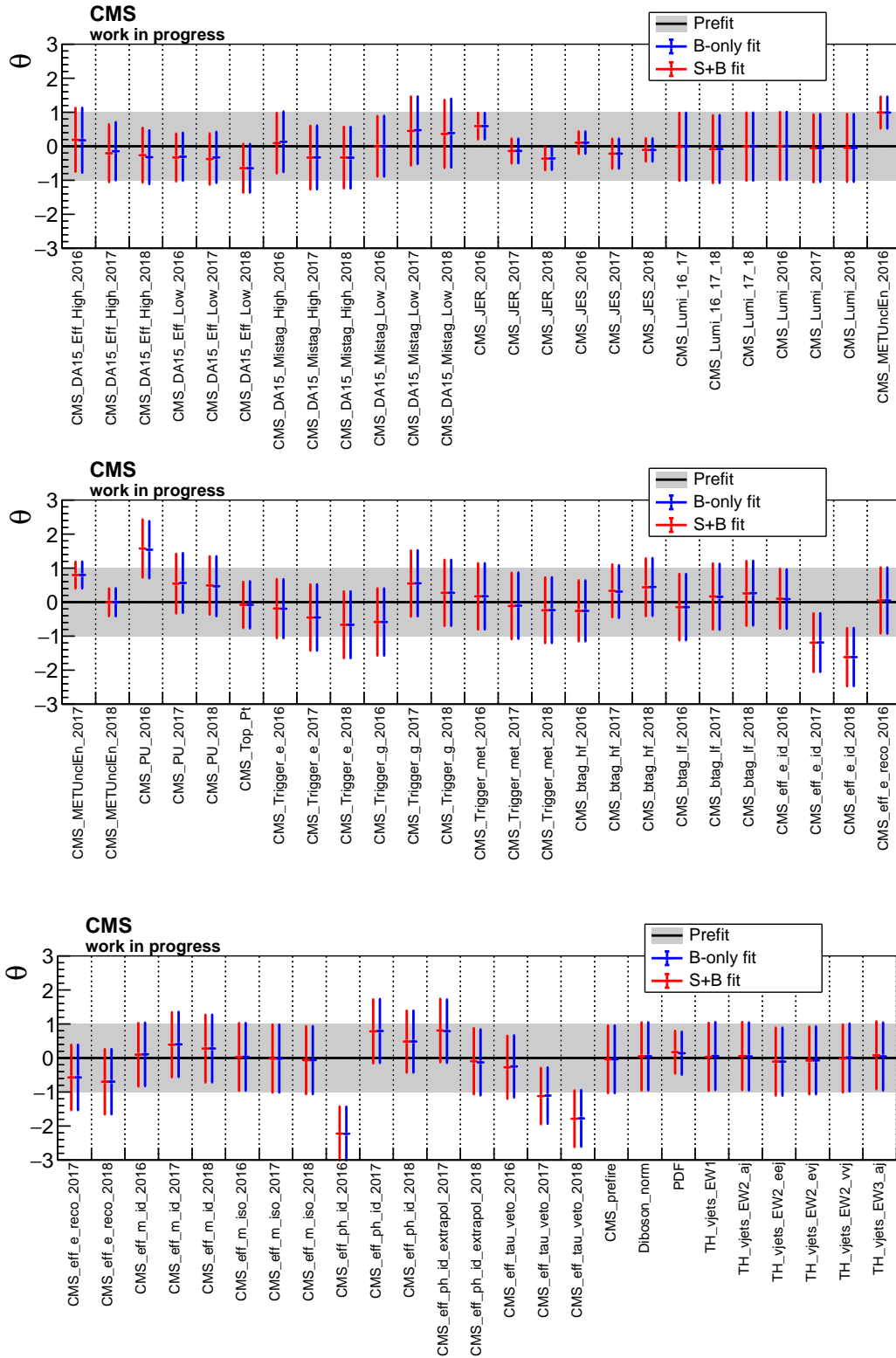
Figure D.62: Maximum likelihood estimators and their corresponding $\pm 1\sigma$ uncertainty of the nuisance parameters after the maximum likelihood fit of the background-only and signal-plus-background model to the data in all analysis regions. The points represent the value of the maximum likelihood estimators and the error bars their corresponding $\pm 1\sigma$ uncertainties. The different nuisance parameters can be identified with the corresponding systematic uncertainties by using the labels given in Tab. 5.12, Tab. 5.13, and Tab. 5.14.
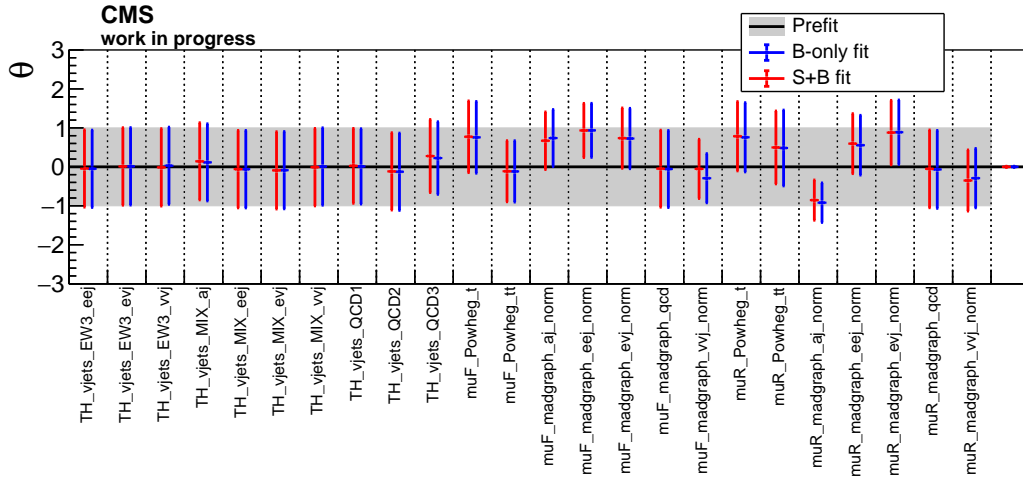
Figure D.63: Maximum likelihood estimators and their corresponding $\pm 1\sigma$ uncertainty of the nuisance parameters after the maximum likelihood fit of the background-only and signal-plus-background model to the data in all analysis regions. The points represent the value of the maximum likelihood estimators and the error bars their corresponding $\pm 1\sigma$ uncertainties. The different nuisance parameters can be identified with the corresponding systematic uncertainties by using the labels given in Tab. 5.12, Tab. 5.13, and Tab. 5.14.
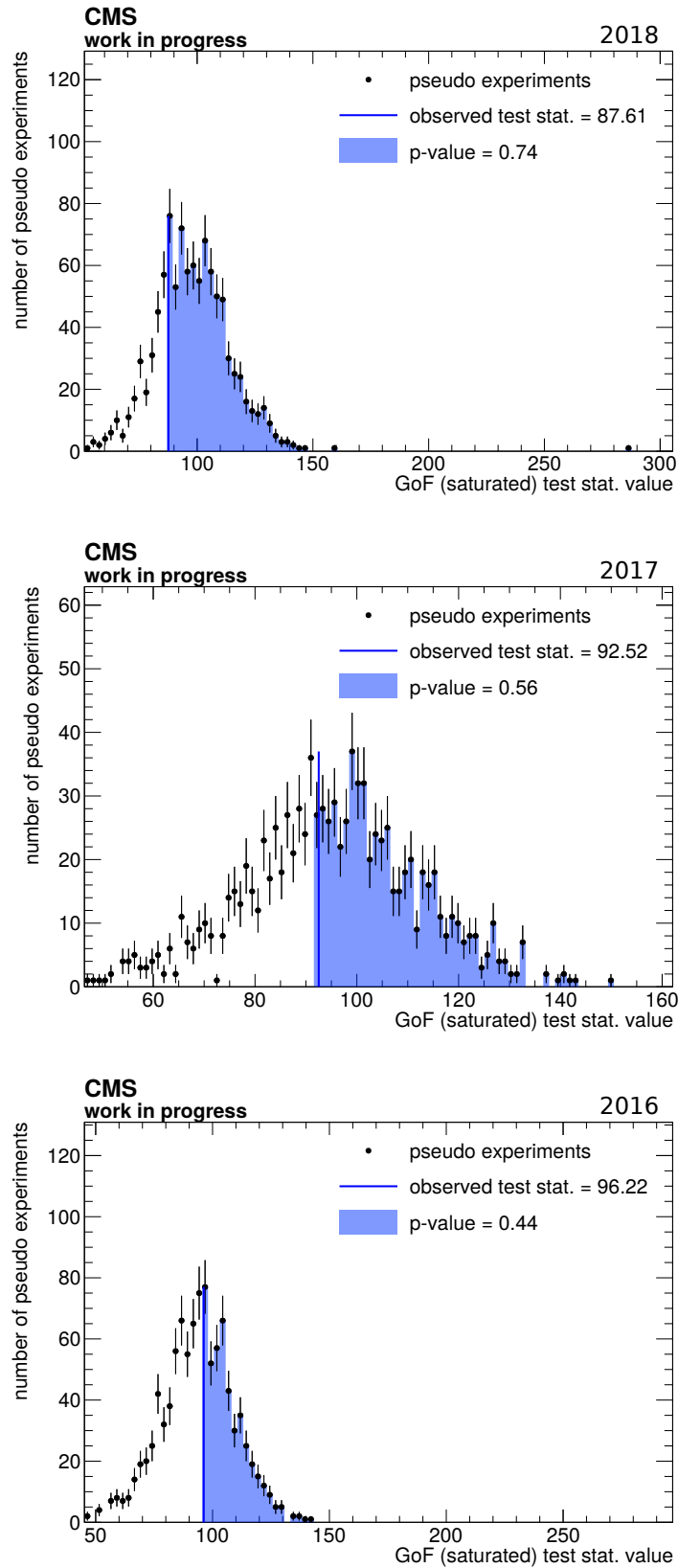
Figure D.64: Distributions of the test statistic of the saturated goodness-of-fit test for a-posteriori toy datasets sampled from the a-posteriori probability density function of the statistical model after a maximum likelihood fit to all analysis regions in the 2018 (top), 2017 (center), and 2016 (bottom) data era separately.
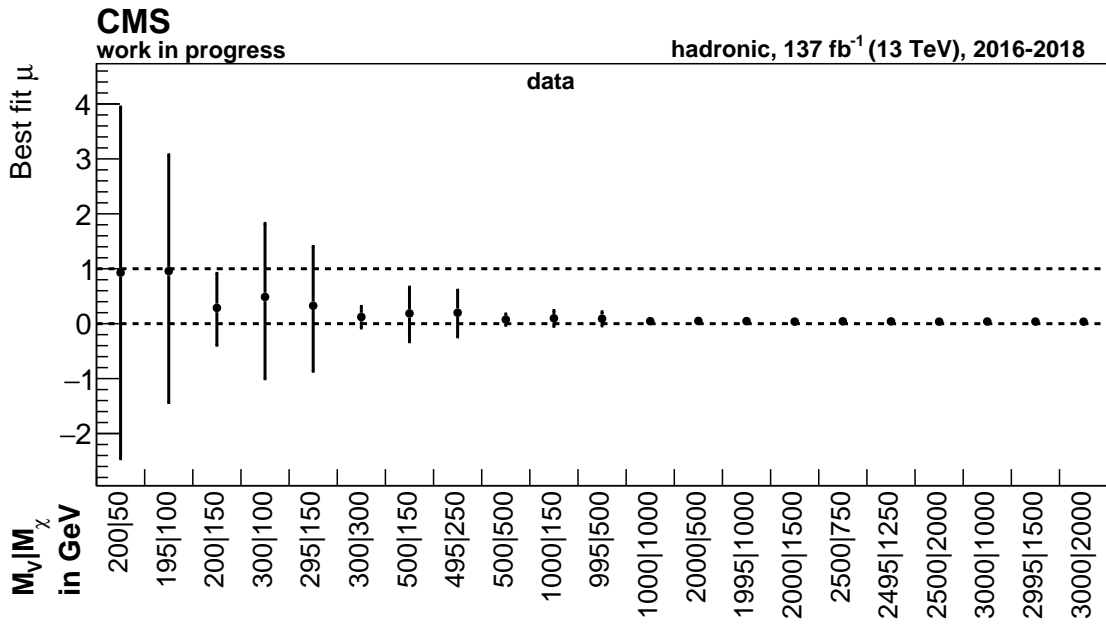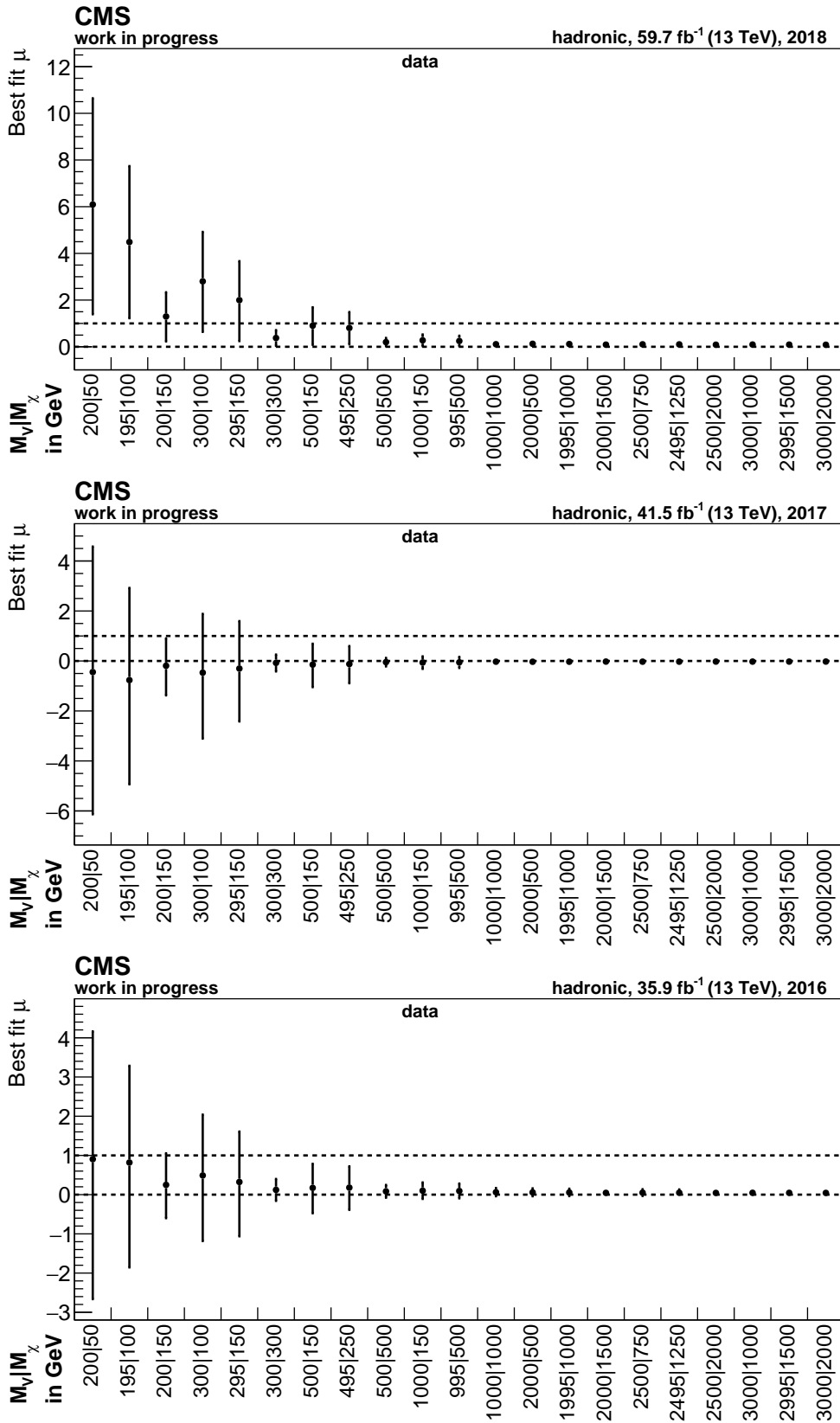
Figure D.65: Maximum likelihood estimators and their corresponding $\pm 1\sigma$ uncertainty of the signal strength modifier for different mono-top signals after a simultaneous maximum likelihood fit to data in all analysis regions of all data eras. The mono-top signals are scaled to a cross section of $0.1\,\mathrm{pb}$. The mass of the hypothetical vector mediator is represented by M_V and the mass of the DM candidates by M_χ.
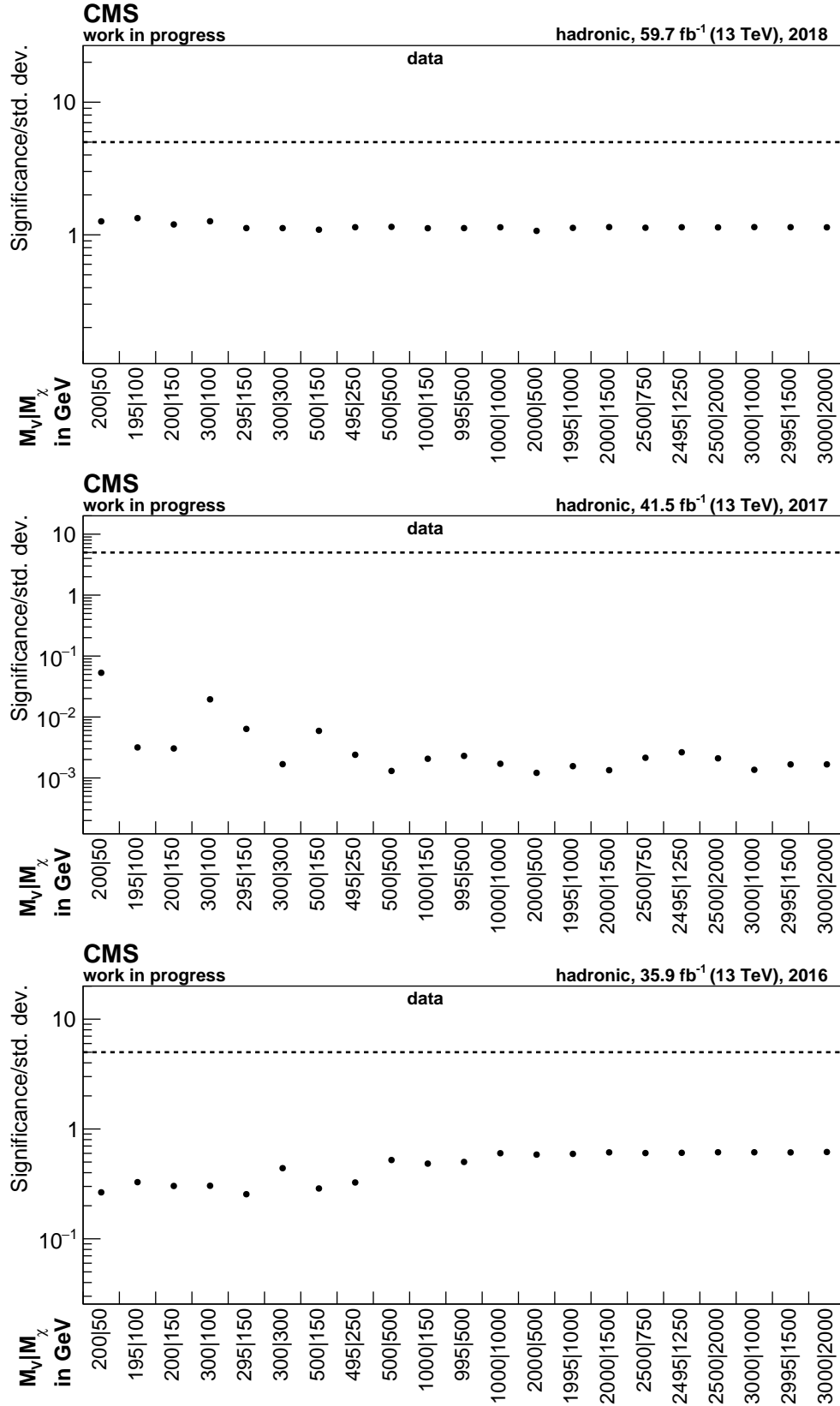
Figure D.66: Observed significances in units of the standard deviation of the standard normal distribution for different mono-top signals in the 2018 (top), 2017 (center), and 2016 (bottom) data era. The mass of the hypothetical vector mediator is represented by M_V and the mass of the DM candidates by M_χ. The 5σ discovery significance is represented by the dashed line.

Figure D.67: Maximum likelihood estimators and their corresponding $\pm 1\sigma$ uncertainty of the signal strength modifier for different mono-top signals after a maximum likelihood fit to data in all analysis regions in the 2018 (top), 2017 (center), and 2016 (bottom) data era. The mono-top signals are scaled to a cross section of 0.1 pb. The mass of the hypothetical vector mediator is represented by M_V and the mass of the DM candidates by M_χ.
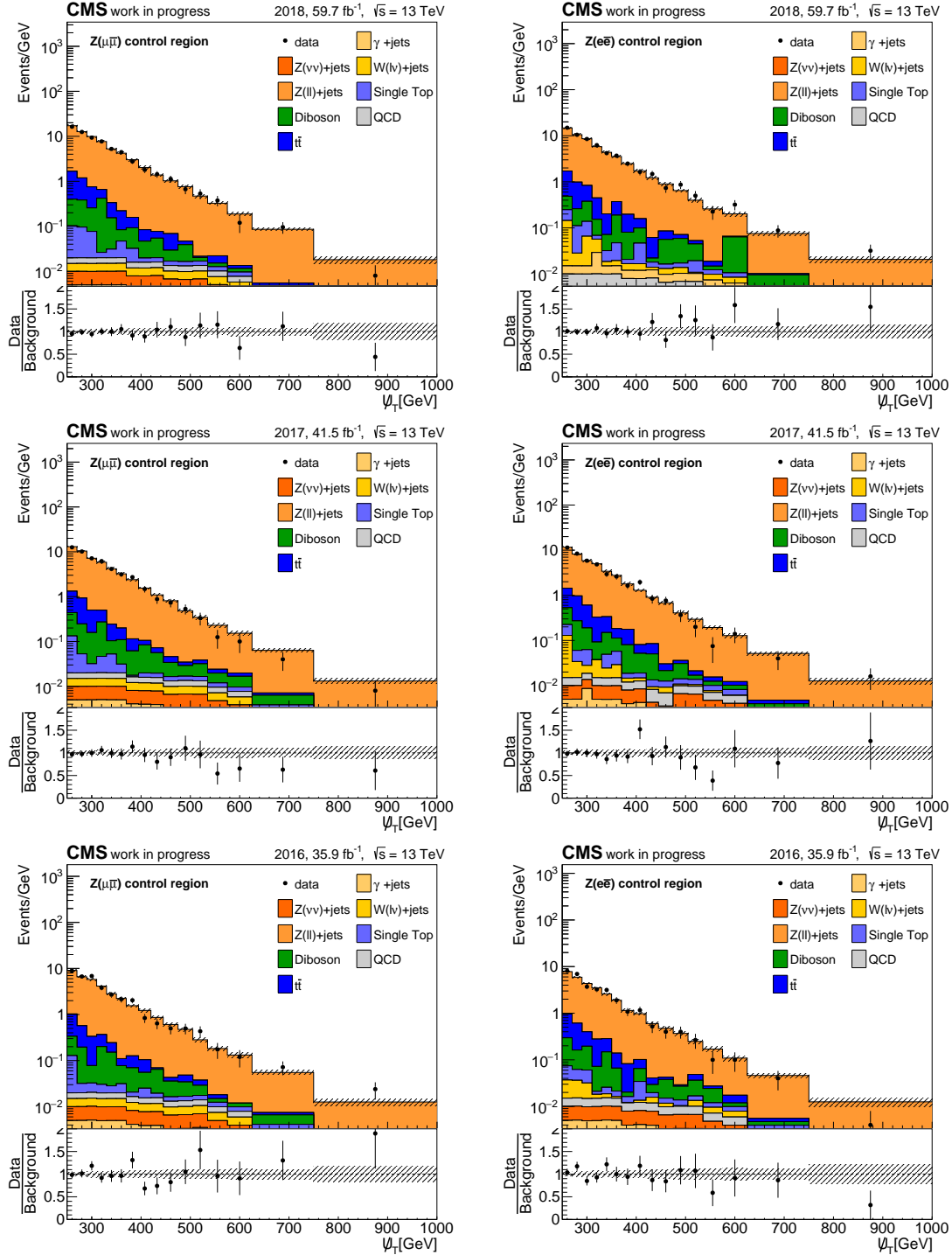
Figure D.68: A-posteriori distributions of the hadronic recoil in the Z boson control regions in the separate data eras. The hatched uncertainty band represents the total a-posteriori uncertainty of the background processes. The black error bars represent the inherent statistical uncertainty of the data.
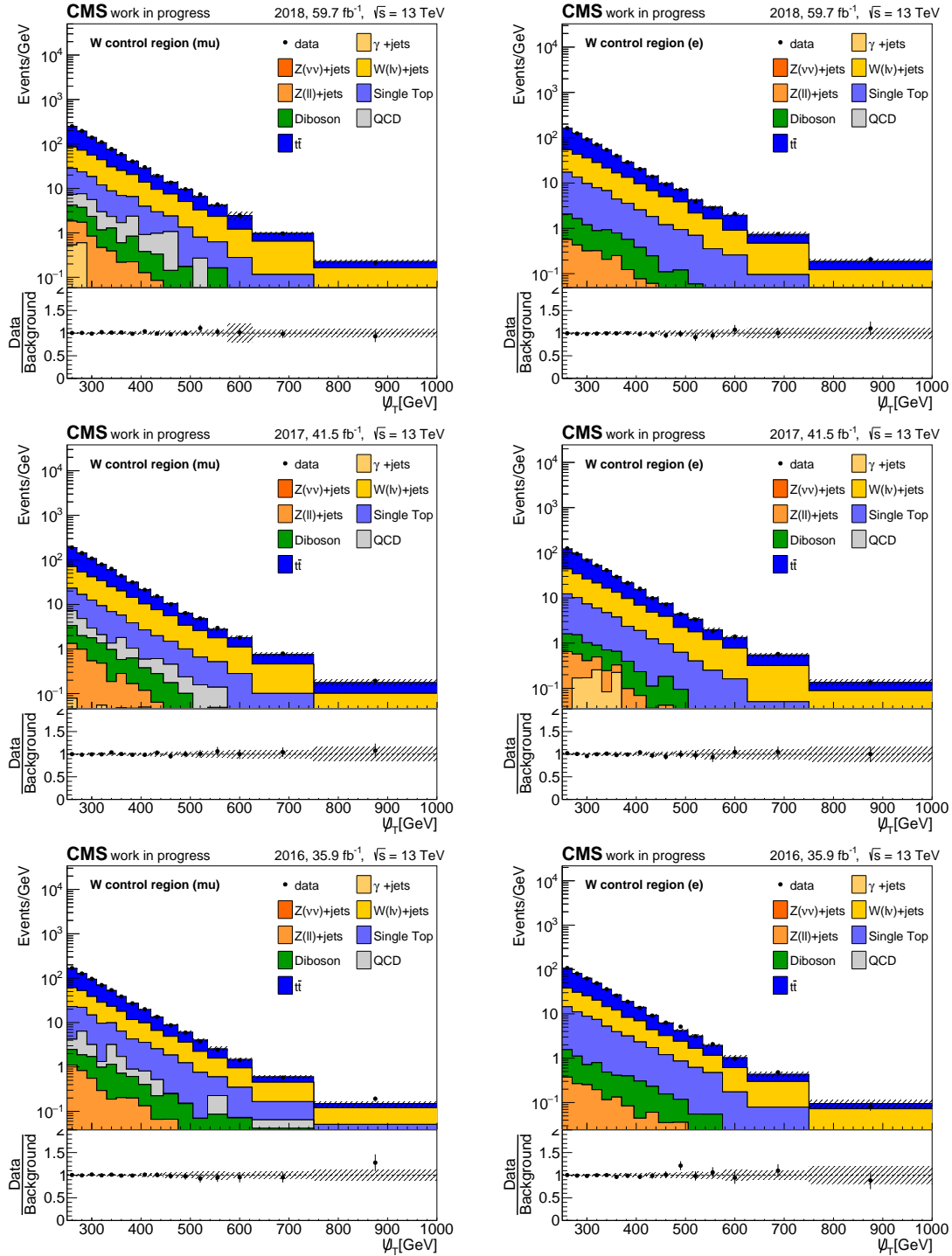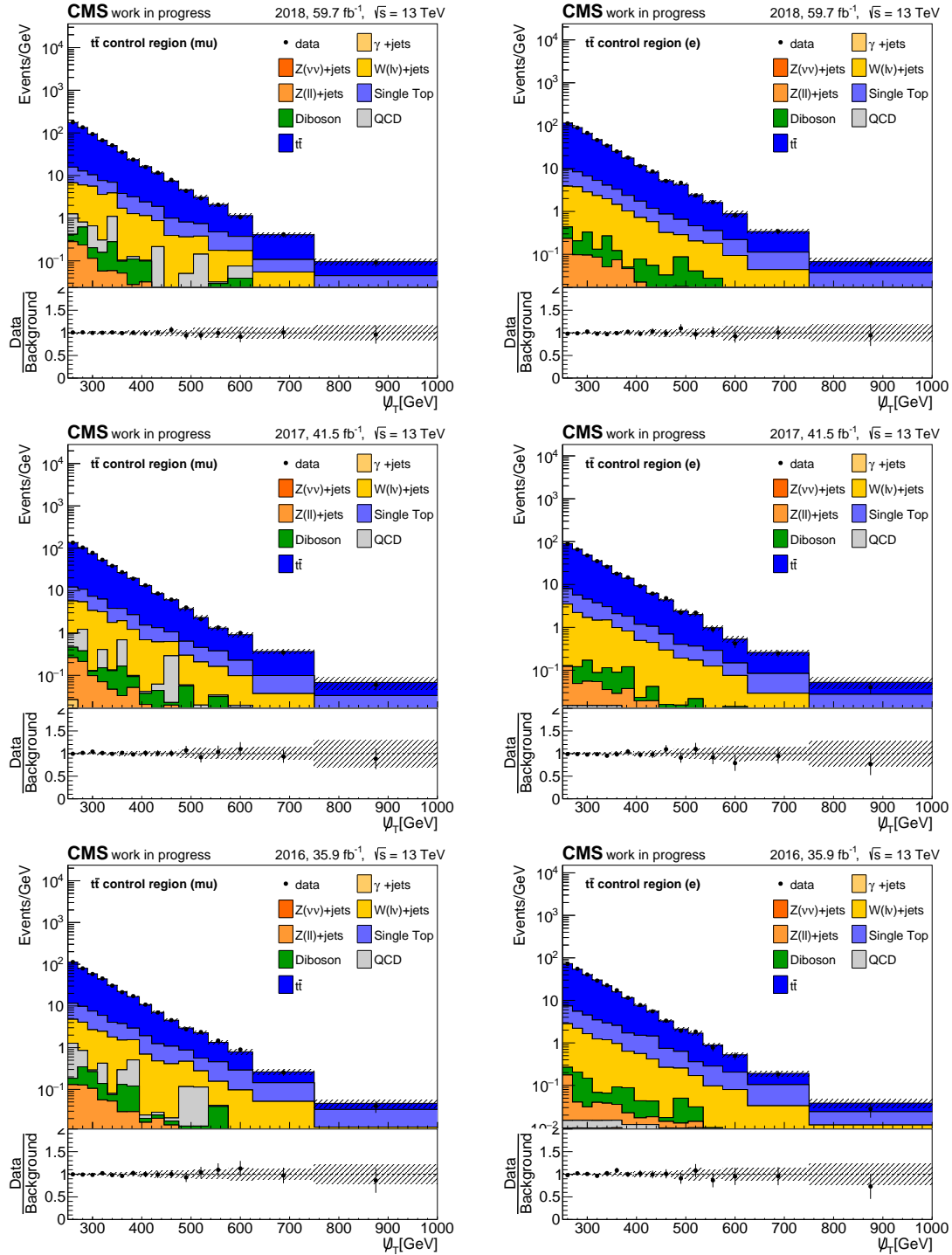
Figure D.69: A-posteriori distributions of the hadronic recoil in the W boson control regions in the separate data eras. The hatched uncertainty band represents the total a-posteriori uncertainty of the background processes. The black error bars represent the inherent statistical uncertainty of the data.

Figure D.70: A-posteriori distributions of the hadronic recoil in the $t\bar{t}$ control regions in the separate data eras. The hatched uncertainty band represents the total a-posteriori uncertainty of the background processes. The black error bars represent the inherent statistical uncertainty of the data.
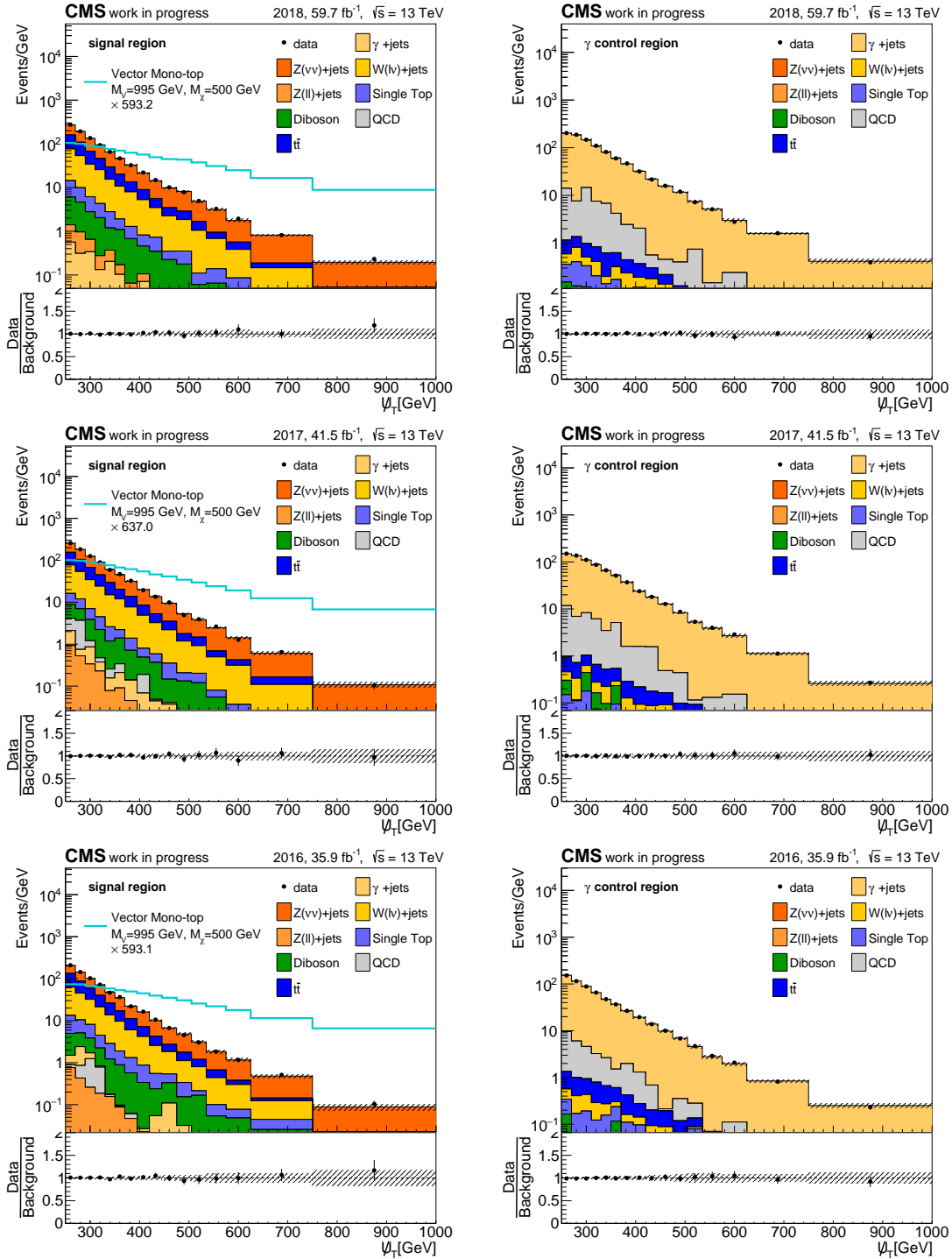
Figure D.71: A-posteriori distributions of the hadronic recoil in the signal regions as well as the photon control regions in the separate data eras. One mono-top signal sample, scaled to the total yield of all background processes, is overlaid. The corresponding scale factor is given in the legend. The hatched uncertainty band represents the total a-posteriori uncertainty of the background processes. The black error bars represent the inherent statistical uncertainty of the data.
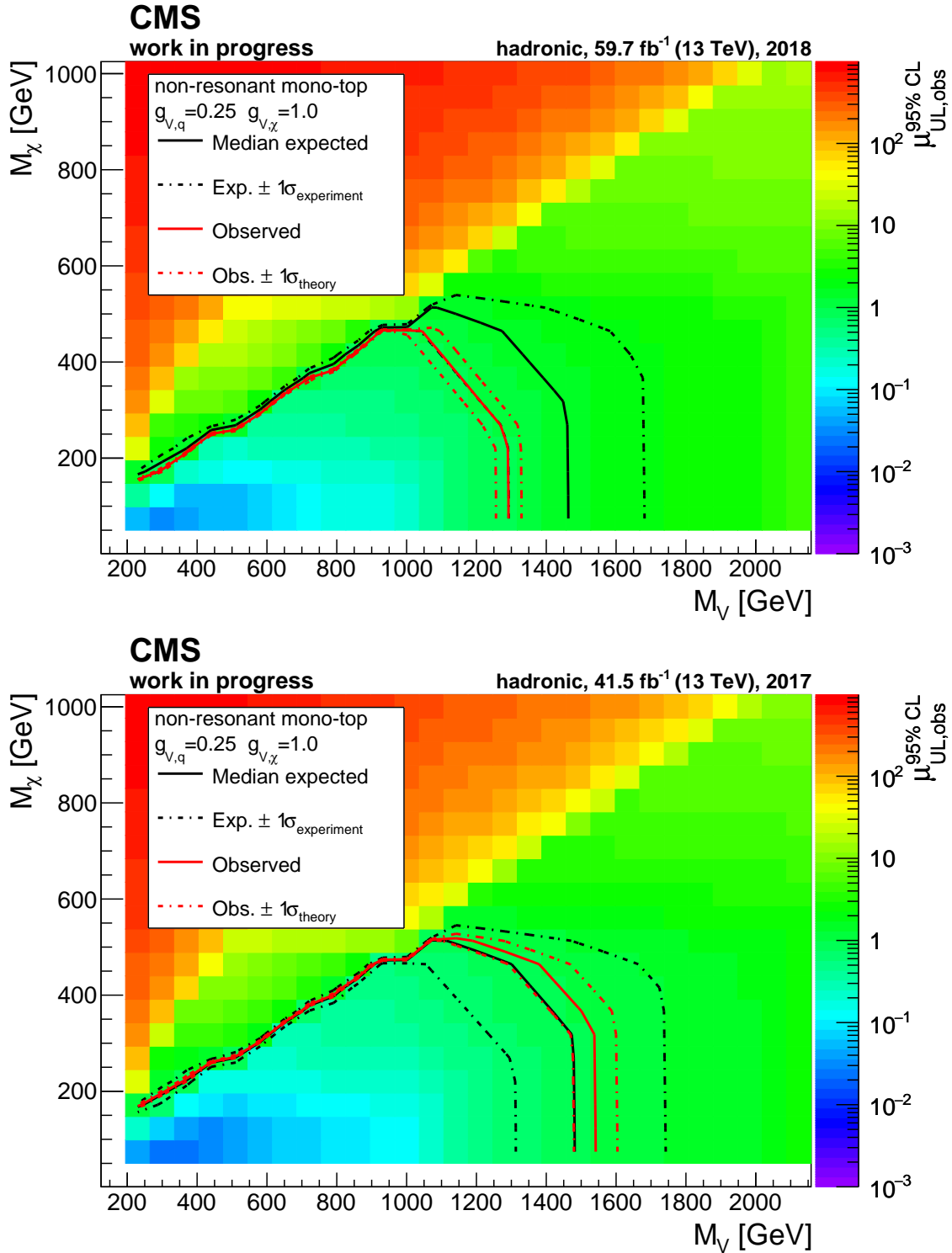
Figure D.72: Observed upper exclusion limits of the signal strength modifier at 95% confidence-level as a function of the mediator mass M_V and the DM candidate mass M_χ for the 2018 (top) and the 2017 (bottom) data era. The colored area represents the observed upper limits. The solid black and red line represent the contours for which the median expected upper limit and the observed upper limit is equal to unity, respectively. The dashed black lines represent the 68% confidence interval for the expected upper limit to be equal to unity considering all uncertainties relevant for the description of the background processes. The area within the red solid line is the observed exclusion area at 95% confidence-level. The dashed red lines show the observed exclusion areas assuming a change of the mono-top cross section by $\pm 1\sigma$.
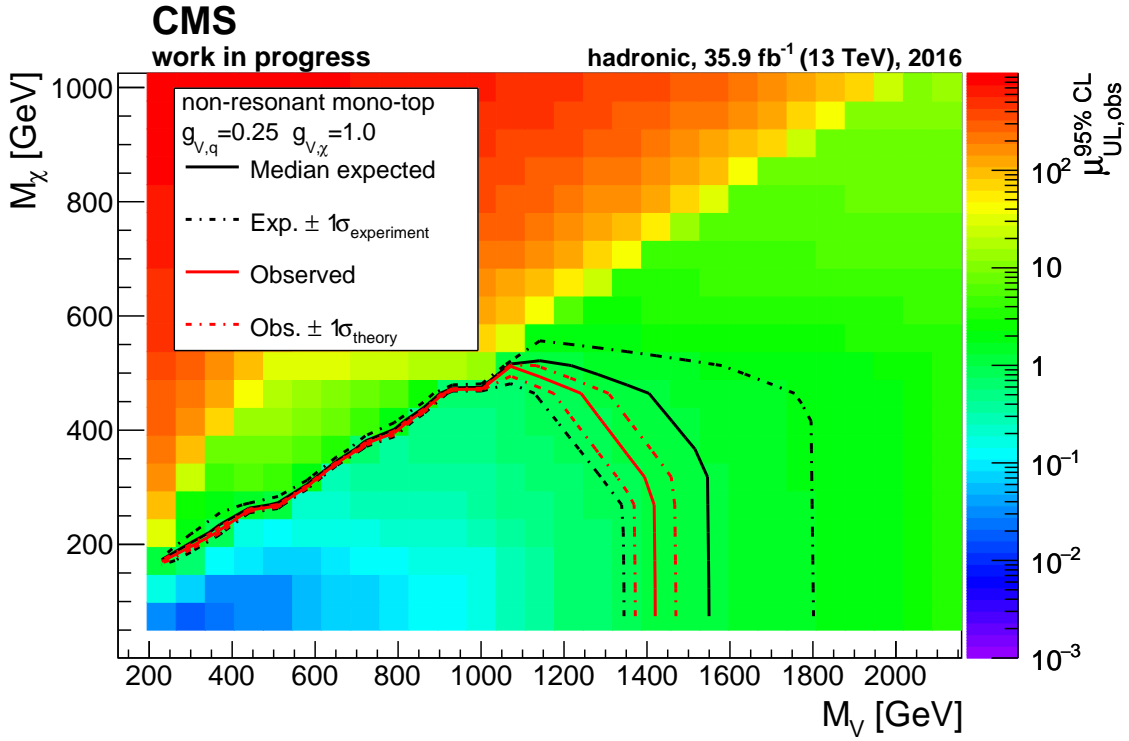
Figure D.73: Observed upper exclusion limits of the signal strength modifier at 95% confidence-level as a function of the mediator mass M_V and the DM candidate mass M_χ for the 2016 data era. The colored area represents the observed upper limits. The solid black and red line represent the contours for which the median expected upper limit and the observed upper limit is equal to unity, respectively. The dashed black lines represent the 68% confidence interval for the expected upper limit to be equal to unity considering all uncertainties relevant for the description of the background processes. The area within the red solid line is the observed exclusion area at 95% confidence-level. The dashed red lines show the observed exclusion areas assuming a change of the mono-top cross section by $\pm 1\sigma$.

E Preliminary studies for the leptonic mono-top analysis

E.1 Analysis strategy

In the leptonic mono-top analysis, the leptonic top quark decay is exploited. Because there is an additional neutrino present in these events, the $\vec{E}_T$ is determined by the two DM candidates and the neutrino. Since the top quark mostly recoils against the mediator, this implies that the neutrino is also approximately recoiling against the two DM candidates. Because of this, the overall $\vec{E}_T$ in the event is decreased for the same transverse momentum of the mediator compared to the hadronic mono-top analysis. Therefore, the threshold of $\not{E}_T$ is set lower than in the hadronic channel. Furthermore, the final state consists of a charged lepton and a jet originating from a bottom quark. Both of these objects are clear signatures and can be used to build the signal region in the leptonic mono-top analysis. Similar to the hadronic mono-top analysis, in the leptonic mono-top analysis several SM processes feature the same final state signature as the signal process.

First, the production of events containing a W boson and additional jets with the decay $W \rightarrow l\nu$ results in a charged lepton with $\vec{E}_T$ as well. Then, either a jet originating from a light flavor quark or gluon can be misidentified as a jet originating from a bottom quark or bottom quarks can be created by QCD activity. Although the discriminant to distinguish jets originating from bottom quarks is used at a working point of 1% mistagging probability, the large cross section of $W + jets$ results in a significant contribution of this process in the signal region.

Second, the production of top-quark-antiquark-pair events is another important SM background. Due to the involved bottom quarks, the b-tagging requirement is fulfilled as well as the presence of a charged lepton due to leptonic top quark decays. Also, as was already explained, the cross section of approximately 832 pb (see Tab. 5.1) is high compared to the signal cross section. Therefore, the production of top-quark-antiquark pair events is expected to be a major background as well.

Although the missing transverse momentum is a possible option to use for the search in the leptonic analysis channel, another quantity called the transverse mass m_T, see the review article *Kinematics* in [2], is exploited. It is calculated from the transverse momentum of the charged lepton $p_{T,l}$ and the missing transverse momentum $\vec{E}_T$:

$$m_T = \sqrt{2p_{T,l}\vec{E}_T(1 - \cos\Delta\phi(l, \vec{E}_T))} \tag{6.1}$$

This quantity has a distinct signature for processes involving a W boson with $W \rightarrow l\bar{\nu}$. The transverse mass of the system of charged lepton and $\vec{E}_T$ is smaller or equal to the mass of the W boson for on-shell decays. This can be understood by transforming to the reference frame in which the W boson is at rest. In this frame, the charged lepton and the neutrino are produced back-to-back. Therefore, their transverse momentum has to be equal in magnitude but opposite in direction ($\Delta\phi(l, \vec{E}_T) = \pi$). The magnitude, however, has a maximum value of $m_W/2$ because of energy conservation. In this case, $m_T = m_W$. The magnitude of the transverse momentum can also be smaller than $m_W/2$, which then corresponds to $m_T < m_W$. Finally, due to an enhancement of the p_T distribution for $p_T \rightarrow m_W/2$, also known as the Jacobian peak, a peak-like structure at the W boson mass with a large drop for $m_T > 80$ GeV is expected. Contributions of $W \rightarrow l\bar{\nu}$ processes beyond the W boson mass are only due to incorrect measurements of the transverse momentum of the charged lepton or neutrino as well as off-shell decays of the W boson.

On the contrary for leptonic mono-top events, large contributions are expected for m_T values larger than the W boson mass. This is due to the fact that for leptonic mono-top

events, the missing transverse momentum and the charged lepton do not both originate from the W boson resonance. The $\vec{E}_T$ in these events originates mainly from the two DM candidates, while only the charged lepton originates from the W boson. The differences between these distributions are studied in more detail in the next section on generator studies.

Using the transverse mass as the discriminant in the leptonic mono-top analysis, signal and control regions can be created to determine a possible signal contribution as well as the normalization of the main backgrounds, $W + $ jets and $t\bar{t}$ from data. To create these phase spaces, the number of jets identified to originate from bottom quarks can be used.

E.2 Generator studies

In the leptonic analysis channel, the transverse mass is considered as the discriminating observable used to distinguish the phase space of SM processes and possible leptonic mono-top signatures. Because of this, the transverse mass is studied for mono-top models in which the missing transverse momentum is generated by the neutrino and the two DM candidates and is compared to the transverse mass for generic SM W boson processes in which the missing transverse momentum is only generated by the neutrino originating from the W boson decay. In order to check this expectation, the same signal samples as in section 5.2 are used. The distribution of the transverse mass for SM W boson decays is presented in Fig. E.74.
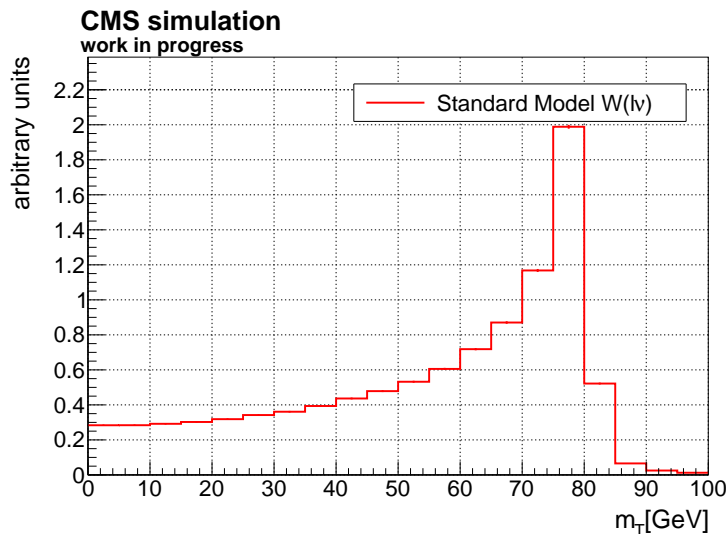

Figure E.74: Distribution of the transverse mass using the lepton and the neutrino from the W boson decay.

As expected, the transverse mass calculated using the charged lepton and the neutrino from the W boson increases over the range from $0\,\text{GeV}$ to the W boson mass of approximately $80\,\text{GeV}$ and then drops sharply. The contributions with a transverse mass larger than the W boson mass are due to events in which the W boson is produced off-shell.

On the contrary, the transverse mass calculated from the charged lepton and the missing transverse momentum originating from the neutrino and the two DM candidates in leptonic mono-top events shows a significantly different behavior, see Fig. E.75. Although all distributions still show a maximum at the W boson mass, the distributions do not drop sharply for larger transverse masses. Instead, all distributions show a much slower decrease

towards larger transverse masses. In addition, the larger the masses of the involved mediator, the more the transverse mass tends towards larger values.

These distributions motivate and confirm the usage of the transverse mass to search for mono-top signatures in the leptonic channel. For transverse masses higher than the W boson mass, SM contributions are strongly suppressed due to the fact that only off-shell W boson decays can produce transverse masses in this range or on reconstruction level also events in which the lepton or missing transverse momentum is measured incorrectly.
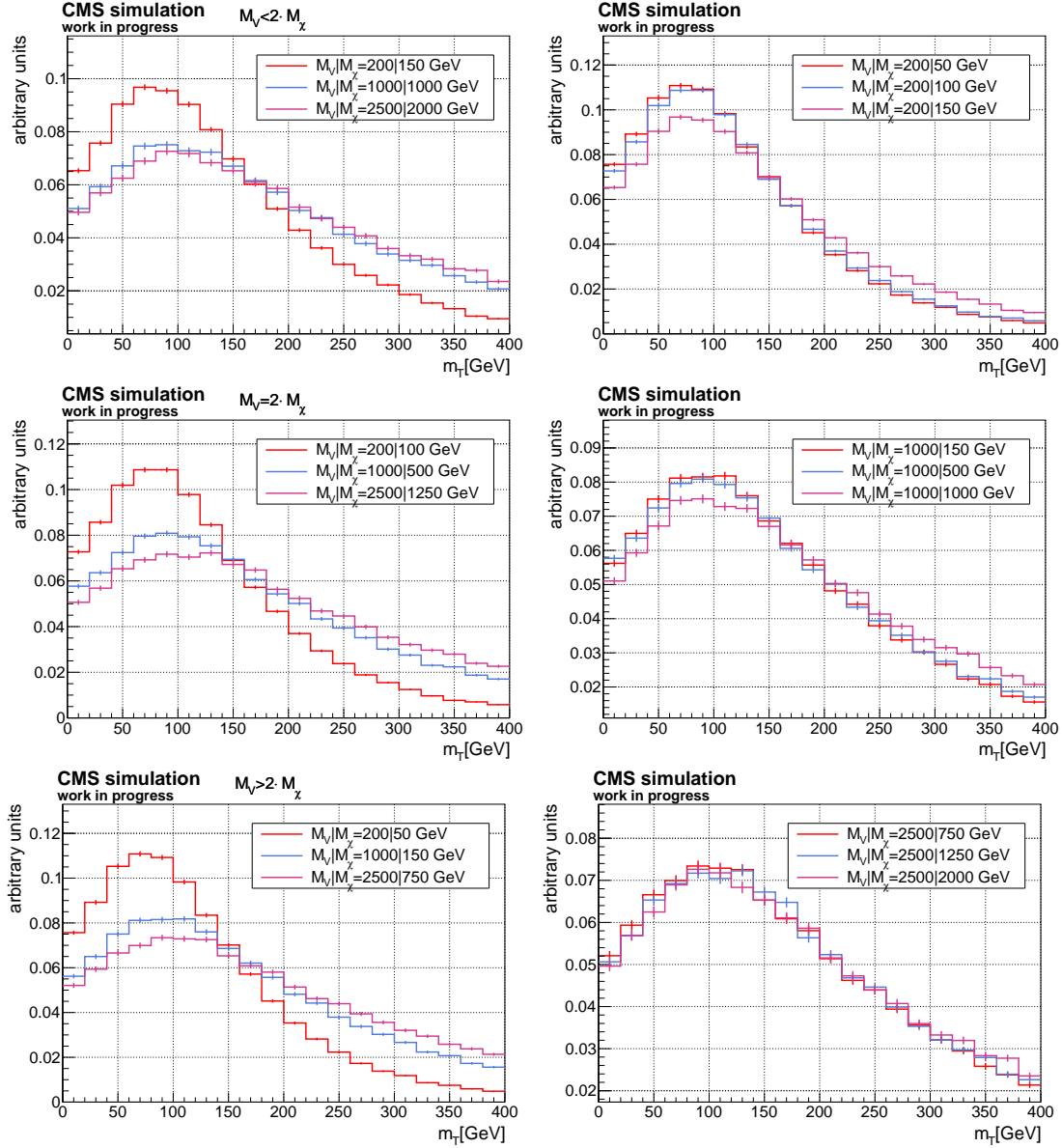

Figure E.75: Distribution of the transverse mass of the charged lepton and the missing transverse momentum in mono-top models with different mediator (V) and DM candidate (χ) masses, M_V and M_χ, respectively. In the left-hand column, the distributions are split according to the mass hierarchy of the mediator and the DM candidates. In the upper left-hand panel, the mediator mass is lower than two times the mass of the DM candidate. In the center left-hand panel, the mediator mass is two times the DM candidate mass. In the bottom left-hand panel, the mediator is heavier than two times the DM candidate mass. In the right-hand column, the distributions are split according to the mediator mass. All distributions are normalized to a yield of one event.

Danksagung

Die Anfertigung dieser Arbeit wäre ohne die Unterstützung durch andere Personen in dieser Form nicht möglich gewesen. Diesen Personen möchte ich mit den folgenden Worten meinen Dank aussprechen.

Als erstes gilt mein größter Dank meiner Familie, speziell meinen Eltern Carmen und Bruno Waßmer sowie meinem Bruder Tobias Waßmer. Ohne eure Unterstützung besonders in den letzten Monaten, wäre diese Arbeit nicht möglich gewesen. Weiterhin möchte ich euch dafür danken, dass ihr mir diesen Weg ermöglicht habt. Bedanken möchte ich mich auch bei meinen Freunden, welche mir ebenfalls immer unterstützend zur Seite standen.

Als nächstes gilt mein Dank Prof. Dr. Ulrich Husemann, welcher mich im Rahmen meiner Masterarbeit der Teilchenphysik näher brachte und schließlich mir die Promotion innerhalb seiner Arbeitsgruppe ermöglicht hat. Ebenso bedanke ich mich für die Möglichkeit an Konferenzen, Workshops sowie Sommerschulen teilnehmen zu durften. Zusätzlich möchte ich mich für die Unterstützung und Betreuung während der Promotion sowie beim Anfertigen der Dissertation bedanken.

Weiterhin bedanke ich mich bei Prof. Dr. Thomas Müller für die Übernahme des Korreferats und die damit einhergehende Unterstützung durch das Institut für Experimentelle Teilchenphysik. Zusätzlich bedanke ich mich für das Wecken meines Interesses für Teilchenphysik in der gleichnamigen Vorlesung während meines Masters.

Ich bedanke mich auch bei Dr. Matthias Schröder für die Betreuung während eines Großteils meiner Promotion und auch während meiner Masterarbeit.

Ein spezieller Dank richte ich an Philip Keicher, Sebastian Wieland, Jan van der Linden, Nikita Shadskiy, Dr. Karim El Morabit und Dr. Simon Kudella für die schöne Zeit innerhalb und außerhalb unserer Arbeitsgruppe.

Ein weiterer großer Dank geht an meine aktuellen und ehemaligen Kollegen sowie den Mitgliedern des Instituts für Experimentelle Teilchenphysik. Das ETP wird mir stets positiv in Erinnerung bleiben.

Zuletzt bedanke ich mich beim Graduiertenkolleg GRK 1694: Elementarteilchenphysik bei höchster Energie und höchs- ter Präzision sowie der Karlsruher Schule für Elementarteilchen- und Astroteilchenphysik: Wissenschaft und Technologie (KSETA) für zahlreiche Kurse und Kolloquien sowie für die finanzielle Unterstüzung für die Teilnahme an internationalen Veranstaltungen in der Teilchenphysik.